Special Issue Reprint

Feature Papers in Eng 2024

Volume II

Edited by
Antonio Gil Bravo

mdpi.com/journal/eng

MDPI

Feature Papers in Eng 2024—Volume II

Feature Papers in Eng 2024—Volume II

Guest Editor

Antonio Gil Bravo

Guest Editor
Antonio Gil Bravo
INAMAT2
Universidad Pública de
Navarra
Pamplona
Spain

This is a reprint of the Special Issue, published open access by the journal *Eng* (ISSN 2673-4117), freely accessible at: https://www.mdpi.com/journal/eng/special_issues/NL9E2PWG88.

For citation purposes, cite each article independently as indicated on the article page online and as indicated below:

Lastname, A.A.; Lastname, B.B. Article Title. *Journal Name* **Year**, *Volume Number*, Page Range.

Contents

Exploring the Frontier of 3D Bioprinting for Tendon Regeneration: A Review

Josée Rosset [1], Emmanuel Olaniyanu [1], Kevin Stein [1], Nátaly Domingues Almeida [2,3] and Rodrigo França [1,2,*]

[1] Department of Biomedical Engineering, Price Faculty of Engineering, University of Manitoba, Winnipeg, MB R3T 5V6, Canada
[2] Department of Restorative-Dentistry, College of Dentistry, University of Manitoba, Winnipeg, MB R3E 0W2, Canada
[3] Department of Diagnosis and Surgery, University of the State of São Paulo, São José dos Campos 12245-000, SP, Brazil
[*] Correspondence: rodrigo.franca@umanitoba.ca

Abstract: The technology of 3D bioprinting has sparked interest in improving tendon repair and regeneration, promoting quality of life. To perform this procedure, surgical intervention is often necessary to restore functional capacity. In this way, 3D bioprinting offers a scaffold design, producing tendons with precise microarchitectures, promoting the growth of new tissues. Furthermore, it may incorporate bioactive compounds that can further stimulate repair. This review elucidates how 3D bioprinting holds promise for tendon repair and regeneration, detailing the steps involved and the various approaches employed. They demonstrate future challenges and perspectives and provide valuable information on the concept, bioprinting design, and 3D bioprinting techniques for the repair of tendon injuries.

Keywords: tendon injuries; 3D bioprinting; review

1. Introduction

Tendons are an integral component of the musculoskeletal system, serving as a critical medium in the transmission of force from muscle to bone during joint movement and maintenance of posture. The structure of tendons can vary depending on their specific function but can be generally described as a collection of tightly packed, longitudinally arranged, collagen fibrils embedded within a highly hydrated matrix of proteoglycans and glycoproteins. The collagen fibrils are organized in hierarchical manner, first bundling as fibers, which further bundle as fascicles [1].

Each fascicle is wrapped in a connective tissue layer called the endotenon, which binds adjacent fascicles to form the full tendon unit, which is itself wrapped by the epitenon. These connective tissue sheaths provide structural integrity, facilitate the sliding of tendon fibres, and serve as vascular and neural conduits [2]. The primary cell population found in tendons are tenocytes, a class of specialized fibroblast cells which are responsible for the synthesis and turnover of the extracellular matrix [1].

At the termini of the tendon structure, specialized junctions can be found. The myotendinous junction (MTJ) represents the interface between the tendon and muscle. Here, the collagen fibres of the tendon interdigitate with the muscle's sarcolemma through finger-like projections, enhancing the interface surface area. At the other end of the tendon, there is the osteotendinous junction (OTJ), which connects the structure to bone. This insertion point forms a complex and specialized interface that can be either fibrous, where the tendon inserts directly into the bone, or the fibrocartilage. Both the MTJ and OTJ are biomechanically optimized to minimize stress concentration and facilitate efficient force transfer [1].

Due to their high mechanical strength, tendons exhibit viscoelastic characteristics. This means that their mechanical behaviour varies with the rate of strain applied. At lower strain rates, tendons become more deformable, allowing them to absorb more mechanical energy but also causing them to become less effective at bearing mechanical loads. Conversely, at higher strain rates, tendons stiffen, enhancing their ability to transmit substantial muscular loads to bones [3].

Additionally, tendons demonstrate a phenomenon known as "creep", where they elongate over time under a constant load, and "stress relaxation", where the stress within a tendon decreases under a constant strain [4]. Though most commonly occurring during sports participation, tendon ruptures can occur spontaneously during routine activities as well, usually as a consequence of underlying degenerative changes within the tendon matrix [5]. Although such severe acute tendon injuries have the potential for functional recovery, the affected tendon seldom returns to its original pre-injury state [6]. Chronic tendinopathies, on the other hand, are degenerative in nature and develop over an extended period as a result of prolonged overuse or repetitive mechanical stress.

Current treatment strategies for tendon injuries involve a combination of non-surgical and surgical approaches, each with its inherent limitations and challenges. Non-surgical treatment often serves as the first line of management, especially for less severe tendon injuries. For some tendinopathies, extracorporeal shock wave therapy (ESWT) or platelet-rich plasma (PRP) injections may also be used to help stimulate healing [7,8]. While non-surgical treatments can be effective for many patients, they may not always promote complete recovery, especially in chronic cases or with significant tendon damage.

In severe cases, such as significant tears or complete ruptures, surgical tendon repair is often necessary for re-establishing the structural integrity and functionality of the tendon. In cases where the tendon has been severely damaged, a graft may also be required to replace the injured tissue. However, despite advancements in surgical methods, patients often face a long and challenging recovery process. Furthermore, current surgical treatments are often unable to fully restore the tendon to its pre-injury state, leading to a higher risk of re-injury or chronic disability [8]. This gap in treatment efficacy highlights the need for innovative solutions that can more closely mimic the natural architecture and function of healthy tendons.

Emerging techniques, using tissue engineering, offer promising avenues for enhancing tendon repair and regeneration. Among these, tendon-specific stem/progenitor cell (TSPC) therapy and 3D scaffolding stand out for their innovative approaches to facilitate the natural healing process. This method leverages the inherent ability of TSPCs to differentiate into tendon cells, and other supporting cells, to promote the regeneration of damaged tendon structures [9]. Advances in 3D scaffolding techniques, such as electrospinning and soft lithography, have opened new avenues for creating tendon scaffolds with precise microarchitectures [8].

3D printing offers unparalleled control over scaffold design, enabling the fabrication of structures that precisely match the patient's anatomy and injury specifics [10]. This personalized approach not only supports the integration and growth of new tissue but also opens the door to incorporating bioactive compounds that can further stimulate healing. The versatility and precision of 3D printing hold significant promise for overcoming the limitations of current tendon repair methods, marking a new frontier in the field of regenerative medicine.

In this review, we elucidate the main advances, challenges, and future directions in tendon repair. Furthermore, several bioprinting techniques that can be used have been described. Therefore, this review aims to address the concept of 3D bioprinting, bioprinting design, and techniques for tendon injury repair.

2. 3D Printing

The additive manufacturing technique of 3D bioprinting is based on depositing biomaterials, or bioink, on a microscale to create structures that can imitate natural tissues. As

opposed to traditional printing of tissue engineering scaffolds, bioprinting involves live cells mixed with biomaterials being directly deposed. In cell-free printing, the cells are seeded onto the scaffold afterwards [11]. The bioprinting process begins with a digital design of the desired structure, which is then divided into thin layers for printing. It typically involves an extruder being controlled by a three-axis mechanical platform. The movement of the platform is determined by coordinates related to the digital design. Many of the steps remain the same as conventional 3D printing, with different methods for bioprinting including extrusion-based, inkjet, and light-based techniques [12].

2.1. Inkjet Bioprinting

Inkjet bioprinting is a technique that involves the precise ejection of small droplets of bioink, which is a mixture of cells and hydrogel, stored in an ink cartridge. The print head, controlled by a mechanical lifting platform, releases these droplets through electrostatic or piezoelectric stimulation. This method allows for high-resolution printing and maintains high cell viability, making it particularly valuable in academic research. While not as widely commercialized as other bioprinting techniques, inkjet bioprinting is favoured in research settings due to its ability to produce detailed and accurate tissue constructs. The high resolution of this technique enables the creation of complex tissue structures with precise cell placement, which is critical for replicating the intricate architecture of natural tissues. Inkjet bioprinting also allows for the simultaneous deposition of multiple cell types and biomaterials, facilitating the creation of heterogeneous tissue constructs that better mimic the natural cellular environment. This capability is essential for developing functional tissues that can integrate seamlessly with the patient's existing biological structures. Despite its advantages, inkjet bioprinting faces challenges such as the need for bioinks with suitable viscosity and the potential for nozzle clogging. However, ongoing research and technological advancements continue to address these issues, further enhancing the feasibility and effectiveness of inkjet bioprinting for tissue engineering applications [13]. While not as widely commercialized, inkjet bioprinting is prevalent in academic research due to its high resolution and cell viability [14].

2.2. Extrusion-Based Bioprinting

Extrusion-based bioprinting is a widely used technique in tissue engineering, particularly for tendon regeneration, due to its ability to print continuous filaments of bioink. This method involves the deposition of bioink through a nozzle, using either pneumatic, mechanical, or solenoid forces to extrude the material layer by layer onto a substrate. The bioink typically consists of a mixture of cells and biocompatible hydrogels that provide the necessary support for cell growth and differentiation. One of the significant advantages of extrusion-based bioprinting is its versatility in handling a wide range of bioink viscosities, allowing for the use of more complex and mechanically robust materials. This is particularly beneficial for tendon regeneration, where the printed constructs need to mimic the high tensile strength and elasticity of natural tendons.

The technique also allows for the incorporation of gradient materials and the creation of anisotropic structures, which are essential for replicating the hierarchical organization of tendon tissues. By adjusting the printing parameters, such as nozzle diameter, extrusion speed, and layer thickness, researchers can fine-tune the mechanical properties and microarchitecture of the printed tendons to closely match those of native tissues [13]. However, extrusion-based bioprinting faces challenges, including maintaining cell viability during the extrusion process and ensuring uniform cell distribution within the printed construct. High shear forces during extrusion can lead to cell damage, while uneven cell distribution can affect the overall functionality of the printed tendon. To mitigate these issues, advancements in nozzle design, bioink formulation, and printing protocols are being continually developed.

Despite these challenges, extrusion-based bioprinting remains a promising approach for tendon regeneration. Its ability to produce large-scale, mechanically stable constructs with precise control over the spatial distribution of cells and biomaterials makes it a

valuable tool in the field of regenerative medicine. Ongoing research and technological innovations are expected to further enhance the capabilities of extrusion-based bioprinting, paving the way for more effective and reliable tendon repair solutions [14]. This method is compatible with a variety of hydrogels and supports high cell densities, making it suitable for musculoskeletal tissue engineering [15].

2.3. Stereolithography

Stereolithography (SLA) is a sophisticated bioprinting technique that utilizes light to cure liquid photopolymer resins into solid structures with high precision. This process involves the use of a laser or digital light projector to selectively polymerize the bioink layer by layer, creating highly detailed and complex tissue constructs. SLA is particularly advantageous for tendon regeneration due to its ability to produce constructs with fine resolution and intricate geometries.

One of the primary benefits of SLA is its exceptional accuracy and surface finish, which are crucial for replicating the detailed microarchitecture of tendon tissues. The high resolution of SLA enables the fabrication of constructs that closely mimic the natural extracellular matrix, providing an optimal environment for cell attachment, proliferation, and differentiation. This precision is essential for developing functional tendons that can effectively integrate with the surrounding tissues.

SLA also allows for the incorporation of various bioactive molecules and growth factors within the printed constructs, enhancing the regenerative potential of the engineered tendons. By embedding these bioactive compounds within the scaffold, SLA can promote cellular activities such as migration, proliferation, and matrix synthesis, which are vital for tendon healing and regeneration.

Despite its advantages, SLA faces several challenges in tendon bioprinting. One of the main limitations is the need for photopolymerizable bioinks that are both biocompatible and capable of supporting cell viability. The exposure to light and the photoinitiators used in the process can potentially affect cell health and functionality. Additionally, the mechanical properties of the printed constructs must be optimized to match those of native tendons, which requires the careful selection and formulation of the bioinks.

To address these challenges, ongoing research is focused on developing new photopolymerizable bioinks that are tailored for tendon regeneration. Innovations in bioink composition, such as the incorporation of natural polymers and hybrid materials, are being explored to enhance the biocompatibility and mechanical strength of the printed constructs. Furthermore, advancements in SLA technology, including multi-material printing and dynamic light projection, are expanding the capabilities of this technique for more complex and functional tendon tissue engineering.

In summary, stereolithography holds significant promise for the bioprinting of tendons, offering unparalleled precision and the ability to create highly detailed and functional tissue constructs. Continued research and technological developments are expected to overcome current limitations, paving the way for more effective and reliable tendon repair and regeneration strategies [12].

2.4. Laser-Assisted Bioprinting

Laser-assisted bioprinting (LAB) is a cutting-edge technique that leverages laser energy to precisely deposit bioink onto a substrate. This method involves the use of a focused laser beam to generate high-pressure bubbles that propel droplets of bioink from a donor slide to the target area. LAB offers several advantages for tendon regeneration, including high resolution, precise cell placement, and minimal shear stress, which collectively enhance cell viability and functionality.

One of the standout features of LAB is its ability to achieve high spatial resolution, enabling the creation of intricate and finely detailed tendon constructs. This precision is vital for replicating the complex hierarchical structure of tendons, which includes aligned collagen fibres and specialized cellular arrangements. By accurately positioning cells and

biomaterials, LAB can produce constructs that closely mimic the native tendon architecture, promoting effective integration and function. LAB also supports the use of a wide range of bioinks, including those with varying viscosities and compositions. This flexibility allows researchers to incorporate different cell types, growth factors, and extracellular matrix components into the printed constructs, enhancing their biological and mechanical properties. Such versatility is particularly beneficial for tendon regeneration, where the engineered tissues must withstand significant mechanical loads while supporting cellular activities essential for healing [16].

Despite its advantages, LAB faces several challenges in the context of tendon bioprinting. One of the primary concerns is the potential for laser-induced damage to cells and biomaterials. The high energy required for the printing process can generate localized heat, which may affect cell viability and the integrity of the bioink. To mitigate these effects, ongoing research is focused on optimizing laser parameters and developing more resilient bioinks that can withstand the laser-assisted printing process. Another challenge is the scalability of LAB for producing larger tissue constructs. While LAB excels in precision and detail, scaling up the process to create larger, clinically relevant tendon grafts remains a complex task. Efforts are being made to improve the throughput and efficiency of LAB, including the development of multi-laser systems and automated printing platforms [17].

2.5. Fused Deposition Modeling

Fused Deposition Modeling (FDM) is a widely utilized extrusion-based bioprinting technique that involves the layer-by-layer deposition of thermoplastic materials to create three-dimensional structures. In the context of tendon regeneration, FDM offers a robust and versatile approach to fabricating scaffolds that can support cell growth and tissue development. This method uses a heated nozzle to extrude bioink, typically composed of biodegradable polymers and cells, onto a build platform, where it solidifies to form the desired structure. One of the primary advantages of FDM is its ability to produce mechanically strong and stable scaffolds, which are essential for mimicking the load-bearing properties of natural tendons. The technique allows for precise control over the scaffold's architecture, including pore size, shape, and distribution, which are critical parameters for facilitating nutrient diffusion, waste removal, and cellular infiltration. By optimizing these parameters, FDM can create scaffolds that promote effective tissue integration and regeneration [10,17].

FDM is also highly adaptable, capable of processing a wide range of thermoplastic materials, including polylactic acid (PLA), polycaprolactone (PCL), and other biocompatible polymers. These materials can be tailored to achieve specific mechanical properties and degradation rates, ensuring that the scaffold provides adequate support during the initial stages of tendon healing and gradually degrades as the new tissue forms. Additionally, FDM can incorporate bioactive molecules and growth factors into the bioink, enhancing the scaffold's regenerative potential. However, FDM faces several challenges in tendon bioprinting. One significant limitation is the relatively high processing temperatures required to melt the thermoplastic materials, which can affect cell viability. To address this issue, researchers are exploring the use of temperature-sensitive bioinks and developing hybrid printing techniques that combine FDM with other bioprinting methods to preserve cell viability. Another challenge is achieving the fine resolution needed to replicate the intricate microarchitecture of tendons. Advances in nozzle design and printing technology are being pursued to enhance the precision and detail of FDM-printed constructs.

Despite these challenges, FDM remains a promising technique for tendon regeneration. Its ability to produce durable, customizable scaffolds with controlled architecture makes it a valuable tool in the field of tissue engineering. Ongoing research and technological innovations are expected to further improve the capabilities of FDM, enabling the creation of more effective and reliable tendon repair solutions [10].

3. Bioinks

Bioinks are a cornerstone in the field of bioprinting, providing the essential medium that supports cells during the printing process and ultimately forms the scaffold for tissue regeneration. For tendon bioprinting, the development of suitable bioinks is critical, as they must not only support cell viability and proliferation but also replicate the mechanical properties and biological functions of natural tendon tissue [18].

3.1. Composition and Properties

The ideal bioink for tendon bioprinting should exhibit several key properties. Biocompatibility is paramount to ensure that the bioink does not provoke an adverse immune response and supports cell adhesion, growth, and differentiation [17]. Additionally, the bioink must have appropriate rheological properties, such as viscosity and shear-thinning behaviour, to facilitate smooth extrusion and precise deposition during the printing process. Mechanical strength and elasticity are also crucial, as the bioink must withstand the mechanical demands of the tendon while maintaining its structural integrity.

3.2. Natural and Synthetic Polymers

Bioinks can be derived from both natural and synthetic polymers, each offering distinct advantages. Natural polymers, such as collagen, gelatin, and hyaluronic acid, are favoured for their inherent biocompatibility and their ability to promote cell–matrix interactions. These materials closely mimic the extracellular matrix (ECM) of native tissues, providing a familiar environment for cells. However, natural polymers often lack the mechanical strength required for tendon applications and may degrade too quickly.

Synthetic polymers, such as polycaprolactone (PCL), polylactic acid (PLA), and polyethylene glycol (PEG), offer greater control over mechanical properties and degradation rates. These materials can be engineered to provide the necessary support during the initial stages of tendon healing and gradually degrade as the new tissue forms. Combining natural and synthetic polymers in hybrid bioinks can leverage the strengths of both, creating a balanced environment that supports both mechanical integrity and biological functionality [19]. Table 1 displays the biomaterials currently in use for tendon bioprinting, highlighting their properties and applications.

3.3. Functionalization and Bioactive Additives

To enhance the regenerative potential of bioinks, they can be functionalized with bioactive molecules, such as growth factors, peptides, and cytokines. These additives can promote cellular activities essential for tendon healing, including migration, proliferation, and matrix synthesis. For instance, incorporating transforming growth factor-beta (TGF-β) or bone morphogenetic proteins (BMPs) into bioinks can stimulate tenogenic differentiation and improve the overall quality of the regenerated tissue [17–19].

3.4. Challenges and Future Directions of Bioinks

Despite significant advancements, several challenges remain in the development of bioinks for tendon regeneration. Achieving the optimal balance between printability, mechanical strength, and biological functionality is a complex task. Additionally, ensuring uniform cell distribution and maintaining cell viability during the printing process are critical considerations. To address these challenges, ongoing research is focused on developing novel bioink formulations and optimizing printing parameters.

Future directions in bioink development include the exploration of smart bioinks that can respond to environmental cues, such as temperature, pH, or mechanical stress, to enhance tissue regeneration. Advances in nanotechnology and biomaterials science are also expected to contribute to the creation of more sophisticated bioinks that can better replicate the dynamic and hierarchical nature of tendon tissues [10–29].

Table 1. Biomaterials and their properties and application in tendon bioprinting.

Biomaterial	Properties	Applications in Tendon Bioprinting
Collagen [26–28]	Natural polymer, high biocompatibility, promotes cell adhesion and proliferation	Mimics native extracellular matrix (ECM), supports cellular alignment and growth, used in scaffold fabrication
Polylactic Acid (PLA) [19]	Biodegradable, good mechanical strength, tunable degradation rate	Used in FDM printing, provides structural support, and can be combined with other materials for enhanced properties
Polycaprolactone (PCL) [25]	Biodegradable, flexible, slow degradation rate	Provides long-term mechanical support, used in combination with bioactive molecules for enhanced regeneration
Gelatin Methacrylate (GelMA) [10]	Photocrosslinkable, good cell compatibility, adjustable mechanical properties	Used in Digital Light Processing (DLP) printing, supports cell encapsulation and tissue formation, and can be modified for improved properties
Silk Fibroin [10]	High tensile strength, biocompatible, promotes cell attachment	Used for creating mechanically robust scaffolds, supports tendon-like mechanical properties and tissue regeneration
Alginate [11]	Biocompatible, easy to process, forms hydrogels upon crosslinking	Used as a bioink component, provides a hydrated environment for cells, often combined with other materials for improved stability
Hyaluronic Acid [11,19]	Natural polymer promotes cell migration and proliferation, and hydrophilic	Enhances scaffold hydration and cell migration, used in combination with other materials for improved mechanical properties
Decellularized Extracellular Matrix (dECM) [11]	Contains native ECM components, promotes cell attachment and differentiation	Used to create bioactive scaffolds that closely mimic the native tendon environment, support tissue-specific regeneration

4. Tendon 3D Bioprinting

4.1. Functional Properties of Healthy Tendons

While all tendons act as tensile support, also known as the positional role, some tendons can also perform the role of energy storage [21]. As a result, the functional properties of tendons can differ based on their classification, anatomical location, physical training, age, and other factors [22]. In general, the Young Modulus of healthy tendons can range from 800 to 1500 MPa. The stress at failure can range from 50 MPa to 200 MPa and the strain failure can range from 12 to 22% [21,23].

4.2. Functional Properties of 3D Bioprinting Tendons

To fully replace a healthy tendon, a 3D bio-printed tendon must exhibit similar mechanical strength. Most attempts at 3D bioprinting fall under two categories; organic and semi-synthetic [24]. The synthetic materials are used to support the mechanical strength of the tendon or serve as scaffolding for the cell structures. A general overview of 3D bioprinting is depicted in Figure 1. The process of 3D bioprinting begins with acquiring images of the organ or segment of interest through CT scan or MRI. These images are then used to create a segmented 3D model, which is converted into a suitable format. Following this, the appropriate bioprinter and bioink are selected for the construction of the 3D tissues. This process allows for the precise and customized fabrication of complex biological structures with potential applications in tissue engineering and regenerative medicine. Unfortunately, even in the best cases, neither organic nor semi-synthetic 3D bio-printed tendons exhibit similar mechanical characteristics to healthy tendons [25–27]. One study found that in optimal conditions, Electronically Aligned Collagen (ELAC), had a wet Young's modulus of 900 MPa, a wet ultimate stress of 105 MPa and a wet ultimate

strain of 10% [28]. Unfortunately, the ideal conditions of the ELAC are not biocompatible, making such a solution unviable as a tendon replacement. Due to this the current gold standard for tendon treatment are either tendon autografts or allografts.
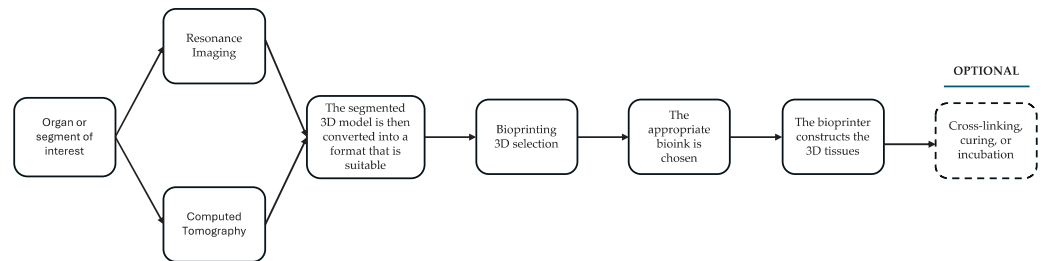
Figure 1. Bioprinting design process.

In recent years, tough and stretchable hydrogels (e.g., GelMA, Silk Fibroin) have garnered considerable interest for their potential applications in tendon repair, owing to their ability to withstand high mechanical loads and their flexibility, both of which are crucial characteristics of natural tendons [29]. These hydrogels are engineered to maintain their structural integrity under stress, providing a robust scaffold for cell attachment and growth. Koo et al. (2023) [30] made noteworthy contributions to this field by developing a novel hydrogel that combines toughness and stretchability, positioning it as an ideal candidate for tendon repair. Their research demonstrated the hydrogel's ability to endure repeated mechanical loading without significant degradation, closely mimicking the behaviour of natural tendons. The composition of the hydrogel included a combination of synthetic and natural polymers, striking a balance between mechanical strength and biocompatibility.

The key features of Koo et al.'s hydrogel include high tensile strength, crucial for supporting the mechanical loads experienced by tendons, as well as elasticity that allows the material to stretch and return to its original shape, akin to natural tendon tissue. Moreover, the hydrogel supports cell viability and proliferation, essential for tissue regeneration, and exhibits self-healing properties, which could be beneficial for repairing micro-damages occurring during normal tendon function [30].

Furthermore, other researchers [11–23,31,32] have also made significant progress in developing tough and stretchable hydrogels for tendon repair. These studies have focused on enhancing the mechanical properties and biological functionality of hydrogels through various approaches, such as composite hydrogels, double-network hydrogels, and bioactive hydrogels. Composite hydrogels involve combining natural and synthetic polymers to create materials with improved mechanical properties and biocompatibility, while double-network hydrogels consist of two interpenetrating polymer networks, one providing elasticity and the other offering toughness to achieve a balance between flexibility and strength. Additionally, bioactive hydrogels incorporate growth factors or peptides to promote cell differentiation, tissue regeneration, adhesion, and proliferation, facilitating better tissue integration.

In Table 2, each technique is paired with examples of how it has been applied in tendon repair, showcasing the practical use cases and the benefits they offer.

While these bioprinting techniques offer numerous advantages for tendon repair applications, they also face several limitations. Inkjet bioprinting, despite its high precision, often struggles with viscous bioinks and may cause cell damage due to shear stress during droplet formation [23]. Extrusion-based bioprinting, while versatile, can compromise cell viability due to the pressure required for extrusion and may have lower resolution compared to other methods [33]. Stereolithography (SLA) is limited by the availability of biocompatible, photocrosslinkable materials and potential cytotoxicity from residual photoinitiators [34]. Laser-assisted bioprinting (LAB), though highly precise, faces challenges in scaling up for larger constructs and can be prohibitively expensive [35]. Fused Deposition Modeling (FDM), while cost-effective, is primarily limited to thermoplastic materials and

often lacks the resolution needed for intricate cellular-level structures [36]. Additionally, all these techniques face common challenges in recreating the complex hierarchical structure and mechanical properties of native tendons, ensuring the long-term stability of the printed constructs in vivo, and achieving proper vascularization and innervation of the engineered tissue. Furthermore, the translation of these technologies from laboratory settings to clinical applications is hindered by regulatory hurdles, scalability issues, and the need for standardization in bioink formulations and printing protocols.

Table 2. Correlation between bioprinting techniques and biomaterials for tendon repair: applications and advantages.

Bioprinting Technique and References	Example of Application	Advantages
Inkjet Bioprinting [23]	Creating cell-laden constructs for tendon repair by precisely depositing droplets of bioink containing tendon-derived cells and growth factors.	High resolution and precision, ability to print multiple cell types and bioactive molecules simultaneously, relatively low cost, and rapid printing speed.
Extrusion-Based Bioprinting [33]	Fabricating PCL scaffolds that support tenocyte proliferation and alignment, enhancing tendon regeneration.	Ability to print a wide range of biomaterials, high mechanical strength of printed constructs, suitability for creating large and complex structures, incorporation of cells and growth factors within the bioink.
Stereolithography (SLA) [34]	Creating high-resolution GelMA-based scaffolds with intricate microarchitectures that mimic the native tendon structure, promoting cell viability and alignment.	High resolution and precision, ability to create complex and detailed structures, suitability for printing photocrosslinkable hydrogels.
Laser-Assisted Bioprinting (LAB) [35]	Depositing cells and biomaterials with high precision to create constructs that promote tendon regeneration, such as patterning tenocytes and ECM components.	High precision and resolution, ability to print cells and biomaterials without direct contact, minimal thermal damage to cells, creation of highly detailed and organized tissue constructs.
Fused Deposition Modeling (FDM) [36]	Fabricating PCL scaffolds that mimic the mechanical properties of native tendons, supporting cell attachment, proliferation, and alignment.	High mechanical strength and stability of printed constructs, ability to print a wide range of thermoplastic materials, suitability for creating large and complex structures, relatively cost-effective and widely accessible.

5. Challenges and Future Perspectives

Tendons are subject to tensile loads exerted by the body's muscles but require more recovery time. Thus, tendon injuries can occur even when the surrounding muscle suffers little to no injuries. Since the issue of tendinopathy is not limited to tendon damage, a more holistic approach must be taken to completely resolve the issue both in the short and long term. A multi-pronged strategy must be followed to stop the degeneration of the cells, promote proper function of the support cells, and stop inflammation of the cells in the area.

One of the challenges involves using a material that is strong enough to withstand the tensile loads that tendons are subject to, while also serving as a good environment for future cell development [28]. Most tendon material development focuses on creating collagen-based tissue mimics. While there have been some improvements in the strength of tissue mimics, the overarching results demonstrate that they are not strong enough to withstand the tensile loads that tendons are normally subject to [24,28]. It is probable that emerging technologies such as Digital Light Processing (DLP) and volume printing will bring gains in the field of bioprinting. DLP uses a digital light projector to cure photopolymer resins layer by layer, allowing for high-resolution and rapid fabrication of complex structures. Its precision and speed make it a promising technique for creating detailed tissue constructs. Volume printing, including techniques such as volumetric

bioprinting, enables the simultaneous solidification of entire 3D structures within a single step. This approach significantly reduces printing time and can produce highly complex geometries with excellent cell viability [13,31,32].

Another challenge has to do with the difficulty of replicating the organized matrix of the tendons. The extracellular matrix (ECM) of the tendon is one of the characteristics of healthy tendon tissue. It is primarily composed of collagen organized in a unique pattern, allowing the tendon to perform its function as medium of force transfer [21]. When tendinopathy occurs, the organized matrix changes, making the tendon tissue weaker and thicker.

Replacement tendon tissue must replicate both the tensile strength and the unique matrix of the tendon to restore the full function of the tendon. This replication of the ECM requires fine 3D bioprinting. Recent studies have shown that electrohydrodynamic jet 3D printing or E-jetting is capable of printing tendon scaffolding with enough precision to mimic the unique order of the ECM from fibre to fascicle level. Unfortunately, such collagen-based tissue biomimics are currently unable to match the tensile strength of healthy tendons [25]. The mechanical properties of tendons, such as tensile strength, elasticity, and viscoelasticity, are crucial for their function. Biomimetic scaffolds aim to replicate these properties to provide adequate support during the healing process and to withstand physiological loads. Materials such as polylactic acid (PLA), polycaprolactone (PCL), and other biocompatible polymers are often used in bioprinting due to their tunable mechanical properties. By adjusting the composition and structure of the bioink, researchers can create scaffolds with mechanical properties that match those of native tendons. Additionally, incorporating reinforcing elements like nanofibers or microfibers can enhance the scaffold's strength and durability. Also, successful tendon repair requires the scaffold to support cellular activities such as proliferation, differentiation, and ECM production. By mimicking the biochemical cues present in native tendons, biomimetic scaffolds can promote the recruitment and differentiation of tendon-derived stem cells or other progenitor cells. The use of growth factors like transforming growth factor-beta (TGF-β) and bone morphogenetic proteins (BMPs) can further stimulate tendon regeneration. Additionally, the scaffold should facilitate vascularization to ensure adequate nutrient and oxygen supply, which is essential for tissue survival and integration [25].

Restoring the tendon repair process is also an obstacle, as one of the important functions of the tendons is the ability to repair damage it sustains due to excessive loads. This repair process is part of the normal function of the tendon and if performed sparingly it can cause the tendon to strengthen [29]. However, when the tendons are exposed to an excessive load it can damage the tendon and change its response to future loads. Tendons that are tendinopathic are not only weak, they also are less able to repair future damage to the tendon. This starts a process of the tendon gradually losing tensile strength due to its inability to reinforce itself when exposed to a load. This makes the tendon predisposed to injury in the future. The most common cause of tendinopathy is the exposure of the tendon to high-volume repetitive loads [23]. To restore proper function of the tendon, the oxidative and apoptotic process must be stopped. This prevents the further deterioration of the tendon in the case that a 3D bio-printed tendon is grafted in.

6. Conclusions

While the main function of tendons is the transfer and/or storage of tensile force produced by muscles, the fulfillment of that function is dependent on many mechanical and biological properties of tendons. The goal of 3D bioprinting design is to fulfil both those requirements. While there are design options that maximize either the mechanical or biological requirements of a tendon there is often a trade-off to maximizing one or the other. Modern 3D bio-printed tendons currently are not significantly comparable to healthy tendons or even tendon autographs and allographs. Further research will need to be performed holistically to design a 3D bio-printed tendon that is both mechanically and biologically viable.

References

1. Thorpe, C.T.; Screen, H.R.C. Tendon Structure and Composition. In *Metabolic Influences on Risk for Tendon Disorders*; Ackermann, P.W., Hart, D.A., Eds.; Springer International Publishing: Cham, Switzerland, 2016; pp. 3–10.

2. Benjamin, M.; Kaiser, E.; Milz, S. Structure-function relationships in tendons: A review. *J. Anat.* **2008**, *212*, 211–228. [CrossRef] [PubMed]

3. Wang, J.H.-C.; Guo, Q.; Li, B. Tendon biomechanics and mechanobiology—A mini-review of basic concepts and recent advancements. *J. Hand Ther.* **2012**, *25*, 133–141. [CrossRef] [PubMed]

4. Nordin, M.; Frankel, V.H. Basic Biomechanics of the Musculoskeletal System, 4th ed.Lippincott Williams & Wilkins: Baltimore, MD, USA, 2012.

5. Resch, H.; Breitfuss, H. Spontaneous tendon ruptures. Etiology, pathogenesis and therapy. *Orthopade* **1995**, *24*, 209–219. [PubMed]

6. Snedeker, J.G.; Foolen, J. Tendon injury and repair—A perspective on the basic mechanisms of tendon disease and future clinical therapy. *Acta Biomater.* **2017**, *63*, 18–36. [CrossRef]

7. França, R.; Winkler, J.; Hsu, H.H.; Rahimnejad, M.; Abdali, Z. *Dental Biomaterials*; 3D Printing — Additive Manufacturing of Dental BiomaterialsWorld Scientific Series: From Biomaterials Towards Medical Devices; World Scientific: Singapore, 2018; pp. 421–462.

8. Bianchi, E.; Ruggeri, M.; Rossi, S.; Vigani, B.; Miele, D.; Bonferoni, M.C.; Sandri, G.; Ferrari, F. Innovative Strategies in Tendon Tissue Engineering. *Pharmaceutics* **2021**, *13*, 89. [CrossRef] [PubMed]

9. Wang, J.H.-C.; Nirmala, X. Application of Tendon Stem/Progenitor Cells and Platelet-Rich Plasma to Treat Tendon Injuries. *Oper. Tech. Orthop.* **2016**, *26*, 68–72. [CrossRef] [PubMed]

10. Alhaskawi, A.; Zhou, H.; Dong, Y.; Zou, X.; Ezzi, S.H.A.; Kota, V.G.; Abdulla, M.H.A.; Tu, T.; Alenikova, O.; Abdalbary, S.; et al. Advancements in 3D-printed artificial tendon. *J. Biomed. Mater. Res. Part B Appl. Biomater.* **2024**, *112*, e35364. [CrossRef]

11. Gao, Q.; Zhao, H.M.; Yang, F.F.; Fu, J.-Z.; He, Y. Practical Laboratory Methods for 3D Bioprinting. In *3D Bioprinting for Reconstructive Surgery*; Elsevier: Amsterdam, The Netherlands, 2018; pp. 7–32.

12. Derakhshanfar, S.; Mbeleck, R.; Xu, K.; Zhang, X.; Zhong, W.; Xing, M. 3D Bioprinting for Biomedical Devices and Tissue Engineering: A Review of Recent Trends and Advances. *Bioact. Mater.* **2018**, *3*, 144–156. [CrossRef]

13. Vanaei, S.; Parizi, M.S.; Vanaei, S.; Salemizadehparizi, F.; Vanaei, H.R. An Overview on Materials and Techniques in 3D Bioprinting Toward Biomedical Application. *Eng. Regen.* **2021**, *2*, 1–18. [CrossRef]

14. Rahimnejad, M.; Rezvaninejad, R.; Rezvaninejad, R.; França, R. Biomaterials in bone and mineralized tissue engineering using 3D printing and bioprinting technologies. *Biomed. Phys. Eng. Express* **2021**, *7*, 062001.

15. Murphy, S.V.; Atala, A. 3D bioprinting of tissues and organs. *Nat. Biotechnol.* **2014**, *32*, 773–785. [CrossRef] [PubMed]

16. Dou, C.; Perez, V.; Qu, J.; Tsin, A.; Xu, B.; Li, J. A State-of-the-Art Review of Laser-Assisted Bioprinting and Its Future Research Trends. *ChemBioEng Rev.* **2021**, *8*, 517–534. [CrossRef]

17. Sorkio, A.; Koch, L.; Koivusalo, L.; Deiwick, A.; Miettinen, S.; Chichkov, B.; Skottman, H. Human Stem Cell Based Corneal Tissue Mimicking Structures Using Laser-Assisted 3D Bioprinting and Functional Bioinks. *Biomaterials* **2018**, *171*, 57–71. [CrossRef] [PubMed]

18. Gungor-Ozkerim, P.S.; Inci, I.; Zhang, Y.S.; Khademhosseini, A.; Dokmeci, M.R. Bioinks for 3D Bioprinting: An Overview. *Biomater. Sci.* **2018**, *6*, 915–946. [CrossRef] [PubMed]

19. Benwood, C.; Chrenek, J.; Kirsch, R.L.; Masri, N.Z.; Richards, H.; Teetzen, K.; Willerth, S.M. Natural Biomaterials and Their Use as Bioinks for Printing Tissues. *Bioengineering* **2021**, *8*, 27. [CrossRef] [PubMed]

20. Papaioannou, T.G.; Manolesou, D.; Dimakakos, E.; Tsoucalas, G.; Vavuranakis, M.; Tousoulis, D. 3D Bioprinting Methods and Techniques: Applications on Artificial Blood Vessel Fabrication. *Acta Cardiol. Sin.* **2019**, *35*, 284–289. [CrossRef] [PubMed]

21. Screen, H.R.C.; Berk, D.E.; Kadler, K.E.; Ramirez, F.; Young, M.F. Tendon functional extracellular matrix. *J. Orthop. Res.* **2015**, *33*, 793–799. [CrossRef] [PubMed]

22. Maganaris, C.N.; Paul, J.P. In vivo human tendon mechanical properties. *J. Physiol.* **1999**, *521 Pt 1*, 307–313. [CrossRef] [PubMed]

23. Xu, Y.; Murrell, G.A.C. The basic science of tendinopathy. *Clin. Orthop. Relat. Res.* **2008**, *466*, 1528–1538. [CrossRef]

24. Potyondy, T.; Uquillas, J.A.; Tebon, P.J.; Byambaa, B.; Hasan, A.; Tavafoghi, M.; Mary, H.; Aninwene, G.E.; Pountos, I.; Khademhosseini, A.; et al. Recent advances in 3D bioprinting of musculoskeletal tissues. *Biofabrication* **2021**, *13*, 022001. [CrossRef]

25. Wu, Y.; Jyh, F.; YS, W.; Sun, J. Fabrication of 3D scaffolds via E-jet printing for tendon tissue repair. In Proceedings of the ASME 2015 International Manufacturing Science and Engineering Conference, Charlotte, NC, USA, 8–12 June 2015.

26. Mozdzen, L.C.; Rodgers, R.; Banks, J.M.; Bailey, R.C.; Harley, B.A. Increasing the strength and bioactivity of collagen scaffolds using customizable arrays of 3D-printed polymer fibers. *Acta Biomater.* **2016**, *33*, 25–33. [CrossRef] [PubMed]

27. Kishore, V.; Uquillas, J.A.; Dubikovsky, A.; Alshehabat, M.A.; Snyder, P.W.; Breur, G.J.; Akkus, O. In vivo response to electrochemically aligned collagen bioscaffolds. *J. Biomed. Mater. Res. Part B Appl. Biomater.* **2012**, *100*, 400–408. [CrossRef] [PubMed]

28. Uquillas, J.A.; Kishore, V.; Akkus, O. Genipin crosslinking elevates the strength of electrochemically aligned collagen to the level of tendons. *J. Mech. Behav. Biomed. Mater.* **2012**, *15*, 176–189. [CrossRef] [PubMed]

29. Viidik, A. The effect of training on the tensile strength of isolated rabbit tendons. *Scand. J. Plast. Reconstr. Surg.* **1967**, *1*, 141–147. [CrossRef] [PubMed]

30. Koo, B.-H.; Lee, Y.-J.; Park, N.R.; Heo, S.C.; Hudson, D.M.; Fernandes, A.A.; Friday, C.S.; Hast, M.W.; Corr, D.T.; Keene, D.R.; et al. Characterization of TGFβ1-induced tendon-like structure in the scaffold-free three-dimensional tendon cell culture system. *Sci. Rep.* **2024**, *14*, 9495. [CrossRef] [PubMed]

31. Skylar-Scott, M.A.; Uzel, S.G.M.; Nam, L.L.; Ahrens, J.H.; Truby, R.L.; Damaraju, S.; Lewis, J.A. Biomanufacturing of Organ-Specific Tissues with High Cellular Density and Embedded Vascular Channels. *Sci. Adv.* **2019**, *5*, 2459. [CrossRef] [PubMed]

32. Grigoryan, B.; Paulsen, S.J.; Corbett, D.C.; Sazer, D.W.; Fortin, C.L.; Zaita, A.J.; Greenfield, P.T.; Calafat, N.J.; Gounley, J.P.; Ta, A.H.; et al. Multivascular Networks and Functional Intravascular Topologies within Biocompatible Hydrogels. *Science* **2019**, *364*, 458–464. [CrossRef] [PubMed]

33. Liu, Y.; Lim, J.; Teoh, S.H. Review: Development of clinically relevant scaffolds for vascularised bone tissue engineering. *Biotechnol. Adv.* **2018**, *36*, 684–702.

34. Visser, J.; Peters, B.; Burger, T.J.; Boomstra, J.; Dhert, W.J.A.; Melchels, F.P.W.; Malda, J. Biofabrication of multi-material anatomically shaped tissue constructs. *Biofabrication* **2015**, *7*, 035009.

35. Koch, L.; Deiwick, A.; Schlie, S.; Michael, S.; Gruene, M.; Coger, V.; Zychlinski, D.; Schambach, A.; Reimers, K.; Vogt, P.M.; et al. Skin tissue generation by laser cell printing. *Biotechnol. Bioeng.* **2012**, *109*, 1855–1863. [CrossRef]

36. Costa, P.F.; Vaquette, C.; Zhang, Q.; Reis, R.L.; Ivanovski, S.; Hutmacher, D.W. Advanced tissue engineering scaffold design for regeneration of the complex hierarchical periodontal structure. *J. Clin. Periodontol.* **2013**, *41*, 283–294. [CrossRef] [PubMed]

Decarbonizing Nitrogen Fertilizer for Agriculture with Nonthermal Plasma Technology

Xiaofei Philip Ye

Department of Biosystems Engineering and Soil Science, The University of Tennessee, Knoxville, TN 37996, USA; xye2@utk.edu; Tel.: +1-(865)-974-7129

Abstract: Synthetic nitrogen fertilizer is the backbone of modern agriculture, helping to feed ~50% of the world's population. However, the current industrial production, distribution, and use of nitrogen fertilizers are built on an unsustainable foundation of fossil resources, and are energy-intensive, environmentally polluting, and inefficient in their usage. With the rapidly declining cost of renewable electricity, such as solar and wind, it is time to develop and implement the decentralized production and application of nitrogen fertilizer with nonthermal plasma technologies. Such locally sourced production at the farm site, using only air and water as feedstock, circumvents the need for the extensive capital investment and infrastructure required for synthetic nitrogen fertilizer production and storage, as well as the complex and costly distribution networks. It will be adaptive to the intermittency of the solar/wind electricity supply, leave no carbon footprint, and also have the advantage of being easily switched on/off, immediately responding to weather changes and local conditions, such as soil, climate, crops, and farming business models, for precision agriculture.

Keywords: decarbonization; nitrogen fertilizer; nonthermal plasma; Haber–Bosch process; nitrogen fixation; continuous process; ammonia; nitrate; sustainability

1. Background Information

1.1. Current Unsustainable System for Nitrogen Fertilizers

The availability of nitrogen fertilizers (N-fertilizers) is crucial for achieving an optimal agricultural yield, because nitrogen is the most common limiting nutrient for plants. Ammonia and nitric acid are the primary raw materials used to produce almost all nitrogen-based synthetic fertilizers, and their demand is closely tied to global population growth and food demand. However, unless environmentally friendly alternatives are adopted, current methods established on the foundation of the Haber–Bosch process (HB process) for producing ammonia and its derivatives could lead to carbon emissions of over 1300 million tons of CO_2 per year by 2050, and significantly impact the world's energy infrastructure [1].

Industrial nitrogen fixation was first commercialized as the thermal-plasma-based Birkeland–Eyde process to produce nitrogen oxides (NO_x) and nitric acid about a century ago, which was economically outcompeted by the centralized, large-scale HB process, using an ultra-pure nitrogen and hydrogen feed (mainly from natural gas and some coal) at high temperature and pressure (>450 °C, 150–350 atm) to catalytically synthesize ammonia that dominates the production of N-fertilizers today. As the result, although nearly 50% of the nitrogen found in the human body has passed through the HB process [2], the production of ammonia is unsustainable, because making this single chemical consumes approximately 2% of the world's annual energy supply and accounts for 1.4% of the annual global carbon emissions, higher than any another chemical [1,3]; this does not include methane emitted from such facilities, which is thought to be underestimated by as much as 50 times, and the number increases further if CO_2 emissions associated with natural gas extraction are included [4,5].

Unfortunately, the production of almost all synthetic N-fertilizers relies on the HB process. Urea is produced from synthetic ammonia and carbon dioxide, and urea manufacturers are always located adjacent to the site where the ammonia is manufactured. The industrial production of ammonium nitrate, the dominant form of nitrate and ammonium fertilizer accounting for 43% of all N-fertilizers [6], entails the acid–base reaction of ammonia with nitric acid. The nitric acid is industrially produced via the Ostwald process that oxidizes ammonia, in the presence of a noble metal catalyst such as platinum with 10% rhodium (top two most expensive metals), to nitric oxide (NO), and, in a second step, NO is further oxidized to yield nitrogen dioxide (NO_2), which is absorbed by water to form nitric acid while reducing a portion of NO_2 back to NO that must be recycled. Evidently, the production of nitrate is a detour—nitrogen in N_2 (oxidation state 0) is first reduced to ammonia (oxidation state -3), and then the ammonia is oxidized to NO and NO_2 (oxidation state +2 and +4, respectively), where extensive energy and fossil fuels are consumed [7]. Furthermore, the tail gas stream in an Ostwald process contains nitrogen oxides (NO_x, mainly NO and NO_2), a gas much more harmful than CO_2 to the climate and environment. To dispose of this pollutant, the industry usually catalytically (again using a noble metal catalyst such as platinum or palladium) reduces the NO_x back to harmless nitrogen gas based on the reaction of NO_x with a fossil fuel, such as hydrogen, methane, butane, propane, or light naphtha [8].

Today, the HB process alone is responsible for the production of over 170 million tons of ammonia, and emits over 300 million tons of CO_2 per year [1,3]. However, the emission of greenhouse gases and pollutants does not just end there. Over 86% of global ammonia produced is applied as N-fertilizer in a variety of chemical forms, among which only about 50% is used by crops, and the rest is lost to the atmosphere via volatilization and denitrification or to ground water through leaching; in some cases, the loss can go up to 70% due to the excessive amount, the low plant population, poor application methods, etc. [9].

Further, global ammonia production has been exclusively established at centralized large scales to be economical, requiring massive capital and infrastructure for H_2 feedstock generation and ammonia storage, and demanding an extensive, costly, and hazardous distribution system [10]. The fossil-fuel-based transportation for the distribution system was not accounted for in the CO_2 emission stated above. Consequently, although the HB process has approached the theoretical limit after continuous development and optimization for more than a century, holding an unbeatable position in terms of energy efficiency despite having great environmental flaws, there is a large variation in the prices and inequality in the accessibility to N-fertilizers globally. For instance, in Sub-Saharan Africa, where sunshine is abundant, low crop yields are associated with low fertilizer use due to high prices [11].

From a systematic engineering view, the current industrial production, distribution, and use of N-fertilizers were built on an unsustainable foundation of fossil resources, and are energy-intensive, inefficient, and environmentally polluting.

1.2. Endeavor to Decarbonize N-Fertilizer Production

The production of N-fertilizer utilizing renewable resources to decarbonize the process has received attention on a global scale driven by the fast declining cost of solar and wind electricity, and sustainability concerns were further incentivized by public policy measures such as a carbon tax [12,13]. In general, research and development endeavors for decarbonizing nitrogen fixation follow either the nitrogen reduction route to fix nitrogen in the form of ammonia (NH_3) or the oxidation path to produce nitrogen oxides (NO_x).

Current efforts in the ammonia route focus on decarbonizing the production of ammonia, not just for fertilizer, but as a platform chemical and energy vector, striving to reduce the specific energy input while increasing the ammonia production rate to achieve Haber–Bosch parity [14]. As a transitional step, the Generation 1 technology for sustainable ammonia production, referred to as "blue ammonia", involves the use of carbon sequestration or offsets to bring the net carbon impact of the ammonia production to near-zero [4].

Recently, two major technologies were extensively researched. The Generation 2 technology still produces ammonia from the HB process, but uses "green" hydrogen from water electrolysis instead of fossil resources, requiring an enormous amount of specialized water and being limited by the energy and economic efficiency of the electrolysis equipment. Further, the HB process must run continuously, and is poorly adaptive to the day–night cycle of solar energy or the intermittency of wind energy [4]. Generation 3 technologies bypass the HB process through the electrocatalytic nitrogen reduction reaction (eNRR) of N_2 to NH_3 with a promising energy efficiency, which has recently gained increasing attention [4]. However, the low ammonia production rate and system stability, the requirement for expensive ultra-dry and oxygen-free organic solvents, or pure nitrogen and hydrogen feedstocks, and platinum and lithium metal requirements are significant drawbacks of this pathway [4,15]. Other methods include the plasma-catalysis of gaseous H_2 and N_2 to NH_3, metallocomplex nitrogen fixation, photochemical synthesis, and bio-catalysis, all of which are currently at the lab research stage, hardly to be practically applicable, scaled up, and economically competitive with the HB process [13,16,17].

In the oxidation path to fix nitrogen in the form of nitrogen oxides (NO_x), air NTP plasma technologies should be the focus, practically because the free atmospheric air is the predominant source of chemically inert N_2. It is noteworthy that the Birkeland–Eyde process to produce NO_x is the first thermal-plasma-based N_2-oxidation concept, which only utilizes around 3–4% of the applied energy in chemical reactions, the remaining applied energy being wasted as heat [18]. The theoretical energy efficiency of thermal plasma is 0.86 MJ/mol of nitrogen oxide (NO), which could be achieved under hypothetical conditions of 20–30 Bars, 3000–3500 K, and a 10^7 K/s cooling rate [19], higher than that of the HB process for N fixation into ammonia (0.48 MJ/mol ammonia produced). The renewed interest in plasma-based N fixation focuses on nonthermal or warm plasma, which has a lower theoretical energy cost than the HB process, and is projected to become a highly competitive alternative, if the actual energy cost can be significantly reduced [7]. In the case of NO_x production, nonthermal plasma (NTP) has a much lower theoretical limit of energy consumption (0.2 MJ/mol in vacuum) than the HB process [20].

However, comparing the energy efficiency of different technologies for the production of ammonia or NO_x could be misleading. Most of the studies in the oxidation path estimated the energy efficiency based on the end product of NO_x gas (mainly the mixture of NO_2 and NO, e.g., in [15,21–27]), which cannot be directly used as an N-fertilizer. NO needs to be further oxidized to NO_2, which then dissolves in water to form nitric acid, but part of the NO_2 would be reacted back to NO. Further, the nitrate fertilizer in the form of nitric acid is highly acidic, limiting its use to alkaline soil or otherwise requiring neutralization before use. For the production and application of N-fertilizers, we need to take a holistic view at the cost of practical end uses, as well as the cost to our health and environment.

1.3. Booming Renewable Electricity and Its Intermittency

The industry of renewable electricity is fast expanding and the cost of solar/wind electricity is rapidly declining (Figure 1). A U.S. Department of Energy study found that renewable electricity generation from technologies that are commercially available today, in combination with a more flexible electric system, is more than adequate to supply 80% of total U.S. electricity generation in 2050 while meeting the electricity demand on an hourly basis in every region of the country. This study explores the implications and challenges of very high renewable electricity generation levels—from 30% up to 90%, focusing on 80%, of all U.S. electricity generation—in 2050. At such high levels of renewable electricity generation, the unique characteristics of some renewable resources, specifically the geographical distribution and variability and uncertainty in output, pose challenges to the operability of the nation's electric system [28].
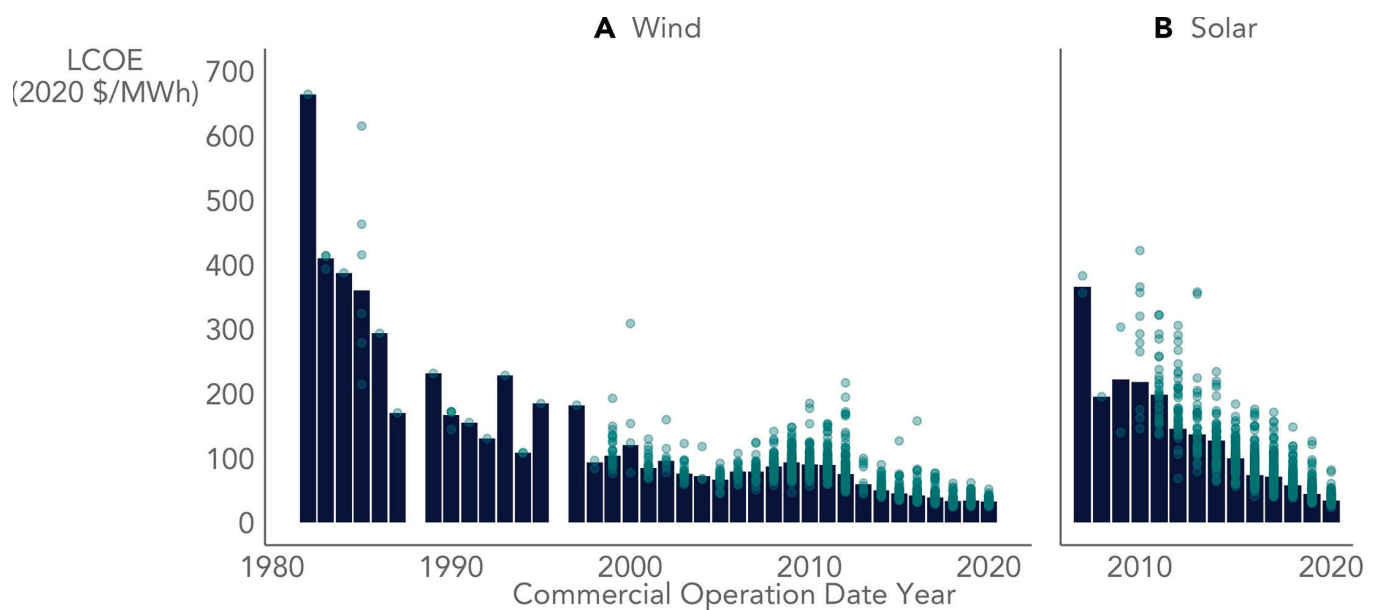
Figure 1. Historical non-normalized levelized cost of electricity (LCOE) of utility-scale wind (**A**) and solar (**B**) energy in the United States [29].

Critics of renewable energy frequently highlight that technologies such as wind and solar only generate electricity when specific natural conditions are met—wind blowing or sun shining. They argue that the widespread adoption of renewable energy is hindered until cost-effective electricity storage technologies are developed. The challenge in integrating variable electricity sources arises from the grid's historical design centered on large, controllable generators. Modern grid operators employ a three-phase planning approach to ensure power plants generate sufficient electricity precisely when needed to consistently and reliably meet demand. Due to the limited storage capacity within the grid, maintaining a continuous balance between the electricity supply and demand is critical to preventing potential blackout events or other systemic failures. Consequently, our modern power grid has been established with a significant overcapacity in order to satisfy the peak load demand in a narrow window of time [30]. Intermittent renewables are challenging because they disrupt the conventional methods for planning the daily operation of the electric grid.

In this respect, the decentralized production of N-fertilizers with NTP technologies are adaptive to the intermittency of renewable electricity and the need of the power grid by "storing" electricity into valuable chemicals, and have a high potential to change the landscape of N-fertilizers, because the production process can be easily switched on and off.

2. Perspective: Decarbonizing N-Fertilizer with NTP Technologies

2.1. Decentralized N-Fertilizer Production and Application Based on NTP

Nitrogen (N) is a critical element essential for optimal plant growth and development. Plants utilize nitrogen primarily in the forms of nitrate (NO_3^-) and ammonium (NH_4^+). Ammonium ions readily bind to negatively charged soil particles, preventing their leaching. Throughout the growing season, soil micro-organisms convert ammonium into nitrate, the primary form of nitrogen absorbed by plants [31]. However, microbial processes like denitrification also convert nitrate and nitrite (NO_2^-) into gaseous nitrogen forms, predominantly nitrogen (N_2) and nitrous oxide (N_2O) [32]. Nitrous oxide is a potent, long-lived greenhouse gas with 300 times the warming potential of CO_2 [33]. Nitrate, being negatively charged, dissolves in water and moves through the soil with the soil water movement. During rainfall, nitrate can percolate downward through the soil profile, potentially entering tiles or drainage channels and becoming lost from agricultural production. This leaching process is the primary mechanism causing nitrogen loss from coarse-textured sandy soils. Nitrite is a less common form of nitrogen in the soil, and it is

typically produced by the breakdown of organic matter or the action of nitrifying bacteria. Nitrite is also absorbed by plant roots, but it is less readily available to plants than nitrate and could be toxic to plants, especially at higher concentrations [34–36]. Each form of N-fertilizers has specific properties that determine when, where, and how various fertilizer materials can be used [31].

We need to re-examine our current system for N-fertilizer production and distribution established on the foundation of the HB process. A recent spike in the prices of N-fertilizers (in U.S., the farmer-paid price for anhydrous ammonia increased from $487/ton in 2020 to $1516/ton as of March 2022), due to the disruption of the natural gas supply chain, intensifies the alarm on this fragile and unsustainable system [37].

Given that over 86% of the global ammonia production involves either the direct application to soil as ammonia fertilizer or conversion into other forms such as ammonium, nitrate, and urea, it results in a complex distribution network, uneven access to nitrogen fertilizers, and significant application losses [9]. Therefore, there is an urgent and practical need to develop an N-fertilizer production system that utilizes renewable electricity (solar or wind) and NTP technologies for a sustainable decentralized production and application in the future. Such a system would utilize water, air, and electricity as the primary inputs to synthesize an aqueous mixture of nitrate and ammonium suitable for the direct application to crops. This approach facilitates local production at the farm level, allowing installation either independently or integrated with existing irrigation systems. It can operate effectively with an intermittent solar or wind electricity supply, resulting in zero carbon emissions. Furthermore, it can enable rapid startup and shutdown, promptly responding to weather fluctuations and local agricultural conditions such as the soil type, climate, crop varieties, and farming practices, for precision agriculture.

Prospectively, the implementation of such an N-fertilizer system will require the demonstration of the following: (1) a scalable modular system that can deliver sufficient aqueous N-fertilizer according to the demand of an agricultural land, small or large, (2) a sufficiently low electric energy cost to be economically competitive, and (3) evidence that the N-fertilizer product can be directly applied to grow crops/vegetables and totally replace synthetic N-fertilizers.

2.2. Plasma-Activated Water and the Applications in Agriculture

Plasma-activated water (PAW), commonly derived from the interaction of atmospheric plasma with water in a batch mode, has attracted widespread attention, with applications ranging from microbial decontamination in the food industry to medical wound healing. Importantly, it is considered a supplement to chemical fertilizers in agriculture because it is rich in fixed nitrogen in the forms of nitrate and nitrite. Other reported benefits of PAW in agriculture include enhancing seed germination, increasing rooting speed, promoting plant growth, enhancing drought tolerance and resistance to abiotic stresses, and controlling plant diseases and pests, due to the presence of reactive oxygen and nitrogen species (RONS), such as hydroxyl radicals ($\cdot$OH), hydrogen peroxide (H_2O_2), ozone (O_3), and nitrate/nitrite (NO_3^- and NO_2^-) [38–41]. Although there are reported negative effects of high-concentration PAW on plants [39,42], a recent study concluded that PAW application, even at high amounts, has no negative influence on the physicochemical properties of soil and it can be safely applied in sustainable, environmentally friendly agriculture [43].

Although the benefits of PAW for agriculture production deserve further research, PAW is not a well-defined product; different methods of generating PAW lead to different contents of reactive chemical species, and most of them are transient, which will ultimately affect the activity of the resulting PAW for different applications. To the prospect of this article, the fixed N content in PAW is insufficient to replace synthetic N-fertilizers.

2.3. On-Site Production of Liquid N-Fertilizer

As discussed in Section 2.1, the decentralized N-fertilizer production utilizing air, water, and renewable electricity holds significant promise for the on-site production of

liquid N-fertilizer. This approach circumvents the need for the extensive capital investment and infrastructure required for ammonia production and storage, as well as the complex and costly distribution networks associated with synthetic N-fertilizers. Moreover, it eliminates the necessity for downstream separations or additional processes to obtain nitrate, ammonium, or urea, as the desired product would be a blend of nitrate and ammonium directly suitable for application to crops and vegetables.

The key to achieving such production capabilities lies in the development of nitrogen fixation technologies based on NTP in continuous reactors that can achieve a high productivity of nitrate and ammonium at sufficiently low electricity costs to be economically viable for agriculture. Recent research has increasingly focused on understanding the interaction between plasma and water, aiming to advance the fundamental knowledge at the largely unexplored interface of NTP and water for engineering development [44–46]. Despite advancements in energy efficiency in nitrogen fixation using NTP technologies, few reported developments have successfully balanced a high productivity with the low electricity costs required for continuous operation and practical applicability in agricultural settings.

2.3.1. Recent Development of a Continuous NTP Reaction System for N-Fertilizer

The author has recently developed a continuous NTP reaction system (denoted as cNTP-H_2O hereafter) for the distributed on-site production and delivery of N-fertilizer [47], as presented in Figure 2. This design enables a high rate of water-flow-through operation, continuously delivering an aqueous N-fertilizer, mainly in the forms of nitrate and ammonium with a trace of nitrite.
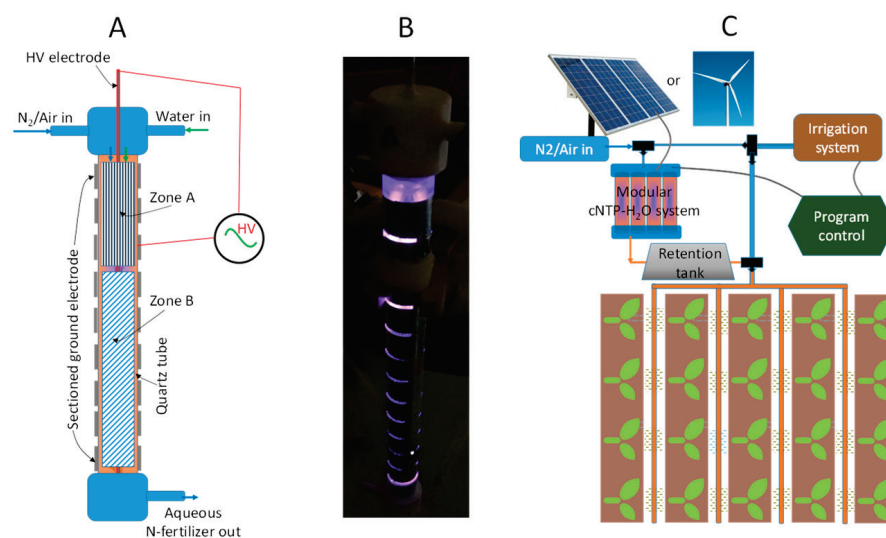
Figure 2. (**A**) Schematic unit-cell design of the cNTP-H_2O system; (**B**) photo image showing a discharging unit-cell against dark background; and (**C**) vision of integrating modular cNTP-H_2O system with irrigation.

The modular cNTP-H_2O system consists of uniquely designed unit-cells, featuring a two-zone, configurable high-voltage (HV) electrode and ground electrode to generate dielectric barrier discharge (DBD) plasma, as schematically presented in Figure 2A. Figure 2B shows the photo image of a discharging unit-cell against a dark background during operation. It is envisaged that the system can be scaled up by the parallel connection of a number of unit-cells and coupled to an irrigation line as illustrated in Figure 2C. Importantly, this invention establishes an innovative platform for research and development, which will allow us to configure the reactor (e.g., the shape, geometry, and metal materials for the two zones of HV electrode) and tune the product composition of nitrate/nitrite and ammonium, aiming to maximize the productivity of the N-fertilizer while minimizing the energy cost.

Interest in exploring the interaction between plasma and water has grown due to its potential to enhance the efficiency of nitrogen fixation, producing an aqueous N-fertilizer.

Redox reactions induced by NTP occur not only at the plasma/air and plasma/water interfaces, but also in the volume of the aqueous phase [48]. Both the oxidation and reduction of nitrogen can be achieved using NTP with water, despite thermodynamic or kinetic limitations at ambient conditions, leading to the production of both NO_x and ammonium [49]. Although this is still a largely unexplored area, good discussions on the mechanisms and pathways for the formation of reactive oxygen and nitrogen species (RONS) leading to the production of NO_x and ammonium can be found in recent publications [44–46]. However, most highly reactive plasma species have a very short half-life in the order of a few nanoseconds to a few milliseconds. Therefore, it is important to consider not only the generation of these reactive species, but also their efficient delivery into liquid products when designing an NTP reaction system.

In the design of the cNTP-H_2O system, both water and air simultaneously flow through plasma discharge zones, intensifying the interfacial reactions to enhance mass transfer and tune the production of fixed nitrogen continuously. In addition to common RONS generated in air plasma, the presence of water in the plasma also generates solvated electrons, hydrogen radicals ($H^\bullet$), hydroxyl radicals ($^\bullet OH$), perhydroxyl radicals ($HOO^\bullet$), and hydrogen peroxide (H_2O_2), which are among the strongest reduction or oxidation agents for nitrogen fixation [48,50,51]. The presence of water helps quench the RONS produced by NTP, rapidly converting them into more stable N-containing compounds. This quenching effect helps prevent the back reactions of RONS. Water also acts as an absorption medium in situ for the fixed N, effectively removing it from the gas phase where back reactions are more likely to occur, shifting the equilibrium towards product formation.

For the cNTP-H_2O system, we designed multiple plasma discharge regimes within one unit-cell, which make efficient utilization of the applied power and reduce energy consumption. As an example, the generation of RONS and reactive hydrogen species can be greatly enhanced as the glow discharge acts as an excitation pre-treatment in Zone A prior to the filament discharge in Zone B. The designed turbulent flows of air and water transiently pass through the multiple plasma discharge regimes, undergoing intensified contact and mixing, while the produced NO_x and ammonium are absorbed by water in situ, further driving reactions toward a higher yield of fixed nitrogen.

Different configurations of the cNTP-H_2O system were tested and key results are summarized in Table 1, which also includes preliminary economic estimations. Table 1 shows the significant progress of improving the energy efficiency and production rate of fixed nitrogen by configuring the cNTP-H_2O system and operation parameters.

There is potential to significantly improve the performance of the cNTP-H_2O system through systematic optimization. A major challenge arises from balancing minimizing the energy cost and maximizing the production rate, which is a complex function of a multitude of factors including the plasma discharge type, the reactor geometry/configuration, the discharge operating parameters, and the presence of catalysts. Two targets that could be potentially achieved after the optimization for practical implementation are also listed in Table 1. Target 1 has a high optimized production rate, and Target 2 has a high optimized energy efficiency. If one of the targets is achieved, solar panels with a surface area of only about 1% of a land area will produce sufficient N-fertilizer for the land. Although the specific energy cost is still higher than that of the HB process, they are potentially viable at the farm site without the emissions and distribution costs associated with the HB process.

Table 1. Test results of the cNTP-H$_2$O system with preliminary economic estimations.

Unit-Cell Configuration	Unit Feed Gas and Flow Rate (mL/min) [1]	Unit Feed Water Content and Flow Rate (mL/min) [2]	Total N Production Rate per Unit-Cell (mg-N/min) [3]	NH$_4$-N Production Rate per Unit-Cell (mg-N/min)	Energy Efficiency (kWh/mol-N) [4]	Number of Unit-Cells for 115 lb N per Acre [5]	Electricity Cost for 115 lb N ($/Season) [6]	% Surface Area of Solar Panel [7]
A	N$_2$/400	DW/48	834.2	15.4	42.5	1737	4752	36.3
B	N$_2$/500	DW (2% ethanol)/47	808.4	503.6	42.4	1792	4743	36.2
C	N$_2$/400	DW/48	1629.1	129.0	25.5	889	2850	21.8
D	N$_2$/580 + H$_2$/80	DW/50	1095.0	865.2	42.4	1323	4740	36.2
E	Air/2302	DW/48	4094.4	94.0	10.4	354	1159	8.8
F	Air/2302 + H$_2$/80	DW/50	3800.0	257.1	12.3	381	1380	10.5
G	Air/3800	TW/95	8265.0	14.3	5.3	175	587	4.5
Target 1	**Air**	**TW/100**	**30,000**	**3000.0**	**1.6**	**48**	**174**	**1.3**
Target 2	**Air**	**TW/100**	**11,000**	**1100.0**	**1.1**	**132**	**119**	**0.9**

[1] The feed gas was either pure nitrogen, air (79% nitrogen, 21% oxygen), or air/nitrogen plus (+) hydrogen gas with flow rate indicated. [2] The feed water was either distilled water (DW), tap water (TW), or DW added with 2% ethanol. [3] This is based on the production of total fixed nitrogen, including NO$_3^-$, NO$_2^-$, and NH$_4^+$ in the aqueous N-fertilizer. [4] This is calculated based on the summation of measured NO$_3^-$, NO$_2^-$, and NH$_4^+$, and the measurement of NTP power consumption using Lissajous parallelogram method [52]. [5] This is calculated practically assuming that the reaction system is powered by intermittent solar or wind electricity for a typical crop growing season of 600 h (6 h per day for 100 days). We aim to demonstrate the economic feasibility of replacing the use of synthetic N-fertilizer at an ideal rate of 115 lb-N per acre per season for corn production, which is arguably the most demanding agricultural practice for N-fertilizer. Nationally, the weighted average of corn N inputs (188 kg-N per hectare) based on corn-planted area exceeded N needs (115 lb-N per acre) by 60 kg-N per hectare, with N surplus found in 80% of all U.S. corn-producing counties [53]. [6] This is calculated assuming that levelized cost of renewable electricity is $0.03/KWh. The levelized cost of electricity (LCOE) is a measure of the average net present cost of electricity generation for a generator over its lifetime. It is used for investment planning and to compare different methods of electricity generation on a consistent basis. It can include the cost of capital, decommissioning, fuel costs, fixed and variable operations and maintenance costs, financing costs, and an assumed utilization rate. In 2020, the LCOE of utility-scale solar and wind reached down to $0.03/KWh, and further decline in the future is forecasted [54]. [7] Using installed solar panels as example, the number gives a visual estimation of the panel surface area for providing 115 lb-N/acre. The footprint of the corresponding cNTP-H$_2$O system is much smaller and can easily fit under the solar panels. The area occupied by solar panels is estimated based on the total wattage required to power the calculated number of cNTP-H$_2$O unit-cells and that the area of a 1 KW panel is 5.56 m^2 [55]. It is noteworthy that, in the case of installed solar panel operation, only 600 h are dedicated to power the cNTP-H$_2$O modules for a crop-growing season; the electricity generated in the rest of time can be sold to the grid.

2.3.2. Implications and Significance of the cNTP-H$_2$O System

The implications for further development are listed below:

- Hydrogen is the limiting reactant in the reduction pathway to make ammonium. This limiting reactant could be supplemented by H$_2$ gas or ethanol, and potentially by methane, which can be generated at the farm site via anaerobic digestion; however, the use of an extra hydrogen source or enriched N$_2$ or O$_2$ input will inevitably increase the cost for the production of the N-fertilizer.
- Compared to the reduction pathway for making ammonium, the oxidation pathway to produce an aqueous N-fertilizer rich in nitrate from air and water is advantageous; the key is to minimize the energy cost, and the content of nitrite to avoid toxicity to plants.
- Using air as a feed gas to the cNTP-H$_2$O system, the fixed N in the product is dominantly in the form of nitrate, with less than 10 ppm of nitrite in all the cases listed in Table 1, which can be directly utilized by plants. Importantly, the nitrate concentration reached an unprecedented 380 ppm (Entry G in Table 1), ideal for fertigation.
- It appeared that the metal material of the electrode that was in contact with reactants affected the performance. Therefore, catalysts can be added onto the electrode (e.g., coating/embedding catalysts onto the electrode), which may potentially improve the reaction kinetics and product yield significantly.
- With the non-equilibrium DBD plasma, the cNTP-H$_2$O system runs at non-equilibrium steady states; thus, the NTP thermodynamics and kinetics, transport processes, and chemical reaction kinetics all influence the production rate and product composition. Therefore, it is possible, based on the cNTP-H$_2$O platform, to further improve the production rate and specific electric energy consumption through the optimization of the process parameters and configurations.

The significance of the results can be revealed by benchmarking against published data, as shown in Figure 3. Because there are different technologies using different feedstocks for nitrogen fixation (e.g., air, N$_2$, or artificially mixed N$_2$/O$_2$ with various ratios as the nitrogen source; and pure H$_2$ or water as the hydrogen source), preventing straightforward and fair comparisons, we benchmark against four categories of promising technologies: (1) the electrocatalytic nitrogen reduction of N$_2$ to NH$_3$ (eNRR-NH$_3$) [15,56–67], (2) the lithium-mediated electrocatalytic nitrogen reduction of N$_2$ to NH$_3$ (Li-eNRR-NH$_3$) [68–74], (3) the plasma-driven NO$_x$ production (NTP-NO$_x$) [15,21–26], and (4) the plasma-driven NH$_3$ production from N$_2$ and water (NTP/H$_2$O-NH$_3$) [75–79].

It should be pointed out that: (1) although the research effort worldwide focuses on reducing the specific energy consumption to achieve Haber–Bosch parity, both a high production rate and low specific energy consumption are required for practical implementation; (2) we had to use the logarithmic scale for the plot in Figure 3 in order to capture the large variation in both the production rate and specific energy consumption reported in the literature; (3) except for the NTP-NO$_x$ category, most other technologies require N$_2$ gas instead of air as feedstock, potentially increasing the production cost; and, (4) even in the NTP-NO$_x$ category, the artificial mixture of N$_2$/O$_2$ with various ratios, instead of air, were commonly used to improve the NO$_x$ yield, and the reported yields were based on the measurement of the produced NO$_x$ gas, not ready to be used as N-fertilizer. Nonetheless, Figure 3 provides an overview of the significant status of the cNTP-H$_2$O system.

For the eNRR-NH$_3$ and Li-eNRR-NH$_3$ technologies to make ammonia, although some achieved a very low specific energy consumption, the production rates were too low for practical applications; the only promising one in the eNRR-NH$_3$ category used a hybrid method, in which NTP was first used to produce NO$_x$, then the NO$_x$ was fed to an eNRR cell to make ammonia [15]. Furthermore, a low system stability, the requirement for expensive ultra-dry and oxygen-free organic solvents, or the demand for pure nitrogen and hydrogen feedstocks, and platinum and lithium metal, result in low levels of technology readiness [4,15].
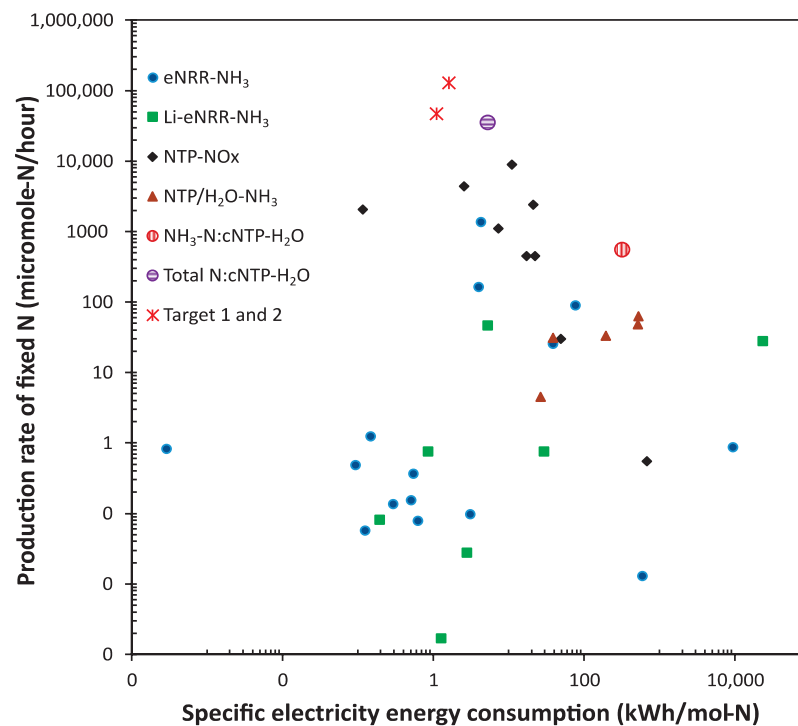
Figure 3. Benchmarking the performance of the cNTP-H$_2$O system against literature data.

Generally, the NTP-NO$_x$ technologies have a higher production rate and moderate specific energy consumption, but most of these studies reported NO as the major product. Although a recent study in this category [26] claimed a record-low specific energy consumption of 0.42 MJ per mol of fixed N (mainly NO) by using a pulsed plasma jet, the production rate is very low (~480 μg-N/min).

Comparing the cNTP-H$_2$O result (Entry C in Table 1) with those reported using NTP/H$_2$O-NH$_3$ technologies and N$_2$ gas as the feed for ammonia production, a much higher production rate was achieved using the cNTP-H$_2$O system, although the specific energy consumption is at the higher end of this category (but it is at the lower end considering the total fixed N). In terms of the total fixed N using air as the feed, we achieved the highest production rate compared with others in the category of NTP-NO$_x$, and the specific energy consumption is at the lower end (Entry G in Table 1). Importantly, the product of the cNTP-H$_2$O system is an aqueous mixture of nitrate and ammonium, which can be directly applied to plants.

Another important consideration in the development of the cNTP-H$_2$O system is practicality. Although the concentration of the fixed N in the aqueous N-fertilizer product (Entry G in Table 1) is about 87 mg-N/L, mainly in the form of NO$_3^-$, the pH is nearly neutral, which can be directly applied to plants without neutralization. This is because tap water has a buffering effect due to its carbonate hardness (KH) and general hardness (GH). Especially, the GH measures the concentration of calcium, magnesium, and other mineral ions present in the water, ranging from 10 to over 300 mg/L depending on the locations. In fact, nitric acid is used to dissolve the mineral deposition in irrigation systems [80], and calcium/magnesium nitrates are excellent fertilizers. Further, the pH of the aqueous N-fertilizer could be tuned by adjusting the process parameters of the cNTP-H$_2$O system according to specific applications, e.g., for citrus trees that prefer slightly acidic soil, or for alkaline soil.

3. Conclusions and Prospects

With the advancement in the fundamental sciences of nonthermal plasma and engineering development in recent years, the implementation of the decentralized on-site

production of N-fertilizer is urgently needed and practically feasible. It has taken more than a century of continuous development and optimization for the HB process to achieve its current level of energy efficiency of approximately 0.5 MJ/mol, which is near its theoretical limit. However, we must point out that the HB process is just one step in the extensive chain of the synthetic N-fertilizer production and distribution entailing heavy emissions and pollutions, which could be largely bypassed by implementing the on-site production of the N-fertilizer using NTP technologies.

We would like to point out the following for accelerating the implementation:

(1)   Minimizing the electric energy cost with NTP technologies without sacrificing productivity should be the priority, because this is directly related to the economic competitiveness. This requires the fundamental research of plasma physics and chemistry, and the reaction kinetics and engineering, especially at the NTP/water interface. Further, the design of the electric power supply directly converting solar or wind electricity to high voltage for better efficiency, although it is out of the scope of this article, is an important aspect for the on-site N-fertilizer production that will certainly improve the performance and energy efficiency. For example, nanosecond-pulsed high voltage has the potential to significantly reduce plasma energy consumption [81], but this type of power supply is expensive. We call on the development of efficient and inexpensive power supplies dedicated to N-fertilizer production with NTP technologies.

(2)   The involvement of agronomists, plant scientists, and soil scientists is crucial for the implementation of the on-site N-fertilizer production and application. As for any disruptive technologies, the new technologies and N-fertilizer products require testing and validation, involving field tests, nutrient uptake studies, soil health monitoring, crop management and improvement, the optimization of fertilizer application, farmer education and training, and an economic and environmental impact assessment. In some cases, the implementation may require the adjustment of current agricultural practices.

(3)   In the early stage of a new technology, process modeling and techno-economic analysis (TEA) can help to assess potential economic feasibilities, bottlenecks, and operation targets for process improvement, and identify further research and development effort requirements. Life cycle analysis (LCA) will evaluate the reduction of greenhouse gas emissions and the environmental impact, resource efficiency, the impact on the ecosystem and human health, and long-term sustainability. Results from the TEA and LCA will also help mitigate socioeconomic and behavioral challenges in adopting new technologies, facilitating the effort of technology transfer for real-world applications.

Opportunities for the on-site N-fertilizer production with NTP technologies are already here.

Agrivoltaics is an innovative approach that combines solar energy production with agriculture on the same land, offering dual land use, a symbiotic relationship, and resource efficiency. Agrivoltaics is wide-spreading globally, and there are more than 300 identified agrivoltaic projects in the United States, representing over 2.8 GW of solar capacity [82]. Assuming only 600 h of usage of the solar capacity for a crop-growing season and that the energy cost of the on-site N-fertilizer production reaches 0.5 MJ/mol-N of Haber–Bosch parity, the 2.8 GW solar capacity would produce 0.17 million tons of fixed N, equivalent to 0.5 million tons of ammonium nitrate fertilizer on site, cutting down the CO_2 emission from the production alone by 0.8 million tons [83].

The NTP-produced N-fertilizer can be combined with animal waste management to treat animal manure, resulting in antimicrobial effects and a higher N content compared to untreated manure, and reducing ammonia and methane emissions [84,85].

Controlled Environment Agriculture (CEA) is an advanced approach to food production that uses technology to create optimal growing conditions for crops. We expect that CEA is ideal for starting the implementation of NTP-produced N-fertilizer, because of its investment in emerging technologies and the need to use nitrate N-fertilizer [86]. A current

trend in new CEA facilities is to implement micro-grids of renewable electricity [87], thus enabling local N-fertilizer production with NTP technologies.

Conflicts of Interest: The author has a patent pending related to the cNTP-H$_2$O system.

References

1. Lim, J.; Fernández, C.A.; Lee, S.W.; Hatzell, M.C. Ammonia and Nitric Acid Demands for Fertilizer Use in 2050. *ACS Energy Lett.* **2021**, *6*, 3676–3685. [CrossRef]
2. Erisman, J.W.; Sutton, M.A.; Galloway, J.; Klimont, Z.; Winiwarter, W. How a century of ammonia synthesis changed the world. *Nat. Geosci.* **2008**, *1*, 636–639. [CrossRef]
3. Gielen, D.; Bennaceur, K.; Kerr, T.; Tam, C.; Tanaka, K.; Taylor, M.; Taylor, P. *Tracking Industrial Energy Efficiency and CO$_2$ Emissions*; IEA: Paris, France, 2007.
4. MacFarlane, D.R.; Cherepanov, P.V.; Choi, J.; Suryanto, B.H.R.; Hodgetts, R.Y.; Bakker, J.M.; Ferrero Vallana, F.M.; Simonov, A.N. A Roadmap to the Ammonia Economy. *Joule* **2020**, *4*, 1186–1205. [CrossRef]
5. Zhou, X.; Passow, F.H.; Rudek, J.; von Fisher, J.C.; Hamburg, S.P.; Albertson, J.D. Estimation of methane emissions from the U.S. ammonia fertilizer industry using a mobile sensing approach. *Elem. Sci. Anthr.* **2019**, *7*, 19. [CrossRef]
6. Ahlgren, S.; Baky, A.; Bernesson, S.; Nordberg, Å.; Norén, O.; Hansson, P.-A. Ammonium nitrate fertiliser production based on biomass—Environmental effects from a life cycle perspective. *Bioresour. Technol.* **2008**, *99*, 8034–8041. [CrossRef]
7. Rouwenhorst, K.H.R.; Jardali, F.; Bogaerts, A.; Lefferts, L. From the Birkeland–Eyde process towards energy-efficient plasma-based NO$_X$ synthesis: A techno-economic analysis. *Energy Environ. Sci.* **2021**, *14*, 2520–2534. [CrossRef]
8. Searles, R. Pollution from Nitric Acid Plants. *Platin. Met. Rev.* **1973**, *17*, 57–63. [CrossRef]
9. Anas, M.; Liao, F.; Verma, K.K.; Sarwar, M.A.; Mahmood, A.; Chen, Z.-L.; Li, Q.; Zeng, X.-P.; Liu, Y.; Li, Y.-R. Fate of nitrogen in agriculture and environment: Agronomic, eco-physiological and molecular approaches to improve nitrogen use efficiency. *Biol. Res.* **2020**, *53*, 47. [CrossRef]
10. Smith, C.; Hill, A.K.; Torrente-Murciano, L. Current and future role of Haber–Bosch ammonia in a carbon-free energy landscape. *Energy Environ. Sci.* **2020**, *13*, 331–344. [CrossRef]
11. Bonilla Cedrez, C.; Chamberlin, J.; Guo, Z.; Hijmans, R.J. Spatial variation in fertilizer prices in Sub-Saharan Africa. *PLoS ONE* **2020**, *15*, e0227764. [CrossRef]
12. Ghavam, S.; Vahdati, M.; Wilson, I.A.G.; Styring, P. Sustainable Ammonia Production Processes. *Front. Energy Res.* **2021**, *9*, 580808. [CrossRef]
13. Rouwenhorst, K.H.R.; Engelmann, Y.; van 't Veer, K.; Postma, R.S.; Bogaerts, A.; Lefferts, L. Plasma-driven catalysis: Green ammonia synthesis with intermittent electricity. *Green Chem.* **2020**, *22*, 6258–6287. [CrossRef]
14. Fernandez, C.A.; Hatzell, M.C. Editors' Choice—Economic Considerations for Low-Temperature Electrochemical Ammonia Production: Achieving Haber-Bosch Parity. *J. Electrochem. Soc.* **2020**, *167*, 143504. [CrossRef]
15. Sun, J.; Alam, D.; Daiyan, R.; Masood, H.; Zhang, T.; Zhou, R.; Cullen, P.J.; Lovell, E.C.; Jalili, A.; Amal, R. A hybrid plasma electrocatalytic process for sustainable ammonia production. *Energy Environ. Sci.* **2021**, *14*, 865–872. [CrossRef]
16. Rouwenhorst, K.H.R.; Krzywda, P.M.; Benes, N.E.; Mul, G.; Lefferts, L. Ammonia, 4. Green Ammonia Production. In *Ullmann's Encyclopedia of Industrial Chemistry*; Verlag Chemie: Hoboken, NJ, USA, 2020; pp. 1–20.
17. Cherkasov, N.; Ibhadon, A.O.; Fitzpatrick, P. A review of the existing and alternative methods for greener nitrogen fixation. *Chem. Eng. Process. Process Intensif.* **2015**, *90*, 24–33. [CrossRef]
18. Patil, B.S.; Wang, Q.; Hessel, V.; Lang, J. Plasma N$_2$-fixation: 1900–2014. *Catal. Today* **2015**, *256*, 49–66. [CrossRef]
19. Rusanov, V.D.; Fridman, A.A.; Sholin, G.V. The physics of a chemically active plasma with nonequilibrium vibrational excitation of molecules. *Sov. Phys. Uspekhi* **1981**, *24*, 447–474. [CrossRef]
20. Li, S.; Medrano, J.A.; Hessel, V.; Gallucci, F. Recent Progress of Plasma-Assisted Nitrogen Fixation Research: A Review. *Processes* **2018**, *6*, 248. [CrossRef]
21. Lu, P.; Boehm, D.; Bourke, P.; Cullen, P.J. Achieving reactive species specificity within plasma-activated water through selective generation using air spark and glow discharges. *Plasma Process. Polym.* **2017**, *14*, 1600207. [CrossRef]
22. Nakaso, T.; Harigai, T.; Kusumawan, S.A.; Shimomura, T.; Tanimoto, T.; Suda, Y.; Takikawa, H. Multi-spark discharge system for preparation of nutritious water. In *AIP Conference Proceedings*; AIP Publishing: Long Island, NY, USA, 2018; Volume 1929.
23. Ogawa, K.; Oh, J.-S.; Gaur, N.; Hong, S.-H.; Kurita, H.; Mizuno, A.; Hatta, A.; Short, R.D.; Ito, M.; Szili, E.J. Modulating the concentrations of reactive oxygen and nitrogen species and oxygen in water with helium and argon gas and plasma jets. *Jpn. J. Appl. Phys.* **2019**, *58*, SAAB01. [CrossRef]
24. Tachibana, K.; Nakamura, T. Comparative study of discharge schemes for production rates and ratios of reactive oxygen and nitrogen species in plasma activated water. *J. Phys. D Appl. Phys.* **2019**, *52*, 385202. [CrossRef]

25. Uchida, G.; Takenaka, K.; Takeda, K.; Ishikawa, K.; Hori, M.; Setsuhara, Y. Selective production of reactive oxygen and nitrogen species in the plasma-treated water by using a nonthermal high-frequency plasma jet. *Jpn. J. Appl. Phys.* **2018**, *57*, 0102B4. [CrossRef]

26. Vervloessem, E.; Gorbanev, Y.; Nikiforov, A.; De Geyter, N.; Bogaerts, A. Sustainable NOx production from air in pulsed plasma: Elucidating the chemistry behind the low energy consumption. *Green Chem.* **2022**, *24*, 916–929. [CrossRef]

27. Muzammil, I.; Lee, D.H.; Dinh, D.K.; Kang, H.; Roh, S.A.; Kim, Y.-N.; Choi, S.; Jung, C.; Song, Y.-H. A novel energy efficient path for nitrogen fixation using a non-thermal arc. *RSC Adv.* **2021**, *11*, 12729–12738. [CrossRef] [PubMed]

28. Hand, M.M.B.S.; DeMeo, E.; Reilly, J.M.; Mai, T.; Arent, D.; Porro, G.; Meshek, M.; Sandor, D. *Renewable Electricity Futures Study*; DOE, Ed.; National Renewable Energy Laboratory: Golden, CO, USA, 2012.

29. Bolinger, M.; Wiser, R.; O'Shaughnessy, E. Levelized cost-based learning analysis of utility-scale wind and solar in the United States. *iScience* **2022**, *25*, 104378. [CrossRef]

30. Sovacool, B.K. The intermittency of wind, solar, and renewable electricity generators: Technical barrier or rhetorical excuse? *Util. Policy* **2009**, *17*, 288–296. [CrossRef]

31. Mengel, D.B. Types and Uses of Nitrogen Fertilizers for Crop Production; Purdue University and U.S. Department of Agriculture cooperating: Cooperative Extension work in Agriculture and Home Economics, State of Indiana. 2020. Available online: https://www.extension.purdue.edu/extmedia/AY/AY-204.html (accessed on 11 April 2024).

32. Takai, K. The Nitrogen Cycle: A Large, Fast, and Mystifying Cycle. *Microbes Environ.* **2019**, *34*, 223–225. [CrossRef] [PubMed]

33. Tian, H.; Xu, R.; Canadell, J.G.; Thompson, R.L.; Winiwarter, W.; Suntharalingam, P.; Davidson, E.A.; Ciais, P.; Jackson, R.B.; Janssens-Maenhout, G.; et al. A comprehensive quantification of global nitrous oxide sources and sinks. *Nature* **2020**, *586*, 248–256. [CrossRef] [PubMed]

34. Masclaux-Daubresse, C.; Daniel-Vedele, F.; Dechorgnat, J.; Chardon, F.; Gaufichon, L.; Suzuki, A. Nitrogen uptake, assimilation and remobilization in plants: Challenges for sustainable and productive agriculture. *Ann Bot* **2010**, *105*, 1141–1157. [CrossRef]

35. Osawa, T. Nitrite toxicities in vegetable crops I. Effect of nitrite and pH levels in nutrient solution on growth of vegetable crops. *J. Jpn. Soc. Hortic. Sci.* **1971**, *40*, 395–400. [CrossRef]

36. Oke, O.L. Nitrite Toxicity to Plants. *Nature* **1966**, *212*, 528. [CrossRef]

37. Schnitkey, G.; Paulson, N.; Zulauf, C.; Swanson, K.; Colussi, J.; Baltz, J. Weekly Farm Economics: Nitrogen Fertilizer Prices and Supply in Light of the Ukraine-Russia Conflict. *Farmdoc Dly.* **2022**, *12*, 45.

38. Guo, D.; Liu, H.; Zhou, L.; Xie, J.; He, C. Plasma-activated water production and its application in agriculture. *J. Sci. Food Agric.* **2021**, *101*, 4891–4899. [CrossRef]

39. Stoleru, V.; Burlica, R.; Mihalache, G.; Dirlau, D.; Padureanu, S.; Teliban, G.-C.; Astanei, D.; Cojocaru, A.; Beniuga, O.; Patras, A. Plant growth promotion effect of plasma activated water on *Lactuca sativa* L. cultivated in two different volumes of substrate. *Sci. Rep.* **2020**, *10*, 20920. [CrossRef]

40. Danilejko, Y.K.; Belov, S.V.; Egorov, A.B.; Lukanin, V.I.; Sidorov, V.A.; Apasheva, L.M.; Dushkov, V.Y.; Budnik, M.I.; Belyakov, A.M.; Kulik, K.N.; et al. Increase of Productivity and Neutralization of Pathological Processes in Plants of Grain and Fruit Crops with the Help of Aqueous Solutions Activated by Plasma of High-Frequency Glow Discharge. *Plants* **2021**, *10*, 2161. [CrossRef]

41. Subramanian, P.S.G.; J, A.; P, L.; Rao, H.; Shivapuji, A.M.; Girard-Lauriault, P.-L.; Rao, L. Plasma-activated water from DBD as a source of nitrogen for agriculture: Specific energy and stability studies. *J. Appl. Phys.* **2021**, *129*, 090401. [CrossRef]

42. Hou, C.-Y.; Kong, T.-K.; Lin, C.-M.; Chen, H.-L. The Effects of Plasma-Activated Water on Heavy Metals Accumulation in Water Spinach. *Appl. Sci.* **2021**, *11*, 5304. [CrossRef]

43. Šimečková, J.; Krčma, F.; Klofáč, D.; Dostál, L.; Kozáková, Z. Influence of Plasma-Activated Water on Physical and Physical–Chemical Soil Properties. *Water* **2020**, *12*, 2357. [CrossRef]

44. Huang, Z.; Xiao, A.; Liu, D.; Lu, X.; Ostrikov, K. Plasma-water-based nitrogen fixation: Status, mechanisms, and opportunities. *Plasma Process. Polym.* **2022**, *19*, 2100198. [CrossRef]

45. Peng, P.; Chen, P.; Addy, M.; Cheng, Y.; Zhang, Y.; Anderson, E.; Zhou, N.; Schiappacasse, C.; Hatzenbeller, R.; Fan, L.; et al. In situ plasma-assisted atmospheric nitrogen fixation using water and spray-type jet plasma. *Chem. Commun.* **2018**, *54*, 2886–2889. [CrossRef]

46. Zhao, X.; Tian, Y. Sustainable nitrogen fixation by plasma-liquid interactions. *Cell Rep. Phys. Sci.* **2023**, *4*, 101618. [CrossRef]

47. Ye, X. Non-Thermal Plasma Reaction Assembly for Continuous Aqueous Nitrogen-Based Fertilizer Production and Method Thereof. University of Tennessee Research Foundation: Provisional Application for Patent UTRF 24035-01 (8597-3017-1), 12 December 2023.

48. Volkov, A.G.; Bookal, A.; Hairston, J.S.; Roberts, J.; Taengwa, G.; Patel, D. Mechanisms of multielectron reactions at the plasma/water interface: Interfacial catalysis, RONS, nitrogen fixation, and plasma activated water. *Electrochim. Acta* **2021**, *385*, 138441. [CrossRef]

49. Sakakura, T.; Murakami, N.; Takatsuji, Y.; Haruyama, T. Nitrogen Fixation in a Plasma/Liquid Interfacial Reaction and Its Switching between Reduction and Oxidation. *J. Phys. Chem. C* **2020**, *124*, 9401–9408. [CrossRef]

50. Rumbach, P.; Bartels, D.M.; Sankaran, R.M.; Go, D.B. The solvation of electrons by an atmospheric-pressure plasma. *Nat. Commun.* **2015**, *6*, 7248. [CrossRef]

51. Liu, J.; He, B.; Chen, Q.; Li, J.; Xiong, Q.; Yue, G.; Zhang, X.; Yang, S.; Liu, H.; Liu, Q.H. Direct synthesis of hydrogen peroxide from plasma-water interactions. *Sci. Rep.* **2016**, *6*, 38454. [CrossRef]

52. Manley, T.C. The electric characteristics of the ozonator discharge. *Trans. Electrochem. Soc.* **1943**, *84*, 12. [CrossRef]

53. Xia, Y.; Kwon, H.; Wander, M. Developing county-level data of nitrogen fertilizer and manure inputs for corn production in the United States. *J. Clean. Prod.* **2021**, *309*, 126957. [CrossRef]

54. Ramasamy, V.; Feldman, D. *U.S. Solar Photovoltaic System and Energy Storage Cost Benchmarks: Q1 2021*; G. National Renewable Energy Lab. (NREL): Golden, CO, USA, 2021.

55. RAYmaps. How to Calculate the Surface Area Required by Solar Panels. Available online: https://www.raymaps.com/index.php/how-to-calculate-the-area-required-by-solar-panels/ (accessed on 10 June 2024).

56. Lamichhane, P.; Adhikari, B.C.; Nguyen, L.N.; Paneru, R.; Ghimire, B.; Mumtaz, S.; Lim, J.S.; Hong, Y.J.; Choi, E.H. Sustainable nitrogen fixation from synergistic effect of photo-electrochemical water splitting and atmospheric pressure N_2 plasma. *Plasma Sources Sci. Technol.* **2020**, *29*, 045026. [CrossRef]

57. Kumari, S.; Pishgar, S.; Schwarting, M.E.; Paxton, W.F.; Spurgeon, J.M. Synergistic plasma-assisted electrochemical reduction of nitrogen to ammonia. *Chem. Commun.* **2018**, *54*, 13347–13350. [CrossRef]

58. Suryanto, B.H.R.; Wang, D.; Azofra, L.M.; Harb, M.; Cavallo, L.; Jalili, R.; Mitchell, D.R.G.; Chatti, M.; MacFarlane, D.R. MoS_2 Polymorphic Engineering Enhances Selectivity in the Electrochemical Reduction of Nitrogen to Ammonia. *ACS Energy Lett.* **2019**, *4*, 430–435. [CrossRef]

59. Shi, M.-M.; Bao, D.; Wulan, B.-R.; Li, Y.-H.; Zhang, Y.-F.; Yan, J.-M.; Jiang, Q. Au Sub-Nanoclusters on TiO_2 toward Highly Efficient and Selective Electrocatalyst for N_2 Conversion to NH_3 at Ambient Conditions. *Adv. Mater.* **2017**, *29*, 1606550. [CrossRef] [PubMed]

60. Kong, J.; Lim, A.; Yoon, C.; Jang, J.H.; Ham, H.C.; Han, J.; Nam, S.; Kim, D.; Sung, Y.-E.; Choi, J.; et al. Electrochemical Synthesis of NH3 at Low Temperature and Atmospheric Pressure Using a γ-Fe_2O_3 Catalyst. *ACS Sustain. Chem. Eng.* **2017**, *5*, 10986–10995. [CrossRef]

61. Zhang, L.; Ding, L.X.; Chen, G.F.; Yang, X.; Wang, H. Ammonia Synthesis Under Ambient Conditions: Selective Electroreduction of Dinitrogen to Ammonia on Black Phosphorus Nanosheets. *Angew. Chem. Int. Ed. Engl.* **2019**, *58*, 2612–2616. [CrossRef] [PubMed]

62. Bao, D.; Zhang, Q.; Meng, F.-L.; Zhong, H.-X.; Shi, M.-M.; Zhang, Y.; Yan, J.-M.; Jiang, Q.; Zhang, X.-B. Electrochemical Reduction of N_2 under Ambient Conditions for Artificial N_2 Fixation and Renewable Energy Storage Using N_2/NH_3 Cycle. *Adv. Mater.* **2017**, *29*, 1604799. [CrossRef] [PubMed]

63. Jin, H.; Li, L.; Liu, X.; Tang, C.; Xu, W.; Chen, S.; Song, L.; Zheng, Y.; Qiao, S.-Z. Nitrogen Vacancies on 2D Layered W_2N_3: A Stable and Efficient Active Site for Nitrogen Reduction Reaction. *Adv. Mater.* **2019**, *31*, 1902709. [CrossRef] [PubMed]

64. Wang, J.; Yu, L.; Hu, L.; Chen, G.; Xin, H.; Feng, X. Ambient ammonia synthesis via palladium-catalyzed electrohydrogenation of dinitrogen at low overpotential. *Nat. Commun.* **2018**, *9*, 1795. [CrossRef] [PubMed]

65. Chen, S.; Perathoner, S.; Ampelli, C.; Mebrahtu, C.; Su, D.; Centi, G. Electrocatalytic Synthesis of Ammonia at Room Temperature and Atmospheric Pressure from Water and Nitrogen on a Carbon-Nanotube-Based Electrocatalyst. *Angew. Chem. Int. Ed.* **2017**, *56*, 2699–2703. [CrossRef] [PubMed]

66. Li, S.-J.; Bao, D.; Shi, M.-M.; Wulan, B.-R.; Yan, J.-M.; Jiang, Q. Amorphizing of Au Nanoparticles by CeOx–RGO Hybrid Support towards Highly Efficient Electrocatalyst for N_2 Reduction under Ambient Conditions. *Adv. Mater.* **2017**, *29*, 1700001. [CrossRef] [PubMed]

67. Mukherjee, S.; Cullen, D.A.; Karakalos, S.G.; Liu, K.; Zhang, H.; Zhao, S.; Xu, H.; More, K.L.; Wang, G.; Wu, G. Metal-organic framework-derived nitrogen-doped highly disordered carbon for electrochemical ammonia synthesis using N_2 and H_2O in alkaline electrolytes. *Nano Energy* **2018**, *48*, 217–226. [CrossRef]

68. Lazouski, N.; Chung, M.; Williams, K.; Gala, M.L.; Manthiram, K. Non-aqueous gas diffusion electrodes for rapid ammonia synthesis from nitrogen and water-splitting-derived hydrogen. *Nat. Catal.* **2020**, *3*, 463–469. [CrossRef]

69. Lazouski, N.; Schiffer, Z.J.; Williams, K.; Manthiram, K. Understanding Continuous Lithium-Mediated Electrochemical Nitrogen Reduction. *Joule* **2019**, *3*, 1127–1139. [CrossRef]

70. Lee, H.K.; Koh, C.S.L.; Lee, Y.H.; Liu, C.; Phang, I.Y.; Han, X.; Tsung, C.-K.; Ling, X.Y. Favoring the unfavored: Selective electrochemical nitrogen fixation using a reticular chemistry approach. *Sci. Adv.* **2018**, *4*, eaar3208. [CrossRef] [PubMed]

71. Zhou, F.; Azofra, L.M.; Ali, M.; Kar, M.; Simonov, A.N.; McDonnell-Worth, C.; Sun, C.; Zhang, X.; MacFarlane, D.R. Electro-synthesis of ammonia from nitrogen at ambient temperature and pressure in ionic liquids. *Energy Environ. Sci.* **2017**, *10*, 2516–2520. [CrossRef]

72. Andersen, S.Z.; Čolić, V.; Yang, S.; Schwalbe, J.A.; Nielander, A.C.; McEnaney, J.M.; Enemark-Rasmussen, K.; Baker, J.G.; Singh, A.R.; Rohr, B.A.; et al. A rigorous electrochemical ammonia synthesis protocol with quantitative isotope measurements. *Nature* **2019**, *570*, 504–508. [CrossRef] [PubMed]

73. Kim, K.; Yoo, C.-Y.; Kim, J.-N.; Yoon, H.C.; Han, J.-I. Electrochemical Synthesis of Ammonia from Water and Nitrogen in Ethylenediamine under Ambient Temperature and Pressure. *J. Electrochem. Soc.* **2016**, *163*, F1523. [CrossRef]

74. Chen, G.-F.; Cao, X.; Wu, S.; Zeng, X.; Ding, L.-X.; Zhu, M.; Wang, H. Ammonia Electrosynthesis with High Selectivity under Ambient Conditions via a Li^+ Incorporation Strategy. *J. Am. Chem. Soc.* **2017**, *139*, 9771–9774. [CrossRef] [PubMed]

75. Peng, P.; Schiappacasse, C.; Zhou, N.; Addy, M.; Cheng, Y.; Zhang, Y.; Anderson, E.; Chen, D.; Wang, Y.; Liu, Y.; et al. Plasma in situ gas—Liquid nitrogen fixation using concentrated high-intensity electric field. *J. Phys. D Appl. Phys.* **2019**, *52*, 494001. [CrossRef]

76. Toth, J.R.; Abuyazid, N.H.; Lacks, D.J.; Renner, J.N.; Sankaran, R.M. A Plasma-Water Droplet Reactor for Process-Intensified, Continuous Nitrogen Fixation at Atmospheric Pressure. *ACS Sustain. Chem. Eng.* **2020**, *8*, 14845–14854. [CrossRef]

77. Hawtof, R.; Ghosh, S.; Guarr, E.; Xu, C.; Mohan Sankaran, R.; Renner, J.N. Catalyst-free, highly selective synthesis of ammonia from nitrogen and water by a plasma electrolytic system. *Sci. Adv.* **2019**, *5*, eaat5778. [CrossRef]

78. Gorbanev, Y.; Vervloessem, E.; Nikiforov, A.; Bogaerts, A. Nitrogen Fixation with Water Vapor by Nonequilibrium Plasma: Toward Sustainable Ammonia Production. *ACS Sustain. Chem. Eng.* **2020**, *8*, 2996–3004. [CrossRef]

79. Indumathy, B.; Ananthanarasimhan, J.; Rao, L.; Yugeswaran, S.; Ananthapadmanabhan, P.V. Catalyst-free production of ammonia by means of interaction between a gliding arc plasma and water surface. *J. Phys. D Appl. Phys.* **2022**, *55*, 395501. [CrossRef]

80. Chant, J. How Nitric Acid is used in the Horticulture Industry. Available online: https://www.monarchchemicals.co.uk/Information/News-Events/795-/How-Nitric-Acid-is-used-in-the-Horticulture-Industry (accessed on 2 June 2024).

81. Huiskamp, T. Nanosecond pulsed streamer discharges Part I: Generation, source-plasma interaction and energy-efficiency optimization. *Plasma Sources Sci. Technol.* **2020**, *29*, 023002. [CrossRef]

82. DOE, Agrivoltaics: Solar and Agriculture Co-Location. Office of Energy Efficiency & Renewable Energy, Department of Energy. Available online: https://www.energy.gov/eere/solar/agrivoltaics-solar-and-agriculture-co-location (accessed on 4 May 2024).

83. Mares, B.P.F.A.J.W. Greenhouse Gas Index for Products in 39 Industrial Sectors: Nitrogenous Fertilizer Manufacturing. NAICS CODE 325311. Resources for the Future. 2022. Available online: https://media.rff.org/documents/WP_22-16_M8.pdf (accessed on 11 May 2024).

84. Mousavi, H.; Cottis, T.; Pommeresche, R.; Dörsch, P.; Solberg, S.Ø. Plasma-Treated Nitrogen-Enriched Manure Does Not Impose Adverse Effects on Soil Fauna Feeding Activity or Springtails and Earthworms Abundance. *Agronomy* **2022**, *12*, 2314. [CrossRef]

85. Nyvold, M.; Dörsch, P. Complete elimination of methane formation in stored livestock manure using plasma technology. *Front. Sustain. Food Syst.* **2024**, *8*, 1370542. [CrossRef]

86. Ragaveena, S.; Edward, A.S.; Surendran, U. Smart controlled environment agriculture methods: A holistic review. *Rev. Environ. Sci. Bio/Technol.* **2021**, *20*, 887–913. [CrossRef]

87. Uddin, M.; Mo, H.; Dong, D.; Elsawah, S.; Zhu, J.; Guerrero, J.M. Microgrids: A review, outstanding issues and future trends. *Energy Strategy Rev.* **2023**, *49*, 101127. [CrossRef]

Assessing CNN Architectures for Estimating Correct Posture in Cruise Machinists

Fabian Arun Panaite [1], Monica Leba [1,*] and Andreea Cristina Ionica [2]

[1] Department of System Control and Computer Engineering, University of Petrosani, Universitatii 20, 332006 Petrosani, Romania; fabianpanaite@upet.ro
[2] Department of Management and Industrial Engineering, University of Petrosani, Universitatii 20, 332006 Petrosani, Romania; andreeaionica@upet.ro
* Correspondence: monicaleba@upet.ro or monicaleba@yahoo.com

Abstract: Cruise machinists operate in dynamic and physically demanding environments where improper posture can lead to musculoskeletal disorders, adversely affecting their health and work efficiency. Current ergonomic assessments in such settings are often generic and not tailored to the unique challenges of maritime operations. This paper presents a novel application of artificial intelligence tools for real-time posture estimation specifically designed for cruise machinists. The primary aim is to enhance occupational health and safety by providing precise, real-time feedback on ergonomic practices. We developed a dataset by capturing video recordings of cruise machinists at work, which were processed to extract skeletal outlines using advanced computer vision techniques. This dataset was used to train deep neural networks, optimizing them for accuracy in diverse and constrained shipboard environments. The networks were tested across various computational platforms to ensure robustness and adaptability. The AI model demonstrated high efficacy in recognizing both correct and incorrect postures under real-world conditions aboard ships. The system significantly outperformed traditional ergonomic assessment tools in terms of speed, accuracy, and the ability to provide instant feedback. The findings suggest that AI-enhanced ergonomic assessments could be a transformative approach for occupational health across various industries.

1. Introduction

Cruise ships are a popular mode of transportation and leisure, attracting millions of passengers each year. However, the cruise industry also employs a significant number of crew members, including machinists responsible for the operation and maintenance of the ship's engines and mechanical systems. Unfortunately, the work environment on cruise ships can be hazardous, and machinists are at a high risk of work-related accidents and injuries.

According to [1], the rate of work-related injuries among cruise ship machinists is significantly higher than the national average for the maritime industry. The study found that the most common types of injuries were musculoskeletal disorders, such as back injuries and sprains, as well as burns and lacerations. These injuries can have a significant impact on the health and well-being of the affected workers, as well as the overall efficiency and productivity of the cruise ship's operations.

To address this issue, cruise lines have implemented various prevention methods, such as providing personal protective equipment (PPE), implementing safety protocols, and offering training programs for machinists [2]. However, these approaches have had limited success in reducing the overall rate of work-related accidents. One potential solution to this problem is the use of AI-based training methods, which could provide more personalized and adaptive learning experiences for machinists, leading to improved safety outcomes.

Ref. [3] explored the use of AI-based training for maritime workers, including machinists. The researchers developed a virtual reality-based training system that used machine learning algorithms to assess the trainee's performance and provide personalized feedback and guidance. The results of the study showed that the AI-based training system was more effective in improving safety knowledge and skills compared to traditional training methods.

Given the significant risks faced by cruise ship machinists and the limitations of existing prevention methods, there is a clear need to explore more effective training solutions that leverage the power of AI. By developing and implementing AI-based training programs, cruise lines can potentially reduce the rate of work-related accidents, improve the health and safety of their employees, and enhance the overall efficiency and productivity of their operations.

This paper advocates for the adoption of an innovative solution: an AI Motion Analysis application. This application harnesses the power of machine learning algorithms and video capture technology to autonomously analyze and differentiate between optimal and suboptimal movements. By empowering trainees to independently practice and evaluate their techniques using readily available camera devices, this system eliminates the dependency on additional resources and human oversight.

Numerous studies have underscored the efficacy of training muscle memory, particularly when coupled with stability optimization strategies. Through the proposed application, training becomes not only more efficient but also accessible, as it can be conducted at the convenience of the trainee. Moreover, the objective nature of computer-based assessments ensures fair evaluations devoid of human subjectivity, thereby enhancing the overall effectiveness of training initiatives and safeguarding personnel health and safety.

The paper advances the application of convolutional neural networks (CNNs) for ergonomic posture evaluation, specifically tailored to the unique environment of cruise machinists. Our research directly targets the maritime industry, focusing on cruise machinists—a group often overlooked in ergonomic studies despite their high risk of posture-related injuries. The solutions we develop are not only theoretically robust but also practically applicable in improving workplace safety and ergonomics aboard cruise ships. By improving posture monitoring through advanced AI tools, our work supports the development of safer working environments and better health outcomes for a critical workforce.

To address the identified training gaps for cruise machinists, we compiled and processed a dataset using specialized software to extract frames from videos, augment images, identify key skeletal inflection points, and isolate skeletal outlines for training a neural network, ensuring unbiased learning across diverse human dimensions and proportions. The dual approach using two distinct CNN architectures—SqueezeNet and GoogleNet— allows us to explore and compare the efficacy of different models in a real-world setting, significantly contributing to the body of knowledge on practical CNN applications. Cross-platform training and evaluation not only tests the models' performance across different hardware but also makes our findings highly relevant for real-world deployments, where such flexibility in resource utilization is crucial.

Our study not only pushes forward the state of the art in applying deep learning to ergonomic assessments but also provides a tailored, robust, and versatile solution to a critical, industry-specific problem. We believe these contributions are of substantial importance to both the academic community and the maritime industry.

The subsequent sections of this paper continue as follows. Section 2: Literature Review offers an exploration of scientific literature about lifting techniques; muscle memory; factors influencing skill acquisition; and advancements in data acquisition, machine learning, and neural networks. Section 3: Materials and Methods is where the methodology employed in the study is presented, containing experimental procedures and data collection methods deployed to evaluate lifting posture correctness. Section 4: Experimental Design describes the careful attention devoted to crafting an experimental design characterized by effectiveness and efficiency. This phase involved the development of a robust system comprising

optimized hardware and software components tailored for seamless data collection and analysis. Section 5: Results and Discussion is where the findings of the study take center stage, accompanied by a thorough comparative analysis of the employed methods' metrics. Section 6: Conclusion is where the key findings and implications are synthesized, emphasizing the significance of the proposed AI Motion Analysis application in elevating workplace ergonomics and safety standards.

2. Related Work

Identifying correct posture in the workplace is essential for preventing musculoskeletal disorders (MSDs) and promoting overall well-being among workers. This literature review synthesizes recent research efforts aimed at evaluating posture and its implications for ergonomics and health.

The authors of [4] proposed a novel, vision-based, real-time method for evaluating postural risk factors associated with MSDs. By leveraging advanced computer vision techniques, their approach offers promising avenues for accurately assessing posture-related risks in real-world work settings. Similarly, an incremental Deep Neural Networks-based posture recognition model has been developed that is specifically tailored for ergonomic risk assessment in construction contexts [5]. The model demonstrates the potential of machine learning in providing precise and efficient solutions for identifying posture-related hazards.

Another work [6] explored ergonomic posture recognition using 3D view-invariant features from a single ordinary camera. The method capitalizes on innovative feature extraction techniques to overcome challenges related to viewpoint variations, paving the way for robust posture assessment systems. Complementing these technological advancements, insights from biomechanics studies are crucial for understanding the mechanical stability of the spine and its implications for injury and chronic low back pain [7,8].

Effective ergonomic interventions necessitate a comprehensive understanding of how various factors influence posture. For instance, lifting tasks pose significant risks to musculoskeletal health, with factors such as load knowledge and lifting height playing pivotal roles [9,10], for which there are proposed general lifting equations based on mechanical work during manual lifting, providing a theoretical framework for assessing lifting-related risks [11].

Furthermore, participatory ergonomic approaches have shown promise in reducing musculoskeletal exposure among workers [12]. By involving workers in the design and implementation of ergonomic interventions, these approaches ensure interventions are tailored to specific workplace contexts, thereby enhancing their effectiveness and acceptance.

In the construction industry, where non-routine work tasks are prevalent, reliable exposure assessment strategies are essential for identifying physical ergonomic stressors [13]. In [14], the authors conducted a postural analysis of building construction workers using ergonomic principles, highlighting the importance of addressing workplace-specific challenges to promote worker well-being.

Moreover, advancements in musculoskeletal modeling enable accurate estimation of spinal loading and muscle forces during lifting tasks, facilitating the design of ergonomic interventions tailored to individual needs [8]. Similarly, stretcher and backboard-related paramedic lifting tasks are ranked based on their biomechanical demands on the low back, providing insights for optimizing task design and training protocols [15].

Recent studies have also emphasized the importance of ergonomic analysis tools in identifying work-related MSDs, such as the efficacy of ergonomic analysis tools in industrial settings, highlighting their role in early detection and prevention of MSDs [16], and lifting hazards in a cabinet manufacturing company and proposed controls to mitigate risks associated with manual handling tasks [17].

Additionally, the accuracy of identifying low or high-risk lifting during standardized lifting situations was assessed, contributing to the development of reliable ergonomic assessment methods [18]. Acute effects of plyometric exercise on maximum squat performance in male athletes was examined, shedding light on the potential benefits of exercise interventions for improving posture and musculoskeletal health [19].

The literature reviewed underscores the multifaceted nature of identifying correct posture in the workplace. By integrating insights from computer vision, biomechanics, participatory ergonomics, and musculoskeletal modeling, researchers and practitioners can develop comprehensive strategies for mitigating posture-related risks and promoting occupational health and safety. Continued interdisciplinary research efforts are warranted to address evolving workplace challenges and ensure the well-being of workers across various industries.

However, these studies also exhibit certain limitations that underscore the novelty and importance of the proposed research on using AI tools for posture estimation in cruise machinists. Many of the related works focus on specific industries such as construction or healthcare; for example, ergonomic risk assessment for construction workers or the biomechanical demands on paramedics. This indicates a gap in research tailored to the unique environment of cruise ships, where space constraints, ship motion, and specific operational tasks might present unique challenges not addressed by these industry-specific studies. While papers such as [4,6] have incorporated advanced computer vision and machine learning techniques for posture recognition, these applications are generally in controlled or semi-controlled environments. The dynamic and often unpredictable environment aboard a cruise ship requires a robust AI system capable of handling diverse scenarios and lighting conditions, which may not be fully addressed by the existing models. The real-time vision-based method mentioned in paper [4] introduces the potential for immediate posture correction feedback, but it is not clear how well these systems perform in non-static, high-movement scenarios typical for cruise machinists. The research on AI tools for cruise machinists aims to fill this gap by developing models that not only assess posture in real-time but are also optimized for the highly mobile maritime context. Existing methods, such as those using 3D view-invariant features, attempt to address viewpoint variations. However, on a cruise ship, the varied and confined spaces could present extreme variations in viewpoint, which demands even more sophisticated adaptation from the AI models. Our research aims to develop an AI system that effectively manages these extreme variations, ensuring accurate posture assessment from any angle. While existing studies lay a strong foundation for using technology in ergonomic assessments, the proposed research on AI tools for posture estimation among cruise machinists addresses several unmet needs. It offers novel contributions by tailoring AI capabilities to the distinctive and challenging environment of cruise ships, ensuring that posture evaluation is accurate, comprehensive, and adaptable to highly variable operational contexts.

3. Materials and Methods

Despite the growing integration of AI tools across various sectors, as resulting from the literature review, there remains a notable research gap in their application specifically for the training of cruise machinists. While AI has been leveraged for operational efficiency and safety in many industrial settings, its potential to enhance the training programs for cruise machinists has not been fully explored. This gap highlights an opportunity to develop and implement AI-driven solutions that could significantly improve the training processes, safety standards, and ergonomic practices for machinists on cruise ships.

The problem to be addressed is the absence of AI-enhanced training solutions for cruise machinists, leading to suboptimal training outcomes and compromised safety and efficiency in cruise ship operations. The objective of this research is to develop and implement AI-based training tools designed for cruise machinists, aimed at enhancing the effectiveness of their training, improving safety compliance, and increasing operational efficiency on cruise ships. In order to achieve this objective, the methodology part contains the development steps of an AI-based tool. The paper ends with a comparative analysis in order to give the best suited solution for the identified problem, as shown in Figure 1.
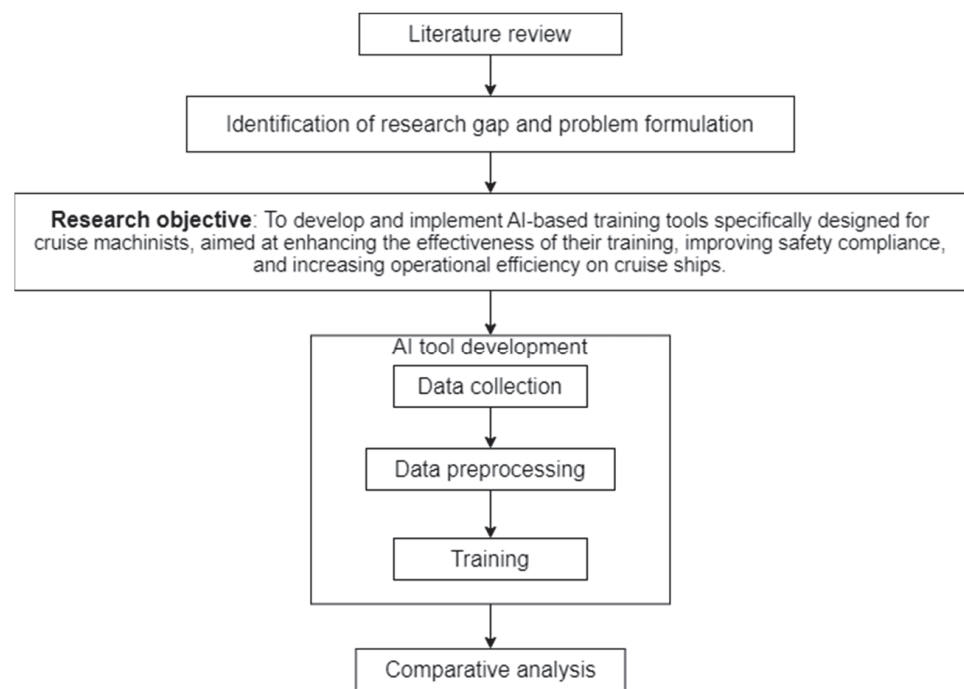
Figure 1. Methodology flowchart.

In this study, we employed pre-trained convolutional neural networks (CNNs) to recognize correct postures and positions during work for cruise machinists. Pre-trained CNNs are advantageous in this context due to their proven effectiveness in image recognition tasks, which allows for a significant reduction in the need for large amounts of labeled training data and diminishes training time. Leveraging these pre-existing networks that have been trained on vast and diverse datasets, such as ImageNet, enables the extraction of high-level features from the posture data captured by onboard cameras. These features are crucial for accurately categorizing postures as correct or incorrect based on ergonomic standards.

For this application, the selection of an appropriate pre-trained network is key, as it must efficiently handle the specific nuances of posture recognition in varied and dynamic maritime environments. The networks were fine-tuned on a smaller, domain-specific dataset composed of annotated images depicting various machinist lifting activities. This dataset included a range of postures captured under different conditions of lighting and background, mimicking the real-world scenario aboard cruise ships. The fine-tuning process involved adjusting the final layers of the networks so they become more specialized to the task-specific features of our ergonomic assessment criteria.

SqueezeNet offers an excellent model size and computational efficiency due to its use of squeeze and expand layers that reduce parameter count without a significant drop in accuracy. This makes SqueezeNet an attractive choice for deployment in environments where computational resources are limited, such as onboard systems on cruise ships. Despite its efficiency, SqueezeNet might struggle with lower accuracy in capturing highly detailed features compared to more complex models. Its performance can falter with very fine distinctions required in the ergonomic assessment of cruise machinists' postures.

GoogleNet, or Inception v1, introduces an inception module that uses different kernel sizes in the same layer, allowing it to capture information at various scales effectively. This ability makes GoogleNet particularly suitable for posture recognition, as it can detect details across diverse scenarios and varied scales, which are common in the unpredictable environments of cruise ships. The complexity of GoogleNet's architecture, while beneficial for feature detection, also means it requires more computational power and memory, potentially making it less ideal for deployment in resource-constrained onboard environ-

ments. Additionally, its complex structure may lead to longer training times during the fine-tuning phase.

Choosing the appropriate CNN architecture is critical in this project, balancing between computational efficiency and the ability to accurately recognize and analyze ergonomic postures. Each network offers distinct advantages and disadvantages, necessitating a careful consideration of the specific requirements and constraints of the setting. The analysis of these networks provides insights into optimizing model selection and tuning strategies to enhance posture recognition accuracy and operational efficiency aboard cruise ships.

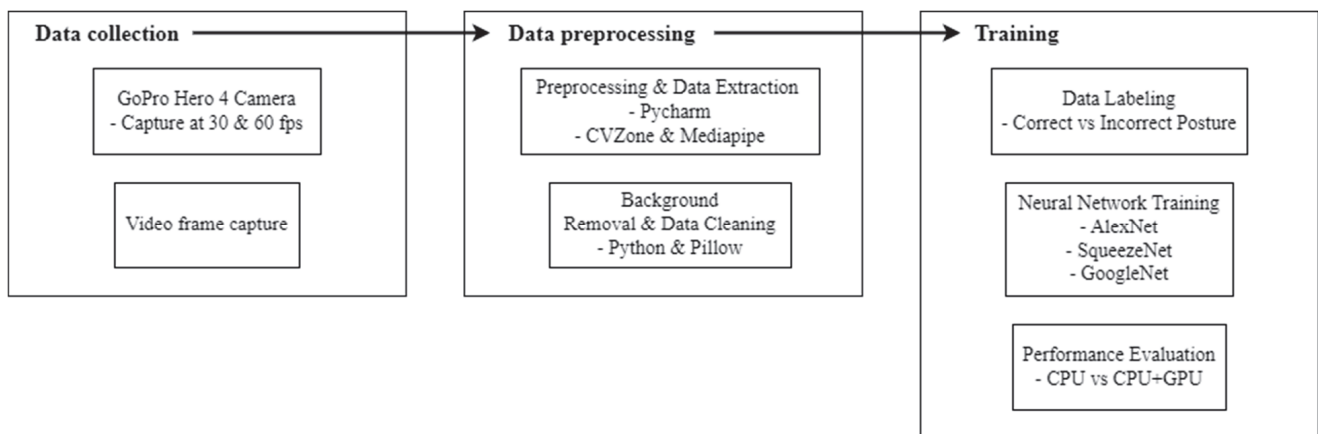In Figure 2 is presented the research flowchart that is further discussed.

Figure 2. Research flowchart.

Data Collection: The research started with data acquisition using a GoPro Hero 4 camera, which captured the activities of cruise machinists at frame rates of 30 and 60 frames per second (fps). This device was chosen for its ability to record high-definition video in 720p MP4 format, allowing for clear and precise capture of detailed movements essential for the analysis. The versatility of this camera supported our objectives to observe and document complex machinist operations under varying light and motion conditions. In designing the system, it was crucial to integrate both effective and efficient technological solutions. The software stack for this project was centered around Pycharm, which facilitated the development environment for scripting and testing. Essential libraries such as CVZone and Mediapipe were integrated within the Pycharm environment to handle the capture and initial processing of motion data from the video files. Libraries from MATLAB were also employed, guaranteeing compatibility across different operating systems, thus maintaining the system's technological edge without being hindered by hardware resource discrepancies.

Data Preprocessing: Following data collection, video frames were extracted and subsequently preprocessed (Figure 3). During this phase, each frame was processed through a Python (version 3.10.12) script which utilized non-intrusive techniques to extract 3D view-invariant relative joint positions and angles. This method ensured that the data remained independent of camera viewpoint variations, which is critical for accurate posture analysis in a dynamic environment. The application prototype used in this project incorporated the Python libraries within a script to refine the capture of worker motion. The motion data extracted then underwent a thorough cleaning process using another Python script leveraging the Pillow library. This script removed backgrounds from captured images, replacing them with a simplified 8-bit color (dark blue in our case) to enhance the clarity of the skeleton representation of the body positions. After the cleaning and extraction phase, each frame was analyzed to remove any with invalid data or missing elements. At this stage, all data were labeled into two categories: correct posture and incorrect posture. This labeled data then formed the basis for training the neural networks.
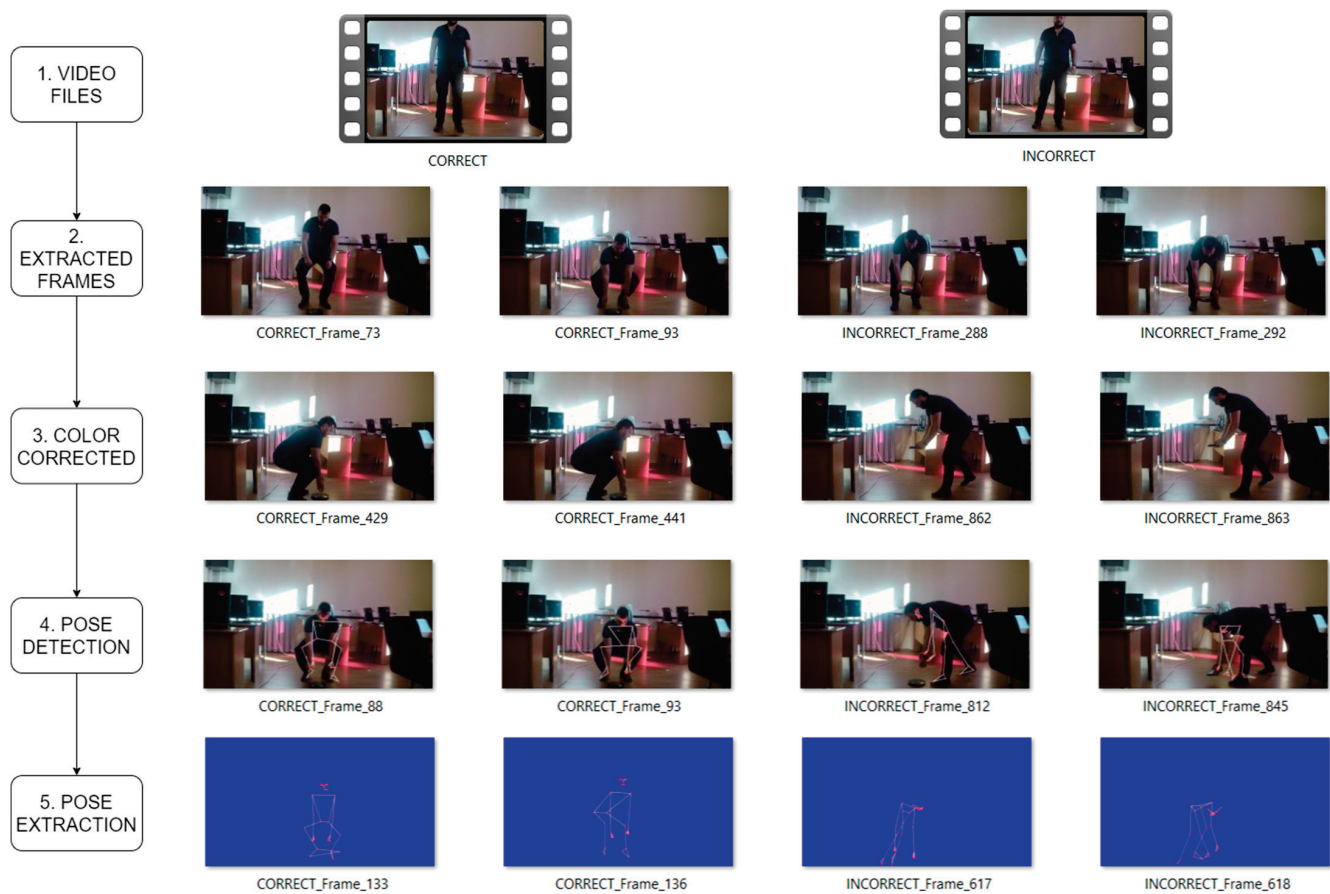
Figure 3. Dataset preprocessing flow.

Dataset Analysis: The dataset critical for our study comprised video footage specifically selected to capture a comprehensive array of postural dynamics of cruise machinists engaged in various lifting tasks. These activities were chosen for their relevance in assessing the ergonomic risks associated with routine maritime mechanical operations. To ensure the robustness and accuracy of the training data, a meticulous preprocessing protocol was followed. Initially, the raw video footage was processed to isolate key frames that accurately represent typical postures machinists assume during their work. This selection process was guided by both the frequency of specific postures in the footage and their significance from an ergonomic perspective. Subsequent to frame selection, a detailed annotation process was undertaken. Each frame was labeled as "CORRECT" or "INCORRECT" based on stringent ergonomic criteria developed by occupational health experts. These criteria were established based on current best practices in ergonomic assessments, ensuring that the labels reflect meaningful distinctions in posture quality that could impact machinist health and safety. The annotation process involved multiple expert reviewers to minimize subjectivity and enhance the reliability of the posture classifications. This dual-review system ensured that each frame's label was as objective as possible, providing a solid foundation for the subsequent machine learning training process. The consistency and accuracy of these labels are crucial, as they directly influence the learning outcomes of the neural network models. The labeled dataset not only serves as the basis for training our CNN models but also plays a critical role in validating their effectiveness in real-world ergonomic assessments.

Training: We employed the two pre-trained networks—SqueezeNet and GoogleNet—for their suitability to the task. SqueezeNet and GoogleNet demonstrated over 90% accuracy, confirming their effectiveness for the project's needs. Both networks were further trained

using configurations that employed just the CPU, as well as combinations of the CPU and GPU, to compare performance metrics under different computational loads.

SqueezeNet has a total of 18 layers, structured to maximize efficiency and performance. The architecture begins with a standard convolutional layer with 96 filters of size 7×7, followed by a ReLU activation and a max-pooling layer. This is followed by eight Fire modules, which consist of a squeeze layer and an expand layer. The Fire modules are arranged in the following sequence: Fire module 2, Fire module 3, Fire module 4 (followed by a max-pooling layer), Fire module 5, Fire module 6, Fire module 7 (followed by a max-pooling layer), Fire module 8, and Fire module 9. After the Fire modules, there is another convolutional layer with 1000 filters of size 1×1, followed by a ReLU activation. The architecture concludes with a global average pooling layer, which averages the spatial dimensions of the feature maps, and a softmax classifier that outputs the probability distribution over 1000 classes.

GoogleNet, also known as Inception v1, has a complex architecture with 22 layers, designed to achieve high performance in image classification tasks. The architecture begins with two standard convolutional layers followed by max-pooling layers. The core innovation of GoogleNet is the Inception module, which allows the network to capture multi-scale information by performing 1×1, 3×3, and 5×5 convolutions in parallel within each module, followed by a max-pooling layer. These outputs are concatenated along the channel dimension. The network includes nine Inception modules stacked linearly, interspersed with max-pooling layers to reduce the spatial dimensions. Following the Inception modules, the architecture ends with an average pooling layer, a dropout layer, a fully connected layer with 1000 units, and a softmax classifier for outputting the probability distribution over the classes. Additionally, GoogleNet includes auxiliary classifiers connected to intermediate layers to improve gradient flow and provide regularization during training. This design significantly reduces the number of parameters while maintaining high accuracy.

To modify SqueezeNet and GoogleNet to output two classes instead of their default number of classes, the final layers of each network were adjusted to accommodate binary classification. For SqueezeNet, modifying the last convolutional layer in the classifier section was necessary to change the output to two classes, ensuring that the network outputs two class scores by reducing the dimensionality of the feature maps to match the number of classes. Similarly, for GoogleNet (Inception v1), the adjustment involved editing the number of outputs in the final fully connected layer to output only two scores instead of the original 1000. This modification required unlocking and editing the final layer's configuration to reduce the number of class scores. Both networks were then fine-tuned on the new binary classification dataset to optimize performance for the new task.

This methodological approach not only ensured the high accuracy and relevance of the posture recognition system but also underscored the necessity for continuous technological adaptation and enhancement to meet and exceed the demanding standards of modern work ergonomics. By integrating advanced computational methods and machine learning techniques, this research illustrates the potential of AI-driven solutions to significantly improve occupational safety in dynamic environments such as those encountered by cruise machinists.

4. Experiment

4.1. Experiment Design

The central aim of this study was to assess and compare the efficacy of two advanced CNN models, SqueezeNet and GoogleNet, when trained across two different computational platforms: CPUs and GPUs. The objective focused on determining the optimal model and hardware combination for accurately estimating correct postures in cruise machinists, who are particularly susceptible to ergonomic risks due to the physically demanding nature of their work.

The dataset integral to this research was derived from video recordings that captured a broad spectrum of postural dynamics of cruise machinists engaged in lifting tasks.

Advanced image processing techniques were employed to preprocess this footage, enhancing frame quality and isolating the subjects from their environments. This involved segmentation to separate the subjects from the background, normalization to standardize the intensity of images, and augmentation to artificially expand the dataset under varied conditions, simulating real-world scenarios.

Each frame extracted during preprocessing was meticulously annotated as "CORRECT" or "INCORRECT", based on ergonomic guidelines provided by occupational health experts. This annotation was crucial for training the models to recognize and differentiate between ergonomically safe and risky postures. A total of 1006 data points were annotated, with a distribution of 559 labeled as "CORRECT" and 447 as "INCORRECT" (Figure 4). This data formed the backbone of our analysis, serving as the basis for training and validating the CNN models.
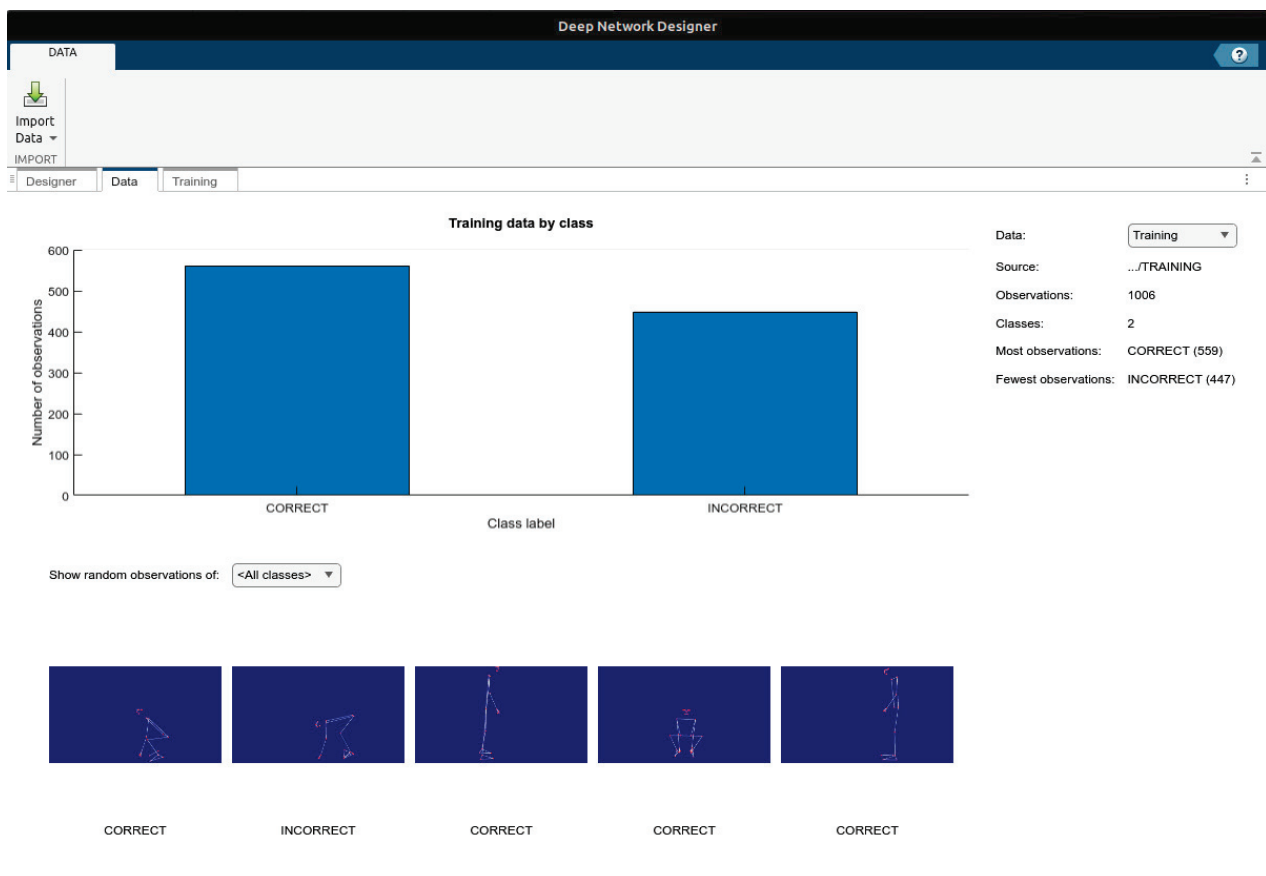

Figure 4. Dataset analysis.

Both SqueezeNet and GoogleNet were subjected to structured training and validation phases. Each model was trained on 80% of the data and validated on the remaining 20%. The training was conducted with batch sizes and learning rates adjusted according to the computational limits of the CPUs and GPUs to ensure consistent learning conditions. The models underwent training over multiple epochs, ceasing only when no significant improvement in validation accuracy was observed, to prevent overfitting and to ensure comprehensive learning.

The experiment utilized mid-range to high-end commercial CPUs and GPUs to reflect a realistic work scenario. This choice was intended to provide insights applicable to potential real-world applications and to test the models under conditions that might be encountered in an actual work setting.

The performance of each model was systematically evaluated using a variety of metrics including accuracy, precision, recall, and F1-score. These metrics were chosen to provide a

holistic view of each model's capability to accurately classify postures as "CORRECT" or "INCORRECT". Additionally, training efficiency was assessed by monitoring the duration and computational resource utilization during the model training sessions.

To facilitate a detailed analysis of the training outcomes, the Deep Network Designer software (version 23.2) was employed. This tool helped visually represent the structure and distribution of the dataset, as well as the training progress of each model, enabling a comprehensive evaluation of the models' performance across different computational platforms.

We employ the Cross-Entropy Loss as our loss function because our task involves classification. This function evaluates the model's performance by comparing the predicted labels with the actual labels. The general formula for Cross-Entropy Loss is:

$$J = -\frac{1}{N} \sum_{i=1}^{N} \sum_{c=1}^{C} y_{ic} \log(\widehat{y}_{ic}) \tag{1}$$

where

N represents the total number of samples in the current batch;
C represents the total number of classes in the classification problem;
y_{ic} is a binary indicator that is 1 if the actual class of sample i is c, and 0 if it is not, and essentially marks the true label of each sample;
$\widehat{y}_{ic}$ is the predicted probability that the model assigns to the sample i being in class c. These probabilities are the output of a softmax function at the final layer of the network.

For our models, the formula for Cross-Entropy Loss is defined as:

$$J = -\frac{1}{10} \sum_{i=1}^{10} (y_{i1} \cdot \log(\widehat{y}_{i1}) + y_{i2} \cdot \log(\widehat{y}_{i2})) \tag{2}$$

We use as optimizer Stochastic Gradient Descent with Momentum (SGDM), that is an optimization algorithm used for training neural networks, namely a variant of gradient descent where the model parameters are updated using a small subset (mini-batch) of the training data, rather than the entire dataset. This approach helps in speeding up the training process and allows for more frequent updates of the model parameters. The momentum is an enhancement to the basic SGD algorithm that helps accelerate the convergence of the training process. It does this by adding a fraction of the previous update to the current update. This helps in smoothing out the oscillations in the gradients and leads to faster convergence.

In mathematical terms, the update rule for SGD with momentum uses the following formulas:

$$v_{t+1} = \mu v_t - \alpha \nabla_\theta J(\theta_t) \tag{3}$$

$$\theta_{t+1} = \theta_t + v_{t+1} \tag{4}$$

where

v_t is the accumulated past gradients, scaled by the momentum coefficient, and helps to smooth out the gradient updates and accelerates convergence;
μ is the momentum coefficient that determines the contribution of the past gradients, for which the value in our models is 0.9;
α is the learning rate, which controls the size of the steps taken towards the minimum of the loss function, for which the value in our models is 0.001;
$\nabla_\theta J(\theta_t)$ is the gradient of the loss function with respect to the parameters θ at the current time step t and indicates the direction and rate of change of the loss function;
θ_t represents the current values of the model parameters;
θ_{t+1} represents the updated values of the model parameters after applying the velocity term.

This experimental design was crafted to rigorously assess the implications of each model's performance across varied hardware setups. By aligning the experimental ap-

proach closely with practical demands, this study aims to significantly advance the application of AI in enhancing occupational health and safety standards, providing valuable insights for the deployment of AI-driven posture estimation tools in work environments.

4.2. Experiment Implementation

For SqueezeNet, the training dashboard visualizations were instrumental in monitoring the model's progress and efficacy throughout the training phase on a GPU, as depicted in Figure 5. The accuracy trends, initially starting at lower levels, showed a consistent increase across iterations, eventually stabilizing above 90%. This upward trajectory in both training and validation accuracies, highlighted by circular indicators at significant points, emphasized the model's capacity to generalize well beyond the training data, achieving a final validation accuracy of 91.32%.

Figure 5. Training SqueezeNet on GPU.

Parallel to this, the loss trends presented in the lower graph of the dashboard and in Table 1 delineated a continuous decrease in both training and validation loss, indicating effective learning and model convergence. The model underwent a rigorous training regimen, consisting of 32 epochs with 114 iterations each, culminating in a total of 3648 iterations. This training was executed efficiently on a single GPU, taking approximately 15 min and 57 s, underscoring the GPU's capacity to facilitate rapid computational processing.

Table 1. Final losses.

	SqueezeNet on CPU	SqueezeNet on GPU	GoogleNet on CPU	GoogleNet on CPU
Final training loss	0.6	0.5	0.25	0.3
Final validation loss	0.4	0.4	0.2	0.25

In contrast, the training dashboard for SqueezeNet on a CPU, shown in Figure 6, documented a notably higher final validation accuracy of 95.14%. This improvement suggests that the extended training duration, which totaled 44 min and 51 s, allowed for more thorough optimization of model weights, despite the inherently slower processing capabilities of CPUs.
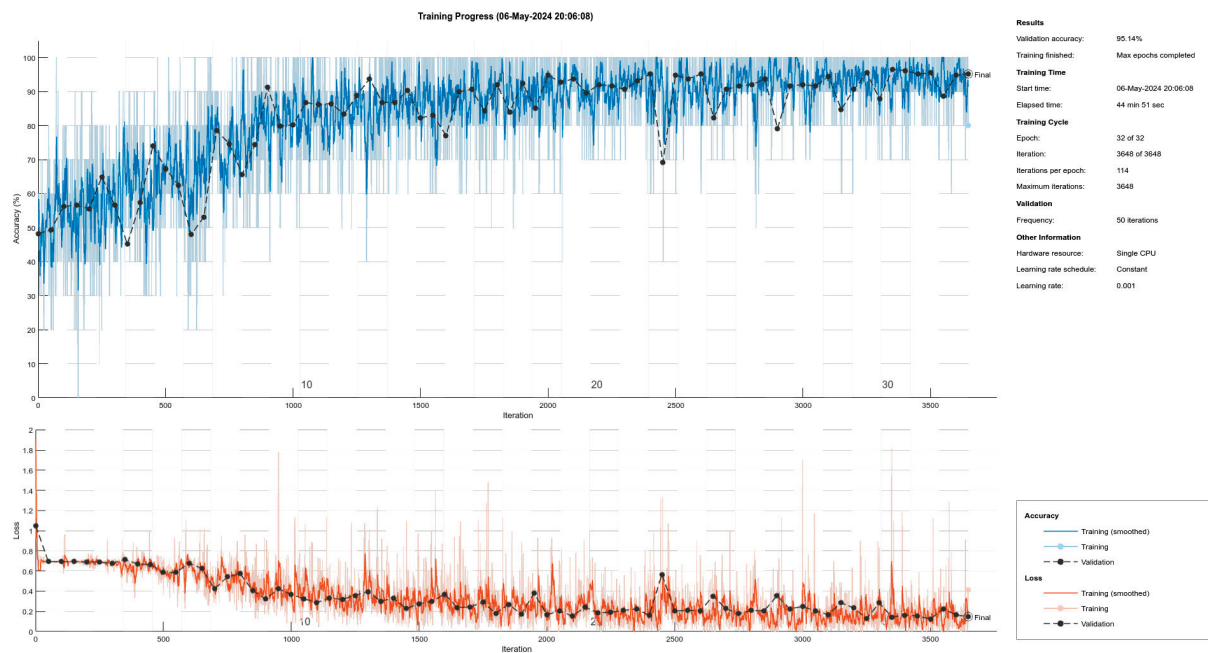
Figure 6. Training SqueezeNet on CPU.

The loss metrics for the CPU model (Table 1) similarly demonstrated a steady decline, mirroring the GPU's performance but with the added benefit of achieving a higher validation accuracy. This points to the CPU's effectiveness in handling deep learning tasks where precision is important, albeit at a slower pace.

The training of GoogleNet provided further insights into the performance disparities between CPU and GPU environments. As shown in Figure 7, the GPU-trained GoogleNet model displayed a quick improvement in validation accuracy, peaking at 97.22% within just 19 min and 26 s. The loss trends followed a declining trajectory, consistent with an effective learning process (Table 1).
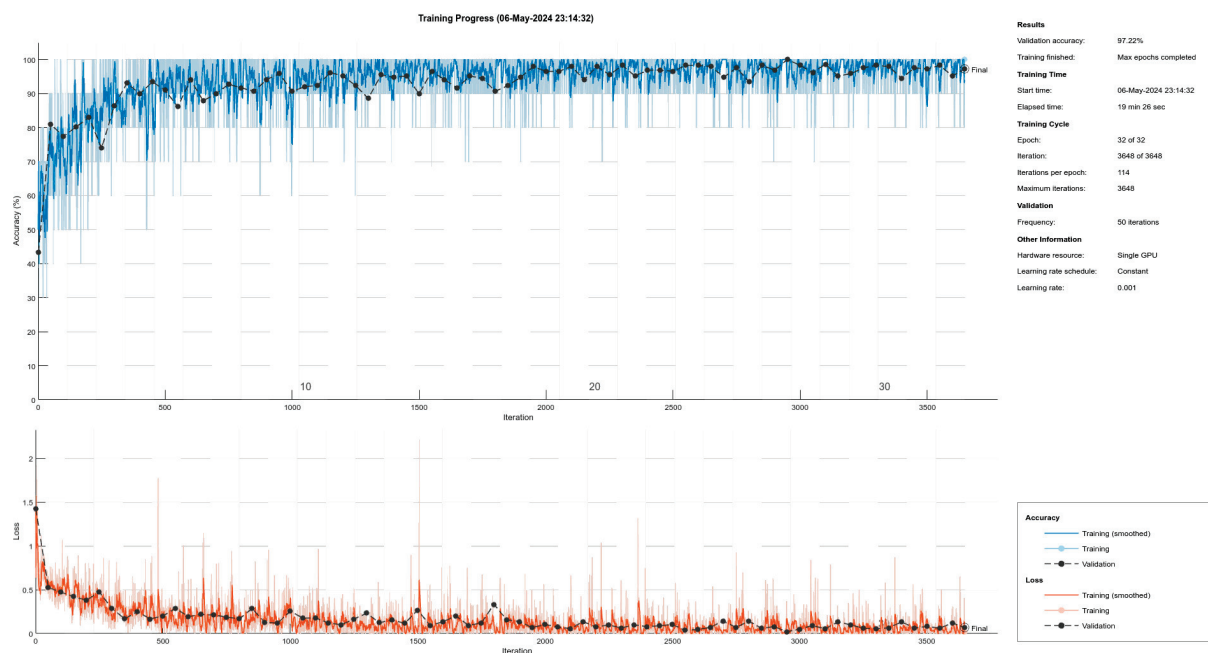

Figure 7. Training GoogleNet on GPU.

Conversely, as illustrated in Figure 8, the GoogleNet model trained on a CPU achieved a slightly higher validation accuracy of 97.57%, albeit over a considerably longer duration of 89 min and 29 s. This extended period allowed for deeper model refinement, which was particularly evident in the stabilization of accuracy and loss rates at the later stages of training (Table 1).
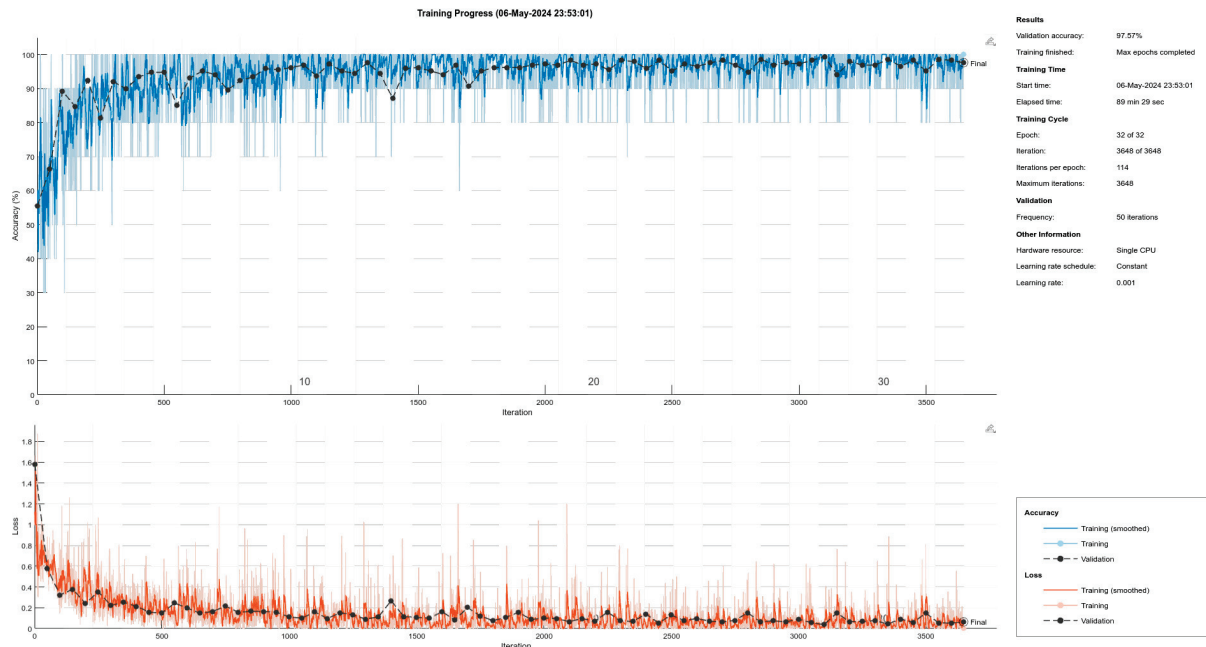

Figure 8. Training GoogleNet on CPU.

The experiment underscored the critical trade-offs between training on CPUs and GPUs. While GPUs offered speed and efficiency, CPU training resulted in marginally higher accuracies, demonstrating the importance of selecting hardware based on specific performance needs and time efficiencies. This comparative analysis between the computational platforms provides essential insights into the deployment strategies for deep learning models, emphasizing the need to balance speed, scalability, and precision based on available resources and project requirements.

This experiment not only highlighted the strengths and limitations of each model across different hardware but also reinforced the significance of strategic hardware selection in optimizing deep learning implementations for practical, real-world applications.
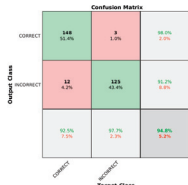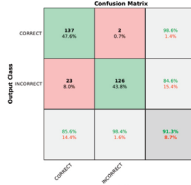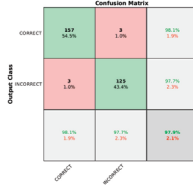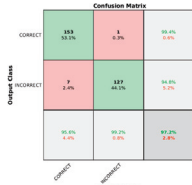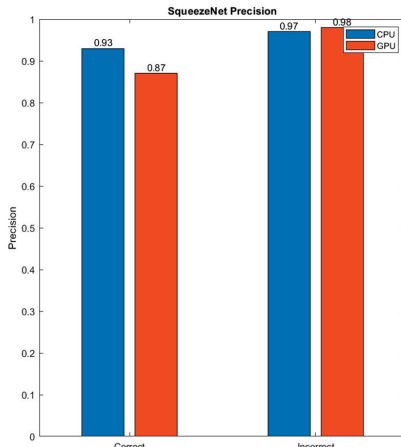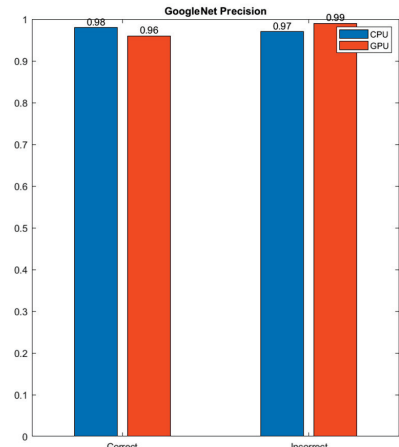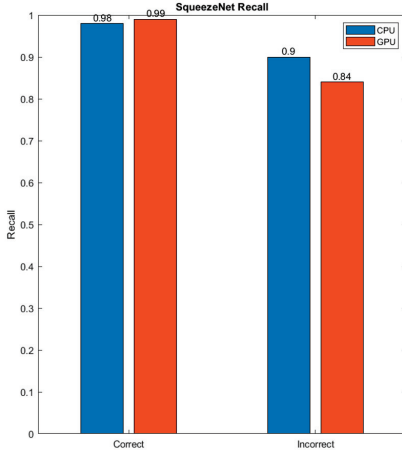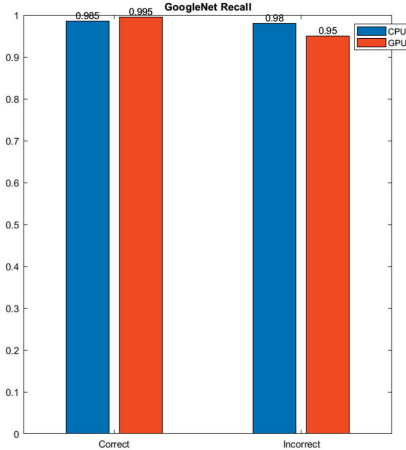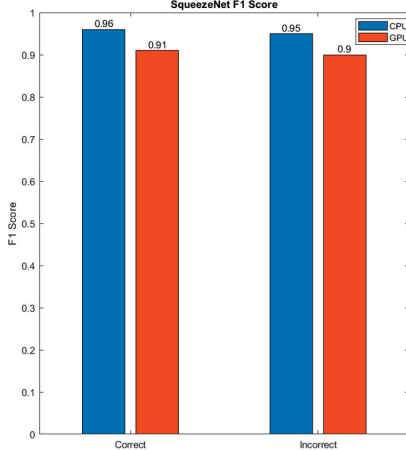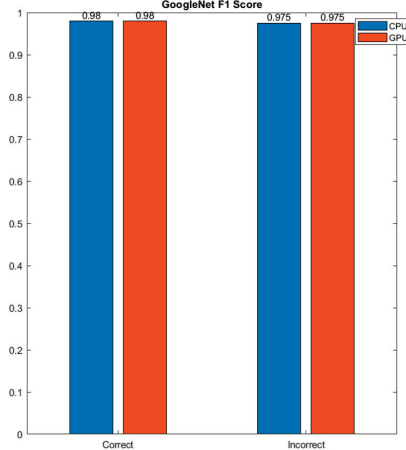
5. Results and Findings

In the evaluation phase of our study, the performance of the two types of pre-trained CNNs, SqueezeNet and GoogleNet, was assessed. These networks were trained on both GPU and CPU hardware settings to determine their efficacy and efficiency under different computational conditions. An overview of the comparison of the performance of the two CNNs based on the resulting metrics is presented in Table 2, followed by detailed comparative analysis.

5.1. Comparative Analysis of SqueezeNet Training on CPU and GPU

This evaluation specifically focuses on various metrics including the confusion matrix, precision, recall, and F1-score for each class (Table 2). This analysis is critical, as it helps identify the optimal operational conditions for the SqueezeNet model, ensuring that it is not only efficient in terms of computational resource usage but also maintains high accuracy in practical applications. Through this investigation, we seek to understand the trade-offs involved in deploying deep learning models across different hardware platforms, providing insights into how each platform supports the model's ability to classify accurately and reliably.

Table 2. Performance comparative metrics.

	SqueezeNet on CPU	SqueezeNet on GPU	GoogleNet on CPU	GoogleNet on CPU
Confusion matrix				
Precision				
Recall				
F1-Score				
Training time	44 min 51 s	15 min 57 s	89 min 29 s	19 min 26 s
Training accuracy	95.14%	91.32%	97.57%	97.22%

The confusion matrices offer a detailed view into the performance of the SqueezeNet CNN trained on two different hardware setups: CPU and GPU. These matrices are critical for understanding not just the overall accuracy but also the model's ability to correctly classify observations into either the "CORRECT" or "INCORRECT" class.

The comparison between the two hardware platforms indicates some crucial differences. The CPU seems to provide a balanced performance, achieving high accuracy in classifying both "CORRECT" and "INCORRECT instances. This balance might be due to the CPU's ability to manage the training process more steadily over time, allowing for more stable learning dynamics. On the other hand, the GPU, despite its faster processing capabilities and ability to handle more extensive data manipulations efficiently, shows a tendency to yield slightly lower precision in classifying "INCORRECT" cases.

Both training environments show high overall accuracy, but the choice between CPU and GPU may depend on specific requirements of the classification task. For applications where minimizing false positives is crucial, CPU-based training might be preferable due to its slightly better balance in handling both classes. In scenarios where speed and handling large datasets are more critical, and slight variations in false-positive rates are acceptable, GPU-based training would be advantageous. This analysis demonstrates the importance of selecting the appropriate hardware based on the specific performance metrics crucial to the task's success.

The evaluation of the SqueezeNet model trained on both CPU and GPU platforms reveals consistency in performance across various metrics—specifically, precision, recall, and F1-score. This analysis compares these key performance indicators to assess how each training environment affects the model's ability to accurately classify observations into "CORRECT" and "INCORRECT" classes.

In terms of precision, both models show slightly higher scores for the "INCORRECT" class compared to the "CORRECT" class. This suggests that both the CPU and GPU models are marginally better at correctly identifying negative instances without mistakenly classifying positive instances as negative.

Regarding recall, both the CPU and GPU models demonstrate higher recall scores for the "CORRECT" class compared to the "INCORRECT" class. This indicates a tendency of both models to capture a majority of the actual "CORRECT" instances, albeit at the risk of missing some "INCORRECT" instances.

Both the CPU and GPU-trained models exhibit high F1 scores for each class, nearing 1.0. This indicates a well-balanced performance, where both models effectively handle the classification tasks with minimal disparity between the classes. The similar F1 scores across both platforms suggest that regardless of the computational power, the model maintains a robust balance between precision and recall, ensuring effective overall performance. The consistency in performance metrics across CPU and GPU training suggests that SqueezeNet is relatively stable and not overly sensitive to the underlying hardware when it comes to classification accuracy. Both platforms manage to sustain a balance between identifying true positives and avoiding false positives, albeit with slight variations in their precision and recall rates across different classes.

Given the specific requirements of the application, which involve identifying and flagging incorrect lifting positions of heavy objects, and considering the evaluated metrics, SqueezeNet trained on a CPU demonstrates superior results. This finding underscores the model's robustness in accurately detecting and classifying incorrect postures, an essential feature for enhancing workplace safety and reducing ergonomic risks among workers engaged in physically demanding tasks.

5.2. Comparative Analysis of GoogleNet Training on CPU and GPU

This comparative analysis is essential for understanding how each platform influences the model's accuracy and its ability to classify instances into "CORRECT" and "INCORRECT" categories efficiently. Through this examination, we seek to highlight the strengths

and limitations of each training setup, providing insights into the optimal deployment scenarios for the GoogleNet model based on specific performance criteria.

The confusion matrices for GoogleNet trained on CPU and GPU provide insightful data into the performance characteristics of each hardware environment. Analyzing these matrices helps to understand how each platform handles the classification of "CORRECT" and "INCORRECT" classes under similar training conditions but different computational resources (Table 2).

The confusion matrix from the model trained on a CPU shows a higher overall accuracy compared to the GPU, with a very high correct classification rate for both "CORRECT" and "INCORRECT" classes. These results indicate a strong performance with minimal error rates, suggesting that CPU training, despite generally being slower, can achieve high accuracy in classification tasks.

Conversely, the GPU-trained model, while also performing well, exhibited a slight decrease in accuracy. The overall pattern suggests that while the GPU model is very effective in correctly identifying "INCORRECT" instances, it is slightly less reliable for "CORRECT" classifications compared to the CPU model.

In both cases, the models show very low false-positive rates for the 'INCORRECT' class, which is crucial in applications where it is important not to mistakenly label an instance as "INCORRECT". However, the GPU model seems to be more prone to false negatives in the "CORRECT" class than the CPU model.

Both the CPU and GPU-trained models exhibit very high F1 scores close to 1.0 for both classes. This indicates an excellent balance of precision and recall, suggesting that the models are well-tuned and perform robustly in distinguishing between "CORRECT" and "INCORRECT" classifications. The consistency of high F1 scores across both hardware platforms highlights the model's capacity to maintain performance stability regardless of the computational environment.

In terms of precision, both models demonstrate high accuracy, with scores nearing perfection. Notably, both models exhibit slightly higher precision for the "INCORRECT" class compared to the "CORRECT" class. This trend suggests that both the CPU and GPU models are particularly effective at avoiding false positives when identifying "INCORRECT" instances, which is crucial for applications where the cost of incorrectly rejecting a correct instance is high.

As for recall, both models again perform very well, with the "CORRECT" class showing marginally higher recall than the "INCORRECT" class.

The parallel performance of GoogleNet across the CPU and GPU environments in terms of precision and recall underscores a consistent model behavior, which is an excellent indicator of the model's robust generalization capabilities. Both models manage to achieve high precision and recall, ensuring that the trade-offs between these metrics are minimized. This consistency is especially noteworthy given the different processing powers and architectures of CPUs and GPUs, which can often lead to variations in training dynamics and outcomes.

Considering the specific needs of the application along with the performance metrics obtained, GoogleNet trained on a GPU emerges as the more suitable option, due to the shorter training time. This approach leverages the GPU's capability to handle the model's complexity effectively, ensuring optimal performance in accurately identifying critical postural assessments, which is crucial for the application's success.

Moreover, the dataset comprises 1006 images, of which 559 are labeled as "CORRECT" and 447 as "INCORRECT". This represents a slight imbalance, with approximately a 10% difference between the two classes. Observations during training indicate that this imbalance does not adversely affect the F1 score of the models, and the difference in accuracy between the two classes remains below 5% across most configurations. An exception was noted with the SqueezeNet model trained on a GPU, where the accuracy for the "INCORRECT" class was nearly 15% higher than that for the "CORRECT" class. Despite the minor discrepancy in the number of images between the classes, this imbalance

does not negatively impact the precision of the models. This finding underscores the robustness of the training process and the models' ability to handle slight variations in class distribution effectively.

6. Conclusions

Lifting heavy objects is the most widespread activity among cruise ship crews, and the integration of AI tools into the training protocol is a significant advancement in promoting safe and efficient work practices.

The current training protocol for cruise machinists includes both demonstration and practical exercises. Simply put, a qualified instructor demonstrates the correct technique for lifting heavy objects, such as a toolbox. The instructor stands with feet a shoulder-width apart, positions themselves close to the object, and bends their knees slightly while keeping the back straight and head up. They then lift the object using leg strength, keeping it close to the body. Following this demonstration, each machinist practices lifting a similar object, receiving real-time feedback and corrections to ensure proper form and technique. This hands-on approach enables machinists to apply the principles demonstrated, fostering the development of muscle memory essential for safe lifting practices. Supervision is provided by a certified safety instructor or an experienced crew member with specialized training in ergonomics and heavy lifting techniques.

The newly developed AI tool enhances this training protocol by providing additional, complex support. It can observe and analyze the posture of multiple machinists simultaneously across different workstations, offering instant feedback and corrective advice. This capability allows the AI tool to effectively augment the role of safety instructors, enabling more comprehensive and efficient training sessions. By integrating this AI technology, the training process not only becomes more scalable but also gains a higher level of precision in monitoring and improving the ergonomic practices of crew members.

When comparing the performance of SqueezeNet trained on a CPU and GoogleNet trained on a GPU for the task of identifying incorrect lifting postures by cruise machinists, several distinctions emerge that are crucial for application-specific decisions. Both models exhibit high levels of accuracy and F1-scores, demonstrating their robustness in classification tasks. However, GoogleNet on a GPU shows a particularly strong performance, making it the preferable choice for activities involving the lifting of heavy objects.

While SqueezeNet offers consistent performance across both CPU and GPU platforms and excels in environments with limited computational resources due to its efficient architecture, it does not match the slightly superior metrics achieved by GoogleNet. Specifically, GoogleNet's recall for the "CORRECT" class is notably higher, suggesting its enhanced capability to capture all relevant instances without missing many. This feature is vital in settings where missing a correct instance could result in increased risk of injury, making high recall an essential metric.

In terms of training efficiency, GoogleNet, despite its complex architecture requiring longer training times on CPUs, benefits significantly from the accelerated processing capabilities of GPUs. This harnessing of GPU capabilities allows GoogleNet to maintain high precision and accuracy, crucial for the demanding requirements of ergonomics in occupational health. On the other hand, the quicker training times of SqueezeNet, while advantageous in constrained environments, may not always meet the stringent accuracy requirements needed for precise ergonomic assessment.

The higher validation accuracy and precision of GoogleNet when trained on a GPU confirm its suitability for critical applications where the stakes of incorrect classification are high, such as in ensuring the safety of cruise machinists during heavy lifting tasks. Thus, for projects where accuracy and the ability to handle complex scenarios are paramount, and where computational resources allow, GoogleNet on a GPU stands out as the better option, outweighing the benefits of SqueezeNet's speed and efficiency in resource-constrained settings. This analysis highlights the importance of aligning the model selection and

training platform with specific operational goals and constraints, ensuring the deployment of the most effective AI solution for the task at hand.

The study presented significant insights into the use of AI for posture evaluation, yet it also revealed certain limitations that could direct future research efforts. One of the primary limitations involves the image preprocessing technique which renders the skeletal outline against a blue background. This blue background, while visually distinct, occupies a significant portion of the image. The extensive presence of this uniform background could potentially slow down the process by including many irrelevant elements when discriminating between "CORRECT" and "INCORRECT" postures. Such a background might inadvertently influence the AI's learning and operational efficiency, as the system spends computational resources processing areas of the image that do not contribute to posture analysis.

Additionally, the potential for generating false "INCORRECT" results in scenarios where a subject is standing with a slight forward lean due to an anatomically poor posture poses a challenge. This misclassification can lead to incorrect training or feedback, potentially reinforcing bad habits rather than correcting them. This limitation underscores the need for more refined posture recognition capabilities that can differentiate between intentional poses and those resulting from an individual's physical limitations.

Regarding the dataset, its enhancement could significantly improve the model's accuracy. Currently, the dataset could benefit from including a broader range of images capturing a variety of subjects interacting with different types of objects varying in shape, size, and weight. Expanding the dataset in this manner would not only provide a richer set of training data but also enhance the model's ability to generalize across real-world scenarios, which is critical for the robust performance of AI systems in diverse operational settings.

Looking forward to further research, there are several paths to explore. One potential improvement could involve the enhancement of the image preprocessing step. This could include thickening the lines that form the subject's outline in the images, which may aid in more accurate and efficient feature extraction by the AI. Additionally, incorporating an algorithm for a bounding box that isolates only the part of the image containing the outline could streamline the processing. This modification would ensure that the AI focuses solely on the relevant features of posture, thereby improving both the speed and accuracy of the posture evaluation process. Such advancements would address the current limitations and deploy more effective and efficient AI tools for ergonomic assessment in various industrial settings.

References

1. Abdallah, S.; Genaidy, A.; Karwowski, W.; Shell, R.; Sonbol, A.; Ravelo, E. Theoretical basis for general lifting equations based on mechanical work performed during manual lifting. *Theor. Issues Ergon. Sci.* **2007**, *8*, 551–564. [CrossRef]
2. Armstrong, D.P.; Makhoul, P.J.; Sinden, K.E.; Fischer, S.L. Ranking stretcher and backboard related paramedic lifting tasks based on their biomechanical demand on the low back. *IISE Trans. Occup. Ergon. Hum. Factors* **2019**, *7*, 9–19. [CrossRef]
3. Brandt, M.; Madeleine, P.; Samani, A.; Jakobsen, M.D.; Skals, S.; Vinstrup, J. Accuracy of identification of low or high risk lifting during standardised lifting situations. *Ergonomics* **2017**, *61*, 710–719. [CrossRef] [PubMed]
4. Capodaglio, E.M. Participatory ergonomics for the reduction of musculoskeletal exposure of maintenance workers. *J. Occup. Environ. Hyg.* **2020**, *17*, 376–386. [CrossRef] [PubMed]
5. Cholewicki, J.; McGill, S.M. Mechanical stability of the in vivo lumbar spine: Implications for injury and chronic low back pain. *Clin. Biomech.* **1996**, *11*, 1–15. [CrossRef] [PubMed]
6. Jensen, R.L.; Ebben, W.P. Acute effects of plyometric exercise on maximum squat performance in male athletes. *J. Strength Cond. Res.* **2003**, *17*, 68–71.
7. Johnson, L.; Williams, K. Evaluating the effectiveness of safety protocols for cruise ship machinists. *Safety Sci.* **2019**, *117*, 123–132.
8. Kim, H.-K.; Zhang, Y. Estimation of lumbar spinal loading and trunk muscle forces during asymmetric lifting tasks: Application of whole-body musculoskeletal modelling in OpenSim. *Ergonomics* **2016**, *59*, 563–576. [CrossRef] [PubMed]
9. Kulkarni, V.S.; Devalkar, R.V. Postural analysis of building construction workers using ergonomics. *Int. J. Constr. Manag.* **2018**, *18*, 464–471. [CrossRef]
10. Lee, S.; Park, J. AI-based training for maritime workers: A virtual reality approach. In Proceedings of the International Conference on Intelligent Transportation Systems (ITSC), Macau, China, 8–12 October 2021; pp. 1234–1239.
11. Li, L.; Martin, T.; Xu, X. A novel vision-based real-time method for evaluating postural risk factors associated with musculoskeletal disorders. *Appl. Ergon.* **2020**, *87*, 103138. [CrossRef] [PubMed]
12. Liu, J.; Qu, X.; Liu, Y. Influence of load knowledge on lifting biomechanics. *J. Occup. Environ. Hyg.* **2022**, *19*, 230–235. [CrossRef] [PubMed]
13. Ngo, B.P.T.; Yazdani, A.; Carlan, N.; Wells, R. Lifting height as the dominant risk factor for low-back pain and loading during manual materials handling: A scoping review. *IISE Trans. Occup. Ergon. Hum. Factors* **2017**, *5*, 158–171. [CrossRef]
14. Paquet, V.; Punnett, L.; Woskie, S.; Buchholz, B. Reliable exposure assessment strategies for physical ergonomics stressors in construction and other non-routinized work. *Ergonomics* **2007**, *50*, 1200–1219. [CrossRef] [PubMed]
15. Pascual, S.A.; Naqvi, S. An investigation of ergonomics analysis tools used in industry in the identification of work-related musculoskeletal disorders. *J. Occup. Environ. Hyg.* **2015**, *5*, 237–245. [CrossRef] [PubMed]
16. Schneider, S.; Grant, K.A.; Habes, D.J.; Bertsche, P.K. Ergonomics: Lifting hazards at a cabinet manufacturing company: Evaluation and recommended controls. *Appl. Occup. Environ. Hyg.* **1997**, *12*, 253–258. [CrossRef]
17. Smith, J.; Jones, M. Work-related injuries among cruise ship machinists. *J. Occup. Environ. Med.* **2020**, *62*, 345–352.
18. Zhang, H.; Yan, X.; Li, H. Ergonomic posture recognition using 3D view-invariant features from a single ordinary camera. *Autom. Constr.* **2018**, *93*, 233–243. [CrossRef]
19. Zhao, J.; Obonyo, E. Applying incremental Deep Neural Networks-based posture recognition model for ergonomics risk assessment in construction. *Adv. Eng. Inform.* **2021**, *50*, 101374. [CrossRef]

MDPI

Article

Analysis and Prediction of Spring-Back in Cylindrical Helical Springs Using Analytical and Numerical Models

Nicola Zani and Luigi Solazzi *

Department of Mechanical and Industrial Engineering, University of Brescia, Via Branze, 38, 25123 Brescia, Italy; nicola.zani@unibs.it
* Correspondence: luigi.solazzi@unibs.it; Tel.: +39-030-3715577

Abstract: This research focuses on cylindrical helical springs with circular cross-sections made from carbon steel (SH 0.82% C) and stainless steel (AISI 302). The transformation from a linear bar to a circular spiral involves numerous factors such as material mechanical behavior, stress–strain relationships and residual stresses. This research investigates the spring-back phenomenon, which affects the final diameter of helical springs post-manufacture, using analytical, experimental and numerical methods. An analytical model, derived from the mechanical bending process, was proposed to predict spring-back, and its accuracy was validated against experimental data. This study also employed finite element simulations to analyze elastic recovery, confirming the analytical predictions. Results indicated that the spring-back ratio k could be expressed as an exponential function of the spring index C (the ratio between the final diameter of the spring D_2 and the diameter of the wire D_W), with a maximum error of 4.80% for stainless steel and 3.62% for carbon steel. This study's findings provide valuable insights into optimizing the spring manufacturing process, enhancing the precision of spring diameter predictions, and potentially reducing production errors and material waste.

Keywords: helical springs; elastic recovery; finite element models

1. Introduction

Springs are one of the most important components used in various industrial applications. Broadly speaking, it can be said that there are no machines that do not utilize this component. The primary applications of springs include addressing vibration-related problems to reduce dynamic effects, preventing shock loads, applying force in a specific pattern, and more.

For the purposes mentioned above, numerous types of springs are used in the automotive sector. For example, Salah [1] discussed the design of coil springs for automotive suspension systems, while Solazzi [2] presented the design of a torsion spring bar for the cab suspension system of an industrial vehicle.

One of the most important parameters in the design of springs is the evaluation of their dynamic behavior, which is related to both the natural frequencies of vibration and the displacement of the spring under a specific load. This aspect is crucial because it can either increase or decrease the displacement or transmission force between the two elements connected by the spring [3–5].

The static axial load also influences the magnitude of natural frequencies [6]. The design problem of coil springs, particularly the estimation of deflections or the stress state of the wire, is highly complex due to its nonlinear nature [7]. This can be evaluated using analytical or numerical methods [8–10]. Recently, to reduce component weight, innovative materials have been introduced for the construction of coil springs [11–13].

Both the design and manufacturing processes of coil springs are very complicated. This complexity arises because the process begins with a linear straight bar that is transformed

into a circular spiral, forming the coil spring. This process involves many factors, such as the mechanical behavior of the material, including the stress–strain curve (particularly Young's modulus and yield stress [14], plasticity, and residual stress [15,16]. Additionally, whether the material exhibits kinematic or isotropic hardening [14] significantly affects the mechanical behavior.

Helical compression springs for automotive suspensions are made using either cold coiling or hot coiling processes. In hot coiling, steel wire is heated above the austenitizing temperature, coiled, quenched, and tempered, which can cause decarburization and surface scaling, detrimental to fatigue performance. In cold coiling, wire is coiled at room temperature, preset with torsion residual stress, and shot peened, avoiding decarburization and scaling since stress relief occurs below the austenitizing temperature. Optimizing stress management in springs involves balancing stress relief temperature, wire strength, shot peening intensity, and presetting conditions. Understanding the effects of each processing step on residual coiling stresses is essential for achieving optimal residual stress in helical springs. Kobelev [16] presented a model to simulate residual stresses in helical springs due to pre-setting, using the deformational theory of plasticity. It provided analytical formulas to assess residual stresses, changes in spring shape, and pre-setting force over spring travel. The method allowed expressing torque as a function of spring travel and residual stresses in a closed form. The analysis included elastic–plastic bending and torsion, offering closed-form solutions for preset moments and elastic spring-back.

There is little literature on experimental measurements of spring-back in helical springs and its analytical prediction based on experimental values. In this paper, we focused on cylindrical helical springs with circular cross-sections made of two different steels. The bending theory of plates was applied to verify its applicability in spring production. In plate production, elastic recovery can simply be measured as the variation in the angle between the bent part before and after recovery, in relation to the angle produced by the tool, or by the ratio of these angles. Numerous diagrams allow manufacturers to account for recovery in sheet production, typically reporting the recovery with respect to the ratio between the angle after recovery and plate thickness. Marciniak [17] and Gardiner [18] first proposed an analytical solution to predict elastic recovery, but they only hypothesized a perfectly plastic elastic behavior. Gonzalez-Coleo et al. [15] later introduced a model that considered hardening after yielding. The main drawback of these studies is that they are based on the elastic curve formulation, which is consistent with small thickness geometries; indeed, in these studies, the error in the estimation of recovery increased with increasing sheet thickness. Furthermore, larger thicknesses are affected by different hardening areas that are not considered in the models.

In this article, the bending theory of plates is used to predict the elastic recovery of cylindrical springs with circular cross-sections. First, the machine used to produce these springs will be described, and data will be collected for different sizes and two materials. Then, a model for estimating recovery will be proposed, and the equation proposed in [15] will be validated. Finally, as an alternative to analytical models, a numerical finite element model with a nonlinear solver will be proposed.

2. Experimental Details

Modern machines used to produce cylindrical helical springs are numerically controlled with 4 to 12 axes. These machines consist of a straightening and feeding area for the wire and a winding-cutting area for the spring. The wire, unwound from a coil, passes through a series of straightening rollers and then through two or four pairs of rollers that press the wire from above and below, rotating and pushing it to the next stage. Figure 1 shows a machine that produces springs from wire with diameters ranging from 2.5 to 8 mm.

Figure 1. Bench machine for 2.5–8 mm springs.

Figure 2 shows a detailed view of the feeding and winding section with the following components: (1) feed rollers, which pull the wire from the coil (fed from the left in this photo) and push it to the right; (2) vertical pitch, which moves up and down to deform the wire and create the spring's pitch; (3) cutter, which cuts the wire against the central mandrel; (4) horizontal pitch, which has the same function as the vertical pitch but is used for springs with larger diameters; (5) coiling fingers, which guide and bend the wire to form the helix; and (6) central mandrel. Smaller machines have six axes, while larger ones have ten axes, with four motors controlling the diameter (radial and tangential movement for the two winding tips) and an additional one for the rotation of the lower tip.
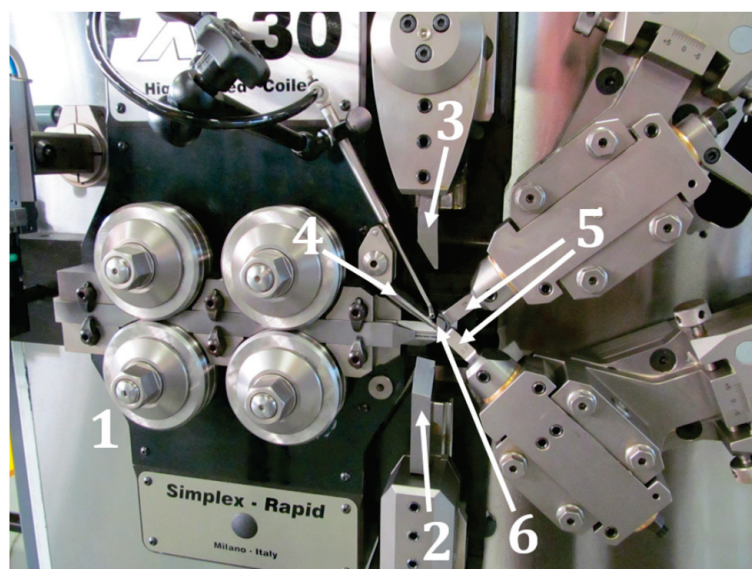

Figure 2. Detail of machine coiling systems: (1) feed rollers, (2) vertical pitch, (3) cutter, (4) horizontal pitch, (5) coiling fingers, and (6) central mandrel.

To regulate the coiling diameter on a machine and control the diameter axes via the system interface, manual adjustments are required for the axial position and vertical plane rotation at the first and second winding points. These tasks are crucial during winding to center the spring relative to the axis of the central pin, ensuring that the wire is cut at the highest horizontal point of the coil and that the contact point of the wire with the tips is centered within the channel. A crucial aspect of spring production is the diameter variation due to spring-back phenomena.

Given the manual nature of these adjustments, achieving accurate and repeatable positioning of the winding tips to form an exact circle is challenging. Indeed, with identical diameter axis positions displayed on the control, incorrect adjustments can result in springs with diameters differing by up to several millimeters. To quantify this effect, for each wire size, the position of the diameter axis relative to the winding diameter was documented alongside the winding and ΔD graphs (where ΔD is the diameter variation due to spring-back phenomena).

The relationship between the electronically set diameter interval and the measured diameter difference exhibits a consistent and repeatable trend.

Accurate measurements of the cut spring can be obtained using a centesimal caliper. However, measuring the winding diameter is more challenging; only half a coil can be measured on the machine, and the space for the caliper is very limited for small spring diameters. Additionally, small wire diameters are very flexible, and even slightly excessive pressure from the caliper can result in inaccurate measurements. The maximum estimated error for these measurements was approximately 0.2 mm, an acceptable margin for this work.

Springs with wire diameters ranging from 0.05 to 12 mm for this study were selected. The investigated springs were made of carbon steel type SH (0.82% C) and stainless steel AISI 302, which are among the most common materials for producing small and medium-sized springs. The chemical compositions of these steels are reported in Tables 1 and 2. Table 3 reports the ultimate tensile stress and the yield stress.

Table 1. Chemical composition of the SH steel (EN 10270-1) [19].

C	Si	Mn	P	S	Cu
0.35–1.00	0.10–0.30	0.50–1.20	0.035 max	0.035 max	0.20 max

Table 2. Chemical composition of the AISI 302 steel (EN 10270/3 [20]; DIN EN ISO 6931-1 [21]).

C	Si	Mn	P	S	N	Cr	Mo	Ni
0.05–0.15	≤2.00	≤2.00	≤0.045	≤0.015	≤0.10	16.0–19.0	≤0.80	6.0–9.5

Table 3. Mechanical properties according to the wire diameters.

Carbon Steel			Stainless Steel		
D_W [mm]	σ_R [MPa]	σ_y [MPa]	D_W [mm]	σ_R [MPa]	σ_y [MPa]
0.25	2690	1883	0.25	2310	1617
0.6	2423	1696	0.6	2060	1442
0.9	2100	1606	1.5	1900	1330
1.5	2098	1469	2.5	1784	1249
2.5	1886	1320			
6	1648	1154			

Various springs were manufactured for each wire size and material type, with a spring index ranging from 4 to 25. The spring index C is defined as the ratio between the final diameter of the spring D_2 and the diameter of the wire D_W.

For each spring size, we measured the diameter across the two winding points to calculate the diameter increase. Figure 3 illustrates the diameter variation ($\Delta D = D_2 - D_1$) of the spring before (D_1) and after spring-back (D_2) for carbon steel springs (a) and stainless-steel springs (b) according to the spring index C. The higher elastic return in stainless steel can be ascribed to the lower Young modulus (185 GPa for the stainless steel and 206 GPa for the carbon steel) combined with the lower yield strength.
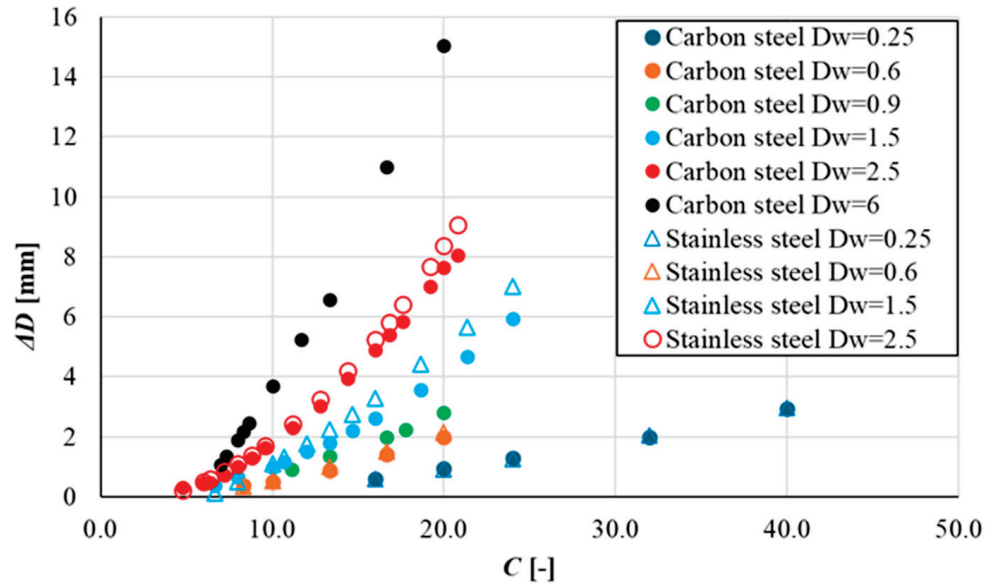
Figure 3. Experimental correlation between index factor C and spring-back.

3. Analytical Approaches

This section reviews various approaches for predicting the spring-back.

The first method we investigate is derived from the mechanical bending process and based on the spring-back ratio k, defined as follows [22]:

$$k = \frac{D_1 + D_W}{D_2 + D_W} = \frac{\alpha_2}{\alpha_1} \tag{1}$$

where α_1 and α_2 are for the bending angles (see Figure 4). This approach has been widely adopted for several materials, but curves for the steels investigated in this paper are not available.
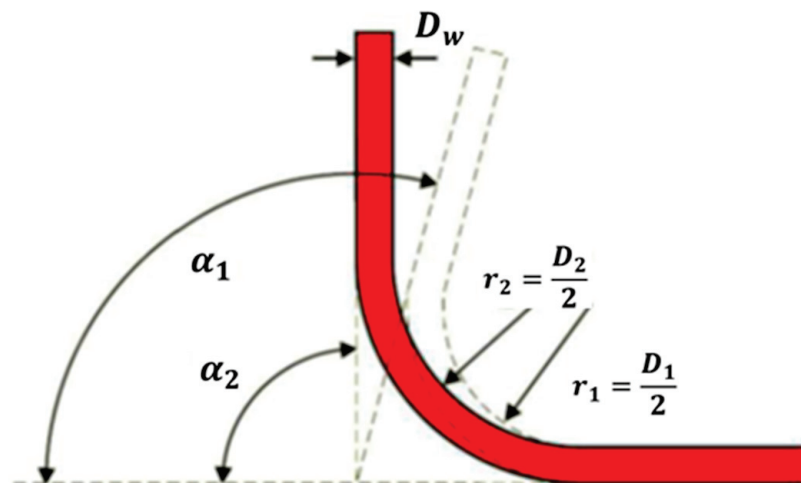
Figure 4. Definition of angles and radii r_1 and r_2 before recovery (1) and after recovery (2).

Figure 5 shows the spring-back parameter *k* as a function of the spring index *C* for the two materials. An exponential function was chosen to fit the points:

$$k = a_1 \, e^{a_2 C} \tag{2}$$

where Table 4 reports the estimated variables for carbon steel and stainless steel, with each coefficient of determination R^2.

Tables 5 and 6 report the spring geometrical parameters, the *k* parameter derived by applying Equation (1) and using the diameters D_1 and D_2 estimated during the spring production process (k_{exp}), and the *k* parameter calculated from Equation (2). The maximum error is about 3.62% and 4.80% for carbon and stainless steels, respectively.
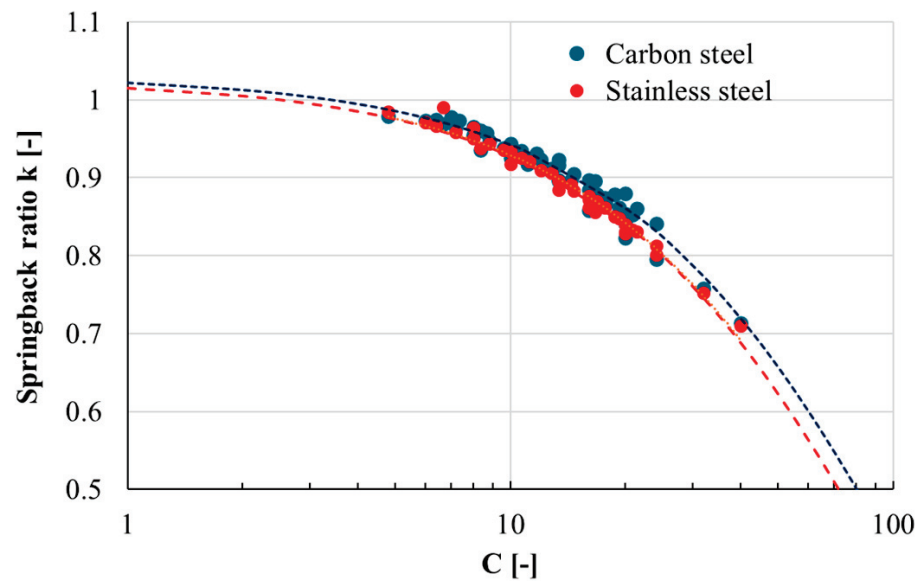
Figure 5. Spring-back parameter *k* of carbon steel and stainless steel as a function of spring index *C* (dotted lines represent the interpolation curves).

Table 4. Coefficient of interpolation for Equation (2).

| Material	a_1	a_2	R^2
Carbon steel	1.0309	−0.009	0.96
Stainless steel	1.0257	−0.01	0.98

Gonzalez-Coleo et al. [15] recovery model was based on the plasticity constitutive law of the steel:

$$1 - \frac{r_1}{r_2} = -8\frac{(1-n)}{(n+2)}\left(\frac{r_1\sigma_y}{D_W E}\right)^3 + 3\frac{2^{1-n}}{(n+2)}\left(\frac{r_1\sigma_y}{D_W E}\right)^{1-n} \tag{3}$$

where *n* is the nondimensional hardening exponent describing the plastic trend of the tensile test, *E* the Young's modulus, σ_y the yield stress, r_1 the radius curvature before the spring-back, r_2 the radius curvature after the spring-back. The yield stresses are reported in Table 4, while the strain hardening exponent is 0.1. Table 7 shows the relative error between the nominal diameter experimentally found and that calculated from Equation (3); the error increases with the spring index *C*. The error can be ascribed to the fact that Equation (3) focuses solely on the bending phenomenon. As the spring diameter increases, it is overly simplistic to consider only bending; torque should be included as well, for instance.

Table 5. Spring geometry details and results from spring-back recovery *k* for carbon steel (k_{exp} is the parameter experimentally found; k_{int} is the one calculated from Equation (2)).

D_W [mm]	D_2 [mm]	D_1 [mm]	k_{exp}	k_{int}	Error *k*	D_W [mm]	D_2 [mm]	D_1 [mm]	k_{exp}	k_{int}	Error *k*
0.25	4	3.40	0.859	0.886	3.13%	2.5	12	11.70	0.979	0.985	0.60%
0.25	5	4.07	0.823	0.853	3.62%	2.5	15	14.53	0.973	0.974	0.09%
0.25	6	4.72	0.795	0.821	3.23%	2.5	16	15.53	0.975	0.970	0.44%
0.25	8	6.00	0.758	0.761	0.43%	2.5	18	17.28	0.965	0.963	0.20%
0.25	10	7.07	0.714	0.705	1.26%	2.5	20	19.00	0.956	0.956	0.01%
0.6	5	4.64	0.936	0.953	1.81%	2.5	22	20.70	0.947	0.948	0.15%
0.6	6	5.51	0.926	0.938	1.29%	2.5	24	22.36	0.938	0.941	0.33%
0.6	8	7.12	0.898	0.908	1.20%	2.5	28	25.70	0.925	0.927	0.26%
0.6	10	8.60	0.868	0.880	1.40%	2.5	32	28.98	0.912	0.913	0.06%
0.6	12	10.00	0.841	0.853	1.36%	2.5	36	32.05	0.897	0.899	0.21%
0.9	10	9.10	0.917	0.928	1.13%	2.5	40	35.10	0.885	0.886	0.11%
0.9	12	10.66	0.896	0.908	1.37%	2.5	42	36.60	0.879	0.879	0.04%
0.9	15	13.00	0.874	0.880	0.67%	2.5	44	38.15	0.874	0.872	0.21%
0.9	16	13.75	0.867	0.871	0.46%	2.5	48	41.00	0.861	0.859	0.26%
0.9	18	15.20	0.852	0.853	0.10%	2.5	50	42.35	0.854	0.853	0.19%
1.5	10	9.64	0.969	0.968	0.09%	2.5	52	43.94	0.852	0.846	0.69%
1.5	12	11.36	0.953	0.956	0.32%	6	42	40.93	0.978	0.965	1.32%
1.5	15	14.03	0.941	0.938	0.38%	6	44	42.66	0.973	0.962	1.18%
1.5	16	14.85	0.934	0.932	0.27%	6	48	46.11	0.965	0.956	0.97%
1.5	18	16.50	0.923	0.920	0.33%	6	50	47.83	0.961	0.953	0.90%
1.5	20	18.20	0.916	0.908	0.86%	6	52	49.54	0.958	0.950	0.83%
1.5	22	19.78	0.906	0.897	0.94%	6	60	56.32	0.944	0.938	0.70%
1.5	24	21.38	0.897	0.886	1.29%	6	70	64.77	0.931	0.923	0.89%
1.5	28	24.42	0.879	0.864	1.72%	6	80	73.42	0.923	0.908	1.63%
1.5	32	27.32	0.860	0.842	2.13%	6	100	89.00	0.896	0.880	1.80%
1.5	36	30.06	0.842	0.821	2.46%						

Table 6. Spring geometry details and results from spring-back recovery *k* for stainless steel (k_{exp} is the parameter experimentally found; k_{int} is the one calculated from Equation (2)).

D_W [mm]	D_2 [mm]	D_1 [mm]	k_{exp}	k_{int}	Error *k*	D_W [mm]	D_2 [mm]	D_1 [mm]	k_{exp}	k_{int}	Error *k*
0.25	4	3.41	0.862	0.874	1.91%	2.5	12	11.77	0.984	0.978	1.13%
0.25	5	4.10	0.829	0.840	1.89%	2.5	15	14.50	0.971	0.966	0.84%
0.25	6	4.76	0.801	0.807	1.23%	2.5	16	15.39	0.967	0.962	0.77%
0.25	8	5.96	0.753	0.745	1.26%	2.5	18	17.16	0.959	0.954	0.63%
0.25	10	7.03	0.710	0.688	4.80%	2.5	20	18.90	0.951	0.947	0.51%
0.6	5	4.65	0.938	0.944	0.59%	2.5	22	20.61	0.943	0.939	0.41%
0.6	6	5.46	0.917	0.928	1.29%	2.5	24	22.29	0.936	0.932	0.32%
0.6	8	7.00	0.884	0.898	1.91%	2.5	28	25.58	0.921	0.917	0.15%
0.6	10	8.48	0.856	0.868	1.94%	2.5	32	28.75	0.906	0.902	0.01%
0.6	12	9.87	0.831	0.840	1.64%	2.5	36	31.81	0.891	0.888	0.11%
1.5	10	9.89	0.990	0.960	3.32%	2.5	40	34.76	0.877	0.874	0.23%
1.5	12	11.52	0.964	0.947	1.87%	2.5	42	36.19	0.869	0.867	0.28%
1.5	15	13.91	0.934	0.928	0.49%	2.5	44	37.59	0.862	0.860	0.34%
1.5	16	14.69	0.925	0.922	0.18%	2.5	48	40.31	0.848	0.847	0.44%
1.5	18	16.24	0.910	0.910	0.28%	2.5	50	41.63	0.841	0.840	0.50%
1.5	20	17.77	0.896	0.898	0.57%	2.5	52	42.92	0.833	0.833	0.55%
1.5	22	19.26	0.883	0.886	0.72%						
1.5	24	20.73	0.872	0.874	0.78%						
1.5	28	23.59	0.851	0.851	0.65%						
1.5	32	26.35	0.831	0.829	0.28%						
1.5	36	29.00	0.813	0.807	0.27%						

Table 7. Spring recovery according to Equation (3) for carbon steel and relative error with respect to experimental results.

D_W [mm]	σ_y [MPa]	C [-]	D_2 exp. [mm]	D_2 calc. [mm]	Error D_2	D_W [mm]	σ_y [MPa]	C [-]	D_2 exp. [mm]	D_2 calc. [mm]	Error D_2
0.25	1883	8.0	4	4.3	9%	2.5	1469	2.4	12	12.5	4%
0.25	1883	10.0	5	5.5	9%	2.5	1469	3.0	15	15.8	5%
0.25	1883	12.0	6	6.7	11%	2.5	1469	3.2	16	17.0	6%
0.25	1883	16.0	8	9.4	17%	2.5	1469	3.6	18	19.1	6%
0.25	1883	20.0	10	12.1	21%	2.5	1469	4.0	20	21.2	6%
0.6	1696	4.2	5	5.3	5%	2.5	1469	4.4	22	23.3	6%
0.6	1696	5.0	6	6.4	7%	2.5	1469	4.8	24	25.4	6%
0.6	1696	6.7	8	8.6	8%	2.5	1469	5.6	28	29.7	6%
0.6	1696	8.3	10	10.9	9%	2.5	1469	6.4	32	34.1	7%
0.6	1696	10.0	12	13.1	9%	2.5	1469	7.2	36	38.4	7%
0.9	1606	5.6	10	10.6	6%	2.5	1469	8.0	40	42.8	7%
0.9	1606	6.7	12	12.8	7%	2.5	1469	8.4	42	45.0	7%
0.9	1606	8.3	15	16.2	8%	2.5	1469	8.8	44	47.3	8%
0.9	1606	8.9	16	17.4	9%	2.5	1469	9.6	48	51.7	8%
0.9	1606	10.0	18	19.7	10%	2.5	1469	10.0	50	53.8	8%
1.5	1320	3.3	10	10.5	5%	2.5	1469	10.4	52	56.3	8%
1.5	1320	4.0	12	12.5	4%	6	1154	3.5	42	44.3	5%
1.5	1320	5.0	15	15.8	5%	6	1154	3.7	44	46.3	5%
1.5	1320	5.3	16	16.9	5%	6	1154	4.0	48	50.3	5%
1.5	1320	6.0	18	19.0	6%	6	1154	4.2	50	52.4	5%
1.5	1320	6.7	20	21.2	6%	6	1154	4.3	52	54.4	5%
1.5	1320	7.3	22	23.4	6%	6	1154	5.0	60	62.6	4%
1.5	1320	8.0	24	25.6	7%	6	1154	5.8	70	73.1	4%
1.5	1320	9.3	28	30.0	7%	6	1154	6.7	80	84.2	5%
1.5	1320	10.7	32	34.4	8%	6	1154	8.3	100	105.0	5%
1.5	1320	12.0	36	38.8	8%	6	1154	10.0	120	127.4	6%

4. Numerical Simulations

We conducted finite element simulations to investigate the effect of elastic return in spring production using Ansys. This analysis requires a nonlinear solver. The model contains six components, as labeled in Figure 6: spring steel wire (1), coiling mandrel (2), and two rollers that bend the wire on the inner disc (3), which are joined to the support braces (4). Except for the wire, all components are designated as rigid, allowing the mesh to be generated solely on the surfaces in contact with the wire, preventing deformations of the rollers or arms that could result in inaccurate calculations and extended solving times.
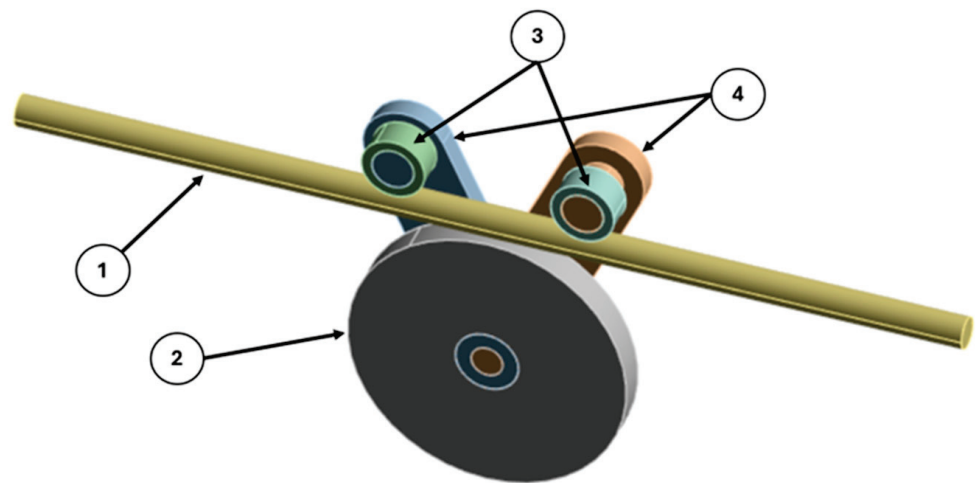
Figure 6. Finite element model: (1) spring steel wire, (2) coiling mandrel, (3) rollers, and (4) support braces.

SH class steel was characterized using the tensile test chart of the same type and batch of material used in the coiling tests previously reported. Table 8 lists the mechanical properties of the steel. To account for the plastic behavior, we implemented an elastic–plastic constitutive model; in detail, a bilinear law approximated the stress–strain tensile curve.

Table 8. Mechanical properties implemented in finite element simulations.

Properties	Value
Density [kg/m^3]	7850
Young's modulus [GPa]	197
Poisson's ratio [-]	0.3
Yield strength [MPa]	1154
Tangent modulus [MPa]	117

The two support braces are attached to the central disc using revolute joints, allowing them to rotate. Similarly, the two rollers are attached to the upper pivots of the arms using revolute joints, enabling their rotation. The central disc is fixed to the ground. The wire is constrained from moving vertically, keeping it centered on the disc and rollers throughout the process. The bending operation is performed by rotating the arms: the right arm rotates clockwise up to 90° and then back to 75°, while the left arm rotates counterclockwise up to 90° and then back to 75°. This motion retracts the rollers, releasing the wire.

The interaction between the wire and the rollers is set through a contact constraint with an Augmented Lagrange method. This was chosen because it provides more accurate results than those obtained through a Pure Penalty method and shorter calculation times, much less than what is required by Normal Lagrange. Additionally, the chosen method does not present any risk of contact vibration (which is possible with Normal Lagrange) and has low permissible contact penetration values. The pure penalty method allows high overlapping values, which result in inaccurate diameter measurements.

The contact behavior is set to asymmetric, and the friction coefficient is set at 0.4. The coiling tools of the actual machine are made of lapped tungsten carbide, while the wire is covered with a thin layer of stearate, which reduces friction during the forming process.

The components are discretized using tetrahedral elements. For the simulation with 6 mm diameter wire and 65 mm coiling diameter, the number of nodes is 26,894, and the number of elements is 5871, as shown in Figure 7. These belong mostly to the steel wire since all other elements are rigid, and the mesh is generated only on the surfaces of the components that come into contact with the wire. Figures 8 and 9 illustrate the progression of the wire throughout the simulations.

a)   b)
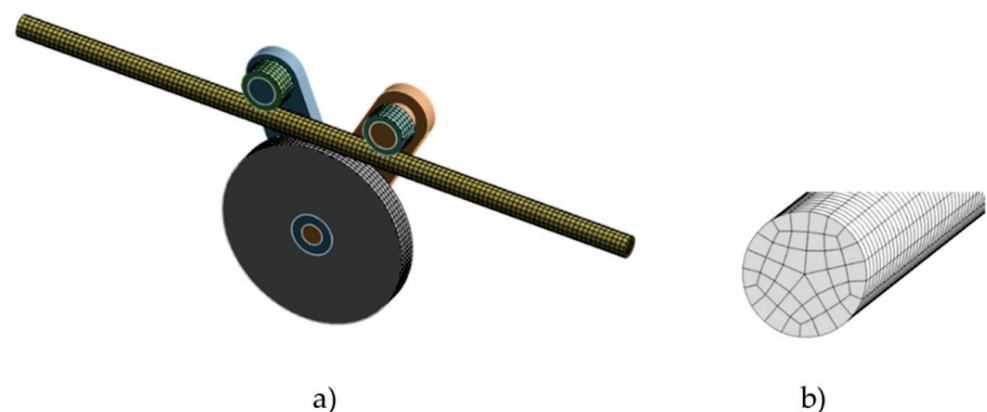
Figure 7. Detail of model mesh: (**a**) overall model; (**b**) wire detail.
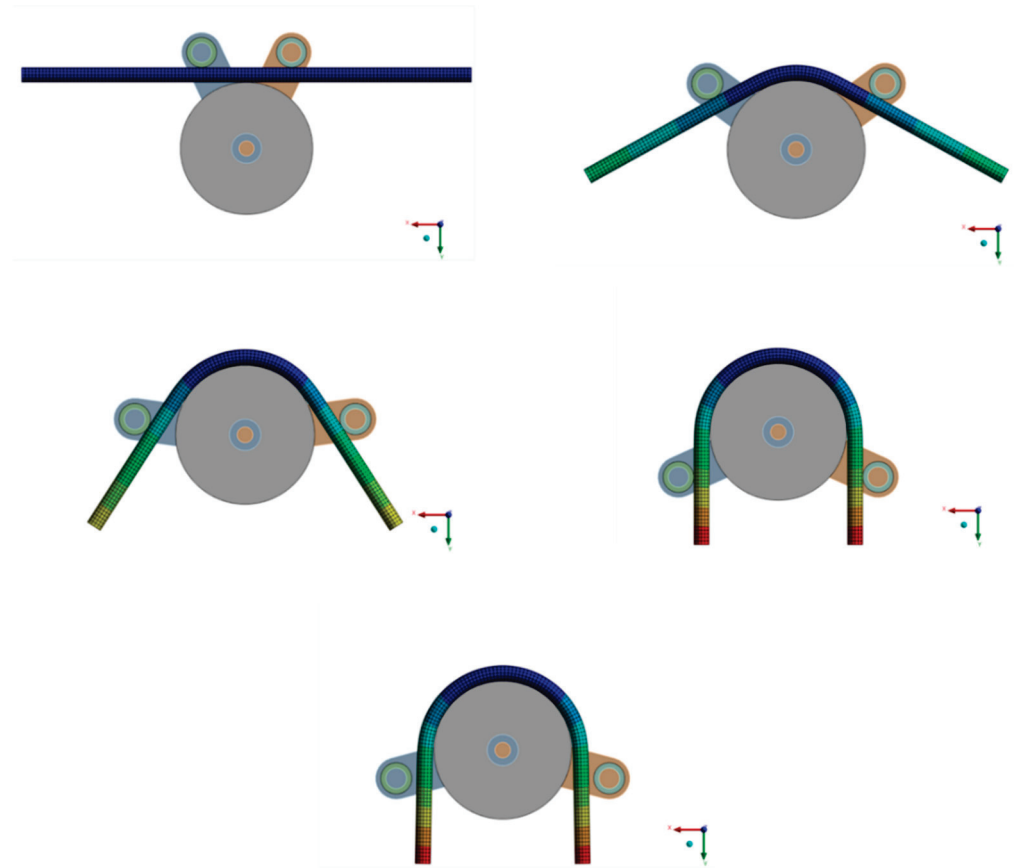
Figure 8. Deformation steps during the simulation.
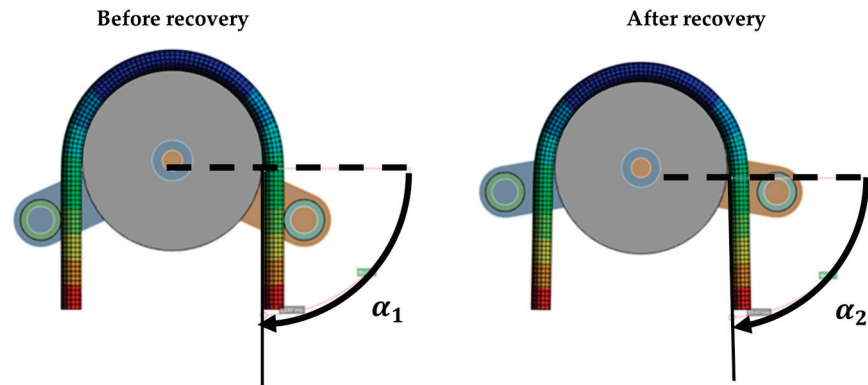
Figure 9. Elastic return detail.

The simulations results were calculated based on the parameter k. Firstly, the angles α_1 and α_2 were estimated from the simulations as shown in Figure 9. Subsequently, k_{FEM} using Equation (1) and, finally, the final diameter $D_{2,\,FEM}$ according to the following equations:

$$D_{2,FEM} = \frac{1}{k_{FEM}}(D_1 + s) - s \tag{4}$$

where $D_{2,FEM}$ is the diameter after the spring-back estimated by the finite element mode, D_1 is the diameter before the spring-back and D_w the wire diameter.

Table 9 shows the simulation results. The extent of spring-back increases nonlinearly as the spring index increases. Of note, the relative errors found in the numerical models are consistent with those calculated with Equation (3). The relative errors are not more than

8%. However, the computation time (in general more than 5 h) makes simulations a less practical method compared to an analytical prediction.

Table 9. Detail of finite elements model results.

D_1 [mm]	$D_{2,exp}$ [mm]	α_1 [°]	α_2 [°]	k_{FEM} [-]	$D_{2,FEM}$ [mm]	% Error D_2
50	52.6	90.62	89.36	0.986	50.79	3%
65	70.3	91.53	89.7	0.980	66.45	5%
75	82.6	91.6	90	0.983	76.44	7%
80	88.8	91.38	90	0.985	81.32	8%

5. Conclusions

This research provided an in-depth analysis of the spring-back phenomenon in cylindrical helical springs made of carbon steel and stainless steel. By employing both experimental measurements and analytical models, the exponential relationship between the spring-back ratio k (Equation (1)) and the spring index C (the ratio between the final diameter of the spring D_2 and the diameter of the wire $2s$) is determined. The maximum errors for the predicted spring-back were 4.80% for stainless steel and 3.62% for carbon steel, demonstrating the model's accuracy. Furthermore, a model requiring the initial diameter, thickness, and plastic properties of the material as input data were employed. The outcomes of this model were dependent on the spring index C, with the error increasing as C increased.

Additionally, finite element simulations corroborated the analytical predictions, though they required significant computation time. These findings offer valuable insights for optimizing spring manufacturing processes, enhancing precision, and minimizing material waste.

Future work could explore more geometries and materials to further refine predictive models and improve manufacturing efficiency.

References

1. Salah, H.R.A.; Mostafa, A.; Eslam, E.; Youssef, T.; Ibrahim, S.; Mina, S. 3D Design of helical spring for automotive independent suspension system under fatigue test conditions. In *Applied Mathematics, Modelling and Computer Simulation*; IOS Press: Amsterdam, The Netherlands, 2023. [CrossRef]
2. Solazzi, L. Design of a truck cab torsion bar. *Int. J. Heavy Veh. Syst.* **2019**, *26*, 692–706. [CrossRef]
3. Yildirim, Y. Expressions for predicting fundamental natural frequencies of non-cylindrical helical springs. *J. Sound Vib.* **2002**, *252*, 479–491. [CrossRef]
4. Yildirim, V. Free vibration of uniaxial composite cylindrical helical springs with circular section. *J. Sound Vib.* **2001**, *239*, 321–333. [CrossRef]
5. Yu, A.M.; Hao, Y. Free vibration analysis of cylindrical helical springs with noncircular cross-sections. *J. Sound Vib.* **2011**, *330*, 2628–2639. [CrossRef]

6. Kobelev, V. Effect of static axial compression on the natural frequencies of helical springs. *Multidiscip. Model. Mater. Struct.* **2014**, *10*, 379–398. [CrossRef]

7. Zhuo, Y.; Qi, Z.; Zhang, J.; Wang, G. A geometrically nonlinear spring element for structural analysis of helical springs. *Arch. Appl. Mech.* **2022**, *92*, 1789–1821. [CrossRef]

8. Yu, A.; Yang, C. Formulation and evaluation of an analytical study for cylindrical helical springs. *Acta Mech. Solida Sin.* **2010**, *23*, 85–94. [CrossRef]

9. Čakmak, D.; Tomičević, Z.; Senjanović, I.; Wolf, H.; Božić, Ž.; Semenski, D. A Study on Cylindrical Coil Spring Deflection and Stress Done Using Analytical and Numerical Methods. *Int. J. Eng. Model.* **2022**, *35*, 57–81. [CrossRef]

10. Kamil, F.; Abdulshaheed, A.G.; Kadhom, M.A. Development of a computational system to design a helical spring. *Int. Rev. Appl. Sci. Eng.* **2014**. [CrossRef]

11. Chen, L.; Wu, L.; Fu, H.; Tang, Y. Design and Performance Evaluation of Polymer Matrix Composite Helical Springs. *Polymers* **2022**, *14*, 3900. [CrossRef] [PubMed]

12. Wu, L.; Chen, L.; Fu, H.; Jiang, Q.; Wu, X.; Tang, Y. Carbon fiber composite multistrand helical springs with adjustable spring constant: Design and mechanism studies. *J. Mater. Res. Technol.* **2020**, *9*, 5067–5076. [CrossRef]

13. Nirala, A.; Kumar, N.; Bandhu Singh, D.; Kumar Singh, A.; Kumar Sharma, S.; Kumar Yadav, J.; Prasad, H.; Chandan, S.; Kumar Shrivastava, A. Simulation analysis of composite helical spring for compression, torsional and transverse mode. *Mater. Today Proc.* **2020**, *28*, 2263–2267. [CrossRef]

14. Kobelev, V. Elastic–plastic deformation and residual stresses in helical springs. *Multidiscip. Model. Mater. Struct.* **2020**, *16*, 448–475. [CrossRef]

15. González-Coneo, J.; Gonzalez-Olier, C.; Pedraza-Yepes, C.; Higuera-Cobos, O.; Troncoso-Palacio, A. Analytical method for elastic recovery prediction of air bending sheet. *J. Appl. Eng. Sci.* **2023**, *21*, 973–981. [CrossRef]

16. Kobelev, V. Elastic-plastic work-hardening deformation under combined bending and torsion and residual stresses in helical springs. *Int. J. Mater. Form.* **2010**, *3* (Suppl. S1), 869–888. [CrossRef]

17. Marciniak, Z.; Duncan, J.L.; Hu, S.J. *Mechanical of Sheet Metal Forming*; Elsevier: Oxford, UK, 2002. [CrossRef]

18. Gardiner, F.J. The springback of metals. *Trans. ASME* **1957**, *79*, 1–7. [CrossRef]

19. *EN 10270-1*; Steel wire for mechanical springs. Part 1: Patented cold drawn unalloyed spring steel wire. iTeh Standards: Newark, DE, USA, 2017.

20. *EN 10270/3*; Steel wire for mechanical springs. Part 3: Stainless spring steel wire. iTeh Standards: Newark, DE, USA, 2011.

21. *DIN EN ISO 6931-1*; Stainless steels for springs—Part 1: Wire. ISO: Geneva, Switzerland, 2016.

22. Kalpakjian, S.; Schmid, S. *Manufacturing Engineering & Technology*, 7th ed.; Pearson Publishing Company: Upper Saddle River, NJ, USA, 2014.

Development, Designing and Testing of a New Test Rig for Studying Innovative Polycrystalline Diamond Bearings

Alessio Cascino *, Andrea Amedei, Enrico Meli and Andrea Rindi

Department of Industrial Engineering (DIEF), University of Florence, 50121 Florence, Italy;
andrea.amedei@unifi.it (A.A.); enrico.meli@unifi.it (E.M.); andrea.rindi@unifi.it (A.R.)
* Correspondence: alessio.cascino@unifi.it

Abstract: This paper reports the preliminary experimental studies carried out on an innovative sliding bearing made of polycrystalline diamond, a material with excellent mechanical and chemical characteristics, used mainly in the drilling industry. Bearings crafted from this material do not necessitate lubrication due to their extremely low coefficient of friction and high resistance to wear. For this reason, they are prime candidates for replacing traditional oil bearings, eliminating the need for auxiliary systems and thereby reducing environmental risks. In this regard, an innovative test rig was designed, capable of reaching speeds up to 6000 rpm both in vertical and horizontal configurations thanks to a novel tilting frame. Moreover, with a high modularity it was possible to test three different kinds of radial PCD bearings. Dynamic data were acquired and elaborated to evaluate orbits, acceleration and absorbed torque, to finally compare these different configurations to better understand how dynamic behavior is influenced by bearings' geometrical characteristics.

Keywords: polycrystalline diamond bearing; rotordynamics; experimental test rig

1. Introduction

In the introduction, this recent technology is analyzed, discussing the physical properties of the material and the applications of this type of component.

1.1. Polycrystalline Diamond Technology

Synthetic diamond is made of the same material as natural diamonds: pure carbon, crystallized in an isotropic 3D form. It differs from both natural diamond (which is created by geological processes) and diamond simulant (which is made of non-diamond material). Studies on these types of materials are reported in [1–3]. Records of attempted diamond synthesis date back to the turn of the twentieth century. Numerous scientists claimed to have successfully synthesized diamonds between 1879 and 1928, but none were confirmed. In the 1940s, systematic research began in the United States, Sweden and the Soviet Union to grow diamonds, which culminated in the first reproducible synthesis of diamond in 1954. Nowadays, four manufacturing processes have been discovered: Chemical Vapor Deposition synthesis (CVD), High-Pressure High-Temperature synthesis (HPHT), detonation synthesis and high-power ultrasound synthesis. CVD and HPHT processes still dominate the production of synthetics diamonds. The detonation process entered the market in the late 1990s. Here, the detonation of carbon-containing explosives creates nanometer-sized diamond grains. The high-power ultrasound process currently has no commercial application. The properties of synthetic diamond depend on the manufacturing process. However, some synthetic diamonds (whether formed by HPHT or CVD) have properties such as hardness, thermal conductivity and electron mobility that are superior to those of most naturally formed diamonds. Synthetic diamond is widely used in abrasives, in cutting and polishing tools and in heat sinks. Electronic applications of synthetic diamond are being developed, including high-power switches at power stations, high-frequency field-effect

transistors and light-emitting diodes. Synthetic diamond detectors of ultraviolet (UV) light or high-energy particles are used at high-energy research facilities and are available commercially. Because of its unique combination of thermal and chemical stability, low thermal expansion and high optical transparency in a wide spectral range, synthetic diamond is becoming the most popular material for optical windows in high-power CO_2 lasers and gyrotrons. It is estimated that 98% of industrial-grade diamond demand is supplied with synthetic diamonds. In Table 1, some mechanical properties of PCD are reported. Because diamond bonds are so short, they are extremely strong, leading to its very high hardness. Diamond is the hardest known material. It has the highest thermal conductivity of any other material, four times that of copper. Vibrational energy can travel extremely quickly through the lattice. The strength of the bonds resists disruption, giving diamond a high melting point, 500 °C above tungsten. The diamond structure allows sound to propagate at an extreme velocity. It is very stiff, with a coefficient of thermal expansion less than silicon. Diamond has a low coefficient of friction and it is more slippery than teflon. It is chemically inert: acids do not attack it and it is biologically compatible.

Table 1. Extreme properties of diamond.

Property	Value
Density	$4–4.35 \times 10^6$ [kg/m^3]
Young's Modulus	850–1000 [GPa]
Poisson Ratio	0.1
Hardness	50–100 [GPa Knoop]
Thermal Conductivity	500–2000 [W/mK]
Melting Point	4000 [°C]
Sonic Velocity	18,000 [m/s]
Coefficient of Thermal Expansion	1.1×10^{-6} [1/K]
Optical Index Refraction	2.42
Coefficient of Friction	0.01–0.07
Biologically Compatible	Pure carbon

1.2. Applications

Most industrial applications of synthetic diamond have long been associated with its hardness. This property makes diamond the ideal material for machine tools and cutting tools, as shown in Figure 1.

Figure 1. Some kinds of PCD drilling tools [4].

As the hardest known naturally occurring material, diamond can be used to polish, cut or wear away any material, including other diamonds. Common industrial applications include diamond-tipped drill bits and saws, and the use of diamond powder as an abrasive. These are by far the largest industrial applications of synthetic diamond. While natural

diamond is also used for these purposes, synthetic HPHT diamond is more popular, mostly because of the better reproducibility of its mechanical properties. Diamond is not suitable for machining ferrous alloys at high speeds, as carbon is soluble in iron at the high temperatures created by high-speed machining, leading to greatly increased wear on diamond tools compared to alternatives. The usual form of diamond in cutting tools is micron-sized grains dispersed in a metal matrix (usually cobalt) sintered onto the tool. This is typically referred to in industry as polycrystalline diamond (PCD). PCD-tipped tools can be found in mining and cutting applications. For the past fifteen years, work has been done to coat metallic tools with CVD diamond, and though the work shows promise, it has not significantly replaced traditional PCD tools. Abrasive particles, high temperatures, corrosive chemicals, and high loads all contribute to failure in bearings used in down-hole drilling tools. Polycrystalline diamond (PCD) bearings outperform other bearing technologies in these harsh conditions due to the unmatched properties of diamond.

PCD bearings are specifically designed to sustain thrust loads, radial loads or a combination of them. Figure 2 illustrates some kinds of PCD bearings. Drilling tool bearing applications include thrust bearing in turbo-drills and thrust or radial bearing in drilling motors, coring tools and power generation turbines. The keys element for a PCD bearing are extreme hardness and high thermal conductivity, which lead to wear resistance and heat removal. In addition, high strength and toughness and low friction make this material very interesting for application on bearings. They simplify equipment and assemblies by eliminating the need for seals and auxiliary lubrication systems. Research on this type of material and its application is focused on wear and abrasion behavior [5–8]. In [9], an important study about life behavior and a lubrication regime is reported. Studies on friction, constant load life and loading capacity are shown for various types of thrust bearings. In [10], a methodology for the designing and building of simple foil thrust bearings intended for parametric performance testing and low marginal costs is described. A test rig for the measurement of the load performance of water-lubricated hydrostatic/hydrodynamic thrust bearings operating under conditions typical of cryogenic turbo pumps (TPs) is reported in [11]. Studies have been carried out mainly on the wear and the life limit of these bearings, without focusing too much on the rotor dynamics aspects, due also to the low speeds in their usual application. One of the characteristic and fundamental aspects of this type of bearing concerns the low dry friction coefficient, which allows it to be used without the aid of synthetic lubricants such as grease and oil. It also has a very high resistance to chemical agents and corrosive environments and can withstand very high loads. The strategic importance that these bearings could have in turbomachinery applications (especially for subsea and remote location oil and gas extraction) becomes immediately evident for various reasons. Some studies about subsea electric pumps are reported in [12,13]. Currently, the most important concerns in subsea applications are represented by higher costs than surface applications with the same system components, both in terms of initial costs and maintenance. For this reason, the possibility of completely removing the auxiliary systems for oil circulation, often very unreliable systems that lead to the interruption of the correct functioning of the machine, is a significant strategic advantage. Furthermore, the use of PCD bearings allows the complete removal of the seals necessary to separate the process fluids from the auxiliary ones; therefore, the use of multiphase machines leads to an increase in the quantity of fluid processed. These machines have very high rotational speeds for the typical applications of these bearings. It is necessary, then, to carry out research aimed at understanding the physical phenomena concerning their behavior and develop a mathematical model that predicts their behavior. With the aim of testing different classes of radial PCD bearings, an innovative test rig was designed. Thanks to its high modularity, three different kinds of radial PCD bearings can be tested. In addition, the test rig has a tilting frame which allows it to reach speeds up to 6000 rpm in both vertical and horizontal configurations.

Figure 2. PCD bearings on the left and real view of PCD bearing samples (rotor and stator rings) on the right.

In the subsequent sections, in addition to the proposed methodology, the design of the bench is described in detail: the mechanical design, transmission system, cooling system, and an overall view of the acquisition systems are appropriately discussed. The experimental results are then presented by processing the acquired data extensively in both the time and frequency domains, considering orbital displacements, torque absorption and frequency response spectrums. Finally, the results are summarized and discussed for each configuration.

2. Materials and Methods

2.1. Methodology

The present activity can be divided into two fundamental parts, one experimental and one numerical, followed by the validation of the numerical model with the experimental data, as briefly summarized in Figure 3. Contact models represent a fundamental aspect of the numerical approach of the project. The selection of an appropriate model for a given contact problem is still an important and challenging issue to be addressed. Some really good reviews of contact force models that are used in the dynamical analysis of multibody systems can be found in [14–16]. The present paper is focused only on the experimental part of the work, with the objective to describe the innovative test rig in detail and present the main results obtained from the experimental test campaign that was carried out.
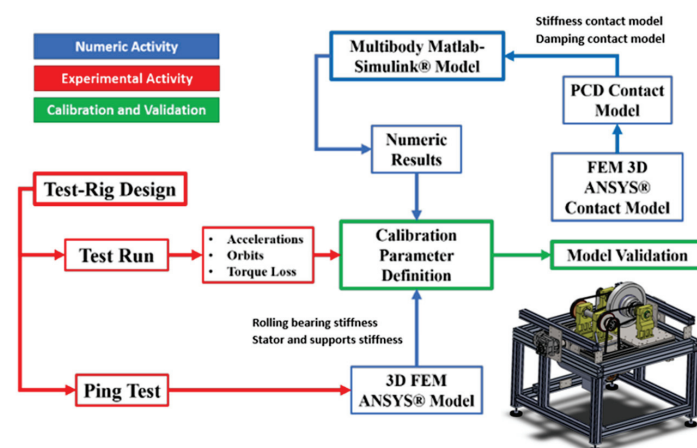
Figure 3. Activity workflow.

The test rig was equipped with various sensors to measure stator accelerations, rotor orbits and the torque absorbed by the PCD bearing. A cooling system was required. Three different types of bearings were tested. The main difference between them is the rotor–stator clearance in the radial direction, from which the name of the testcase is determined: "Baseline" (50 µm), "Low" (40 µm) and "High" (200 µm). Just the "baseline" was tested in the horizontal and vertical configurations. Raw data were acquired and elaborated to understand the behavior of the rotor, as shown within next paragraphs.

2.2. PCD Test Rig Design

The test rig was intended to simulate the behavior of a special design of turbomachinery, in which the individual impellers have independent drives, each driven by a permanent magnet motor, in a configuration with the permanent magnets mounted in the rotor itself, which therefore act as both a motor and an impeller. The main purpose of the test rig was to represent a single rotor in this turbomachinery system, where each rotor was independent from the others, using different kinds of PCD bearings and configurations at several different rotational speeds. The critical parameters and specifications considered during the design of the rig were a maximum main rotor speed of 6000 rpm, modularity, easy variation of rotational axis inclination, decoupling the dynamic behavior of the rotor from the rest of the test rig and rotor inertial properties similar to a real machine. The test rig has a strong integration with heat dissipation and dynamic data acquisition systems. The main physical quantities of interest to better understand the dynamic behavior of the PCD were the rotor displacements (to plot orbits), stator accelerations (to better understand the rotor–stator interaction) and torque on stator, to evaluate the power loss from PCD bearings. The next paragraphs provide a precise and comprehensive explanation of each mechanical component, the cooling circuit and the measurement system, including the specification used when designing the rig and the acquisition system and selecting the instrumentation.

2.3. Mechanical Design

The system is characterized by the presence of a 15 kW electric motor (slow shaft) which, through a secondary transmission shaft, used to avoid a high transmission ratio between low and fast shaft, rotates the disk containing the PCD bearings (the fastest axis) around the main statoric shaft, as shown in Figure 4a. These three axes are supported by steel pedestals, which are bolted to a base plate reinforced with an aluminum frame. A tilting frame is linked to an aluminum fixed frame with two hinges. They allow the base to be tilted easily from a horizontal to a vertical configuration and vice versa, as shown in Figure 4b. The chassis is covered by a steel enclosure that serves as a containment shield in case of failure. Figure 4c illustrates it.
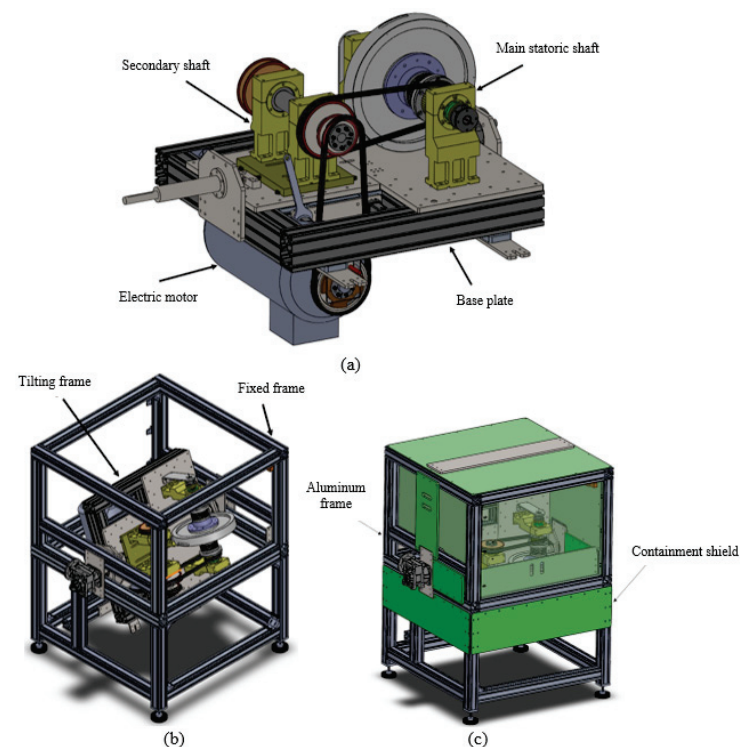

Figure 4. Test rig CAD model overview: (**a**) tilting base with motor, secondary shaft and main axis; (**b**) frame definition; and (**c**) aluminum frame with steel armor.

One of the most difficult goals to achieve was the decoupling of the main rotor from the rest of the test rig. In fact, on the prototype machine the rotors are essentially free to move axially and to rotate around axes perpendicular to the longitudinal axis, until the complete recovery of the clearance. Therefore, one of the requirements of the drive coupling must be to minimize the spring-back forces opposing these degrees of freedom, so that these potential movements can also be represented. The two options explored were an elastic and a magnetic coupling. The main parameters chosen for the execution of the project "trade-off" were the following: the ability of the solution to represent the physics of real-application turbomachines, constructive simplicity, TRL (technology readiness level) and time and costs for finding the component. Table 2 describes how the two options present themselves in relation to the project requirements.

Table 2. Main characteristics of the different transmission systems.

Requirements	Magnetic Joint	Elastic Joint
Representativeness of the solution	Transmission without physical contact.	System able to "decouple" quite effectively.
Constructive simplicity	Simple and space-saving configuration.	Overall dimensions greater than the magnetic coupling.
TRL	Custom component (low TRL).	Known and referenced component.
Time and costs	High, custom product.	Low, standard product.

The two solutions were almost equivalent in their ability to effectively represent the behavior of the real turbomachine. Furthermore, the magnetic coupling had some advantages in terms of simplicity of configuration. However, the TRL and the time and costs associated with procurement oriented the choice to the advantage of the more conventional flexible coupling. Torque transmission is accomplished by a timing pulley–belt system. The number of belts from the secondary shaft to the rotor system depends on the configuration. The horizontal configuration (Figure 5a,c) includes two belts and a symmetric transmission system. Instead, in the vertical configuration (Figure 5b,d), the left belt and pulley system is substituted by an axial PCD bearing to react to the gravitational force, so the torque transmission is provided by a single belt. On the main stationary shaft, the timing pulley is supported on roller bearings, and the torque is transmitted to the rotor by 2 (or 1 in the vertical configuration) high-precision and torsional stiff metal bellow couplings. The main purpose of the metal bellow is to decouple the dynamic response of the rotor (and so the PCD) from the rest of the rotational parts of the test rig. Thanks to the high modularity of the design, changing configurations is a simple and fast procedure.

2.4. Cooling System Design

The cooling system is composed of a 500 L water tank, a recirculation pump and a bypass valve to control the water temperature, measured with a thermocouple, grouped in a simple steel frame (Figure 6). The bypass valve is activated when the temperature is too high in order to mix the high-temperature water with the coolest water inside the tank. During operation, temperatures exceeding 90 °C were never recorded. The system allows the control of the water flow and the temperature. The cooling water enters the PCD bearings through some cavities and channels machined into the stationary shaft. Looking at the cross-section of the main shaft in the vertical configuration in Figure 7a, it is possible to see the water-cooling circuit inside the statoric axis. Blue arrows mean cold water while red arrows mean hot water. An axial channel brings the water from the inlet to the center of the PCD bearing. Then, three radial channels arranged at 120° (visible in Figure 7b) bring the water into a groove just under the PCD and then thirteen holes on the inner ring uniformly distribute the water on the PCD pad, where cooling takes place.
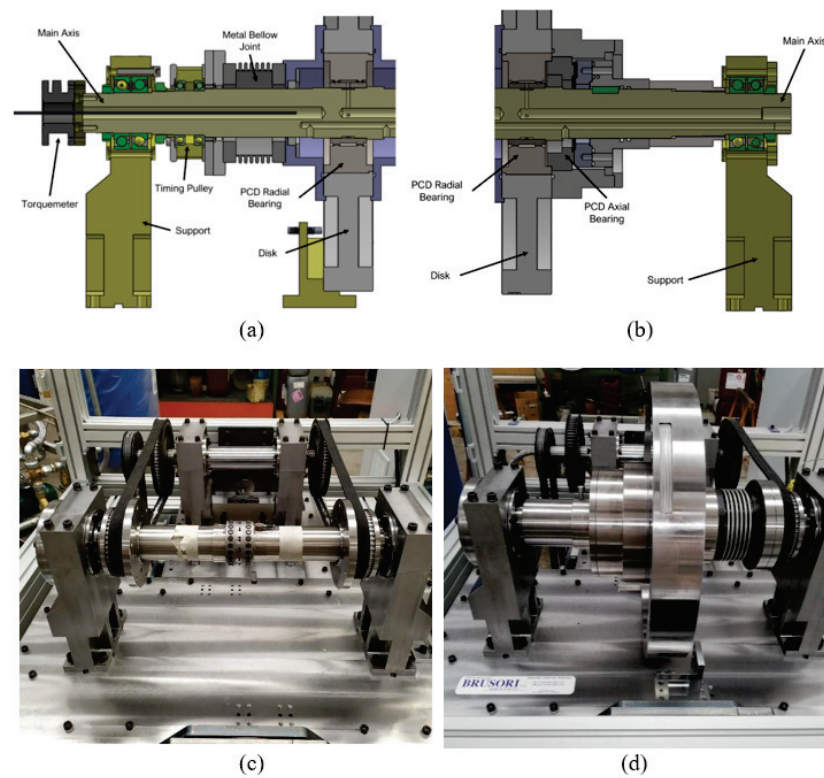
Figure 5. (**a**) Cross-section of partial main axis in horizontal configuration, (**b**) cross-section of partial main axis in vertical configuration, (**c**) torque transmission system: horizontal configuration with symmetric belt–pulley system on main axis, and (**d**) torque transmission system: vertical configuration with asymmetrical transmission system on main axis.

Subsequently, hot water flows into two rotating chambers connected with the outlet channel, thanks to two holes in the lower side of the stationary shaft. The axial PCD cooling circuit is used only for the vertical configuration: cooling water passes through a series of holes and channels until it reaches the axial PCD pads. After cooling action, hot water reaches the same outlet channel as seen for radial PCD cooling in the previously described way (Figure 8).
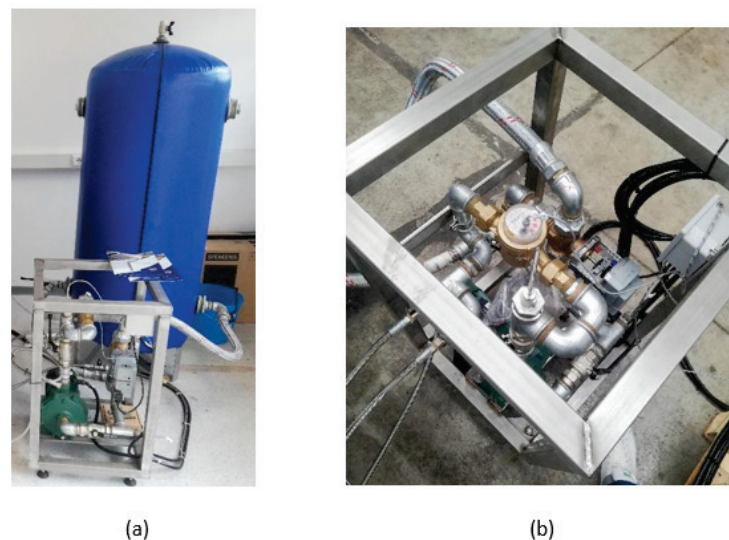
Figure 6. Cooling system: (**a**) cold water tank; (**b**) steel frame with recirculation pump and bypass valve.
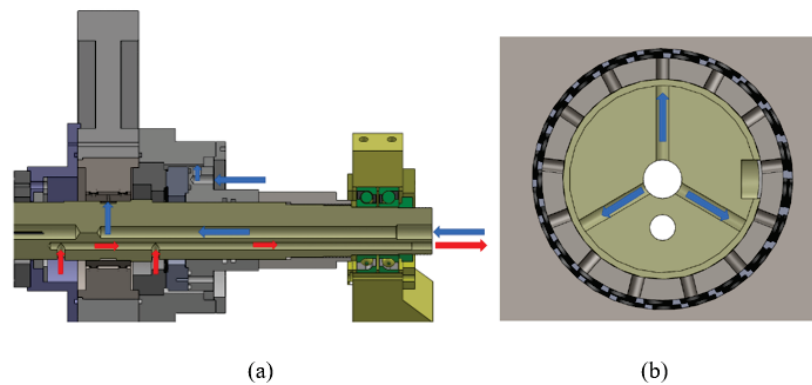
Figure 7. (**a**) Main axis cross-section (water circulation) and (**b**) mid-plane main axis cross-section: the three radial channels arranged at 120°.
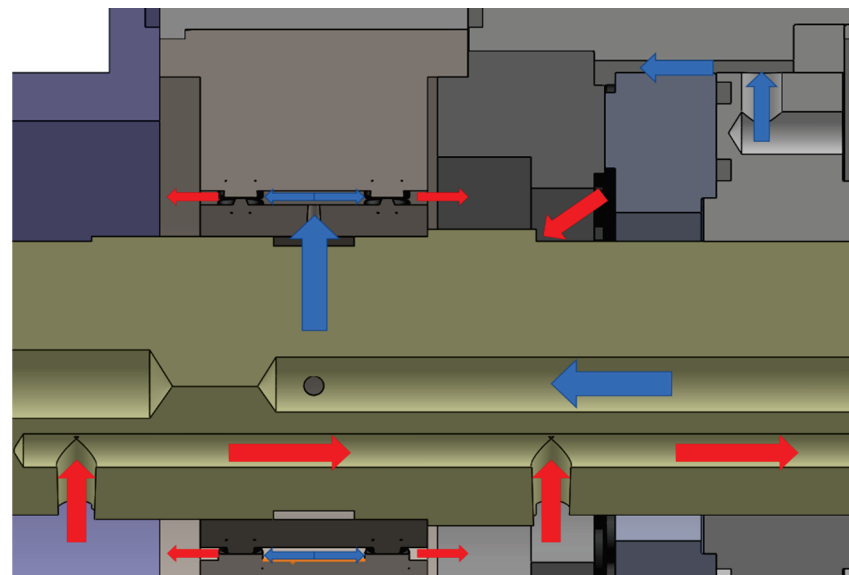
Figure 8. Focus on cooling water flows inside the main shaft: radial and axial PCD cooling. (Blue arrows mean cold water while red arrows mean hot water.)

2.5. Acquisition Data System Design

The aim of the measurement system was to evaluate: the torque and power loss by PCD bearings, acceleration of the support and base and displacement of the rotor (both axial and radial), the orbits and dynamics of the rotor and the radial acceleration induced by the rotor on the stationary shaft, and the exchanged forces during tests, and the PCD temperature. These quantities were measured by the following sensors: 1 torquemeter, 2 external single-axis accelerometers, 2 internal single-axis accelerometers, 4 eddy current sensors (2 radial and 2 axial), 6 thermocouples of type K (TC) for the PCD and 1 thermocouple for cooling system. The torquemeter, visible in Figure 9a with the tag T, is a reaction torquemeter and acts as the torsional constraint for the main axis which is connected to the pedestals via roller bearings. This configuration allows the direct measurement of the PCD bearing reaction torque (the power loss by the roller bearing under the pulley was neglected). Figure 9a also depicts the external accelerometers with the tag Aext1 used to measure the pedestal and base vibrations. The accelerometers are fixed on the main axis with an angular relative position of 90°, as depicted in Figure 9b, as near as possible to the mid-plane of the rotor, to evaluate the acceleration of the main axes when subjected to the forces generated by the rotor. The thermocouples are placed inside the PCD inner ring, as near as possible to the PCD pads, to control and evaluate the effect of friction and the water cooling system.

(a)
(b)
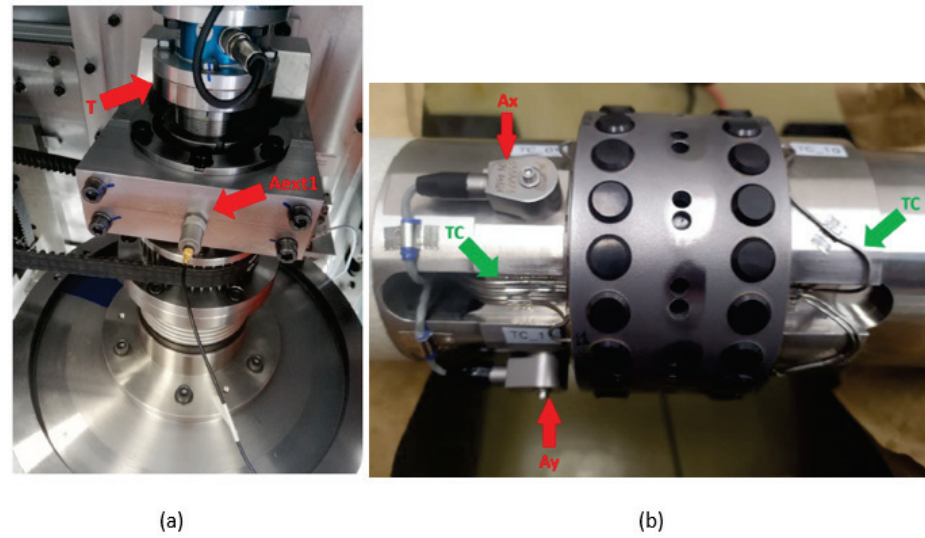
Figure 9. (**a**) Torquemeter (T) and an external accelerometer (Aext1) and (**b**) internal accelerometers (Ax and Ay) and internal thermocouples (TCs).

The probes are positioned by two brackets (Figure 10a) bolted to the base plate. Both radial and axial probes have an angular relative position of 90°. The axial probes face opposite sides of the rotor, so it was possible to characterize the displacement of the rotor. Figure 10b shows a close-up view of one of the proximity probes.

(a)
(b)
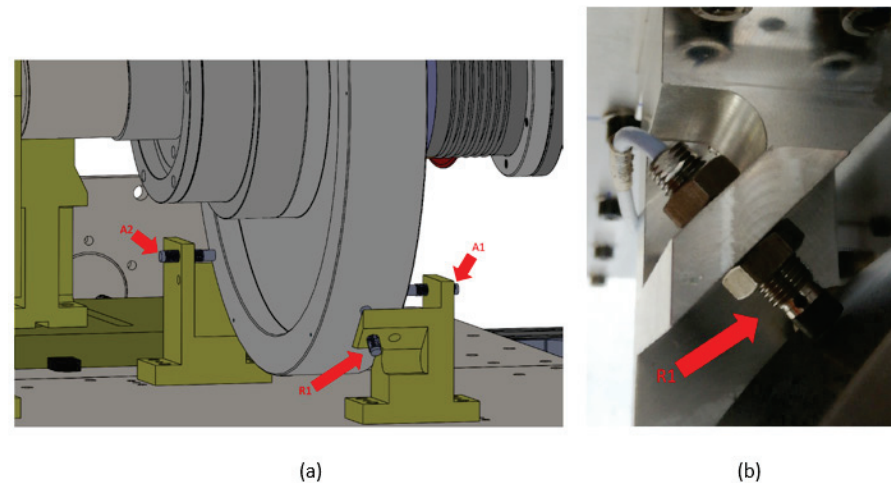
Figure 10. (**a**) Radial (R1) and axial (A1 and A2) proximitors. (**b**) Real position of a radial proximitor (R1).

The dynamic acquisition system (shown in Figure 11) consists of the following: a proximitor for each eddy current probe, a charge amplifier for the external accelerometer and a specific board (NISCB-68) to read signals with the chassis, a chassis (NI PXI 1042) with 2 boards to acquire dynamic signals (NI PXI 4472 and NI PXI 6259 respectively) and 1 board (NI PXI 8336) to communicate with the scientific workstation and a scientific workstation (HP Z720) with a specific board (NI MXI-4) to communicate with the acquiring chassis using an optical fiber.
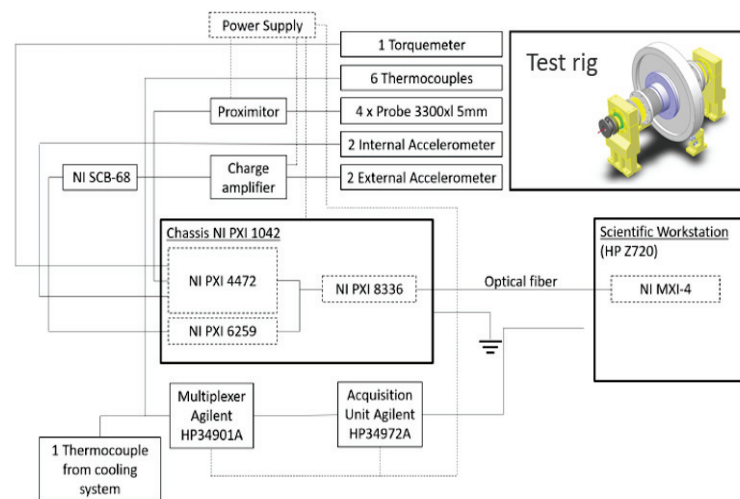
Figure 11. Dynamic acquisition system scheme.

The torquemeter and internal accelerometer are powered directly by one board present in the chassis. The proximity probes and external accelerometer need an independent power supply. To transfer the signal from the acquiring system to the scientific workstation, an optical fiber cable was used.

2.6. Signal Elaboration Workflow

The elaboration of the experimental signals obtained from the test runs of the test rig was divided into 3 main phases: reference system rotation, time series steady-state range selection and filter application.

2.6.1. Reference System Rotation

This transformation was necessary considering that the experimental and numerical results had different reference systems. To be more easily compared, it was necessary to make a rigid rotation of the reference systems and, consequently, of the time series. A scheme representing the cross-section of the center of the test rig is shown in Figure 12. The proximity probes and the accelerometers are represented in blue, with their reference system in red (Ox1y1) and yellow (Ox2y2), respectively, while the numeric reference is in black (Oxy). Note that the sensor reference systems were rotated by 180°. In green are reported two example signals for displacements (r1 and r2) and in orange are reported accelerations (a1 and a2).
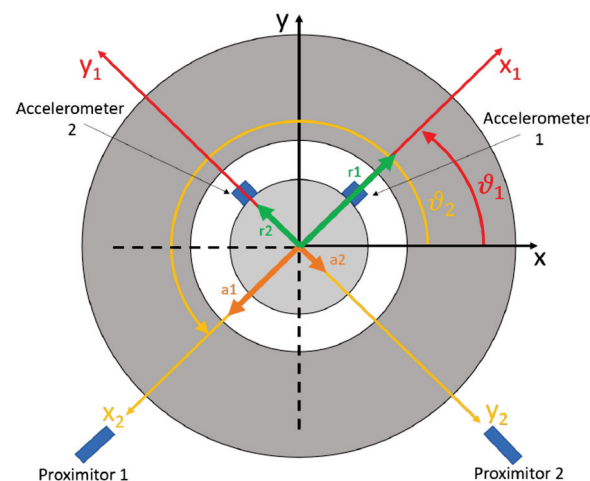
Figure 12. Reference systems' rotation from experimental to numeric.

Considering the scheme described in Figure 12, with the angle θ_1 between the proximitor reference system and the numeric reference system of 45°, with the Equation (1) it was possible to rotate the time series of the rotor displacements:

$$\begin{cases} r_x = r_1 \cos\theta_1 - r_2 \sin\theta_2 \\ r_y = r_1 \sin\theta_1 + r_2 \cos\theta_1 \end{cases} \tag{1}$$

In Figure 13, an example of proximity signal rotation is shown. In particular, Figure 13a,c illustrate the time series of the x and y proximity probes, respectively. Figure 13b illustrates the effective rotation of the orbit.

(a) proximity probe 1

(b) orbits
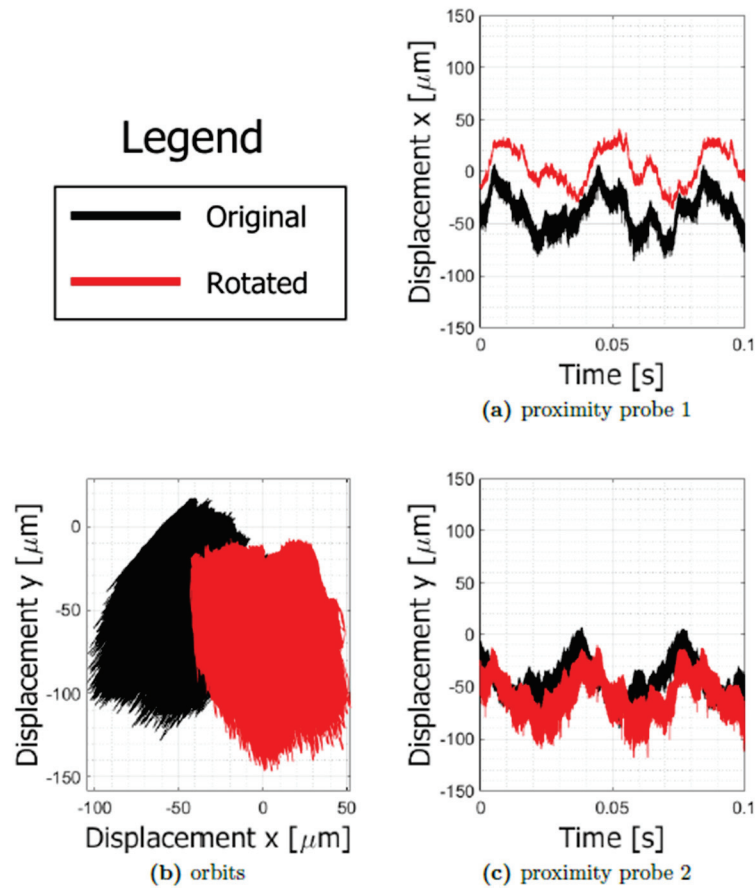
(c) proximity probe 2

Figure 13. Proximity probe signal rotation example.

As seen for the proximity, acceleration signals also needed to be rotated due to the different reference system. Referring to Figure 12, considering the angle between the reference systems θ equal to 135°, with Equation (2) it was possible to rotate the acceleration time series:

$$\begin{cases} a_x = -a_1 \sin\theta_2 + a_2 \cos\theta_2 \\ a_y = -a_1 \cos\theta_2 - a_2 \sin\theta_2 \end{cases} \tag{2}$$

2.6.2. Steady-State Signal Ranging

This type of post process was applied to all accelerometer signals because the acceleration values developed on the stator axis exceeded those that had been predicted. Consequently, the accelerometers often went into saturation, with a behavior similar to that reported in Figure 14, highlighted with red ellipses.
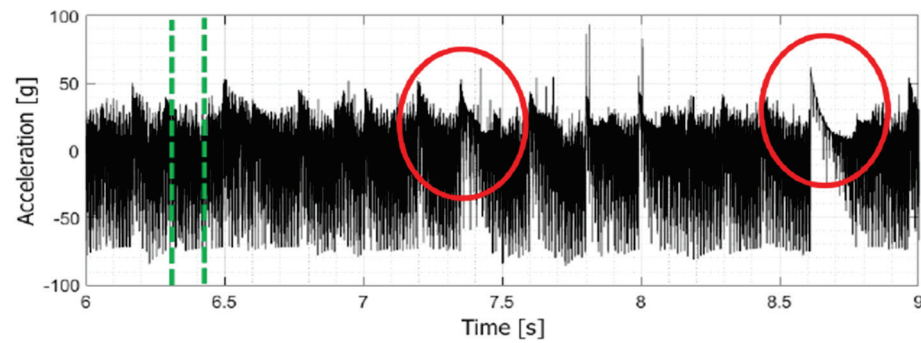
Figure 14. Accelerometer signal saturated time.

For this reason, signal ranging was applied to obtain a steady-state signal. In the example, zooming in on the range defined by dashed green lines, the time series shown in Figure 15 was obtained, useful for frequency-domain consideration.
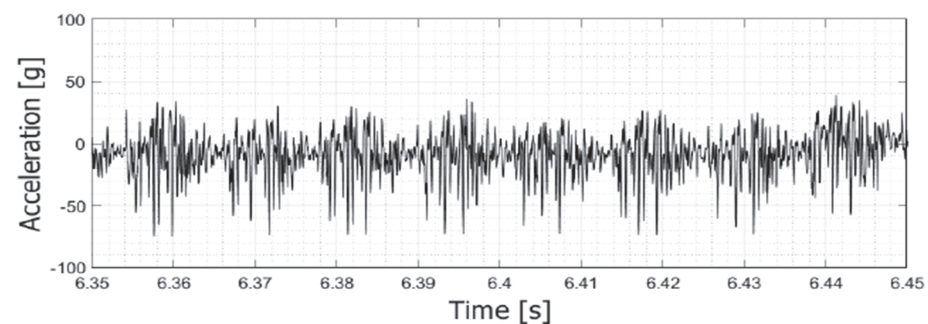
Figure 15. Accelerometer steady-state signal.

2.6.3. Filtering

A filter operation was necessary due to the electrical noise in the signals. During the monitoring of a proximity probe and an accelerometer, both at 0 rpm of the rotor, two high peaks were appreciable, denoting that electrical noise affected the signals at 4000 and 8000 Hz. For this reason, the use of a lowpass filter was a good strategy to remove the noise. A problem arose when supersynchronous frequency components exceeding 4000 Hz were present in the signals (especially in the accelerometers). In these cases, by applying a simple lowpass filter, important parts of the signal were lost. The solution was to apply a multipass filter, trying to remove only the frequencies that represented the noise. The torquemeter was not affected by electrical noise, so no filter was applied. For the displacement signals, the cut frequency for the lowpass filter was between 400 Hz and 1700 Hz, depending on the Fast Fourier Transform (FFT) plot for each test run. For acceleration, as exposed previously, a lowpass filter is not always a good choice to elaborate the signals, especially when the rotation rate is such as to generate supersynchronous frequency components over 4000 Hz. However, in this activity, there were no supersynchronous frequency components and a lowpass filter at 4000 Hz was sufficient to clear the signals of noise.

3. Experimental Results and Discussions

The tested configurations of the test rig were Horizontal "Baseline" (HB), Vertical "Baseline" (VB), Vertical "Low Clearance" (VL) and Vertical "High Clearance" (VH). Geometrical and inertial properties of the tested configurations are reported within Table 3 while Figure 16 illustrates the drawings of the radial PCD inner ring for baseline and low/high clearance configurations.

Table 3. Some geometrical and inertial properties for the tested configurations.

Parameter		HB	VB	VL	VH
Rotor Mass	[kg]	55	61	63	63
Rotor Polar Inertia	[kg·m^2]	1.26	1.31	1.34	1.34
Rotor Diametral Inertia	[kg·m^2]	0.66	0.72	0.77	0.77
Radial Clearance	[μm]	50	50	40	200
PCD Statoric Mass	[kg]	0.517	0.517	3.103	3.103
Pad Rows Distance	[m]	0.029	0.029	0.029	0.029
Rotor–Stator Interface Radius	[m]	0.039	0.039	0.052	0.052
Female PCD Ring Pad Number	[−]	22	22	31	31
Male PCD Ring Pad Number	[−]	21	21	30	30
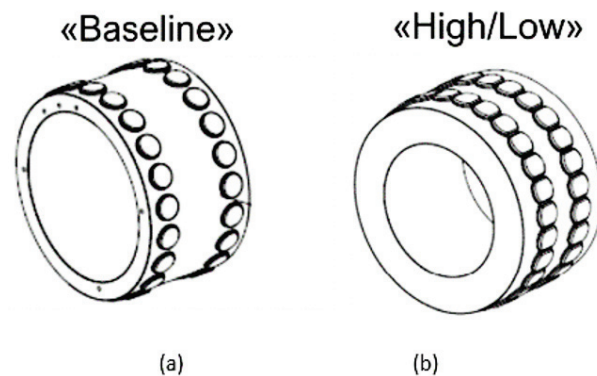
Figure 16. Bearing drawings: (**a**) baseline and (**b**) high/low clearance configurations.

In addition to the masses and inertias of the rotor, among the geometric features of the bearing, it is necessary to highlight the different radial clearances and the different number of pads, which modify accelerometer signals in terms of frequency and amplitude. Firstly, some useful comparisons between configurations are presented in terms of orbits, mean and peak-to-peak values and frequency spectrum, in the function of rotational speed.

3.1. Comparison of Horizontal "Baseline" vs. Vertical "Baseline"

These two configurations were different just for the effect of gravity acceleration and the rotor mass and inertia. The PCD bearing mounted was the same, with the same geometrical characteristics. Time and frequency domains are discussed in detail in the following paragraphs. The same approach is adopted for both configurations analyzed.

3.1.1. Time-Domain Analysis

A comparison between the orbits for the tested configuration is reported in Figure 17. The dashed blue line, representing the clearance circle, is centered in the nominal axis of the stator. This circle is just a representation; the real center depends on the stator deformation. In black are shown the results for the Horizontal "Baseline" case, while in red are those for the Vertical "Baseline". The effect of gravity is evident at all revolution speeds. Furthermore, the shape of the orbits is different; in particular, the horizontal configuration has a preferential area of rubbing due to gravity which, at lower rotation speeds, pulls the rotor downwards. Beyond a certain speed, the orbit has a shape very similar to that of the vertical configuration, always maintaining a downward translation.

Considering now the torque absorption, for which the mean values versus rotational speed for both the configurations are reported in Figure 18, it can be noted that up to 1000 rpm the vertical configuration has the lower absorption. In the range from 1500 to 3500 rpm, the average value is about the same, followed by a marked increase over 4000 rpm, in which the vertical configuration comes to absorb an additional 25% in respect to the horizontal one. This increase is mainly justified by the fact that the vertical configuration requires a thrust PCD bearing, which also absorbs a fair amount of torque. The

higher values of the horizontal configuration at low speeds depend probably on the type of contact: at this speed there are many impulses were generated by high frictional forces.

(a) 3000 rpm

(b) 3500 rpm

(c) 4000 rpm

(d) 4500 rpm

(e) 5500 rpm
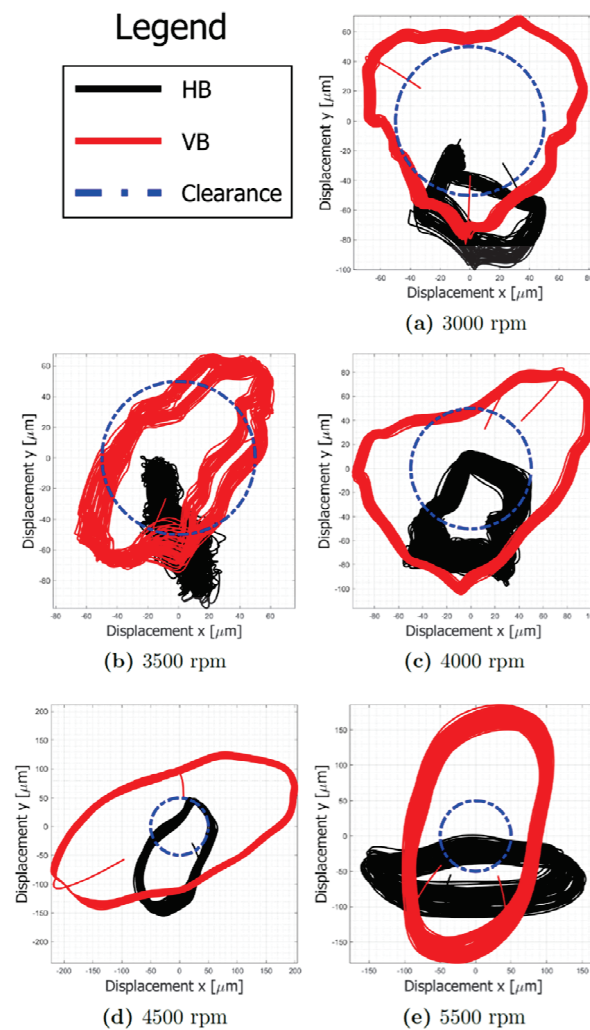
Figure 17. Orbit comparison between Horizontal "Baseline" and Vertical "Baseline".
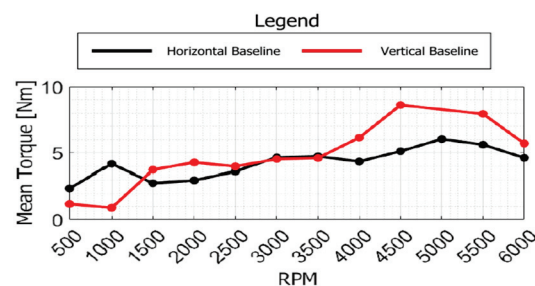
Figure 18. Torque mean value comparison between Horizontal "Baseline" and Vertical "Baseline".

3.1.2. Frequency-Domain Analysis

Now the signals from the proximitor, accelerometer and torquemeter will be analyzed using a frequency spectrum cascade. Considering the proximitor signals, reported in Figure 19a and Figure 19b for the Horizontal "Baseline" and Vertical "Baseline", respectively, it can be observed that the main frequency of the components is represented by the synchronous frequency, for both configurations. In some speed runs, the rise in the x2 component is visible, but always lower than x1.
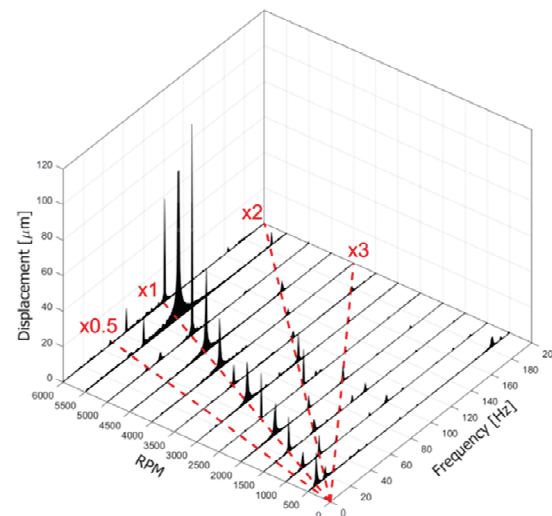
(a) Horizontal Baseline
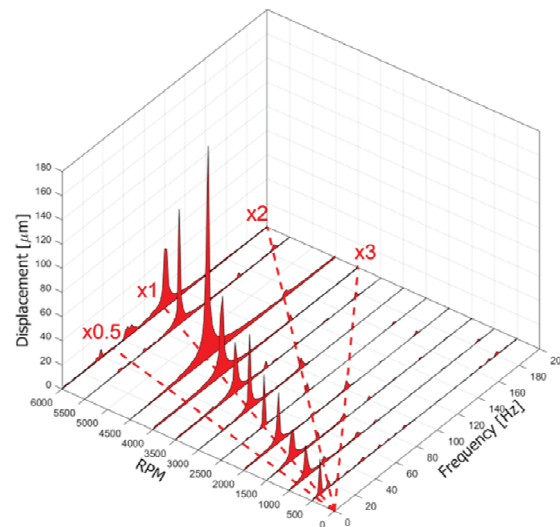
(b) Vertical Baseline

Figure 19. Frequency spectrum cascade comparison for proximitor.

Turning to accelerations and remembering that the number of pads for the PCD bearing is 21 for the male and 22 for the female ring, we can easily see how the main frequency components are multiples of the number of pads. Waterfall diagrams are visible in Figure 20a and Figure 20b for the Horizontal "Baseline" and Vertical "Baseline", respectively. Lower synchronous components (such as x1, x2 etc.) are not evident at speeds lower than 3000 rpm. Some of them appear from 3500 rpm, but always with an amplitude lower than the pad multiple.

To compare the configurations at different revolution speeds, FFT areas are plotted in Figure 21. Assuming that the acceleration is a measure of the force exchanged during the contact of the PCD bearing, and therefore a measure of the dynamic stress induced by the rotor, it can be observed that the accelerations are lower for the Vertical "Baseline" configuration up to 3500 rpm, where they go over those of the horizontal configuration. Subsequently, immediately after 5000 rpm, the vertical configuration shows a better behavior.
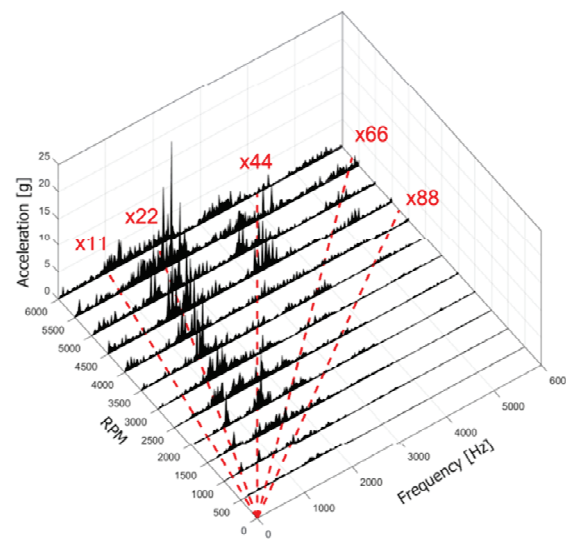
(a) Horizontal Baseline
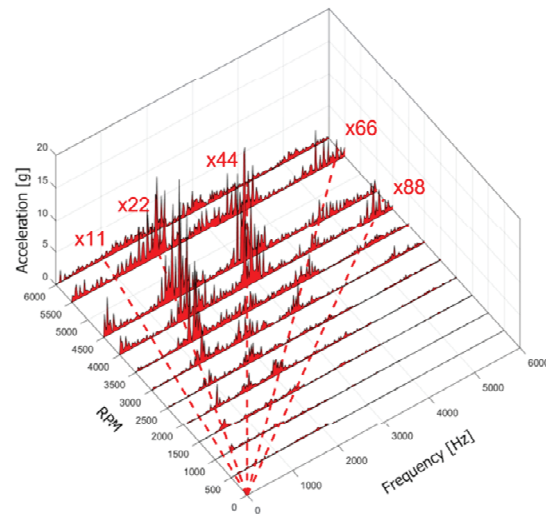
(b) Vertical Baseline

Figure 20. Frequency spectrum cascade comparison for accelerometer.
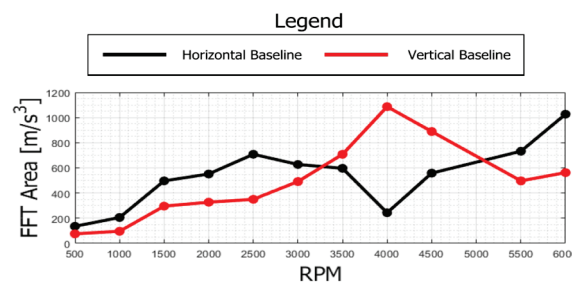
Figure 21. Acceleration FFT area comparison.

Focusing on some working speeds, frequency spectra comparison is shown in Figure 22. Conforming to the trend described in Figure 21, at 3500 and 4500 rpm vertical peaks are somewhat higher than the horizontal ones. Instead, at 5500 rpm the accelerometer in the x direction for the horizontal configuration shows a pad synchronous peak higher than that of the vertical configuration. Looking at the torque absorption in Figure 23a,b for the Horizontal "Baseline" and Vertical "Baseline", respectively, the behavior is a little bit different for each configuration. In particular, for the HB, the main frequency component is

the synchronous one but from 3500 rpm x2 arise until they become higher than x1. In one case, at 4000 rpm, the x3 component is higher than x1 and x2. Finally, at 3000 rpm, x4 is higher than x1. Instead, for VB, x1 increases linearly with the revolution speed except for 6000 rpm. x2 is almost always present, and higher than x1 just from 3000 to 4000 rpm. x3 is present and the highest at 2500 rpm.
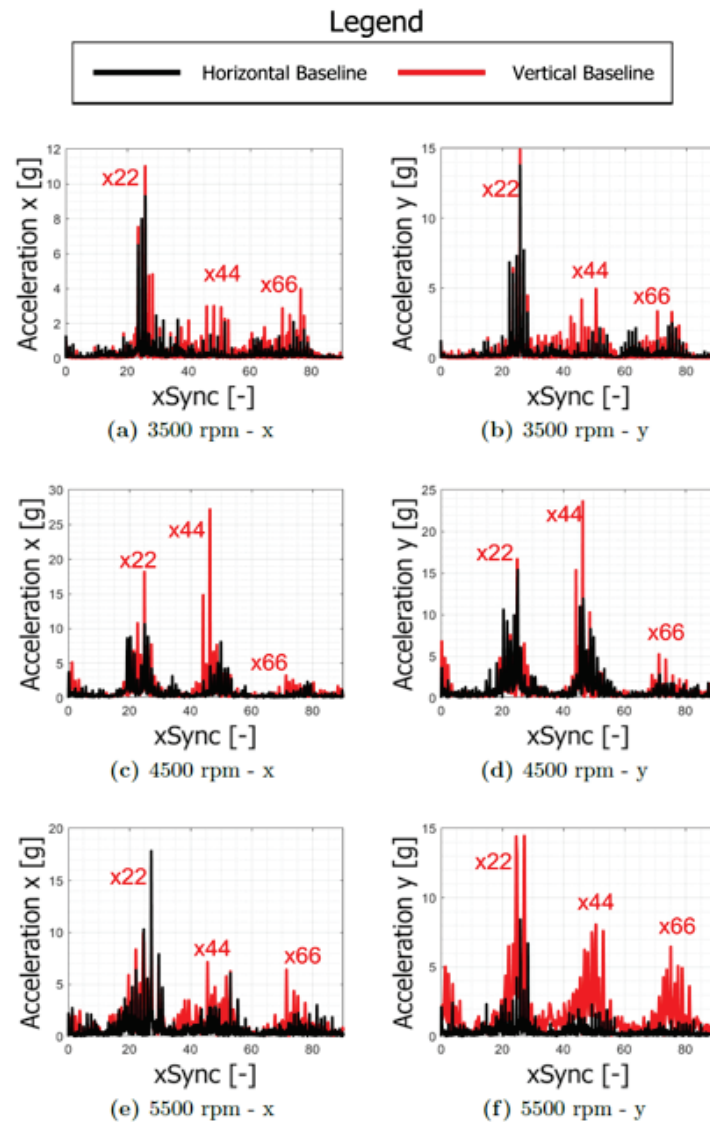
Figure 22. Frequency spectrum comparison for Horizontal and Vertical Baseline.

3.2. Comparison of Vertical "Baseline", "Low" and "High"

These three configurations were different just for the radial clearance, which was equal to 50 μm for the Vertical "Baseline", 40 μm for the Vertical "Low" and 200 μm for the Vertical "High".

3.2.1. Time-Domain Analysis

A comparison between the orbits normalized with respect to the radial clearance for the three tested configurations is visible in Figure 24. The "Baseline", "Low" and "High" clearance vertical configurations, respectively, are represented in the solid red, blue and green lines. The black dashed circle line represents the normalized clearance circle. For VB, a preferential direction of stretching for the orbit is quite clear, while the VL and VH orbits are much more circular. From 3000 rpm, the VH orbit is quite chaotic in comparison to the

other two, but always circular-shaped. In Figure 25 are shown the mean torque absorptions for the three configurations. All of them have the same axial PCD bearing, so it is possible to perform a direct comparison. All of the mean values get higher the higher the revolution speed. A geometrical parameter that affects this measure is the rotor–stator interface radius; look at Table 3. For the lower value of the interface radius (39 mm), VB has generally the lower mean torque absorption. The other two configurations have the same interface radius (52 mm); for 500 and 1000 rpm, the lower value for VH can be justified because the stiffness of the metal bellows draws the rotor to the center, avoiding contact. For higher revolution speeds, the mean torque is almost the same for both the VL and VH configurations.
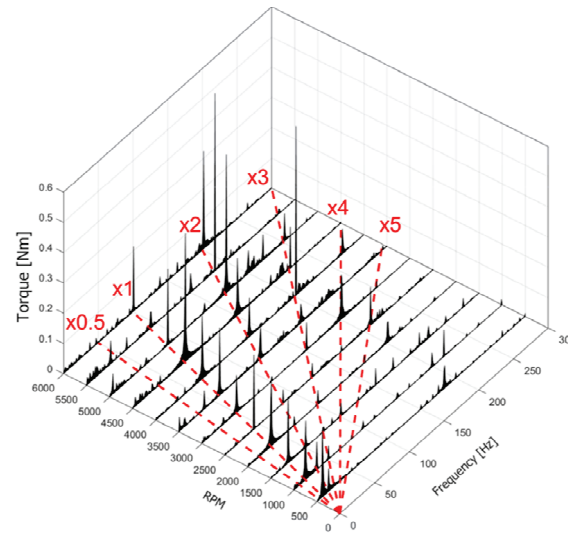
(a) Horizontal Baseline
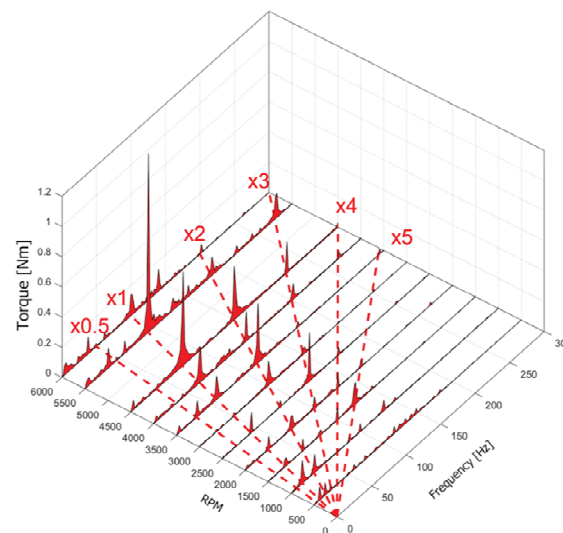
(b) Vertical Baseline

Figure 23. Frequency spectrum cascade comparison for torquemeter.
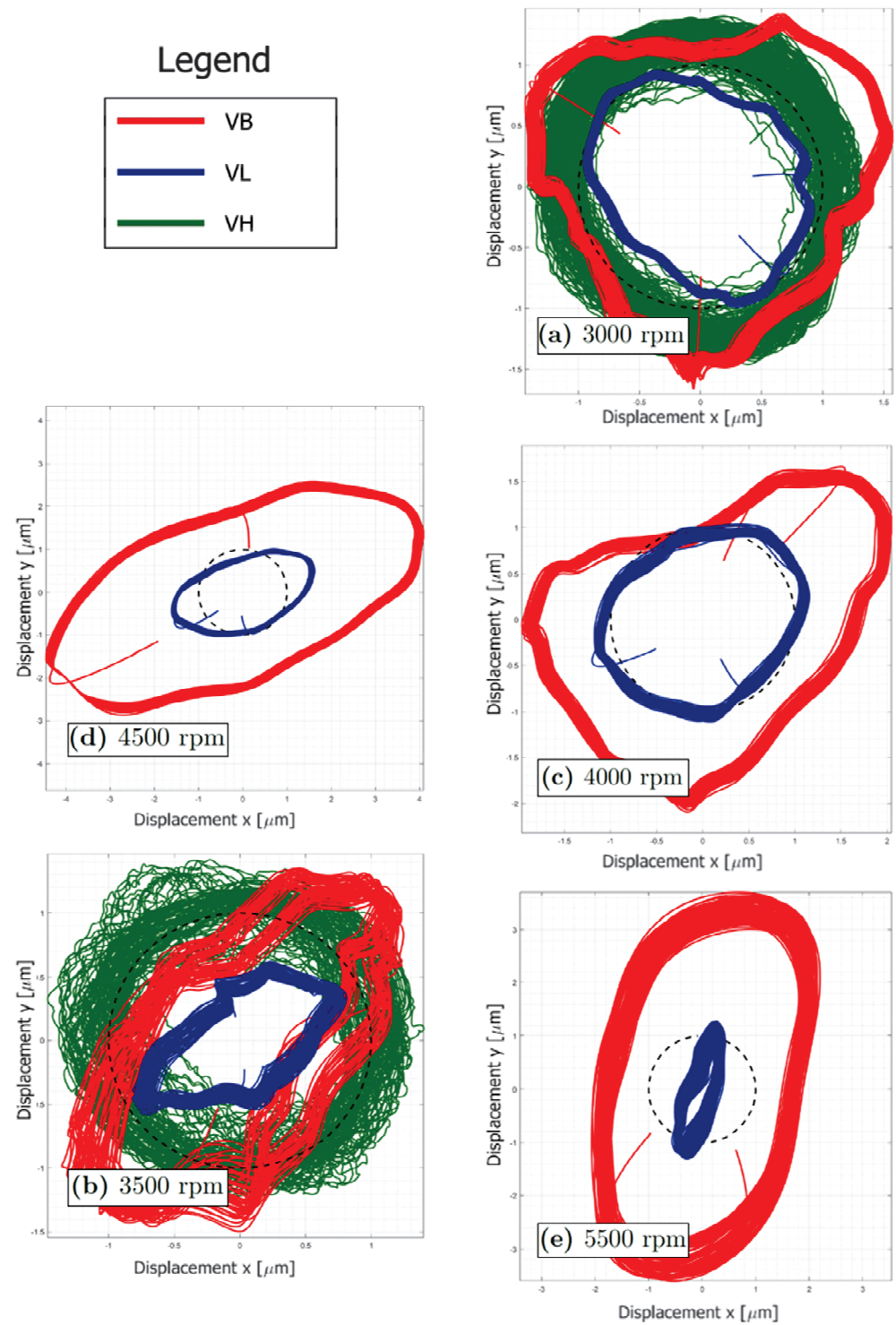
Figure 24. Orbit comparison between Vertical "Baseline", "Low" and "High" clearance.
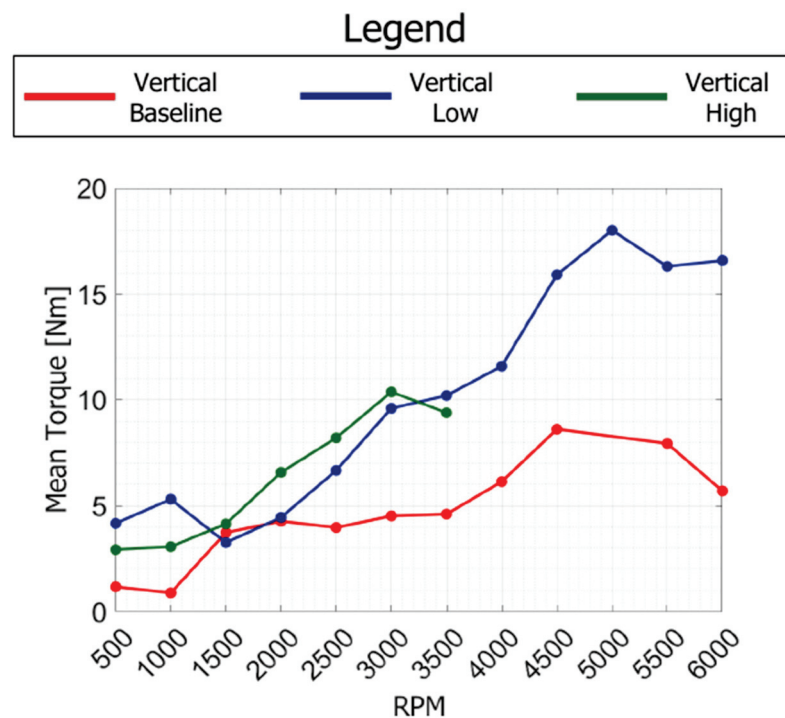
Figure 25. Torque mean value comparison between Vertical "Baseline", "Low" and "High" clearance.

3.2.2. Frequency-Domain Analysis

Now the signals from the proximitor, accelerometer and torquemeter will be analyzed using the frequency spectrum cascade. Considering the proximitor signals, reported in Figure 26 for all vertical configurations, it is possible to see that the main frequency component is represented by the synchronous peak. The High clearance configuration does not experience any supersynchronous frequency components, while, at a higher speed, the spectrum suggests an extreme shock and chaotic motion. For the "baseline" and "low" configurations, in some speed runs it a rise in the x2 component can be observed, always lower than that of x1. Concerning the accelerations, in Figure 27 the comparison between the FFT area is shown, in order to evaluate which configuration is the most critical considering the stator dynamic load. At the lower speeds (500 and 1000 rpm) the "high" clearance configuration is near zero in acceleration. When impact occurs, from 1500 to 2500 rpm, "high" overcomes "low" clearance. Over 3000 rpm, "high" clearance is the highest in terms of acceleration's FFT area. It is evident that clearance really affects the stator–rotor force interaction.

In Figure 28 are shown the waterfall diagrams for the three configurations. It is theoretically plausible that the supersynchronous components derive from the pad number. Remembering Table 3 and looking at the pad number, the Vertical "Baseline" configuration experiences x22, in strong accordance with this theory. On the other hand, the "low" and "high" configurations, despite a number of pads of 25 for the male ring and 26 for the female ring, experience multiple x30, x60 and x90. Frequency spectra comparison for the three configurations at the main running speeds (3000, 3500, 4000, 4500, 5500 and 6000 rpm) are shown in Figure 29. Interestingly, the VB configuration experiences the highest accelerations up to 6000 rpm, where there is a drastic reduction in peaks. The VH configuration has the lowest peaks. This is probably due to the increased clearance that permits the metal bellows to slow down the rotor before impact.
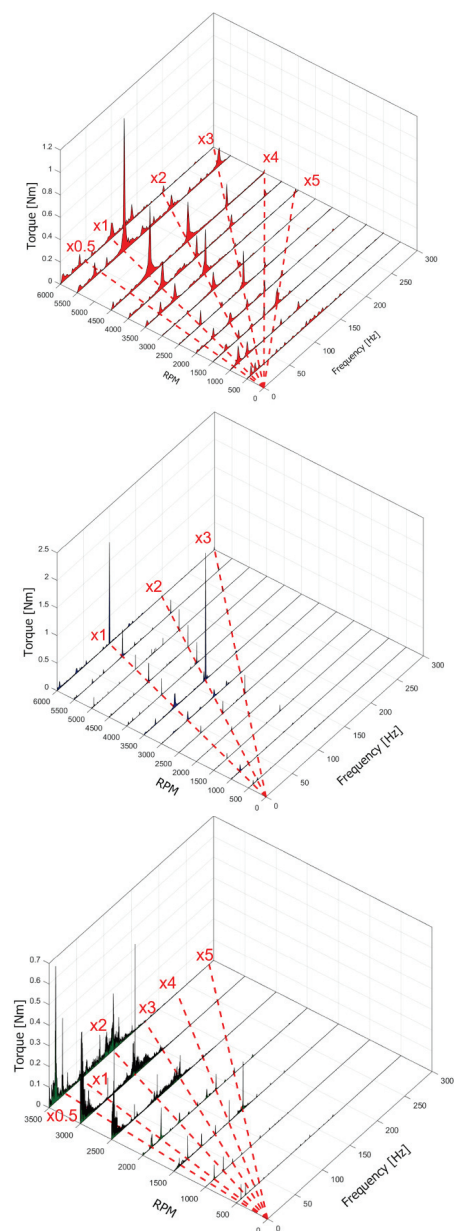
Figure 26. Frequency spectrum cascade comparison for proximity probe (Vertical Baseline, Vertical Low and Vertical High).
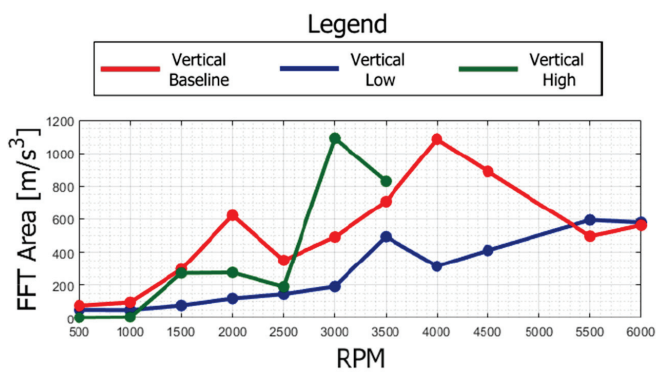
Figure 27. Acceleration FFT area comparison between Vertical "Baseline", "Low" and "High" clearance.
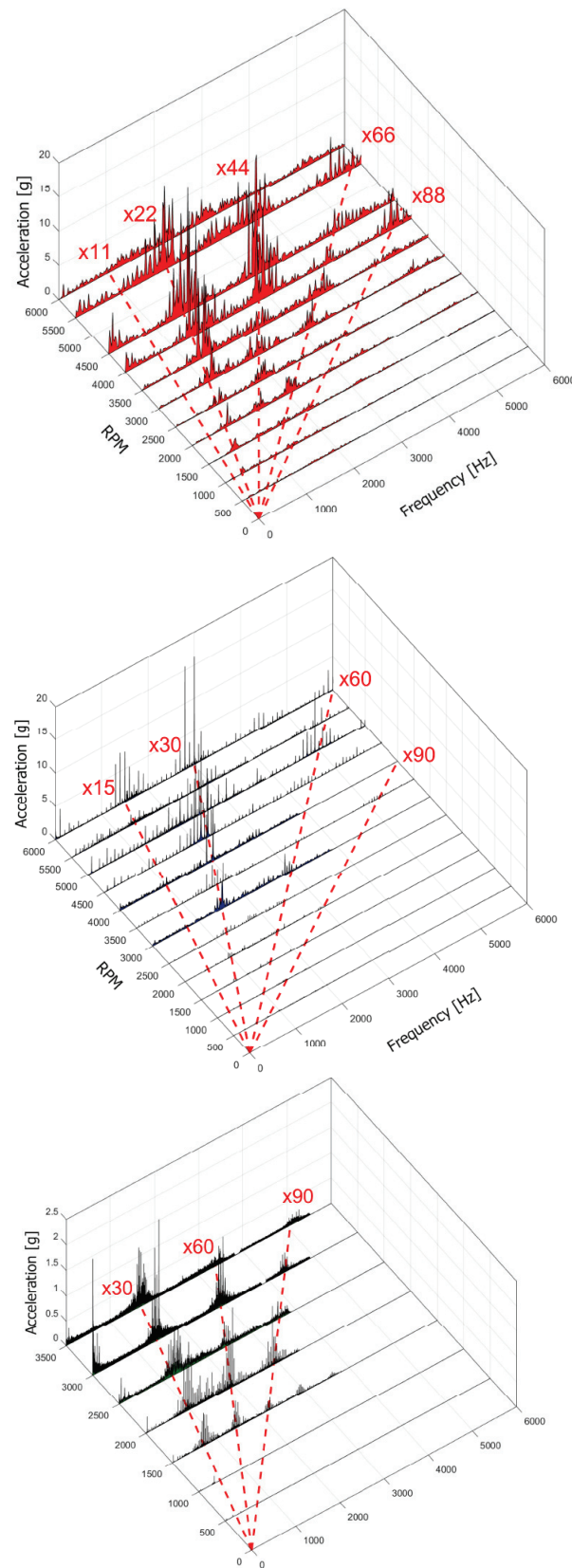
Figure 28. Frequency spectrum cascade comparison for accelerometer (Vertical Baseline, Vertical Low and Vertical High).
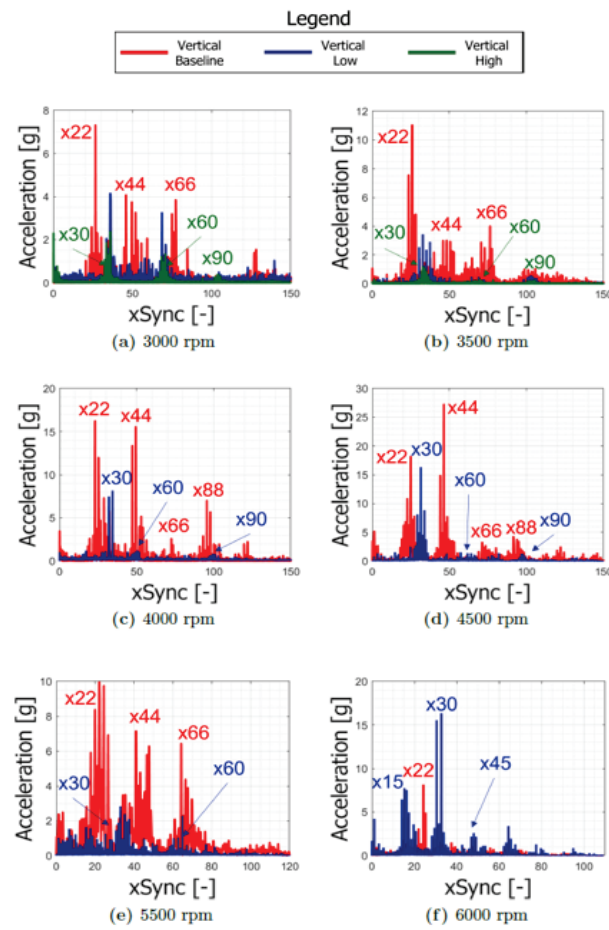
Figure 29. Frequency spectrum cascade comparison for "Vertical Baseline", "Vertical Low" and "Vertical High".

At 3000 rpm, this trend reverses and VL has peaks greater than VH. At the overspeed of 6000 rpm, the "low" clearance configuration has the highest acceleration peak at x30, and x15 and x45. Passing now to the torque absorption, depicted in Figure 30, VH has a more chaotic frequency spectrum, probably caused by the high-impact frequency. At 1500 rpm, it is possible to see the higher peak at the x5 supersynchronous component. VL has a cleaner behavior. The synchronous component is always similar to x2 except for 6000 rpm where it is higher. At 3500 rpm, the highest peak appears at the x3 supersynchronous component.
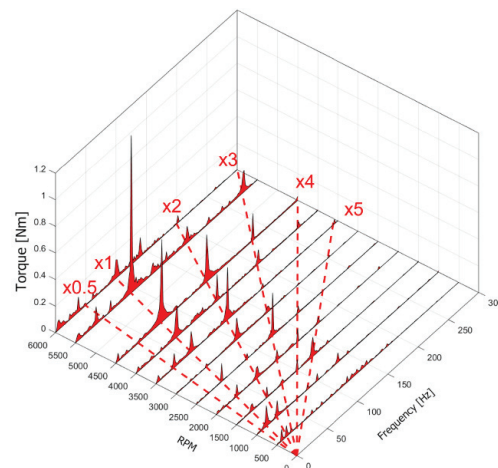
Figure 30. *Cont.*
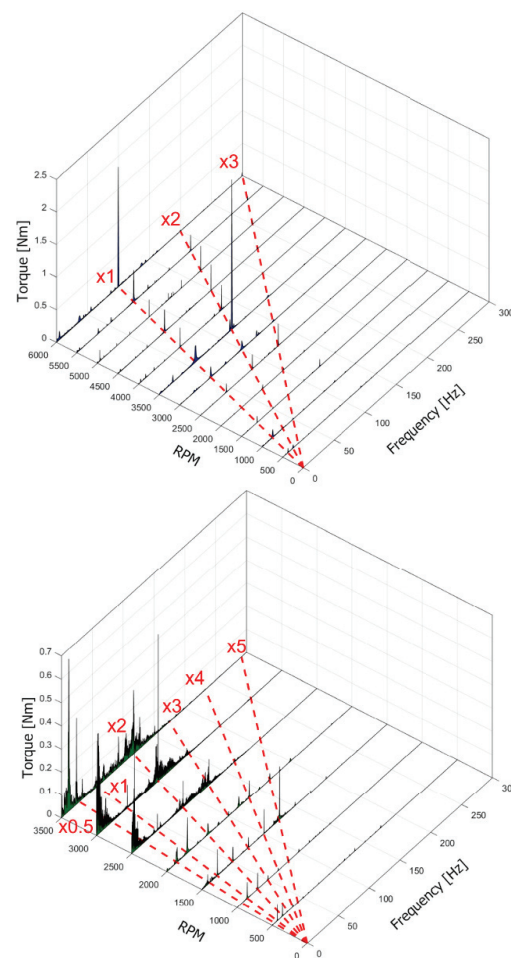
Figure 30. Frequency spectrum cascade comparison for torquemeter (Vertical Baseline, Vertical Low and Vertical High).

4. Conclusions and Future Developments

In the present activity, a rotor dynamics test bench was designed and instrumented to study the behavior of a turbomachinery rotor resting on innovative polycrystalline diamond (PCD) plain bearings. The aim of the work was to acquire the orbits, stator accelerations and absorbed torque for various types of bearings ("Baseline", "Low" and "High") in various configurations ("Horizontal" and "Vertical") and consequently carry out comparisons between them. Much experimental data was acquired. As for the experimental results, within this paragraph the comparisons between the reference configurations are discussed.

4.1. Horizontal Baseline vs. Vertical Baseline

The behavior of the vertical configuration is certainly more stable due to the nature of the continuous contact present between the rotor and stator, which generates more "common" orbits in rotor dynamics. On the other hand, the horizontal configuration presents an intermittent contact at lower speeds and consequently the generated acceleration results were higher. However, it is extremely important to take into account the dynamic behavior of the stator, as any unexpected resonances could increase the order of magnitude of the accelerations and consequently compromise the operation of the machine, even if apparently the behavior could be quieter. From a frequency-domain point of view, the presence of a supersynchronous multiple of the number of pads was immediately noticed. These peaks very often turned out to be higher than the synchronous ones, and therefore must necessarily be taken into consideration in the design phase. As far as the absorbed torque is concerned, the configurations are essentially the same. Considering that in the Vertical Baseline configuration there is an additional PCD thrust bearing, below 3500 rpm

the torque of the Vertical Baseline is lower than that of the Horizontal Baseline. This can be explained by the nature of continuous contact which reduces the frictional force compared to intermittent contact. At high speeds, when the nature of the contact is the same (and therefore the orbits are almost elliptical), the Vertical Baseline absorbs more power due to the axial PCD.

4.2. Vertical Baseline vs Vertical Low vs. Vertical High

With the same orientation, the main difference between these configurations consists in the interface radius between the rotor and stator and the radial clearance present in the PCD bearings; the latter is the parameter that, in this case, distinguishes the type of contact (with the same unbalance and rotation speed). From the orbits, it can be deduced that for the Vertical Low and Vertical Baseline configurations, the behavior is stable with continuous contact, at least at industrially useful speeds. In the Vertical High configuration, on the other hand, since there is a lot of radial gap available, the rotor comes into contact only from 1000 rpm upwards. Consequently, its behavior is very unstable and with intermittent contact. As for the accelerations, we have seen how the Vertical Baseline presents higher accelerations, especially from 3000 rpm onwards. In the frequency domain, the presence of a supersynchronous multiple of the number of pads is still evident. Finally, with regard to the absorbed torque, it was immediately clear that the fundamental difference is caused by the interface radius between the rotor and stator.

As an extension to the present study, the definition of an effective numerical model for the prediction of the test rig performance will represent the most important development. This will be essential to make the global method more effective and faster. In addition, the high modularity of the system could allow the testing of several and different working conditions, with the objective to extend the adoption of the PCD bearing to other turbomachinery applications.

References

1. Barnard, A.S. *The Diamond Formula: Diamond Synthesis: A Gemmological Perspective*; Butter-worth-Heinemann: Oxford, MA, USA, 2000.
2. Donoghue, M. *Gems: Their Sources, Descriptions and Identification*; Butterworth-Heinemann: Oxford, MA, USA, 2006.
3. Spear, K. *Synthetic Diamond: Emerging CVD Science and Technology*; Wiley: New York, NY, USA, 1994.
4. US Synthetic (CHAMPION X), PCD Drilling Tools. Available online: https://www.championx.com/products-and-solutions/drilling-technologies/diamond-bearings (accessed on 5 June 2024).
5. Lingwall, B.; Sexton, T.; Cooley, C. Polycrystalline diamond bearing testing for marine hydrokinetic application. *Wear* **2013**, *302*, 1514–1519. [CrossRef]
6. Knuteson, C.; Sexton, T.; Cooley, C. Wear-in behavior of polycrystalline diamond thrust bearings. *Wear* **2011**, *271*, 2106–2110. [CrossRef]

7. Sexton, T.; Cooley, C. Polycrystalline diamond thrust bearings for down-hole oil and gas drilling tools. *Wear* **2009**, *267*, 1041–1045. [CrossRef]

8. Bromaghin, A.; Ali, M.; Ravens, T.; Petersen, T.; Hoffman, J. Experimental study of abrasion characteristics for critical sliding components for use in hydrokinetic devices. *Renew. Energy* **2014**, *66*, 205–214. [CrossRef]

9. Cooley, C.; Khonsari, M.; Lingwall, B. *The Development of Open Water-Lubricated Polycrystalline Diamond (PCD) Thrust Bearings for Use in Marine Hydrokinetic (MHK) Energy Machines*; Technical Report; US Synthetic Bearings: The Woodlands, TX, USA, 2012.

10. Dykas, B.; Bruckner, R.; DellaCorte, C.; Edmonds, B.; Prahl, J. Design, Fabrication, and Performance of Foil Gas Thrust Bearings for Microturbomachinery Applications. *J. Eng. Gas Turbines Power* **2008**, *131*, 012301. [CrossRef]

11. Andrés, L.S.; Phillips, S.; Childs, D. A Water-Lubricated Hybrid Thrust Bearing: Measurements and Predictions of Static Load Performance. *J. Eng. Gas Turbines Power* **2016**, *139*, 022506. [CrossRef]

12. Norrbin, C.S.; Childs, D.W. Lateral Equilibrium Position Analysis Program with Applications to Electric Submersible Pumps. *J. Eng. Gas Turbines Power* **2018**, *140*, 38482. [CrossRef]

13. Norrbin, C.S.; Childs, D.W.; Phillips, S. Including Housing–Casing Fluid in a Lateral Rotordynamics Analysis on Electric Submersible Pumps. *J. Eng. Gas Turbines Power* **2017**, *139*, 062505. [CrossRef]

14. Gilardi, G.; Sharf, I. Literature survey of contact dynamics modelling. *Mech. Mach. Theory* **2002**, *37*, 1213–1239. [CrossRef]

15. Machado, M.; Moreira, P.; Flores, P.; Lankarani, H.M. Compliant contact force models in multibody dynamics: Evolution of the Hertz contact theory. *Mech. Mach. Theory* **2012**, *53*, 99–121. [CrossRef]

16. Skrinjar, L.; Slavič, J.; Boltežar, M. A review of continuous contact-force models in multibody dynamics. *Int. J. Mech. Sci.* **2018**, *145*, 171–187. [CrossRef]

Article

Engineering Biomedical Problems to Detect Carcinomas: A Tomographic Impedance Approach

Filippo Laganà [1,†], **Danilo Prattico** [2,*,†], **Domenico De Carlo** [2], **Giuseppe Oliva** [1], **Salvatore A. Pullano** [1] and **Salvatore Calcagno** [2,*]

1. Department of Health Science, Magna Graecia University, I-88100 Catanzaro, Italy; filippo.lagana@unicz.it (F.L.); giuseppe.oliva@unicz.it (G.O.); pullano@unicz.it (S.A.P.)
2. DICEAM Department, Mediterranea University, I-89122 Reggio Calabria, Italy; domenico.decarlo@unirc.it
*   Correspondence: danilo.prattico@unirc.it (D.P.); calcagno@unirc.it (S.C.)
†   These authors contributed equally to this work.

Abstract: Computed tomography (CT), magnetic resonance imaging (MRI), and radiography expose patients to electromagnetic fields (EMFs) and ionizing radiation. As an alternative, Electrical Impedance Tomography (EIT) offers a less EMF-influenced method for imaging by measuring superficial skin currents to provide a map of the body's conductivity. EIT allows for functional monitoring of anatomical regions using low electromagnetic fields and minimal exposure times. This paper investigates the application of EIT for the morphological and functional assessment of tissues. Using the Finite Element Method (FEM) (Comsol 5.2), both two-dimensional and three-dimensional models and simulations of physiological and pathological tissues were developed to replicate EIT operations. The primary objective is to detect carcinoma by analysing the electrical impedance response to externally applied excitations. An eight-electrode tomograph was utilised for this purpose, specifically targeting epithelial tissue. The study allowed the characterisation of tomographs of any size and, therefore, the possibility to verify both their geometric profile and the ideal value of the excitation current to be delivered per second of the type of tissue to be analysed. Simulations were conducted to observe electrical impedance variations within a homogeneously modelled tissue and a carcinoma characterized by regular geometry. The outcomes demonstrated the potential of EIT as a viable technique for carcinoma detection, emphasizing its utility in medical diagnostics with reduced EMF exposure.

Keywords: biomedical signal; electronic systems; electrical impedance tomography

1. Introduction

Electrical Impedance Tomography (EIT) is a non-invasive imaging modality that exploits the varying electrical impedance properties of biological tissues [1]. EIT operates on the principle that different tissues exhibit distinct impedance responses when subjected to a small, alternating current, a variance attributed to the tissues' intrinsic electrical conductivity and permittivity characteristics influenced by factors such as cellular structure, fluid content, and pathological alterations. The result is a map of the electrical conductivity of the analyzed area [2]. An EIT system typically consists of a series of surface electrodes arranged around the periphery of the region of interest. Adhesive electrodes are placed on the skin, and an alternating electric current, typically a few milliamps and within the range of 10 to 100 kHz—below the threshold of nerve stimulation—is applied between pairs of electrodes [3]. Voltage measurements are then collected using additional electrodes, requiring numerous stimulation patterns to gather comprehensive data. These measurements are processed through sophisticated reconstruction algorithms to generate cross-sectional images depicting the internal impedance distribution of the tissues. A primary advantage of the EIT is its ability to provide functional images in real-time, along with its ability to

produce thousands of images per second. Its main limitation is its low spatial resolution because recordings are typically made by applying current to the organism or system under examination, using a series of electrodes, and measuring the voltage developed between other electrodes. The electric current usually flows through the sample by ionic conduction, and therefore, measurements can provide information on changes in ion mobility, such as viscosity and temperature. The impedance of ice, for example, is much higher than that of water, so EIT measurements can provide information on freezing and thawing. Unlike traditional imaging techniques such as CT and MRI, which predominantly offer anatomical details, EIT can monitor dynamic physiological processes, including respiration, cardiac function, and blood flow.

EIT systems employ the finite element method (FEM) for image reconstruction and visualisation, solving iterative algorithms to produce detailed images. Electrical Capacitance Tomography (ECT), a related technique, retrieves information on the distribution of contents within closed vessels, providing cross-sectional images, volume fraction measurements, and flow analysis through dielectric properties. The sensitivity of EIT to impedance variations renders it an effective tool for detecting pathological conditions [4]. For example, tumours or lesions that alter the normal impedance profile of tissues can be identified through EIT imaging. The technique shows promise in the early detection of conditions such as breast cancer, lung pathologies, and brain injuries. In EIT, the electrical current flows through ionic conductors, providing information about ion mobility, viscosity, and temperature changes. Data acquisition methods in EIT include the "Adjacent strategy" and the "Opposite Potentials Method" [5,6]. Despite its potential, EIT faces challenges, notably the lower spatial resolution of its images compared to other imaging modalities. This limitation arises from the ill-posed nature of the inverse problem involved in reconstructing impedance distributions from surface measurements. Enhancing image resolution and accuracy necessitates the development of advanced reconstruction algorithms and improved electrode configurations. The image reconstruction process begins with defining a physical model for the observations derived from equations linking the measurements of potentials, injected currents, and resistivity distribution based on Maxwell's equations [7,8]. While the governing equation for the body's interior remains constant across models, the boundary conditions differ. The interpretation of EIT images can be complex, requiring the integration of EIT data with other imaging modalities and clinical information to enhance diagnostic accuracy. Ongoing research aims to address these limitations and expand the clinical applications of EIT, demonstrating its potential as a valuable tool in medical diagnostics and patient care. In this paper, a comprehensive modeling of Electrical Impedance Tomography (EIT) is presented, examining the most widely used physical models. The research focuses on analysing epithelial tissue using EIT to identify any carcinomas present within it. Different mathematical formulations of EIT problem are possible, i.e., using integral boundary equations [9] usually solved using the Galerkin method [10,11] in conjunction with GMRES or BiCGSTAb methods [12], or differential models solved using the difference finite (DF) approach [13]. In this work, Finite Element Method (FEM) software (Version 5.2) is employed to model a cylindrical EIT system with eight electrodes. Subsequently, the electrical and magnetic properties of the tomograph and the tissue sample are meticulously configured. The analysis involves applying a potential difference across the electrodes, generating an induced current within the material immersed in a saline solution. The resultant impedance variations are then evaluated and analysed to detect abnormalities. In summary, Electrical Impedance Tomography offers a valuable, non-invasive approach for both functional and pathological imaging. Its ability to provide real-time monitoring and detect tissue abnormalities through impedance variations makes it a promising tool in medical diagnostics and patient care. Ongoing advancements in algorithm development, hardware design, and clinical integration are crucial to fully harness the potential of EIT in various medical applications. The present document is organised as follows: Section 2 lists similar works in which there are different points of view from the one presented in the paper. Section 3 discusses the EIT mathematical model and epithelial tissue, particularly the

physical and mathematical characteristics. Section 4 describes the model implemented in the Comsol (Version 5.2) Multiphysics environment. Section 5 reports the results obtained from the processing of the experimental data. Finally, conclusions are drawn.

2. Related Works

Electrical impedance tomography (EIT) has emerged as a significant innovation that has revolutionised critical care [14]. Even still, compared to other imaging techniques, such as computerised thermography (TC), EIT has a lower reconstruction quality and needs more processing resources for medical applications [15]. However, in recent years, EIT has been widely used, with excellent results, thanks in part to the evolution of the tomographs, which have new features [16]. Over time, the information obtained has been combined with the patient's vital signs automatically and in real-time and provides the doctor with timely and in-depth information even during the visit. Electrical impedance tomography, which has proven to be incredibly helpful and has been more readily incorporated into routine clinical practice, is primarily responsible for making this feasible. In the past, the EIT was not widely utilised in hospitals, and those who did thought its primary applications were in research and critical care. However, those very same researchers have demonstrated that EIT is not only useful in resuscitation but also in the operating room, directly contributing significantly at the patient's bedside without requiring the patient to wait for data processing or the outcome of potentially lengthy investigations. The image reconstruction procedure is the main area of attention for EIT improvement. Through a complex process, the conductivity distribution of the body is described by coherent pictures created from recorded voltage variations. Complex methods developed to solve the inverse issue of determining internal conductivity from surface voltage measurements are used to perform this task. Due to the small number of electrodes and the complicated three-dimensional structure of the human anatomy, these algorithms handle the challenges presented by the limited data that are accessible [17]. Numerous factors, including the number and configuration of measuring electrodes, measurement precision, applied voltage and injected current patterns, and measurement accuracy, impact the quality of the EIT image reconstruction [18]. Small intrusive spikes are used to circumvent the high-impedance area of the stratum corneum in a minimally invasive electrical impedance-based approach to assess the electrical impedance of the skin [19]. This method involves inserting tiny, intrusive spikes into the targeted skin layer to measure changes associated with disease [20]. This technique's ability to identify malignancies linked to the skin's deeper layers is one of its main advantages. Based on our investigation of the literature, we have categorised minimally invasive approaches into three categories: electrical impedance tomography (EIT), electrical impedance scanning, and minimally invasive electrical impedance spectroscopy. Using a variety of potential methods, EIT has been suggested as a legitimate way to determine the patient's ideal PEEP [21,22]. Therefore, electrical impedance measurement plays an important role in showing morphological changes related to the growth of the cancerous skin lesion [23].

Multi-frequency impedance spectra are used to detect the electrical bio-impedance of different skin lesions [24,25]. To improve the signal-to-noise ratio, impedance is measured using an impedance spectrometer between 1 kHz and 1 MHz of various skin tumours, including melanoma. By applying a small AC voltage and comparing the measured current with the voltage, the impedance between two electrodes is measured.

Impedance variation is used to detect skin cancer using information about the shape, structure and orientation of cells, the integrity of cell membranes, the relative properties of intra- and extra-cellular fluids and ionic composition. Electrical impedance helps differentiate cancerous from non-cancerous cells in the range of 1 kHz to 2.5 MHz [26]. Bio-impedance spectroscopy is also available in portable form and is used to monitor the physiological system [27]. The latest advances in electrical bio-impedance approaches for skin cancer diagnosis are shown in Table 1.

Table 1. Electrical bio-impedance techniques for skin cancer diagnosis.

Signal Used	Description	Merits	Demerits	Reference
1 kHz and 1000 kHz	Distinguishes the skin cancer from the benign lesions using multi-frequency impedance spectra	The result obtained is more accurate than conventional methods	Distinguishing the tumours takes more time, and false results may also be obtained	[24]
1–1000 kHz	Compares the detection of skin cancer by a non-invasive probe and micro-invasive electrode system, whose surface is furnished with tiny spikes which get penetrated to the stratum corneum	The electrode system produces a better result	Minimally invasive technique	[28]
1 kHz and 1 MHz	Describes the method for detecting skin cancer using electric impedance. The electric impedance of the biological system decreases with the increase in frequency	High resolution	Multivariate and the impedance is complex	[29]
1 kHz to 2.5 MHz	Accuracy of electrical impedance to classify malignant melanoma from benign tumour by automated classification algorithm	Accuracy is high	Various algorithm is needed for the classification of skin cancer	[25]
1–100 kHz	Non-invasive approach for detecting the presence of skin lesions by measuring the impedance change	Low-cost and portable	Electrodes are used, which cause discomfort	[30]
1 kHz to 2.5 MHz	EIS algorithm is used on lesions to differentiate normal skin from abnormal lesions	High resolution	An experienced physician is required	[20]
20 kHz to 1 MHz	A portable bio-impedance system is used to diagnose skin cancer based on the magnitude ratio and phase detection method	Act as a great tool for monitoring the physiological conditions of the biological system	High cost	[27]

After outlining some research on EIT to overcome the problem of detecting skin cancer and smaller lesions on highly vascularised body regions, the paper focuses in Section 3 on the materials and methodologies applied to the study in this paper.

3. Materials and Methods

In the EIT reconstruction problem, the initial step involves constructing a physical model for the observations. This requires deriving equations that establish relationships between the measured voltages, injected currents and the resistivity distribution. These equations are based on Maxwell's fundamental equations of electromagnetism. While the equation governing the interior of the body remains consistent across all EIT models, the boundary conditions differ. This section will present and discuss the various physical models that are most commonly employed in EIT.

3.1. EIT Mathematical Model

EIT involves encircling the body with a series of electrodes, typically numbering 16 or 32. Small alternating currents are applied to these electrodes at frequencies ranging from 10 kHz to 100 kHz. The resulting voltages are then measured, either between adjacent electrodes or relative to a reference electrode. The current can be applied between pairs of electrodes or distributed among all the electrodes [31]. Considering the human body as a conductor through which electric charges flow, these charges, according to Biot-Savart's law,

generate an induced magnetic field. Therefore, the study of Maxwell's equations becomes critical in understanding these phenomena [32]. The human body contains billions of free ions and complex proteins, such as haemoglobin, circulating in the blood.

Consequently, it is reasonable to apply the laws of electromagnetism to the human body [33]. For instance, the resistance of the human body is approximately 600 Ohms, and the brain exhibits a potential difference of 25 millivolts [34]. Additionally, the neurons maintain a potential difference of 70 millivolts between the outside of the myelin sheath and the inside of the axon [35]. In our analysis, the human body is considered a non-homogeneous medium. Consequently, Maxwell's equations can be expressed in the following form:

$$\nabla \times E = -\partial B / \partial t \tag{1}$$

$$\nabla \times H = J + \partial D / \partial t \tag{2}$$

Here, E represents the electric field, H the magnetic field, B the magnetic induction, D the electric displacement field, and J the current density. In the phasor domino $\widetilde{E} = E e^{j\omega t}$ and $\widetilde{B} = B e^{j\omega t}$. In addition, in an isotropic linear medium, $D = \varepsilon E$, $B = \mu H$, $J = \sigma E$ are also valid, where ε is the permittivity, μ is the permeability and σ is the conductivity of the medium.

In Electrical Impedance Tomography (EIT), bodies are typically approximated as isotropic. Given that the current injection is sinusoidal, the fields can be represented as (3):

$$E = \widetilde{E} e^{jwt}, \; B = \widetilde{B} e^{jwt} \tag{3}$$

In EIT, current sources are represented by J_s. Thus, the current density J can be decomposed into two components: $J_0 = \sigma E$, the Ohmic current, and J_s, the source current. Consequently, the Equations are (4) and (5):

$$\nabla \times E = -j\omega\mu H \tag{4}$$

$$\nabla \times H = J_s + (\sigma + j\omega\varepsilon)E \tag{5}$$

These modified Maxwell's equations can be simplified under certain approximations. For instance, considering static conditions, where the induced electric field from magnetic induction is negligible, we have (6):

$$E = -\nabla u - \frac{\partial A}{\partial t} \tag{6}$$

If the magnetic vector potential A is neglected, this approximation is valid if (7):

$$\omega\mu\sigma L_c \left(1 + \frac{\omega\varepsilon}{\sigma}\right) \ll 1 \tag{7}$$

where L_c represents the characteristic length scale of the most significant distance variations, thus justifying the neglect of magnetic induction effects.

Another common approximation in EIT is the neglect of capacitive effects, which is valid if (8):

$$\left(\frac{\omega\varepsilon}{\sigma}\right) \ll 1 \tag{8}$$

With these approximations, Maxwell's equations for a linear, isotropic, and quasi-static medium become (9) and (10):

$$E = -\nabla u \tag{9}$$

$$\nabla \times H = J_s + \sigma E \tag{10}$$

Taking the divergence of both sides and substituting, we obtain the simplified form (11):

$$\nabla \cdot (\sigma \nabla u) = 0 \tag{11}$$

within the body for EIT, assuming no internal sources ($J_s = 0$).

3.2. Boundary Conditions

Considering the scenario depicted in Figure 1, a small cylindrical volume element is positioned on the surface of an object, with its top and bottom surfaces nearly parallel to the boundary.
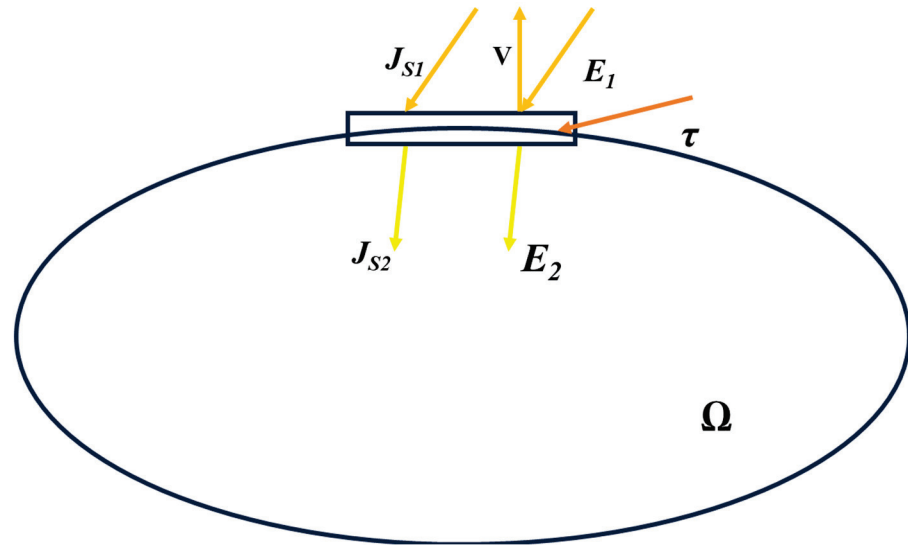
Figure 1. Determination of circumference conditions. J_{s1} and J_{s2} are the current densities outside and inside the object, respectively. E_1 and E_2 are the corresponding electrical fields.

Integrating the Equation (12) over a volume τ is obtained:

$$\nabla \cdot \sigma E = -\nabla \cdot J_s \tag{12}$$

$$\int_\tau \nabla \cdot \sigma E \, d\tau = -\int_\tau \nabla \cdot J_s d\tau \tag{13}$$

and using the divergence theorem, we have (14):

$$\int_S \sigma E \cdot \nu \, dS = -\int_S \nu \cdot J_s dS \tag{14}$$

where S is the contour of τ and ν is the normal. When the volume $\tau \to 0$, the top and bottom of the cylinder coincide. Since $J_s = 0$ inside the object and, on the other hand, $E = 0$ outside the object, the Equation is

$$\sigma E \cdot \nu |_{inside} = \nu \cdot J |_{outside} \tag{15}$$

Considering $E = -\nabla u$, the boundary condition comes from

$$\sigma \frac{\partial u}{\partial \nu} = -J_s \cdot \nu = j \tag{16}$$

where j is the negative normal component of J_s.

3.3. Epithelial Tissue

The skin comprises three primary layers: the epidermis, dermis, and hypodermis, each with a heterogeneous structure and distinct electrodermal activity [36]. Understanding the electrical conductivity and permittivity of these layers in response to a stimulus provides insights into various biological processes. Research has shown that specific pathological conditions, such as tumours, lead to significant variations in electrical conductivity and permittivity compared to healthy tissue. However, the dielectric properties of tumours exhibit substantial variability and cannot be generalised.

For the purposes of this study, we model the skin as a homogeneous layer in terms of its electrical characteristics. At low frequencies (up to 100 kHz), the ionic conductivity is considered to be 2 S/m, with the extra-cellular fluid comprising approximately 10% of solid tissues [37–39]. This results in a low-frequency conductivity of about 0.14 S/m. At frequencies between 100 kHz and 300 MHz, the cellular membrane acts as a capacitor in short-circuit, allowing us to apply mixture theory by considering the proteins contained within the cells.

At frequencies above 300 MHz, three phenomena are observed: interfacial polarisation between electrolytes in solution and proteins, which are poorly conductive (as described by the Maxwell-Wagner relaxation model) with a relaxation frequency around 300 MHz; losses due to small polar molecules such as amino acids or polar side chains of proteins, which have relaxation frequencies greater than 100 MHz; and pure water relaxation, occurring at a frequency of approximately 20 GHz. For frequencies much lower than the critical frequency ($f << f_c$), we can make certain assumptions regarding the electrical properties of the skin, as described in Equation (17).

$$\Sigma = [2\pi f^2 \, (\varepsilon_s - \varepsilon_\infty)\varepsilon_0 / f_c] / [1 + (f / f_c)^2] \tag{17}$$

Additionally, the conductivity of tissues and proteins in solution includes the contribution of dipolar relaxation of bound water, known as δ-type relaxation, with a critical frequency (f_c) approximately an order of magnitude smaller than that of free water. Therefore, the total conductivity is defined by three main contributions: (a) ionic conductivity, (b) relaxation due to bound water, and (c) relaxation due to free water. Conductivity can be represented as the sum of a dipolar and an ionic term (18):

$$\sigma = \frac{\left[2\pi f^2 * (\varepsilon_S - \varepsilon_\infty) * \varepsilon_0 / f_c\right]}{\left[1 + \left(\frac{f}{f_c}\right)^2\right]} + \sigma_s \tag{18}$$

where ε_s, ε_∞, and f_c pertain to the dipolar contribution of pure water, and σ_S represents ionic conductivity. Assuming non-conductive proteins, we can rewrite the Equation for conductivity derived from mixture theory in the case of $\sigma_i << \sigma_a$ as follows in Equation (19).

Considering a proportional coefficient *k* that scales the conductivity contributions can be written as follows:

$$\sigma \approx k \frac{(1 - \rho')\sigma_a}{1 + \rho'/2} + \frac{9\rho'\sigma_i}{(2 + \rho')^2} \tag{19}$$

where *k* is the proportional coefficient, σ_i is the conductivity contribution of the protein-water bound system, and $\rho\prime$ is the volume fraction of protein dissolved in the solution. The addition of *k* allows the entire expression to be scaled up to account for factors such as tissue-specific properties and experimental conditions that influence conductivity measurements. By increasing the frequency, the membrane, schematised with a capacitor, can be considered a short circuit, and the theory of mixtures can then be applied, considering the proteins contained inside the cell [40]. The difference with dispersion is that the effect of ionic conductivity is less influential than that due to the presence of proteins in the solution. At frequencies above 300 MHz, the ionic conductivity curve shows little variation as the frequency varies and can, therefore, be considered almost constant. At high frequencies,

losses can occur due to small polar molecules, such as amino acids in solution, or due to the polar side chains of proteins. At low frequencies, the denominator approaches one and remains the only square dependency of the numerator. The asymptotic trend tends to be a constant value, as predictable from physical considerations on mobility. For tissues with high water content, in the frequency range between 3 and 5 GHz, this increase in conductivity is of the same order of magnitude as ionic. The proposed study addresses the complex field of biological tissue transplantation, a transformative area in modern medicine that has revolutionised the treatment of several serious diseases. For successful transplantation, the harvested tissues must be thoroughly analysed to ensure the absence of malignant cells [41]. Previous research on the electrical properties of biological tissues has demonstrated that the electrical impedance of malignant tissues is significantly different from that of normal tissues or benign tumours. This study aims to demonstrate the effectiveness of Electrical Impedance Tomography (EIT) in detecting carcinogenic tissues within other tissue types. In EIT, an electric current is injected through a pair of electrodes, and the resulting variation in impedance across the tissue, with and without carcinoma, is measured. The electrodes are arranged in a circular configuration around a container filled with a saline solution to maintain the viability of the tissue. The following section will discuss the development of the Finite Element Method (FEM) model and the results obtained from the study.

4. Model Realisation in COMSOL-Multiphysics®

The goal of Section 4 is to analyse a sample of epithelial tissue through an electrical impedance tomograph. The tomograph must be able to detect the presence of carcinomas inside the tissue through the FEM simulation software (Version 5.2). Tissues taken and subsequently transplanted into the body of patients must be analysed to ensure that they do not have tumour cells in them. Studies on the electrical properties of biological tissues have shown that the electrical impedance in malignant tissues is significantly different from that of normal tissues or benign tumours [42]. With EIT, an electric current is injected through a pair of electrodes and then the change in impedance on the tissue with and without carcinoma is evaluated. The electrodes are placed circularly on a vessel containing a saline solution to preserve the tissue. This section is organised according to a standardised structure. The initial experimental step involves varying the electrical parameters of the tomograph, such as the thickness and type of skin. Subsequently, the electrical properties of the carcinoma are defined. This section is organised according to a standardised structure. The initial experimental step involves varying the electrical parameters of the tomograph, such as the thickness and type of skin. Subsequently, the electrical properties of the carcinoma are defined. EIT systems generally estimate the distribution of transverse sections of an object by conducting measurements under specified boundary conditions. These non-invasive measurements are sensitive to the electrical properties of the examined objects. To this end, the model, developed in the Comsol Multiphysics® (Version 5.2) environment, simulates the tomograph by realising its cylindrical geometry (both two-dimensional initially and three-dimensionally subsequently), the eight electrodes to which to apply the potential values and the geometry of the tissue to be analysed. The aim is to understand how the model of the impedance electric tomograph facilitates the detection of carcinomas within the epithelial tissue. The study takes into account the dominant equations for both 2D and 3D geometry modelling using four numerically tested models:

- 2D tomograph model analysing a tissue sample without carcinoma;
- 2D tomograph model analysing a tissue sample with the presence of carcinoma;
- 3D tomograph model analysing a tissue sample without carcinoma;
- 3D tomograph model analysing a tissue sample with the presence of carcinoma.

Two main configurations are considered for the electrical impedance tomograph:

- Adjacent potential configuration;
- Opposite potential configuration.

The thickness of the epithelial tissue ranges from a minimum of 0.5 mm (cornea) to a maximum of 4 mm (nape of the neck). The potential values considered range from 0.05 V to a maximum of 10 V, which are within the tolerable limits for the type of tissue under examination. In the multi-physics domain, the coupling between different phenomena extends beyond electromagnetic interactions to include couplings with acoustics, structural mechanics, and variations in material properties. Due to the impossibility of creating a mesh over an infinite volume, it is necessary to define a finite volume for discretisation and calculation of the solution. This is achieved by placing the x–y plane at z = 0.

The subsequent step involves modelling the tissue sample for analysis. The skin tissue, characterised by its irregular shape and distinct edges, was considered. The presence of carcinoma within the skin was then simulated.

The values for conductivity and permittivity were obtained through studies [43–45] that developed software to calculate the electrical parameters of tissues at various frequencies. By initiating the simulation calculations, a series of electromagnetic parameters are generated, which can then be applied to our model for further analysis.

The primary electrical measurement considered in this study is the variation in the electrical impedance of the tissue sample. Given that the tissue size is an order of magnitude smaller than that of the tomograph, the initial step involves scaling down the tomograph accordingly. This adjustment ensures that the simulation accurately reflects the conditions relevant to the tissue under examination. The geometry shown in Figure 2 is implemented to represent the ideal tomograph model.
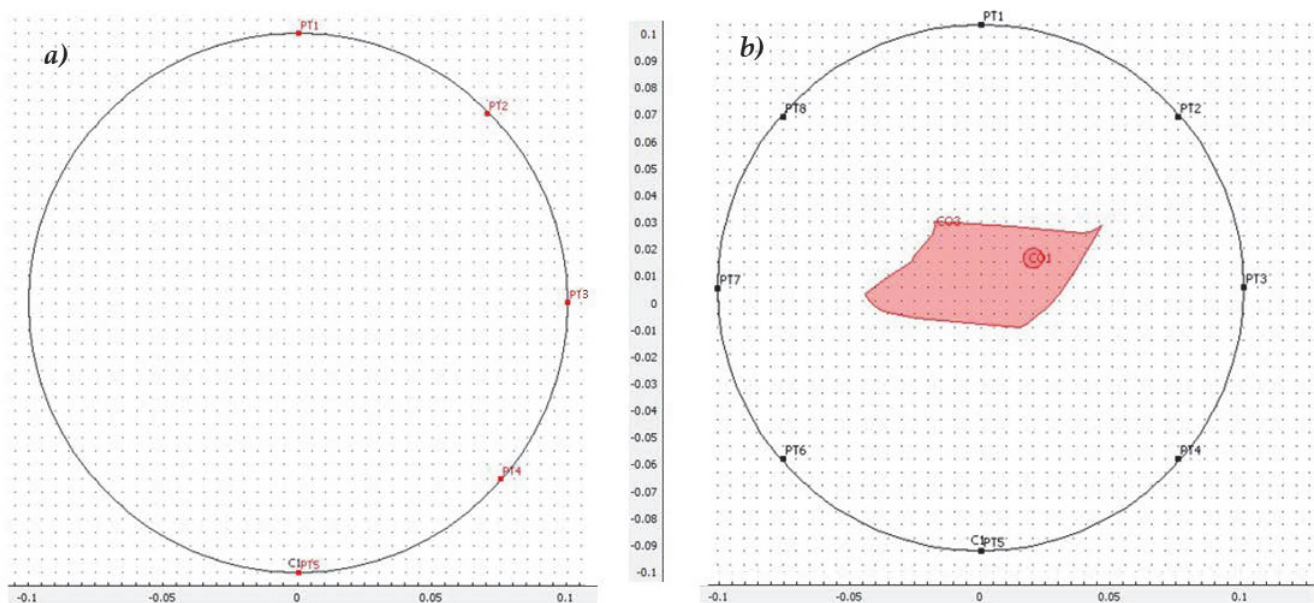
Figure 2. Geometry: (**a**) Realisation of electrodes through point modelling; (**b**) modelling of irregularly shaped skin tissue and carcinoma.

The geometry of the circle has a length (x) of 0.13 m and a height (y) of 0.1 m; the base is the centre, and the angle of rotation is 0°. It is now necessary to draw the electrodes by modelling them as points, so one by one, we position the points, representing the electrodes on the circle as shown in Figure 2a.

It is important to initially set the grid of points with a step of 0.005 m for the X- and Y-axes so that the electrodes can be positioned, as far as possible, in diametrically opposite positions. The next step is to prepare the tissue sample to be analysed. To make the simulation more real, let us consider the irregular shape of the skin tissue, which usually has obvious edges. Subsequently, inserting a small circle will simulate the presence of carcinoma on the skin tissue. Once the geometry of the system is complete, we move on to set the physical data for the various objects. Based on these considerations, it is essential

to set the physical parameters for the sample by incorporating the established values for conductivity and permittivity, as summarised in Table 2.

Table 2. Characteristics of biological tissues dry skin.

Thickness [m]	Applied Potential [V]	Conductivity [S/m]	Permittivity	Frequency [Hz]
0.005	0.05	0.0002	1136	50

The analysis was performed on a sample of skin tissue, considering that our device works with a mains frequency of 50 [Hz]. The various potential areas are outlined on both the tomograph and the sample [46].

The next step is to suppress the sub-domain of the tomograph because the order of magnitude of the sample is much smaller, and we cannot show the electrical measurements well. At the same time, we have to show the electrical impedance variation of the sample, which is the main objective of the paper. The distribution of the flow lines of the electric field, shown in Figure 3, is interesting to better understand how much we can exploit the software to represent the electrical quantities on the sample we are interested in.
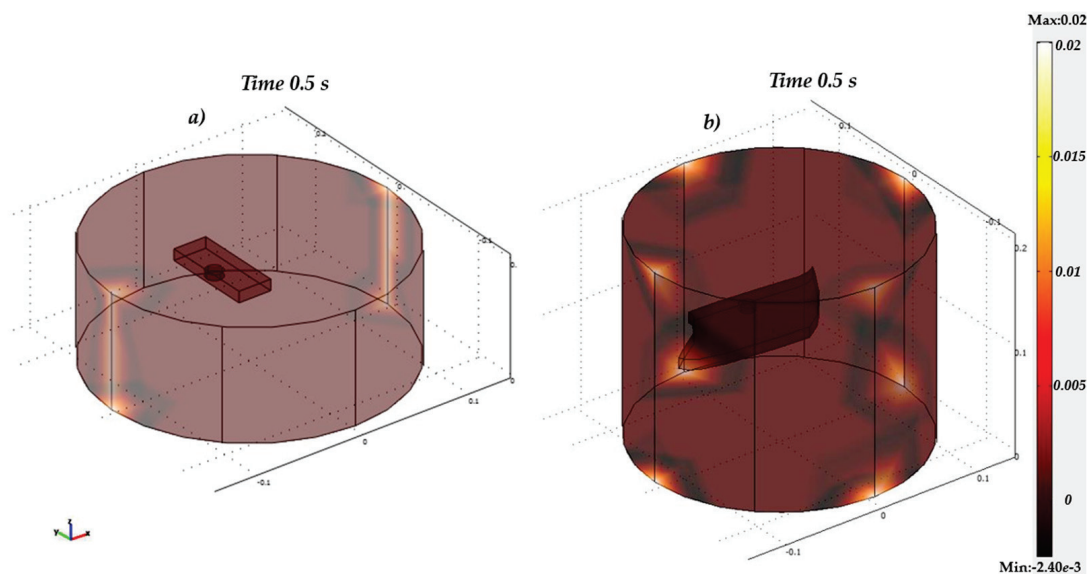
Figure 3. Three-dimensional (3D) model: (**a**) Electrical potential trend on the tomograph and sample; (**b**) time-change of the electric potential.

The two-dimensional problem described so far was subsequently realised with a three-dimensional approach in order to make the simulation of the proposed model as real as possible (Figure 3).

In the next section, the results of the three-dimensional simulations of the tomograph will be analysed in detail, varying its electrical characteristics appropriately in order to obtain the best visualisation of the impedance variation for the detection of the tumour cell. Other parameters (potentials, dimensions, etc.) will also be modified in order to obtain results that are exhaustive for the purpose of the paper.

5. Results

The final part presents the obtained results, which enable the evaluation of the most effective configuration for carcinoma detection. By varying the electrical parameters of the tomograph, the thickness and/or type of skin, and, finally, by providing the electrical properties of the carcinoma, we illustrate the results obtained, allowing us to assess which configuration may be most effective in detecting the carcinoma itself. In general, electrical

tomography systems provide an estimate of the transverse distribution of an object by making measurements with appropriate boundary conditions. These measurements, which are non-invasive in nature, are sensitive to the electrical properties of the objects under examination. Modelling the system in two dimensions, as covered extensively in the study [46], studied a simple model of skin tissue. From Figure 4, it can be seen that the impedance variation occurs with an abrupt jump when it encounters the edges of the tissue at its actual position within our tomograph at various instants of solution time.
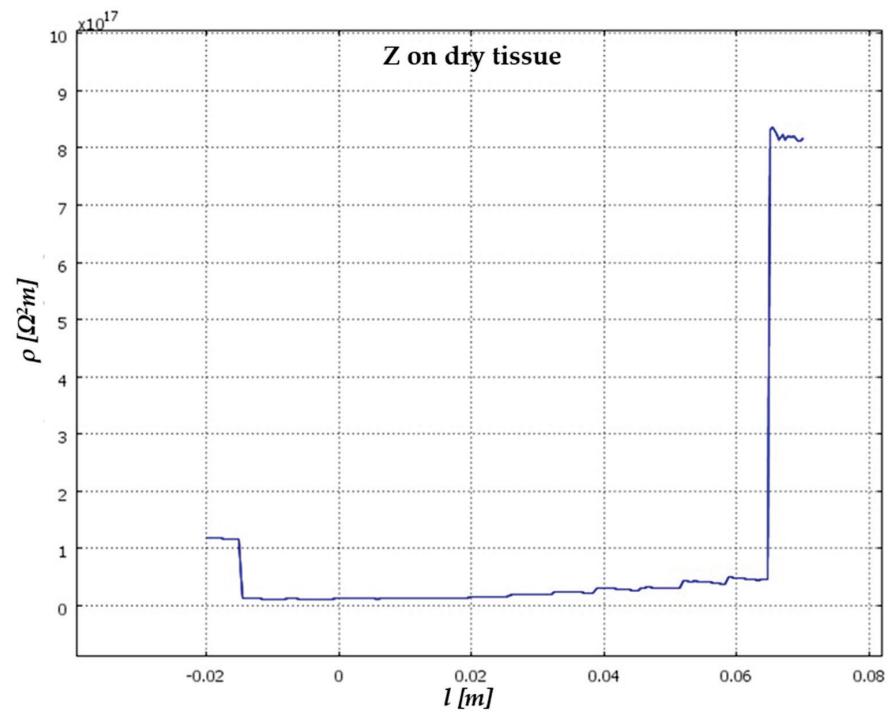
Figure 4. Cartesian representation of electrical impedance variation on dry tissue.

The trend of the impedance changes on the tissue, set appropriately on the plotting parameters, is shown in Figure 4. Specifically, the y-axis shows the surface resistivity, which is represented as a function of the intrinsic properties and geometry of the investigated material. The impedance Z of a tissue can be described as a function of frequency f, taking into account the resistive (R) and reactive (X) components. For dry tissues, the resistive component R is significant due to the lower moisture content. The relationship between voltage V, current I and impedance Z is given by Ohm's law. Applying this law to dry tissue, Z will primarily reflect a higher resistance. Resistance changes its behaviour as the length of the current flowing through the tissue is indicated on the x-axis.

The impedance variation determined considers the frequency constant and changes as the surface resistivity varies. For dry tissue, this paper uses a simple model in which the impedance of the tissue, comprising a resistive and a capacitive component, changes as a constant current flow through the medium considered (the skin) as the surface resistivity changes.

Maintaining the same settings for the tomograph, we proceed to vary the tissue type by considering wet tissue. The electrical and geometrical parameters for this wet tissue are provided in Table 3.

Table 3. Characteristics of biological tissues wet skin.

Thickness [m]	Applied Potential [V]	Conductivity [S/m]	Permittivity	Frequency [Hz]
0.005	0.05	0.0002	1136	50

The results obtained by restarting the calculation simulation are shown in Figure 5.
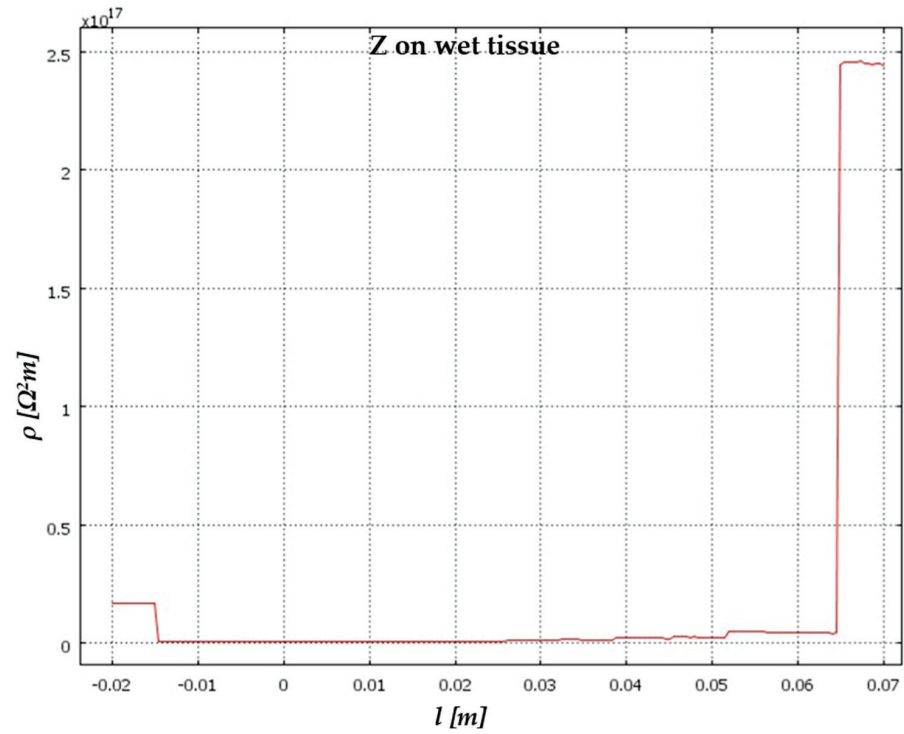
Figure 5. Cartesian representation of electrical impedance variation on wet tissue.

Comparing the two results obtained (Figure 6) highlights the significant differences in impedance values between the tissue types. This initial result is crucial for distinguishing between various tissue types, as it allows for their identification based on a range of pre-established impedance values.
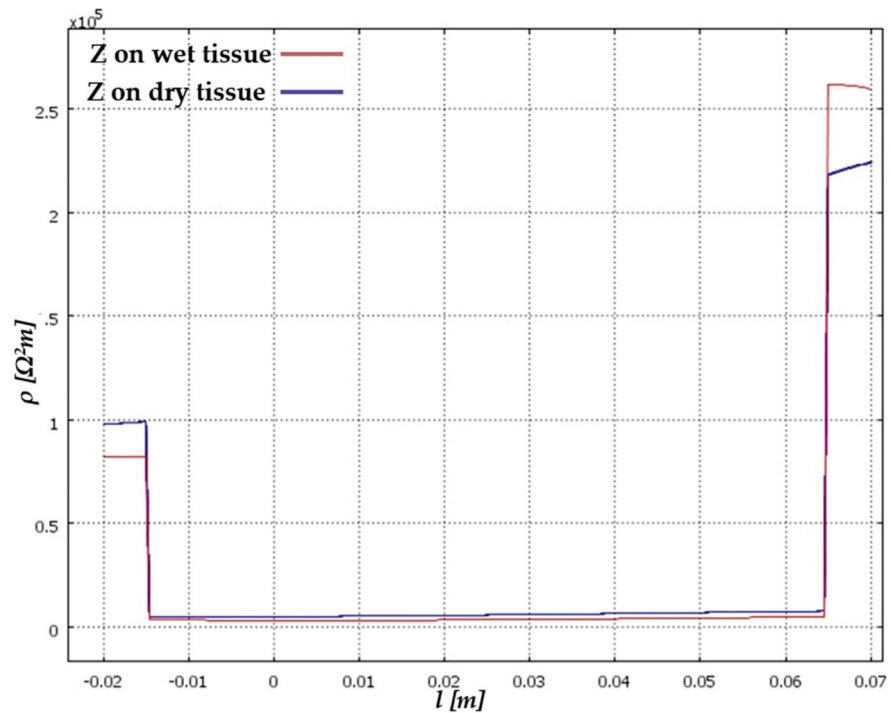
Figure 6. Comparison of electrical impedance variations between the two types of tissues considering a potential difference of 1 V. DRY = BLUE − WET = RED.

In comparing the variations in electrical impedance between the two types of epithelial tissue, this study also focused on the analysis of a sample of epithelial tissue containing a carcinoma. In these cases, the thickness is significantly reduced, and the conductivity is significantly higher. Electrosurgery and radiotherapy are effective alternatives for this type of cancer, particularly in the case of large carcinomas, but they can damage the lungs and cause major respiratory symptoms, such as dyspnea (difficulty breathing), coughing, and even pneumonia [47,48]. Carcinomas exhibit conductivity values that are 6–7 times greater than those of normal tissue, attributable to the higher water content within the malignant tissue [49]. Table 4 summarises the values adopted for this new simulation, reflecting the distinct electrical properties of carcinomatous tissue.

Table 4. Characteristics of biological tissues wet skin in the presence of carcinoma.

Type of Tissue	Thickness [m]	Applied Potential [V]	Conductivity [S/m]	Permittivity	Frequency [Hz]
Wet	0.03	0.05	0.0042719	51,274	50
Cancer	0.0001	0.05	0.0013	1	50

The biological attributes of moistened skin tissue in the presence of carcinoma manifest distinct electrical properties, encompassing alterations in conductivity, permittivity, and other pertinent parameters compared to healthy tissue. These modifications are pivotal for the identification and diagnosis of pathological conditions such as carcinoma. Moreover, the distinctive electrical signatures exhibited by carcinoma tissue offer valuable insights into medical imaging techniques and diagnostic methodologies.

The solution depicted in Figure 7 illustrates how, despite the analysis of tissue with a heightened water concentration akin to that of the tumour, it remains feasible to visibly and quantitatively pinpoint the carcinoma within its precise location within the examined tissue.
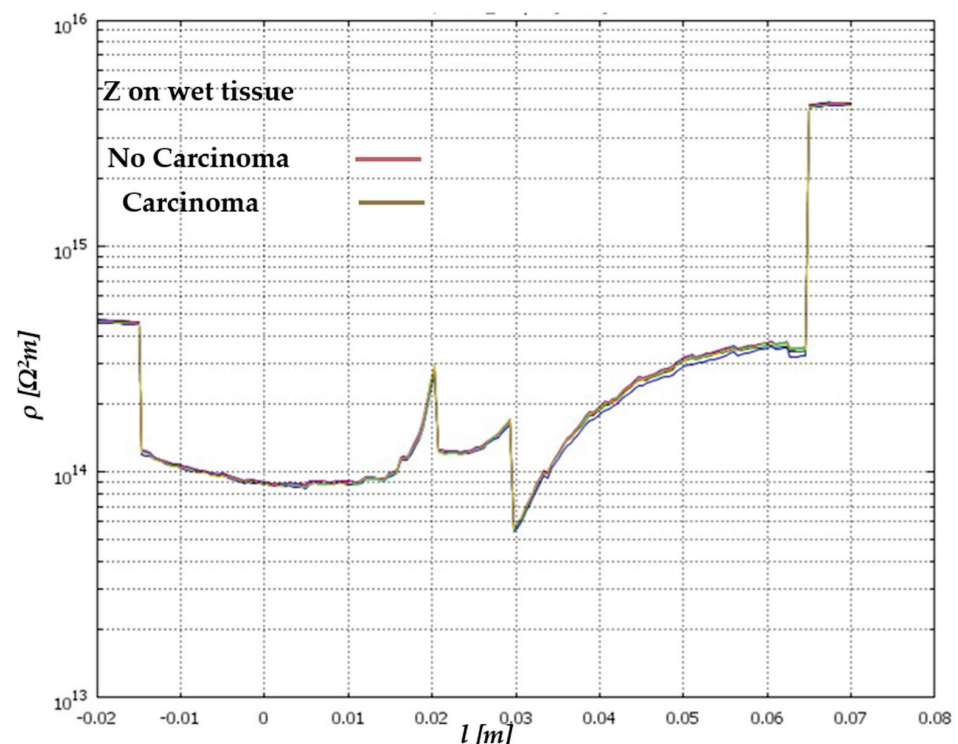
Figure 7. Change in electrical impedance on wet tissue: The red curve represents the change in electrical impedance on skin without carcinoma; the brown curve represents the change in electrical impedance on skin with carcinoma.

The biological attributes of moistened skin tissue in the presence of carcinoma manifest distinct electrical properties, encompassing alterations in conductivity, permittivity, and other pertinent parameters compared to healthy tissue. These modifications are pivotal for the identification and diagnosis of pathological conditions such as carcinoma.

Moreover, the distinctive electrical signatures exhibited by carcinoma tissue offer valuable insights into medical imaging techniques and diagnostic methodologies. The solution (Figure 7—brown curve) shows how, despite the analysis of tissue with a high-water concentration similar to that of the tumour, it is possible to visually and quantitatively identify the carcinoma in its precise position within the examined tissue. The two-dimensional model successfully demonstrated how tomographic analysis, coupled with variations in electrical impedance across biological tissues, serves as an effective means for detecting cancerous cells within tissues intended for human transplantation. The two-dimensional model was able to show how this tomographic analysis, linked to the variation of electrical impedance on biological tissues, can be considered an effective tool for detecting cancer cells in tissues to be transplanted into humans [46]. We thus also wanted to develop the study on a three-dimensional model to try to make our modelling even more real. The first step is to set the parameters shown in Table 5. Initially, employing the adjacent strategy and deactivating the tomograph, the solution is computed.

Table 5. Electrical and geometric parameters three-dimensional model.

Type of Tissue	Dimensions XYZ [m]	Applied Potential [V]	Conductivity [S/m]	Permittivity	Frequency [Hz]
Dry	$0.08 \times 0.03 \times 0.01$	0.05	0.0002	1136	50
Wet	$0.08 \times 0.03 \times 0.01$	0.05	0.0042719	51,274	50

By repeating the simulation for both tissue types, the alterations in electrical impedance are depicted in Figure 8. This comparative analysis provides valuable insights into the distinct electrical properties exhibited by different tissue compositions, particularly in the context of detecting pathological conditions such as carcinoma.
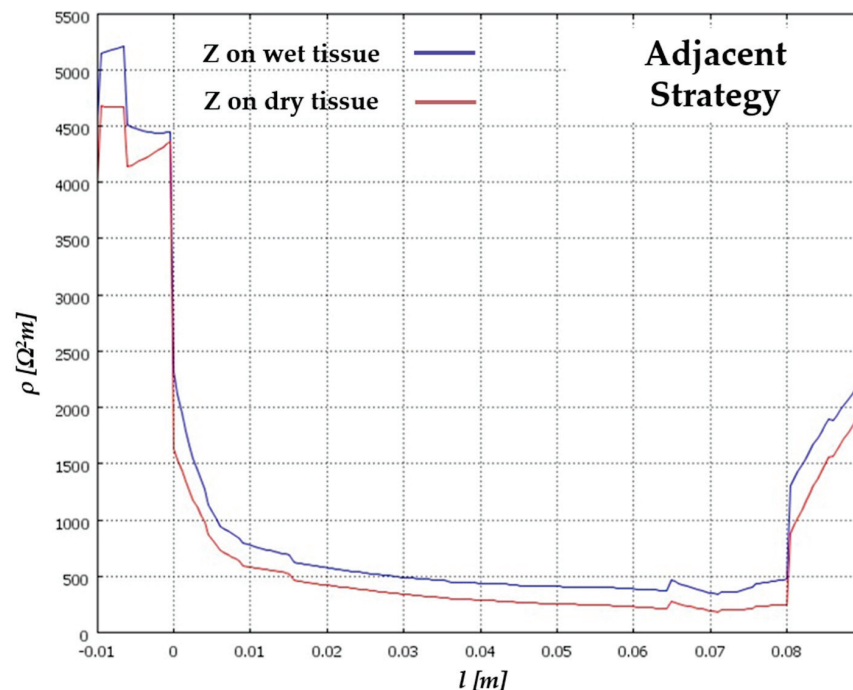
Figure 8. Electrical impedance variation on epithelial tissue obtained by the method of adjacent potentials.

Once more, the efficacy of the tomograph is evident, clearly delineating the alteration in electrical impedance between the two tissue types. Notably, the values depicted on the Y-axis exhibit a considerable increase compared to the two-dimensional scenario. This discrepancy is attributed to the three-dimensional implementation, wherein the potential is uniformly applied along a line, contrasting with the two-dimensional model where the potential was localised to a point. This observation underscores the importance of considering the dimensionality of the model when interpreting impedance variations in biological tissues. The configuration dictated by the method of opposing potentials is shown in Figure 9.
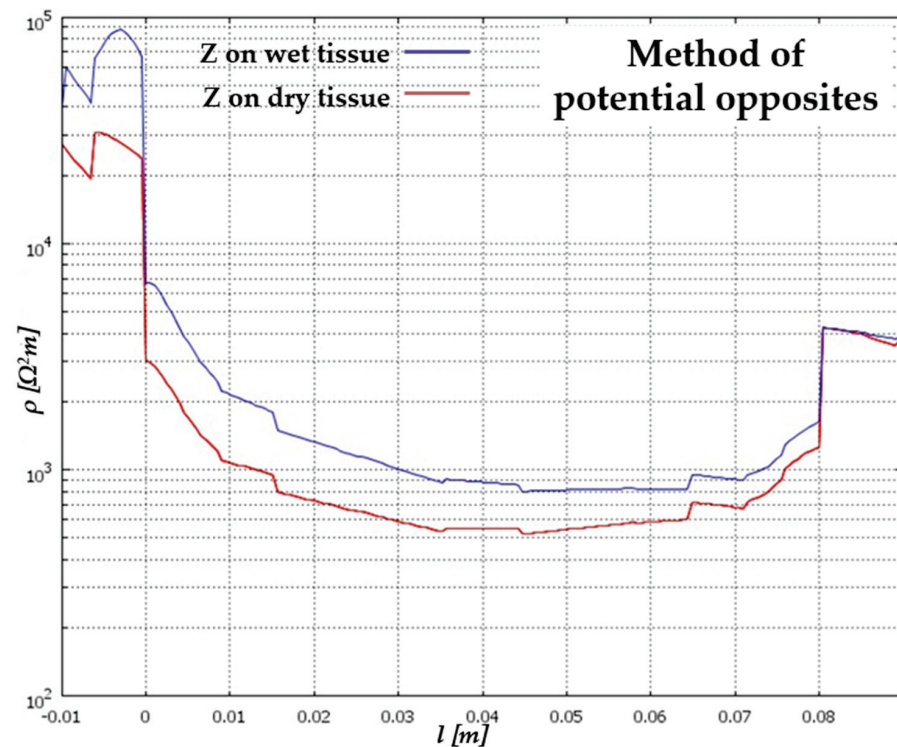
Figure 9. Variation of electrical impedance on the two epithelial tissues obtained by the method of opposite potentials.

Once more, employing the method of opposite potentials enhances our ability to observe the fluctuations in electrical impedance between the two tissue types. This approach provides greater clarity in discerning the differences in electrical properties between the tissues, facilitating the identification of pathological conditions such as carcinoma. The three-dimensional depiction of the carcinoma is geometrically approximated as a cylinder, with the method of adjacent potentials being employed once more for analysis. This approach allows for a comprehensive evaluation of the electrical impedance variations within the tissue, offering insights into the presence and characteristics of pathological conditions such as carcinoma. To better observe the cross-section we refer to for our analysis, we consider the Y–Z representation of the model, as shown in Figure 10.

By contrasting a tissue exhibiting a higher water concentration with one affected by carcinoma, the presence of carcinoma can be discerned at the same location as the drier tissue, as depicted in Figure 11.
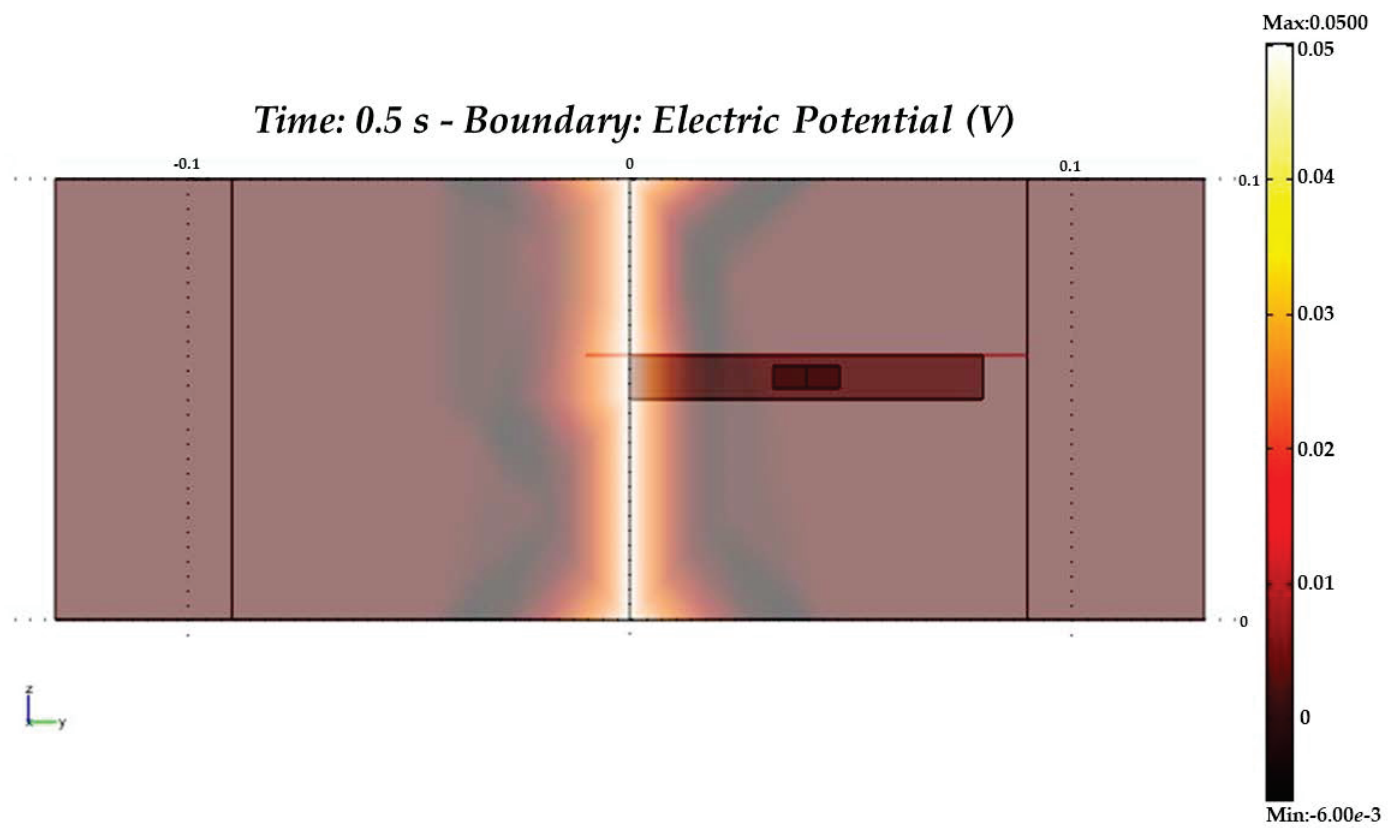
Figure 10. Y–Z plane of the cross-section for calculating the surface electrical impedance variation on epithelial tissue with the presence of carcinoma.
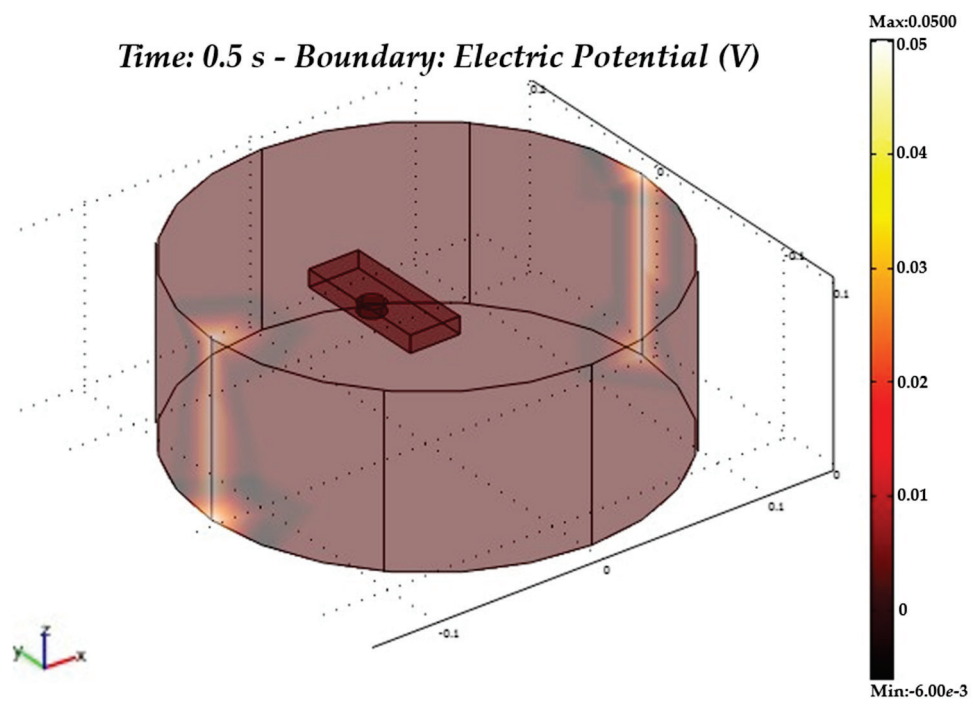
Figure 11. Variation of electrical impedance on epithelial tissue with the presence of carcinoma obtained by the method of the opposite potentials.

The analysis shown in Figure 12 highlights the distinct electrical signatures associated with carcinoma within biological tissues, facilitating their identification through non-invasive imaging techniques.
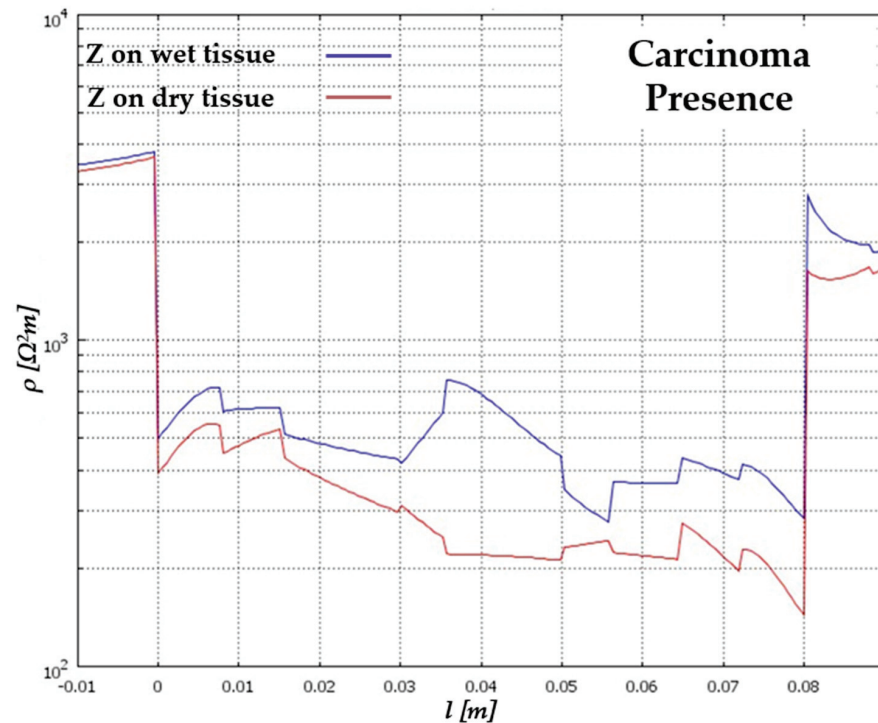
Figure 12. Superficial electrical impedance variation on epithelial tissue with the presence of carcinoma on wet tissue (blue curve) and on dry tissue (red curve).

This observation underscores the potential of electrical impedance tomography in detecting pathological conditions within biological tissues, irrespective of variations in moisture content. The comparison between the two tissue types reveals the pattern of electrical impedance variation in epithelial tissue with the presence of carcinoma, derived using the method of opposite potentials (Figure 13). Even for the three-dimensional case, as was legitimate to expect from the two-dimensional (2D) analysis, the method of potential opposites turns out to be significantly more sensitive and effective than the adjacent potential method. This analysis highlights the distinct electrical signatures associated with carcinoma within biological tissues, facilitating their identification through non-invasive imaging techniques.

Furthermore, in the three-dimensional scenario, consistent with the observations from the two-dimensional analysis, the method employing opposite potentials demonstrates notably higher sensitivity and efficacy compared to the adjacent potential's method, as evident in Figure 13. These simulations conducted via electrical impedance tomography underscore the potential for future practical experimentation, offering several advantages:

- Simplified implementation of the instrumentation due to the accessibility and cost-effectiveness of materials utilised;
- Immediate detection of carcinoma presence and concurrent localization within the examined tissue;
- Non-invasive analysis, ensuring no harm to the tissue being scrutinised;
- Convenient electrical measurement facilitated by sensors or other cost-effective devices.
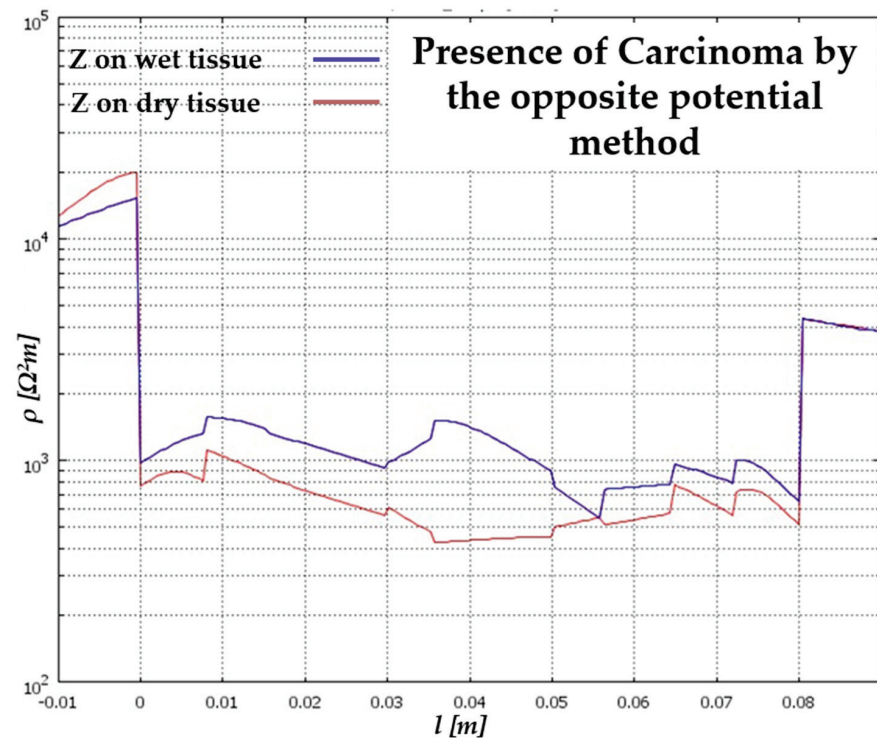
Figure 13. Electrical impedance variation on epithelial tissue with the presence of carcinoma was obtained by the method of opposite potentials on wet tissue (blue curve) and on dry tissue (red curve).

6. Conclusions

The advancement of non-invasive diagnostic techniques for detecting carcinomas is experiencing rapid growth, primarily driven by technological advancements in both hardware and software support systems. This study specifically focused on analyzing epithelial tissue using electrical impedance tomography (EIT) to identify any carcinomas present within it. The approach involved detecting carcinoma through its response to externally applied excitation generated by a potential applied through an experimental tomograph, facilitating the determination of changes in electrical impedance. It is worth pointing out that the paper proposed is the evolution of the model already implemented in 2D by the research group in a previous work. The results produced in this paper are obtained by considering variations in electrical impedance in homogeneous tissue without simulating the cellular structure entirely to avoid computational complexity. For this reason, the results obtained are limited to a limited number of data points. However, the implemented equations govern the approach for the modelling of 2D and three-dimensional (3D) geometries through four numerically tested models, specifically a 2D tomograph model that analyses a tissue sample without carcinoma; a 2D tomograph model that analyses a tissue sample with carcinoma; a 3D tomograph model that analyses a tissue sample without carcinoma; and a 3D tomograph model that analyses a tissue sample with carcinoma. Furthermore, for each model, the two main configurations, i.e., the adjacent potential and the opposite potential, were considered for the electrical impedance tomograph. It is essential to note that the simulation considered electrical impedance variations in the tissue homogeneously without simulating the intricate cellular structure to avoid computational complexity. Additionally, both the tissue and carcinoma were modelled with regular geometry during the simulation phase, simplifying the mesh calculation process. The selection of the 8-electrode tomograph, after multiple simulations, aimed to achieve adequate resolution in measuring impedance variation. Contact impedance between electrodes and skin is a critical factor that significantly influences the quality and reliability of acquired biopotential signals. This paper recognises that high contact impedance can introduce noise and artefacts, thus compromising the accuracy of measurements. In the proposed method, to mitigate the

impact of contact impedance, changes in electrical impedance on epithelial tissue are detected with point values by performing a longitudinal scan in a direction coincident with one of the tissue axes for carcinoma detection of an unstratified sample. However, employing a greater number of electrodes could yield more meaningful measurements, a possibility warranting further investigation for enhancing carcinoma detection efficacy. This consideration is important because it provides reassuring answers and opens up new fields of research for the creation of EIT devices that improve the visual process to detect skin cancer. High-tech imaging devices can provide additional accurate data to help doctors monitor and manage specific patients. Real-world application poses challenges not captured by software simulations, such as non-uniform stratified sample structures and instrumentation-induced noise during the measurement phase, necessitating consideration. Regarding the experimental phase, conducting numerous tests suggested potential refinements for practical device implementation, which could be further optimized in future developments. In the simulation phase, the software package allows tomography of any size to be characterised, with the possibility of verifying both the geometric profile and the ideal value of the excitation current to be delivered according to the type of tissue to be analysed. In electrical impedance tomography (EIT), the choice between the use of voltage and current sources is crucial and has significant implications for the method of data acquisition, the quality of reconstructed images, and the accuracy of impedance measurements. The implemented model uses a constant current source, such that it remains unchanged with respect to the size of the skin under examination. This is particularly useful when considering carcinoma on the skin, as the tumour involves impedance variability, as demonstrated by the results obtained. To achieve high levels of accuracy, it is necessary to use very precise and stable current control circuits to ensure that the current delivered is exactly as desired. Finally, prolonged use of high currents can cause polarisation of the electrodes, altering the accuracy of measurements. Future endeavors may involve modifying the model to analyze transplantable organs adjusting geometric, electrical, and biological characteristics accordingly. This iterative approach holds promise for advancing diagnostic capabilities in medical settings.

Author Contributions: Conceptualization, F.L. and G.O.; methodology, D.D.C. and S.A.P.; software, D.P. and F.L.; validation, D.D.C. and F.L.; formal analysis, F.L. and D.P.; investigation, S.C., D.D.C. and F.L.; resources, D.D.C. and F.L.; data curation, D.D.C. and F.L.; writing—original draft preparation, D.P.; writing—review and editing, G.O. and S.A.P.; supervision, S.A.P. and S.C. All authors have read and agreed to the published version of the manuscript.

Informed Consent Statement: Not applicable.

Data Availability Statement: The data are contained within this article.

Conflicts of Interest: The authors declare no conflicts of interest.

References

1. Wu, Y.; Hanzaee, F.F.; Jiang, D.; Bayford, R.H.; Demosthenous, A. Electrical Impedance Tomography for Biomedical Applications: Circuits and Systems Review. *IEEE Open J. Circuits Syst.* **2021**, *2*, 380–397. [CrossRef]
2. Padilha Leitzke, J.; Zangl, H. A review on electrical impedance tomography spectroscopy. *Sensors* **2020**, *20*, 5160. [CrossRef] [PubMed]
3. Seçkin, A.Ç.; Ateş, B.; Seçkin, M. Review on Wearable Technology in sports: Concepts, Challenges and opportunities. *Appl. Sci.* **2023**, *13*, 10399. [CrossRef]
4. Ke, X.Y.; Hou, W.; Huang, Q. Advances in electrical impedance tomography-based brain imaging. *Mil. Med. Res.* **2022**, *9*, 10. [CrossRef] [PubMed]
5. Adam, E.E.B.; Babikir, E. Survey on medical imaging of electrical impedance tomography (EIT) by variable current pattern methods. *J. IoT Soc. Mob. Anal. Cloud* **2021**, *3*, 82–95.

6. Zhang, H.; Kalra, A.; Lowe, A.; Yu, Y.; Anand, G. A hydrogel-based electronic skin for touch detection using electrical impedance tomography. *Sensors* **2023**, *23*, 1571. [CrossRef] [PubMed]
7. Li, Y.; Wang, N.; Fan, L.F.; Wang, Y.Q.; Zhao, P.F.; Huang, L.; Wang, Z.Y. Imaging spatial-temporal distribution of moisture in intact maize ear. *Measurement* **2022**, *202*, 111809. [CrossRef]
8. Khan, T.A.; Ling, S.H.; Rizvi, A.A. Optimisation of electrical Impedance tomography image reconstruction error using heuristic algorithms. *Artif. Intell. Rev.* **2023**, *56*, 15079–15099. [CrossRef]
9. Tyni, T.; Stinchcombe, A.R.; Alexakis, S. A boundary integral equation method for the complete electrode model in electrical impedance tomography with tests on experimental data. *SIAM J. Imaging Sci.* **2024**, *17*, 672–705. [CrossRef]
10. Angiulli, G.; Versaci, M.; Calcagno, S. Computation of the cutoff wavenumbers of metallic waveguides with symmetries by using a nonlinear eigenproblem formulation: A group theoretical approach. *Mathematics* **2020**, *8*, 489. [CrossRef]
11. Jain, H.; Isaacson, D.; Edic, P.M.; Newell, J.C. Electrical impedance tomography of complex conductivity distributions with noncircular boundary. *IEEE Trans. Biomed. Eng.* **1997**, *44*, 1051–1060. [CrossRef] [PubMed]
12. Angiulli, G.; Cacciola, M.; Calcagno, S.; De Carlo, D.; Morabito, C.F.; Sgró, A.; Versaci, M. A numerical study on the performances of the flexible BiCGStab to solve the discretized E-field integral equation. *Int. J. Appl. Electromagn. Mech.* **2014**, *46*, 547–553. [CrossRef]
13. Kulkarni, R.; Boverman, G.; Isaacson, D.; Saulnier, G.; Newell, J.C. Layered model for breasts in electrical impedance tomography. In Proceedings of the 2007 29th Annual International Conference of the IEEE Engineering in Medicine and Biology Society, Lyon, France, 22–26 August 2007; pp. 4150–4153.
14. Cappellini, I.; Campagnola, L.; Consales, G. Electrical Impedance Tomography, Artificial Intelligence, and Variable Ventilation: Transforming Respiratory Monitoring and Treatment in Critical Care. *J. Pers. Med.* **2024**, *14*, 677. [CrossRef]
15. Pennati, F.; Angelucci, A.; Morelli, L.; Bardini, S.; Barzanti, E.; Cavallini, F.; Conelli, A.; Di Federico, G.; Paganelli, C.; Aliverti, A. Electrical Impedance Tomography: From the Traditional Design to the Novel Frontier of Wearables. *Sensors* **2023**, *23*, 1182. [CrossRef] [PubMed]
16. Singh, R.K.; Nayak, N.P.; Behl, T.; Arora, R.; Anwer, M.K.; Gulati, M.; Bungau, S.G.; Brisc, M.C. Exploring the Intersection of Geophysics and Diagnostic Imaging in the Health Sciences. *Diagnostics* **2024**, *14*, 139. [CrossRef]
17. Bianco, M.G.; Quattrone, A.; Sarica, A.; Vescio, B.; Buonocore, J.; Vaccaro, M.G.; Aracri, F.; Calomino, C.; Gramigna, V.; Quattrone, A. Cortical atrophy distinguishes idiopathic normal pressure hydrocephalus from progressive supranuclear palsy: A machine learning approach. *Park. Relat. Disord.* **2022**, *103*, 7–14.
18. Tang, M.; Wang, W.; Wheeler, J.; McCormick, M.; Dong, X. The number of electrodes and basis functions in EIT image reconstruction. *Physiol. Meas.* **2002**, *23*, 129–140. [CrossRef]
19. Sarac, E.; Meiwes, A.; Eigentler, T.K.; Forchhammer, S.; Kofler, L.; Häfner, H.M.; Garbe, C. Diagnostic accuracy of electrical impedance spectroscopy in non-melanoma skin cancer. *Acta Derm. Venereol.* **2020**, *100*, adv00328. [CrossRef]
20. Braun, R.P.; Mangana, J.; Goldinger, S.; French, L.; Dummer, R.; Marghoob, A.A. Electrical Impedance Spectroscopy in Skin Cancer Diagnosis. *Dermatol. Clin.* **2017**, *35*, 489–493. [CrossRef]
21. Becher, T.; Buchholz, V.; Hassel, D.; Meinel, T.; Schädler, D.; Frerichs, I.; Weiler, N. Individualization of PEEP and tidal in ARDS patients with electrical impedance tomography: A pilot feasibility study. *Ann. Intensive Care* **2021**, *11*, 89. [CrossRef]
22. Zhao, Z.; Steinmann, D.; Frerichs, I.; Guttmann, J.; Möller, K. PEEP titration guided by ventilation homogeneity: A feasibility study using electrical impedance tomography. *Crit. Care* **2010**, *14*, R8. [CrossRef]
23. Glickman, Y.A.; Filo, O.; David, M.; Yayon, A.; Topaz, M.; Zamir, B.; Kenan, G. Electrical impedance scanning: A new approach to skin cancer diagnosis. *Ski. Res. Technol.* **2003**, *9*, 262–268. [CrossRef]
24. Aberg, P.; Nicander, I.; Hansson, J.; Geladi, P.; Holmgren, U.; Ollmar, S. Skin cancer identification using multifrequency electrical impedance—A potential screening tool. *IEEE Trans. Biomed. Eng.* **2004**, *51*, 2097–2102. [CrossRef]
25. Åberg, P.; Birgersson, U.; Elsner, P.; Mohr, P.; Ollmar, S. Electrical impedance spectroscopy and the diagnostic accuracy for malignant melanoma. *Exp. Dermatol.* **2011**, *20*, 648–652. [CrossRef]
26. Mohr, P.; Birgersson, U.; Berking, C.; Henderson, C.; Trefzer, U.; Kemeny, L.; Paoli, J. Electrical impedance spectroscopy as a potential adjunct diagnostic tool for cutaneous melanoma. *Ski. Res. Technol.* **2013**, *19*, 75–83. [CrossRef]
27. Yang, Y.; Wang, J.; Yu, G.; Niu, F.; He, P. Design and preliminary evaluation of a portable device for the measurement of bioimpedance spectroscopy. *Physiol. Meas.* **2006**, *27*, 1293. [CrossRef]
28. Åberg, P.; Geladi, P.; Nicander, I.; Hansson, J.; Holmgren, U.; Ollmar, S. Non-invasive and microinvasive electrical impedance spectra of skin cancer—A comparison between two techniques. *Ski. Res. Technol.* **2005**, *11*, 281–286. [CrossRef]
29. Narayanamurthy, V.; Padmapriya, P.; Noorasafrin, A.; Pooja, B.; Hema, K.; Nithyakalyani, K.; Samsuri, F. Skin cancer detection using non-invasive techniques. *RSC Adv.* **2018**, *8*, 28095–28130. [CrossRef]
30. Kamat, D.K.; Chavan, A.P.; Patil, P.M. Bio-impedance measurement system for analysis of skin diseases. *Int. J. Appl. Innov. Eng. Manag.* **2014**, *3*, 92–96.
31. Zhao, Z.; Zhu, H.; Li, X.; Sun, L.; He, F.; Chung, J.E.; Xie, C. Ultraflexible electrode arrays for months-long high-density electrophysiological mapping of thousands of neurons in rodents. *Nat. Biomed. Eng.* **2023**, *7*, 520–532. [CrossRef] [PubMed]
32. Eisenberg, R.S. Maxwell equations without a polarization field, Using a paradigm from biophysics. *Entropy* **2021**, *23*, 172. [CrossRef]

33. Abdul-Al, M.; Amar, A.S.; Elfergani, I.; Littlehales, R.; Ojaroudi Parchin, N.; Al-Yasir, Y.; Abd-Alhameed, R.A. Wireless electromagnetic radiation assessment based on the specific absorption rate (SAR): A review case study. *Electronics* **2022**, *11*, 511. [CrossRef]

34. Wust, P.; Stein, U.; Ghadjar, P. Non-thermal membrane effects of electromagnetic fields and therapeutic applications in oncology. *Int. J. Hyperth.* **2021**, *38*, 715–731. [CrossRef]

35. Mazuir, E.; Fricker, D.; Sol-Foulon, N. Neuron–oligodendrocyte communication in myelination of cortical GABAergic cells. *Life* **2021**, *11*, 216. [CrossRef]

36. Wu, H.; Zhou, W.; Yang, Y.; Jia, J.; Bagnaninchi, P. Exploring the potential of electrical impedance tomography for tissue engineering applications. *Materials* **2018**, *11*, 930. [CrossRef]

37. Yilmaz, T.; Ates Alkan, F. In vivo dielectric properties of healthy and benign rat mammary tissues from 500 MHz to 18 GHz. *Sensors* **2020**, *20*, 2214. [CrossRef]

38. Laganà, F.; Britti, D.; Fiorillo, A.S.; Pullano, S.A. New Surface Electrical Charge Detection System for Ecology and Insect Monitoring. In Proceedings of the 2023 IEEE International Workshop on Biomedical Applications, Technologies and Sensors, BATS 2023—Proceedings, Catanzaro, Italy, 28–29 September 2023.

39. Di Meo, S.; Bonello, J.; Farhat, I.; Farrugia, L.; Pasian, M.; Camilleri Podesta, M.T.; Sammut, C.V. The variability of dielectric permittivity of biological tissues with water content. *J. Electromagn. Waves Appl.* **2022**, *36*, 48–68. [CrossRef]

40. Seweryn, A. Interactions between surfactants and the skin—Theory and practice. *Adv. Colloid Interface Sci.* **2018**, *256*, 242–255. [CrossRef]

41. Pullano, S.A.; Greco, M.; Islam, S.K.; Fiorillo, A.S. Thermoelectrical Characterization of Cells Using a Pyroelectric Sensor. In Proceedings of the 2023 IEEE SENSORS, Vienna, Austria, 29 October–1 November 2023.

42. Tang, J.; Lu, M.; Xie, Y.; Yin, W. A Novel Efficient FEM Thin shell model for bio-impedance analysis. *Biosensors* **2020**, *10*, 69. [CrossRef]

43. Pullano, S.A.; Greco, M.; Foti, D.P.; Brunetti, A.; Fiorillo, A.S. Dual Pyroelectric Sensor for Thermal Characterization of Cell Lines. In Proceedings of the 2021 IEEE Sensors Applications Symposium (SAS), Virtual Conference, Sundsvall, Sweden, 23–25 August 2021.

44. Laganà, F.; De Carlo, D.; Calcagno, S.; Pullano, S.A.; Critello, D.; Falcone, F.; Fiorillo, A.S. Computational model of cell deformation under fluid flow-based rolling. In Proceedings of the 7th IEEE International Conference on E-Health and Bioengineering, EHB 2019, Iasi, Romania, 21–23 November 2019.

45. Lee, S.; Ozkavukcu, S.; Ku, S.Y. Current and future perspectives for improving ovarian tissue cryopreservation and transplantation outcomes for cancer patients. *Reprod. Sci.* **2021**, *28*, 1746–1758. [CrossRef]

46. Laganà, F.; De Carlo, D.; Calcagno, S.; Oliva, G.; Pullano, S.A.; Fiorillo, A.S. Modeling of Electrical Impedance Tomography for Carcinoma Detection. In Proceedings of the 10th E-Health and Bioengineering Conference EHB 2022, Virtual Conference, Iasi, Romania, 17–18 November 2022. [CrossRef]

47. Menniti, M.; Oliva, G.; Laganà, F.; Bianco, M.G.; Fiorillo, A.S.; Pullano, S.A. Portable Non-Invasive Ventilator for Homecare and Patients Monitoring System. In Proceedings of the 2023 IEEE International Symposium on Medical Measurements and Applications (MeMeA), Jeju, Republic of Korea, 14–16 June 2023; pp. 1–5. [CrossRef]

48. Menniti, M.; Laganà, F.; Oliva, G.; Bianco, M.; Fiorillo, A.S.; Pullano, S.A. Development of Non-Invasive Ventilator for Homecare and Patient Monitoring System. *Electronics* **2024**, *13*, 790. [CrossRef]

49. Vaupel, P.; Piazena, H. Hyperhydration of cancers: A characteristic biophysical trait strongly increasing O_2, CO_2, glucose and lactate diffusivities, and improving thermophysical properties of solid malignancies. In *International Society on Oxygen Transport to Tissue*; Springer International Publishing: Cham, Switzerland, 2022; pp. 135–145.

Review

Bone Drilling: Review with Lab Case Study of Bone Layer Classification Using Vibration Signal and Deep Learning Methods

Wahyu Caesarendra [1,2]

1   Faculty of Integrated Technologies, Universiti Brunei Darussalam, Jalan Tungku Link,
    Gadong BE1410, Brunei; wahyu.caesarendra@ubd.edu.bn
2   Faculty of Mechanical Engineering, Opole University of Technology, 76 Proszkowska St., 45-758 Opole, Poland

Abstract: In orthopedics, bone drilling is a crucial part of a surgical method commonly carried out for internal fixation in bone fracture treatment. The primary purpose of bone drilling is the creation of holes for screw insertion to immobilize fractured parts. The bone drilling task depends on the orthopedist and surgeon's high level of skill and experience. This paper aimed to provide a summary of previously published review studies in the field of bone drilling. This review paper also presents a comprehensive review of the application of machine learning for bone drilling and as a future direction for automation systems. This review can also help medical surgeons and bone drillers understand the latest improvements through parameter selection and optimization strategies to reduce bone damage in bone drilling procedures. Apart from the review, bone drilling vibration data collected in a university laboratory experiment is also presented in this study. The vibration data consist of three different layers of femur cow bone, which are processed and classified using several deep learning (DL) methods such as long short-term memory (LSTM), convolutional neural network (CNN), and recurrent neural network (RNN). These DL methods are used in the bone drilling lab case study to prove that the layers of bone drilling are associated with the vibration signal and that they can be classified and predicted using DL methods. The result shows that LSTM is outperformed by CNN and RNN.

Keywords: bone drilling parameters; bone drilling vibration; bone layer classification; deep learning; machine learning

1. Introduction

Bone drilling is a medical procedure that involves the creation of small holes or drilling into bones for various purposes, including diagnosis, treatment, and research. Although bone drilling may be invasive, this technique has become an integral part of modern medical science, and it offers various important benefits. Bone drilling plays a crucial role in accurately diagnosing various diseases and conditions. In addition to diagnosis, bone drilling also makes a significant contribution to medical research. The development of safer and more precise drilling equipment and techniques has become possible because of the efforts of scientists and doctors. These innovations have a positive impact on patient safety and the effectiveness of medical procedures and can help reduce the risk of complications and speed up the healing process. In bone drilling, inner base bone structures that are examined and treated with nails and screws are generally composed of three layers, namely first cortical, spongy, and second cortical [1].

Currently, manual hand drilling is still the main method in orthopedic surgery in which the process is solely controlled by a surgeon and orthopedist. Bone drilling requires the orthopedist's and the surgeon's extensive experience and dexterity. The drilling procedures are performed without visual guidance, making it difficult for surgeons to determine the depth of the holes they are creating [2]. As a result, the effectiveness of the bone drilling

process is strongly dependent on the surgeon's skill and ability to evaluate the drilling operation based on their own understanding [3]. The bone drilling experience by the surgeon is subjective; for example, the applied force given by the surgeon depends on the drill bit speed, the bone condition, and the type of drill bit [4,5].

A recent study that compares ultrasonic-assisted drilling (UAD) to conventional drilling in bone surgeries is presented in [6]. The study examines optimal drilling parameters such as drilling force, temperature elevation, osteonecrosis, and micro-crack formation. The study found that the ultrasonic drilling resulted in less force and did not produce micro-cracks in cortical bone compared to the conventional drilling. However, it has the side effect in which the temperature elevation is higher than in conventional drilling. In addition, histopathological and scanning electron microscopic (SEM) analysis is conducted to evaluate the osteonecrosis and structural damage. The result shows that UAD is more advantageous for bone surgeries than the conventional method because it can reduce tissue damage. Another comparison study of conventional and UAD techniques is presented in [7]. The study presents in detail the comparative analysis of diametric delamination in the drilling of cortical bone using conventional drilling and UAD techniques. A coordinate measuring machine (CMM) is used in the study to characterize delamination during bone drilling. A quantitative comparison was also presented in the study with the finding that UAD causes less delamination than conventional drilling, with maximum delamination for UAD and conventional drilling of 8.54% and 9.15%, respectively. Ultrasonic actuation application in bone drilling is also presented in [8]. The objective is to reduce the cutting force and temperature during the bone drilling. The comparison study between conventional drilling and UAD is discussed. The study found that UAD has a higher viability and greater pullout strength, which can potentially lead to low-trauma surgeries.

Recently, bone drilling research has mostly focused on monitoring techniques and drilling parameters. An automated bone drilling system and a bone-drilling medical training system (MTS) [9] are the future directions of this particular research area. The bone drilling MTS is a sophisticated tool designed to train medical professionals in the application of force during bone drilling procedures. This system operates in a virtual environment (VE) and aims to teach users how to apply force within a specific range, thereby maintaining a constant drilling thrust velocity. The virtual reality (VR) simulator consists of visual, acoustic, and haptic warning signals [9]. Another study that presents the training system with 3 degrees of freedom (DOF) force feedback is presented in [10]. Another proposed MTS concept is presented in [11]. The concept generally consists of the following: (1) The system architecture based on haptic display (HD) and graphical user interface (GUI); (2) A control system using proportional derivative (PD) position control.

A comprehensive review of surgical simulators for orthopedic and neurosurgeries, which focuses on haptic and VR technologies, is presented in [12]. The review paper informs that the main part of the orthopedic simulator is the haptic system. The haptic system in the simulator is expected to provide tactile sensations that mimic the real-life feel of orthopedic surgery. The haptic system is supported by force feedback, which is calculated based on the interaction between virtual tools and the simulated anatomy [12]. More details of the review on MTS and potential automated systems in bone drilling are presented in Section 3.

A current review paper provides a different side of bone drilling, which discusses the vibration analysis of different bone layers and the application of the DL methods. The structure of the paper following the introduction is as follows: Section 2 presents a summary of the previously published review paper on bone drilling. A brief review of the MTS and robotic drilling as potential future technologies are discussed in Section 3. Section 4 presents a review of published papers on bone drilling vibration analysis and the application of ML methods for bone layer classifications. Section 5 presents the bone drilling lab's experimental setup and procedure. An application of DL methods is presented in Sections 6 and 7. A detailed description of the LSTM method and its results is presented in Section 6. For other DL methods, i.e., convolutional neural network (CNN) and recurrent

neural network (RNN), a performance comparison is presented in Section 7. Section 8 presents the conclusions and the future direction of the study. For ease of understanding in reading this review paper, which consists of a lot of terminologies, an abbreviation table is provided and presented in Table 1.

Table 1. Abbreviations of terminologies used in the paper.

Full Terminology	Abbreviation
Acoustic Emission	AE
Artificial Neural Network	ANN
Analysis of Variance	ANOVA
Computer-Aided Orthopedic Surgery	CAOS
Coordinate Measuring Machine	CMM
Computer Numerical Control	CNC
Convolutional Neural Network	CNN
Deep Learning	DL
Direct Current	DC
Degree of Freedom	DOF
Decision Tree	DT
Genetic Algorithm	GA
Grey Fuzzy Reasoning Grade	GFRG
Grey Relation Analysis	GRA
Graphical User Interface	GUI
Haptic Display	HD
Human-Robot Interaction	HRI
High-Speed Steel	HSS
K-Nearest Neighbors	KNN
Laser-Assisted Drilling	LAD
Leaning-based Guidance	LbG
Long Short-Term Memory	LSTM
Mean Absolute Error	MAE
Machine Learning	ML
Mean Square Error	MSE
Medical Training System	MTS
National Instrument	NI
Proportional Derivative	PD
Radial Basis Function Neural Network	RBFNN
Random Forest	RF
Rotation Per Minute	RPM
Root Mean Square Error	RMSE
Rotary Ultrasonic Bone Drilling	RUBD
Response Surface Methodology	RSM
Scanning Electron Microscopic	SEM
Support Vector Machine	SVM
Ultrasonic-Assisted Drilling	UAD
Virtual Environment	VE
Virtual Reality	VR
Water Jet-Assisted Drilling	WJAD

2. Previous Review Studies on Bone Drilling

Extensive review studies related to bone drilling have been presented. Information about what is the difference between the present review paper and other published review papers is presented in Table 2. The following is a more detailed description of Table 2:

A detailed review paper of various studies on bone drilling is presented in [4]. The paper compares various studies on bone drilling, highlighting the influence of bone drilling parameters and drill specifications to find the optimized bone drill specifications for a better outcome. The study described that a significant risk during drilling is the increase in bone temperature, which can lead to osteonecrosis and can affect the stability and strength of the bone fixation. In their future directions section, the authors emphasize the need for

more advanced drilling methods, precise experimental setups, and automated systems to minimize human error and reduce associated risks. At the end of the paper, the authors provided eight points for future works, one of which is to improve the control penetration of the manual skill in typical bone drilling by developing automated drilling systems using a fuzzy logic controller that analyzes the current consumption by the direct current (DC) motor.

A study that presents practicality, limitations, and complications related to surgical drill bits in bone drilling is discussed in [13]. The study starts with the types and anatomy of surgical drill bits, followed by the cutting operation, which caused heat generation. Mechanical properties of the drill bit, such as moment of inertia, wear, and dulling of the cutting face, are also explained. Intraoperative and postoperative complications of the drill bit during surgical bone drilling are also presented comprehensively. A study also summarizes the previous research related to the thermonecrosis biological models. In the future direction, the study mentioned that ultrasonic or vibration-assisted drilling is one technology to reduce both axial thrust force and drilling torque.

A review that focused on cutting force and temperature variation in bone drilling is presented in [14]. Drilling accurate position holes and maintaining clean surrounding holes are crucial. The study also mentioned the importance of maintaining a temperature of less than 47 °C during drilling to avoid bone cell death due to the occurrence of thermal osteonecrosis. Drill design, drill parameters, and coolant were reported as the important factors for controlling heat in the bone drilling. Other factors, such as spindle speed and feed rate, are also important to avoid bone damage.

A comprehensive review of the mechanical and thermal responses in bone drilling, which is a critical aspect of various procedures, is presented in [15]. The discussion of the paper includes the bone structure, drill-bit geometry, operating conditions of bone drilling, and techniques and optimization. In bone structure, the inhomogeneity and anisotropy of bone tissues and their impact on drilling outcomes are discussed. The influence of drill-bit design on the efficiency and safety of bone drilling is a part of the drill-bit geometry section. The effect of drilling parameters such as spindle speed and feed rate on the mechanical and thermal responses during drilling is presented in the operating condition of the bone drilling section. Current techniques used in bone drilling and parameters optimization are presented in the last part of the review paper. However, future works or future direction was not provided.

Another review that discusses the factors affecting heat generation in bone drilling is presented in [16]. The paper focused on the thermal osteonecrosis that occurred during the bone drilling. The study suggests the need for more in vivo studies on human bone and how drilling parameters interact to influence heat generation. However, there is a challenge in the measurement method of bone temperature due to the complex properties of bone tissue and the lack of a standard procedure.

Another comprehensive review on the bone drilling process investigation and possible research is presented in [17]. A typical schematic diagram of the bone drilling process is provided. Factors influencing bone drilling efficiency and temperature rise are also discussed. The study mainly focused on the investigations of conventional bone drilling to obtain information such as bone type, experimental type, experimental details, and research outcome. To complement the conventional bone drilling review, the authors also provided the investigations of non-conventional bone drilling studies such as ultrasonic-assisted drilling (UAD) [18], vibrational drilling technique [19], water-jet drilling [20], automatic drilling process [21], and acoustic emission (AE) based monitoring process [22]. In the summary section, the authors highlight that most of the previously published research articles presented temperature measurement and analysis during orthopedic drilling. Another summary can be read in detail in the paper.

Heat is one of the major issues in the bone drilling procedure, and the study in [23] presents the factors that affect drilling behavior to prevent excessive heat generation. The study also discusses a model of bone drilling to find the relationships between the drilling parameters. The study also highlights the necessity of the improved drill bit to minimize thermal and mechanical damage to the bone in the future direction. The development and application of a robotic bone drilling system as an advanced bone drilling procedure is also necessary and emphasized in the paper.

A state-of-the-art review and comprehensive analysis of orthopedic drilling are presented in [24]. The review summarized numerous articles on conventional and non-conventional drilling parameters and their technologies. Bone drilling characteristics and control variables were presented in very detail and inclusively. Apart from the detailed review, non-conventional techniques in orthopedic drilling are also described. It includes water jet-assisted drilling (WJAD), laser-assisted drilling (LAD), and UAD. Design of experiments and modeling in orthopedic drilling based on the Taguchi method, analysis of variance (ANOVA), and fuzzy logic are also presented. The review paper also provided several future directions, two of which are as follows: (1) The vibrational bone drilling with an internal closed-loop irrigation system is potentially used to minimize heat and thrust force; (2) Robotic bone drilling with multiobjective optimization can reduce thermal and mechanical damage.

A review paper that highlights the use of robotics and autonomous systems designed in bone drilling as part of computer-aided orthopedic surgery (CAOS) is presented in [25]. The robotic autonomous systems were designed to optimize drilling speed, safety, and effectiveness of various drilling parameters. The study also reviews several potential signal processing-based approaches for detecting a condition when a drill bit breaks through bone. Therefore, The authors stated that signal processing methods for motor current, drilling sound, and vibration signal for breakthrough detection in conventional drills are viable new research topics.

A review that focuses on the advancements in surgical drill bit design and its impact on reducing thermomechanical damage during bone drilling is presented in [26]. The paper discusses how different geometries of drill bits influence bone damage, especially the importance of precise cutting tools to prevent damage to surrounding tissues. The review explores various drill bit geometries, highlighting how each design influences bone damage. The general objective of the review is to provide guidelines for designing drill bits to minimize damage and improve the effectiveness and safety of bone drilling surgeries. The paper suggests future research directions for improving surgical drill bit design, including flexible drill bits and chip-breaker designs, to enhance safety.

Jung et al. [27] present internal and external factors on heat generation. Drill properties, drill diameter, drill coating, and wear are categorized as internal factors. The external factors include drilling speed or feed rate, drilling depth, cooling, drilling energy, methodology used, and patient individual factors. An almost similar review that also discussed drill bit heat generation on surgical bone drilling is presented in [28]. The paper highlights that drill bit design is one of the important factors in reducing thermal damage during surgical bone drilling. In addition, other key parameters, such as feed rate and applied force, also contribute to heat generation. Another review paper on the impact of temperature on the bone drilling process is presented in [29]. The review paper encapsulates several related studies that emphasize the critical role of temperature control in the bone drilling process.

Table 2. Highlight the previously published review papers on bone drilling.

Reference and Publication Year	Content of the Review Paper and Significant	Future Study and Future Direction

Bertollo and Walsh (2011) [13]	- Types and anatomy of surgical drill-bit
	- Drilling and cutting operations
	- Mechanical properties
	- Complications
	   - Drill bit wear or breakage
	   - Heat generation
	   - Postoperative complications
	- Biological models of bone research
	- Measurement methods
		Improving drill-bit design for better surgical outcomes and patient recovery.
		Ultrasonic-assisted drilling reduces axial thrust force and drilling torque.

Pandey et al. (2013) [4]	- Thermal osteonecrosis
	- Bone drilling parameters:
	   - Drilling parameters, e.g., drilling speed and feed rate
	   - Drill specifications, e.g., drill diameter and cutting face
	- Temperature measurement
		Predicting model development for the relationship between drilling force, drill temperature, and surface roughness [1].

Ginta et al. (2014) [14]	- Cutting force in bone drilling - Temperature variation in one drilling	Not available

Lee et al. (2018) [15]	- Experimental conditions:
	   - Cutting direction
	   - Operating condition
	- Dill-bit geometry
	- Bone chips
	- Bone drilling techniques
	- Parameter optimization
		Not available

Timon et al. (2019) [16]	- Bone drilling parameters - Temperature measurement - Experiment setup - Thermal osteonecrosis	Not available

Bohra et al. (2019) [17]	- Typical process of bone drilling
	- Factors influencing the efficiency and temperature rise of bone drilling:
	   - Variables of the drilling process
	   - Drill-bit specifications
	- Investigations of conventional drilling studies
	- Investigations of non-conventional drilling studies
	   - Ultrasonic assisted drilling
	   - Vibrational drilling technique
	   - Water-jet drilling
	   - Automatic drilling process
	   - Acoustic emission based monitoring
		Acoustic emission (AE) based technique can improve bone surgical quality in micro-drilling and support bone surgery robot systems in the future.

Samarasinghe et al. (2020) [23]	- Thermal necrosis - Factors affecting the drilling process - Rotational speed and feed rate - Drill geometry - Effect of hole depth - Effect of bone structure - Modeling of bone drilling - Robotic drilling	Improve the prediction model using the force variation based on bone layers. Enhance hand-held drill with intelligent sensors and data acquisition system.

Table 2. *Cont.*

Reference and Publication Year	Content of the Review Paper and Significant	Future Study and Future Direction

Jamil et al. (2020) [24]	- Bone drilling characteristics:
	   - Temperature
	   - Drilling force and torque
	   - Surface roughness and drill tool wear, etc.
	- Control variables of bone drilling
	- Non-conventional techniques:
	   - Water-jet-assisted drilling
	   - Laser-assisted drilling
	   - Ultrasonic-assisted drilling
	- Modeling and design of experiment in bone drilling
		Robotic bone drilling with multiobjective optimization can reduce thermal and mechanical damage [2].

Torun et al. (2020) [25]	- Breakthrough detection
	- Robotic drilling
	- Experimental parameters:
	   - Force and moment parameter
	   - Temperature control
		Signal information and processing to identify different bone densities from motor current, drilling sound, and vibration is one of the future directions.

Akhbar and Sulong (2021) [26]	- Thermomechanical damage - Surgical drill bit specifications - Surgical drill bit design	A flexible drill design.

Jung et al. (2021) [27]	- Influencing factors in bone drilling
	   - Internal factors
	   - External factors
	- Finite element method simulation
	- In vivo examination results
		Not available

Islam et al. (2022) [28]	- Thermomechanical properties - Bone drilling practice - Conventional vs. non-conventional bone drilling - Heat generation in bone drilling - Bone drilling characterization - Drill bit geometry - Temperature measurement - Challenges in bone drilling	Use more suitable drill bit geometry. Use medical-grade material for the drill bit.
Chouhan et al. (2023) [29]	- Temperature effect in bone drilling - Numerical simulation	Not available

[1] A more detail of the future study of Ref. [4] is explained in the paragraph in Section 2. [2] An interested reader for a detailed future work may read the article in Ref. [24].

3. A Brief Review of Medical Training System and Robotic Drilling

A medical training system (MTS) development for bone drilling is presented in [9]. The main objective of the training system development is to train and enhance the medical professionals' skills via VE. In particular, it controls the force in a certain range and maintains the drill thrust velocity constant at a certain time. Multi-user is the unique feature of the proposed MTS. One of the important parts of the training system is the haptic feedback for simulating realistic bone drilling sensations. The training system was validated through user tests and assessed using Euclidean distance.

A virtual training simulation approach called machine learning-based guidance (LbG) was introduced in [30]. The LbG approach aims for kinesthetic human-robot interaction (HRI) in virtual training simulations, particularly for bone surgical drilling. A femur bone drilling simulation is developed based on haptic feedback and X-ray views to help orthopedic residents practice, train, and improve their skills. The skill level of users and surgical

expertise were assessed using machine learning tools. In addition, the virtual training system uses adaptive LbG forces, which are informed by expert surgeon knowledge, to enhance the resident's performance during simulation.

Another study that applied haptic feedback for virtual reality (VR) simulation of surgical drilling is presented in [31]. The general objective of the study is to shift surgical training to VR simulation for otolaryngology and temporal bone dissection due to the complexity of anatomy. The haptic feedback in the VR simulation is used to provide a realistic sense of touch, especially the rendering of vibrations during surgical drill use. In detail, the ability of four different haptic hand controllers was evaluated to render realistic drill vibrations in VR surgical training. Some future applications of the study are as follows: (1) To enhance VR surgical simulators by incorporating vibrotactile feedback; (2) To improve the training experience in bone drilling procedures.

The application of physical and virtual prototypes for temporal bone drilling simulation is discussed in [32]. The authors mentioned that a combined method of physical and virtual prototypes offers advantages such as ease of access, the possibility of repeated practice, and the absence of ethical issues. The future work of the study is to develop and use virtual reality in bone surgical simulation.

4. An Application of Vibration and Machine Learning Methods for Bone Drilling

This section presents a review on techniques in bone drilling experiments with vibration, ultrasonic, and acoustic emission signals. This section also presents an application of various machine learning (ML) methods for optimization, regression, and classification in bone drilling studies.

4.1. Bone Drilling Vibration

When a drill bit makes mechanical contact with bone during bone drilling, it applies force to the bone surface, causing it to penetrate and trigger a vibration signal. The vibration signal exhibited from this process can be captured using an accelerometer. A study of vibration signal characteristics for bone drilling, especially for bone layer classification, is presented in [33]. The vibration signal dataset was acquired intermittently when the drill bit passed through three different layers: periosteum, first cortical, and spongy. Time and frequency domain features were extracted for the acquired vibration signal for three different layers. The features analysis results of the frequency domain show outperformed time domain features, indicating that frequency domain features have more information related to the bone layer compared to the time domain features. This is because the frequency characteristics of the vibration signal generated during bone drilling correspond to the structure and condition of the bone layer itself. Different bone densities will exhibit different frequency characteristics of the vibration signal. These properties can be investigated further using various signal and image processing techniques.

Another study found that the vibration signal during the milling of the ventral cortical bone (VCB), which has a higher density, is different from that during the milling of the cancellous bone (CCB) [34]. Cortical bone tends to show higher frequency responses, reflecting greater hardness and density, whereas cancellous bone exhibits lower frequency responses due to its porous structure. These studies [34,35] provide strong evidence that cortical and cancellous bones differ in the frequency patterns of the vibration signals.

A novel ultrasonic vibration-assisted drilling (UVD) technique for precise bone surgery is presented by Kong and Lee [36]. An analytical force model is developed for ultrasonic vibration-assisted bone drilling. In comparison to traditional drilling techniques, force and torque were significantly decreased in an experimental study on bovine bone utilizing ultrasonically assisted drilling [18]. The study found that sensors-aided drilling, with a vibration frequency of 20 kHz and amplitude of 4–20 μm, produced lower temperatures than conventional drills [3,37].

4.2. Applied Machine Learning Methods

An application of the machine learning (ML) method for optimum bone drilling parameters prediction is presented in [38]. A genetic algorithm (GA) is used to find a minimum thrust force value from the combination of the bone drilling parameters during bone drilling. A mathematical model of the thrust force as a function of spindle speed and feed rate is calculated using response surface methodology (RSM). In the study, the optimal value of the spindle speed and the feed rate to achieve the minimum thrust force during bone drilling is developed using the GA method. The GA method uses a developed RSM of thrust force as an objective function. The GA optimization result shows that a feed rate of 30 mm/min and a spindle speed of 1000 rpm are the optimal parameters for the minimum thrust force value. The GA predicted result is also compared to the experiment result for a similar feed rate and spindle speed value of 710 rpm.

Pandey et al. [39] presented a combined method to obtain an optimized grey fuzzy reasoning grade (GFRG) from all quality characteristics of bone drilling. The combined method consists of two methods: grey relation analysis (GRA) and fuzzy logic. The GFRG determines the optimal combination of bone drilling parameters that minimize temperature, force, and surface roughness. The highest GFRG is obtained at the speed of 500 rpm and the feed rate of 40 mm/min.

A study that reported the application of radial basis function neural network (RBFNN) for drill wear classification in bone drilling is available [40]. The RBFNN is utilized to develop a drill wear classification model based on a multi-sensor approach. The features for the RBFNN classification model were extracted from signals such as cutting forces, servomotor drive currents, and acoustic emission (AE).

Various ML models such as k-nearest neighbors (KNN), support vector regression (SVR), decision tree (DT), and random forest (RF) were used for predicting temperature elevation rotary ultrasonic bone drilling (RUBD) [41]. The machine learning models were compared with the response surface methodology (RSM) analysis. The result shows that SVR is the most outperformed model for this application compared to other ML methods.

The monitoring and prediction of temperature elevation during real-time in vivo medical surgery is a challenging task. A study that presents the Ridge regression for prediction of the temperature rise during orthopedic bone drilling is presented by Agarwal et al. [42]. The Ridge regression model is compared with other ML models such as multilayer perceptron (MLP), lasso regression, and multi-linear regression. The performance metrics such as mean square error (MSE), root mean square error (RMSE), and mean absolute error (MAE) show that the error metrics of the Ridge regression are lower than other ML models, indicating that the proposed method outperformed other models. In another study by Agarwal et al. [43], the Ridge regression was compared with other ML models such as lassor regression, SVR, multi-linear regression, and artificial neural network (ANN). Ridge regression and other ML methods are used to predict the surface roughness and cutting force during rotary ultrasonic bone drilling. According to the statistical analysis of the predictive results, it was observed that Ridge regression has the least error metrics compared to other ML methods in terms of surface roughness prediction. In the case of the cutting force prediction, SVR was the most accurate model compared to the other ML models.

KNN and ensemble classifiers were utilized in [44] for breakthrough detection in robotic orthopedic surgery. A feature set containing closed-loop control signals and force sensor data were used as the training datasets to develop the prediction models. It was found that the ML models accurately detected the breakthrough during bone drilling operations. The best accuracy of breakthrough detection is $98.1 \pm 0.2\%$ for sheep femur bone.

A successful strategy for identifying bone drilling levels (bone layers) using a customized convolutional neural network (CNN) is described in [35]. The CNN classification used vibration signals from a three-axial accelerometer attached to the cow femur bone. The CNN accurately classified raw vibration signals from the three-axial accelerometer into three distinct bone layers: periosteum (the outermost layer), first cortical (the next layer

beneath the periosteum), and spongy (the innermost layer). A summary of the application of ML methods in bone drilling is presented in Table 3.

Table 3. Summary of the application of machine learning methods on bone drilling.

Author (Year)	Data Used in the Machine Learning Method	Machine Learning Method	Machine Learning Is Used for?	The Purpose of Using Machine Learning Method
Pandey et al. (2014) [38]	Temperature, force, and surface roughness	Grey relation analysis and fuzzy logic	Optimization	To determine the optimal combination of bone drilling parameters that minimize temperature, force, and surface roughness.
Pandey et al. (2014) [39]	Temperature, force, and surface roughness	Grey fuzzy reasoning grade	Classification	To find an optimal value of feed rate (mm/min) and speed (rpm).
Staroveski et al. (2015) [40]	Cutting forces, servomotor drive currents, and acoustic emission	Radial basis function neural network	Classification	To develop a drill wear classification model based on a multi-sensor approach.
Torun et al. (2020) [44]	Closed-loop signal and force sensor data	*K*-nearest neighbors and ensemble classifier	Classification	To detect breakthroughs and estimate the condition of the drill bit in robotic bone drilling.
Agarwal et al. (2022) [41]	Temperature	*K*-nearest neighbors Support vector regression Decision trees Random forest	Regression	To introduce different ML predicting methods for the temperature elevations of rotary ultrasonic bone drilling.
Agarwal et al. (2022) [42]	Temperature	Multilayer perceptron Lasso regression Ridge regression	Regression	To predict temperature rise during bone drilling.
Agarwal et al. (2022) [43]	Surface roughness and cutting force	Ridge regression, lasso regression, support vector regression, multi-linear regression, artificial neural network	Regression	To predict the surface roughness and cutting force during rotary ultrasonic bone drilling.
Caesarendra et al. (2024) [35]	Vibration signal	Convolutional neural network	Classification	To classify three bone layers based on vibration signal.

5. Experimental Procedure of Bone Drilling

5.1. Previous Studies

Several tools are required in the drilling process, namely the hand drill machines and drill bits. Currently, the drilling speed of the hand drill machine varies between 500 and 1500 rpm. The reason for this difference is that some manufacturers have also introduced high speeds as an advantage in their marketing activities. Drill bits are also employed in preparing bone tunnels, for instance, in anterior ligament reconstructions. Typically, drilling is utilized to create holes in the bone before inserting screws. Nevertheless, since rigid bone is invariably surrounded by soft tissues like muscles, fat, ligaments, and tendons, which allow for bone movement, the bone can deviate from its normal position due to the shearing forces exerted by the drilling tool. The process of drilling a bone is depicted in a typical block diagram in Figure 1.
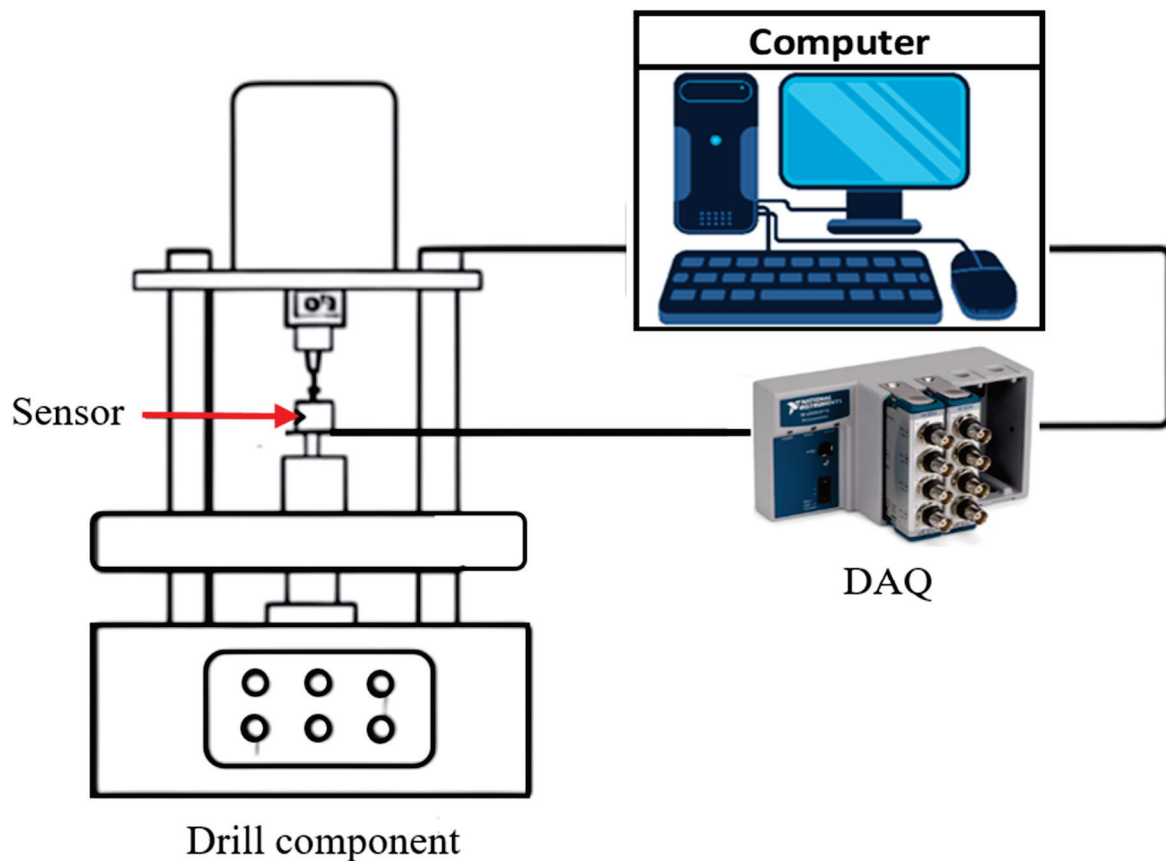
Figure 1. Schematic block diagram of typical bone drilling experiment.

Several other critical performance characteristics that determine the success of bone drilling include the straightness of the created hole, an efficient coefficient of friction, and healing time. Therefore, during surgical procedures, the force exerted by the surgeon and the position of the drill bit must be accurate. The accuracy of drilled holes during orthopedic fracture treatment relies greatly on the manual skills of the surgeon. However, currently, bone drilling tools used in surgeries do not include any mechanisms for penetration control. Thus, an automatic drilling system must be developed to minimize human errors during bone drilling. Much research has been conducted to explore new drill-bit designs [13–16] and new drilling techniques [17–19]. This was performed to avoid the accumulation of heat at the point where the drill was located.

In [45], there are two approaches to minimize thermal damage during bone drilling. The first strategy involves employing a higher feed rate to decrease the duration of the drilling process. The second method involves utilizing a lower feed rate to achieve a lower maximum temperature.

Bone drilling has been studied in past decades and is still a promising and developing research area. Table 4 shows the selected research from 1976 to 2023 that briefly described the bone sample used, the experimental description and procedure, and the outcome of the study.

Table 4. Review paper on experimental bone drilling.

Author (Year)	Bone Sample	Brief Experimental Description	The Outcome of the Study
Chen and Gundjian (1976) [46]	Bovine femur	The bovine femur was split into seven thin-disc samples. Each thin-disc sample dimension is approximately 1 mm thick and 3 mm in diameter.	The material characteristic that affects the bone's maximum temperature when a heat source is present is specific heat.
Cordioli and Majzoub (1997) [47]	Bovine cortical femur bone	The bone sample was drilled with a diameter of 2 and 3 mm running at 1500 rpm and 200 N of axial force.	Correlation between drilling depth and maximum temperature.
Hillery et al. (1999) [48]	Femur heads, Bovine tibia	The drilling machine was operated from 400 to 2000 rpm with an interval of 200 rpm. The feed rate during the bone drilling was 50 mm/min.	The temperature increased with the increasing depth of the hole. The optimal speed range is between 800 and 1400 rpm with a drill bit diameter of 3.2 mm.
Lee et al. (2012) [49]	Bovine femur	Each bone specimen was attached to a drilling dynamometer. The controlled parameters for the drilling time are gauge torque and thrust.	Presented a novel method based on a CNC system for temperature measurement, various thermocouples, and an accurate position.
Pandey et al. (2014) [50]	Bovine bone	Using an MTAB 3-axis Flex mill. Temperature data were gathered using a K-type Extech thermocouple and data-gathering software.	The study found that drill diameter had the greatest influence among these variables based on the result of the Taguchi method.
Sarparast et al. (2020) [51]	Bovine femur	A high-speed electrical motor with a rotational speed higher than 10,000 rpm was mounted in the lathe machine. High-speed steel (HSS) drill bit that was 2 mm in diameter was selected for the experiment. The lathe machine was run with an increasing feed rate from 10 to 50 mm/min. Single footing load cells and k-type thermocouples are used for force and temperature measurement.	Bone drilling optimum (minimum) temperature was revealed at a rotational speed of 12,000 rpm and feed rate of 50 mm/min. By increasing the feed rate slightly, it increases the process force, which can also lead to the increasing temperature.
Alam et al. (2023) [52]	Femoral and tibia bones	A custom-made drilling setup with a feedback control system for force, torque, and temperature was used in drilling tests. Small holes of 1.5 mm in diameter through the bone were produced with rotational speed of 400 rpm and feed rate of 40 mm/min.	Increasing pressure on a worn drill is necessary when drilling passes through the hard cortex of the bone. The torque in bone drilling has a direct relationship with the depth of drilling. Bone temperature was increased when the drill progressed to wear.

5.2. Bone Drilling Lab Experiment of the Present Study

A bone drilling lab experiment utilized a Dobot Magician robot, National Instrument (NI) data acquisition (DAQ) module NI-9345, Brüel & Kjær three-axis accelerometer type 4535-B, and standalone academic LabVIEW software. A Dobot Magician robot was connected to a PC with available software for robot programming. A schematic of the bone drilling lab experiment is presented in Figure 2.

Layer	Depth (mm)
Periosteum	2 − 3
First cortical	0.7 − 0.86
Spongy	1.09 − 2.12
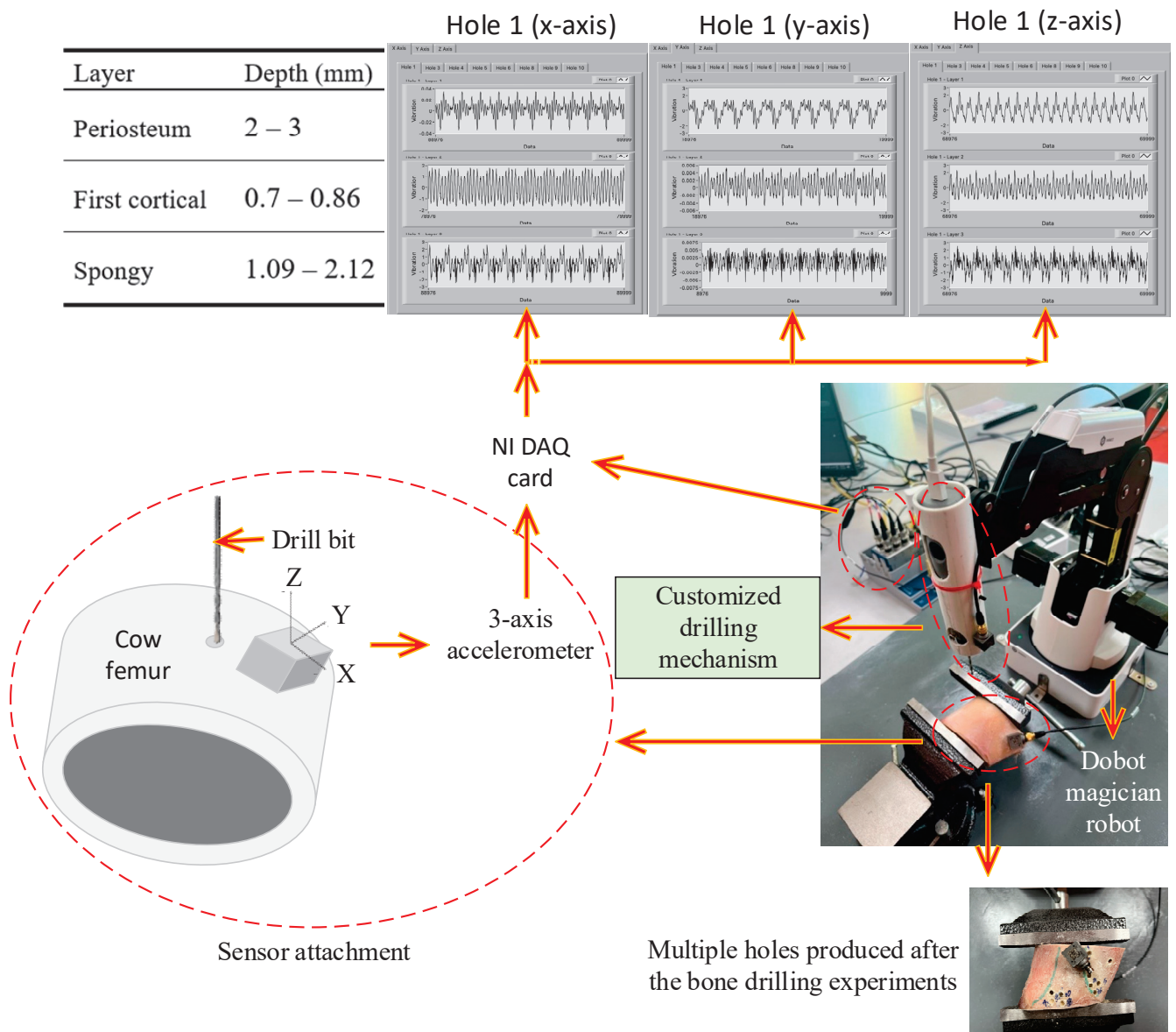
Figure 2. Schematic diagram of the bone drilling experiment.

The original end effector of the Dobot Magician robot was replaced with the customized drilling mechanism, as presented in Figure 2. In the bone drilling experiment, each layer's depth penetration is accurately controlled by the Dobot Magician robot. Bone drilling vibration was performed intermittently from the periosteum layer (the outermost layer), first cortical layer (the layer beneath the periosteum layer), and spongy layer (the innermost layer) as illustrated in the table part of Figure 2. The vibration signal was acquired using a three-axial accelerometer B&K type 4535-B-001 with a sensitivity for the x-, y-, and z-axis of 96.44, 100.4, and 100.6 mV/g, respectively. A LabVIEW block diagram for the bone drilling vibration experiment was developed, and the vibration data were acquired with a sampling rate of 5 kHz. The drill was run at 500 rpm and a feed rate of 0.002 to 0.006 in/min during the experiment. The drill geometry was chosen as a twisted drill bit with a 3.5 mm diameter. The vibration data were collected in 5 s for each layer and saved in the Microsoft Excel 2013 Worksheet. The experiment does not involve data processing because the vibration signal is not filtered or denoised. This is to simplify the method by excluding the data processing step and to examine the robustness of deep learning methods in predicting and classifying the raw vibration signals of bone drilling.

The three-axial accelerometer was mounted to the bone that would be drilled, and another one was attached to the customized drilling mechanism to receive vibration signals during the drilling operation, as presented in Figure 2. The drill bit was then placed at the anterior surface of the proximal femur and drilled in clockwise rotation continuously. A fresh frozen cow femur was used in this research because this type of bone has almost similar characteristics to human bone [16]. The sample was fixed with a laboratory clamp while the drilling process was performed. The total number of holes produced in the experiment was 10. However, two holes did not go through the bone (holes #2 and #7). The remaining eight holes were successfully drilled through the bone sample.

The vibration signal of the bone drilling experiment (hole #5) for three different layers is presented in Figures 3–5. Figure 3 presents the bone drilling vibration data (x-axis) for the duration of one second. Figure 3a, Figure 3b, and Figure 3c are the vibration signals from different layers: periosteum, first cortical, and spongy, respectively. The vibration signals from several layers are difficult to differentiate. On the other hand, the vibration signal displays a distinct form, as seen in Zoom in portions of Figure 3a–c, if it was only plotted for 0.2 s (0.5~0.7 s) for zooming purposes. Another information that can be revealed in Figure 3 is the vibration signal amplitude of each layer. The deeper the drill bit comes in, the higher the amplitude (in mV) of the vibration signal.
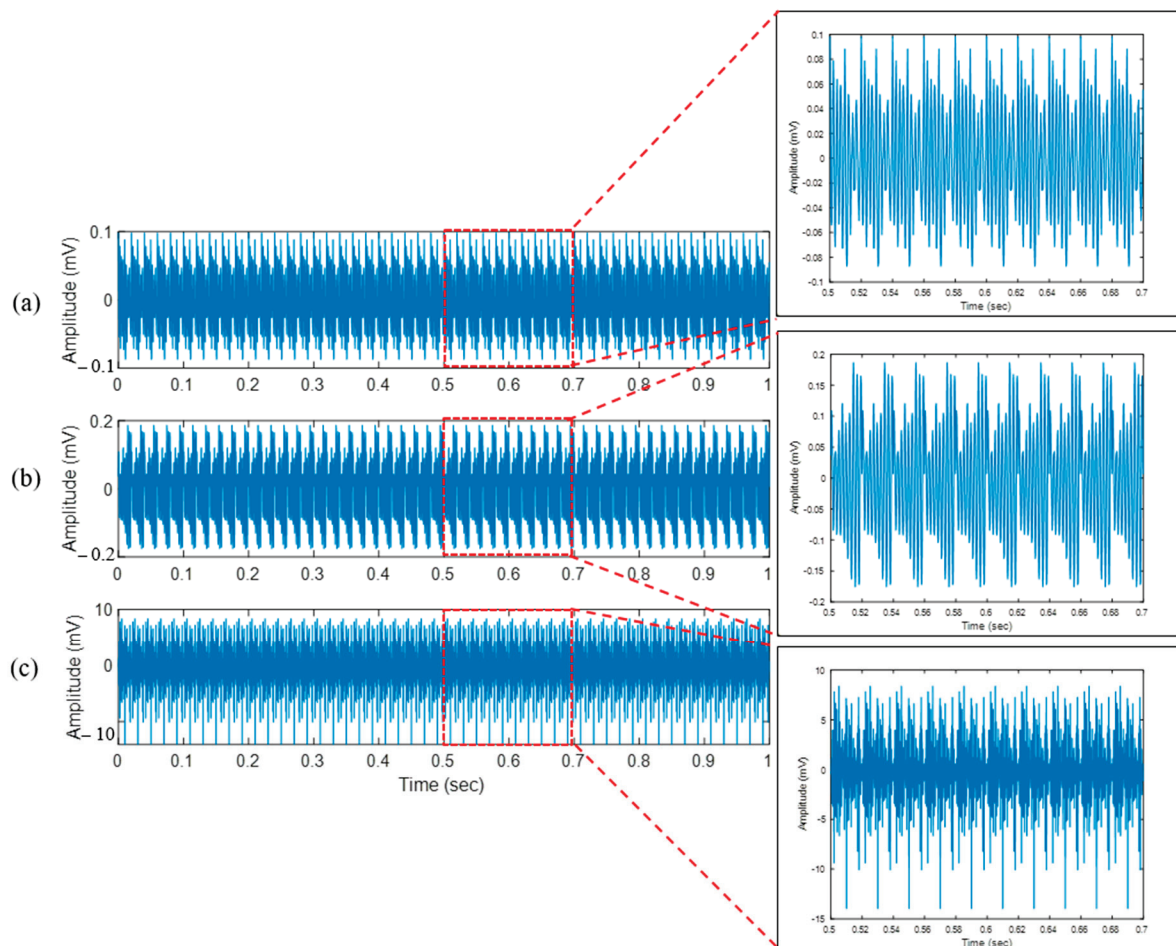
Figure 3. Bone drilling vibration signal (x-axis) of three different layers: (**a**) Periosteum; (**b**) First cortical; (**c**) Spongy.

Figure 4 presents the bone drilling vibration data (y-axis) for the duration of one second. Figure 4a, Figure 4b, and Figure 4c are the vibration signals from different layers: periosteum, first cortical, and spongy, respectively. Similar to Figure 3, the vibration signals of three different layers in Figure 4 are also difficult to distinguish visually. However, zooming in on the vibration signal for 0.2 s (0.5~0.7 s results in a distinct form and amplitude, as seen in Figure 4a–c.

Figure 5 presents the bone drilling vibration data (z-axis) for the duration of one second. Figure 5a, Figure 5b, and Figure 5c are the vibration signals from the periosteum layer, first cortical layer, and spongy layer, respectively. Similar to Figures 3 and 4, the vibration signals of three separate layers in Figure 5 are visually indistinguishable. Zooming in on the vibration signal for 0.2 s (0.5–0.7 s) results in a changed shape and amplitude.
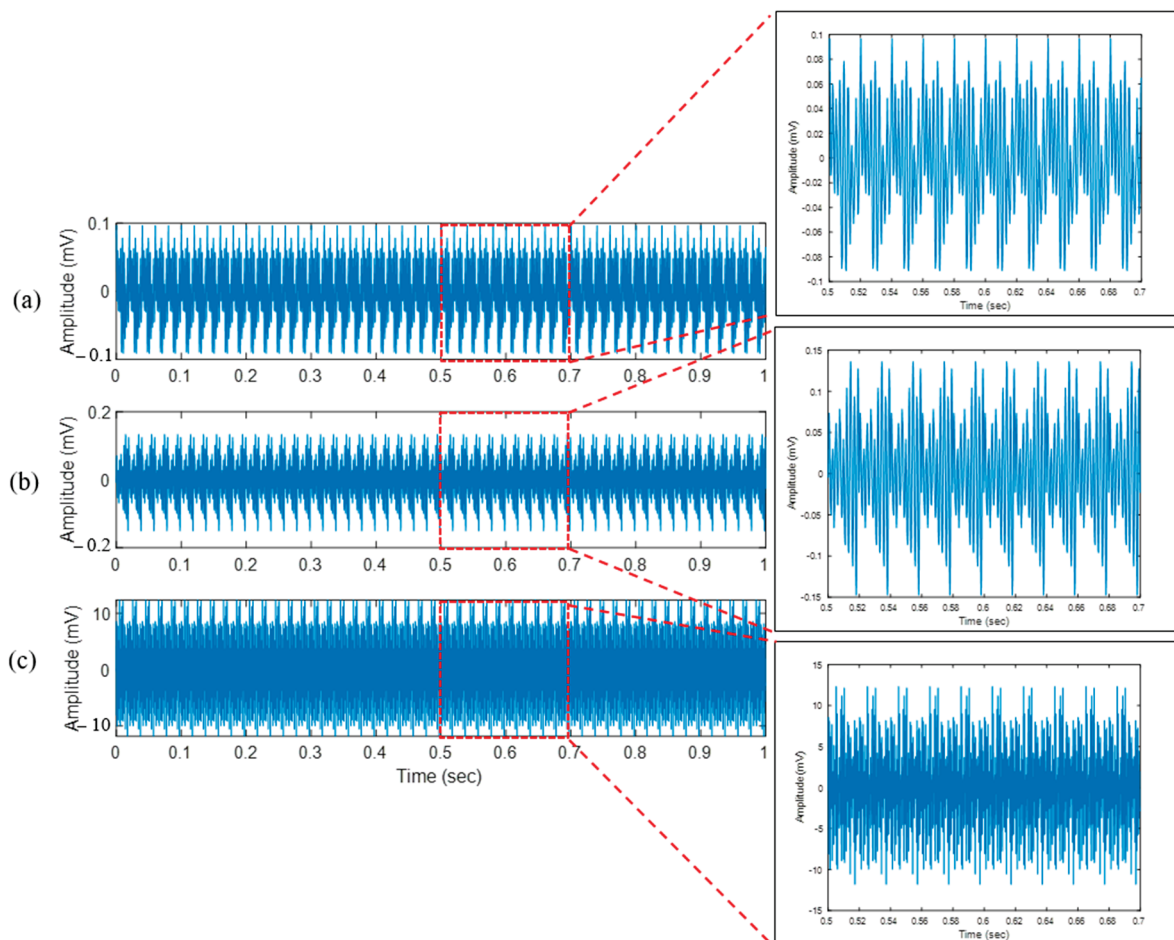
Figure 4. Bone drilling vibration signal (y-axis) of three different layers: (**a**) Periosteum; (**b**) First cortical; (**c**) Spongy.

Table 5 shows the root mean square (RMS) of the vibration amplitude during bone drilling. It is demonstrated that as the drill bit penetrates deeper, the RMS amplitude increases. It implies that each layer's bone structure is different, and when the drill bit makes contact with the bone structure, the vibration signal is triggered. In particular, the RPM values increase significantly from the first cortical to spongy layer than from the periosteum to the first cortical layer. It shows that the spongy layer is less rigid and dense than the periosteum and first cortical layer.
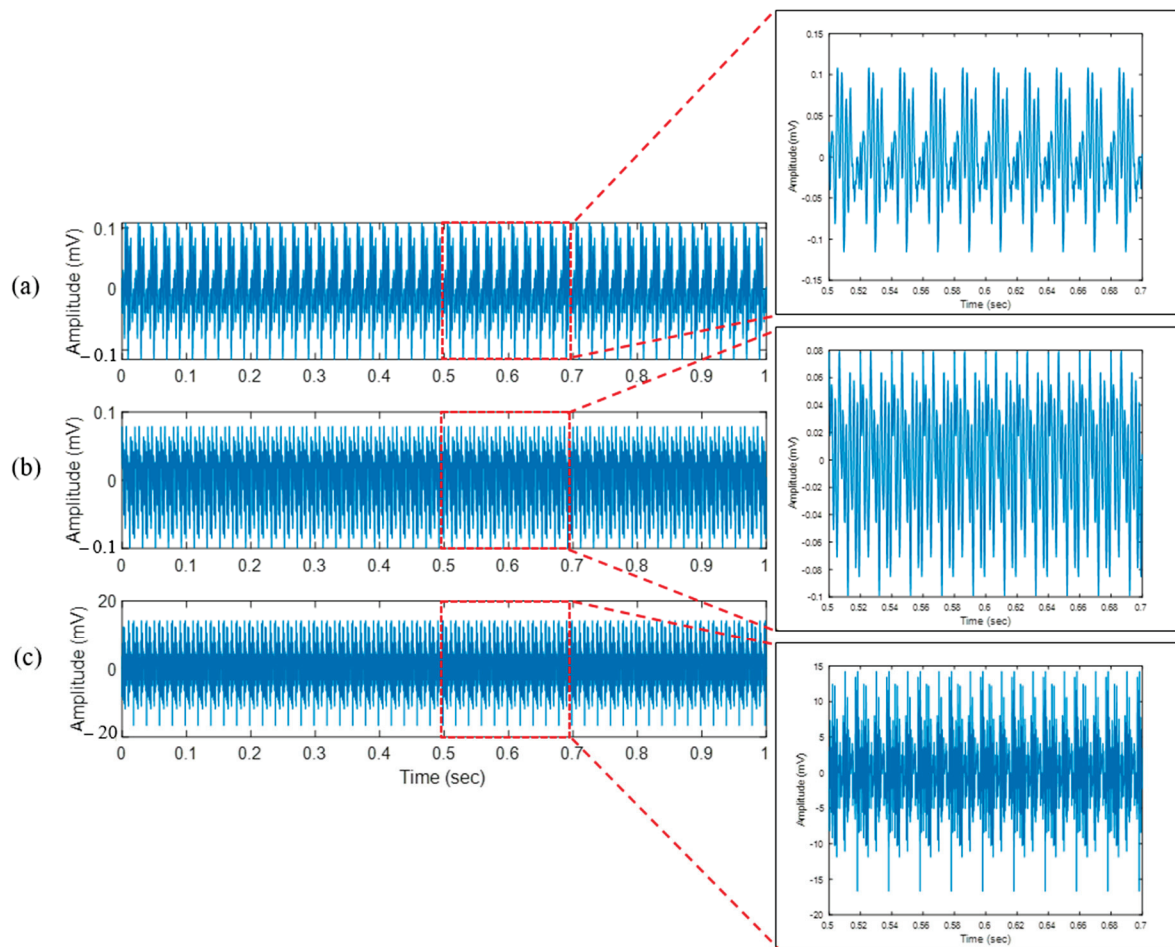
Figure 5. Bone drilling vibration signal (z-axis) of three different layers: (**a**) Periosteum; (**b**) First cortical; (**c**) Spongy.

Table 5. Vibration amplitude of different axes and different layers represented by RMS.

Layer	RMS of x-Axis Vibration (mV)	RMS of y-Axis Vibration (mV)	RMS of z-Axis Vibration (mV)
Periosteum (layer 1)	0.04	0.04	0.04
First cortical (layer 2)	0.09	0.06	0.05
Spongy (layer 3)	4.04	5.51	5.85

6. Long Term-Short Memory Method

Long short-term memory (LSTM) is a type of recurrent neural network (RNN) architecture that processes sequential input. The LSTM is an improved method of RNN, which was designed by Hochreiter and Schmidhuber for sequence prediction tasks [53]. In addition, the LSTM method excels in capturing long-term dependencies in sequence data and handling the vanishing gradient problem [53]. The LSTM method has been applied previously in an ECG-rhythm classification study [54] and has been used to optimize reactive power usage in high-rise buildings [55]. According to the summary of the machine learning application presented in Table 3, LSTM has not been used for orthopedic bone drilling; this is the motivation for selecting the LSTM method in the present bone layer classification study.

An example application of the LSTM method for reproducing variable forces in haptic technology focusing on tactile feedback enhancement in real-time robotic surgery simulation is presented in [56]. The LSTM method is used in the study to replicate varied force feedback during a skin layer surgical procedure. The LSTM method is also applied in the study to increase force prediction accuracy in robotic surgery simulation. This is

because the bone experiment was conducted intermittently from the periosteum, through the first cortical, and ended at spongy; a sequential method is suitable for this type of data. This is the main reason why LSTM was selected in this study.

6.1. LSTM Architecture

The characteristic of LSTM is a chain of repeating modules, as presented in Figure 6a. Each module looks at some input x_t and outputs a hidden state value h_t. A loop passes information from one network phase to the next. The difference between RNN and LSTM is in the construction of the chained units. The unit of standard RNN has a simple structure, like a single tanh layer, while LSTM has a more complicated unit, as presented in Figure 6b. The keys of LSTM are cell state and gates. The cell state is kind of like a conveyor belt. The cell state (memory) learns new information from the input. The LSTM can remove or add information to the cell state (C_t) using a mechanism called gates. Gates can remove or add information to the cell state. Gates decides whether information should be added to the units or not. In general, the gate equation is presented in (1) [57]:

$$Gate_{(f,i,o)} (h_{t-1}, x_t) = \sigma(U\, h_{t-1} + W\, x_t + b),$$ (1)

where U, W, and b are the parameters of the door. In this equation, the parameters of each door are different. The variable x_t in the current input, and h_{t-1} is the previous hidden state.
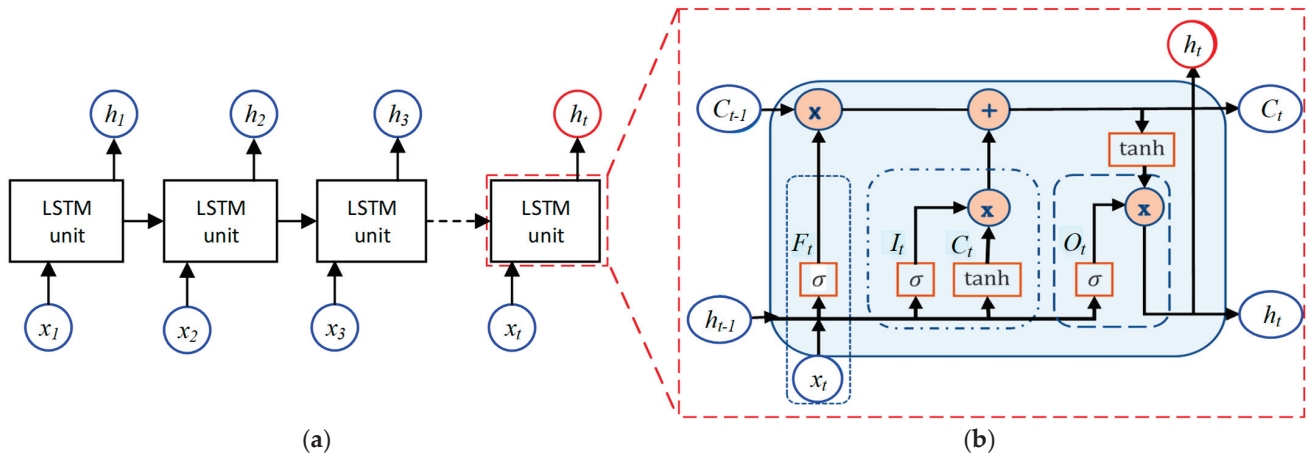
Figure 6. LSTM architecture: (**a**) LSTM chain; (**b**) LSTM unit construction.

There are three gates in an LSTM unit: forget gate, input gate, and output gate. Forget gate (F_t) controls which information should be removed from the cell state. Input gate (I_t) determines which information from the previous timestamps should be remembered or forgotten. The input gate also controls how much new information is added to the cell state. Output gate (O_t) selects useful information from the current cell state and produces it as the output. The output gate additionally sends updated data to the following timestamp.

The forget gate (F_t), input gate (I_t), and output gate (O_t) equations are presented in (2)–(4), respectively [57].

$$F_t = \sigma(U_f\, h_{t-1} + W_f\, x_t + b_f),$$ (2)

$$I_t = \sigma(U_i\, h_{t-1} + W_i\, x_t + b_i),$$ (3)

$$O_t = \sigma(U_o\, h_{t-1} + W_o\, x_t + b_o),$$ (4)

6.2. LSTM Model

During the Lab experiment, eight holes were successfully drilled through the femur bone in the bone drilling experiment. They were holes #1, #3, #4, #5, #6, #8, #9, and #10.

Among the eight datasets, holes #1 and #3 were not included in DL multiclassification and prediction. Six holes were used in LSTM, CNN, and RNN training and testing (holes #4, #5, #6, #8, #9, and #10). Holes #1 and #3 were not included because they were corrupted by an expected noise after initial dataset checking using MATLAB. The assessment was conducted visually and was not explained in detail in this paper.

In this study, the LSTM algorithm that is available in TensorFlow Keras was used. To develop the LSTM model, 70% of the vibration data were used for training, and 30% of the data were used for testing. The validation data were obtained from 20% of the training data. The LSTM architecture used in this project is presented in Table 6, and the summary is as follows: Input Layer → LSTM Layer (return_sequences = True) → LSTM Layer → Flatten Layer → Dense Layer (Output Layer). With this architecture, the model can accept the sequential vibration data from the x-, y-, and z-axis for each layer. The sequential vibration data were processed in two LSTM layers to obtain the prediction model for multiclass classification. The 'softmax' activation function was selected as the dense layer.

Table 6. LSTM architecture for multiclass classification.

Layer (Type)	Output Shape	Param #
input_1 (InputLayer)	[(None, 3, 1)]	0
Astm (LSTM)	[(None, 3, 32)]	4352
lstm_1 (LSTM)	(None, 32)	8320
flatten (Flatten)	(None, 32)	0
dense (Dense)	(None, 3)	99

Total params: 12,771 (49.89 KB)
Trainable params: 12,771 (49.89 KB)
Non-trainable params: 0 (0.00 Byte)

6.3. LSTM Classification Results and Discussion

In the multi-classification model development, the LSTM model is configured with an 'adam' optimizer and a 'categorical_crossentropy' loss function. Some 'callback' functions, such as EarlyStopping, ModelCheckpoint, and LearningRateScheduler, are also used to control the training process. An 'accuracy' metric to evaluate the model's performance is used during the training process. The model evaluation is presented in Figure 7 with a test loss of 0.018 and test accuracy of 0.993.
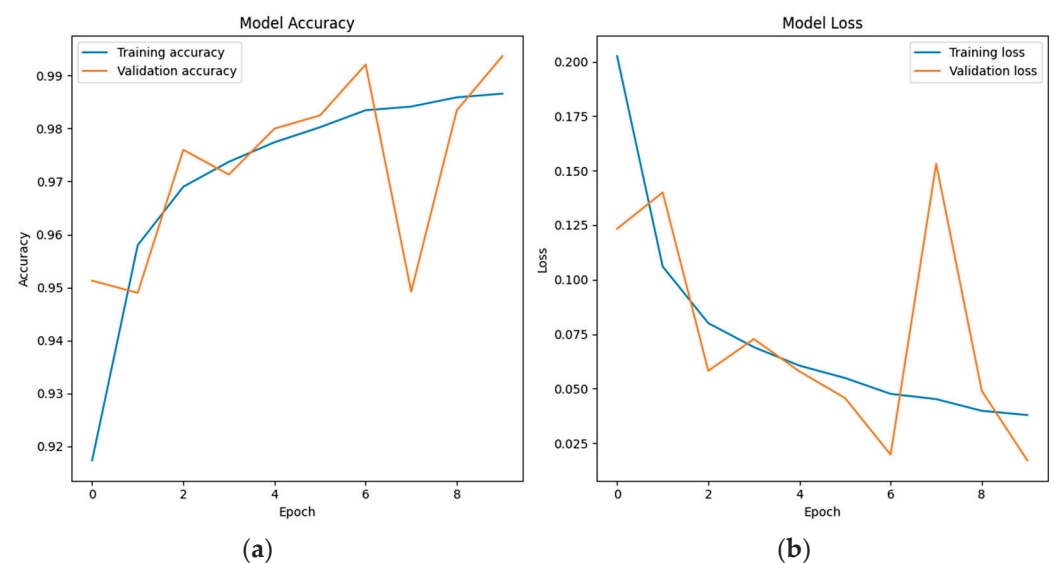
Figure 7. (**a**) Model accuracy of LSTM; (**b**) Model loss of LSTM.

Table 7 shows a classification report of LSTM, which provides detailed information regarding model performance for each target class. The evaluation of layer 1 (periosteum) shows that the model has a result of 0.99 for precision, recall, and *F*1-score. In layer 2 (first cortical), the model also has a result of 0.99 for precision, recall, and *F*1-score. In the case of layer 3 (spongy), it produces the highest result of 1 for recall and 0.99 for both precision and *F*1-score. Figure 8 shows the precision–recall curve of all three layers was close to 1.

Table 7. LSTM classification report.

	Precision	**Recall**	**F1-Score**	**Support**
Periosteum (layer 1)	0.99	0.99	0.99	45,042
First cortical (layer 2)	0.99	0.99	0.99	44,948
Spongy (layer 3)	0.99	1	0.99	45,010
Accuracy			0.99	135,000
Macro avg	0.99	0.99	0.99	135,000
Weighted avg	0.99	0.99	0.99	135,000
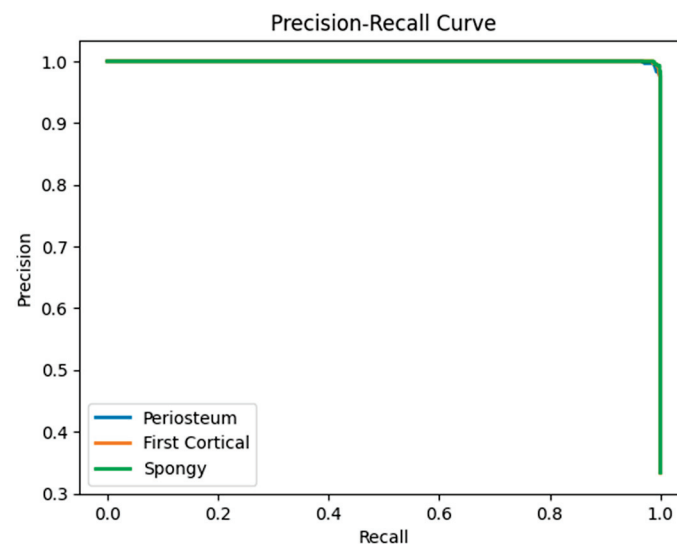
Figure 8. Precision–recall curve of the LSTM classification model.

A confusion matrix for the training and testing of the LSTM model with 10 epochs is presented in Figure 9. It is shown the classification of the three bone layers is generally successful. However, there were very few misclassification results, as presented in the confusion matrix of training and testing. In the confusion matrix of training, 366 out of the total 104,957 data points of the periosteum layer wwere misclassified in the first cortical layer, which is about a 0.35% incorrect prediction, and 694 out of the total 104,957 data points of the periosteum layer were predicted as a spongy layer, which resulted in a 0.66% error. For the first cortical layer, 698 out of the total 105,052 data points were misclassified as the periosteum layer (0.66% error), and there is no first cortical data classified as spongy. Another minor misclassification is also found in the first cortical layer, with 346 out of 104,644 data predicted in the periosteum layer, which is about 0.33% classification error, and zero spongy data were classified in the periosteum.

In the testing confusion matrix, 134 and 306 out of 45,042 periosteum data were misclassified in a first cortical layer and spongy layer, respectively, which resulted in 0.3% and 0.68% incorrect prediction error. Similar to the training confusion matrix, only 302 out of the first 44,948 cortical data points were predicted in the periosteum layer, which is about a 0.67% classification error, and no data were classified as spongy. A better classification result is found in the spongy data, with only 154 out of 44,856 data predicted in the first cortical layer, which is about 0.34% classification error, and zero spongy data were classified in the periosteum layer.
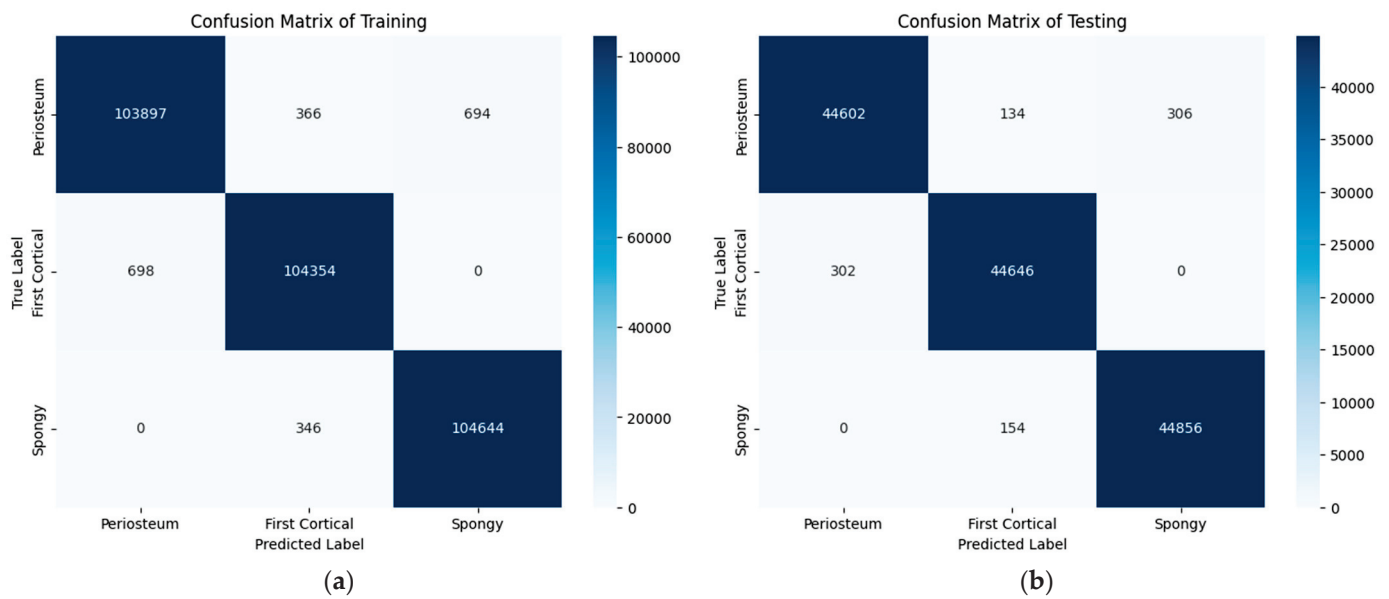
Figure 9. LSTM Confusion matrix: (**a**) Training; (**b**) Testing.

7. Other Deep Learning (DL) Methods for Performance Comparison with LSTM

Two other DL methods were selected for performance comparisons with LSTM: CNN and RNN.

7.1. Brief Information of Convolutional Neural Network (CNN)

Convolutional neural network (CNN) is a popular network design for deep learning that is particularly useful for detecting patterns in 2D (image) data. CNN uses layers of interconnected neurons, including convolutional layers that learn features directly from data. These filters slide over input features, extracting relevant patterns. CNN has been used in previous studies, e.g., for automated Cobb angle measurement [58], for bird sound classification [59], and for vibration signal analysis in belt grinding tool wear prediction [60].

CNNs were initially created for the application in images or 2D (image) data; however, there is an increasing trend of CNN applications in 1D data, especially in audio signals, time-series data, biomedical data, structural health monitoring data, and fault detection-based vibration data. A review of the application of CNNs in 1D data is presented in [61]. The review paper also described in detail the fundamental theory and architecture of applied 1D CNNs. In the review, the 1D CNNs were applied to the speech signal, ECG signal for arrhythmia detection, and vibration data for structural damage detection. The review discovered that 1D CNNs have advantages compared to 2D CNNs due to the simpler and more compact configuration. In detail, there are three main advantages of 1D CNNs: (1) Lower computational complexity; (2) Feasibility for real-time; (3) Low-cost hardware implementation [61].

7.2. CNN Classification Results and Discussion

Similar to the LSTM model, the CNN model is also configured with an 'adam' optimizer and 'categorical_crossentropy' loss function in the application of a multiclass classification of bone layers. An 'accuracy' metric to evaluate the model's performance is used during the training process. The model evaluation is presented in Figure 10.

Table 8 shows a CNN classification report of bone layers. The evaluation result of layer 1 (periosteum) shows the model has 0.95 for precision and 0.94 for both recall and *F*1-score. In layer 2 (first cortical), the model has 0.95 for precision, 0.97 for recall, and 0.96 for *F*1-score. In the case of layer 3 (spongy), it has 0.95 for precision, 0.93 for recall, and 0.94 for *F*1-score. The overall multi-classification accuracy of RNN is 0.95. The precision–recall

curve is presented in Figure 11; it is shown that the first cortical layer has better results compared to the other two layers (periosteum and spongy).

Figure 10. (**a**) Model accuracy of CNN; (**b**) Model loss of CNN.

Table 8. CNN classification report.

|	**Precision**	**Recall**	**F1-Score**	**Support**
Periosteum (layer 1)	0.95	0.94	0.94	45,042
First cortical (layer 2)	0.95	0.97	0.96	44,948
Spongy (layer 3)	0.95	0.93	0.94	45,010
Accuracy			0.95	135,000
Macro avg	0.95	0.95	0.95	135,000
Weighted avg	0.95	0.95	0.95	135,000
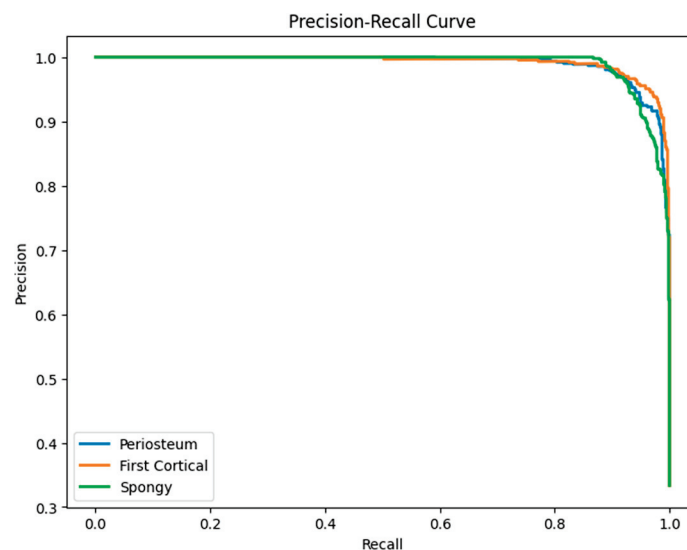
Figure 11. Precision–recall curve of the CNN classification model.

A confusion matrix for the training and testing of the CNN model with 10 epochs is presented in Figure 12. There were greater misclassification results as presented in the CNN confusion matrix of training and testing, compared to the LSTM confusion

matrix. In the confusion matrix of training, 2086 out of the total 104,957 layer 1 data points were misclassified in layer 2, which is about a 1.99% incorrect prediction; 4022 out of the total 104,957 layer 1 data points were predicted as layer 3, which resulted in a 3.83% classification error. For layer 2 prediction, 2094 out of the total 105,052 layer 2 data points were misclassified as layer 1 (1.99% error), and 1205 out of the total 105,052 layer 2 data points were predicted incorrectly as layer 3 (1.15% error). Another misclassification is also found in layer 3, with 3321 out of the total 104,990 layer 3 data points being predicted in layer 1, which is about a 3.16% classification error, and 3482 out of the total 104,990 layer 3 data points being predicted in layer 2, which is about 3.32% prediction error.

Figure 12. CNN Confusion matrix: (**a**) Training; (**b**) Testing.

In the confusion matrix of testing, 914 and 1728 out of the total 45,042 layer 1 data points were misclassified in layer 2 and layer 3, respectively, which produced prediction errors of 2.03% and 3.84% for each layer. In layer 2, 906 out of the total 44,948 layer 2 data points were predicted in layer 1 with a 2.02% classification error, and 545 out of the total 44,948 layer 2 data points were misclassified in layer 3 with a 1.21% prediction error. For layer 3 classification, 1429 out of the total 45,010 layer 3 data points were predicted in layer 1 with a 3.17% classification error, and 1518 out of the total 45,010 layer 3 data points were misclassified in layer 2 with a 3.37% prediction error.

7.3. Brief Information of Recurrent Neural Network (RNN)

A recurrent neural network (RNN) is a superset of a feedforward neural network (FFNN) that is enhanced by the addition of edges spanning neighboring time steps, which gives the model an understanding of time [62]. The RNN makes use of sequential information and can, therefore, simultaneously model sequential and time dependencies on multiple scales. This enables a unidirectional process to take information from the past to process later inputs. A basic RNN model is presented in Figure 13a.

Figure 13b illustrates the architecture of a single RNN cell. Each cell has two inputs and two outputs at each time step. For the inputs, $a^{(t-1)}$ and $x^{(t)}$ denote the hidden state from the previous cell and the current time step's input data, respectively. The inputs interact with the weights and biases (W_{aa}, W_{ax}, and b_a), which are reused in each time step. The new hidden state at the end of each cell is then used to calculate the prediction during the forward propagation using a softmax function, s. The indifferent new hidden value is carried forward; the two needed outputs are produced, which are the hidden state and predictions, as represented by $a^{(t)}$ and $\hat{y}^{(t)}$.

(**a**)

(**b**)
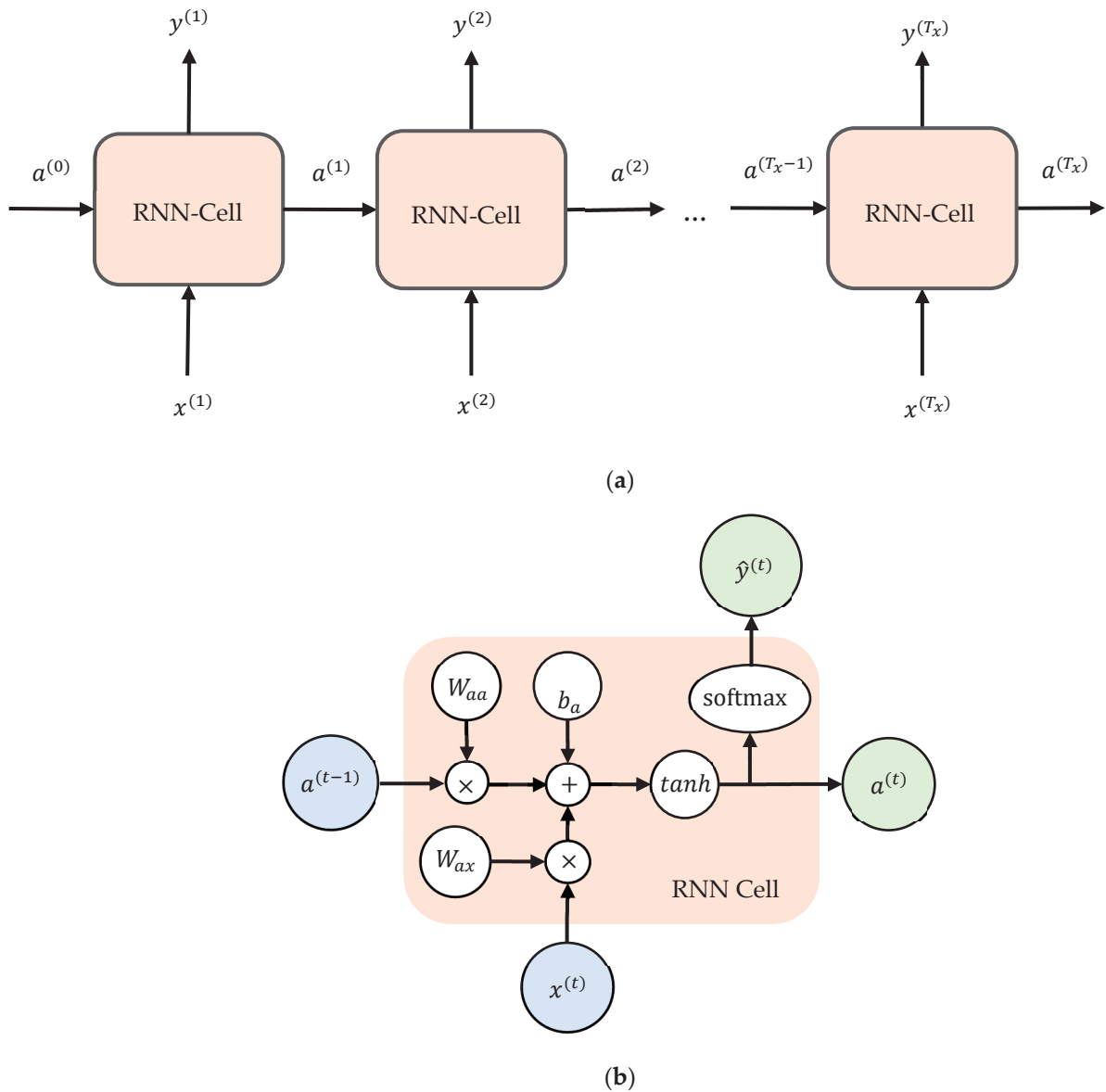
Figure 13. (**a**) Basic RNN model. (**b**) Basic RNN cell. Adapted from [63].

7.4. RNN Classification Results and Discussion

Similar to the LSTM and CNN model, the RNN model also is configured with an 'adam' optimizer, and 'categorical_crossentropy' loss function in the application of a multiclass classification of bone layers. An 'accuracy' metric to evaluate the model's performance is also used during the training process. The model evaluation is presented in Figure 14.

Table 9 shows an RNN model performance for each target class. The classification report of (periosteum (layer 1) shows that the model has 0.96 for recall and 0.95 for both precision and $F1$-score. In the first cortical (layer 2), the model has 0.97 for precision and 0.96 for both recall and $F1$-score. In the case of spongy (layer 3), the precision, recall, and $F1$-score of the model are 0.94, 0.96, and 0.95, respectively. The overall multi-classification accuracy of RNN is 0.96. The precision–recall curve is presented in Figure 15; it shows that the first cortical layer has better results compared to the other two layers (periosteum and spongy), which is similar to the CNN result.
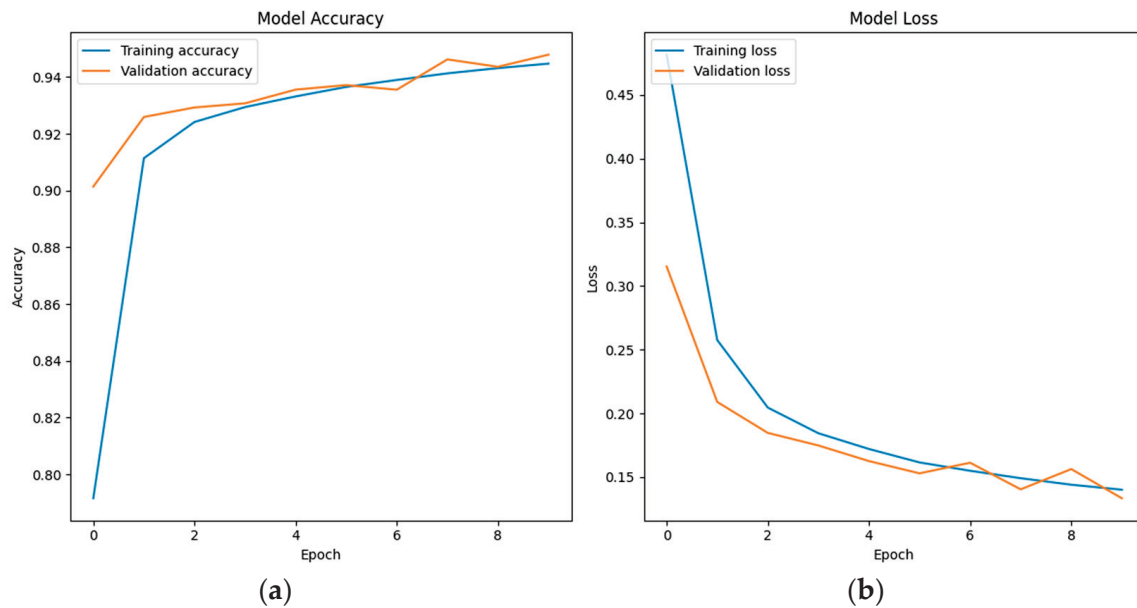
(a)   **(b)**
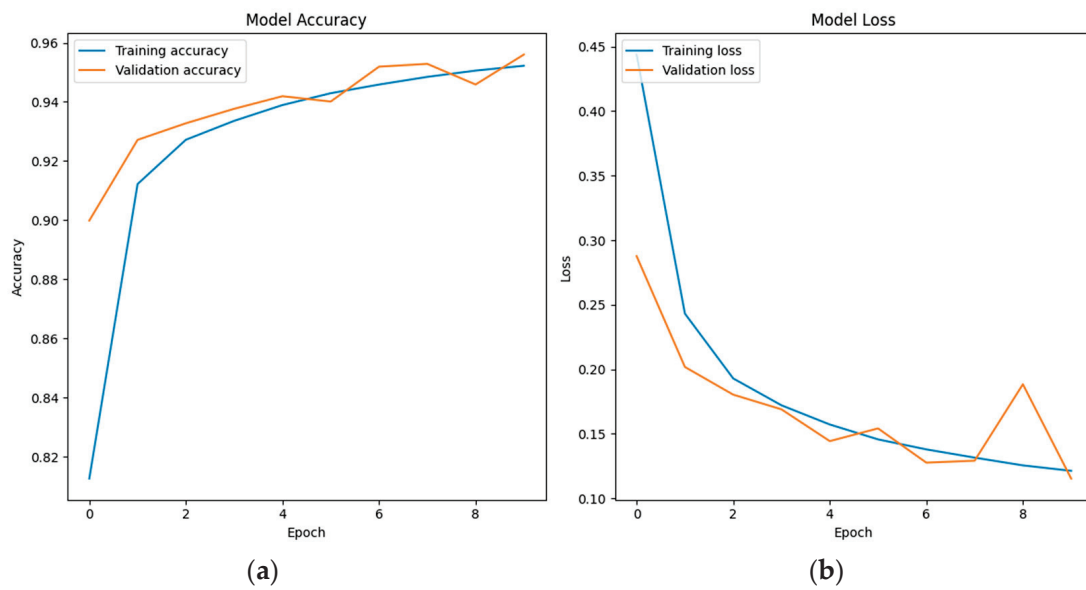
Figure 14. (**a**) Model accuracy of RNN; (**b**) Model loss of RNN.

Table 9. RNN classification report.

|	Precision	Recall	*F*1-Score	Support
Periosteum (layer 1)	0.95	0.96	0.95	45,042
First cortical (layer 2)	0.97	0.96	0.96	44,948
Spongy (layer 3)	0.94	0.96	0.95	45,010
Accuracy			0.96	135,000
Macro avg	0.96	0.96	0.96	135,000
Weighted avg	0.96	0.96	0.96	135,000
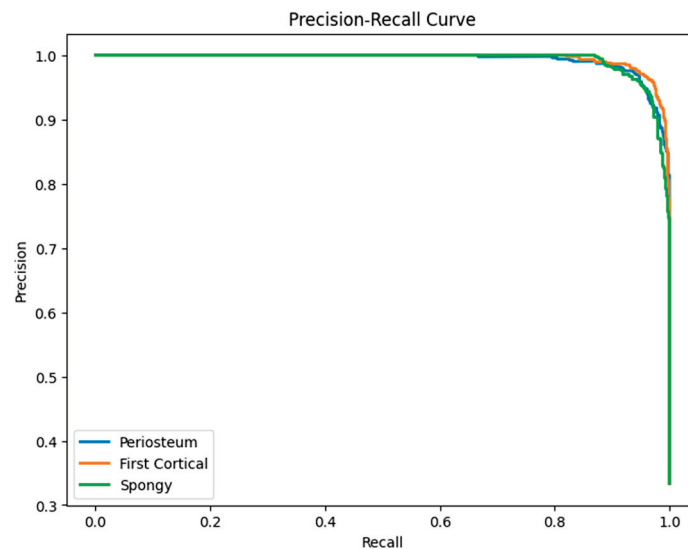
Figure 15. Precision–recall curve of the RNN classification model.

A confusion matrix for the training and testing process of RNN model development with 10 epochs is presented in Figure 16. In general, the confusion matrix result of the RNN is slightly better than that of the CNN. However, it does not perform as well as LSTM. For the confusion matrix of training, 1202 out of the total 104,957 layer 1 data points were misclassified in layer 2 with a 1.15% classification error, and 3341 out of the total 104,957 layer 1 data points were predicted incorrectly in layer 3 with a 3.18% prediction

error. In layer 2, 1928 out of the total 105,052 layer 2 data points were predicted incorrectly in layer 1 with a 1.84% error, and 2855 out of the total 105,052 layer 2 data points were misclassified in layer 3 with a 2.72% error. In layer 3, 3164 and 1572 out of the total 104,990 layer 3 data points were misclassified in layer 1 and layer 2, respectively, with 3.01% and 1.5% prediction error for layer 1 and layer 2, respectively.
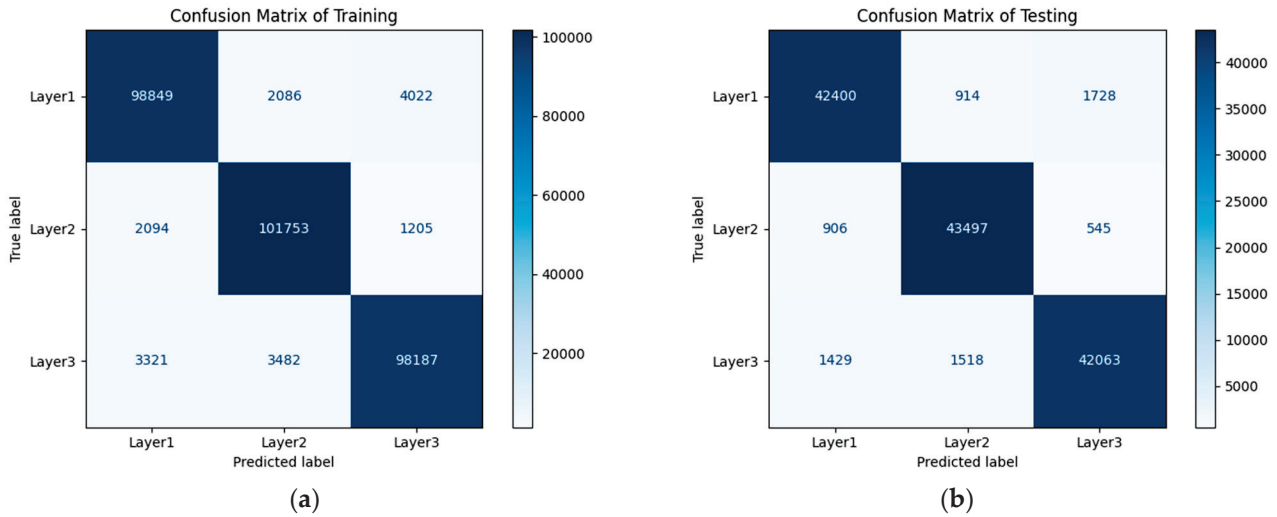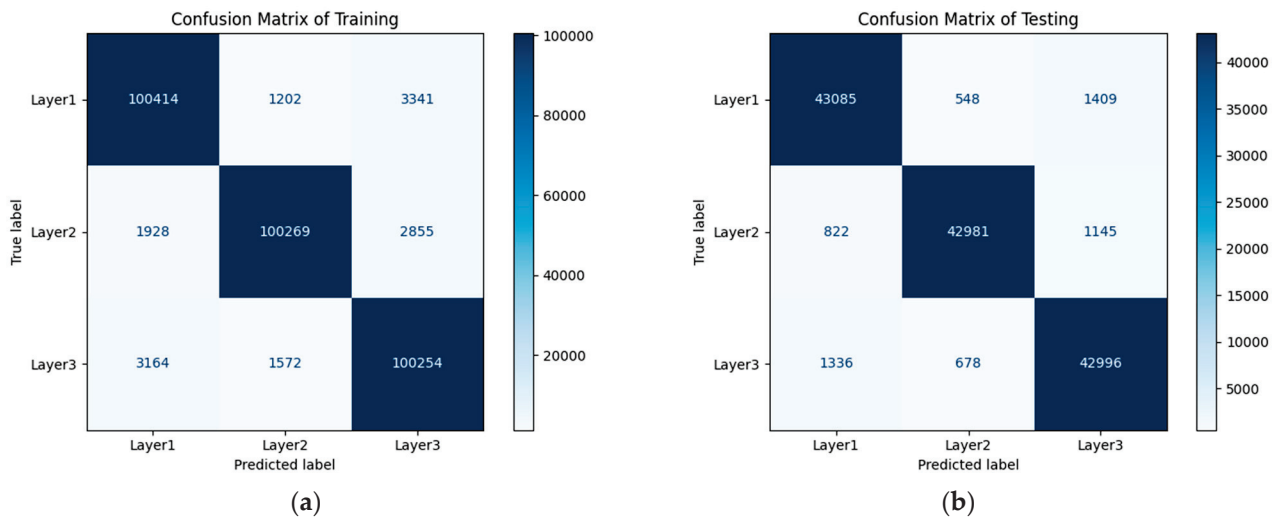

Figure 16. RNN Confusion matrix: (**a**) Training; (**b**) Testing.

In the confusion matrix of testing, 548 and 1409 out of the total 45,042 layer 1 data points were predicted incorrectly in layer 2 and layer 3, respectively. This misclassification results in a prediction error of 1.22% for layer 2 and 3.13% for layer 3. In layer 2 classification, 822 out of the total 44,948 layer 2 data points were predicted incorrectly in layer 1 with a 1.83% classification error, and 1145 out of 44,948 were misclassified in layer 3 with a 2.55% prediction error. For layer 3 classification, 1336 and 678 out of the total 45,010 layer 3 data points were predicted in layer 1 and layer 2, respectively, with a 2.97% classification error in layer 1 and a 1.51% prediction error in layer 2.

8. Conclusions

A review of an orthopedic bone drilling study with an example of bone layer classification using vibration signal and deep learning methods such as LSTM, CNN, and RNN is presented. This review aimed to provide a state-of-the-art bone drilling study that will be useful for researchers developing a new method or a new research direction. One summary that can be highlighted according to the review is the potential research direction and future work in the development of the medical training system simulation that comprises sensor and robotic technologies, haptic mechanisms, and real-time monitoring systems. Sensor technology is one of the main factors in the simulation of medical training systems for providing user feedback. This paper presented a potential sensor input-based accelerometer or vibration signal to enable user feedback information in conducting bone drilling.

Three DL methods, i.e., LSTM, CNN, and RNN, are selected to describe the benefit of utilizing the vibration signal for bone drilling study, especially for bone layer classification. The following are a few of the multi-classifications of bone layers based on the three applied DL methods:

- With an almost similar DL model development parameters and epoch number, the LSTM shows that it is better than CNN and RNN for vibration data (1D data) of bone layer classification.
- The overall multi-classification accuracy of LSTM, CNN, and RNN, according to the classification report tables, is 0.99, 0.95, and 0.96. This indicates that LSTM is outperformed by CNN and RNN.

- The bone layer classification study based on vibration signals is still developing. This study can be particularly useful in medical procedures in bone drilling, where accurate identification of different bone layers is crucial.
- The future work related to the bone drilling experiment is to generate more datasets and to use other potential methods.

References

1. Torun, Y.; Malatyali, S. Power Analysis of Robotic Medical Drill with Different Control Approaches. *Cumhur. Sci. J.* **2020**, *41*, 527–533. [CrossRef]
2. Tsai, M.-D.; Hsieh, M.-S.; Tsai, C.-H. Bone Drilling Haptic Interaction for Orthopedic Surgical Simulator. *Comput. Biol. Med.* **2007**, *37*, 1709–1718. [CrossRef] [PubMed]
3. Gupta, V.; Pandey, P.M.; Silberschmidt, V.V. Rotary Ultrasonic Bone Drilling: Improved Pullout Strength and Reduced Damage. *Med. Eng. Phys.* **2017**, *41*, 1–8. [CrossRef] [PubMed]
4. Pandey, R.K.; Panda, S.S. Drilling of Bone: A Comprehensive Review. *J. Clin. Orthop. Trauma* **2013**, *4*, 15–30. [CrossRef] [PubMed]
5. Han, Y.; Lv, Q.; Song, Y.; Zhang, Q. Influence of Parameters on Temperature Rise and Chips Morphology in Low-Frequency Vibration-Assisted Bone Drilling. *Med. Eng. Phys.* **2022**, *103*, 103791. [CrossRef] [PubMed]
6. Pourgiv, S.; Mosavar, A.; Jamshidi, N.; Mohammadi, A. Ultrasonic-Assisted Drilling of Cortical and Cancellous Bone in a Comparative Point of View. *Heliyon* **2024**, *10*, e26248. [CrossRef] [PubMed]
7. Singh, G.; Babbar, A.; Jain, V.; Gupta, D. Comparative Statement for Diametric Delamination in Drilling of Cortical Bone with Conventional and Ultrasonic Assisted Drilling Techniques. *J. Orthop.* **2021**, *25*, 53–58. [CrossRef] [PubMed]
8. Agarwal, R.; Gupta, V.; Singh, J. Leveraging Ultrasonic Actuation during Inclined Orthopaedic Bone Drilling: An Experimental and Histological Study. *Appl. Acoust.* **2023**, *211*, 109520. [CrossRef]
9. Esen, H.; Yano, K.; Buss, M. Bone Drilling Medical Training System. In *The Sense of Touch and Its Rendering*; Bicchi, A., Buss, M., Ernst, M.O., Peer, A., Eds.; Springer: Berlin/Heidelberg, Germany, 2008; Volume 45, pp. 245–278. ISBN 978-3-540-79034-1. Springer Tracts in Advanced Robotics.
10. Esen, H.; Yano, K.; Buss, M. A Virtual Environment Medical Training System for Bone Drilling with 3 DOF Force Feedback. In Proceedings of the 2004 IEEE/RSJ International Conference on Intelligent Robots and Systems (IROS) (IEEE Cat. No.04CH37566), Sendai, Japan, 28 September–2 October 2004; IEEE: New York, NY, USA, 2004; Volume 4, pp. 3631–3636.
11. Esen, H.; Yano, K.; Buss, M. A Control Algorithm and Preliminary User Studies for a Bone Drilling Medical Training System. In Proceedings of the 12th IEEE International Workshop on Robot and Human Interactive Communication, 2003. Proceedings. ROMAN 2003, Millbrae, CA, USA, 2 November 2003; IEEE: New York, NY, USA, 2003; pp. 153–158.
12. Syamlan, A.; Fathurachman; Denis, K.; Vander Poorten, E.; Pramujati, B.; Tjahjowidodo, T. Haptic/Virtual Reality Orthopedic Surgical Simulators: A Literature Review. *Virtual Real.* **2022**, *26*, 1795–1825. [CrossRef]
13. Bertollo, N.; Robert, W. Drilling of Bone: Practicality, Limitations and Complications Associated with Surgical Drill-Bits. In *Biomechanics in Applications*; Klika, V., Ed.; InTech: London, UK, 2011; ISBN 978-953-307-969-1.
14. Ginta, T.L.; Ari-Wahjoedi, B. Cutting Force and Temperature Variation in Bone Drilling—A Review. *Adv. Mater. Res.* **2013**, *845*, 934–938. [CrossRef]
15. Lee, J.; Chavez, C.L.; Park, J. Parameters Affecting Mechanical and Thermal Responses in Bone Drilling: A Review. *J. Biomech.* **2018**, *71*, 4–21. [CrossRef] [PubMed]
16. Timon, C.; Keady, C. Thermal Osteonecrosis Caused by Bone Drilling in Orthopedic Surgery: A Literature Review. *Cureus* **2019**, *11*, e5226. [CrossRef]
17. Bohra, A.; Chandrasekaran, M.; Teyi, N. Bone Drilling Investigation and Possible Research: A State of the Art Review. *AIP Conf. Proc.* **2019**, *2128*, 050022.
18. Alam, K.; Mitrofanov, A.V.; Silberschmidt, V.V. Experimental Investigations of Forces and Torque in Conventional and Ultrasonically-Assisted Drilling of Cortical Bone. *Med. Eng. Phys.* **2011**, *33*, 234–239. [CrossRef]
19. Wang, Y.; Cao, M.; Zhao, Y.; Zhou, G.; Liu, W.; Li, D. Experimental Investigations on Microcracks in Vibrational and Conventional Drilling of Cortical Bone. *J. Nanomater.* **2013**, *2013*, 1–5. [CrossRef]
20. Den Dunnen, S.; Mulder, L.; Kerkhoffs, G.M.M.J.; Dankelman, J.; Tuijthof, G.J.M. Waterjet Drilling in Porcine Bone: The Effect of the Nozzle Diameter and Bone Architecture on the Hole Dimensions. *J. Mech. Behav. Biomed. Mater.* **2013**, *27*, 84–93. [CrossRef] [PubMed]

21. Wang, W.; Shi, Y.; Yang, N.; Yuan, X. Experimental Analysis of Drilling Process in Cortical Bone. *Med. Eng. Phys.* **2014**, *36*, 261–266. [CrossRef]

22. Liao, Z.; Axinte, D.A. On Monitoring Chip Formation, Penetration Depth and Cutting Malfunctions in Bone Micro-Drilling via Acoustic Emission. *J. Mater. Process. Technol.* **2016**, *229*, 82–93. [CrossRef]

23. Samarasinghe, C.; Uddin, M.; Bari, S.; Xian, C. Surgical Bone Drilling: A Review. In Proceedings of the Volume 3: Biomedical and Biotechnology Engineering; American Society of Mechanical Engineers, Salt Lake City, UT, USA, 11 November 2019; p. V003T04A054.

24. Jamil, M.; Rafique, S.; Khan, A.M.; Hegab, H.; Mia, M.; Gupta, M.K.; Song, Q. Comprehensive Analysis on Orthopedic Drilling: A State-of-the-Art Review. *Proc. Inst. Mech. Eng.* **2020**, *234*, 537–561. [CrossRef]

25. Torun, Y.; Pazarci, O.; Ozturk, A. Current Approaches to Bone-Drilling Procedures with Orthopedic Drills. *Cyprus J. Med. Sci.* **2020**, *5*, 93–98. [CrossRef]

26. Akhbar, M.F.A.; Sulong, A.W. Surgical Drill Bit Design and Thermomechanical Damage in Bone Drilling: A Review. *Ann. Biomed. Eng.* **2021**, *49*, 29–56. [CrossRef] [PubMed]

27. Jung, O.; Lindner, C.; Pantermehl, S.; Barbeck, M. Heat Development During Medical Drilling: Influencing Factors and Examination Methods—Overview and First Results. *Vivo* **2021**, *35*, 3011–3017. [CrossRef]

28. Islam, M.A.; Kamarrudin, N.S.; Daud, R.; Mohd Noor, S.N.F.; Azmi, A.I.; Razlan, Z.M. A Review of Surgical Bone Drilling and Drill Bit Heat Generation for Implantation. *Metals* **2022**, *12*, 1900. [CrossRef]

29. Chouhan, P.S.; Dwivedi, V. Temperature Distribution in Bone Drilling: A Review. *Int. J. Res. Publ. Rev.* **2023**, *4*, 2616–2618.

30. Zahedi, E.; Khosravian, F.; Wang, W.; Armand, M.; Dargahi, J.; Zadeh, M. Towards Skill Transfer via Learning-Based Guidance in Human-Robot Interaction: An Application to Orthopaedic Surgical Drilling Skill. *J. Intell. Robot. Syst.* **2020**, *98*, 667–678. [CrossRef]

31. Ghasemloonia, A.; Baxandall, S.; Zareinia, K.; Lui, J.T.; Dort, J.C.; Sutherland, G.R.; Chan, S. Evaluation of Haptic Interfaces for Simulation of Drill Vibration in Virtual Temporal Bone Surgery. *Comput. Biol. Med.* **2016**, *78*, 9–17. [CrossRef] [PubMed]

32. Aussedat, C.; Venail, F.; Marx, M.; Boullaud, L.; Bakhos, D. Training in Temporal Bone Drilling. *Eur. Ann. Otorhinolaryngol. Head Neck Dis.* **2022**, *139*, 140–145. [CrossRef] [PubMed]

33. Wulandari, P.; Caesarendra, W.; Lai, D.T.C.; Surindra, M.D.; Królczyk, G.; Tjahjowidodo, T. A Study of Vibration Signal Feature Extraction for Bone Drilling Layer Classification. In Proceedings of the 2023 8th International Conference on Mechanical Engineering and Robotics Research (ICMERR), Krakow, Poland, 8–10 December 2023; IEEE: New York, NY, USA, 2023; pp. 50–54.

34. Wang, R.; Bai, H.; Xia, G.; Zhou, J.; Dai, Y.; Xue, Y. Identification of Milling Status Based on Vibration Signals Using Artificial Intelligence in Robot-Assisted Cervical Laminectomy. *Eur. J. Med. Res.* **2023**, *28*, 203. [CrossRef]

35. Caesarendra, W.; Wulandari, P.; Gatnar, K. Bone Drilling Vibration Signal Classification Using Convolutional Neural Network to Determine Bone Layers. In *Lecture Notes in Electrical Engineering, Proceedings of the 4th International Conference on Electronics, Biomedical Engineering, and Health Informatics, Surabaya, Indonesia, 28 April 2024*; Triwiyanto, T., Rizal, A., Caesarendra, W., Eds.; Springer: Singapore, 2024; Volume 1182, pp. 577–592.

36. Kong, F.; Lee, Y.-S. Analytical Modeling of Ultrasonic Vibration Assisted Drilling of Bones for Medical Surgical Applications. In *Volume 2: Materials; Biomanufacturing; Properties, Applications and Systems; Sustainable Manufacturing, Proceedings of the ASME 2015 International Manufacturing Science and Engineering Conference, Charlotte, NC, USA, 8 June 2015*; American Society of Mechanical Engineers: New York, NY, USA, 2015; p. V002T03A008.

37. Gupta, V.; Pandey, P.M. Experimental Investigation and Statistical Modeling of Temperature Rise in Rotary Ultrasonic Bone Drilling. *Med. Eng. Phys.* **2016**, *38*, 1330–1338. [CrossRef]

38. Pandey, R.K.; Panda, S.S. Genetic Algorithm Based Prediction of an Optimum Parametric Combination for Minimum Thrust Force in Bone Drilling. In *Recent Advances in Information and Communication Technology*; Boonkrong, S., Unger, H., Meesad, P., Eds.; Springer International Publishing: Cham, Switzerland, 2014; Volume 265, pp. 103–112. ISBN 978-3-319-06537-3. Advances in Intelligent Systems and Computing.

39. Pandey, R.K.; Panda, S.S. Optimization of Bone Drilling Parameters Using Grey-Based Fuzzy Algorithm. *Measurement* **2014**, *47*, 386–392. [CrossRef]

40. Staroveski, T.; Brezak, D.; Udiljak, T. Drill Wear Monitoring in Cortical Bone Drilling. *Med. Eng. Phys.* **2015**, *37*, 560–566. [CrossRef]

41. Agarwal, R.; Singh, J.; Gupta, V. Prediction of Temperature Elevation in Rotary Ultrasonic Bone Drilling Using Machine Learning Models: An in-Vitro Experimental Study. *Med. Eng. Phys.* **2022**, *110*, 103869. [CrossRef]

42. Agarwal, R.; Singh, J.; Gupta, V. An Intelligent Approach to Predict Thermal Injuries during Orthopaedic Bone Drilling Using Machine Learning. *J. Braz. Soc. Mech. Sci. Eng.* **2022**, *44*, 320. [CrossRef]

43. Agarwal, R.; Gupta, V.; Singh, J.; Jain, V. Prediction of Surface Roughness and Cutting Force Induced during Rotary Ultrasonic Bone Drilling via Statistical and Machine Learning Algorithms. *Proc. Inst. Mech. Eng. Part C J. Mech. Eng. Sci.* **2022**, *236*, 11123–11135. [CrossRef]

44. Torun, Y.; Öztürk, A. A New Breakthrough Detection Method for Bone Drilling in Robotic Orthopedic Surgery with Closed-Loop Control Approach. *Ann. Biomed. Eng.* **2020**, *48*, 1218–1229. [CrossRef]

45. Song, S.; Cheng, X.; Li, T.; Shi, M.; Zheng, G.; Liu, H. Experimental Study of Bone Drilling by Kirschner Wire. *Med. Eng. Phys.* **2022**, *106*, 103835. [CrossRef] [PubMed]

46. Chen, H.L.; Gundjian, A.A. Specific Heat of Bone. *Med. Biol. Eng.* **1976**, *14*, 548–550. [CrossRef] [PubMed]
47. Cordioli, G.; Majzoub, Z. Heat Generation during Implant Site Preparation: An in Vitro Study. *Int. J. Oral Maxillofac. Implants* **1997**, *12*, 186–193. [PubMed]
48. Hillery, M.T.; Shuaib, I. Temperature Effects in the Drilling of Human and Bovine Bone. *J. Mater. Process. Technol.* **1999**, *92–93*, 302–308. [CrossRef]
49. Lee, J.; Gozen, B.A.; Ozdoganlar, O.B. Modeling and Experimentation of Bone Drilling Forces. *J. Biomech.* **2012**, *45*, 1076–1083. [CrossRef] [PubMed]
50. Pandey, R.K.; Panda, S.S. Optimization of Multiple Quality Characteristics in Bone Drilling Using Grey Relational Analysis. *J. Orthop.* **2015**, *12*, 39–45. [CrossRef] [PubMed]
51. Sarparast, M.; Ghoreishi, M.; Jahangirpoor, T.; Tahmasbi, V. Experimental and Finite Element Investigation of High-Speed Bone Drilling: Evaluation of Force and Temperature. *J. Braz. Soc. Mech. Sci. Eng.* **2020**, *42*, 349. [CrossRef]
52. Alam, K.; Qamar, S.Z.; Iqbal, M.; Piya, S.; Al-Kindi, M.; Qureshi, A.; Al-Ghaithi, A.; Al-Sumri, B.; Silberschmidt, V.V. Effect of Drill Quality on Biological Damage in Bone Drilling. *Sci. Rep.* **2023**, *13*, 6234. [CrossRef] [PubMed]
53. Hochreiter, S.; Schmidhuber, J. Long Short-Term Memory. *Neural Comput.* **1997**, *9*, 1735–1780. [CrossRef] [PubMed]
54. Darmawahyuni, A.; Nurmaini, S.; Sukemi; Caesarendra, W.; Bhayyu, V.; Rachmatullah, M.N. Firdaus Deep Learning with a Recurrent Network Structure in the Sequence Modeling of Imbalanced Data for ECG-Rhythm Classifier. *Algorithms* **2019**, *12*, 118. [CrossRef]
55. Rofii, A.; Soerowirdjo, B.; Irawan, R.; Caesarendra, W. Utilize the Prediction Results from the Neural Network Gate Recurrent Unit (GRU) Model to Optimize Reactive Power Usage in High-Rise Buildings. *Int. J. Robot. Control Syst.* **2024**, *4*, 628–654.
56. Sabique, P.V.; Pasupathy, G.; Ramachandran, S. A Data Driven Recurrent Neural Network Approach for Reproduction of Variable Visuo-Haptic Force Feedback in Surgical Tool Insertion. *Expert Syst. Appl.* **2024**, *238*, 122221. [CrossRef]
57. Lu, S.; Yang, J.; Yang, B.; Li, X.; Yin, Z.; Yin, L.; Zheng, W. Surgical Instrument Posture Estimation and Tracking Based on LSTM. *ICT Express* **2024**, *10*, 465–471. [CrossRef]
58. Caesarendra, W.; Rahmaniar, W.; Mathew, J.; Thien, A. Automated Cobb Angle Measurement for Adolescent Idiopathic Scoliosis Using Convolutional Neural Network. *Diagnostics* **2022**, *12*, 396. [CrossRef]
59. Permana, S.D.H.; Saputra, G.; Arifitama, B.; Yaddarabullah; Caesarendra, W.; Rahim, R. Classification of Bird Sounds as an Early Warning Method of Forest Fires Using Convolutional Neural Network (CNN) Algorithm. *J. King Saud Univ.-Comput. Inf. Sci.* **2022**, *34*, 4345–4357. [CrossRef]
60. Caesarendra, W.; Triwiyanto, T.; Pandiyan, V.; Glowacz, A.; Permana, S.D.H.; Tjahjowidodo, T. A CNN Prediction Method for Belt Grinding Tool Wear in a Polishing Process Utilizing 3-Axes Force and Vibration Data. *Electronics* **2021**, *10*, 1429. [CrossRef]
61. Kiranyaz, S.; Avci, O.; Abdeljaber, O.; Ince, T.; Gabbouj, M.; Inman, D.J. 1D Convolutional Neural Networks and Applications: A Survey. *Mech. Syst. Signal Process.* **2021**, *151*, 107398. [CrossRef]
62. Lipton, Z.C.; Berkowitz, J.; Elkan, C. A Critical Review of Recurrent Neural Networks for Sequence Learning. *arXiv* **2015**, arXiv:1506.00019.
63. Huang, H. Building Your Recurrent Neural Network—Step by Step 2018. Available online: https://github.com/Kulbear/deep-learning-coursera/blob/master/Sequence%20Models/Building%20a%20Recurrent%20Neural%20Network%20-%20Step%20by%20Step%20-%20v2.ipynb (accessed on 3 July 2024).

Control of Floating Body Waves Due to an Airplane Takeoff from a Very Large Floating Airport

Taro Kakinuma [1],* and Yusei Fukuura [2]

1   Graduate School of Science and Engineering, Kagoshima University, Kagoshima 890-0065, Japan
2   Civil Engineering Department, Kumamoto Prefectural Government, Kumamoto 862-8570, Japan;
    yuusei0802@icloud.com
*   Correspondence: taro@oce.kagoshima-u.ac.jp; Tel.: +81-99-285-8467

Abstract: Numerical simulations were generated to investigate the response of a very large floating airport to an airplane takeoff, using the set of nonlinear shallow water equations of velocity potential for water waves interacting with a floating thin plate. We have proposed two methods to reduce persistent airport vibration: reflectance reduction by decreasing the flexural rigidity in airport edge parts and amplification reduction by decreasing the still water depth partially under airport runways. First, when the flexural rigidity is uniformly decreased in an airport edge part, the reflectance of the floating body waves due to a B737 was reduced because of the multiple reflections. However, the wave reflectance for a B747 increased, depending on the conditions. A too-long edge part was not effective in reducing the wave reflectance. Conversely, when the flexural rigidity is linearly decreased in an airport edge part, the wave reflectance was reduced for both airplanes. Second, when the still water depth under an airport runway is partially reduced at the location where floating body waves are amplified, the wave heights of floating body waves tended to decrease as the still water depth in the shallower area decreased.

1. Introduction

A very large floating structure, namely VLFS, can be used for various purposes—an offshore airport, power plant, storage facility, evacuation area, etc. When designing a VLFS with hydroelasticity, the interaction between structure oscillation and fluid motion should be considered. Hydroelastic platforms can also be seen in nature, such as wide ice plates floating at the sea surface [1]. The response of an ice plate to a moving load on it has been investigated [2–4], and these results are useful in VLFS design. In addition, the hydroelasticity of a floating body can be used to obtain sustainable energy by converting water wave energy (e.g., [5,6]).

Regarding the response of a VLFS to long waves including tsunamis, the Boussinesq-type equations for surface waves were solved numerically using a finite difference method (FDM), to examine the relationship between the bending moment and flexural rigidity of a thin plate floating on a progressing solitary wave [7]. The interaction of a thin plate with an incident solitary wave was also investigated by coupling a finite element method (FEM) and boundary element method (BEM) in the vertical two dimensions [8]. This interaction was reproduced in the hydraulic experiments, in which the solitary waves were disintegrated by the floating thin plate, as their nonlinearity was strong [8]. The results—that the wave heights of the incident waves decreased because of the generation of floating body waves—suggest that the wave height of a huge tsunami decreases after propagating through an offshore VLFS. Such tsunami height reduction using a VLFS was discussed based on the numerical simulation of water waves interacting with a floating

thin plate using an FDM [9]. In addition, when density stratification is developed under a hydroelastic structure, a two-dimensional problem in the vertical section was formulated with the framework of a linear potential theory [10], and the surface and internal waves due to a moving load on a VLFS in the vertical two-dimensions were examined with an FDM, considering both the nonlinearity and dispersion of water waves [11]. If a load on a VLFS moves at a speed close to the internal-mode speed, internal waves can be generated in a pycnocline, etc., which will particularly affect nearshore environments.

One of the artificial loads on a VLFS is an airplane moving on a very large floating airport. For example, the drag against an airplane taking off from a floating airport of infinite length was evaluated numerically, using the Fourier transform theory for different flexural rigidities of the airport [12]. Conversely, the transient response of a floating airport subjected to a landing airplane load was studied using an FEM [13]. A BEM was also applied to simulate the response of a hydroelastic plate to a moving weight in the coexistence field of linear waves and a current [14]. Under the combined loads of water waves and an airplane landing or taking off, the drag induced on the airplane by the deformed runway, as well as the time variation of the airport profile, was obtained using both an FEM-scheme-based method and Wilson's θ method [15]. To study the hydroelastic response of floating composite plates subjected to moving loads, a combination of a BEM and moving element method (MEM) was utilized [16]. Moreover, the horizontally two-dimensional responses of a floating airport to the landing and takeoff of an airplane were investigated with the time-domain mode-expansion method [17], and also simulated using an FDM [18].

Thus, an airplane running on a very large floating airport generates floating body waves, that is, floating airport vibration. If airplanes land or take off while floating airport vibration remains, unexpected large floating body waves may occur because of wave superposition. Furthermore, if large floating body vibration remains for a long time because of the wave reflections at the ends of the floating airport, airplane operations will be hindered, accelerating the airport deterioration. To mitigate the hydroelastic vibration of a VLFS under sea wave action, several methods have been proposed: for example, the introduction of floating breakwaters [19], aircushions [20], and member connectors [21]. The reduction of the resonance phenomena due to the presence of a breakwater near a VLFS was also investigated [22].

In the present study, to reduce the persistence of large floating body waves due to an airplane taking off from a very large floating airport, we propose two methods as follows:

1. Reducing the flexural rigidity in a floating airport edge;
2. Reducing the still water depth under a floating airport runway.

We have examined the effectiveness of these methods based on one-dimensional numerical calculations with an FDM. In the computation, an offshore airport was assumed to be a floating thin plate without viscous or structural damping, as well as fluid damping, and was installed in a calm water without wind waves, for simplicity. The governing equations were the nonlinear shallow water equations on velocity potential, which were obtained by reducing the equations derived based on a variational principle for water waves, interacting with horizontal flexural thin plates [23]. In the numerical calculations, the flexural rigidity was given at the location of a thin plate, to express the thin plate covering part of the water area. With this method, it is possible to consider both the reflection and transmission of floating body waves at the ends of the thin plate, which were not discussed for infinitely long and wide airports. The oscillations of floating airports due to a takeoff of two types of jetliners are discussed.

2. Numerical Calculation Method

2.1. Governing Equations

The illustration in Figure 1 is our schematic for a system consisting of a fluid and thin plate. The *x*-axis is the horizontal axis, in the direction of which surface waves propagate. In the present study, an airplane moves in the positive direction of the *x*-axis, so the airport

end at the larger x is called the front end, and the other the rear end, to distinguish between them. Conversely, the z-axis is the vertical axis, the origin of which is located at the surface in the stationary state, and the positive direction of z is vertically upward.
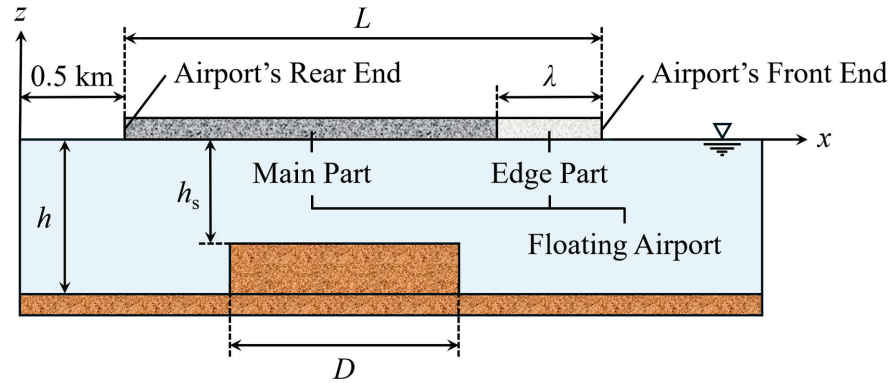
Figure 1. Schematic for a water area with a hydroelastic airport floating at the water surface.

The floating airport is assumed to be a thin plate, where the horizontal length scale is assumed to be much larger than the thickness, so that the differences of curvature between the upper surface, neutral plane, and lower surface of the thin plate are ignored. The energy attenuation inside the airport is not considered, as described above. Therefore, the governing equation of motion for the floating airport is the following classical equation to describe the oscillation of an elastic thin plate as

$$m\delta \frac{\partial^2 \eta}{\partial t^2} + B\nabla^2\,\nabla^2\eta + mg\delta + p_0 - p_1 = 0, \tag{1}$$

where η is the surface displacement, B is the flexural rigidity of the thin plate, and ∇ is the horizontal partial differential operator when also considering the y-axis, perpendicular to the x-axis in the horizontal plane. Although both the plate density m and vertical width δ are assumed to be constant throughout the thin plate, the flexural rigidity B can be distributed along the thin plate. The pressures at the upper and lower faces of the thin plate are p_0 and p_1, respectively.

When the representative values of wave height, wavelength, fluid depth, and density are H, l, d, and ρ, respectively, the dimensionless quantities are

$$\left.\begin{array}{l} x^* = \frac{x}{l}, \quad y^* = \frac{y}{l}, \quad t^* = \frac{\sqrt{gd}}{l}t, \quad \nabla^* = l\nabla, \quad \frac{\partial}{\partial t^*} = \left(\frac{\partial}{\partial t}\right)^* = \frac{l}{\sqrt{gd}}\frac{\partial}{\partial t}, \\[2mm] \eta^* = \frac{\eta}{H}, \quad \delta^* = \frac{\delta}{H}, \quad m^* = \frac{m}{\rho}, \quad B^* = \frac{B}{\rho g l^4}, \quad p_e^* = \frac{p_e}{\rho g d} \end{array}\right\}, \tag{2}$$

where $e = 0$ and 1.

We substitute Equation (2) into Equation (1), and obtain

$$\varepsilon^2\sigma^2 m^*\delta^* \frac{\partial^2 \eta^*}{\partial t^{*2}} + \varepsilon\, B^*\nabla^{*2}\,\nabla^{*2}\eta^* + \varepsilon m^*\delta^* + p_0^* - p_1^* = 0, \tag{3}$$

where $\varepsilon = H/d$ and $\sigma = d/l$ are the representative ratio of wave height to water depth, and that of water depth to wavelength, respectively. In the manner similar to that of [7], the water area is assumed to be relatively shallow, so the orders of the parameters are $O(\varepsilon) = O(\sigma^2) \ll 1$. Thus, the first term on the left-hand side of Equation (3) can be ignored. Without this term, we obtain the plate equation for the dimensional quantities as

$$B\nabla^2\,\nabla^2\eta + mg\delta + p_0 - p_1 = 0. \tag{4}$$

Conversely, a set of water wave equations were derived for multi-layer fluids [24], by applying a variational principle that referenced the functional for water surface waves [25]

based on the functional with rotation [26]. In the derivation, the fluids were inviscid and incompressible, and the fluid motion was irrotational, resulting in the existence of velocity potentials. In the present study, we adopt just the first term of the expanded velocity potential for one-layer cases with one-dimensional wave propagation, i.e., *N* = 1 and *i* = 1 in [23]. Therefore, using Equation (4), the governing equations are reduced to

$$\frac{\partial \eta}{\partial t} + \frac{\partial}{\partial x}\left[(\eta - b)\frac{\partial \varphi}{\partial x}\right] = 0, \tag{5}$$

$$\frac{\partial \varphi}{\partial t} + \frac{1}{2}\left(\frac{\partial \varphi}{\partial x}\right)^2 + g\eta + \frac{B}{\rho}\frac{\partial^2}{\partial x^2}\frac{\partial^2}{\partial x^2}\eta + \frac{p_0}{\rho} = 0, \tag{6}$$

where *b* and *φ* are the seabed position and velocity potential, respectively, and the sea water density ρ is 1030 kg/m^3. The gravitational acceleration *g* is 9.8 m/s^2, and the load of an airplane per unit length is given as p_0. Equation (5) is the equation of continuity, whereas Equation (6) is the nonlinear shallow water equation on velocity potential, that is, the Bernoulli equation at the surface, considering the flexural rigidity of a floating thin plate. Both surface tension and capillary action were ignored, and friction was also ignored for simplicity.

2.2. Numerical Method

The governing equations—Equations (5) and (6)—were solved numerically using a finite difference method with central and forward difference schemes for space and time, respectively. The initial value of velocity potential, $\phi(x, 0 \text{ s})$, was 0.0 m^2/s at any location. In this paper, the values are written without considering significant digits, although the calculations were conducted using 64-bit floating point numbers.

To verify the accuracy of the governing equations, the reproducibility of the response of a floating thin plate was examined by comparing the results of the existing hydraulic experiments [8] and those of numerical computation [18]. In the present study, the grid size Δx was 20 m and the time interval Δt was 0.01 s, after verification.

We performed numerical calculations for the one-dimensional propagations of surface waves generated by two sizes of airplanes with different weights. When the hydroelastic runway is not so wide compared to the spacing of the airplane's left and right landing gears, 1D wave propagation would be dominant.

3. Calculation Conditions

An airport with length *L* of 5 km or 15 km was floating at the sea surface in 0.5 km $\leq x \leq$ 5.5 km or 0.5 km $\leq x \leq$ 15.5 km, respectively, and an airplane ran on the floating airport in the positive direction of the *x*-axis from *x* = 1 km, whereafter it took off. The airport length of 15 km was an unrealistic value which was set to ignore wave reflections at the front end of the airport.

We considered two sizes of airplanes, i.e., B747-400 and B737-800, manufactured by the Boeing Company, which we call B747 and B737, respectively, in this paper. The former is a large airplane, known as "jumbo jet", which is no longer operated for passenger transport because it is not in keeping with the current economic situation, but is used to transport an airplane after renovation. Conversely, the latter is operated on many routes. The weights of a B747 and B737 were set at 397,000 kgs and 79,000 kgs, respectively, referring to the maximum takeoff weights [27]. The unit "kgs" is often used for the mass of airplanes in aviation industry and is the same as "kg" in physics. In the present calculations, the total tire contact distance of both the B747 and B737 was assumed to be 9.8 m, considering the unit width of 1 m.

The running distances of the B747 and B737 were 3 km and 2 km, respectively, on the floating airport. We assumed that the airplane runs at a constant running acceleration on the airport when taking off. We considered the cases in which an airplane plays a rolling start, i.e., the airplane starts running to take off immediately after arriving at the starting

point. Therefore, at the starting time, both the running speed and load of the airplane were assumed to be zero. In addition, we assumed that the point load due to the airplanes is constant while running on the airport. The calculation conditions of the airplanes are listed in Table 1.

Table 1. Calculation conditions of the airplanes. The takeoff speed is the airplane speed when the airplane leaves the airport.

Case	Type	Weight (kgs)	Takeoff Speed (m/s)	Running Acceleration (m/s^2)	Running Distance (km)	Running Time (s)
A	B747-400	397,000	83	1.15	3	72.2
B	B737-800	79,000	78	1.52	2	51.3

Regarding the airports, the values of flexural rigidity B were determined with reference to those obtained during the prototype test using the Mega-Float airport [28]. The flexural rigidity B was given in the area covered by the airport, which made it possible to consider both the reflection and transmission of waves at the ends of the floating airports, as described above.

When the flexural rigidity is uniformly reduced in an edge part of an airport, i.e., in $5.5 \text{ km} - \lambda \leq x \leq 5.5 \text{ km}$, where λ is the length of the edge part, the calculation conditions of the flexural rigidity are described in Table 2. The flexural rigidities of the main and edge parts of the airport are B_{main} and B_{edge}, respectively. When $B_{edge} = B_{main} = 1.0 \times 10^{11}$ Nm, the flexural rigidity is uniform throughout the airport. In the case names, "E" stands for edge related, and "S" and "L" indicate that the edge part is short and long, respectively. The still water depth h is uniformly 50 m.

Table 2. Calculation conditions when the flexural rigidity is uniformly reduced in an edge part of the airports, i.e., in $5.5 \text{ km} - \lambda \leq x \leq 5.5 \text{ km}$. The flexural rigidities of the main and edge parts of the airports are B_{main} and B_{edge}, respectively.

Case	Length of the Edge Part	Flexural Rigidity of the Main Part	Flexural Rigidity of the Edge Part	Airport Length	Still Water Depth
	λ (km)	B_{main} (Nm)	B_{edge} (Nm)	L (km)	h (m)
ES	0.5	10^{11}	10^6–10^{11}	5	50
EL	1				

Conversely, when the flexural rigidity is linearly reduced in an edge part of an airport, i.e., in $5.5 \text{ km} - \lambda \leq x \leq 5.5 \text{ km}$, the calculation conditions of the flexural rigidity are described in Table 3, in which the flexural rigidities of the main part and front end of the airports are B_{main} and B_{end}, respectively. The "C" of the case names represents a continuous reduction of flexural rigidity in an edge part of the airport.

Table 3. Calculation conditions when the flexural rigidity is linearly reduced from B_{main} to B_{end} in an edge part of the airports, i.e., in $5.5 \text{ km} - \lambda \leq x \leq 5.5 \text{ km}$, where the flexural rigidities of the main part and front end of the airports are B_{main} and B_{end}, respectively.

Case	Length of the Edge Part	Flexural Rigidity of the Main Part	Flexural Rigidity at the Front End	Airport Length	Still Water Depth
	λ (km)	B_{main} (Nm)	B_{end} (Nm)	L (km)	h (m)
CS	0.5	10^{11}	10^6–10^{11}	5	50
CL	1				

Moreover, when the still water depth is uniformly reduced at 1.5 km $\leq x \leq$ 1.5 km + *D*, where *D* is the length of the shallower area, the calculation conditions of the still water depth are described in Table 4. The length *L* and flexural rigidity *B* of the airport are 15 km and 1.0×10^{10} Nm, respectively. In the case names, "D" stands for water depth related, and "S" and "L" indicate that the shallower area is short and long, respectively.

Table 4. Calculation conditions when the still water depth is uniformly reduced at 1.5 km $\leq x \leq$ 1.5 km + *D*, at which the still water depth is h_s.

Case	Flexural Rigidity of the airport	Airport Length	Length of the Shallower Area	Still Water Depth in the Shallower Area	Still Water Depth Outside the Shallower Area
	B (Nm)	*L* (km)	*D* (km)	h_s (m)	*h* (m)
DS	10^{10}	15	0.5	10–50	50
DL			2.5		

The case names are expressed by combining two case names described above, i.e., "A" or "B" in Table 1 and one of the names in Tables 2–4. For example, in Case ADS, a B747 takes off from the floating airport with a flexural rigidity of 1.0×10^{10} Nm and a length of 15 km.

4. Reflection Control of Floating Body Waves by Reducing the Flexural Rigidity Uniformly in a Floating Airport Edge

4.1. Floating Body Waves Due to an Airplane Takeoff without Reflection Control

First, we numerically simulated the motion of a finite-length floating airport without any reflection control over a flat seabed. Figure 2 depicts the time variation of the floating airport and water surface profiles when a B747 takes off from the floating airport with a constant flexural rigidity of 1.0×10^{11} Nm in Case AES. In the figure, the black dotted line indicates the location of the airplane running on the floating airport. The calculation conditions in this case are listed in Tables 1 and 2.

Figure 2. Profiles of the floating airport and water surface at every 5 s when a B747 takes off from an airport with a constant flexural rigidity of 1.0×10^{11} Nm in Case AES, the conditions of which are described in Tables 1 and 2. The black dotted line indicates the location of the airplane running on the floating airport.

After the airplane began to take off, both the wave height and wavelength of the floating body waves generated by the running airplane increased as the airplane moved faster. As detailed in [11,18], floating body waves are significantly amplified when the moving speed of a point load on a floating thin plate is roughly close to the phase velocity of the linear shallow water waves, i.e., $\sqrt{gh}$, in shallow water conditions with a still water depth of h. This is due to the resonance similar to that occurring in tsunami generation due to air pressure waves, e.g., [29], based on the Proudman resonance [30]. Such resonance phenomena are also known in other transient waves, e.g., [31–36]. In Case AES, $\sqrt{gh}$ was approximately 22 m/s, which corresponded to the running speed of the airplane at $t \simeq 19$ s. Based on Figure 2, the amplification of the floating body waves is noticeable approximately in the time period of 20 s $\leq t \leq$ 40 s, and in the area of 1.2 km $\leq x \leq$ 1.9 km. It should be noted that in order for waves to grow, the airplane needs to be traveling at a speed roughly close to $\sqrt{gh}$ for a sufficient period of time. During this time period, because of the energy being supplied by the running airplane, a forced wave was generated, and in parallel with this, many free waves also continued to occur so as to satisfy the dispersion relation of floating body waves. When the draft of a floating thin plate is assumed to be zero, the linear dispersion relation of floating body waves is expressed by

$$\theta^2 = \left(\frac{Bk^4}{m} + g \right) k \tanh(kh), \tag{7}$$

where θ and k are the angular frequency and wavenumber of floating body waves, respectively, and B and m are the flexural rigidity and density of the floating body, respectively [18,37]. The generated free waves propagated in front of the airplane because the propagation speeds of the floating body waves were larger than the running speed of the airplane during the time period. When $t > 40$ s, the airplane traveled faster, and the resonance effect was reduced, so the distance over which the amplified wave group, or wave clump, with relatively large wave heights existed was limited.

Thereafter, when $t \geq 70$ s, at the front end of the floating airport, part of the wave energy was reflected and the rest was transmitted in the x-axis direction, causing the continued airport vibration even after the airplane took off. The reflected components of the above-described localized wave group propagated in the negative direction of the x-axis, overlapped with the waves traveling in the positive direction of the x-axis, and then were reflected again at the rear end of the floating airport. Thus, the generated and amplified waves are repeatedly reflected and overlapped, causing complex vibrations at a floating airport. If this continues, it is necessary to take a long time interval between landings and takeoffs, so it disrupts airplane operations at the airport and may also accelerate the deterioration of the structure.

Conversely, Figure 3 depicts the time variation of the floating airport and water surface profiles when a B737 takes off from the same floating airport with a constant flexural rigidity of 1.0×10^{11} Nm in Case BES, where the still water depth is 50 m throughout the water area. The calculation conditions in this case are also listed in Tables 1 and 2.

In Case BES, the phase velocity of linear shallow water waves, i.e., $\sqrt{gh}$, is also approximately 22 m/s, which corresponds to the running speed of the airplane at $t \simeq 15$ s. Based on Figure 3, the amplification of the floating body waves is noticeable approximately in the time period of 20 s $\leq t \leq$ 30 s, and in the area of 1.3 km $\leq x \leq$ 1.7 km. Although the wave height was not as large as in the B747 case because a B737 is lighter than a B747, the wave behavior was similar to that seen when the B747 takes off. Even if a B737 runs when the airport is still vibrating, newly generated waves can overlap the existing floating body waves, forming unexpectedly large waves that could disrupt the airplane's takeoff and landing.

Moreover, Figure 4 depicts the time variation of the floating airport and water surface profiles when a B737 takes off from a floating airport with the same airport length of 5 km but with a lower flexural rigidity of 1.0×10^{10} Nm. As indicated in the figure, the decrease in the flexural rigidity of the floating airport resulted in the larger wave heights

of floating body waves. When the flexural rigidity is decreased, the difference in speed between floating body waves and water waves decreases based on the dispersion relation represented by Equation (7), so the wave transmittance at an airport end increases [18]. However, the floating body waves were highly amplified in the present case and the wave heights of the reflected waves increased.
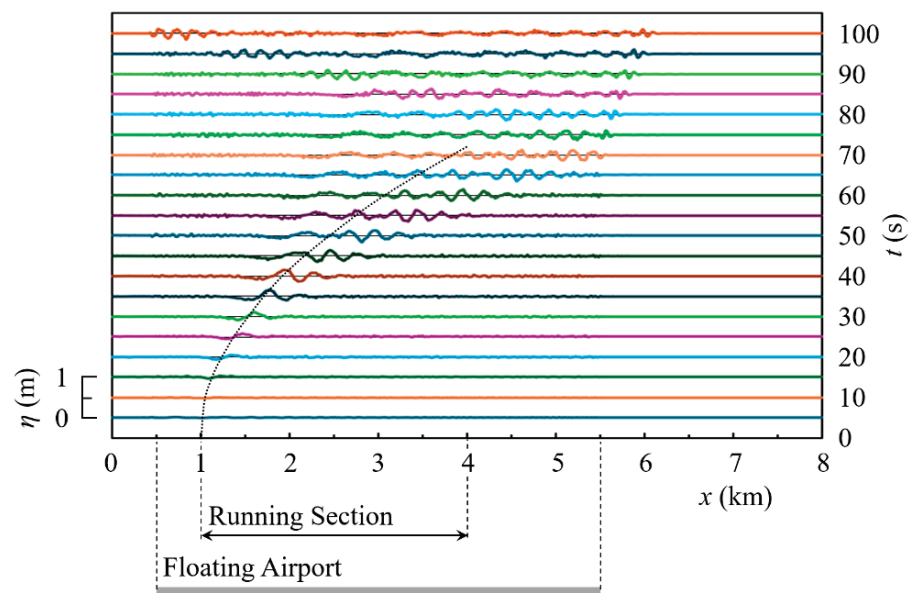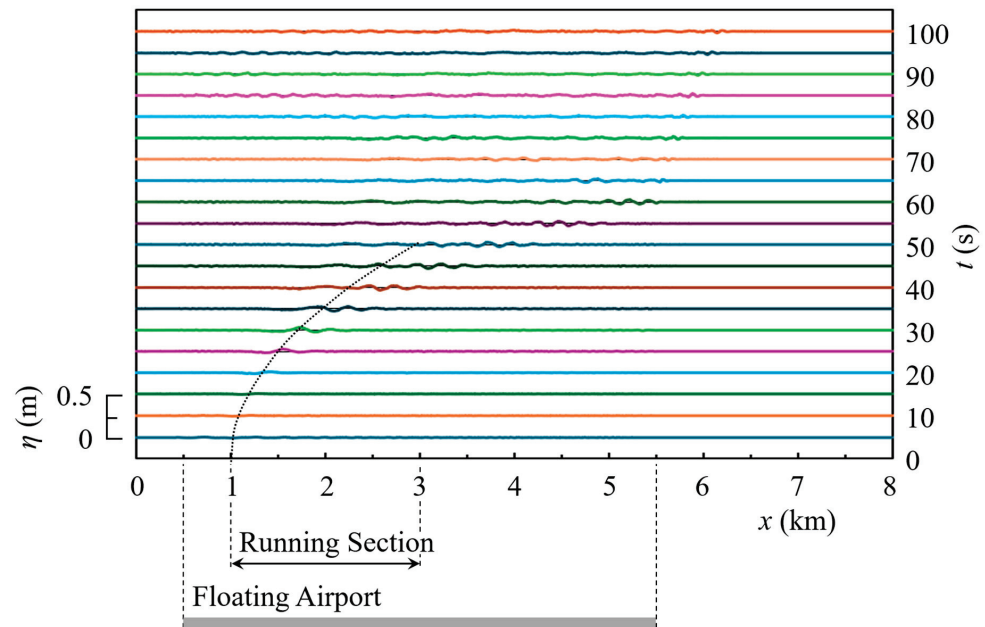

Figure 3. Profiles of the floating airport and water surface at every 5 s when a B737 takes off from an airport with a constant flexural rigidity of 1.0×10^{11} Nm in Case BES, the conditions of which are described in Tables 1 and 2. The black dotted line indicates the location of the airplane running on the floating airport.
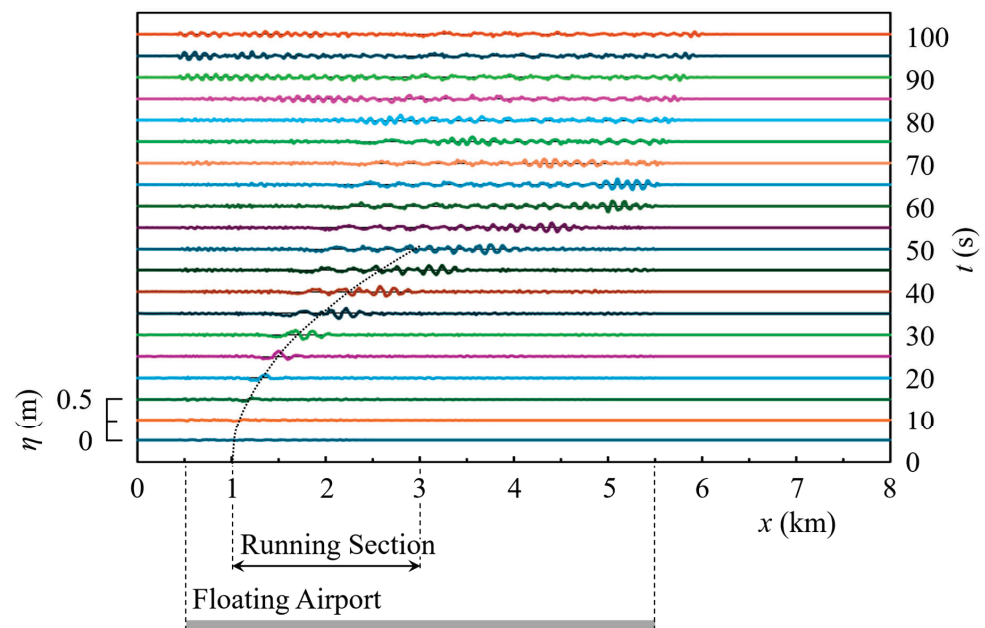
Figure 4. Profiles of the floating airport and water surface at every 5 s when a B737 takes off from an airport with an airport length of 5 km and a constant flexural rigidity of 1.0×10^{10} Nm. The still water depth was 50 m, and the airplane conditions are described in Table 1. The black dotted line indicates the location of the airplane running on the floating airport.

4.2. When Reducing the Flexural Rigidity Uniformly in a Floating Airport Edge

Second, we examine the effectiveness of the reflection reduction techniques under various conditions. One of the methods is to reduce the flexural rigidity in an edge part of an airport uniformly. In Cases AES, AEL, BES, and BEL, the conditions of which are listed in Tables 1 and 2, the flexural rigidity is uniformly reduced to B_{edge} in 5.5 km $- \lambda \leq x \leq 5.5$ km, where λ is the length of the edge part of the airport, and the flexural rigidity of the main part in 0.5 km $\leq x < 5.5$ km $- \lambda$, i.e., B_{main}, is 1.0×10^{11} Nm. Figure 5 depicts the time variation of the floating airport and water surface profiles when the flexural rigidity of the edge part, B_{edge}, is 1.0×10^9 Nm in Case AES. In comparison with Figure 2, the wave heights of the reflected waves are significantly reduced in Figure 5, which is especially clear for the floating body waves at $t \geq 90$ s. This is because the multiple reflections of waves occurred at both the boundary between the main and edge parts and the front end of the airport. At the boundary between the main and edge parts, the difference in flexural rigidity was decreased, so the wave reflectance decreased compared to when the main part is directly connected to the free water surface area, without providing the edge part. Through this boundary, part of the generated floating body waves entered the edge part and were then reflected at the front end of the floating airport, but since the difference in flexural rigidity between the airport and free water surface was also decreased, the wave reflectance at the front end of the airport was also suppressed. Moreover, the multiple reflections at both the part boundary and front end of the airport occurred with a time difference, which also contributed to reducing the wave reflectance.
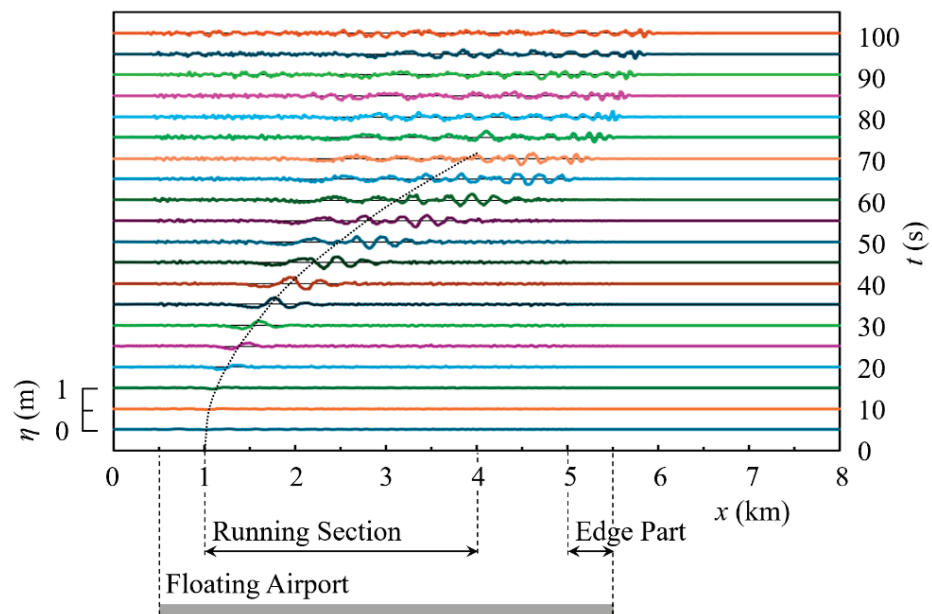
Figure 5. Profiles of the floating airport and water surface at every 5 s when the flexural rigidity of the edge part, B_{edge}, is 1.0×10^9 Nm in Case AES, the conditions of which are described in Tables 1 and 2. The black dotted line indicates the location of the airplane running on the floating airport.

Figure 6 displays the time variation of the floating airport and water surface profiles when the flexural rigidity of the edge part, B_{edge}, is 1.0×10^9 Nm in Case AEL. In this case, the wave heights of the reflected waves were also reduced, as in the case depicted in Figure 5. However, in Figure 6, comparing in detail, the wave heights of the reflected waves are slightly larger than those in Figure 5. The reason is that in Case AEL, the edge part length was longer and the starting location of the edge part was closer to the airplane runway, so still larger waves that were in the deformation process to satisfy the dispersion relation, expressed by Equation (7), were reflected at the boundary between the main and edge parts, leading to the slightly larger wave heights of the reflected waves.
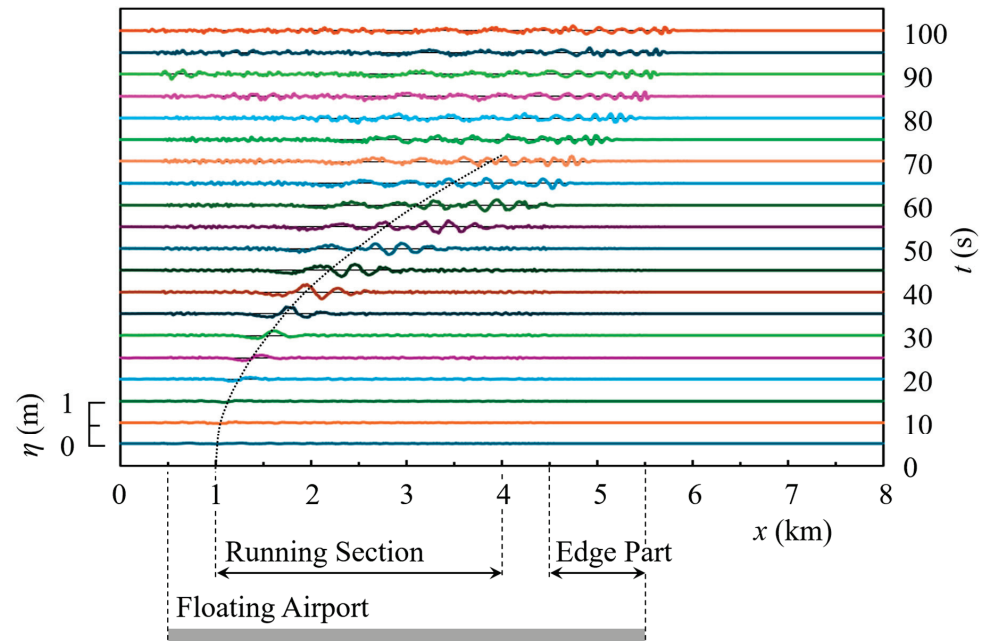
Figure 6. Profiles of the floating airport and water surface at every 5 s when the flexural rigidity of the edge part is 1.0×10^9 Nm in Case AEL, the conditions of which are described in Tables 1 and 2. The black dotted line indicates the location of the airplane running on the floating airport.

The difference in elevation between the maximum and minimum surface displacements—$\eta_{\max}$ and $\eta_{\min}$, respectively—at a location of x is represented as H, i.e.,

$$H = \eta_{\max} - \eta_{\min}. \tag{8}$$

Figure 7 depicts the ratio of the H values between with and without the reflection control, i.e., $R_E = H/H_0$, at $x = 2$ km, where H_0 is the H value when the flexural rigidity in the edge part of the airport, B_{edge}, is not reduced and the flexural rigidity is uniformly 1.0×10^{11} Nm throughout the airport. It should be noted that when using the ratio R_E, reflected waves are not distinguished from newly generated waves, but the H values are compared with and without measures.
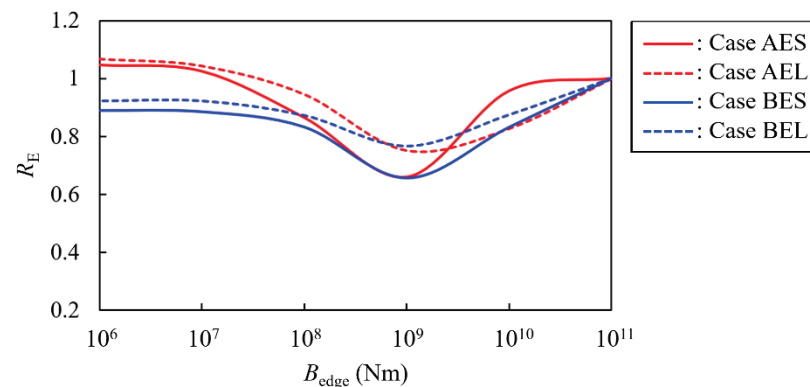
Figure 7. Ratio R_E between the difference in the maximum and minimum surface displacements, H, and that without flexural rigidity reduction in the edge part, H_0, at $x = 2$ km in Cases AES, AEL, BES, and BEL. The calculation conditions are described in Tables 1 and 2.

As indicated in Figure 7, when B_{edge} is close to B_{main}, R_E is not decreased much especially in Case AES. As the difference between B_{edge} and B_{main} increases, R_E decreases more, and when B_{edge} is approximately 1.0×10^9 Nm, R_E is reduced most effectively. However, when B_{edge} is reduced too much, R_E is not decreased much, and R_E

is larger than one when 1.0×10^6 Nm $\leq B_{edge} \leq 1.0 \times 10^{7.2}$ Nm in Case AES and when 1.0×10^6 Nm $\leq B_{edge} \leq 1.0 \times 10^{7.5}$ Nm in Case AEL. Thus, if there is a large difference in flexural rigidity between the main and edge parts of a floating airport, the wave reflectance at this part boundary will be large, which is counterproductive. Therefore, it is necessary to appropriately allow part of the waves to transmit into the edge part and cause above-described multiple reflections at both the part boundary and the end of the airport. It is desirable that the floating body waves are repeatedly reflected and part of the wave energy is trapped in the edge part of the airport, to avoid vibrating the main part of the airport as much as possible.

Conversely, when a B737 takes off in Cases BES and BEL, R_E is reduced even when $B_{edge} \leq 1.0 \times 10^8$ Nm, because the wave height of the generated floating body waves is not large and the wave slope is not steep, resulting in the low reflectance at the boundary between the main and edge parts of the airport. Thus, for recently popular economical airplanes such as a B737, reducing the flexural rigidity of the edge parts uniformly is beneficial to reduce the wave reflectance; however, because there are conditions under which the wave reflectance reaches a minimal value, case studies are required for the design of the edge parts under actual conditions.

5. Reflection Control of Floating Body Waves by Reducing the Flexural Rigidity Linearly in a Floating Airport Edge

In Cases ACS, ACL, BCS, and BCL, the flexural rigidity in the edge part of an airport is linearly reduced, where the conditions are listed in Tables 1 and 3. The flexural rigidity linearly decreases from B_{main} at $x = 5.5$ km $- \lambda$ to B_{end} at $x = 5.5$ km, where λ is the length of the edge part. Figure 8 depicts the ratio R_C between the maximum surface displacements with and without the reflection control, at $x = 3.4$ km, where the ratio R_C is defined as $\eta_{max}/\eta_{max,\,0}$, and η_{max} is the maximum surface displacement at a location of x, whereas $\eta_{max,\,0}$ is η_{max} at the same location when the flexural rigidity in the edge part of the airport, B_{edge}, is not reduced and the flexural rigidity is uniformly 1.0×10^{11} Nm throughout the airport.
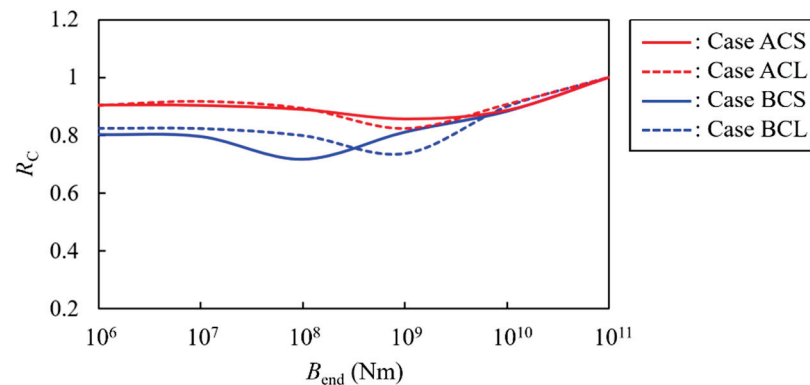
Figure 8. Ratio R_C between the maximum surface displacement η_{max} and that without flexural rigidity reduction, $\eta_{max,\,0}$, at $x = 3.4$ km in Cases ACS, ACL, BCS, and BCL. The calculation conditions are described in Tables 1 and 3.

Figure 8 indicates that in all these cases, there exists a minimal value of R_C, as in the cases in which the flexural rigidity of the edge part is reduced uniformly. It is noteworthy that $R_C < 1.0$ for $B_{end} \leq 1.0 \times 10^{7.5}$ Nm even when a B747 takes off, unlike in Cases AES and AEL. When the flexural rigidity is gradually reduced, wave reflection occurs gradually, so even if the still larger floating body waves enter an edge part before the deformation is completed to satisfy the dispersion relation, i.e., Equation (7), the wave reflectance does not increase significantly. Therefore, the method of reducing the flexural rigidity in edge parts of an airport linearly is effective regardless of the airplane size.

Moreover, for example, in Case ACL, the ratio of the H values, defined in Equation (8), at $x = 4$ km between with and without the reflection control was approximately 0.73 when $0.0 \text{ Nm} \leq B_{\text{end}} \leq 1.0 \times 10^{7.5} \text{ Nm}$. Therefore, if the flexural rigidity at airport ends can be lowered further, this method is more effective and does not have a negative effect even for B747. That is, even when a larger airplane runs on the floating airport, a stable effect can be obtained by gradually and sufficiently lowering the flexural rigidity within the edge part. However, there is a minimal value of the wave reflectance, so to achieve optimal flexural rigidity conditions, such numerical analyses should be performed at the design stage of a floating airport.

Based on Figure 8, in Case BCS, the minimal value of R_{C} is achieved when the flexural rigidity at the front end of the floating airport, B_{end}, is 1.0×10^8 Nm. Figure 9 displays the time variation of the floating airport and water surface profiles under this condition. Compared to Figure 3 without partial reduction of flexural rigidity, the wave heights of the reflected waves are obviously reduced. Even if the flexural rigidity is structurally or economically fixed for most of a floating airport, the wave reflectance can be reduced by modifying the structure or installing accessories to lower the flexural rigidity only near the airport ends, leading to increase in the calmness of the floating airport.
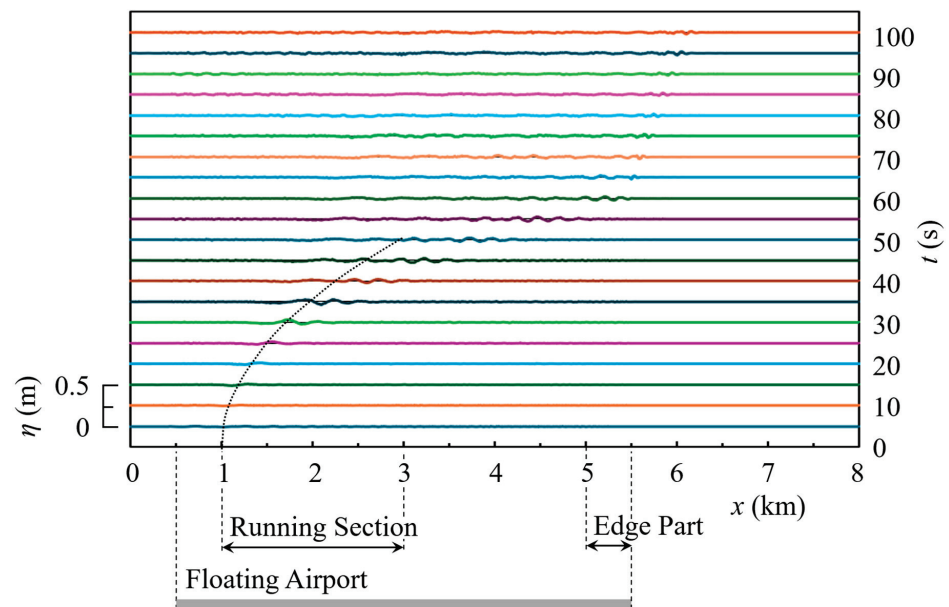
Figure 9. Profiles of the floating airport and water surface at every 5 s when the flexural rigidity at the front end of the airport is 1.0×10^8 Nm in Case BCS, the conditions of which are described in Tables 1 and 3. The black dotted line indicates the location of the airplane running on the floating airport.

Furthermore, in Case BCL, the minimal value of R_{C} is achieved when B_{end} is 1.0×10^9 Nm. Figure 10 depicts the time variation of the floating airport and water surface profiles under this condition. In this case, the wave heights of the reflected waves were reduced almost to the same extent as in the case depicted in Figure 9, and the waveforms showed no significant difference between the two cases.

To understand the difference in the effect of uniformly reducing the flexural rigidity of the edge part versus linearly reducing it, we compare the distributions of H, defined in Equation (8), between these cases. When the H values in Cases AEL and ACL are represented as H_{E} and H_{C}, respectively, Figure 11 depicts the distributions of H_{E} and H_{C}, where $B_{\text{edge}} = 1.0 \times 10^9$ Nm and $B_{\text{end}} = 1.0 \times 10^9$ Nm, respectively. This figure indicates that in Case AEL, the reduction in H_{E} began immediately after the floating body waves entered the edge part, and the energy of the waves reaching the front end of the floating airport decreased. In contrast, in Case ACL, the energy of the waves reaching the airport's front end was larger. Thus, if the flexural rigidity B is decreased spatially suddenly, the

floating wave reflection at the part boundary will be large. In addition, as described in the comparison between Figures 3 and 4, the wave heights of floating body waves increase as B decreases, so the longer distance with lower B will reduce the reflection control effect.
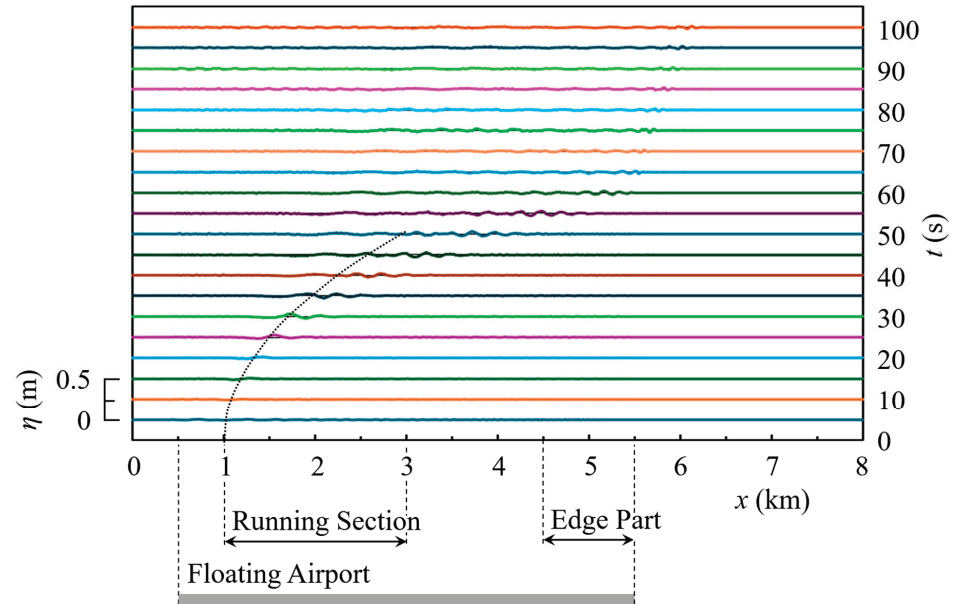
Figure 10. Profiles of the floating airport and water surface at every 5 s when the flexural rigidity at the front end of the airport is 1.0×10^9 Nm in Case BCL, the conditions of which are described in Tables 1 and 3. The black dotted line indicates the location of the airplane running on the floating airport.
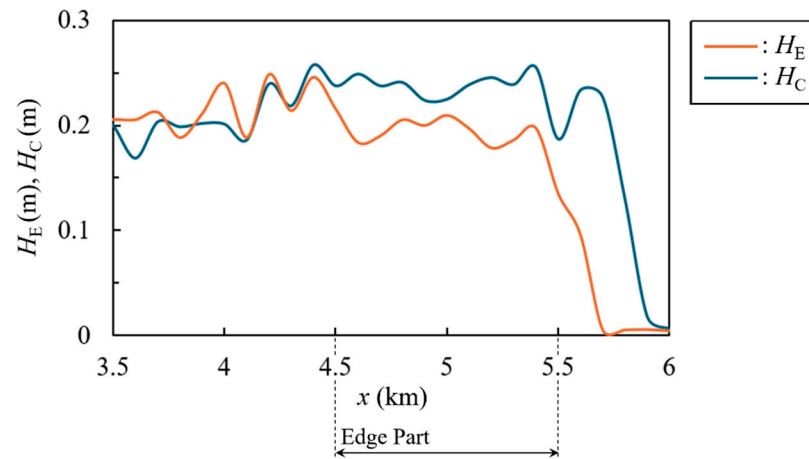
Figure 11. Distributions of the differences between the maximum and minimum surface displacements, H_E and H_C, where $B_{edge} = 1.0 \times 10^9$ Nm in Case AEL and $B_{end} = 1.0 \times 10^9$ Nm in Case ACL, respectively. The calculation conditions are described in Tables 1–3.

When the maximum surface displacements η_{max} at a location of x in Cases AEL and ACL are represented as $\eta_{E, max}$ and $\eta_{C, max}$, respectively, Figure 12 depicts the distributions of $\eta_{E, max}$ and $\eta_{C, max}$, where $B_{edge} = 1.0 \times 10^9$ Nm and $B_{end} = 1.0 \times 10^9$ Nm, respectively. In Case AEL, $\eta_{E, max}$ began to decrease immediately after the floating body waves entered the edge part, similarly to H_E, and gradually decreased in the edge part, although there were ups and downs. Conversely, in Case ACL, $\eta_{C, max}$ increased once immediately after the waves entered the edge part, and then the average height was maintained inside the edge part, which indicates that part of the wave energy was trapped within the edge part. In both cases, the distributions express vibration modes with nodes and antinodes, and

future work is required to investigate the mechanism of mode generation through analyses considering the wave dispersion.
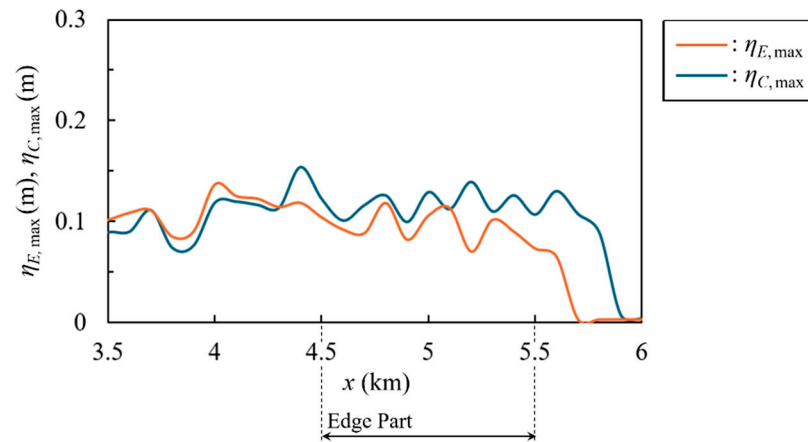
Figure 12. Distributions of the maximum surface displacements $\eta_{E,\,max}$ and $\eta_{C,\,max}$, where B_{edge} = 1.0×10^9 Nm in Case AEL and $B_{end} = 1.0 \times 10^9$ Nm in Case ACL, respectively. The calculation conditions are described in Tables 1–3.

6. Wave Height Control of Floating Body Waves by Partially Reducing the Still Water Depth under a Floating Airport Runway

As described above, resonance occurs when the running speed of an airplane on a floating airport is close to the phase velocity of water waves. In this section, we propose a method to reduce the amplification of floating body waves by decreasing the still water depth under an airport runway over a certain distance to change the wave speeds. In order not to consider both the reflection and transmission of floating body waves at the front end of a floating airport, the airport length is set to be 15 km. Figure 13 displays the time variation of the floating airport and water surface profiles when the still water depth is uniformly 50 m in Cases ADS and ADL.

Figure 13. Profiles of the floating airport and water surface at every 5 s when the still water depth is uniformly 50 m throughout the water area in Cases ADS and ADL, the conditions of which are described in Tables 1 and 4. The black dotted line indicates the location of the airplane running on the floating airport.

Conversely, Figure 14 depicts the time variation of the floating airport and water surface profiles when the still water depth is partially reduced to 10 m at 1.5 km $\leq x \leq$ 2 km in Case ADS. In comparison with Figure 13, the wave amplification due to the resonance is suppressed in Figure 14, and the wave height of the floating body waves propagating in the positive direction of the *x*-axis is reduced. As discussed in Section 4.1, the airplane's running speed and the water wave propagation speed become closer at $t \simeq 19$ s, and larger waves are generated at 20 s $\leq t \leq$ 40 s, i.e., at 1.2 km $\leq x \leq$ 1.9 km, when the still water depth is uniformly 50 m throughout the water area. In the case depicted in Figure 14, by reducing the still water depth where the airplane's speed gradually increased, the difference between the airplane and water wave speeds increased, so the distance at which the resonance effect was larger decreased, resulting in the wave height reduction.

Figure 14. Profiles of the floating airport and water surface at every 5 s when the still water depth in the shallower area is 10 m in Case ADS, the conditions of which are described in Tables 1 and 4. The black dotted line indicates the location of the airplane running on the floating airport.

Regarding changing still water depth, there was concern about wave reflection due to the abrupt change in still water depth. At 0.5 km $\leq x \leq$ 1.5 km in Figure 14, it is certainly observed that floating body waves are traveling back and forth between the rear end of the floating airport and the starting point of the shallower water area, repeating reflections at these two locations, but the wave heights of these floating body waves are not significant.

Figure 15 depicts the time variation of the floating airport and water surface profiles when the still water depth is partially reduced to 10 m at 1.5 km $\leq x \leq$ 4 km in Case ADL. In this case, the wave heights of the floating body waves were reduced more remarkably, decreasing not only the wave heights of the localized wave group with larger wave heights, but also those of the waves following them. As previously described, in order for waves to be amplified, it is necessary that the distance at which the resonance effect is large is sufficient, so making the shallower area longer leads to a more effective reduction in wave height. In addition, the wavelengths in the shallower area are shorter than the corresponding results indicated in Figures 13 and 14. This is because, based on the dispersion relation expressed by Equation (7), as the still water depth is decreased, the wave propagation speed increases and the wavelength decreases [18].
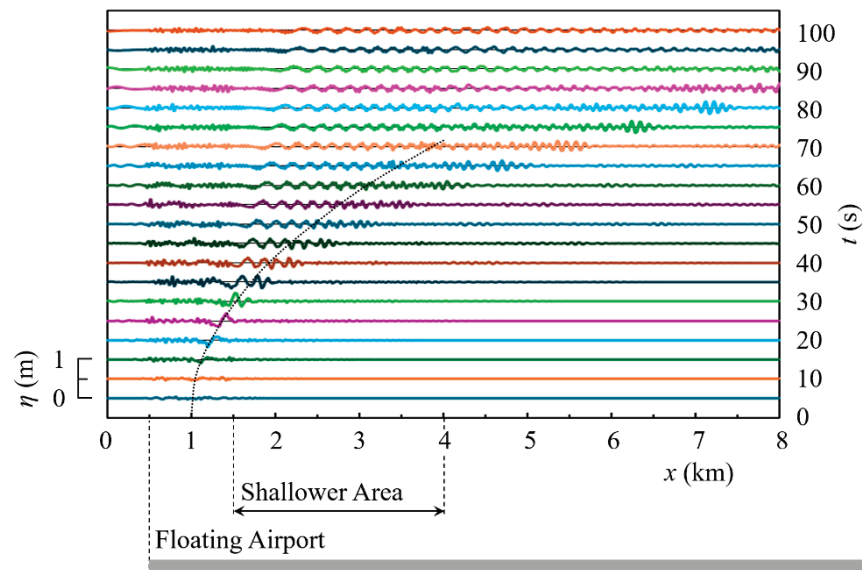
Figure 15. Profiles of the floating airport and water surface at every 5 s when the still water depth in the shallower area is 10 m in Case ADL, the conditions of which are described in Tables 1 and 4. The black dotted line indicates the location of the airplane running on the floating airport.

Moreover, regarding the takeoff of a B737, Figure 16 depicts the time variation of the floating airport and water surface profiles when the still water depth is uniformly 50 m in Cases BDS and BDL. Conversely, when the still water depth is partially reduced to 10 m at 1.5 km $\leq x \leq$ 2 km in Case BDS and at 1.5 km $\leq x \leq$ 4 km in Case BDL, the results are displayed in Figures 17 and 18, respectively. A similar effect was obtained with B737s as with B747s. Although it is better to build a floating airport in a place where the still water depth is not too deep, if it is built in a deeper place, the amplification of floating body waves can be suppressed by reducing the still water depth under the runways using a natural seabed topography, artificial reefs, etc. Furthermore, in the case of landing, the running speed of an airplane gradually slows after its touchdown, so the amplification effect increases as the airplane approaches a stop position when the still water depth is, for example, 50 m [18]. Therefore, it would be favorable for airport operations if the airplane stops at a place where the still water depth is reduced.

Figure 19 depicts the ratio of the H values between with and without the partial reduction in the still water depth, i.e., $R_D = H/H_0$, at $x = 4$ km, where H is evaluated by Equation (8) and H_0 is the H value when the still water depth is uniformly 50 m throughout the water area. This figure indicates that as the still water depth in the shallower area is decreased, the ratio R_D tends to decrease. In both Cases ADL and BDL with a longer shallower area, R_D decreases approximately linearly with decreasing the still water depth, where the gradient R_D/h_s is approximately 0.016 m^{-1}. Conversely, in Cases ADS and BDS, when $h_s < 30$ m, the reduction rate of R_D with respect to the decrease in h_s decreases, from which it can be concluded that when the shallower area is short, reducing h_s beyond a certain level does not significantly increase the wave height reduction effect. In summary, adjusting the still water depth under airport runways over a sufficient distance so that the speeds of airplanes and water waves do not come close to each other, as well as gradually changing the flexural rigidity in the edge parts of the airport, will help to reduce the floating body waves excited by airplanes.
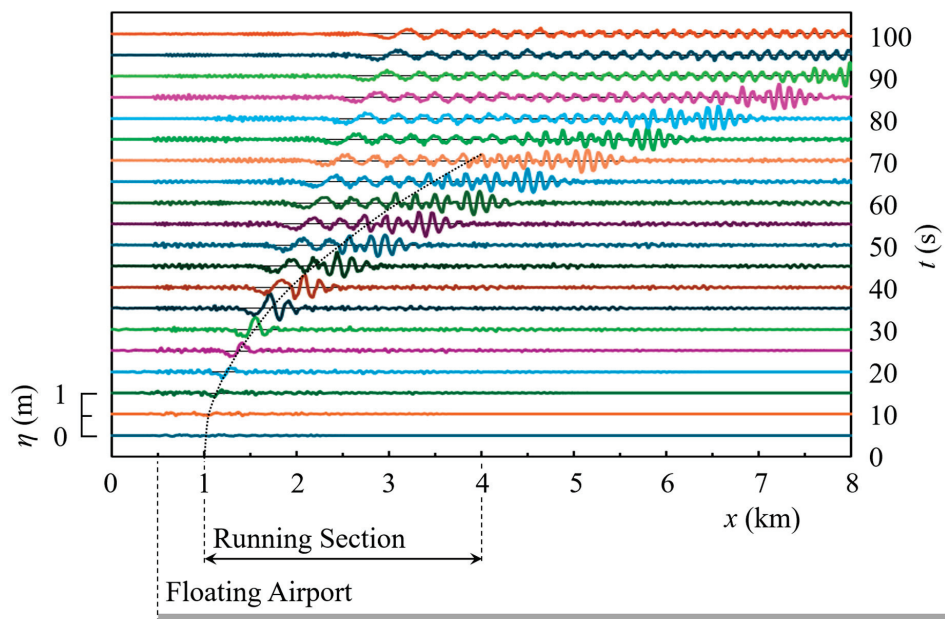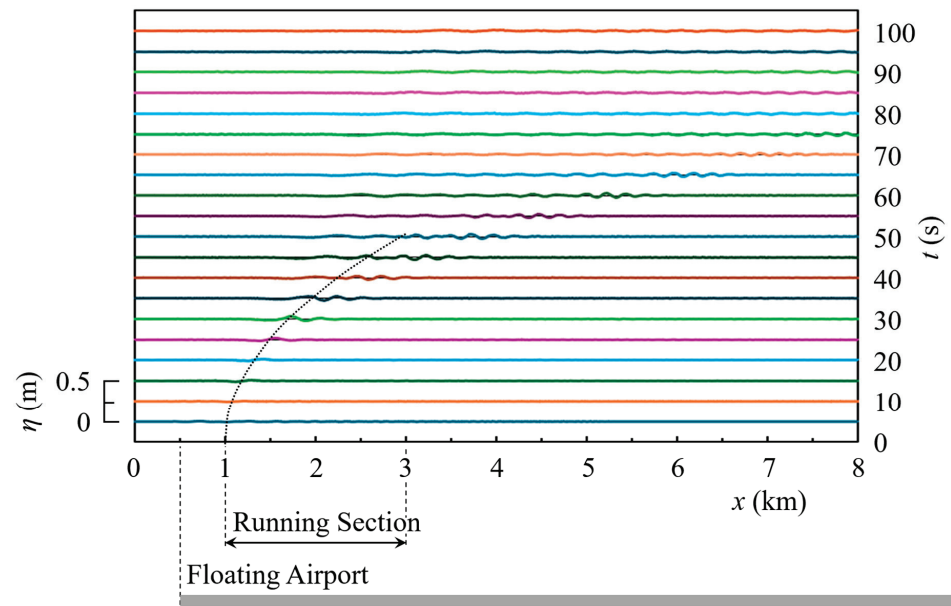
Figure 16. Profiles of the floating airport and water surface at every 5 s when the still water depth is uniformly 50 m throughout the water area in Cases BDS and BDL, the conditions of which are described in Tables 1 and 4. The black dotted line indicates the location of the airplane running on the floating airport.
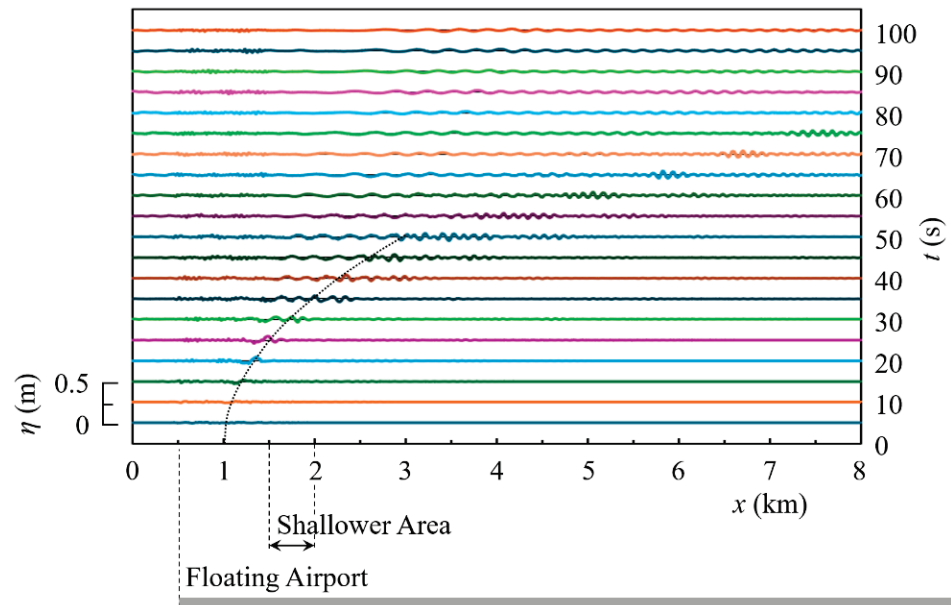
Figure 17. Profiles of the floating airport and water surface at every 5 s when the still water depth in the shallower area is 10 m in Case BDS, the conditions of which are described in Tables 1 and 4. The black dotted line indicates the location of the airplane running on the floating airport.
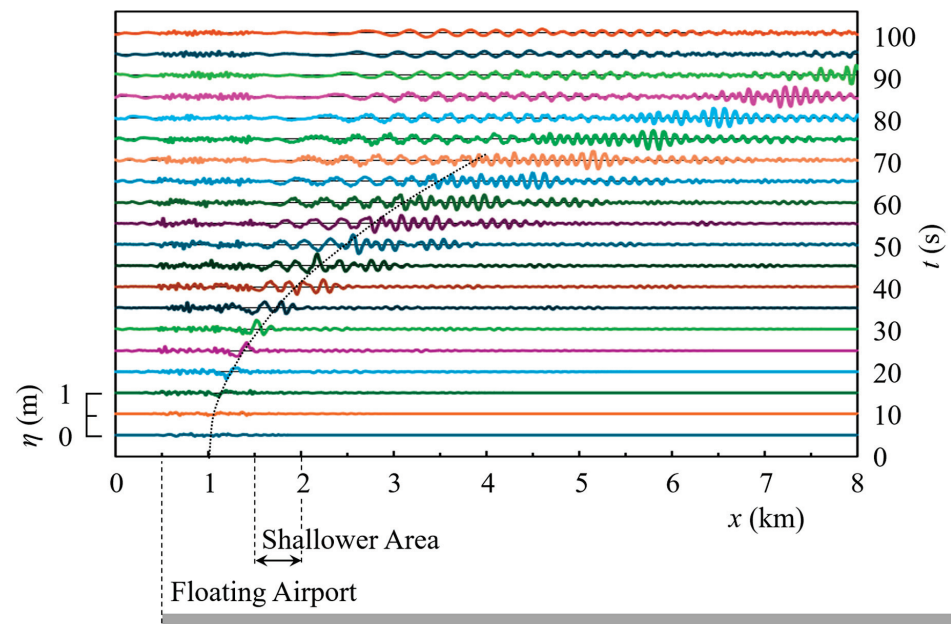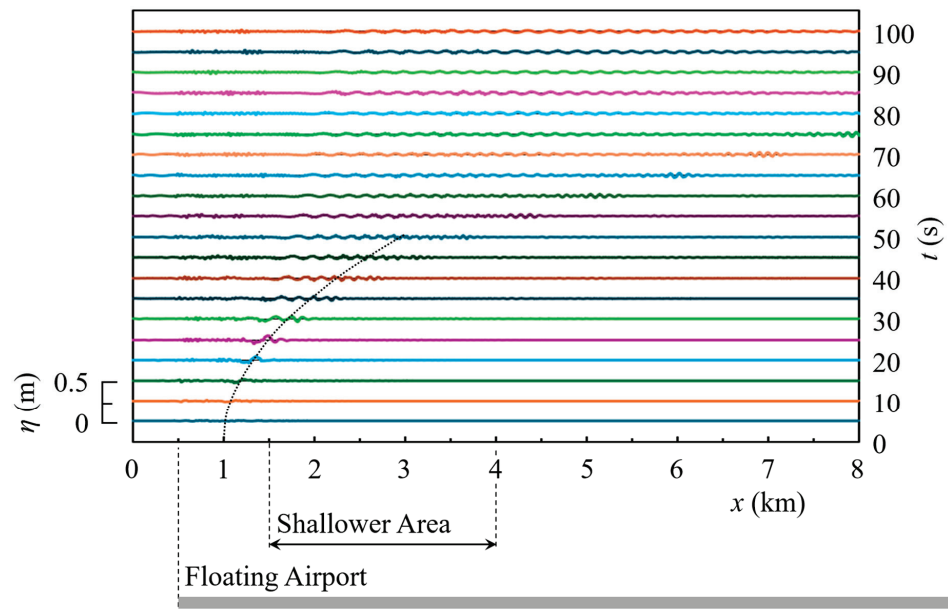
Figure 18. Profiles of the floating airport and water surface at every 5 s when the still water depth in the shallower area is 10 m in Case BDL, the conditions of which are described in Tables 1 and 4. The black dotted line indicates the location of the airplane running on the floating airport.
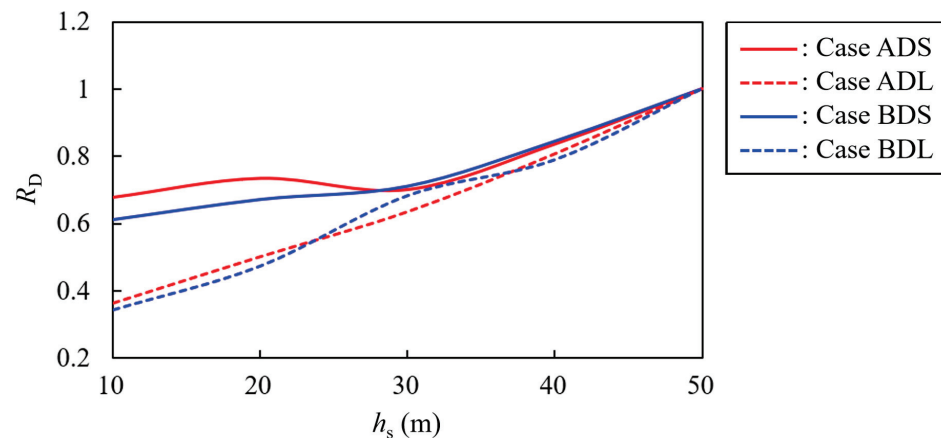
Figure 19. Ratio R_D between the difference in the maximum and minimum surface displacements, H, and that without partial reduction in still water depth, H_0, at $x = 4$ km in Cases ADS, ADL, BDS, and BDL. The calculation conditions are described in Tables 1 and 4.

7. Conclusions

To design a large floating structure that exhibit hydroelastic behavior at the water surface, it is necessary to understand the interaction between the vibration of the floating structure and the motion of the fluid. In this study, the numerical simulations were generated to investigate the response of a very large floating airport to an airplane takeoff, using the set of nonlinear shallow water equations of velocity potential for water waves interacting with a floating thin plate.

We simulated the excitation of floating body waves due to an airplane takeoff. When the running speed of the airplane approached the phase velocity of the water waves, resonance occurred, and a forced wave was excited, generating free waves to satisfy the dispersion relation. As the airplane speed increased more, the resonance effect decreased and a localized wave group with larger wave heights was formed. Thereafter, these floating body waves were reflected and transmitted at the front end of the floating airport, and the vibration of the airport remained even after the airplane took off. Therefore, to reduce such prolonged vibrations, which may disrupt airport operations, we have proposed

two methods to reduce remaining floating body waves caused by an airplane takeoff: reflectance reduction by decreasing the flexural rigidity in the edge parts of an airport and amplification reduction by decreasing the still water depth partially under airport runways.

First, when the flexural rigidity is uniformly decreased in an edge part of the floating airports, the reflectance of the floating body waves due to the B737 was reduced because of the multiple reflections. However, the reflectance of the floating body waves caused by the B747 increased, depending on the conditions. In both cases of the B737 and B747, when the edge part is too long, the still larger waves reached the edge part, so the wave reflectance was not reduced much. There were conditions under which the wave reflectance reached a minimal value, so numerical simulations such as those generated here will be required for optimal design of airport edge parts.

Moreover, when the flexural rigidity is linearly decreased in an edge part of the floating airports, although a minimal value appeared in the wave reflectance, the wave reflectance decreased, never increased under the conditions investigated.

Second, when the still water depth under the airport runways is partially decreased in the section where larger floating body waves are generated, the wave heights of floating body waves tended to decrease as the still water depth in the shallower area decreased. This is because the water wave speed decreased in the shallower area, and the distance with larger resonance effect was shortened, thereby suppressing the amplification of floating body waves.

In conclusion, considering the still water depth under the runways of a floating airport to reduce the distance at which airplane speeds approach water wave speeds, and further gradually decreasing the flexural rigidity in the edge parts of the airport are effective in reducing the persistent airport vibration due to airplane movements. In the future, the behavior of airports with significant frequency dispersion, particularly in a deeper sea, and the vibration modes generated at airports should be investigated with higher-order effects of the velocity potential to consider the dispersion of floating body waves due to both running airplanes and incident ocean waves, including swells. Furthermore, when mooring lines are installed near the ends of a floating airport, they may affect the vibration of the airport ends, changing the reflectance of the floating body waves. It will also be necessary to examine such effects of mooring items, in determining the appropriate mooring methods and locations.

References

1. Squire, V.A.; Dugan, J.P.; Wadhams, P.; Rottier, P.J.; Liu, A.K. Of ocean waves and sea ice. *Annu. Rev. Fluid Mech.* **1995**, *27*, 115–168. [CrossRef]
2. Pӑrӑu, E.; Dias, F. Nonlinear effects in the response of a floating ice plate to a moving load. *J. Fluid Mech.* **2002**, *460*, 281–305. [CrossRef]
3. Dinvay, E.; Kalisch, H.; Pӑrӑu, E. Fully dispersive models for moving loads on ice sheets. *J. Fluid Mech.* **2019**, *876*, 122–149. [CrossRef]

4. Țugulan, C.; Trichtchenko, O.; Părău, E. Three-dimensional waves under ice computed with novel preconditioning methods. *J. Comput. Phys.* **2022**, *459*, 111129. [CrossRef]

5. Renzi, E.; Michele, S.; Zheng, S.; Jin, S.; Greaves, D. Niche applications and flexible devices for wave energy conversion: A review. *Energies* **2021**, *14*, 6537. [CrossRef]

6. Michele, S.; Zheng, S.; Greaves, D. Wave energy extraction from a floating flexible circular plate. *Ocean Eng.* **2022**, *245*, 110275. [CrossRef]

7. Takagi, K. Interaction between solitary wave and floating elastic plate. *J. Waterw. Port Coast. Ocean Eng.* **1997**, *123*, 57–62. [CrossRef]

8. Sakai, S.; Liu, X.; Sasamoto, M.; Kagesa, T. Experimental and numerical study on the hydroelastic behavior of VLFS under tsunami. In *Hydroelasticity in Marine Technology*; Kashiwagi, M., Koterayama, W., Ohkusu, M., Eds.; Yomei Printing Cooperative Society: Fukuoka, Japan, 1998; pp. 385–392. ISBN 4-87780-001-8.

9. Kakinuma, T.; Ochi, N. Tsunami-height reduction using a very large floating structure. In *Mathematical Analysis of Continuum Mechanics and Industrial Applications III, CoMFoS 2018, Mathematics for Industry 34*; Itou, H., Hirano, S., Kimura, M., Kovtunenko, V.A., Khludnev, A.M., Eds.; Springer: Singapore, 2020; pp. 193–202. [CrossRef]

10. Xu, F.; Lu, D.Q. Wave scattering by a thin elastic plate floating on a two-layer fluid. *Int. J. Eng. Sci.* **2010**, *48*, 809–819. [CrossRef]

11. Kakinuma, T.; Yamashita, K.; Nakayama, K. Surface and internal waves due to a moving load on a very large floating structure. *J. Appl. Math.* **2012**, *2012*, 830530. [CrossRef]

12. Kim, J.W.; Webster, W.C. The drag on an airplane taking off from a floating runway. *J. Mar. Sci. Technol.* **1998**, *3*, 76–81. [CrossRef]

13. Watanabe, E.; Utsunomiya, T.; Tanigaki, S. A transient response analysis of a very large floating structure by finite element method. *Struct. Eng. Earthq. Eng. JSCE* **1998**, *15*, 155s–163s. [CrossRef]

14. Hermans, A.J. A boundary element method for the interaction of free-surface waves with a very large floating flexible platform. *J. Fluids Struct.* **2000**, *14*, 943–956. [CrossRef]

15. Endo, H. The behavior of a VLFS and an airplane during takeoff/landing run in wave condition. *Mar. Struct.* **2000**, *13*, 477–491. [CrossRef]

16. Nguyen, X.V.; Luong, V.H.; Cao, T.N.T.; Lieu, X.Q.; Nguyen, T.B. Hydroelastic responses of floating composite plates under moving loads using a hybrid moving element-boundary element method. *Adv. Struct. Eng.* **2020**, *23*, 2759–2775. [CrossRef]

17. Kashiwagi, M. Transient responses of a VLFS during landing and take-off of an airplane. *J. Mar. Sci. Technol.* **2004**, *9*, 14–23. [CrossRef]

18. Kakinuma, T.; Hisada, M. A numerical study on the response of a very large floating airport to airplane movement. *Eng* **2023**, *4*, 1236–1264. [CrossRef]

19. Hong, D.C.; Hong, S.Y.; Hong, S.W. Reduction of hydroelastic responses of a very-long floating structure by a floating oscillating-water-column breakwater system. *Ocean Eng.* **2006**, *33*, 610–634. [CrossRef]

20. van Kessel, J.L.F.; Pinkster, J.A. The effect of aircushion division on the motions of large floating structures. In Proceedings of the ASME 2007 26th International Conference on Offshore Mechanics and Arctic Engineering, San Diego, CA, USA, 10–15 June 2007; Volume 4, pp. 677–686. [CrossRef]

21. Gao, R.P.; Wang, C.M.; Koh, C.G. Reducing hydroelastic response of pontoon-type very large floating structures using flexible connector and gill cells. *Eng. Struct.* **2013**, *52*, 372–383. [CrossRef]

22. Ohmatsu, S. Numerical calculation method for the hydroelastic response of a pontoon-type very large floating structure close to a breakwater. *J. Mar. Sci. Technol.* **2000**, *5*, 147–160. [CrossRef]

23. Kakinuma, T. Nonlinear interaction of surface and internal waves with very large floating or submerged structures. In *Fluid Structure Interaction II*; Chakrabarti, S.K., Brebbia, C.A., Almorza, D., Gonzalez-Palma, R., Eds.; WIT Press: Ashurst, Southampton, UK, 2003; pp. 117–126. Available online: https://www.witpress.com/elibrary/wit-transactions-on-the-built-environment/71/2312 (accessed on 8 June 2024).

24. Kakinuma, T. A set of fully nonlinear equations for surface and internal gravity waves. In *Coastal Engineering V*; Brebbia, C.A., Ed.; WIT Press: Ashurst, Southampton, UK, 2001; pp. 225–234. Available online: https://www.witpress.com/elibrary/wit-transactions-on-the-built-environment/58/3473 (accessed on 8 June 2024).

25. Isobe, M. Time-dependent mild-slope equations for random waves. In *Coastal Engineering 1994*; Edge, B.L., Ed.; ASCE: New York City, NY, USA, 1995; pp. 285–299. [CrossRef]

26. Luke, J.C. A variational principle for a fluid with a free surface. *J. Fluid Mech.* **1967**, *27*, 395–397. [CrossRef]

27. Boeing Japan Homepage. Available online: https://www.boeing.jp/ (accessed on 8 June 2024).

28. Andrianov, A.O.I. Hydroelastic Analysis of Very Large Floating Structures. Doctoral Dissertation, Electrical Engineering, Mathematics and Computer Science, TU Delft, Delft, The Netherlands, 2005. Available online: https://resolver.tudelft.nl/uuid:85cef785-c17c-41d7-9a58-6a183c468523.

29. Kakinuma, T. Tsunamis generated and amplified by atmospheric pressure waves due to an eruption over seabed topography. *Geosciences* **2022**, *12*, 232. [CrossRef]

30. Proudman, J. The effects on the sea of changes in atmospheric pressure. *Geophys. Suppl. Mon. Not. R. Astron. Soc.* **1929**, *2*, 197–209. [CrossRef]

31. Whitham, G.B. *Linear and Nonlinear Waves*; John Wiley & Sons, Inc.: Hoboken, NJ, USA, 1974; pp. 511–532. [CrossRef]

32. Wu, T. Generation of upstream advancing solitons by moving disturbances. *J. Fluid Mech.* **1987**, *184*, 75–99. [CrossRef]

33. Lee, S.; Yates, G.; Wu, T. Experiments and analyses of upstream-advancing solitary waves generated by moving disturbances. *J. Fluid Mech.* **1989**, *199*, 569–593. [CrossRef]
34. Kakinuma, T.; Akiyama, M. Numerical analysis of tsunami generation due to seabed deformation. In *Coastal Engineering 2006*; Smith, J.M., Ed.; World Scientific Publishing Co., Pte. Ltd.: Singapore, 2007; pp. 1490–1502. [CrossRef]
35. Dalphin, J.; Barros, R. Optimal shape of an underwater moving bottom generating surface waves ruled by a forced Korteweg-de Vries equation. *J. Optim. Theory Appl.* **2019**, *180*, 574–607. [CrossRef]
36. Michele, S.; Renzi, E.; Borthwick, A.; Whittaker, C.; Raby, A. Weakly nonlinear theory for dispersive waves generated by moving seabed deformation. *J. Fluid Mech.* **2022**, *937*, A8. [CrossRef]
37. Tsubogo, T. A basic investigation on deflection wave propagation and strength of very large floating structures (The 2nd Report). *J. Soc. Nav. Archit. Jpn.* **1997**, *182*, 381–390. [CrossRef]

Development of a Methodology for Railway Bolster Beam Design Enhancement Using Topological Optimization and Manufacturing Constraints

Alessio Cascino *, Enrico Meli and Andrea Rindi

Department of Industrial Engineering (DIEF), University of Florence, Via Santa Marta, 3, 50139 Florence, Italy; enrico.meli@unifi.it (E.M.); andrea.rindi@unifi.it (A.R.)
* Correspondence: alessio.cascino@unifi.it

Abstract: Rolling stock manufacturers are finding innovative structural solutions to improve the quality and reliability of railway vehicle components. Structural optimization processes represent an effective strategy for reducing manufacturing costs, resulting in geometries that are easier to design and produce combined with innovative materials. In this framework, the present paper proposes the development of a design methodology to innovate a railway bolster beam using topological optimization techniques, assessing the effect of different manufacturing constraints oriented to the casting process. A comprehensive numerical testing campaign was conducted to establish an effective testing procedure. Two different designs were obtained and compared, statically and dynamically, evaluating the difference in terms of mass, mechanical performance and manufacturability. Reductions in stress values up to 70% were observed, along with an 8% increase in the first natural frequency of the component, leading to beneficial effects in terms of stiffness. The methodology shows encouraging results to streamline the design of complex casting components, moving to a new generation of structural railway components.

Keywords: railway vehicle; structural optimization; topological optimization; casting design

1. Introduction

Recently, the demand for efficient and sustainable transportation has continued to grow, and the railway industry can meet this request. The imperative is to ensure the major reliability of its components and minimize the downtime of railway vehicles. For this reason, advancements in manufacturing techniques offer a promising path toward achieving these objectives, opening the door to significant improvements in the design, manufacturing and maintenance of railway components. Casting technologies can play a main role in these improvements, offering versatility, efficiency and cost-effectiveness. Furthermore, casting can be employed for both prototype development and high-volume production, making it a versatile choice for manufacturers seeking flexibility in their operations. It offers excellent material properties and performance characteristics, ensuring the final products meet demanding industry standards and specifications. With reference to the railway sector, main vehicle components like bogie frames and bolster beams have historically been made up with structural steel and complex welding techniques. This allows box-shaped geometries to be easily created to perform correctly under vehicle running conditions. However, all of this comes at a cost in terms of reliability and maintenance times due to the presence of welding, which is the most critical factor for railway components. Furthermore, unlike the casting process, this production method requires significantly longer production times and a limited reproducibility of solutions. In this context, transitioning from components designed for welding to ones designed for casting could be very complex, requiring a wide series of iterations to arrive at a final design. With this objective, structural optimization processes represent an efficient solution to significantly

accelerate the process. In order to create a casting piece, it is essential to consider all the geometric characteristics the piece must possess, from reference dimensions to a geometry that enables the correct execution of the production process. In this paper, the authors compare the development of two different innovative designs for a railway bolster beam using structural optimization processes and manufacturing constraints. The project was conducted by exploiting Finite Element Analysis (FEA) combined with CAD techniques and structural optimization processes. In addition, it explored the use of spheroidal cast iron compared with structural steel. The strength of this non-standard material for the railway field was assessed with particular attention to its fatigue strength. In recent years, austempered ductile cast iron (ADI) has also established itself due to its good mechanical performance. It can be considered an economic substitute for steel in many fields, such as the automotive and railway sectors. Some previous works are available about casting constraints, which is the object of the present work. Wang and Kang [1] proposed a level set-based topology optimization method for the realization of the concept design of casting components. Their method used velocity field design variables and combined the level set method with the gradient-based mathematical programming algorithm, considering the sensitivity scheme of the object's function and constraints. A similar level set method was also introduced by Allaire et al. [2], Xia et al. [3,4] and Liu et al. [5]. Gersborg and Andreasen [6] applied a Heaviside parametrization design to obtain manufacturable cast geometries in a gradient-driven topology optimization. Also, Liu et al. [7] used Heaviside-function-based directional growth topology parameterization (H-DGTP) for the optimization of the layout and height of casting components. Another example for the use of this method was described by Guest et al. [8] for imposing a minimum-length scale on structural members in topology optimization. Schmitt et al. [9] considered a parameter-free shape optimization and developed a new formulation and implementation method for geometric and manufacturing constraints. Harzheim and Graf [10] compared the topology optimization of a casted part with and without manufacturing constraints. The geometries could be manufactured easily, imposing constraints related to the minimum size of the parts and the direction of extraction from the mold. Casting is a near-net-shape process, so a piece can be optimized to reduce the operations required for its finishing. Bhosale and Sapkal [11] considered a carrier for an epicycloidal mechanism to perform topological optimization for mass reduction. As a result of the changes introduced, the cost of production reduced, eliminating many manufacturing steps that would otherwise be necessary. The applications of structural optimization in the railway field are not as widespread as in other sectors. Such methodologies can allow reductions in mass, reductions in stresses, or improvements in the manufacturing processes of parts. Applications of structural optimization are available in the literature considering the various subsystems in which a railway car can be broken down, e.g., via its running gear, car body structure or internal equipment. Regarding internal equipment, some studies have focused on the optimization of the battery mounts of a railway carriage [12] or on the coupling between carriages [13]. Koenig and Friedrich [14] attended to the topological optimization of the body structure of a railway car to reduce its overall mass. The geometry modeled on the basis of the results obtained presented a modular structure for greater design flexibility. A similar approach was adopted by the authors in [15,16] for optimizing a tramway carbody. A design procedure combining the size optimization and modal behavior of the carbody structure was proposed. More generally, procedures to be followed to optimize the body structure of railway vehicles have been described in [17,18]. Srivastava et al. [19] dealt with the structural optimization of both a bogie frame of a freight wagon and its bolster with the aim of reducing the mass of the parts. Initially, an analysis of the original configuration was carried out to understand its performance. Then, a topological optimization was conducted with the SIMP method with the aim of maximizing the stiffness of the structure. After the reconstruction of the geometry, on the basis of the results obtained, a new static verification analysis was carried out. Park and Lee [20] used a genetic algorithm with an artificial neural network to optimize a railway bogie frame. The component was subjected

to fatigue loads, and the authors have implemented a constraint to ensure the resistance of the component to such conditions. The implementation of fatigue constraints, in fact, cannot easily be implemented in the commercial FE software. The proposed method is based on a microgenetic algorithm, the scheme of which referred to the one proposed by Krishnakumar in 1990 [21]. Another application of the proposed method was carried out by Park et al. [22] for the redesign of the bogie frame for a tilting train for the Korean railways. Yamamoto in 2020 [23] used fatigue-constrained shape optimization for the redesign of two wheel models for Japanese railways. In this case, fatigue strength constraints could be introduced in commercial FE software. Other methods in the literature are "trial and error". An example of this procedure was proposed by Abid and Waqas [24] by applying it to a locomotive bolster with the aim of reducing its mass. In the article, some configurations are considered with various changes of geometry features. Fatigue strength and stress concentrations were evaluated for each of them. At the end of the process, it was possible to identify a configuration that would increase the strength of the structure and at the same time reduce its mass. Structural optimization applications other than mass minimization are also available. An interesting example, for the purposes of the research conducted, was analyzed by Cetin et al. [25] with a multi-criterion optimization. The parameters considered in this case are the cost of production, the difficulty of realization and the reliability of the part. Summing up, the present research activity, carried out in collaboration with an industrial partner, had the objective of developing a methodology capable of generating mechanical components for railway use with a design achievable through a sand-casting process. This would allow for the elimination of all welds, which is identified as the most critical aspect from a mechanical fatigue perspective. The method aims to efficiently combine Finite Element Analysis (FEA), structural optimization processes and CAD modeling. In addition to this, manufacturing constraints were included within the optimization step. Regarding these aspects, compared to the just presented state of the art, numerous considerations have been taken into account: the proper generation of symmetries based on the characteristics of the load cases, the selection of minimum component feature sizes to expedite the subsequent geometry reconstruction process, and the assessment of the correct direction for applying constraints. The object of the study was the bolster beam of a currently circulating tram vehicle. It was tested according to two different optimization procedures, thus enabling the assessment of the effects generated by the technological constraints. A robust initial campaign of numerical tests was conducted, and the results obtained are reported in this article. In Section 2, the bolster beam, test conditions and methodology have been presented. In Section 3, the benchmark has been described, including all the optimization settings. In Section 4, results have been discussed in detail and illustrated. Finally, Section 5 reports conclusions and future developments.

2. Materials and Methods

In this section, the methodology proposed by the authors for the innovation of the bolster beam is described. The objective of the present work was to define an effective and lighter design of the component for producing it with casting techniques, passing from traditional structural construction steel to cast iron.

2.1. Model Description: The Bolster Beam

The structure of the original bolster beam, illustrated in Figure 1, was totally made with construction steel and assembled through welding. It was mounted on a tram vehicle, as a linking component between the bogie frame and the carbody. It was connected to the bogie systems through the two arms, while the main interfaces with the carbody were the two upper buffers and the central traction pin.
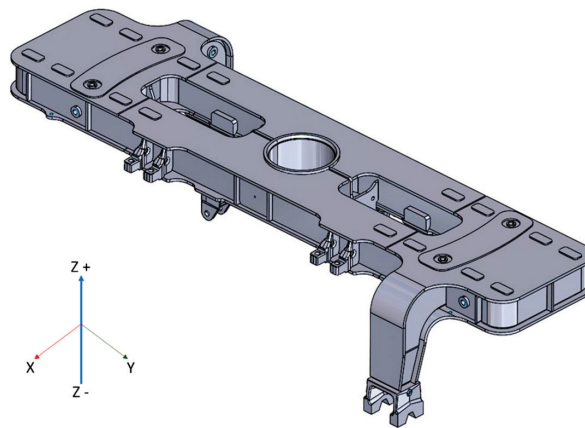
Figure 1. View of the original bolster beam.

As previously mentioned, due to spatial constraints, the two tanks for pneumatic suspensions were positioned within the bolster beam. This solution reduces the complexity of the geometry while ensuring the desired volume. Another important characteristic was the presence of internal reinforcements, that allowed the component to be stiffer and support better bending loads. The torsional behavior was naturally good thanks to the box shape of the component. The original model served as a reference for generating the CAD model used in the optimization process. This model had all available space filled with material to maximize the workspace for the optimization solver while ensuring no interference with other vehicle components. To improve the optimization process and the subsequent redesign of the part, before making the mesh, the model was divided into two regions: design space (black color) and non-design space (gray color), as shown in Figure 2. The first one represented the volume of material that can be altered by the software. It must be maximized to give more freedom to the solver. The non-design space was minimized to only include the interfaces between the body and bogie components, ensuring non-interference and maintaining essential structural connections.
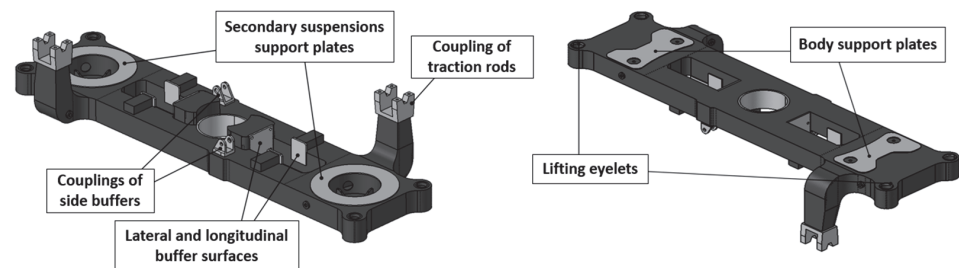
Figure 2. Design space (black) and non-design space regions (gray).

The next step was the generation of the grid. To optimize the number of nodes and elements, their size was adapted to different regions of the bolster, ranging from a minimum of 2.5 mm at the inner cylinders of the tanks to 10 mm for the central body of the structure. For the modeling of the reinforcement ribs inside the tanks, 5 mm elements were used, ensuring a minimum of two elements in the thickness of each geometric feature. To improve the quality of the tetra elements, automatic refinement functions were applied near the edges and fillets. For the support plates of the secondary suspensions and support plates of the body, instead, it was possible to use PENTA elements to reduce their number in those regions that would have required a much finer size of tetra elements. To apply the loads, 1D elements of type RBE3 were used, which prevented the structure from stiffening excessively. The model consisted of 1,073,078 elements and 1,782,362 nodes. To perform the optimization, the class 400 spheroidal graphite cast iron (EN-GJS-450-10) has been considered. This material has good mechanical performances with sufficient strain at

breakage (10% minimum), ensuring good performance in terms of mechanical fatigue behavior. More precisely, the material presented an ultimate tensile stress (σ_u) of 450 MPa and yield stress (σ_Y) of 310 MPa with a Young's module (E) equal to 169,000 MPa. The steel with which it was compared (S355 construction steel), on the other hand, exhibited the following characteristics: ultimate tensile stress (σ_u) of 510 MPa and yield stress (σ_Y) of 355 MPa with a Young's module (E) equal to 210,000 MPa.

2.2. Methodology

The methodology proposed in the present activity aimed to combine CAD and FEM techniques with a structural optimization approach, whose settings were oriented to a casting manufacturing process. All simulations were conducted using the same computer that had the following characteristics: Intel(R) Xeon(R) CPU E5-2643 v4 @ 3.40GHz, RAM 32GB. Two manufacturing constraints have been introduced in the optimization procedure to evaluate the differences between the geometries proposed by the optimization process: "Extraction direction from a mold" and "Minimum feature size" are their reference names. Starting from the CAD model of the component, a detailed FE model was built and tested according to the reference standard EN 13749:2021 [26] with the aim to know the original mechanical behavior of the system.

In detail, 16 load cases have been considered to examine the mechanical performances in different running conditions. This phase has a key importance in the methodology proposed because it could lead to a better comprehension of the mechanical behavior of the structure in its original form. Furthermore, it would not have made sense to optimize a structure that does not support the loads acting on its original configuration After selecting the main interfaces with other vehicle systems, the model was prepared for the topological optimization process by defining the design and non-design spaces. The original model featured a welded, box-shaped structure with all available space filled with material to maximize the optimization solver workspace. Initially, the extreme zones, which functioned as tanks for the vehicle secondary pneumatic suspension, were included. This choice was fundamental to evaluate the internal structural reinforcements of the original configuration, which could generate major complications for the subsequent casting process. When all the volume of the model was defined, the design and non-design space were separated, maintaining the correct interfaces previously found. The optimization process had the objective of minimizing the weighted compliance, calculated on all the main load cases, including static and dynamic ones. As a constraint condition, a limit on the volume fraction has been imposed, as described within the next sections. In addition, three other types of constraints were included: symmetry with respect to the Z-axis, and two technological conditions closely related to casting manufacturing process ("Extraction direction from a mold" and "Minimum feature size"). The first one was imposed to the solver to remove material only in one direction, starting from a reference plane defined by the user, exactly as a piece is extracted from its mold at the end of the casting process. In order to ensure the correct performance of the casting process, the second constraint related to the minimal feature dimension has been imposed. This parameter impacts on the material flow within the mold. A tight flow section could slow down the melted material, leading to the generation of imperfections or localized cooling, which is representative of a non-excellent melting process. In this way, the optimization result could have the minimum size to guarantee the flow of the molten metal in the mold. Once the optimization step was completed, the new geometry was imported in a 3D CAD environment and modeled again. The redesigned bolster beam was then imported in commercial FE software for testing it again according to the reference conditions and to verify its mechanical performances. The overall process is summarized in Figure 3.
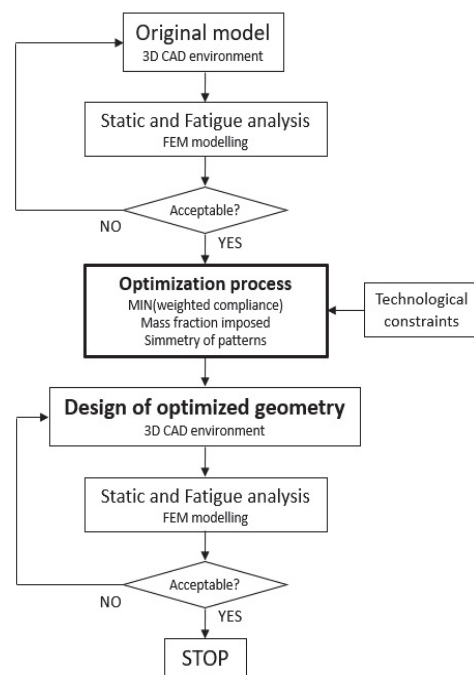
Figure 3. Scheme of the redesign procedure, including optimization process.

2.3. Optimization Settings and Load Cases

With the objective of evaluating the effect of the casting constraints, defined as "Extraction direction from a mold" and "Minimum feature size", two types of optimization processes have been considered. In both cases, a gradient-based optimization method [27] has been adopted for solving the optimization problem. In Case 1, the manufacturing constraints were not imposed. This approach allowed the solver maximum freedom to perform the optimization within the design space. Conversely, in Case 2, manufacturing constraints were imposed. This ensured that the solver produced a result feasible for the casting process. For the second case, two alternatives were considered with different extraction directions: the first one with the extraction direction along the Z-positive direction and the second along the Z-negative direction. To run the optimization, other general settings, common to the three cases, were imposed to the solver. In detail, the optimization objective was to minimize the weighted compliance considering all the load cases introduced in the model and described below. As optimization constraint, the mass fraction, which is the ratio between the final and the initial mass of the design space, was set below 40%. Similarly, the imposition of a symmetry constraint was considered relevant, as the load cases were highly asymmetric. Then, a revolution symmetry was imposed around the Z-axis passing through the central hole of the beam. The main challenges regarding the definition of the optimization settings were the definition of the "Minimum feature size" and the symmetry constraint above described. Numerous tests were needed to find the suitable value for the studied geometry, allowing to achieve the correct level of detail in the optimized geometry. Once identified, it sped up the times in reconstructing the final design of the bolster beam. Table 1 shows the common settings for both test cases and the proposed technological constraints.

Table 1. Optimization settings.

Parameters		Case 1	Case 2a	Case 2b
General settings	Material	Spheroidal graphite cast iron EN-GJS-450-10		
	Symmetry constraint	Cyclic around Z axis		
	Optimization constraint	Mass fraction < 0.4		
	Optimization objective	Min. weighted compliance		
	Load cases considered	Static and fatigue		
Technological constraints	Extraction from mold	-	Z positive	Z negative
	Minimum feature size	-	20 mm	20 mm

Case 1 has been studied as a reference to evaluate the effect of the manufacturing constraints. For Case 2, a main direction of extraction from the mold was imposed: along the positive Z-axis (openings upwards—Case 2a) and along the negative Z-axis (openings downwards—Case 2b). This latter setting was fundamental, because it allowed a simpler process for the creation of the mold. The ability to control the optimization process by incorporating casting properties will enable the adoption of casting for railway components, thereby eliminating critical features such as welds. Additionally, the casting process can reduce the need for extensive inspections and tests typically required for welded components. The load conditions contained in the technical specification, and considered in the optimization, were based on the EN 13749. Other load conditions have been indicated by the producer to ensure the quality and the reliability of the component. Inertial accelerations on the masses attached to the considered part have been defined according to the reference regulation. Overall, 16 load cases have been tested, taking into account some conditions that could occur during the operation and the maintenance of the vehicle (Figure 4). Particularly, we considered the following loads:

- Longitudinal load on the bogie bolster to carbody connection;
- Transversal load on the bogie bolster to carbody connection;
- Truck lifting;
- Truck twist (with also the completing unloading of one wheel);
- Braking forces;
- Internal pressure of the air springs;
- Longitudinal lozenging forces.
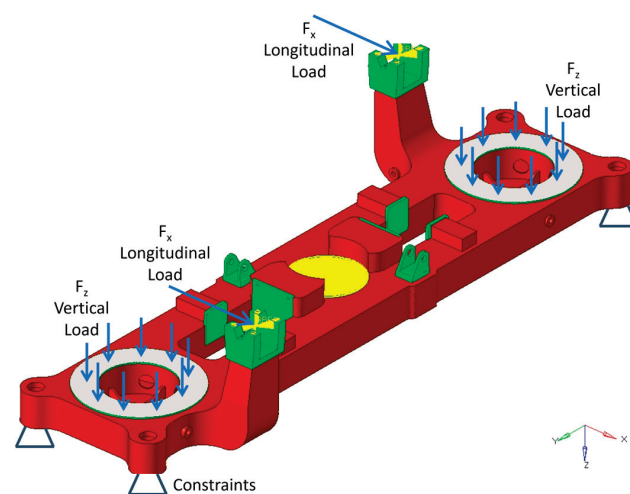
Figure 4. Example of a longitudinal load case condition.

3. Topological Optimization and FEA Results

3.1. Topological Optimization Results

Since the first results obtained with the optimization process, it could be seen that Case 1 has a box-shaped geometry similar to that of the original bolster beam. Case 2a, with extraction direction from a mold constraint along the Z-positive direction, presented some openings upwards. This result could generate problems during the use of the vehicle due to the possibility of the accumulation of liquids or other impurities that degrade the structure, compromising its resistance. The result of Case 2b, with the extraction direction from a mold constraint along the Z-negative direction, on the other hand, allowed to solve this problem and was therefore considered more relevant than the previous one. For these reasons, the most relevant test cases, Case 1 and Case 2b, will be analyzed.

3.1.1. Topology Optimization Results—Case 1

In the first case, the geometry was similar to a box shape, with several lightening holes in the central area, on the arms of the connections for the traction rods and in the area around the tanks (Figure 5a). In the area of the arms, the ribs were reduced, and the material was removed, creating some holes on the outer surfaces. These considerations could reduce the mass of the optimized geometry without compromising the stiffness of the structure. It should be noted that the shape of Case 1 could only be produced using the welding process. After a visual assessment of the optimization results, the geometry, in STEP format, has been exported from the FE software to be imported into a commercial CAD software to perform reconstruction. The geometry was formed by an uneven set of surfaces and therefore could not be used directly for optimized bolster modeling. The bogie bolster was then completely redesigned, taking advantage of the original geometry and coherently with the results provided by the optimizer. Preliminary static analysis on the original model was therefore important for paying attention to the more stressed zone of the component during the redesign phase. The constraints due to the presence of joints to the bogie and to the train carbody were considered to allow the replacement of the new geometry in the assembly. Once the new geometry was ready, the numerical verification analyses on it were carried out considering all the design load cases. This phase was necessary to eliminate possible stress concentrations in a more detailed modeling step and to evaluate the modification introduced in the model. The average size of the elements was 8 mm, while in correspondence with smaller geometrical characteristics, a minimum size of 4 mm was adopted. These values were achievable thanks to the introduction of the Minimum feature size constraint. The main stress concentrations were observed at the fillet between the center of the bolster and the lateral dampers. It should be noted that the concentrations that occur on the structure were very localized and required detailed changes in the geometry. In particular, the geometry of the lateral dampers was modified by taking as reference the geometry of the original bogie bolster provided by the manufacturer, which showed the same distribution. Some holes were realized in this stress concentration zone, eliminating the connection between the lateral damper and the boxed top plate. The idea behind this modeling was to move the point of stress concentration in an area with more resistant material, which was effective, as shown in the following section.

(a)

(b)
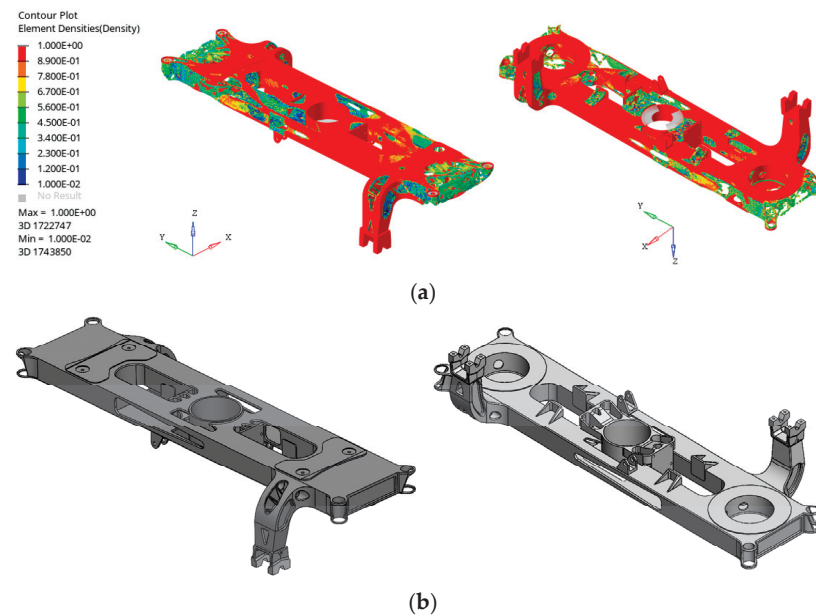
Figure 5. Case 1: (**a**) result of the optimization, element density distribution; (**b**) final geometry of the redesigned bolster beam.

3.1.2. Topology Optimization—Case 2

The effect of the technological constraint was clear: an opened shape was generated for most of the bolster beam, removing material along only a main direction. Instead, in correspondence of the connections for the lateral dampers, a sort of box structure was obtained. This region had to be modified in an opportune way to produce it without the necessity of casting cores. Similar to the previous case, some lightning holes were opened around the air tanks and on the arms for the traction rods. Figure 6a illustrates the optimization result for this step of the analysis. The obtained model had an upper region formed by a plate on which reinforcement ribs were placed to ensure the bending strength of the structure, trying to reduce the mass as much as possible. In the area around the secondary suspension link, the tanks were rebuilt with an appropriate volume. To manufacture this part, casting cores were necessary, particularly for components like the arms. Generally, the casting process necessitated minimizing elements in the undercut areas. When undercuts were unavoidable, specific cores had to be employed and properly connected to the mold. Verification analyses were carried out maintaining all the conditions of the previous step. Some localized stress concentrations were observed at the reinforcement ribs of the lateral and longitudinal dampers and at the connection arms with the traction rods. Then, the geometry of the reinforcement ribs was modified, increasing their dimensions in the critical areas. After a detailed mesh sensitivity analysis, an average element size of approximately 10 mm was achieved. Once again, the effect of the Minimum feature size constraint made the geometry reconstruction process faster and easier, ensuring an optimum detail of the FE model.

From a technological point of view, the fillet radii were increased to avoid excessive dimensional variations, reducing possible defects in the pouring phase of the cast iron within the mold. Regarding the concentrations around the connection arms with the traction rods, the fillet radius was increased, and at the same time, the dimensions of the reinforcements in this part were revised, following the optimization results. In addition, the symmetry of the beam was restored to ensure the resistance of the structure. The final design could be manufactured with casting techniques, achieving the main objective of the activity.

(a)

(b)
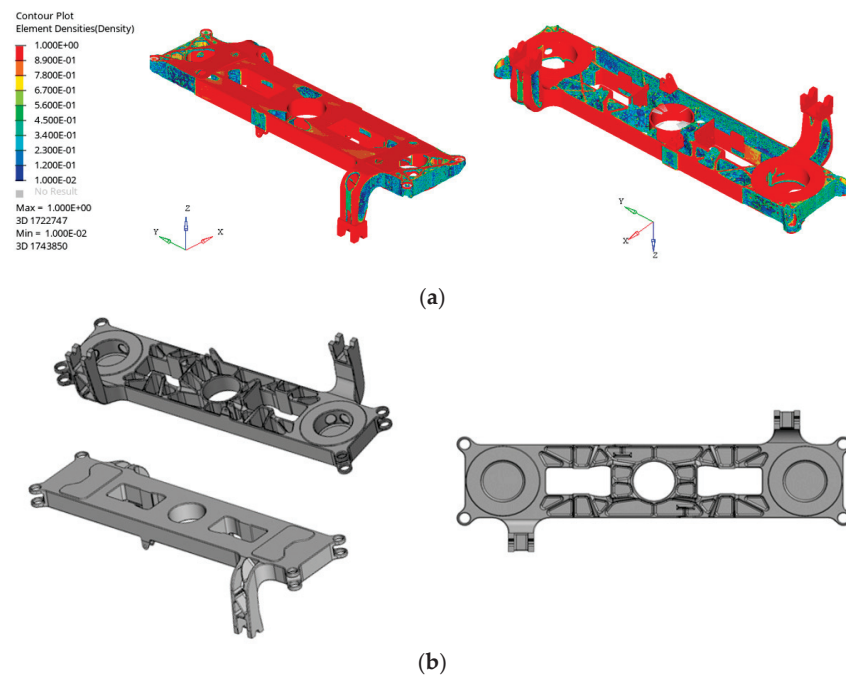
Figure 6. Case 2: (**a**) result of the optimization, element density distribution; (**b**) final geometry of the redesigned bolster beam.

3.2. FEA Verification Results

To conclude the redesign of the bogie bolster beam, static analyses were carried out on the optimized structures. To do this, the design load cases have been considered, as previously seen. The same procedure seen for the previous analyses has been followed, and no changes have been made to the material introduced in the FE software. Below, we reported the most significant results of the simulations for the two geometries proposed. Three different load cases have been described: these conditions were the most critical for the resistance of the structure due to the high stresses generated. In addition, the information obtained from these cases was considered relevant for future activities in detailed design. FE analyses, according to EN 13749, and extremely localized stress concentrations will be assessed in future activity supported by experimental activities carried out by the manufacturer. The longitudinal load case was focused on the truck-to-carbody connection. The longitudinal force was applied partially on the traction rod ends and partially on longitudinal bumper plates. As expected, the main stress concentrations were in the regions near the lateral bumpers and on the reinforcement ribs behind the longitudinal bumper plates. Case 2 showed lower stress due to its innovative design as illustrated in Figure 7a. The transversal force, instead, was applied on the lateral bumper plate along the Y-positive direction. The main stress concentrations were localized near the lateral bumper plate. In detail, for Case 1, the critical regions were on the plate and near the small fillet between the plate and the lateral reinforcement ribs. Regarding Case 2, a stress concentration was detected on the reinforcement rib behind the lateral bumper plate, complying with the permissible value of the material (see Figure 7b). Finally, the lifting load case represented the truck lifting applied on only two eyelets to simulate the non-correct connection of the jacking system to the geometry. The bolster beam, during the lifting operations, had to resist the normal lifting load with a safety factor equal to two. The static analyses conducted on lifting conditions are generally the most critical. Case 1 showed a higher maximum value in a really localized area. The innovative design, instead, was able to distribute better the stress, reducing the stress level on the structure. Figure 7c illustrates the results for this load case. The plasticity effect in localized zones must be evaluated with a non-linear FE analysis.
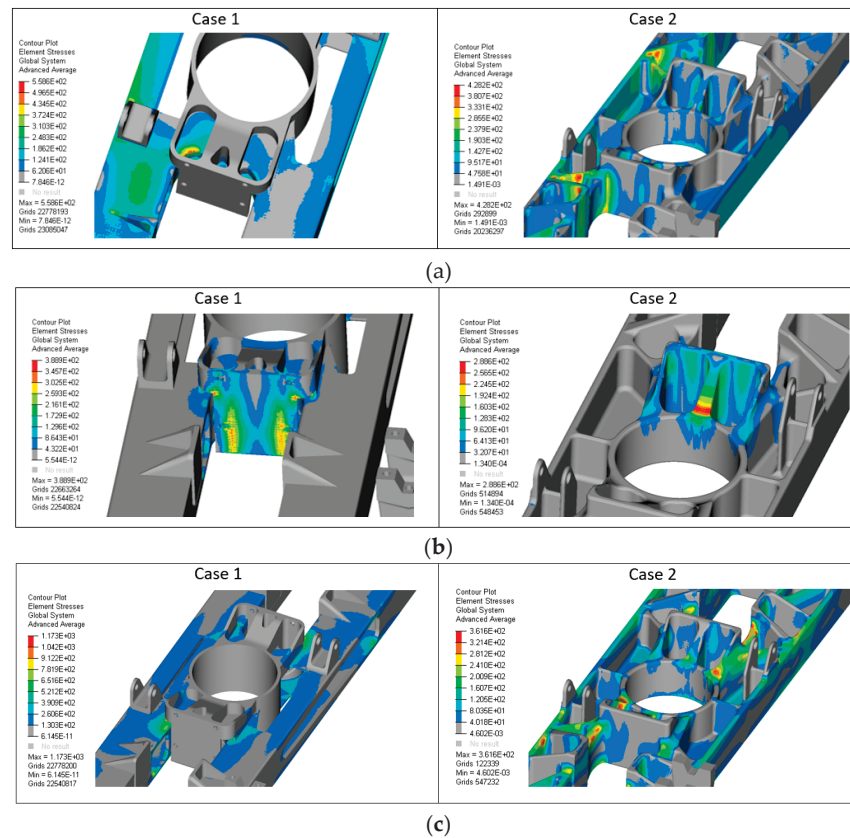
Figure 7. Stress distribution in Case 1 vs. Case 2: (a) longitudinal load case, (b) transversal load case, (c) lifting load case.

4. Results and Discussion

In this section, the comparison between the two solutions is presented from a static and dynamic point of view. In Table 2, the maximum stress values have been summarized for the three load cases reported before. The table reports the "Utilization coefficient" to evaluate stress concentration, which is calculated as the ratio between maximum stress calculated and permissible stress. The maximum allowed value in the linear field is generally equal to 1. However, as in the case under consideration, local exceedances of stresses are permitted, considering the plastic behavior that characterizes metallic materials. In this case, although not required in this research activity, it is possible to proceed with a non-linear calculation. Significantly lower material utilization coefficients can be observed in Case 2, which is producible by casting, ranging from 25% to 70%.

Table 2. Performance comparison between the two optimized geometries.

Load Case	σ_{amm} [MPa]	Case 1		Case 2	
		σ_{max} [MPa]	U [-]	σ_{max} [MPa]	U [-]
Longitudinal		559	1.80	428	1.38
Transversal	310	390	1.26	289	0.93
Lifting		1173	3.78	362	1.17

σ_{max} is the maximum stress evaluated through FE analysis, σ_{amm} is permissible stress, U is the utilization coefficient.

In Case 1, the obtained model was formed by a box-shaped closed geometry with some reinforcement ribs inside it. For its realization, the use of the welding process will be necessary, similar to the original case. This solution had a lower mass compared with the existing bolster produced by the manufacturer (−17.7%), even if the complexity of the

production of the component remained unchanged. In Case 2, the bolster beam was entirely manufacturable by casting due to the introduction of the extraction constraint from the mold during the optimization phase. Another advantage was that the welding inspection steps were no longer required. However, the mass of the component in this case was higher than in the original case (+9.0%). In terms of dynamic behavior, modal analysis carried out in free-free conditions has shown higher frequencies of vibration for the bolster beam feasible through sand casting with an increase of about 8% on the first one. This result was not a given, considering the greater mass. In addition, the nature of the first mode shape was changed: a first torsional mode was observed in Case 1, while a first flexural node with a double-nodal line was observed in Case 2. Figure 8 shows the mode shapes comparison.
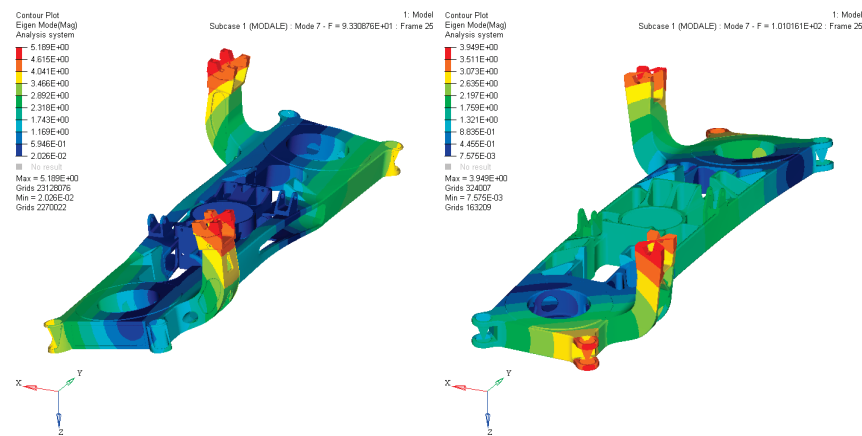
Figure 8. First mode shapes comparison: Case 1 vs. Case 2.

5. Conclusions and Future Developments

In the present work, a structural topological optimization procedure combined with manufacturing constraints has been presented. Two different optimization procedures have been carried out on a railway bolster beam, and the use of spheroidal graphite cast iron has been examined. The two solutions were the result of optimization with different technological constraints that allowed obtaining geometric features for the specific production process. The problems of topological optimization were formulated to minimize the weighted compliance considering both static and fatigue load cases. The first solution (Case 1) has allowed to design a lighter bolster beam, maintaining a box-shaped geometry. The component needed to be produced using a welding-supported process, thus retaining many of the initial component's critical aspects. The second solution (Case 2), as a result of the proposed optimization procedure, has revealed the potential to quickly redesign the geometry of a component that conforms to the requirements of the casting process. Moreover, it led to a stiffer design. Imposing constraints related to the extraction direction from the mold and minimum feature size could facilitate a transition to entirely different manufacturing processes and geometries. This research emphasizes the necessity of continuing to explore optimization procedures within the railway industry. These procedures hold the potential for achieving mass reduction, guiding design innovations, and streamlining production processes. Additionally, integrating fatigue optimization techniques with finite element (FE) analysis, particularly when dealing with time-varying load cases, promises a higher level of precision compared to the capabilities offered by the currently employed FE software. This convergence could mark the inception of a new era in railway component design and validation. The adoption of these innovative methodologies has the capacity to yield substantial advantages within the railway field.

References

1. Wang, Y.; Kang, Z. Structural shape and topology optimization of cast parts using level set method: Structural shape and topology optimization of cast parts using level set method. *Int. J. Numer. Meth. Eng.* **2017**, *111*, 1252–1273. [CrossRef]
2. Allaire, G.; Jouve, F.; Michailidis, G. Casting Constraints in Structural Optimization via a Level-Set Method. Orlando, United States. 2013, p. 10. Available online: https://hal.science/hal-01088775 (accessed on 28 May 2024).
3. Xia, Q.; Shi, T.; Wang, M.Y.; Liu, S. A level set based method for the optimization of cast part. *Struct. Multidisc. Optim.* **2010**, *41*, 735–747. [CrossRef]
4. Xia, Q.; Shi, T.; Wang, M.Y.; Liu, S. Simultaneous optimization of cast part and parting direction using level set method. *Struct. Multidisc. Optim.* **2011**, *44*, 751–759. [CrossRef]
5. Liu, J.; Ma, Y. A survey of manufacturing oriented topology optimization methods. *Adv. Eng. Softw.* **2016**, *100*, 161–175. [CrossRef]
6. Gersborg, A.R.; Andreasen, C.S. An explicit parameterization for casting constraints in gradient driven topology optimization. *Struct. Multidisc. Optim.* **2011**, *44*, 875–881. [CrossRef]
7. Liu, S.; Li, Q.; Chen, W.; Hu, R.; Tong, L. H-DGTP—A Heaviside-function based directional growth topology parameterization for design optimization of stiffener layout and height of thin-walled structures. *Struct. Multidisc. Optim.* **2015**, *52*, 903–913. [CrossRef]
8. Guest, J.K.; Prévost, J.H.; Belytschko, T. Achieving minimum length scale in topology optimization using nodal design variables and projection functions. *Int. J. Numer. Meth. Eng.* **2004**, *61*, 238–254. [CrossRef]
9. Schmitt, O.; Friederich, J.; Riehl, S.; Steinmann, P. On the formulation and implementation of geometric and manufacturing constraints in node–based shape optimization. *Struct. Multidisc. Optim.* **2016**, *53*, 881–892. [CrossRef]
10. Harzheim, L.; Graf, G. A review of optimization of cast parts using topology optimization: I—Topology optimization without manufacturing constraints. *Struct. Multidisc. Optim.* **2005**, *30*, 491–497. [CrossRef]
11. Bhosale, G.H.; Sapkal, S.U. Re-engineering of Cast Product by Topology Optimization. *IJETER* **2021**, *9*, 1211–1216.
12. Luo, Y.; Peng, Y. Topology optimization design of the suspension arm of a certain type of train battery system. *JMESS* **2021**, *7*, 4059–4061.
13. Hoosain, S.E.; Tshabalala, L.; Bester, D.; Chetty, D.; Mukwevho, G. *Additive Manufacturing Case Study in the Railway Industry*; Rapid Product Development Association of South Africa: Pretoria, South Africa, 2020.
14. Koenig, J. *Integral Consideration of the Lightweight Design for Railway Vehicles*; Technical University of Denmark: Lyngby, Denmark, 2011.
15. Cascino, A.; Meli, E.; Rindi, A. Dynamic size optimization approach to support railway carbody lightweight design process. *Proc. Inst. Mech. Eng. Part F: J. Rail Rapid Transit* **2023**, *237*, 871–881. [CrossRef]
16. Cascino, A.; Meli, E.; Rindi, A. A strategy for lightweight designing of a railway vehicle car body including composite material and dynamic structural optimization. *Rail. Eng. Sci.* **2023**, *31*, 340–350. [CrossRef]
17. Kirkayak, L.; Krüger, D.; Malzacher, G.; Gomes Alves, C.; Schmauder, N.; Kopp, G. *Lightweight Design Concept Methodology of the Extended Market Wagon: A Shift2Rail Project*; WCRR: Birmingham, UK, 2022; p. 6.
18. Li, X.; Peng, F.; Yang, Z.; Peng, Y.; Zhou, J. Structural optimization design of a bolster based on simulation driven design method. *Transp. Saf. Environ.* **2023**, *5*, tdac075. [CrossRef]
19. Srivastava, P.K.; Shukla, S. Topology Optimization: Weight Reduction of Indian Railway Freight Bogie Side Frame. *Int. J. Mech. Eng.* **2021**, *6*, 4374–4383.
20. Park, B.H.; Lee, K.Y. Bogie frame design in consideration of fatigue strength and weight reduction. *Proc. Inst. Mech. Eng. Part F J. Rail Rapid Transit.* **2006**, *220*, 201–206. [CrossRef]
21. Krishnakumar, K. Micro-Genetic Algorithms For Stationary And Non-Stationary Function Optimization. In *Intelligent Control and Adaptive Systems*; Rodriguez, G., Ed.; SPIE: Bellingham, WA, USA, 1990; pp. 289–296.
22. Park, B.H.; Kim, N.P.; Kim, J.S.; Lee, K.Y. Optimum design of tilting bogie frame in consideration of fatigue strength and weight. *Veh. Syst. Dyn.* **2006**, *44*, 887–901. [CrossRef]
23. Yamamoto, M. Non-parametric optimization of railway wheel web shape based on fatigue design criteria. *Int. J. Fatigue* **2020**, *134*, 105463. [CrossRef]

24. Abid, M. Analysis and Redesign of Bolster Beam of the Bogie Frame of a Locomotive. *J. Eng. Res.* **2013**, *1*, 271–287.
25. Cetin, M.H.; Alvali, G.T.; Korkmaz, S. Parameter Optimization with Multi-criteria Decision-Making Methods in Rail Transport: A Case Study of Freight Wagon Bogie. *Arab. J. Sci. Eng.* **2021**, *46*, 10059–10076. [CrossRef]
26. *EN 13749:2021*; Railway Applications—Wheelsets and Bogies—Method of Specifying the Structural Requirements of Bogie Frames. iTeh, Inc.: Newark, DE, USA, 2021.
27. Jameson, A. *Gradient Based Optimization Methods*; MAE Technical Report No (2057); Princeton University: Princeton, NJ, USA, 1995.

Machine and Deep Learning Trends in EEG-Based Detection and Diagnosis of Alzheimer's Disease: A Systematic Review

Marcos Aviles *, Luz María Sánchez-Reyes , José Manuel Álvarez-Alvarado and Juvenal Rodríguez-Reséndiz *

Facultad de Ingeniería, Universidad Autónoma de Querétaro, Querétaro 76240, Mexico;
luzmsr@ieee.org (L.M.S.-R.); jmalvarez@uaq.mx (J.M.Á.-A.)
* Correspondence: marcosaviles@ieee.org (M.A.); juvenal@uaq.edu.mx (J.R.-R.)

Abstract: This article presents a systematic review using PRISMA methodology to explore trends in the use of machine and deep learning in diagnosing and detecting Alzheimer's disease using electroencephalography. This review covers studies published between 2013 and 2023, drawing on three leading academic databases: Scopus, Web of Science, and PubMed. The validity of the databases is evaluated considering essential factors such as the arrangement of EEG electrodes, data acquisition methodologies, and the number of participants. Additionally, the specific properties of the databases used in the research are highlighted, including EEG signal classification, filtering, segmentation approaches, and selected features. Finally, the performance metrics of the classification algorithms are evaluated, especially the accuracy achieved, offering a comprehensive view of the current state and future trends in the use of these technologies for the diagnosis of Alzheimer's disease.

Keywords: deep learning; diagnosis of Alzheimer's disease; EEG; machine learning; systematic review

1. Introduction

Alzheimer's disease (AD) is a neurodegenerative pathology that progresses over time and mainly affects older people. Its symptoms vary among those affected but include memory loss, confusion, and extensive cognitive impairment [1,2]. Early identification and accurate diagnosis are essential to provide appropriate medical care and improve the quality of life of patients [3,4]. With technological progress in capturing brain signals, such as the electroencephalogram (EEG), more accurate and effective diagnostic methods have been developed. Due to its non-invasive nature, the EEG records the brain's electrical activity through electrodes on the scalp, offering valuable insights into brain alterations linked to Alzheimer's disease [5–7].

Machine learning (ML) and deep learning (DL) techniques for classifying EEG signals have been established as an expanding area of research. These methods allow the analysis of large volumes of EEG data to identify non-obvious patterns, potentially facilitating the early diagnosis of AD [8,9]. However, the effective implementation of these techniques needs to be improved. Critical factors such as the appropriate choice of EEG databases, a correct arrangement of the electrodes, the selection of an appropriate number of participants, the identification of relevant features for the analysis, the choice of appropriate classification algorithms, and a rigorous evaluation of its performance is decisive in the quality and reliability of the results obtained [10].

This work aims to carry out a systematic review of current trends in the use of ML and DL to detect and diagnose AD through the use of EEG. Fundamental aspects such as preparation prior to data collection is addressed, including the selection of the EEG database, the electrode placement strategy, data acquisition methodologies, and the selection of the number of volunteers. A detailed analysis of ML and DL methods will be carried out, including everything from filtering and segmentation techniques to feature selection. The evaluation metrics used to determine the effectiveness of the classification algorithms

are also reviewed. This article offers a comprehensive overview of the advances and methodologies in applying ML and DL in EEG analysis to diagnose and detect AD early.

The main contributions of the work are:

- Artificial intelligence is a booming branch that offers an alternative to understanding diseases. However, it is susceptible to the input data and its processing. This work analyzes these critical points described in the state of the art.
- No work has been carried out in the last ten years with this approach to analysis; before the application of artificial intelligence algorithms, their selection and classification levels focused on Alzheimer's disease.
- This review covers the analysis of EEG signal databases for use in AI, the demographic data of the patients that comprise them, and the data acquisition paradigms, resulting in a necessary tool for future research.

The structure of the current work is divided as follows: Section 2 exposes the sequential steps that must be followed to implement the proposed review. The results and discoveries obtained are presented in Section 3. Section 4 analyzes and interprets the results. Finally, in Section 5, the areas covered by the scope of this work are exposed.

2. Materials and Methods

The article selection and screening methodology are described in this section. The inclusion and exclusion criteria are detailed to select relevant studies. The searches in scientific databases and the screening process are discussed and divided into two main stages: an initial review based on titles and abstracts and a full-text review. The selection was based on the relevance and relationship to the topic of interest.

Search Strategy

The Preferred Reporting Items for Systematic Reviews and Meta-Analysis (PRISMA) guidelines were used in this systematic review [11]. The systematic search was conducted to identify studies investigating the use of ML and DL methods in the diagnosis of mild cognitive impairment (MCI) and Alzheimer's Disease using EEG. Articles written in English and published between 2013 and 2023 were exclusively selected. The search strategy used the PubMed, Scopus, and Web of Science databases. The following key terms were combined using Boolean operators:

- TITLE-ABS-KEY ((mci OR (mild AND cognitive AND impairment) OR (amnestic AND mild AND cognitive AND impairment) OR Alzheimer) AND (eeg OR electroencephalography) AND (detection OR diagnosis OR classification OR diagnostic) AND ((deep AND learning) OR (machine AND learning)) AND (LIMIT-TO (DOCTYPE, "ar")) AND (LIMIT-TO (PUBYEAR, 2023) OR LIMIT-TO (PUBYEAR, 2022) OR LIMIT-TO (PUBYEAR, 2021) OR LIMIT-TO (PUBYEAR, 2020) OR LIMIT-TO (PUBYEAR, 2019) OR LIMIT-TO (PUBYEAR, 2018) OR LIMIT-TO (PUBYEAR, 2017))).

Three independent reviewers removed duplicates and applied eligibility criteria to select relevant articles. Those who met the following criteria were included:

- Use of AD or MCI databases.
- Use of EEG data.
- Use of classification methods based on ML or DL algorithms.
- The works presenting objective performance measures were included, which allows an accurate evaluation of ML and DL's capacity to diagnose MCI and AD.

Relevant data were extracted from each selected study, including diagnostic methods prior to database acquisition, study groups, sample size, mean age, EEG electrode placement, acquisition, classification techniques used, signal processing, features used for classification, feature evaluation metrics, and the classification percentages obtained. These data allow it to comprehensively analyze the selected studies and evaluate their contribution to diagnosing MCI and AD using EEG. To ensure a systematic and transparent process in this review, the PRISMA methodology was followed. Initially, 425 articles from

the PubMed (107), WOS (141), and Scopus (177) databases were included. Duplicates were subsequently removed, resulting in 241 unique articles. Then, the exclusion criteria were strictly applied, which included cohorts other than Alzheimer's or MCI, the non-use of EEG, the absence of machine learning or deep learning techniques, volunteers with conditions additional to MCI or AD, and the lack of presentation of performance metrics such as algorithm efficiency and incomplete information. After this evaluation, 109 articles met all criteria and were included in this review. The Figure 1 illustrates this selection process in detail.
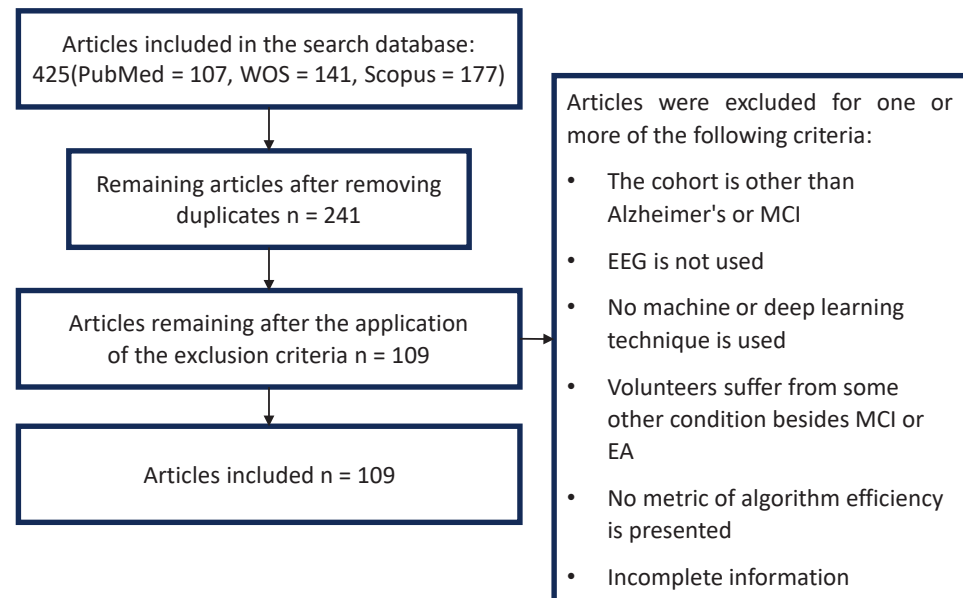
Figure 1. General methodology for the selection of articles.

Additionally, to ensure data integrity and methodological consistency, the following steps were adopted:

- Study selection criteria: Only studies that met predefined inclusion criteria, which guaranteed the use of EEG, were included. These criteria included specifying the EEG acquisition methodology, using cohorts diagnosed with Alzheimer's or MCI, and applying standardized machine learning or deep learning techniques.
- Review of methodologies: The methodologies used in each study for the acquisition and processing of EEG data were reviewed in detail. This included the evaluation of recording parameters, experimental conditions, and preprocessing procedures, ensuring that they met the standards established in the scientific literature.
- Peer review: All studies selected for review underwent a peer review process, ensuring the additional scrutiny of the validity and reliability of the data and methods used.
- Transparency and reproducibility: Studies were considered that provided sufficient detail about their methods and data, allowing the reproducibility of the experiments. Transparency in the presentation of results and analysis methods was also an important criterion for inclusion.

3. Results

In the results section, the findings obtained are presented. This section details significant advances, identifies emerging patterns and trends in current research, and highlights the most effective methodologies and areas requiring further research.

3.1. Traditional Alzheimer's Diagnosis Techniques for Database Formation

The database quality implemented for the classifiers' training is a critical point in ML and DL. In this section, an exhaustive analysis of the diagnostic techniques implemented

before the ML and DL methodology is carried out to diagnose the volunteers and confirm which cohort they belong to. An incorrect diagnosis before the application of artificial intelligence algorithms affects the accuracy of the results and makes it difficult to obtain solid conclusions. If a participant is misdiagnosed, either by classifying them as healthy when they have early disease symptoms or by labeling them as Alzheimer's patients when they are not, the results of classifiers trained with such a database could be biased and lead to wrong conclusions.

In analyzing the diagnostic techniques used in the reviewed studies, several tools and methods widely used to detect dementia and cognitive impairment were identified. The Mini-Mental State Examination (MMSE) is the most used diagnostic technique in 50% of the analyzed studies [5–7,12–19]. This test is used to detect the presence of dementia in psychiatric patients through systematic screening. In addition, it is used to follow the evolution of cognitive deterioration in patients with dementia over time.

Another relevant diagnostic technique is the Montreal Cognitive Assessment (MoCA) [20–24]. This brief screening test assesses cognitive function in six domains: memory, visuospatial capacity, executive function, attention, concentration, working memory, language, and orientation. This test was used in 15% of the papers analyzed and comprehensively assessed cognitive function. As for imaging tests, it was found that magnetic resonance imaging (9.5%), positron emission tomography (4.25%), computed tomography (3.77%), and single-photon emission tomography (2.83%) techniques were also used in the diagnosis of dementia. These techniques allow for the visualization and analysis of the brain to identify possible structural and functional abnormalities.

In addition to these tools, other diagnostic tests were used to a lesser extent. The Neuropsychiatry Unit Cognitive Assessment Tool (NUCOG) was presented in 3.7% of the papers [14,21,25], while the Wechsler Memory Scale represented 2.83% and the Boston Naming Test 1.88%. These tests assess specific aspects of cognitive function and contribute to the accurate diagnosis of dementia. It is essential to highlight that some studies do not specify the initial diagnostic process for creating the database. In these cases, the presence of unspecified brain images was demonstrated in 4.71% of the works, unspecified neurological examinations in 11.3%, diagnosis made by experts in 9.43%, interviews in 5.66%, and 11.3% did not describe any prior diagnostic methodology.

Concerning the diagnostic criteria used in the studies analyzed, several standards and metrics widely used in detecting and diagnosing dementia were identified. One of the most used criteria was the National Institute of Neurological and Communicative Disorders and Stroke and the AD and Related Disorders Association (NINCDS-ADRDA), present in 20.75% of the papers analyzed [26–30]. This criterion establishes the clinical and neuropathological standards for diagnosing AD.

Another main diagnostic criterion was the Dementia Rating (CDR), which was used in 12.26% of the studies [31–35]. The CDR is a clinical tool that assesses and classifies dementia severity across multiple cognitive domains and provides a standardized and reliable measure for diagnosing and monitoring cognitive impairment. The Diagnostic and Statistical Manual of Mental Disorders (DSM), a widely used reference manual in mental health, was also mentioned in 9.43% of the papers. This manual provides diagnostic criteria for various mental disorders, including Alzheimer's disease.

Regarding the National Institute on Aging-Alzheimer's Association (NIA-AA) Criteria, its presence was found in 7.5% of the papers analyzed [36,37]. These criteria have been developed by a collaboration between the National Institute on Aging and the Alzheimer's Association, as well as ongoing updates and consensus for diagnosing and classifying AD. Finally, the RedLat (Standardized Diagnostic Assessment of the Multipartner Consortium to Expand Dementia Research in Latin America) was identified in 1.88% of the studies [23]. This criterion is part of a consortium that aims to standardize the diagnostic evaluations of dementia in Latin America.

These different diagnostic criteria reflect the importance of reliable tools and standards for accurately detecting and classifying dementia in the context of machine research and

deep learning. Choosing the appropriate diagnostic criteria is crucial to guarantee the consistency and comparability of the results obtained in the studies.

3.2. Demographic Data of the Participants from the Databases

Three main aspects are examined: the average age of the participants, the percentage of males and females that make up the sample, and the average education level of the subjects. It is essential to highlight that only some reviewed papers reported the information necessary for these analyses. Of the 109 papers analyzed in this systematic review, 19 articles that did not provide the required statistics were identified [16,38–47]. This lack of information may be due to different reasons, such as the need for greater standardization in the presentation of demographic data.

Regarding the average age of the participants, significant differences were observed between the groups of healthy volunteers, those with MCI, and Alzheimer's patients. The average age for healthy volunteers was 68.53 years, with a standard deviation of 6.18. In the MCI group, the mean age was 70.52 years, with a standard deviation of 5.68. Finally, in the group of patients with Alzheimer's, the average age was 73.66 years, with a standard deviation of 5.58. These differences in average age reflect the progressive nature of Alzheimer's disease, which tends to manifest itself later in life.

Regarding the years of education, it was observed that the healthy volunteers had an average of 11.24 years, with a standard deviation of 2.98. On the other hand, MCI patients had an average of 9.67 years of education, while Alzheimer's disease patients had an average of 9.36 years, with a standard deviation of 2.84. These data indicate that the study participants had varied educational levels, which is essential to remember when interpreting the results and considering possible influences of education on cognitive performance.

Concerning the gender distribution in the databases, differences in the proportion of males and females were found. On average, the databases comprised 47.35% male, with a standard deviation of 10.12, and 53.57% female, with a standard deviation of 12.13. This indicates that, in general, the databases include a slightly higher proportion of females. In addition, the gender distribution by cohort was analyzed in healthy volunteers, MCI, and Alzheimer's patients. For healthy volunteers, it was found that, on average, 24.19% were female, and 18.87% were male. In the MCI group, the proportion of females was 20.47%, while the ratio of males was 19.68% on average. Finally, in the group of Alzheimer's disease patients, the proportion of females was 24.19%, and the balance of males was 21.86% on average. These differences in gender distribution by cohort may be significant in understanding possible variations in disease patterns and clinical manifestations.

This analysis of databases used in Alzheimer's disease screening and diagnosis studies using ML and DL techniques reveals differences in mean age, years of education, and gender distribution between healthy volunteers, MCI, and patient groups with Alzheimer's disease. These findings provide important information about the demographic features of the samples used in the studies, which is essential to interpret and generalize the results obtained.

The balance in the number of cases in the databases impacts the robustness of the model. According to the analysis of the percentages for control cases against cases with the disease, 50.47% of the databases show a difference of less than 10% between the number of cases with the disease and the control cases, which suggests that most of the methods reviewed used a balanced database [12–14,17,20,26,43,48,49]. On the other hand, in 8.5% of the databases, the total number of cases with the disease represents between 70 and 90% of the total cases, that is, they used a database with a bias in the number of cases [7,15,50,51].

3.3. EEG Acquisition

This section analyzes the number of electrodes used, sampling frequencies, and acquisition activities carried out by the volunteers who created the databases.

3.3.1. Number of Electrodes in the Acquisition of EEG Signals

In this context, 63 databases have been analyzed to understand the most used configurations and their relative proportions in scientific papers. Four main configurations were identified from the 63 analyzed databases representing the most used amounts of electrodes. The first uses 19 electrodes, the most frequently used in 19% of the works. As the second most used configuration, the use of 16 electrodes was found to be present in 17.46% of the total databases analyzed. This relatively minor number of electrodes may be due to studies focused on specific brain areas or restrictions in the equipment available for research. Thirdly, it is observed that implementing 32 electrodes is another standard option, being used in 14.28% of the analyzed databases. This configuration offers a greater density of information about brain activity, which is valuable for studies that seek a high level of detail.

On the other hand, it was identified that 21 electrodes also represent a common choice, present in 7.93% of the works analyzed. This configuration may be preferred in studies that seek a balance between information density and available technical resources. It is interesting to note that two configurations that stand out for their high electrode density were found. First, using 64 electrodes in 9.52% of the databases offers much information about brain activity, which is especially useful in research seeking comprehensive coverage. Secondly, it was identified that the configuration of 128 electrodes, although less frequent, was present in 6.34% of the analyzed databases.

Finally, less common configurations were found, corresponding to 25.46%. These include sensor configurations such as 1, 7, 30, and 33, among others. All the above configurations correspond to the international 20–10 system. Table 1 shows the electrode configurations found in the analysis.

Table 1. Electrode configurations in AD analysis.

Ref.	Electrode Configuration
[4,5,7,8,12,13,16,51–59]	19
[29,49,60–65,65]	16
[6,20,35,66–71]	32
[3,72–76]	21
[42,50]	64
[2,23,77,78]	128
[36,37,46,79–83]	Less common configurations

3.3.2. Analysis of Activities in Patients for Clinical Data Collection

In the context of the early detection of AD, the careful examination of the activities of patients becomes crucially important. This detailed analysis of daily actions allows for detailed stratification and helps design a valuable instrument for identifying patterns and early signs of the disease.

The above highlights the relevance of tasks, specifically resting with eyes closed at 58.67%, as a fundamental strategy for acquiring EEG signals. This highlights the importance of these controlled conditions to obtain and record more precise and consistent brain signals to evaluate more precise patterns for feature extraction. According to [84], these activities evidence the synchronous activation of multiple cortical neurons that coordinate to produce signals of considerable amplitude.

Acquisition with eyes open is another popular technique with 9.64% of the reviewed works. Other activities, such as analyzing responses to sound and visual stimuli or cognitive tasks, are intended to evaluate cognitive abilities in older people, represented by 11.73%. This approach not only enables the early detection of patterns associated with Alzheimer's disease, but also facilitates the continuous monitoring of disease progression. Furthermore, these techniques allow the design of a plan for particular interventions and the development of specific therapies and, ultimately, improve the quality of life of those affected by this neurological condition [85].

The other activities involve more specific studies, such as analyzing signals before sleep or after some physical activity, which represent 1.53% and 2.04%, respectively. Table 2 shows some works that apply the various acquisition paradigms for EA classification.

Table 2. Techniques and activities in the acquisition of EEG signals.

Ref.	Acquisition Paradigm
[5,16,18,21,22,24,25,28,29,32,33,38,57–59,70,72,82,83,86,87]	Closed eyes
[2,6,12,27,35,42,47,54,71,73–75,77,79,88–90]	Open eyes
[20,26,33,80,91,92]	Responses to stimuli and cognitive tasks
[19,41,93]	Sleep
[48,49,64]	Physical activity

3.3.3. Sampling Frequencies of EEG Signals

The analysis of the sampling frequencies implemented in the 63 databases reveals that preferences and trends in this field have been obtained. Of the sample frequencies analyzed, it stands out that the most used is 256 Hz, present in a considerable 22.22% of the works reviewed. This choice may be because 256 Hz is a widely accepted standard frequency in the scientific community to accurately and efficiently acquire brain activity data. In second place, there is the frequency of 500 Hz, corresponding to 20.63% of the databases. Thirdly, the 1024 Hz frequency is present in 14.28% of the acquisitions. This choice relates to research seeking a high temporal resolution to capture brain signals. Two other sample rate values used in a similar percentage are 1 kHz and 200 Hz, present in 11.11% and 12.68% of the databases, respectively.

On the other hand, the highest and lowest sampling frequencies found were the 128 Hz frequency used in 6.34% of the cases, while the 5 kHz frequency was used in 3.17% of the databases. These frequencies are related to specific investigations that require very fast or slow sampling to detect particular phenomena in the brain. In the remaining 6.34%, some frequencies were used only once, such as 10 kHz, 2 kHz, and 83.3 Hz. Finally, it is essential to note that a small percentage of works did not report their sampling frequency, in 3.175% of the cases. This highlights the importance of transparency and adequate documentation in the presentation of research results since the sampling frequency is a crucial aspect of the interpretation and replicability of the studies. Table 3 shows the sampling frequencies most implemented in Alzheimer's detection.

Table 3. Sampling frequencies of EEG signals in the analyzed databases.

Ref.	Sampling Frequency
[3,5,7,13,16,28,30,40,51,54–59,63,70,72,73,75,76,87,88,93,94]	256 Hz
[6,12,20,32,36,37,47,69,71,92,95–97]	500 Hz
[8,18,23,49,56,58,60,62,65,66,87,93,98,99]	1024 Hz
[45,48,67,77]	1 kHz
[4,23,61,72,76,90,100]	128 Hz
[91,92]	5 kHz
[26,27,78,79,100]	Frequencies ***

Frequencies *** refer to frequencies of 10 kHz, 2 kHz, and 83.3 Hz.

3.4. Filtering Methods for Signal Processing

The studies analyzed show a significant preference for the combined use of Band-pass and Notch filters, with low cut-off frequencies ranging from 0.1 Hz to 1 Hz, with the most common option being 0.5 Hz, followed by 1 Hz. Finally, the most used low-cost frequency is 0.1 Hz.

On the other hand, high cut-off frequencies are between 30 Hz and 45 Hz. The most used high cut-off frequency is around 30 Hz. The second most used frequencies are close to 45 Hz. Table 4 shows the most common outage frequencies.

Table 4. Low and high cutoff frequencies in the use of filters.

Ref.	Cutoff Frequency
[15,16,23,25,36–41,44,48,49,51,57,60,67,101]	0.5 Hz high pass
[7,9,20,22,52,53,55,56,63,65,69,81,86,92,102,103,103]	1 Hz high pass
[8,12,19,33,34,50,83,99,104]	0.1 Hz high pass
[4,8,16,19,22,25,35,38,40,41,46,56,57,59,60,63,66,79,86,90,96,97,101,103,105]	30 Hz low pass
[7,15,18,23,48–50,53,55,65,70,80,81,89,95,102,106]	45 Hz low pass

Filter type selection varies widely among studies, reflecting differences in analytical needs and methodological preferences, with the most common being the Butterworth filter. Butterworth filters are valued for their flat response in the passband, allowing minimal distortion within the frequency range of interest.

Independent component analysis (ICA) is another frequently cited method used not only as a filter per se but as a technique for artifact removal, underscoring the importance of signal cleaning in EEG preprocessing. This technique is beneficial for identifying and removing signal the components associated with blinks, eye movements, and other non-brain artifacts. Additionally, the specific applications of filters such as Chebyshev, Wavelet, and finite impulse response (FIR) are identified, which are selected for their unique properties that may be particularly beneficial under certain study conditions, such as the need for filters with highly selective frequency responses or the ability to decompose the signal into frequency components for detailed analysis. The choice of filters and preprocessing techniques in EEG analysis is a critical decision that directly influences the quality and interpretation of the collected data. Table 5 shows the most common filter types in the processing of EEG signals for patients with AD.

Table 5. Summary of filters and techniques in AD studies.

Ref.	Filter
[3,4,6,12,14,15,17,26,34,36,46,47,52,62,70,78,91,97,102]	Butterworth
[9,20,33,35,48,59,75,81,83,95,106,107]	ICA
[44,78]	Chebyshev
[28,34]	Elliptical
[31,45]	Wavelet
[4,8,16,19,22,25,35,38,40,41,46,59,60,63,66,79,86,97,101,103]	FIR

3.5. Feature Extraction

The selection and analysis of features represent a fundamental pillar in studying EEG signals from people with AD. This process allows us to identify distinctive patterns in patients' neurological conditions and facilitate discrimination between the different cognitive states and stages of the disease. Through EEG processing and analysis, we seek to extract relevant information hidden in the raw signals, transforming the data into information applicable to diagnosis [108].

Analyzing the features in the time, frequency, and time–frequency domains is a critical task. Each domain offers a unique perspective on brain activity, from the temporality and amplitude of signals to their spectral composition and the interaction between different frequencies over time. It has been determined that 36.49% of the reviewed works focus on analyzing the frequency domain. As for the most-used frequency feature, it is the calculation of power spectral density (PSD) [3,36–38,56,78,95,106]. Another feature in this domain is the coefficients of the Fourier transform [34,58,87]. Likewise, research that focuses on the temporal features of EEG signals makes up 22.97% of the analyzed works. Among the most used time features are statistical indicators such as mean, variance, kurtosis, skewness, and standard deviation [16,17,41,44,109]. Another of the most used features is entropy [22,30,44,76] and principal component analysis [43,47,61,70]. Furthermore, studies that integrate analysis in both the time and frequency domains represent

16.22%. By combining both domains, the calculation of the spectral power and entropy is used [15,19,67,75,83,96,102]. The PSD was also used together with the raw signal [5] or it was used together with the fractal dimension [59,73].

Brain connectivity, which examines the interactions between various brain regions, constitutes 10.81% of the works. Only 6.76% of the research jointly addresses frequency and brain connectivity or time. The most popular features of brain connectivity are network resilience, network clustering coefficient, or versatility [4,18,33,57,62]. Other implemented features are phase locking value and phase lag index [33,77,100]. Finally, a segment equivalent to 6.76% is categorized under various methodologies, including innovative or less conventional approaches in EEG analysis, such as 2D images to save the spatial structure, multiple color channels to represent the spectral dimension [32], and the writing features [42,81]. The left temporal volume and the cortical thickness of the frontal, parietal, and occipital lobes were also used [54].

3.6. Classification Techniques Approach for Alzheimer Detection

Different techniques performed in diagnosing Alzheimer's using classification models are presented in this section. According to [110], patients with Alzheimer's manifest neurological changes that cause physical changes, which is detected through brain signals. With this, classification techniques help detect these symptoms. According to the analysis of the 109 articles in the literature, different techniques associated with the classification of signals have been found. Figure 2 displays the most used classification techniques in the disease of Alzheimer's.
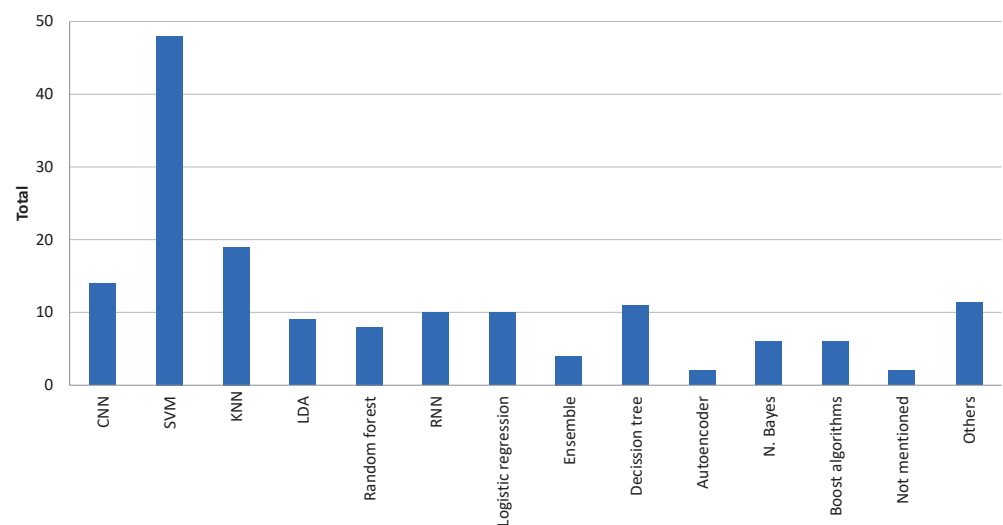
Figure 2. Classification techniques most used in the diagnosis of Alzheimer.

It is found that support vector machine (SVM) is the most popular technique used with around 30.57% of the works. It can handle nonlinear data using kernel functions, allowing complex relationships between features to be represented and improving the classification accuracy [111]. Then, the K-nearest neighbors (KNN) algorithm presents about 12.1% of usage according to the literature. This finding is noteworthy as both methods are supervised training algorithms commonly employed in ML for classification tasks.

Likewise, in recent years, the use of convolutional neural networks (CNN) has been increasing. Among the articles studied, its use is around 8.91%. The tendency to integrate CNN is because they can automatically learn relevant features of the images or input signals using the convolution and pooling layers. This allows the model to autonomously identify complex and significant patterns in the data [112]. On the other hand, decision tree algorithms (DT) present about 7% in the analysis of AD. The recurrent neural network (RNN) algorithms are another trend technique, which represent 6.36%. RNNs benefit

from directly operating on raw data, eliminating the need for a feature extraction step and providing faster responses [113].

One of the current deep learning techniques implemented is the graph neural network (GNNs). Among the analyzed works, only 2.8% used GNN networks. Linear regression algorithms are used in 6.36% of the analyzed works. Random forest (RF) is also another alternative used for extracting features with 5.73%. Other works, such as boost algorithms or latent Dirichlet allocation present about 3.82% and 5.73%, respectively. Another technique employed are the Bayesian-based algorithms, that are presented in 3.82%. Other conventional and not specified works represents the 6.36% of the analyzed works. Finally, ensemble algorithms are used in 2.54% and autoencoder algorithms in 1.27%. Table 6 shows the works where each of the classifiers were implemented.

Table 6. Deep and machine learning classifiers used for EA detection.

Ref.	Classification Technique
[2,4,6,7,13,15–18,20,25,28,29,31,34,36,37,41,44,46,49,54–57,59,62,67,68,70,73,75,78,80,81,83,86,88,89,92,96,103,105,106,109,114]	SVM
[7,13,15,25–27,34,43,44,46,56,57,59,73,89,94,99,104,105]	KNN
[3,7,8,32,38,39,42,45,69,79,90,93,107]	CNN
[7,15,21,34,55,56,58,59,73,78,87]	DT
[24,34,40,50,52,55,61,64,71,91]	RNN
[12,22,41,51,66,78,82,83,97,109]	Linear regression
[1,15,23,33,34,47,78,81,89]	RF
[57,78,81]	Boost
[34–37,44,52,76,83,95]	Latent Dirichlet allocation
[7,15,34,59,83,98]	Bayesian
[7,63,73,83]	Ensemble
[41,109]	Autoencoders
[77,100,115]	GNN
[5,60,65,72,101,102,116]	Other works

3.7. Evaluation Metrics

Accuracy shows the percentage of cases that the model got right. According to Figure 3, it is the most used metric, followed by precision and specificity. Although accuracy is the most used metric, it does not mean that it is the most representative metric of the model. As a complement to accuracy, it is recommended to use precision, recall, and F1 to represent the model regarding prediction quality, quantity, and the visualization of the types of errors. The 55% of the articles use at least three of the metrics, while 20% do not indicate the evaluation metrics [68,71,74,80,82,91,94,99,116].

3.8. Results in the Classification Achieved

In addition to the diversity in methodological approaches, it is crucial to highlight the classification percentages achieved in each domain, which provides insight into the effectiveness of the different techniques. Studies focused on the frequency domain achieved a classification average of 86.82%, while those focused on temporal analysis achieved a similar average of 86.81%. This suggests that both approaches, regardless of their orientation towards frequency spectrum or temporal features, offer comparable results in terms of classification ability. On the other hand, research exploring brain connectivity showed an average classification of 88.58%, indicating a slight advantage in applying this approach to discern between different conditions or brain states. Most notably, studies that combined analyses over time and frequency presented an average classification of 89.72%, suggesting that integrating multiple dimensions of analysis provide a more complete and detailed understanding of brain activity, reflected in a higher classification accuracy. Papers incorporating time, frequency, and brain connectivity analysis achieved an average classification of 89.07%. Finally, the methods classified as diverse achieved the highest average classification, with 92.575%.

Evaluation metrics
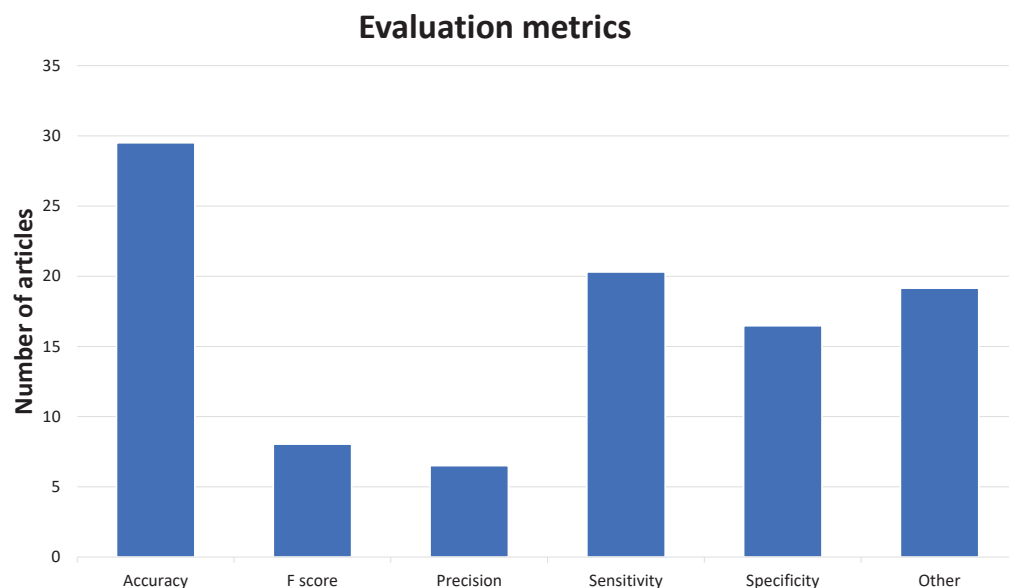
Figure 3. Comparison of the frequency of use of the various evaluation metrics in scientific articles.

4. Discussion

Table 7 highlights the main works analyzed, showing the various classification models used. In addition to selecting specific filtering ranges, sample size and rankings were also obtained.

Table 7. Summary of the main works analyzed.

Reference	N° Volunteers	Classification Model	Filtering Range (Hz)	Performance
[55]	11 healthy, 8 MCI, 19 AD	SVM with radial kernel, multilayer perceptron (MLP) and DT	1–40	DT 94.88% SVM 95.10% MLP 95.55%
[70]	120 healthy and 175 EA	SVM	0.2–47	95%
[64]	28 healthy and 7 MCI	Bidirectional LSTM	3–30	91.93%
[45]	15 healthy and 16 MCI	CNN	8–30	79.66%
[13]	16 healthy and 11 MCI	GRU	0–32	96.91%
[14]	16 healthy and 11 MCI	LSTM	0.5–50	96.41%
[18]	21 healthy and 28 MCI	SVM with Gaussian kernel	0–40	86.6%
[89]	89 EA	SVM with linear and Gaussian kernels, RF and KNN	0.5–45	RMSE of 1.682 between predicted and actual MMSE values when measuring disease progression
[75]	13 healthy, 16 MCI, 15 EA	SVM with Gaussian kernel	0.5–65	88%
[46]	50 healthy and 50 EA	SVM and KNN	0.5–30	94%

Table 7. *Cont.*

Reference	N° Volunteers	Classification Model	Filtering Range (Hz)	Performance
[107]	Synthetic EEG signals were generated from 8 healthy patients and 1 using EA generative adversarial networks and variational autoencoders	EEGNet, DeepConvNet, and EEGNet SSVEP	4–40	50.2%
[73]	15 healthy, 16 MCI and 16 EA	KNN	Iterative filtering	92%
[78]	17 healthy and 19 AD	Logistic regression, SVM, RF, extra trees, DT, stochastic gradient descent, Ada boosting, and gradient boosting	0.4–115 Hz	95.6%
[27]	20 healthy and 20 EA	KNN	2–680	90%
[8]	23 healthy, 56 MCI and 63 AD	CNN	0.1–30	80%
[61]	15 healthy and 20 EA	LSTM	-	97.9%
[81]	39 healthy and 40 MCI	SVM with Gaussian kernel, RF and Xgboost	1–45	XGboost 87.34% SVM 93.7% RF 84.81%
[19]	20 healthy and 20 EA	Cubic SVM and bidirectional GRU (Bi-GRU)	0.1–30	Cubic SVM 90.51% Bi-GRU 93.46%
[7]	11 healthy, 8 MCI and 19 EA	CNN, ensemble, KNN, SVM, naive Bayes, discriminant analysis and DT	1–40	57%
[102]	9 healthy, 6 MCI and 11 EA	MLP	1–45	82.5%
[100]	20 healthy and 20 AD	GNN	0.1–51	92%

Due to the nonlinear nature of EEG signals, models implemented in nature have proven to be robust in terms of their accuracy, since at least a classification model is expected to present a performance of at least 80% based on its precision. With this, it is possible to observe that SVMs are commonly used models for these tasks due to their kernel-based architecture. Furthermore, recent years have seen the implementation of RNN-based classification models, particularly with GRU and LSTM configurations. These models report at least 92% accuracy according to Table 7. It is important to note that the tendency of these models to present prominent results is based on the treatment of the signal and configuration of the parameters, so the remaining models can improve their accuracy if they are correctly adapted.

The analysis of EEG signals for the early diagnosis of the AD using machine and deep learning highlights the importance of carefully selecting databases and analysis methodologies. The adequate preparation and the choice of clear diagnostic criteria are essential to avoid bias in the results. There is a preference for using 19-electrode configurations and selecting specific activities such as rest periods with eyes closed. Different EEG electrode configurations can significantly affect classification results. High-density configurations, which use more electrodes, offer better spatial resolution and brain coverage, allowing for the more precise and subtle details of brain activity to be captured. This may improve the accuracy of diagnoses and the identification of robust features for the detection of AD [67]. However, these configurations also have disadvantages, such as greater complexity, which could make the classification task more complex, longer configuration time, patient discomfort, and higher economic and computational costs [117]. On the other

hand, configurations with fewer electrodes, although more practical and comfortable, can limit the amount of information available and affect the effectiveness of machine and deep learning algorithms. Variability in electrode configurations introduces challenges when comparing results between studies, as different configurations may capture the different aspects of brain activity [118]. Given the above, it is important to standardize electrode configurations or provide detailed analyses on how these configurations can affect the results to improve the comparability and replicability of studies in the field.

Demographic data, such as age and gender distribution, can significantly influence the results of EEG studies used to diagnose AD. The information in this paper shows that notable differences in the mean age of participants were observed between the groups of healthy volunteers, patients with MCI, and patients with Alzheimer's, reflecting the progressive nature of the disease. Specifically, Alzheimer's disease patients had a higher mean age (73.66 years) compared to healthy volunteers (68.53 years) and MCI patients (70.52 years). These age differences may affect EEG results, as aging may influence brain activity patterns regardless of the presence of AD.

Regarding gender, the general distribution showed a slight majority of women (53.57%) in the databases analyzed. Furthermore, the proportion of women and men varied between the different cohort groups, with a higher proportion of women in the healthy volunteer and Alzheimer's patient groups. This gender distribution may be relevant to the results of EEG studies, as there are gender differences in the incidence and progression of AD, which may influence the patterns of brain activity recorded.

The average educational level also varied between groups: it was higher in healthy volunteers than in patients with MCI and Alzheimer's. Education has been identified as a factor that can influence cognitive reserve and, therefore, the results of EEG studies. People with more education may show different patterns of brain activity due to a greater capacity for cognitive compensation against the effects of AD.

The different methods of EEG data acquisition, such as being awake with eyes open, awake with eyes closed, asleep, and responses to cognitive stimuli and tasks, may influence the reliability of the data for diagnosing AD. The most commonly used method is being awake with eyes closed due to its ability to provide a stable baseline and minimize eye noise, thereby facilitating the identification of brain activity patterns indicative of AD, such as generalized slowing of brain waves [119]. This approach is particularly useful for detecting the changes in brain connectivity and complexity characteristic of AD. However, other methods, such as responses to stimuli and cognitive tasks, can offer additional information about cognitive decline and the dynamics of neural networks, although they require more complex experimental designs and are more susceptible to individual variations. A combination of these methods is suggested to obtain a more complete and reliable assessment of brain status in AD.

Regarding the filtering and analysis of the signals, the combination of band-pass and notch filters stands out as a way to maintain valuable information and eliminate noise. This approach is complemented by analysis in the time and frequency domains, prioritizing PSD and descriptive statistics to identify patterns related to Alzheimer's. Exploring brain connectivity also provides deep insights, suggesting that a multidimensional analysis significantly improves classification.

The choice and calibration of classifiers play a crucial role in the effectiveness of the diagnosis. Different classifiers produce varying results on the same data set due to how their parameters are tuned, underscoring the need for careful selection and optimization. Adequate adaptation of the classifier to the features of the dataset is decisive in achieving high classification rates. This aspect and an evaluation of metrics beyond simple accuracy offer a complete view of the classifier's performance and highlight the importance of advanced techniques for artifact removal and feature selection.

Despite its apparent simplicity, accuracy is considered the most used metric as an indicator of success. Accuracy provides a general measure of model performance, indicating the proportion of correct predictions over the total number of cases analyzed. In

addition, it is complemented by sensitivity and specificity. Sensitivity measures the model's ability to correctly identify subjects with AD, which is crucial for early diagnosis and timely treatment. On the other hand, specificity evaluates the model's ability to correctly identify healthy subjects, avoiding false positives that could cause unnecessary anxiety and additional procedures.

The Figure 4 shows that SVM techniques are the predominant technique in the analysis of Alzheimer's. In addition, band-pass filters are the most commonly used when data acquisition is required with eyes-closed patients. It also is observed that the bands with relevant information are those ranging from 1 to 32 Hz. This suggests that the identification of patterns in resting or relaxed conditions is found with this model.
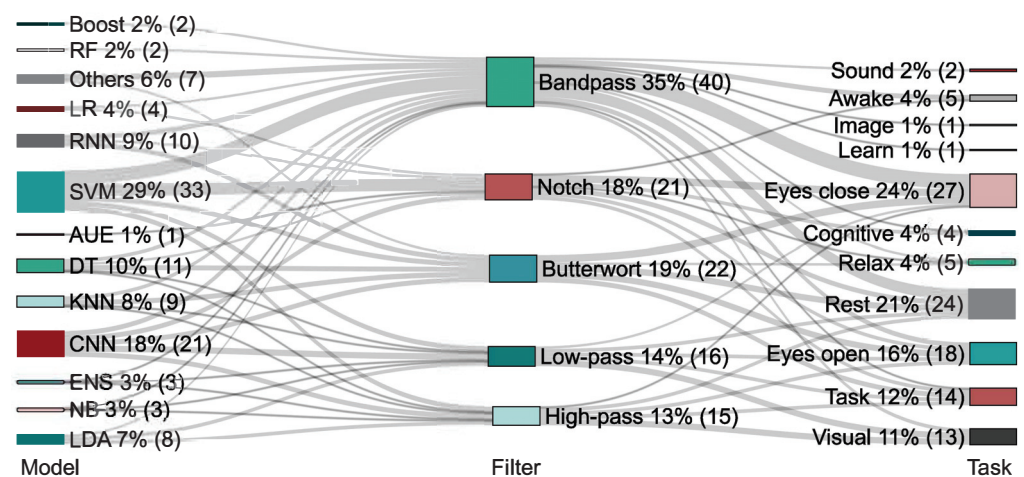
Figure 4. Sankey plot analysis of AI techniques in acquisition tasks.

This analysis suggests that the approaches combining analyses across time, frequency, and brain connectivity, supported by a well-prepared database and the choice of appropriate classifiers, provide the most detailed understanding of brain activity and the greatest accuracy in the classification. Integrating these elements strengthens the ability to detect Alzheimer's in its early stages and improves the development of artificial intelligence models that significantly contribute to combating this disease. In summary, the research highlights the need for a careful approach to data preparation, method selection, and classifier optimization to advance the use of artificial intelligence technologies in ongoing efforts to tackle Alzheimer's disease.

5. Conclusions

The review of recent works in artificial intelligence applied to detecting AD highlights the importance of these technologies in understanding this condition. The studies analyzed have shown promising results, significantly contributing to understanding the disease and developing advanced methodologies for its early detection. In particular, it has been shown that signal processing plays an essential role in improving data collection, highlighting the importance of adjusting data acquisition to specific frequency bands for the design of more accurate and efficient algorithms.

The proposal to adopt strategies that integrate various methodologies promises to increase the effectiveness of traditional methods and to revolutionize the current paradigm towards a more precise and robust classification of EEG signals in people with Alzheimer's. These innovations open new directions in research and development, facilitating the personalization of treatment and disease management with information obtained through advanced AI techniques. In the long term, these technologies provide more accessible and reliable diagnostic tools for early detection.

The importance of the careful analysis of EEG signals using machine and deep learning is highlighted, underlining the need to select databases and analysis methodologies to

avoid biases appropriately. The preparation of data and choosing clear diagnostic criteria are essential. The demographic conformation of the databases and the selection of filtering and analysis methods, such as the combination of band-pass and notch filters, and an analysis in the time and frequency domains, are essential to identify patterns related to Alzheimer's. Furthermore, the precise adaptation and calibration of classifiers highlight the need for careful selection and meticulous optimization to achieve high classification rates.

The combination of detailed analysis in time, frequency, and brain connectivity, supported by a well-prepared database and adequately selected and tuned classifiers, provides a deep understanding of brain activity and the highest classification accuracy. This research emphasizes the need for a rigorous approach in data preparation, methodology selection, and classifier optimization to advance the application of AI technologies in the fight against Alzheimer's, demonstrating the transformative potential of these technologies in personalized medicine and patient management.

The generalization of these findings presents several challenges, given that the manifestation of Alzheimer's can vary significantly depending on genetic, lifestyle, and environmental factors. First, the studies reviewed often use cohorts that may not represent global genetic diversity, limiting the applicability of the results to populations with different backgrounds. Additionally, lifestyle factors such as diet, physical activity level, and sleep habits can influence brain health and EEG patterns. Differences in these factors between the populations studied, and other populations may lead to variations in results and reduce the generalizability of the findings. Environmental factors, such as exposure to toxins, level of education, and access to medical care, also play a crucial role in the manifestation of Alzheimer's. These factors may modify disease progression and associated EEG patterns, making the models developed in one specific context not directly applicable to other settings.

It is important to note that many studies need to detail these aspects in the description of their populations, which adds a layer of uncertainty about the generalizability of the findings. The lack of specific information on genetic, lifestyle, and environmental factors in the cohorts studied may limit the interpretation and application of the results to broader contexts. Although the findings of our review provide a valuable basis for the EEG-based diagnosis of AD, their generalization to different populations requires the careful consideration of multiple variables not anticipated in this review. To improve generalizability, future research should include more diverse cohorts and consider these factors when developing and validating diagnostic models.

Finally, according to our review, a key trend is the application of advanced deep learning techniques, which have shown great potential but are still relatively underexplored compared to more traditional methods such as CNNs, RNNs, and GNNs.

Another promising area is the development of new feature extraction and filtering methods. Advanced preprocessing techniques, such as adaptive filtering, can improve the quality of EEG signals. Feature extraction using nonlinear and multifractal methods can also capture complex brain dynamics indicative of AD. Integrating these techniques with deep learning models can significantly improve the accuracy and effectiveness of the diagnosis.

One of the main challenges for applying deep and machine learning in AD diagnosis is the need for large labeled datasets, which are essential for effectively training deep learning models. Variability in electrode configurations and data acquisition protocols between different studies must be more consistent, making comparing results and replicating studies difficult. Additionally, EEG signals are susceptible to artifacts and noise from various sources, such as eye and muscle movements, which complicates effectively removing these artifacts without losing relevant information.

Another limitation of deep learning models, often called black boxes, is their interpretability. This makes it difficult to understand how and why a model makes certain decisions, a crucial aspect of medical applications. Generalizing the models to different populations is also problematic due to genetic, lifestyle, and environmental differences

that may need to be adequately represented in the study cohorts. The computational requirements to train and deploy deep learning models are significant, requiring specialized hardware and access to high-performance computing infrastructures.

While deep and machine learning techniques present exciting opportunities for EEG-based AD detection, their application is an ongoing area of research and development. Researchers should continue to focus on optimizing and adapting these emerging technologies, as well as developing new feature extraction and filtering methods, to advance the accuracy and effectiveness of Alzheimer's disease diagnosis.

Author Contributions: Conceptualization, M.A.; Data curation, M.A. and J.M.Á.-A.; Formal Analysis, M.A. and L.M.S.-R.; Investigation, M.A., L.M.S.-R., J.R.-R. and J.M.Á.-A.; Methodology, M.A., L.M.S.-R., J.R.-R. and J.M.Á.-A.; Project administration, J.R.-R.; Resources, J.R.-R.; Supervision, M.A. and J.R.-R.; Validation M.A. and J.R-R.; Visualization, J.R.-R.; Writing—original draft, M.A., L.M.S.-R., J.R.-R. and J.M.Á.-A.; Writing—review and editing, M.A., L.M.S.-R., J.R.-R. and J.M.Á.-A. All authors have read and agreed to the published version of the manuscript.

Conflicts of Interest: The authors declare no conflicts of interest.

References

1. Dauwan, M.; Zande, J.J.; Dellen, E.; Sommer, I.E.; Scheltens, P.; Lemstra, A.W.; Stam, C.J. Random forest to differentiate dementia with Lewy bodies from Alzheimer's disease. *Alzheimer's Dement. Diagn. Assess. Dis. Monit.* **2016**, *4*, 99–106. [CrossRef]
2. Cao, J.; Zhao, Y.; Shan, X.; Blackburn, D.; Wei, J.; Erkoyuncu, J.A.; Chen, L.; Sarrigiannis, P.G. Ultra-high-resolution time-frequency analysis of EEG to characterise brain functional connectivity with the application in Alzheimer's disease. *J. Neural Eng.* **2022**, *19*, 046034. [CrossRef]
3. Sidulova, M.; Nehme, N.; Park, C.H. Towards Explainable Image Analysis for Alzheimer's Disease and Mild Cognitive Impairment Diagnosis. In Proceedings of the 2021 IEEE Applied Imagery Pattern Recognition Workshop (AIPR), Washington, DC, USA, 12–14 October 2021. [CrossRef]
4. Duan, F.; Huang, Z.; Sun, Z.; Zhang, Y.; Zhao, Q.; Cichocki, A.; Yang, Z.; Sole-Casals, J. Topological Network Analysis of Early Alzheimer's Disease Based on Resting-State EEG. *IEEE Trans. Neural Syst. Rehabil. Eng.* **2020**, *28*, 2164–2172. [CrossRef]
5. Kashefpoor, M.; Rabbani, H.; Barekatain, M. Supervised dictionary learning of EEG signals for mild cognitive impairment diagnosis. *Biomed. Signal Process. Control.* **2019**, *53*, 101559. [CrossRef]
6. McBride, J.C.; Zhao, X.; Munro, N.B.; Jicha, G.A.; Schmitt, F.A.; Kryscio, R.J.; Smith, C.D.; Jiang, Y. Sugihara causality analysis of scalp EEG for detection of early Alzheimer's disease. *NeuroImage Clin.* **2015**, *7*, 258–265. [CrossRef] [PubMed]
7. Araújo, T.; Teixeira, J.P.; Rodrigues, P.M. Smart-Data-Driven System for Alzheimer Disease Detection through Electroencephalographic Signals. *Bioengineering* **2022**, *9*, 141. [CrossRef] [PubMed]
8. Morabito, F.C.; Campolo, M.; Ieracitano, C.; Ebadi, J.M.; Bonanno, L.; Bramanti, A.; Desalvo, S.; Mammone, N.; Bramanti, P. Deep convolutional neural networks for classification of mild cognitive impaired and Alzheimer's disease patients from scalp EEG recordings. In Proceedings of the 2016 IEEE 2nd International Forum on Research and Technologies for Society and Industry Leveraging a better tomorrow (RTSI), Bologna, Italy, 7–9 September 2016.
9. Drage, R.; Escudero, J.; Parra, M.A.; Scally, B.; Anghinah, R.; Araujo, A.V.L.D.; Basile, L.F.; Abasolo, D. A novel deep learning approach using AlexNet for the classification of electroencephalograms in Alzheimer's Disease and Mild Cognitive Impairment. In Proceedings of the 2022 44th Annual International Conference of the IEEE Engineering in Medicine & Biology Society (EMBC), Glasgow, UK, 11–15 July 2022.
10. Nematzadeh, S.; Kiani, F.; Torkamanian-Afshar, M.; Aydin, N. Tuning hyperparameters of machine learning algorithms and deep neural networks using metaheuristics: A bioinformatics study on biomedical and biological cases. *Comput. Biol. Chem.* **2022**, *97*, 107619. [CrossRef] [PubMed]
11. Grueso, S.; Viejo-Sobera, R. Machine learning methods for predicting progression from mild cognitive impairment to Alzheimer's disease dementia: A systematic review. *Alzheimer's Res. Ther.* **2021**, *13*, 162. [CrossRef] [PubMed]
12. Farina, F.; Emek-Savaş, D.; Rueda-Delgado, L.; Boyle, R.; Kiiski, H.; Yener, G.; Whelan, R. A comparison of resting state EEG and structural MRI for classifying Alzheimer's disease and mild cognitive impairment. *NeuroImage* **2020**, *215*, 116795. [CrossRef]
13. Alvi, A.M.; Siuly, S.; Wang, H.; Wang, K.; Whittaker, F. A deep learning based framework for diagnosis of mild cognitive impairment. *Knowl.-Based Syst.* **2022**, *248*, 108815. [CrossRef]
14. Alvi, A.M.; Siuly, S.; Wang, H. A Long Short-Term Memory Based Framework for Early Detection of Mild Cognitive Impairment From EEG Signals. *IEEE Trans. Emerg. Top. Comput. Intell.* **2023**, *7*, 375–388. [CrossRef]

15. Miltiadous, A.; Tzimourta, K.D.; Giannakeas, N.; Tsipouras, M.G.; Afrantou, T.; Ioannidis, P.; Tzallas, A.T. Alzheimer's Disease and Frontotemporal Dementia: A Robust Classification Method of EEG Signals and a Comparison of Validation Methods. *Diagnostics* **2021**, *11*, 1437. [CrossRef]

16. Yin, J.; Cao, J.; Siuly, S.; Wang, H. An Integrated MCI Detection Framework Based on Spectral-temporal Analysis. *Int. J. Autom. Comput.* **2019**, *16*, 786–799. [CrossRef]

17. Seifallahi, M.; Mehraban, A.H.; Galvin, J.E.; Ghoraani, B. Alzheimer's Disease Detection Using Comprehensive Analysis of Timed Up and Go Test via Kinect V.2 Camera and Machine Learning. *IEEE Trans. Neural Syst. Rehabil. Eng.* **2022**, *30*, 1589–1600. [CrossRef]

18. Li, X.; Yang, C.; Xie, P.; Han, Y.; Su, R.; Li, Z.; Liu, Y. The diagnosis of amnestic mild cognitive impairment by combining the characteristics of brain functional network and support vector machine classifier. *J. Neurosci. Methods* **2021**, *363*, 109334. [CrossRef]

19. Geng, D.; Wang, C.; Fu, Z.; Zhang, Y.; Yang, K.; An, H. Sleep EEG-Based Approach to Detect Mild Cognitive Impairment. *Front. Aging Neurosci.* **2022**, *14*, 865558. [CrossRef]

20. San-Martin, R.; Johns, E.; Quispe Mamani, G.; Tavares, G.; Phillips, N.A.; Fraga, F.J. A method for diagnosis support of mild cognitive impairment through EEG rhythms source location during working memory tasks. *Biomed. Signal Process. Control.* **2021**, *66*, 102499. [CrossRef]

21. Oltu, B.; Akşahin, M.F.; Kibaroğlu, S. A novel electroencephalography based approach for Alzheimer's disease and mild cognitive impairment detection. *Biomed. Signal Process. Control.* **2021**, *63*, 102223. [CrossRef]

22. Rutkowski, T.M.; Abe, M.S.; Komendzinski, T.; Otake-Matsuura, M. Older adult mild cognitive impairment prediction from multiscale entropy EEG patterns in reminiscent interior image working memory paradigm. In Proceedings of the 2021 43rd Annual International Conference of the IEEE Engineering in Medicine & Biology Society (EMBC), Virtual, 1–5 November 2021.

23. Moguilner, S.; Birba, A.; Fittipaldi, S.; Gonzalez-Campo, C.; Tagliazucchi, E.; Reyes, P.; Matallana, D.; Parra, M.A.; Slachevsky, A.; Farías, G.; et al. Multi-feature computational framework for combined signatures of dementia in underrepresented settings. *J. Neural Eng.* **2022**, *19*, 046048. [CrossRef]

24. Fan, C.C.; Xie, H.; Peng, L.; Yang, H.; Ni, Z.L.; Wang, G.; Zhou, Y.J.; Chen, S.; Fang, Z.; Huang, S.; et al. Group Feature Learning and Domain Adversarial Neural Network for aMCI Diagnosis System Based on EEG. In Proceedings of the 2021 IEEE International Conference on Robotics and Automation (ICRA), Xi'an, China, 30 May–5 June 2021; pp. 9340–9346. [CrossRef]

25. Siuly, S.; Alcin, O.F.; Kabir, E.; Sengur, A.; Wang, H.; Zhang, Y.; Whittaker, F. A new framework for automatic detection of patients with mild cognitive impairment using resting-state EEG signals. *IEEE Trans. Neural Syst. Rehabil. Eng.* **2020**, *28*, 1966–1976. [CrossRef]

26. Durongbhan, P.; Zhao, Y.; Chen, L.; Zis, P.; De Marco, M.; Unwin, Z.C.; Venneri, A.; He, X.; Li, S.; Zhao, Y.; et al. A Dementia Classification Framework Using Frequency and Time-Frequency Features Based on EEG Signals. *IEEE Trans. Neural Syst. Rehabil. Eng.* **2019**, *27*, 826–835. [CrossRef] [PubMed]

27. Zhao, Y.; Zhao, Y.; Durongbhan, P.; Chen, L.; Liu, J.; Billings, S.A.; Zis, P.; Unwin, Z.C.; De Marco, M.; Venneri, A.; et al. Imaging of Nonlinear and Dynamic Functional Brain Connectivity Based on EEG Recordings With the Application on the Diagnosis of Alzheimer's Disease. *IEEE Trans. Med. Imaging* **2020**, *39*, 1571–1581. [CrossRef] [PubMed]

28. Trambaiolli, L.R.; Spolaôr, N.; Lorena, A.C.; Anghinah, R.; Sato, J.R. Feature selection before EEG classification supports the diagnosis of Alzheimer's disease. *Clin. Neurophysiol.* **2017**, *128*, 2058–2067. [CrossRef] [PubMed]

29. Nobukawa, S.; Yamanishi, T.; Kasakawa, S.; Nishimura, H.; Kikuchi, M.; Takahashi, T. Classification Methods Based on Complexity and Synchronization of Electroencephalography Signals in Alzheimer's Disease. *Front. Psychiatry* **2020**, *11*, 255. [CrossRef] [PubMed]

30. Fruehwirt, W.; Zhang, P.; Gerstgrasser, M.; Grossegger, D.; Schmidt, R.; Benke, T.; Dal-Bianco, P.; Ransmayr, G.; Weydemann, L.; Garn, H.; et al. Bayesian Gaussian Process Classification from Event-Related Brain Potentials in Alzheimer's Disease. In *Proceedings of the Artificial Intelligence in Medicine*; ten Teije, A., Popow, C., Holmes, J.H., Sacchi, L., Eds.; Springer International Publishing: Cham, Switzerland, 2017; pp. 65–75. [CrossRef]

31. Kanda, P.A.M.; Trambaiolli, L.R.; Lorena, A.C.; Fraga, F.J.; Basile, L.F.I.; Nitrini, R.; Anghinah, R. Clinician's road map to wavelet EEG as an Alzheimer's disease biomarker. *Clin. EEG Neurosci.* **2014**, *45*, 104–112. [CrossRef] [PubMed]

32. Bi, X.; Wang, H. Early Alzheimer's disease diagnosis based on EEG spectral images using deep learning. *Neural Netw.* **2019**, *114*, 119–135. [CrossRef] [PubMed]

33. Youssef, N.; Xiao, S.; Liu, M.; Lian, H.; Li, R.; Chen, X.; Zhang, W.; Zheng, X.; Li, Y.; Li, Y. Functional brain networks in mild cognitive impairment based on resting electroencephalography signals. *Front. Comput. Neurosci.* **2021**, *15*, 698386. [CrossRef]

34. AlSharabi, K.; Bin Salamah, Y.; Abdurraqeeb, A.M.; Aljalal, M.; Alturki, F.A. EEG Signal Processing for Alzheimer's Disorders Using Discrete Wavelet Transform and Machine Learning Approaches. *IEEE Access* **2022**, *10*, 89781–89797. [CrossRef]

35. Zeng, H.; Fang, X.; Zhao, Y.; Wu, J.; Li, M.; Zheng, H.; Xu, F.; Pan, D.; Dai, G. EMCI: A novel EEG-based mental workload assessment index of mild cognitive impairment. *IEEE Trans. Biomed. Circuits Syst.* **2022**, *16*, 902–914. [CrossRef]

36. Trinh, T.T.; Tsai, C.F.; Hsiao, Y.T.; Lee, C.Y.; Wu, C.T.; Liu, Y.H. Identifying Individuals With Mild Cognitive Impairment Using Working Memory-Induced Intra-Subject Variability of Resting-State EEGs. *Front. Comput. Neurosci.* **2021**, *15*, 700467. [CrossRef]

37. Hsiao, Y.T.; Tsai, C.F.; Wu, C.T.; Trinh, T.T.; Lee, C.Y.; Liu, Y.H. MCI Detection Using Kernel Eigen-Relative-Power Features of EEG Signals. *Actuators* **2021**, *10*, 152. [CrossRef]

38. Ieracitano, C.; Mammone, N.; Bramanti, A.; Hussain, A.; Morabito, F.C. A Convolutional Neural Network approach for classification of dementia stages based on 2D-spectral representation of EEG recordings. *Neurocomputing* **2019**, *323*, 96–107. [CrossRef]

39. Ieracitano, C.; Mammone, N.; Hussain, A.; Morabito, F.C. A Convolutional Neural Network based self-learning approach for classifying neurodegenerative states from EEG signals in dementia. In Proceedings of the 2020 International Joint Conference on Neural Networks (IJCNN), Glasgow, UK, 19–24 July 2020.

40. Capecci, E.; Morabito, F.C.; Campolo, M.; Mammone, N.; Labate, D.; Kasabov, N. A feasibility study of using the NeuCube spiking neural network architecture for modelling Alzheimer's disease EEG data. In *Advances in Neural Networks: Computational and Theoretical Issues*; Smart Innovation, Systems and Technologies; Springer International Publishing: Cham, Switzerland, 2015; pp. 159–172.

41. Ieracitano, C.; Mammone, N.; Bramanti, A.; Marino, S.; Hussain, A.; Morabito, F.C. A time-frequency based machine learning system for brain states classification via EEG signal processing. In Proceedings of the 2019 International Joint Conference on Neural Networks (IJCNN), Budapest, Hungary, 14–19 July 2019.

42. You, Z.; Zeng, R.; Lan, X.; Ren, H.; You, Z.; Shi, X.; Zhao, S.; Guo, Y.; Jiang, X.; Hu, X. Alzheimer's Disease Classification With a Cascade Neural Network. *Front. Public Health* **2020**, *8*, 584387. [CrossRef]

43. Biagetti, G.; Crippa, P.; Falaschetti, L.; Luzzi, S.; Turchetti, C. Classification of Alzheimer's Disease from EEG Signal Using Robust-PCA Feature Extraction. *Procedia Comput. Sci.* **2021**, *192*, 3114–3122. [CrossRef]

44. Safi, M.S.; Safi, S.M.M. Early detection of Alzheimer's disease from EEG signals using Hjorth parameters. *Biomed. Signal Process. Control.* **2021**, *65*, 102338. [CrossRef]

45. Wei, J.; Xiao, W.; Zhang, S.; Wang, P. Mild cognitive impairment classification convolutional neural network with attention mechanism. In Proceedings of the 2020 IEEE 16th International Conference on Control & Automation (ICCA), Singapore, 9–11 October 2020.

46. Bairagi, V. EEG signal analysis for early diagnosis of Alzheimer disease using spectral and wavelet based features. *Int. J. Inf. Technol.* **2018**, *10*, 403–412. [CrossRef]

47. Chouvarda, I.; Mpaltadoros, L.; Boutziona, I.; Tsakonas, G.; Tsolaki, M.; Diamantaras, K. Exploring Classification in Open and Closed Eyes EEG Data for People with Cognitive Disorders. In *Proceedings of the 15th International Joint Conference on Biomedical Engineering Systems and Technologies*; SCITEPRESS—Science and Technology Publications: Setubal, Portugal, 2022. [CrossRef]

48. Li, X.; Zhou, H.; Su, R.; Kang, J.; Sun, Y.; Yuan, Y.; Han, Y.; Chen, X.; Xie, P.; Wang, Y.; et al. A mild cognitive impairment diagnostic model based on IAAFT and BiLSTM. *Biomed. Signal Process. Control.* **2023**, *80*, 104349. [CrossRef]

49. Song, Z.; Deng, B.; Wang, J.; Wang, R. Biomarkers for Alzheimer's Disease Defined by a Novel Brain Functional Network Measure. *IEEE Trans. Biomed. Eng.* **2019**, *66*, 41–49. [CrossRef]

50. Sibilano, E.; Brunetti, A.; Buongiorno, D.; Lassi, M.; Grippo, A.; Bessi, V.; Micera, S.; Mazzoni, A.; Bevilacqua, V. An attention-based deep learning approach for the classification of subjective cognitive decline and mild cognitive impairment using resting-state EEG. *J. Neural Eng.* **2023**, *20*, 016048. [CrossRef]

51. Fan, M.; Yang, A.C.; Fuh, J.L.; Chou, C.A. Topological Pattern Recognition of Severe Alzheimer's Disease via Regularized Supervised Learning of EEG Complexity. *Front. Neurosci.* **2018**, *12*, 685. [CrossRef]

52. Ruiz-Gómez, S.; Gómez, C.; Poza, J.; Gutiérrez-Tobal, G.; Tola-Arribas, M.; Cano, M.; Hornero, R. Automated Multiclass Classification of Spontaneous EEG Activity in Alzheimer's Disease and Mild Cognitive Impairment. *Entropy* **2018**, *20*, 35. [CrossRef]

53. Jeong, T.; Park, U.; Kang, S.W. Novel quantitative electroencephalogram feature image adapted for deep learning: Verification through classification of Alzheimer's disease dementia. *Front. Neurosci.* **2022**, *16*, 1033379. [CrossRef]

54. Waser, M.; Benke, T.; Dal-Bianco, P.; Garn, H.; Mosbacher, J.A.; Ransmayr, G.; Schmidt, R.; Seiler, S.; Sorensen, H.B.D.; Jennum, P.J. Neuroimaging markers of global cognition in early Alzheimer's disease: A magnetic resonance imaging–electroencephalography study. *Brain and Behavior* **2018**, *9*, e01197. [CrossRef]

55. Rodrigues, P.M.; Bispo, B.C.; Garrett, C.; Alves, D.; Teixeira, J.P.; Freitas, D. Lacsogram: A new EEG tool to diagnose Alzheimer's disease. *IEEE J. Biomed. Health Inform.* **2021**, *25*, 3384–3395. [CrossRef]

56. Pirrone, D.; Weitschek, E.; Di Paolo, P.; De Salvo, S.; De Cola, M.C. EEG Signal Processing and Supervised Machine Learning to Early Diagnose Alzheimer's Disease. *Appl. Sci.* **2022**, *12*, 5413. [CrossRef]

57. Movahed, R.A.; Hamedani, N.E.; Sadredini, S.Z.; Rezaeian, M.-R. An Automated EEG-based mild cognitive impairment diagnosis framework using spectral and functional connectivity features. In Proceedings of the 2021 28th National and 6th International Iranian Conference on Biomedical Engineering (ICBME), Tehran, Iran, 25–26 November 2021; pp. 271–275. [CrossRef]

58. Fiscon, G.; Weitschek, E.; De Cola, M.C.; Felici, G.; Bertolazzi, P. An integrated approach based on EEG signals processing combined with supervised methods to classify Alzheimer's disease patients. In Proceedings of the 2018 IEEE International Conference on Bioinformatics and Biomedicine (BIBM), Madrid, Spain, 3–6 December 2018. [CrossRef]

59. Movahed, R.A.; Rezaeian, M. Automatic diagnosis of mild cognitive impairment based on spectral, functional connectivity, and nonlinear EEG-based features. *Comput. Math. Methods Med.* **2022**, *2022*, 2014001. [CrossRef]

60. Yu, H.; Lei, X.; Song, Z.; Liu, C.; Wang, J. Supervised Network-Based Fuzzy Learning of EEG Signals for Alzheimer's Disease Identification. *IEEE Trans. Fuzzy Syst.* **2020**, *28*, 60–71. [CrossRef]

61. Alessandrini, M.; Biagetti, G.; Crippa, P.; Falaschetti, L.; Luzzi, S.; Turchetti, C. EEG-Based Alzheimer's Disease Recognition Using Robust-PCA and LSTM Recurrent Neural Network. *Sensors* **2022**, *22*, 3696. [CrossRef]

62. Cai, L.; Wei, X.; Liu, J.; Zhu, L.; Wang, J.; Deng, B.; Yu, H.; Wang, R. Functional Integration and Segregation in Multiplex Brain Networks for Alzheimer's Disease. *Front. Neurosci.* **2020**, *14*, 51. [CrossRef]

63. Williams, P.; White, A.; Merino, R.B.; Hardin, S.; Mizelle, J.C.; Kim, S. Facial Recognition Task for the Classification of Mild Cognitive Impairment with Ensemble Sparse Classifier. In Proceedings of the 2019 41st Annual International Conference of the IEEE Engineering in Medicine and Biology Society (EMBC), Berlin, Germany, 23–27 July 2019; pp. 2242–2245. [CrossRef]

64. Sridhar, S.; Manian, V. EEG and Deep Learning Based Brain Cognitive Function Classification. *Computers* **2020**, *9*, 104. [CrossRef]

65. Su, R.; Li, X.; Li, Z.; Han, Y.; Cui, W.; Xie, P.; Liu, Y. Constructing biomarker for early diagnosis of aMCI based on combination of multiscale fuzzy entropy and functional brain connectivity. *Biomed. Signal Process. Control.* **2021**, *70*, 103000. [CrossRef]

66. Chedid, N.; Tabbal, J.; Kabbara, A.; Allouch, S.; Hassan, M. The development of an automated machine learning pipeline for the detection of Alzheimer's Disease. *Sci. Rep.* **2022**, *12*, 18137. [CrossRef]

67. Lee, K.; Choi, K.M.; Park, S.; Lee, S.H.; Im, C.H. Selection of the optimal channel configuration for implementing wearable EEG devices for the diagnosis of mild cognitive impairment. *Alzheimer's Res. Ther.* **2022**, *14*, 170. [CrossRef]

68. Timothy, L.T.; Krishna, B.M.; Nair, U. Recurrence quantification analysis of mci eeg under resting and visual memory task conditions. *Biomed. Eng. Appl. Basis Commun.* **2019**, *31*, 1950025. [CrossRef]

69. Park, J.; Jang, S.; Gwak, J.; Kim, B.C.; Lee, J.J.; Choi, K.Y.; Lee, K.H.; Jun, S.C.; Jang, G.J.; Ahn, S. Individualized diagnosis of preclinical Alzheimer's Disease using deep neural networks. *Expert Syst. Appl.* **2022**, *210*, 118511. [CrossRef]

70. Vecchio, F.; Miraglia, F.; Alù, F.; Menna, M.; Judica, E.; Cotelli, M.; Rossini, P.M. Classification of Alzheimer's Disease with Respect to Physiological Aging with Innovative EEG Biomarkers in a Machine Learning Implementation. *J. Alzheimer's Dis.* **2020**, *75*, 1253–1261. [CrossRef]

71. Kim, D.; Kim, K. Detection of early stage Alzheimer's disease using EEG relative power with deep neural network. In Proceedings of the 2018 40th Annual International Conference of the IEEE Engineering in Medicine and Biology Society (EMBC), Honolulu, HI, USA, 18–21 July 2018; pp. 352–355.

72. Cejnek, M.; Vysata, O.; Valis, M.; Bukovsky, I. Novelty detection-based approach for Alzheimer's disease and mild cognitive impairment diagnosis from EEG. *Med. Biol. Eng. Comput.* **2021**, *59*, 2287–2296. [CrossRef]

73. Sharma, N.; Kolekar, M.H.; Jha, K. Iterative Filtering Decomposition Based Early Dementia Diagnosis Using EEG With Cognitive Tests. *IEEE Trans. Neural Syst. Rehabil. Eng.* **2020**, *28*, 1890–1898. [CrossRef]

74. Han, S.H.; Pyun, J.M.; Yeo, S.; Kang, D.W.; Jeong, H.T.; Kang, S.W.; Kim, S.; Youn, Y.C. Differences between memory encoding and retrieval failure in mild cognitive impairment: Results from quantitative electroencephalography and magnetic resonance volumetry. *Alzheimer's Res. Ther.* **2021**, *13*, 3. [CrossRef] [PubMed]

75. Sharma, N.; Kolekar, M.; Jha, K.; Kumar, Y. EEG and Cognitive Biomarkers Based Mild Cognitive Impairment Diagnosis. *IRBM* **2019**, *40*, 113–121. [CrossRef]

76. Houmani, N.; Dreyfus, G.; Vialatte, F.B. Epoch-based Entropy for Early Screening of Alzheimer's Disease. *Int. J. Neural Syst.* **2015**, *25*, 1550032. [CrossRef]

77. Shan, X.; Cao, J.; Huo, S.; Chen, L.; Sarrigiannis, P.G.; Zhao, Y. Spatial-temporal graph convolutional network for Alzheimer classification based on brain functional connectivity imaging of electroencephalogram. *Hum. Brain Mapp.* **2022**, *43*, 5194–5209. [CrossRef]

78. Tavares, G.; San-Martin, R.; Ianof, J.N.; Anghinah, R.; Fraga, F.J. Improvement in the automatic classification of Alzheimer's disease using EEG after feature selection. In Proceedings of the 2019 IEEE International Conference on Systems, Man and Cybernetics (SMC), Bari, Italy, 6–9 October 2019. [CrossRef]

79. Li, F.; Matsumori, S.; Egawa, N.; Yoshimoto, S.; Yamashiro, K.; Mizutani, H.; Uchida, N.; Kokuryu, A.; Kuzuya, A.; Kojima, R.; et al. Predictive diagnostic approach to dementia and dementia subtypes using wireless and mobile electroencephalography: A pilot study. *Bioelectricity* **2022**, *4*, 3–11. [CrossRef]

80. Grässler, B.; Herold, F.; Dordevic, M.; Gujar, T.A.; Darius, S.; Böckelmann, I.; Müller, N.G.; Hökelmann, A. Multimodal measurement approach to identify individuals with mild cognitive impairment: Study protocol for a cross-sectional trial. *BMJ Open* **2021**, *11*, e046879. [CrossRef]

81. Chai, J.; Wu, R.; Li, A.; Xue, C.; Qiang, Y.; Zhao, J.; Zhao, Q.; Yang, Q. Classification of mild cognitive impairment based on handwriting dynamics and qEEG. *Comput. Biol. Med.* **2023**, *152*, 106418. [CrossRef]

82. Simpraga, S.; Alvarez-Jimenez, R.; Mansvelder, H.D.; van Gerven, J.M.A.; Groeneveld, G.J.; Poil, S.S.; Linkenkaer-Hansen, K. EEG machine learning for accurate detection of cholinergic intervention and Alzheimer's disease. *Sci. Rep.* **2017**, *7*, 5775. [CrossRef]

83. Ding, Y.; Chu, Y.; Liu, M.; Ling, Z.; Wang, S.; Li, X.; Li, Y. Fully automated discrimination of Alzheimer's disease using resting-state electroencephalography signals. *Quant. Imaging Med. Surg.* **2022**, *12*, 1063–1078. [CrossRef]

84. Schumacher, J.; Thomas, A.J.; Peraza, L.R.; Firbank, M.; Cromarty, R.; Hamilton, C.A.; Donaghy, P.C.; O'Brien, J.T.; Taylor, J.P. EEG alpha reactivity and cholinergic system integrity in Lewy body dementia and Alzheimer's disease. *Alzheimer's Res. Ther.* **2020**, *12*, 46. [CrossRef]

85. Zorick, T.; Landers, J.; Leuchter, A.; Mandelkern, M.A. EEG multifractal analysis correlates with cognitive testing scores and clinical staging in mild cognitive impairment. *J. Clin. Neurosci.* **2020**, *76*, 195–200. [CrossRef]

86. Houmani, N.; Vialatte, F.; Gallego-Jutglà, E.; Dreyfus, G.; Nguyen-Michel, V.H.; Mariani, J.; Kinugawa, K. Diagnosis of Alzheimer's disease with Electroencephalography in a differential framework. *PLoS ONE* **2018**, *13*, e0193607. [CrossRef] [PubMed]

87. Fiscon, G.; Weitschek, E.; Felici, G.; Bertolazzi, P.; De Salvo, S.; Bramanti, P.; De Cola, M.C. Alzheimer's disease patients classification through EEG signals processing. In Proceedings of the 2014 IEEE Symposium on Computational Intelligence and Data Mining (CIDM), Orlando, FL, USA, 9–12 December 2014; pp. 105–112.

88. Perez-Valero, E.; Morillas, C.; Lopez-Gordo, M.A.; Carrera-Muñoz, I.; López-Alcalde, S.; Vílchez-Carrillo, R.M. An Automated Approach for the Detection of Alzheimer's Disease From Resting State Electroencephalography. *Front. Neuroinformatics* **2022**, *16*, 924547. [CrossRef] [PubMed]

89. Jesus, B., Jr.; Cassani, R.; McGeown, W.J.; Cecchi, M.; Fadem, K.C.; Falk, T.H. Multimodal prediction of Alzheimer's disease severity level based on resting-state EEG and structural MRI. *Front. Hum. Neurosci.* **2021**, *15*, 700627. [CrossRef] [PubMed]

90. Fouladi, S.; Safaei, A.A.; Mammone, N.; Ghaderi, F.; Ebadi, M.J. Efficient deep neural networks for classification of Alzheimer's disease and mild cognitive impairment from scalp EEG recordings. *Cognit. Comput.* **2022**, *14*, 1247–1268. [CrossRef]

91. Crook-Rumsey, M.; Howard, C.J.; Doborjeh, Z.; Doborjeh, M.; Ramos, J.I.E.; Kasabov, N.; Sumich, A. Spatiotemporal EEG Dynamics of Prospective Memory in Ageing and Mild Cognitive Impairment. *Cogn. Comput.* **2022**, *15*, 1273–1299. [CrossRef]

92. Zhang, J.; Lu, H.; Zhu, L.; Ren, H.; Dang, G.; Su, X.; Lan, X.; Jiang, X.; Zhang, X.; Feng, J.; et al. Classification of Cognitive Impairment and healthy controls based on Transcranial Magnetic Stimulation Evoked Potentials. *Front. Aging Neurosci.* **2021**, *13*, 804384. [CrossRef] [PubMed]

93. Amini, M.; Pedram, M.M.; Moradi, A.; Ouchani, M. Diagnosis of Alzheimer's Disease by Time-Dependent Power Spectrum Descriptors and Convolutional Neural Network Using EEG Signal. *Comput. Math. Methods Med.* **2021**, *2021*, 5511922. [CrossRef] [PubMed]

94. Cecere, C.; Corrado, C.; Polikar, R. Diagnostic utility of EEG based biomarkers for Alzheimer's disease. In Proceedings of the 2014 40th Annual Northeast Bioengineering Conference (NEBEC), Boston, MA, USA, 25–27 April 2014; pp. 1–2.

95. Cicalese, P.A.; Li, R.; Ahmadi, M.B.; Wang, C.; Francis, J.T.; Selvaraj, S.; Schulz, P.E.; Zhang, Y. An EEG-fNIRS hybridization technique in the four-class classification of alzheimer's disease. *J. Neurosci. Methods* **2020**, *336*, 108618. [CrossRef] [PubMed]

96. Jiang, J.; Zhang, J.; Li, C.; Yu, Z.; Yan, Z.; Jiang, J. Development of a Machine Learning Model to Discriminate Mild Cognitive Impairment Subjects from Normal Controls in Community Screening. *Brain Sci.* **2022**, *12*, 1149. [CrossRef] [PubMed]

97. Jiang, J.; Yan, Z.; Sheng, C.; Wang, M.; Guan, Q.; Yu, Z.; Han, Y.; Jiang, J. A Novel Detection Tool for Mild Cognitive Impairment Patients Based on Eye Movement and Electroencephalogram. *J. Alzheimer's Dis.* **2019**, *72*, 389–399. [CrossRef]

98. Jervis, B.W.; Bigan, C.; Jervis, M.; Besleaga, M. New-onset Alzheimer's disease and normal subjects 100% differentiated by P300. *Am. J. Alzheimer's Dis. Other Dement.* **2019**, *34*, 308–313. [CrossRef]

99. Laskaris, N.; Tarnanas, I.; Tsolaki, M.; Vlaikidis, N.; Karlovasitou, A. Improved detection of amnestic MCI by means of discriminative vector quantization of single-trial cognitive ERP responses. *J. Neurosci. Methods* **2013**, *212*, 344–354. [CrossRef]

100. Klepl, D.; He, F.; Wu, M.; Blackburn, D.J.; Sarrigiannis, P. EEG-based graph neural network classification of Alzheimer's disease: An empirical evaluation of functional connectivity methods. *IEEE Trans. Neural Syst. Rehabil. Eng.* **2022**, *30*, 2651–2660. [CrossRef]

101. Amezquita-Sanchez, J.P.; Mammone, N.; Morabito, F.C.; Marino, S.; Adeli, H. A novel methodology for automated differential diagnosis of mild cognitive impairment and the Alzheimer's disease using EEG signals. *J. Neurosci. Methods* **2019**, *322*, 88–95. [CrossRef]

102. Perez-Valero, E.; Lopez-Gordo, M.Á.; Gutiérrez, C.M.; Carrera-Muñoz, I.; Vílchez-Carrillo, R.M. A self-driven approach for multi-class discrimination in Alzheimer's disease based on wearable EEG. *Comput. Methods Programs Biomed.* **2022**, *220*, 106841. [CrossRef]

103. Mitsukura, Y.; Sumali, B.; Watanabe, H.; Ikaga, T.; Nishimura, T. Frontotemporal EEG as potential biomarker for early MCI: A case-control study. *BMC Psychiatry* **2022**, *22*, 289. [CrossRef]

104. Dimitriadis, S.I.; Laskaris, N.A.; Bitzidou, M.P.; Tarnanas, I.; Tsolaki, M.N. A novel biomarker of amnestic MCI based on dynamic cross-frequency coupling patterns during cognitive brain responses. *Front. Neurosci.* **2015**, *9*, 350. [CrossRef]

105. Kulkarni, N. EEG signal analysis for mild Alzheimer's disease diagnosis by means of spectral- and complexity-based features and machine learning techniques. In Proceedings of the 2nd International Conference on Data Engineering and Communication Technology; Advances in Intelligent Systems and Computing. Springer: Singapore, 2019; pp. 395–403.

106. Cassani, R.; Falk, T. Alzheimer's Disease Diagnosis and Severity Level Detection Based on Electroencephalography Modulation Spectral "Patch" Features. *IEEE J. Biomed. Health Informatics* **2019**, *24*, 1982–1993. [CrossRef]

107. Komolovaitė, D.; Maskeliūnas, R.; Damaševičius, R. Deep convolutional neural network-based visual stimuli classification using electroencephalography signals of healthy and Alzheimer's disease subjects. *Life* **2022**, *12*, 374. [CrossRef]

108. Jovic, A. 1. Feature selection in biomedical signal classification process and current software implementations. In *Intelligent Decision Support Systems*; Borra, S., Dey, N., Bhattacharyya, S., Bouhlel, M.S., Eds.; De Gruyter: Berlin Germany; Boston, MA, USA, 2019; pp. 1–30.

109. Ieracitano, C.; Mammone, N.; Hussain, A.; Morabito, F.C. A novel multi-modal machine learning based approach for automatic classification of EEG recordings in dementia. *Neural Netw.* **2020**, *123*, 176–190. [CrossRef]

110. Adeli, H.; Ghosh-Dastidar, S.; Dadmehr, N. Alzheimer's disease and models of computation: Imaging, classification, and neural models. *J. Alzheimer's Dis.* **2005**, *7*, 187–199. [CrossRef]

111. Parmar, S.K.; Ramwala, O.A.; Paunwala, C.N. Performance evaluation of svm with non-linear kernels for eeg-based dyslexia detection. In Proceedings of the 2021 IEEE 9th Region 10 Humanitarian Technology Conference (R10-HTC), Bangalore, India, 30 September–2 October 2021; pp. 1–6.

112. Roy, A.M. Adaptive transfer learning-based multiscale feature fused deep convolutional neural network for EEG MI multiclassification in brain–computer interface. *Eng. Appl. Artif. Intell.* **2022**, *116*, 105347. [CrossRef]

113. Aviles, M.; Alvarez-Alvarado, J.M.; Robles-Ocampo, J.B.; Sevilla-Camacho, P.Y.; Rodríguez-Reséndiz, J. Optimizing RNNs for EMG signal classification: A novel strategy using Grey Wolf Optimization. *Bioengineering* **2024**, *11*, 77. [CrossRef] [PubMed]

114. Höller, Y.; Bathke, A.C.; Uhl, A.; Strobl, N.; Lang, A.; Bergmann, J.; Nardone, R.; Rossini, F.; Zauner, H.; Kirschner, M.; et al. Combining SPECT and Quantitative EEG Analysis for the Automated Differential Diagnosis of Disorders with Amnestic Symptoms. *Front. Aging Neurosci.* **2017**, *9*, 290. [CrossRef] [PubMed]

115. Klepl, D.; He, F.; Wu, M.; Blackburn, D.J.; Sarrigiannis, P.G. Adaptive Gated Graph Convolutional Network for Explainable Diagnosis of Alzheimer's Disease using EEG Data. *IEEE Trans. Neural Syst. Rehabil. Eng.* **2023**, *31*, 3978–3987. [CrossRef] [PubMed]

116. Tang, T.; Li, H.; Zhou, G.; Gu, X.; Xue, J. Discriminant Subspace Low-Rank Representation Algorithm for Electroencephalography-Based Alzheimer's Disease Recognition. *Front. Aging Neurosci.* **2022**, *14*, 943436. [CrossRef]

117. Gelbard-Sagiv, H.; Pardo, S.; Getter, N.; Guendelman, M.; Benninger, F.; Kraus, D.; Shriki, O.; Ben-Sasson, S. Optimizing electrode configurations for wearable EEG seizure detection using machine learning. *Sensors* **2023**, *23*, 5805. [CrossRef] [PubMed]

118. Westover, M.B.; Gururangan, K.; Markert, M.S.; Blond, B.N.; Lai, S.; Benard, S.; Bickel, S.; Hirsch, L.J.; Parvizi, J. Diagnostic value of electroencephalography with ten electrodes in critically ill patients. *Neurocrit. Care* **2020**, *33*, 479–490. [CrossRef]

119. Wang, R.; He, Q.; Shi, L.; Che, Y.; Xu, H.; Song, C. Automatic detection of Alzheimer's disease from EEG signals using an improved AFS–GA hybrid algorithm. *Cogn. Neurodyn.* **2024**. [CrossRef]

Correlation Analysis between Young Driver Characteristics and Visual/Physiological Attributes at Expressway Exit Ramp

Zeng'an Wang [1], Xinyue Qi [2], Chenzhu Wang [3,*], Said M. Easa [4], Fei Chen [3] and Jianchuan Cheng [3]

[1] Jiangsu Expressway Company Limited, No. 6 Xianlin Avenue, Nanjing 210046, China; wangzengan@email.jchc.cn

[2] School of Technology, Tibet University, Lasa 850001, China; q17852056315@163.com

[3] School of Transportation, Southeast University, 2 Sipailou, Nanjing 210096, China; cf@seu.edu.cn (F.C.); jccheng@seu.edu.cn (J.C.)

[4] Department of Civil Engineering, Toronto Metropolitan University, Toronto, ON M5B 2K3, Canada; seasa@torontomu.ca

[*] Correspondence: wcz@seu.edu.cn

Abstract: More collisions occur at the exit ramps of expressways due to frequent lane-changing behavior and interweaving between vehicles. Young drivers with shorter driving mileage and driving experience, radical driving styles, and worse behavior prediction are likelier to be involved in collisions at the exit ramps. This paper focuses on the correlation analysis between young drivers' characteristics and their visual and physiological attributes at expressway exit ramps. First, the driver's gender, driving experience, and mileage are classified. Then, seven expressway exit models are established using the UC/Win road modeling software. The driver's driving plane vision is divided into four areas using the K-means clustering algorithm. In addition, the driver's visual and heart rate attributes were analyzed at 500 m, 300 m, 200 m, and 100 m away from an expressway exit. The results show that the visual attributes, gender, and driving mileage of young drivers strongly correlate with the fixation times and average saccade amplitude. In contrast, the driving experience has almost no correlation with the fixation behavior of young drivers. Young drivers' driving experience and mileage strongly correlate with cardiac physiological attributes, but there is virtually no correlation with gender. The practical implications of these results should be helpful to highway planners and designers.

Keywords: highway exit; driver; visual characteristics; heart rate; fixation; saccade

1. Introduction

Expressway exit and entrance ramps are complex areas where vehicles merge into or diverge from the stream. At the entrance ramp, vehicles entering the mainline from the ramp compete for suitable headways with the vehicles driving in the merging lane. At the exit ramp, the vehicles slow down for the exit ramp speed. An expressway exit is a highly space-competitive position for vehicles, where traffic accidents are likely to occur at expressway exits. Therefore, studying drivers' driving behavior at expressway exits is warranted. As the most unstable main factor in the human–vehicle–road closed-loop system, drivers often show various characteristics during the driving process. For example, in lane changing, drivers will adopt other processing methods in the selection of the lane-changing timing and the search for surrounding environmental information. The human–machine interaction can be realized only when the vehicle system's performance meets the current driver's characteristics. Research shows that the driving behavior characteristics will show specific rules according to various types. Analyzing and comparing the driver's control of the vehicle and the driver's visual characteristics can provide an essential data basis for predicting expressway lane-changing behavior. Young drivers' characteristics include short mileage, short driving experience, radical driving style, and a challenging behavior.

To the authors' best knowledge, limited studies have addressed young drivers' work-load in the areas with different distances to an expressway exit. Thus, the current study tended to explore the effects of the visual and physiological attributes of young drivers at the expressway exit segments.

2. Literature Review

As indicated in Table 1, the recent literature review shows that most previous research has focused on characterizing drivers' visual and psychophysiological parameters. Still, a limited body of research efforts exists on the correlation between driver characteristics and visual and psychophysiological attributes. There is also little research on young drivers. Therefore, this paper mainly focuses on the correlation between young drivers' characteristics and visual and physiological characteristics at an expressway exit. Therefore, this study aimed to evaluate the correlations between young driver characteristics (gender, driving experience, and driving mileage) and their visual/physiological attributes at expressway exit ramps.

Table 1. A summary of previous research regarding characterizing drivers' visual and psychophysiological parameters.

Previous Research Efforts	Findings	Research Gap
Ji [1] and Sun et al. [2]	The authors classified lane-changing behavior into two categories according to the purpose of lane changing: subjective lane-changing behavior (driven by the driver's subjective desire for better lane-changing benefits)	However, drivers' forced lane-changing behavior at an expressway exit was not analyzed.
Ji [1] and Xiong et al. [3]	They analyzed the conditions of these behaviors and the main influencing factors of drivers' lane-changing behavior, such as drivers' characteristics, vehicle type, traffic flow environmental impact, and road conditions. Finally, they established an urban road vehicle lane-changing model based on driving behavior (subjective lane-changing model, forced lane-changing model)	However, there was no specific correlation analysis between drivers' characteristics and the characterization parameters of lane-changing behavior.
Portera and Bassani [4]	They studied the influencing factors on driving behavior at expressway off-ramps and on-ramps. It was proposed that the radius of the lane circle curve, the position of the entrance and exit ramps, and the length of the ramps significantly influence drivers' driving behavior.	However, the parameters, such as the radius of the lane circle curve, were not mapped to the characterization parameters, such as drivers' visual characteristics.
Yuan [5] and Yu et al. [6]	They fitted the distribution functions of three parameters, i.e., fixation duration, saccade amplitude, and saccade speed. They found that they had approximately logarithmic, exponential, and logarithmic normal distributions, respectively. The proficiency level significantly influences four parameters, by comparing and counting the parameters of proficient and unskilled drivers. The dynamic clustering theory was used to determine the fixation area and to divide the various fixation areas.	However, the differences in proficiency among various types of drivers and their correlation with visual characteristics were not specifically analyzed.
Ji [7]	Three evaluation indexes of visual characteristics were determined: fixing characteristics' evaluation indexes (fixation times, fixation duration, line of vision transfer probability); evaluation indexes of saccade characteristics (saccade duration, saccade range, and saccade speed); head motion evaluation indexes (rotation angle of vertical motion, rotation angle of horizontal motion). The drivers were classified into various styles, and their correlations to fixation, saccade, and head movement behaviors were analyzed.	The influence of drivers' characteristics on visual characteristics was neglected.
Hou [8] and Feng [9]	They determined the driving intent time windows according to the driving style of various drivers. They built GM-HMM and SVM models based on the difference significance analysis [10]. Finally, they concluded that the parameters of drivers' perceptual characteristics of lane-changing intention were the number of rearview mirror views, the average saccade amplitude, and the standard deviation of the head horizontal angle [11].	

Table 1. *Cont.*

Previous Research Efforts	Findings	Research Gap
Wei [12]	They studied the predictions of drivers' lane-changing behavior based on in-depth learning and correlated the visual characteristics with drivers' behavior characteristics.	However, the driver's features were not related to visual attributes.
Wang and Yin [13]	They concluded that driving behavior is influenced by drivers' driving intentions and the driving environment outside the vehicle.	However, the driver's features and psychological characteristics were not analyzed.
Cheng [14], and Cheng and Zhang [15]	They preprocessed and extracted physiological signal data and designed neural network architecture. The changing regularity of drivers' psychological and physiological characteristics during driving was analyzed.	
Mahmud et al. [16]	The effectiveness of dynamic speed feedback signs (DSFSs) as a speed reduction countermeasure was evaluated.	
Tian [17]	The heart rate variability parameter was mainly used to obtain the time-frequency domain index of the ECG signal. The authors studied this aspect and proposed that in the element of ECG detection, the ECG data should generally be paid attention to, mainly analyzing the time-frequency domain index of the ECG signal.	The change in the driver's heart rate during a lane change at an expressway exit was not analyzed.
Sun et al. [2]	They analyzed the correlation between drivers' characteristics and psychophysiological characteristics under natural driving conditions on the expressway.	

3. Experimental Design

3.1. Participants

Various types of young drivers have other physiological characteristics at 500 m, 300 m, 200 m, and 100 m from an expressway exit. The drivers' gender, driving experience, driving mileage, and visual and heart rate attributes were classified. The experiments and questionnaire were completed by 30 people, including 17 males and 13 females. The drivers were all between 18 and 25 years old.

3.2. Material

The experimental platform comprised UC-Win/Road scene modeling software version 1.1, a driving simulator, a driver, an eye tracker, a biofeedback instrument, and an Ergolab (Stockholm, Sweden) human–machine environment synchronization platform. Among them, UC-Win/Road is mainly used to construct road scenes and road alignments conducive to driving fatigue. The driving simulator used in this experiment is shown in Figure 1. The instrument comprises three display panels, real car body instruments, and other parts. At the same time, the actual scene simulation system, the operation system, the sound simulation system, the vehicle dynamics simulation system, and the data recording system constitute the experimental platform. Ergolab human–machine environment synchronization (HMI) is a platform for simultaneous data collection and analysis of human–machine environmental data. It is essential in experimental design, data collection, statistical analysis, and human behavior research.

The biofeedback instrument can collect the driver's physiological and psychological signals in the driving experiment. In this study, an eight-channel multi-parameter biofeedback instrument was used to collect the heart rate data of the experimenter. The biofeedback instrument is small and light, so it will not cause much interference to the driver. The eye tracker model adopted is Tobii Pro Glasses2, which can obtain eye movement signals for subsequent research and analysis.

Figure 1. Driving Simulator.

3.3. Driver Attributes

The main experiment consisted of two parts: the visual characteristics of lane-changing behavior, the acquisition of heart rate data, and the determination of the basic information about the driver. First, the participants were given questionnaires for basic driver information before the experiment, and then the driving simulation was carried out in the UC-Win/Road driving simulation software. The Tobii Pro Glasses2 eye tracker was used to collect the visual characteristics of the drivers, and the biofeedback device was used to collect the participants' heart rates. After the test, the vehicle operation data parameters in the simulator were extracted. After the preliminary processing and analysis of the obtained data, abnormal data were eliminated, and the influencing factors and correlation between the visual characteristics and heart rate of the drivers of various types were finally obtained. The main variables of this experiment were divided as shown in Table 2.

Table 2. Main variables of this experiment.

Variable	Variable Name	Instruction
Independent Variable	Driver Characteristics	Gender, Driving Experience, Driving Mileage
Dependent Variable	Visual attribute (Fixation)	Fixation Times, Percentage of Cumulative Fixation Duration
	Visual attribute (Saccade)	Average Saccade Amplitude, Average Saccade Speed

3.4. Experimental Process

The UC-Win/Road software built a two-way, eight-lane expressway with seven exit ramps. The mainline was a straight line, and the radius of the circular curve was 1500 m; the width of each lane was 3.75 m; the longitudinal slope was 0.305% and −0.286%. For the deceleration lane, the length of the gradient segment was 100 m, the length of the deceleration segment was 150 m, and the total length was 250 m. The ramp had a 350 m circular curve radius, a single lane form, and a lane width of 4.5 m. The ramp signs included exit warning signs, exit signs, straight signs, and the following exit warning signs. The questionnaire was concisely developed, generally with multiple-choice questions to help the respondents complete the questionnaire quickly. The experimental process included the following steps:

Step 1: Questionnaire filling stage

After entering the laboratory, the participants had to first register their primary information (name, gender, serial number, etc.), sign the experimental record form, and then scan the code to fill in the questionnaire. The person in charge of the experiment guided the participants to complete the questionnaire (the specific information is shown in Table 3).

Table 3. Basic driver information questionnaire.

Question	Answer Form
Name	Fill in the Blanks
Gender	Multiple-choice
Driving Experience	Multiple-choice
Whether or Not Owns a Car	Multiple-choice
Driving Hours Per Day	Multiple-choice
Mileage Per Week	Multiple-choice
Mileage Per Year	Multiple-choice
Number of Violations in One Year	Multiple-choice
Number of Accidents in a Year	Multiple-choice
Points Deducted from Driving License within a Year	Fill in the Blanks

Step 2: Instrument Configuration

The person in charge of the experiment introduced the primary experiment situation to the experimenter (the expected experiment time, the method of using the experimental equipment, the experiment process, the steps, etc.). After the introduction of the experiment, the eye tracker and heart rate monitor were worn to detect the visual characteristics and heart rate characteristics of the experimenter during the experiment. The model was initialized and prepared to start the experiment.

Step 3: Driving Simulation

The experiment was divided into seven groups. Each group had a different starting point. When the participants started driving, they were given a driving destination.

4. Methodology

The division method of the driver's field of vision (FOV) plane used in this paper is the dynamic clustering method, with the screenshot shown in Figure 2.

Figure 2. FOV of one sample of participants.

4.1. Design of the k-Means Clustering Algorithm

Let $X = \{x_1, x_2, \cdots, x_i, \cdots, x_n\}$ be n data in R^d space. Before clustering, k should be specified as the number of initial clusters. There are many methods to determine k. Generally, it is determined according to the sample situation and the number of samples. The following are the basic steps of the k-means clustering algorithm:

Step1: Select k objects from n data objects as the initial clustering center, and the similarity $s(x_i - c_j)$ of the remaining points can be derived from the following formula:

$$s(x_i - c_j) = \frac{1}{d(x_i, c_j)} \tag{1}$$

where c_j = the cluster center of class j, and $d(x_i, c_j)$ = the distance between sample x_i and cluster center c_j [18].

The three types of distances are given by:

$$d(x_i, c_j) = \sqrt[p]{\left|x_i^1 - c_j^1\right|^p + \left|x_i^k - c_j^k\right|^p + \left|x_i^d - c_j^d\right|^p} \text{ (Makowski distance)} \quad (2)$$

$$d(x_i, c_j) = \left|x_i^1 - c_j^1\right| + \cdots + \left|x_i^k - c_j^k\right| + \cdots + \left|x_i^d - c_j^d\right| \text{ (Manhattan distance)} \quad (3)$$

$$d(x_i, C_j) = \sqrt{\left(x_i' - c_j^1\right)^2 + \cdots + \left(x_i^k - c_j^k\right)^2 + \ldots \left(x_i^d - c_j^d\right)^2} \text{ (Euclidean distance)} \quad (4)$$

Step2: Calculate the cluster center of each updated class, and assume that the sample in the j class is $\left\{x_{j1}, x_{j2}, \cdots, x_{jn_j}\right\}$; that is, it contains samples, and then the cluster center of this class is $c_j = \left\{c_j^1, c_j^2, \cdots, c_j^k, \cdots, c_j^d\right\}$, where c_j^k is the k attribute of the center c_j of the class, which can be obtained according to the formula:

$$c_j^k = \frac{x_{j1}^k + x_{j1}^k + \cdots + x_{j1}^k}{n_j} \quad (5)$$

Step3: Repeat the steps until the standard detection function converges, as shown in the following formula:

$$J = \sqrt{\frac{\sum_{i=1}^{k}\sum_{j=1}^{n_i}\left(x_{ij} - c_i\right)^2}{n - 1}} \quad (6)$$

Note that k means clustering of the fixation points in the driver's FOV.

4.2. Clustering Algorithm Results

The k means clustering algorithm was used to explore the division law of the driver's FOV plane at the expressway exit. The results showed that the number of drivers' FOV plane divisions at the expressway exit was mainly based on the number of classes selected. A large selection of k value will lead to the angle of the divided field of the vision plane and weak goal. Determining the relationship between the divided FOV plane and its internal targets is challenging. In contrast, the selection of k value is small and the divided areas are less, so it is difficult to determine the characteristics of targets and lines of vision. In this study, according to the driver's main fixation points at the expressway exit, the value of k was preliminarily set as 4, 5, and 6. That is, the FOV plane was divided into 4, 5, and 6 areas for clustering calculation, respectively. The clustering results of k = 4, 5, and 6 are shown in Table 4, while the optimal number of k is 4.

Table 4. Clustering results for various k.

Category	Initial Cluster Center	Final Cluster Center	Number of Cases
		(k = 4)	
1	$(-55.96, -16.88)$	$(-46.54, 13)$	13
2	$(35.36, 3.28)$	$(22.18, 2.76)$	17
3	$(50.99, -20.40)$	$(44.77, -19.65)$	121
4	$(18.44, 21.05)$	$(18.83, 22.04)$	12
		(k = 5)	
1	$(-54.77, -16.45)$	$(-46.54, 13)$	14
2	$(17.45, 22.17)$	$(23.64, 5.63)$	23
3	$(-8.55, -6.04)$	$(2.845, -6.44)$	137
4	$(-47.11, 22.16)$	$(-20.44, -3.39)$	7
5	$(-14.48, -42.37)$	$(-10.81, -27.67)$	14

Table 4. *Cont.*

Category	Initial Cluster Center	Final Cluster Center	Number of Cases
		(*k* = 6)	
1	(17.65, −14.34)	(23.00, 7.45)	21
2	(−11.33, 1.48)	(0.75, −3.91)	21
3	(−13.88, −43.58)	(−19.92, −9.66)	145
4	(−47.45, 21.68)	(−20.68, 4.22)	6
5	(47.65, −22.34)	(47.66, −12.53)	14
6	(16.63, −27.77)	(5.33, −7.44)	3

Thus, the driver's line of vision plane was divided into four areas: front, interior rear-view (RV) mirror, left RV mirror, and right RV mirror. According to the driver's visual characteristics at the expressway exit, this paper dynamically clusters the driver's line of vision points. It puts forward the selective division of the following visual field planes (four types in total): A-front, B-interior RV mirror, C-left RV mirror, and D-right RV mirror. After clustering, each cluster point was reflected in the coordinate system in the driver's FOV. The division of the driver's FOV plane is shown in Figure 3.

Figure 3. Division of driver's FOV plane.

5. Correlation Analysis

The correlation between young drivers' characteristics (gender, driving duration, driving mileage, and driving style), visual attributes (fixation and saccade behavior), and physiological attributes (heart rate difference) was analyzed at 500 m, 300 m, 200 m, and 100 m away from the expressway exit. In the normal driving process, drivers obtain external information in three ways: fixation, saccade, and blinking. Blinking behavior does not represent the driver's visual characteristics, so the saccade and fixation behavior characteristics were selected for analysis. In addition, the heart rate was also selected as the physiological characterization parameter of the driver.

5.1. Fixation Times

The number of fixation times is the total number (frequency) of the driver's fixation on a point or an area in the FOV during driving, and the frequency also shows the driver's attention to the FOV from the side, reflecting the driver's interest in this area. In this paper, the number of drivers' fixation times at a location can represent the change in the driver's focus. The correlation of fixation times of various types of drivers was analyzed regarding gender, driving experience, and driving mileage at various distances from the expressway exit.

5.1.1. Fixation Times by Gender

A comparison of the fixation times of the drivers of both genders at various distances is shown in Figure 4. First, at the expressway exit, the attention to the left RV mirror and the inside RV mirror is low because the driver is about to change lanes to the right, so his attention will mainly focus on the front and right RV mirrors. However, there is a small

difference between the number of female drivers' fixation times on the right RV mirror and the number of fixation times at the front. In contrast, male drivers pay more attention to the right RV mirror and the front, but their attention still mainly stays in the front. Therefore, gender has a strong correlation as a factor affecting the fixation behavior characteristics of young drivers at the expressway exit. This is consistent with recent studies [19].

(**a**)

(**b**)
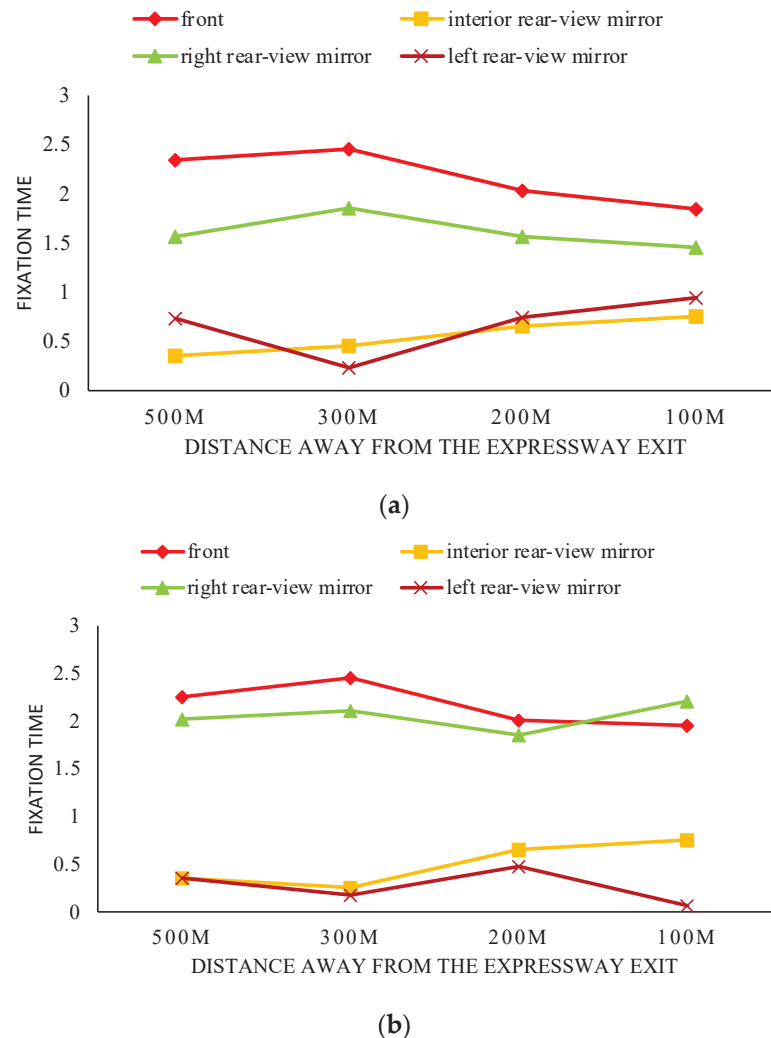
Figure 4. Driver fixation times by gender. (**a**) Male drivers. (**b**) Female drivers.

5.1.2. Fixation Times by Driving Experience

A comparison of the fixation times of drivers with various lengths of driving experience at various distances is shown in Figure 5. Similarly, the driver's attention is mainly focused on the front and right RV mirrors, but when comparing the number of fixation times of drivers of various ages, it is found that the age of driving has little effect on the number of fixation times at the expressway exit. As a result, the driving experience has little correlation with the fixation behavior characteristics of young drivers at the expressway exit.

5.1.3. Fixation Times by Driving Mileage

A comparison of the fixation times of drivers with varying driving mileages at different distances is shown in Figure 6. Similarly, the drivers' attention is mainly focused on the front and the right RV mirrors, but it is noteworthy that the number of eyes on the right RV mirror by drivers with under 10,000 km of driving mileage differs slightly from the number of eyes on the front. On the contrary, drivers with driving mileage of more than 10,000 km

mainly focus on the front. Although the right RV mirror is fixed on more frequently than the left and the interior RV mirror, there is still a large gap compared with the front. Unlike drivers with under 10,000 km of driving mileage, the gap is smaller. Therefore, driving mileage has a strong correlation as a factor affecting the fixation behavior of young drivers at the exit of the highway, especially between drivers with driving mileage above 1000 km and those with driving mileage below 1000 km.
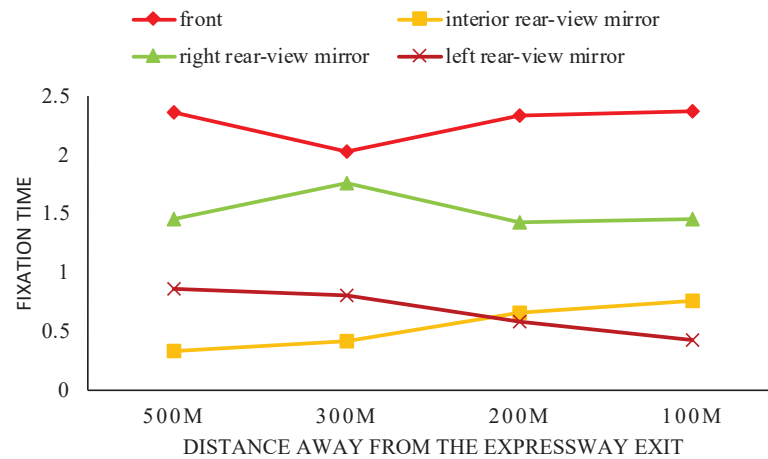
(**a**)
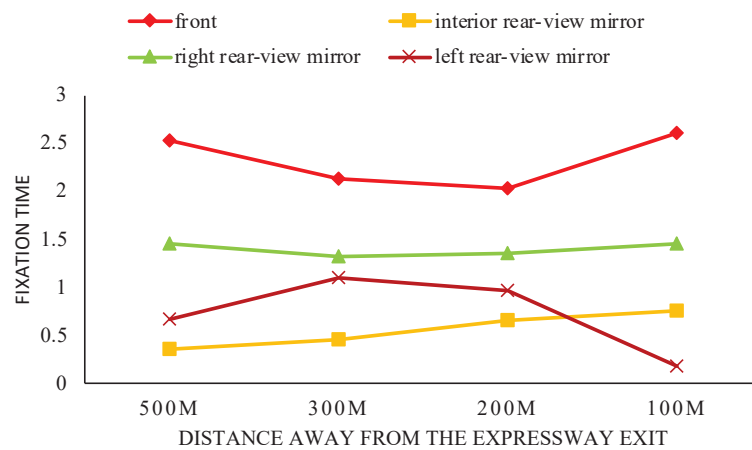
(**b**)
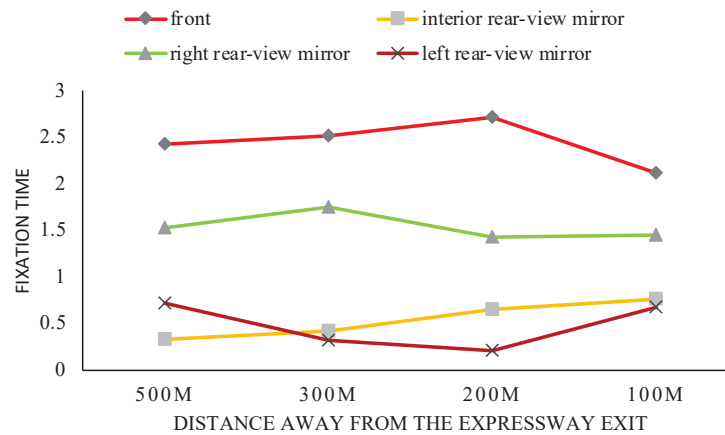
(**c**)

Figure 5. Fixation times by drivers' experience. (**a**) Less than 1 year. (**b**) 1 to 3 years. (**c**) Over 3 years.
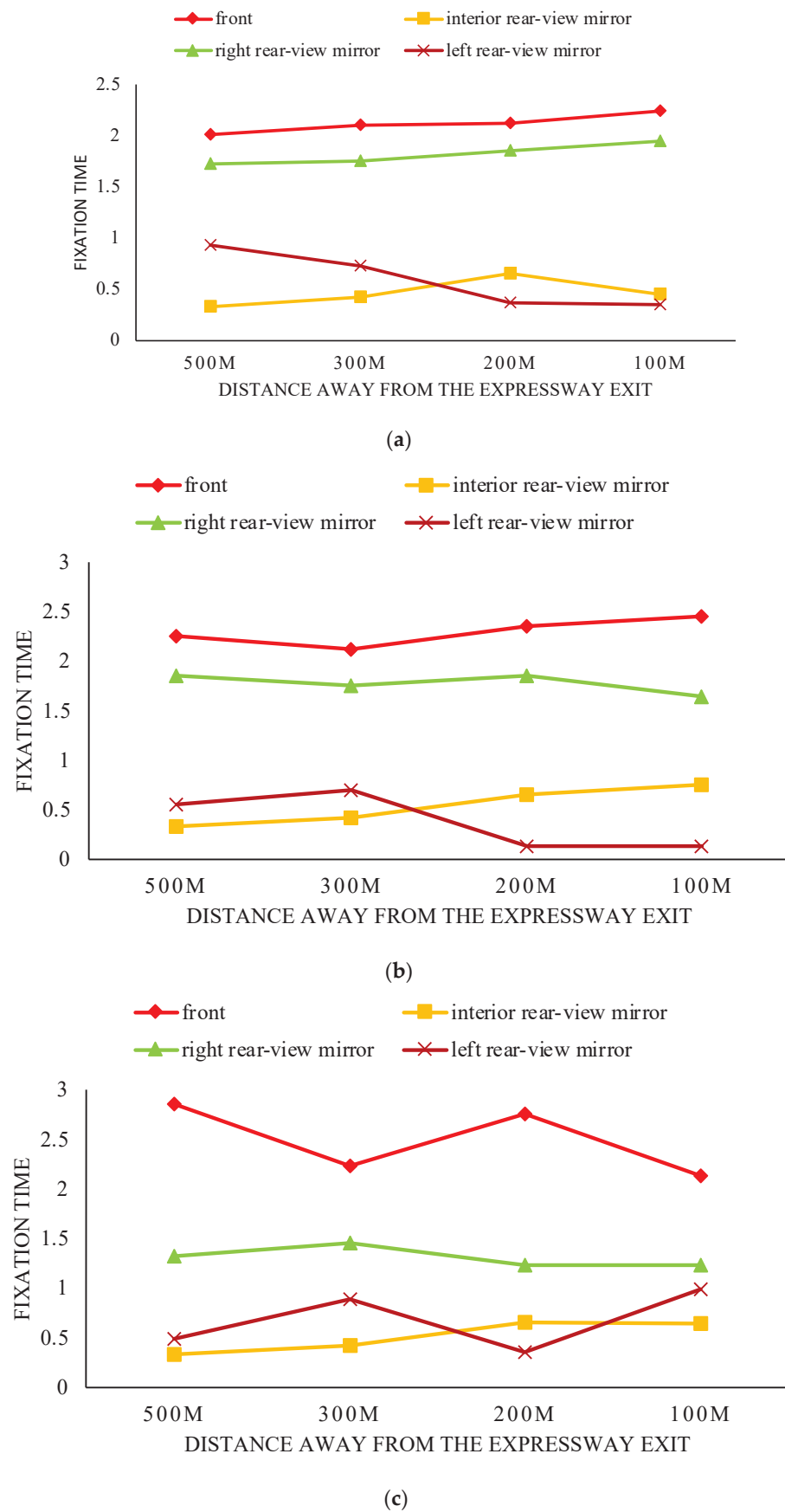
Figure 6. Fixation times for varying driving mileages. (**a**) Less than 5000 km. (**b**) 5000 km−10,000 km. (**c**) Over 10,000 km.

Thus, as far as the fixation behavior characteristics are concerned, gender and driving mileage (driving mileage of 10,000 km) have a greater correlation with the fixation behavior characteristics at the exit of the driver's highway, while driving time has a smaller correlation with the fixation behavior characteristics at the exit of the driver's highway.

5.2. Average Saccade Amplitude

Saccade amplitude describes the extent to which the driver's eye covers when he completes a saccade (the extent to which the driver's eye saccades from the previous focus to the next). Saccade behavior can be represented by the angle between the last fixation behavior and the view of the following fixation behavior (the angle of view variation). In this paper, the average saccade amplitude uses the average vector angle between the two fixation behaviors over a certain period.

The correlation between the average saccade amplitude of various types of drivers is shown in Figure 7 at 500, 300, 200, and 100 m away from the expressway exit in three aspects: gender, driving time, and driving mileage.

Regarding gender, the average saccade amplitude of drivers approaching 200 m and 100 m from the expressway exit increases substantially, as drivers generally choose to change lanes here. It is not difficult to see from the diagram that the average saccade range of male drivers is usually smaller than that of female drivers, especially when the distance is 100 m from the expressway exit and the gap reaches 7.25 degrees. Therefore, gender strongly influences young drivers' saccade behavior characteristics (average saccade range).

Regarding driving age, the driver changes lanes near the expressway exit, so the average saccade increases. It can be seen from the diagram that the average saccade decreases slowly with the increase in the driving experience, which is due to the increase in driver experience but does not change much. Therefore, there is no strong correlation with the age of driving as a factor affecting the saccade behavior characteristics (average saccade amplitude) of young drivers at the exit of a highway.

In terms of the amount of driving mileage, similarly, the driver changes lanes near the expressway exit so that the average saccade will increase. It can be seen from the diagram that as the driving mileage increases, there is a significant correlation between the average saccade amplitude and the driver's driving mileage. Especially when it is more than 10,000 km, the average saccade amplitude of the driver at the expressway exit decreases significantly. Therefore, driving mileage strongly correlates with young drivers' saccade behavior characteristics (average saccade amplitude).

(**a**)
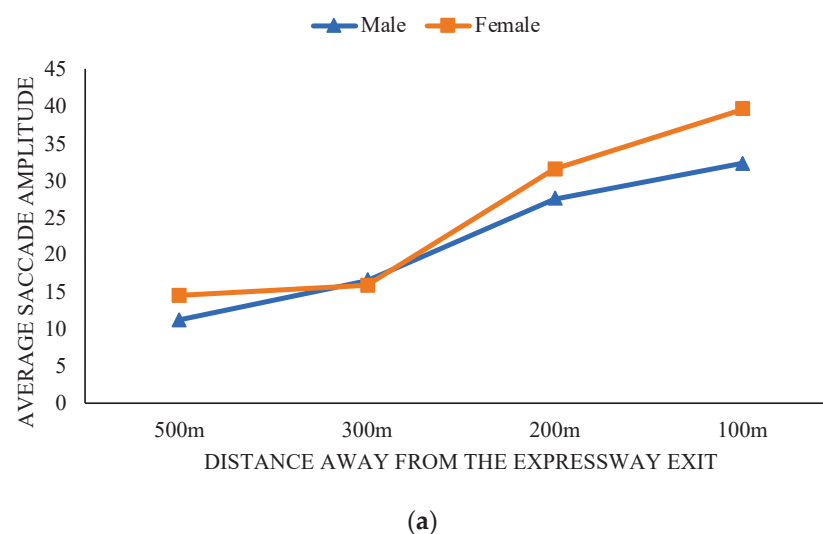
Figure 7. *Cont.*
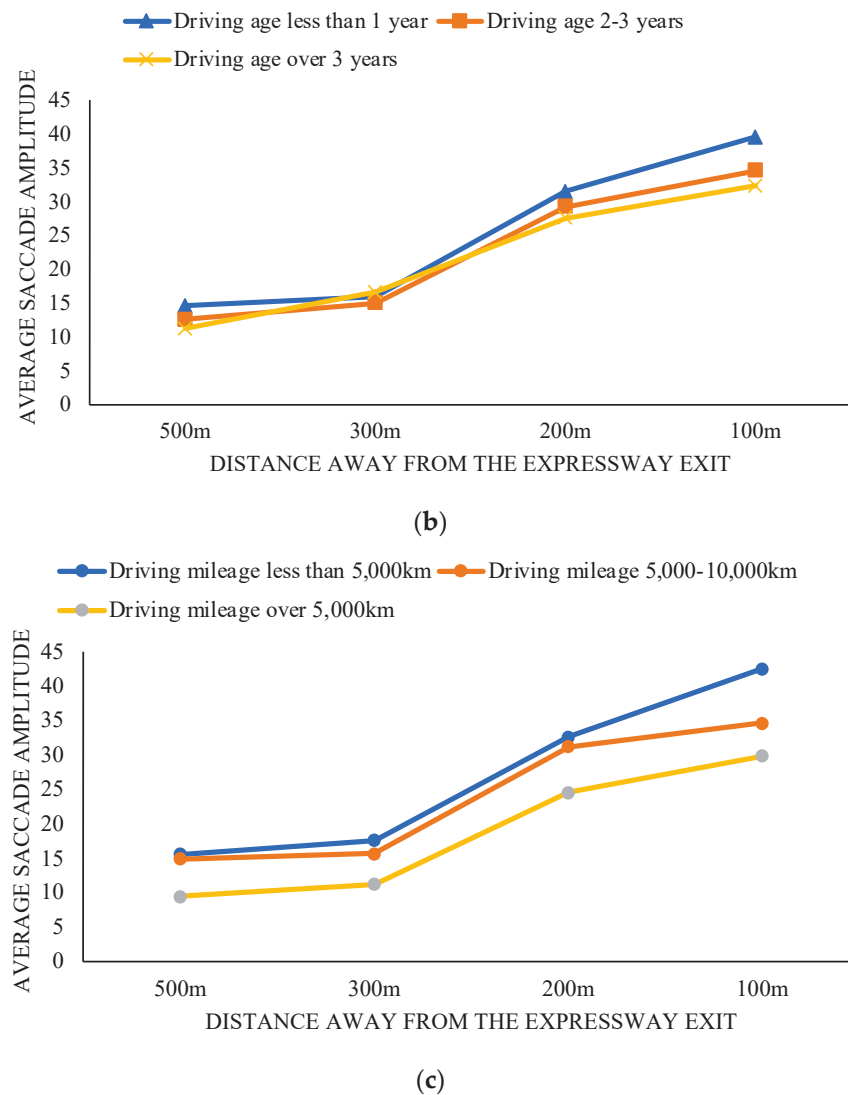
Figure 7. Average saccade amplitude for various driver characteristics. (**a**) Gender. (**b**) Driving experience. (**c**) Driving mileage.

5.3. Heart Rate

Heart rate refers to the number of heartbeats per minute in a normal person's quiet state, also known as the quiet heart rate, which is generally 60 to 100 beats/min. Individual differences can be caused by age, gender, or other physiological attributes. Generally speaking, the younger the age, the faster the heart rate. The slower heartbeat of the elderly than that of the young and the faster heart rate of females than that of males of the same age are both normal physiological phenomena.

The cardio-physiological index selected in this paper is the heart rate index, which was used mainly to obtain the heart rate data of the tested drivers during the experiment through the biofeedback instrument. The feedback from subsequent experimenters shows that the interference from the heart rate detection device with the driver was negligible. Therefore, the heart rate data obtained in this experiment have certain reliability.

The heart rate index in this experiment can roughly reflect the driver's psychological changes while driving the vehicle. The characteristic parameters of the heart rate mainly include the mean value of the heart rate, the difference value of the heart rate, and the rate of change of the heart rate. Because the individual difference in the heart rate index is noticeable, the research on the mean heart rate value is insignificant. Therefore, the characteristic parameter of the heart rate difference is mainly used for statistical analysis

in the subsequent correlation analysis with the steering wheel index. Therefore, when the driver is 500 m away from the expressway exit, the driver's heart rate is highly initial B_0, and then his heart rate at 300 m, 200 m, and 100 m is B_i, and the driver's heart rate difference $Z = B_i - B_0$. The changes in the difference Z between various classifications of drivers' heart rates at 500 m, 300 m, 200 m, and 100 m away from the expressway exit are shown in Figure 8.
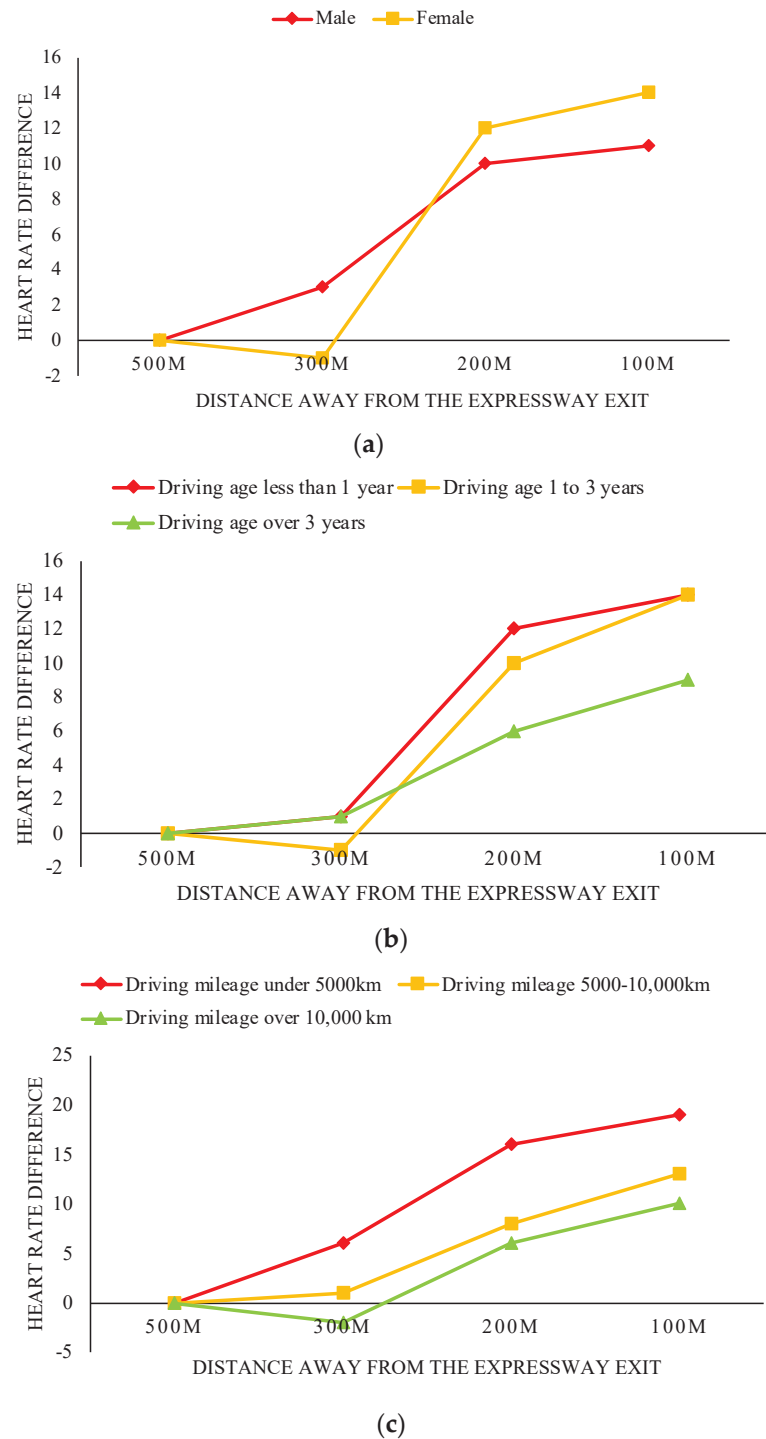

(**a**)

(**b**)

(**c**)

Figure 8. Driver heart rate difference for various driver characteristics. (**a**) Gender. (**b**) Driving experience. (**c**) Driving mileage.

Regarding gender, the driver's heart rate increased significantly at 200 m and 100 m away from the expressway exit because drivers generally choose to change lanes here. In

contrast, the female drivers had a gap in heart rate changes compared with the male drivers, but the gap was not particularly significant, and only about three times per minute. As a result, there is little correlation between gender as a factor influencing the change in heart rate at the expressway exit for young drivers.

Drivers with driving experience of less than 1 year and 2–3 years will have a significant increase in heart rate at 200 m and 100 m from an expressway exit of about 12–14 times/minute. For drivers with driving experience of more than 3 years, the heart rate at 200 m and 100 m from expressway exits will also change significantly, but the change is smaller than that of drivers with driving experience of less than 1 year and 2–3 years. There are only about nine times per minute, so the driving age strongly correlates with the heart rate change at the expressway exit for young drivers, especially drivers with over 3 years and under 3 years of driving experience.

In terms of driving mileage, varying driving mileages characterize the proficiency of the driver's driving behavior. The figure shows a significant difference in heart rate change between drivers with varying driving mileage at the expressway exit. The longer the driving mileage, the smaller the heart rate change at the expressway exit. Therefore, driving mileage has a strong correlation as a factor affecting young drivers' heart rate change at the expressway exit.

6. Concluding Remarks

This paper has focused on the correlation analysis between young drivers' characteristics and visual and physiological attributes at four typical distances of 500 m, 300 m, 200 m, and 100 m from the identification plate at an expressway exit. Based on this study, the following comments are offered:

1. The influence of the driver's characteristics on the number of fixation times is mainly studied for the fixation behavior. The results showed that gender, driving mileage, and fixation number strongly correlate. In contrast, the driving experience has almost no correlation with the fixation behavior characteristics of young drivers at an expressway exit.
2. The effect of driver characteristics on the average saccade magnitude showed that the average saccade magnitude could be affected by gender and driving mileage. At the same time, the driving experience has almost no correlation with the saccade behavior characteristics of young drivers at an expressway exit.
3. Concerning the heart rate, previous studies have shown a significant individual difference in the heart rate and considerable uncertainty in the case of small samples. Therefore, this study mainly analyzed the difference in the heart rate. The correlation between gender and the heart rate was weak, while the correlation between driving experience and driving mileage was strong for the change in the heart rate at an expressway exit.
4. Interestingly, the correlation between the driver's age, the number of fixation times, and the average saccade amplitude was low for young drivers. This is because the number of fixation times and the average saccade are related to the driver's driving experience. The longer the driving experience, the smaller the average saccade, and the less frequently an experienced driver looks at the right rearview mirror since the experienced driver quickly determines the road conditions and opts for the appropriate driving behavior.
5. Most young drivers in China do not necessarily have an immediate chance of obtaining a driver's license. After obtaining their license, they may still go to school or own a vehicle, so the age-responsive driving experience is unacceptable for young drivers. In contrast, driving mileage is a parameter that directly reflects the driver's driving experience. Therefore, the driving experience is directly related to the driver's driving mileage, so driving mileage is strongly related to the number of fixation times and the average saccade range.

6. Several practical implications could be developed based on such findings. For instance, the young drivers could practice their driving skills under the supervision of an experienced driver. An education program could be effective for the young drivers to improve their driving skills and form safe driving habits. The parents are also encouraged to be actively involved in the young drivers' driving education and monitor their progress, such as leaving an expressway at an exit. Moreover, more effective measurements should be set up to improve the driving safety on expressway exit ramps for the highway planners and designers.

References

1. Ji, W. Research on Urban Road Vehicle Lane Change Model Based on Driving Behavior Analysis. Master's Thesis, Harbin University of Technology, Harbin, China, 2018.
2. Sun, H.; Liu, X.; Huang, K. Driver following characteristics based on high-speed natural driving data. *J. Shandong Jiaotong Univ.* **2020**, *28*, 23–29+62.
3. Xiong, X.; Chen, L.; Liang, J.; Cai, Y.; Jiang, H.; Chen, Y. Research on Prediction Method of Dangerous Lane-changing Driving Behavior. *Automot. Eng.* **2017**, *39*, 1040–1046+1067.
4. Portera, A.; Bassani, M. Factors influencing driver behaviour along curved merging interchange terminals. *Transp. Res. Part F Psychol. Behav.* **2020**, *75*, 187–202. [CrossRef]
5. Yuan, W. Experimental Study on Dynamic Visual Characteristics of Automobile Drivers in Urban Road Environment. Ph.D. Thesis, Chang'an University, Xi'an, China, 2008.
6. Yu, Y.; Liang, J.; Chen, L.; Chen, X.; Zhu, N.; Hua, G. Emergency lane-changing behavior prediction method based on Gauss Mixed Hidden Markov Model and Artificial Neural Network. *China Mech. Eng.* **2020**, *31*, 2874–2882+2890.
7. Ji, B. Research on Driving Behavior Forecasting Method Based on Driver Visual Characteristics. Ph.D. Thesis, Jilin University, Changchun, China, 2014.
8. Hou, H. Research on Methods for Identifying Drivers' Interchange Intent on Expressway. Ph.D. Thesis, Jilin University, Changchun, China, 2013.
9. Feng, J. Research on Driving Characteristics of Lane-Changing Vehicles Based on Driver Behavior. Master's Thesis, Wuhan University of Technology, Wuhan, China, 2018.
10. Sheng, Y. Driver Model Considering Visual Cognitive Characteristics. Master's Thesis, Jilin University, Changchun, China, 2020.
11. Tang, L. Analysis and optimization of safety influencing factors at the entrance and exit of Expressway. *Transp. World* **2020**, *19*, 38–39.
12. Wei, C. Driver Changing Behavior Forecast Based on Deep Learning. Master's Thesis, Chang'an University, Xi'an, China, 2020.
13. Wang, Y.; Yin, H. Driving behavior prediction based on AIOHMM model. *Inf. Commun.* **2019**, *3*, 120–123.
14. Cheng, J. Research on the Impact of Emotion on Driving Behavior. Master's Thesis, Southwest Jiaotong University, Chengdu, China, 2019.
15. Cheng, J.; Zhang, Y. Prediction of Vehicle Driving Behavior under Different Emotions. *J. Transp. Eng. Inf.* **2019**, *17*, 125–132.
16. Mahmud, M.; Gates, T.; Savolainen, P.; Safaei, B. Driver response to a dynamic speed feedback sign at a freeway exit ramp considering the sign design and installation characteristics. *Transp. Res. Rec.* **2023**, *2677*, 289–301. [CrossRef]
17. Tian, X. Evaluation and Application of Driver's Mental Load Based on Heart Rate Variability. Master's Thesis, Northern University of Technology, Beijing, China, 2016.

18. Chen, X.; Liu, S.; Zhao, J.; Wu, H.; Xian, J.; Montewka, J. Autonomous port management based AGV path planning and optimization via an ensemble reinforcement learning framework. *Ocean. Coast. Manag.* **2024**, *251*, 107087. [CrossRef]

19. Zhang, D.; Chen, F.; Zhu, J.; Wang, C.; Cheng, J.; Zhang, Y.; Bo, W.; Zhang, P. Research on drivers' hazard perception in plateau environment based on visual characteristics. *Accid. Anal. Prev.* **2022**, *166*, 106540. [CrossRef] [PubMed]

Enhancing Metabolic Syndrome Detection through Blood Tests Using Advanced Machine Learning

Petros Paplomatas [1,*], Dimitris Rigas [2], Athanasia Sergounioti [3] and Aristidis Vrahatis [1,*]

[1] Bioinformatics and Human Electrophysiology Laboratory, Department of Informatics, Ionian University, 49100 Corfu, Greece
[2] Independent Researcher, 33100 Amfissa, Greece; rigas_dimitris@yahoo.gr
[3] Medical Laboratory Department, General Hospital of Amfissa, 33100 Amfissa, Greece; nasiaser@yahoo.gr
[*] Correspondence: petrospaplomatas@gmail.com (P.P.); aris.vrahatis@gmail.com (A.V.)

Abstract: The increasing prevalence of metabolic syndrome (MetS), a serious condition associated with elevated risks of cardiovascular diseases, stroke, and type 2 diabetes, underscores the urgent need for effective diagnostic tools. This research carefully examines the effectiveness of 16 diverse machine learning (ML) models in predicting MetS, a multifaceted health condition linked to increased risks of heart disease and other serious health complications. Utilizing a comprehensive, unpublished dataset of imbalanced blood test results, spanning from 2017 to 2022, from the Laboratory Information System of the General Hospital of Amfissa, Greece, our study embarks on a novel approach to enhance MetS diagnosis. By harnessing the power of advanced ML techniques, we aim to predict MetS with greater accuracy using non-invasive blood test data, thereby reducing the reliance on more invasive diagnostic methods. Central to our methodology is the application of the Borda count method, an innovative technique employed to refine the dataset. This process prioritizes the most relevant variables, as determined by the performance of the leading ML models, ensuring a more focused and effective analysis. Our selection of models, encompassing a wide array of ML techniques, allows for a comprehensive comparison of their individual predictive capabilities in identifying MetS. This study not only illuminates the unique strengths of each ML model in predicting MetS but also reveals the expansive potential of these methods in the broader landscape of health diagnostics. The insights gleaned from our analysis are pivotal in shaping more efficient strategies for the management and prevention of metabolic syndrome, thereby addressing a significant concern in public health.

Keywords: metabolic syndrome (MetS); machine learning (ML); feature importance; Borda count method; predictive modeling; ensemble models; cross-validation; non-invasive diagnostics

1. Introduction

Non-communicable diseases (NCDs), also known as lifestyle-related diseases, are a group of diseases that are not contagious and result from a combination of genetic, behavioral, physiological and environmental factors. The predominant NCDs are cardiovascular diseases (CVD), neoplasms, diabetes mellitus and chronic respiratory diseases [1]. NCSs have emerged as serious threats to health systems globally, as they are held responsible for higher rates of morbidity and mortality than all other causes combined [2], in both the developed and the underdeveloped world [3]. The early detection of NCDs is of paramount importance, since it allows timely treatment which consequently secures a higher probability of a successful outcome [4].

Metabolic syndrome (MetS) represents a significant health challenge, characterized by a cluster of metabolic dysregulations including insulin resistance, central obesity, dyslipidemia, and hypertension. Multiple acquired and genetic entities are involved in the pathogenesis of MetS, most of which contribute to insulin resistance and chronic microinflammation [5]. Most notably, accelerating economic development, an aging population,

changes in lifestyle, and obesity are all contributing to the rising prevalence of MetS. The global prevalence of MetS is estimated to be between 20 and 25%. If not treated, MetS leads to an increased risk of developing diabetes mellitus, cardiovascular diseases (CVDs), cancer [6] and chronic kidney disease [7]. Moreover, MetS has been associated with Alzheimer's disease [8,9], neuroinflammation and neurodegeneration [10], female and male infertility [11,12], chronic obstructive pulmonary disease (COPD) [13,14], autoimmune disorders [15–17] and even ocular [18,19] and dental diseases [20–22].

This predisposition to cardiovascular diseases and type 2 diabetes has further broadened to include complications such as non-alcoholic fatty liver disease, chronic prothrombotic and proinflammatory states, and sleep apnea. Despite efforts by various global health organizations, achieving a universal consensus on the precise definition of MetS remains a significant challenge for healthcare practitioners and researchers [5,23,24]. The widespread prevalence of MetS leads to substantial socio-economic costs due to its associated significant morbidity and mortality. Recognized as a global pandemic, MetS places immense pressure on healthcare systems worldwide. Thus, accurately predicting populations at high risk for MetS and proactively implementing prevention measures have become essential in contemporary healthcare management [25,26].

In response to these challenges, recent years have witnessed a paradigm shift towards leveraging advanced technological methods like machine learning (ML) for understanding and predicting MetS. While traditional analytical methods like linear and logistic regression have their merits, they often come with limitations, including stringent assumptions and challenges in managing multicollinearity. In contrast, ML offers a more nuanced and adaptable approach, potentially overcoming these limitations and providing deeper insights into MetS. This shift towards innovative computational techniques marks a significant advancement in metabolic health research [23].

Delving into the specifics of ML, various models such as decision trees, random forests, support vector machines, and k-NN classifiers have demonstrated notable success in diagnosing MetS. Their ability to employ non-invasive features for prediction sets these models apart, eliminating the need for invasive testing procedures. Furthermore, the capability of ML to intricately analyze metabolic patterns significantly enhances the specificity and sensitivity of MetS diagnosis [24–26].

Acknowledging the critical role of early and accurate diagnosis in managing MetS, our research is geared towards a comprehensive comparative analysis of 16 machine learning methods. This study aims to not only highlight the unique capabilities of each method in predicting MetS but also to showcase the diverse applications of ML in this vital health field. This study aims to achieve two primary objectives: first, to perform a comprehensive comparative analysis of 16 machine learning classifiers in predicting MetS; and second, to introduce the Borda count method as an innovative approach to refine the dataset and enhance predictive accuracy. By implementing the Borda count method, we plan to refine our data according to the relevance of variables identified by the top-performing models. This methodological approach is anticipated to significantly improve the accuracy of our analysis and contribute to the development of more effective management and prevention strategies for MetS, thus addressing a major public health concern.

Recent progress in predicting metabolic syndrome (MetS) has notably utilized machine learning techniques. A pivotal study "Metabolic Syndrome Prediction Models Using Machine Learning" [23] was a crucial work that investigated the efficacy of these methods in MetS prediction, with a novel focus on incorporating Sasang constitution types from traditional Korean medicine into the models. This integration significantly increased the sensitivity of multiple machine learning methodologies, highlighting a unique synergy between traditional medical insights and modern predictive algorithms.

Further, "Metabolic Syndrome Prediction Models" [27] presented a breakthrough in predicting MetS for non-obese Koreans, incorporating both clinical and genetic polymorphism data. This study highlighted the importance of genetic factors in MetS models, particularly for non-obese persons who are often underrepresented in such studies. No-

tably, models using Naïve Bayes classification performed better, especially when genetic information was included.

Nine machine learning classifiers were evaluated in a dataset of 2400 patients [28], resulting in the XGBoost model outperforming the other ones, with an F1 score of 0.913. Using a large-scale Korean health examination dataset of 70,370 records, 13.6% of them diagnosed with MetS [29], a prognostic model was developed having an AUC = 0.889, recall = 0.855, and specificity = 0.773. It is remarkable that using only four features as predictors (waist circumference, systolic and diastolic blood pressures, and sex) in this research, the prediction model performance did not have a difference in model evaluation metrics.

2. Materials and Methods

2.1. Data

In this study, data from the Laboratory Information System (LIS) database of the Medical Laboratory Department at the General Hospital of Amfissa, Greece, covering the period from 2017 to 2022 were analyzed. The focus of our study was a group of 77 individuals, comprising 38 men and 39 women, who met the three laboratory criteria for the diagnosis of metabolic syndrome (MetS) as defined by the revised US National Cholesterol Education Program's Adult Treatment Panel III (NCEP ATP III). These criteria include fasting glucose levels exceeding 100 mg/dL, triglycerides over 150 mg/dL, and HDL cholesterol levels below 40 mg/dL for men and below 50 mg/dL for women. We compared the MetS group with a control group of 63 individuals (31 men and 32 women) who did not meet any of the diagnostic criteria for MetS. The study evaluated a range of variables, including Gender, Age, Glucose, Triglycerides, HDL (High-Density Lipoprotein), SGOT (Serum Glutamic-Oxaloacetic Transaminase), SGPT (Serum Glutamic-Pyruvic Transaminase), GGT (Gamma-Glutamyl Transferase), ALP (Alkaline Phosphatase), HBA1c (Hemoglobin A1c), Urea, Uric Acid, WBC (White Blood Cells), ANC (Absolute Neutrophil Count), ANL (Absolute Neutrophil to Lymphocyte ratio), PLT (Platelet Count), MPV (Mean Platelet Volume), HT (Hematocrit), and Hg (Hemoglobin). The analysis of these variables aimed to enhance the understanding and prediction of MetS, thus contributing to the improvement of diagnosis and treatment strategies.

2.2. Data Preprocessing

In our study, data preprocessing was a critical step, essential for the effective application of sophisticated analytical techniques in machine learning. Understanding the importance of this phase, certain pivotal variables associated with metabolic syndrome (MetS), specifically glucose (GLU), triglycerides (TRIG), and high-density lipoprotein cholesterol (HDL) (US National Cholesterol Education Program's Adult Treatment Panel III (NCEP ATP III)) were removed to mitigate the risk of model overfitting.

By excluding these direct diagnostic markers, the models were enabled to explore and leverage other informative yet less direct indicators in the dataset. This approach was intended to unearth subtle patterns that might be eclipsed by the more direct MetS indicators, thus providing a broader perspective on the disease's markers.

Following the exclusion of these variables, a comprehensive series of data adjustments was undertaken to optimize the dataset for machine learning analysis. Our adjustments included type inference for correct data categorization, the imputation of missing values, and the encoding of categorical variables. Additionally, we applied Z-score normalization to ensure uniformity in feature scale, which is crucial for the comparative evaluation of machine learning models and the enhancement of algorithmic computations.

Finally, to underscore the consistency and reproducibility of our analysis, a session seed was meticulously established. This practice lays a solid foundation for future implementations of machine learning models, ensuring that results are reliable and can be replicated in further studies. Through these detailed preprocessing steps, our dataset was transformed into a robust foundation, setting the stage for an in-depth evaluation of the predictive capabilities of 16 machine learning models in diagnosing MetS.

2.3. Machine Learning Models and Evaluation

A thorough examination of machine learning techniques was carried out, including algorithms such as Quadratic Discriminant Analysis, Naive Bayes, Linear Discriminant Analysis, CatBoost Classifier, Extra Trees Classifier, Random Forest Classifier, Gradient Boosting Classifier, Light Gradient Boosting Machine, Ada Boost Classifier, Extreme Gradient Boosting, Logistic Regression, Ridge Classifier, Decision Tree Classifier, Dummy Classifier, and SVM. An ensemble methodology based on Borda count was used to improve forecast precision even further. The Borda count is a method where candidates or choices are ranked by preference. In this technique, each candidate is assigned a specific number of points based on their position in the ranking, with points calculated relative to the least preferred options. This process determines the overall preference or winner, as the outcome depends not only on who receives the most first-place votes but also on how the competitors are ranked overall, making it more consistent across all models [30].

To ensure robust model evaluation, the study employs a nested 10-fold cross-validation technique, which has been shown to outperform typical k-fold cross-validation in terms of predicted accuracy. An outer k-fold cross-validation loop is used in nested cross-validation to offer a comprehensive assessment of the best model's performance. Each outer fold uses an inner cross-validation loop to fine-tune the model's parameters at the same time [23].

The performance of each method was painstakingly tested across a range of measures, including AUC, recall, precision, F1 score, Kappa, MCC, T-Sec (Time in Seconds), and total accuracy. The models' comparative efficacy was principally assessed using their AUC values, with the detailed metrics summarized in Table 1 [24]. In the world of diagnostic instruments, the importance of sensitivity over specificity is heightened by the urgency of diagnosis and subsequent intervention, unless specificity is significantly degraded [25].

Table 1. Comparison of clustering evaluation metrics between a full feature set and a reduced feature set comprising the top 3 features, highlighting performance changes in terms of separation, spread, and correlation.

Metric	Full Feature Set	Top 3 Features	Improvement Indication
Silhouette Score	0.1151535	0.1051986	Decreased (slight)
Dunn Index	0.0009324	0.0014525	Improved (better separation)
Calinski–Harabasz Index (CH)	169.7546	187.8952	Improved (more defined)
Separation	0.0064366	0.0149632	Improved (increased distance)
Diameter	6.903106	10.30144	Increased (larger spread)
Average Within-Cluster Distance	2.834242	4.094495	Increased (more variance)
Pearson Gamma	0.0948925	0.124181	Improved (stronger correlation)
Within-Cluster Sum of Squares (SS)	7869.409	15,378.26	Increased (more spread)

The Borda count approach was used for feature importance aggregation among several models. For each model, features were ranked in order of relevance, with the most important feature receiving the highest rating and the least important receiving the lowest. These ranks were then aggregated using the Borda count method. The Borda score was calculated by adding the ranks of each feature from the best three models. Instead of relying on a single model's feature importance, which could be skewed or overfitted to a specific dataset, the aggregated Borda scores provided a more holistic and robust perspective of feature significance. This technique ensured that the most relevant traits were consistently recognized as such across various models, improving the dependability of the isolated features and setting the framework for creating more robust ensemble models in later rounds of the study.

3. Results

3.1. Cumulative Insights: Unveiling Model Outcomes

A heatmap was used to compare performance metrics across 16 machine learning algorithms for the initial dataset of 24 features. Each algorithm was evaluated based on key

metrics: accuracy, AUC (Area Under the Curve), recall, precision, Kappa, MCC (Matthews Correlation Coefficient), F1, and T-Sec (Time in Seconds). The heatmap (Figure 1) provides an intuitive and visually appealing depiction of these results.
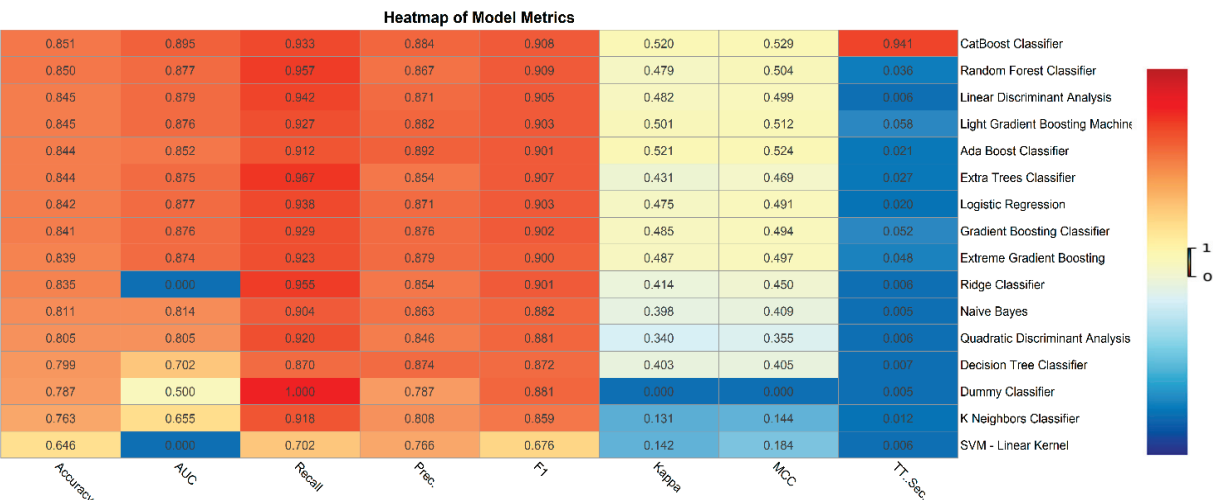
Figure 1. The heatmap displays performance metrics for various machine learning algorithms. Metrics on the x-axis provide insight into each model's capabilities. The color gradient, from dark blue to dark red, represents the range of metric values.

3.2. Visual Representations

A 10-fold cross-validation technique was implemented to achieve a detailed understanding of the model's performance. To highlight the variability and reliability of model outcomes, a shaded region plot was designed (Figure 2). This plot emphasizes the mean values of both accuracy and F1 score for each model.
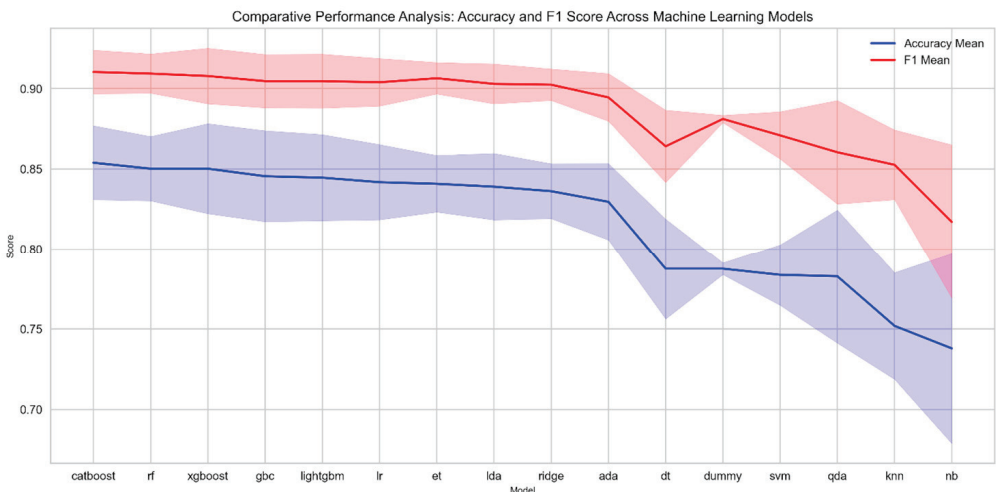
Figure 2. This plot delineates the mean scores of both accuracy (depicted in blue) and F1 (shown in red) for 16 distinct machine learning models. The x-axis signifies each of the models, and the y-axis captures the range of scores. To further understand the variability in model performance, shaded regions are incorporated around each mean line. The regions embody a span of one standard deviation above and below the respective mean scores, providing insight into the distribution and consistency of results for each model.

3.3. Feature Importance Analysis

Understanding the significance of individual features is crucial for interpreting the predictive power and functionality of our models. Based on performance metrics, the top three models identified were CatBoost, Random Forest, and XGBoost. These models

calculate variable importance through internal scoring mechanisms during training. For instance, Random Forest derives importance from the decrease in Gini impurity when a feature is used to split the data; the greater the decrease, the higher the feature's importance score. CatBoost evaluates how each feature influences the loss function, assigning higher importance to features that significantly reduce loss. XGBoost uses gain, coverage, and frequency metrics, where gain measures the improvement in accuracy a feature provides, coverage measures the number of observations a feature affects, and frequency counts how often a feature is used in trees. These scores are extracted post-training to understand each feature's contribution to the model's predictions, enhancing the transparency and interpretability of our predictive models.

3.3.1. Individual Models

Various machine learning models demonstrated distinct feature prioritization. The top three models were evaluated to ascertain the most influential predictors based on their contributions to the models. The CatBoost model identifies hemoglobin A1C (HbA1C) as the most significant predictor, followed by White Blood Cells (WBC), Uric Acid (UA), and Gamma-Glutamyl Transferase (GGT). Conversely, Eosinophils (EOS) and Alkaline Phosphatase (ALP) are found to be less predictive. Similarly, the Random Forest model also ranks HbA1C as the primary predictive feature, with UA closely following in significance. It acknowledges the importance of WBC and GGT but assigns lower predictive value to Mean Platelet Volume (MPV) and Granulocytes (GRAN). Meanwhile, the XGBoost model echoes these trends, reaffirming the central role of HbA1C and also underscoring the relevance of WBC and GGT. However, it places more emphasis on the GRAN feature, marking a slight departure from the CatBoost model's findings.

3.3.2. Borda Count Ensemble Feature Importance

The ensemble method integrates the predictions from the previously discussed three models, combining their distinct strengths for enhanced predictive power. The feature importance analysis of this ensemble approach (Figure 3) offers a comprehensive perspective on which features are most influential in the collective decision-making process of the ensemble model.
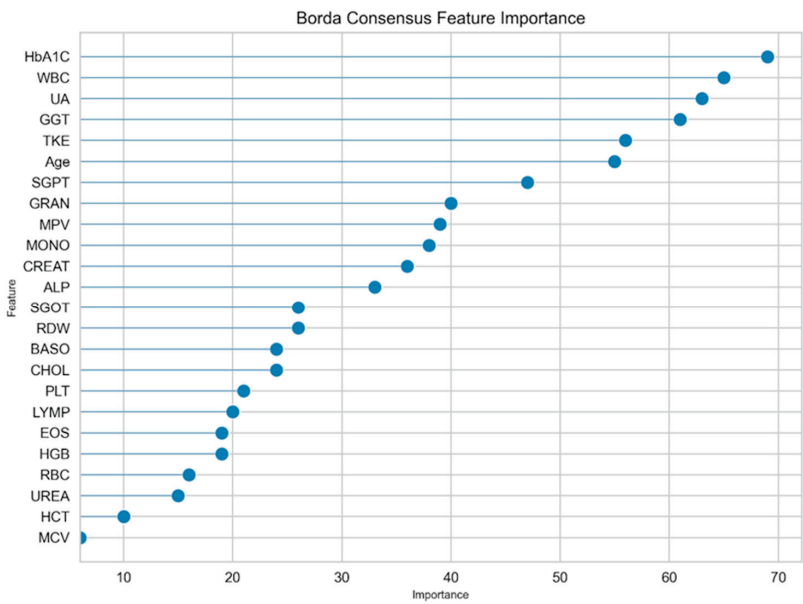
Figure 3. Borda consensus feature importance plot. This visualization represents the aggregated feature importance derived from an ensemble method using the Borda count. Each dot corresponds to a specific feature, with its horizontal position indicating its consensus importance.

3.3.3. Sequential Feature Addition Based on Borda Importance

To further illustrate the cumulative impact of features as they are added sequentially based on their Borda importance, a detailed graph was constructed using the KNN algorithm (Figure 4). KNN was used to determine both accuracy and F1 score for each incremental addition in each feature. The x-axis in this plot lists the features in order of Borda significance, adding one feature each time, and the y-axis shows the associated model accuracy. When the model just includes the first feature (as rated by Borda significance), the F1 score is 56%. Interestingly, a higher accuracy of 85% is attained in the three first features; when the first three features—HbA1C, WBC, and UA—are included, the F1 score is reported to be 55%. This minor decrease in the F1 score, despite the addition of new variables, implies that there is not a significant difference in importance between these features in terms of predictive potential. Based on these findings, the first three features, HbA1C, WBC, and UA, were chosen to create a new comparison for the 16 algorithms that only used these three data. The goal was to investigate if an ensemble approach, which integrates ideas from various algorithms, may improve the model's performance even further when compared to the KNN-based evaluation.
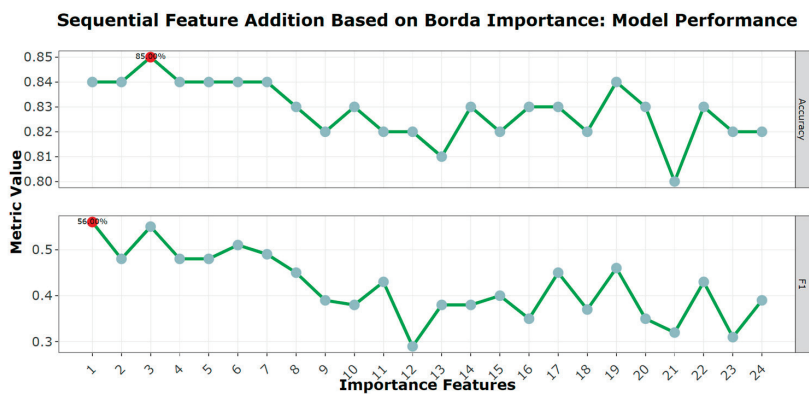
Figure 4. Sequential feature addition based on Borda importance: This plot visualizes how the model's accuracy evolves as features are added in order of their Borda importance using the KNN algorithm. The peaks emphasize the most impactful features, while troughs suggest features that may not substantially contribute to or even slightly hinder the model's accuracy.

3.4. Ensemble Model Results

To determine the efficacy of the selected three features—HbA1C, WBC, and UA—in predicting metabolic conditions, various ensemble models were constructed and evaluated. The heatmap presented (Figure 5) elucidates the performance of these models across a myriad of metrics, including accuracy, AUC, recall, precision, F1 score, Kappa, and MCC.
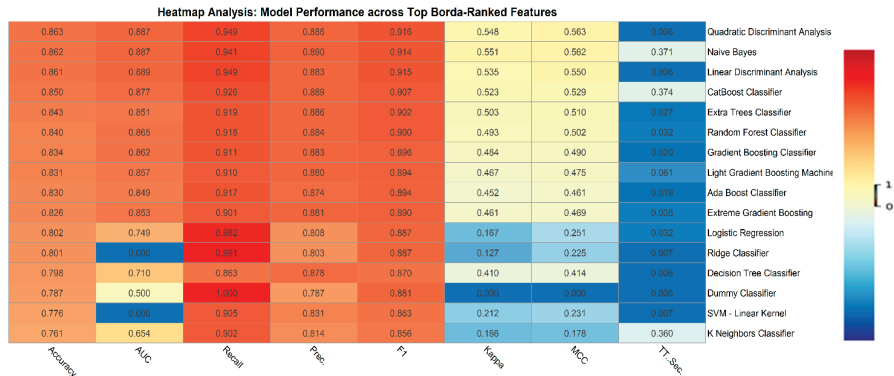
Figure 5. The heatmap showcases the performance metrics of various machine learning models using selected features derived from ensemble methods (HbA1C, WBC, and UA). Metrics on the x-axis indicate the effectiveness of each algorithm. A color gradient transitioning from dark blue to dark red represents the spectrum of metric values.

3.5. Clustering Analysis Post-Ensemble Method: Insights before and after Feature Selection

In our analysis, we employed Uniform Manifold Approximation and Projection (UMAP) for clustering. UMAP is a non-linear dimensionality reduction technique that is particularly effective in preserving the local and global structure of high-dimensional data. It works by constructing a high-dimensional graph representation of the data, which is then optimized to produce a low-dimensional embedding. This method is advantageous for visualizing complex datasets and identifying clusters within the data. UMAP is chosen over other techniques like PCA and t-SNE due to its ability to maintain both local and global data structures, its computational efficiency, and its scalability with large datasets.

Specifically, the UMAP algorithm initializes with a random low-dimensional layout of the data and iteratively adjusts it by minimizing a cross-entropy loss function that quantifies the difference between the high-dimensional and low-dimensional data distributions [31]. The resulting embedding effectively captures the intrinsic geometry of the data, making it an ideal choice for clustering tasks. Our implementation utilized the default settings of the UMAP package in R.

Our clustering analysis was enhanced through the application of a Uniform Manifold Approximation and Projection (UMAP) algorithm, which revealed distinctive patterns in our dataset comprising patients with and without metabolic syndrome (Mets and Non-Mets). Initially, the UMAP algorithm was applied to the entire feature set, resulting in clusters that, while indicative of an underlying structure, showed considerable overlap between the two patient groups (Figure 6). This overlap suggested an absence of clear delineation, potentially due to the confounding influence of less discriminative features. Subsequently, our approach was refined by focusing on the three most important features, as determined by the Borda count ensemble feature importance method. Remarkably, the resultant clusters exhibited a more pronounced separation, with less overlap and more defined grouping (Figure 7). This improvement visually suggests that the selected features capture the essence of the data more effectively, offering a more lucid distinction between Mets and Non-Mets patients. To substantiate these visual observations, we conducted a quantitative analysis, wherein metrics such as silhouette scores and the Dunn index were computed pre- and post-feature selection. The post-selection results showed a marginally lower silhouette score but an improved Dunn index and Calinski–Harabasz score, indicating better-defined clusters despite an increase in within-cluster variance. These mixed results underscore the complexity of the dataset and the trade-off between cluster separation and cohesion. Overall, there is an improvement in clustering performance with the top three features (Table 1). Our findings elucidate the potential of ensemble-based feature selection in enhancing the interpretability of clustering outcomes, which is pivotal for advancing precision medicine in the context of metabolic syndrome.
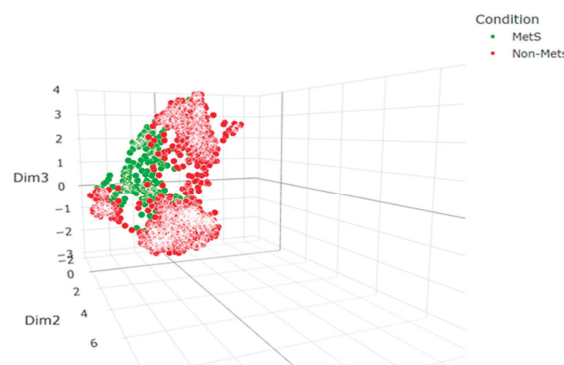
Figure 6. Representation of the clustering results obtained when the Uniform Manifold Approximation and Projection (UMAP) algorithm was applied to the entire feature set of our dataset. In this figure, patients diagnosed with metabolic syndrome are indicated by green points, while those without the syndrome are marked in red.
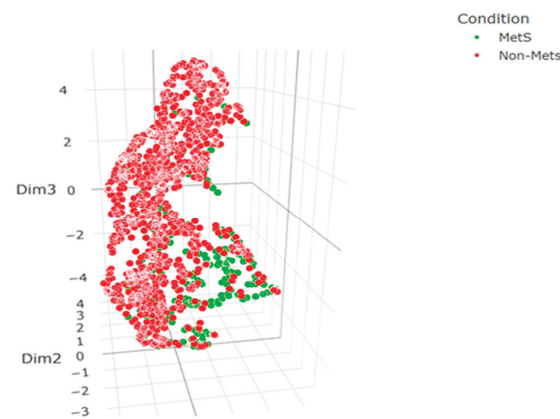
Figure 7. Showcase of the clustering outcome following the application of UMAP on a reduced set of features, specifically the three most significant features as identified using the machine learning model. Similar to Figure 1, green points denote Mets patients and red points represent Non-Mets patients. The axes in this figure also reflect the UMAP components, albeit within a feature space constrained to the three key attributes. The spatial arrangement of points in this reduced dimensionality space demonstrates a more pronounced demarcation between the two patient groups, suggesting that the chosen features offer a sharper distinction in the clustering pattern.

3.6. Model Comparisons

A thorough analysis of the various models using metrics such as AUC, accuracy, recall, precision, Kappa, MCC, and F1 score offers a nuanced understanding of their performance. The CatBoost Classifier stands out with an impressive AUC of 0.941, underlining its capability in class differentiation. While models like the Random Forest Classifier and CatBoost Classifier exhibit strong results in the Kappa and MCC metrics, others like Ridge Classifier and Naive Bayes indicate areas of improvement, especially in terms of recall. The varied performance serves as a reminder of the criticality of selecting models in alignment with specific project objectives, be it a focus on precision or recall.

The ensemble methods bring in a fresh perspective. Despite relying on only three of the original 24 features, many ensemble models demonstrated remarkable performance. This achievement reaffirms the importance of the selected features, HbA1C, WBC, and UA, in diagnosing metabolic conditions. For instance, the Random Forest model, even with a reduced feature set, exhibits a commendable accuracy and F1 score. Such outcomes from ensemble methods underline the potential of feature reduction, especially when it is backed by a solid selection rationale like Borda importance.

Furthermore, the T-Sec metric emphasizes the balance between model performance and computational efficiency. While some models are time-efficient, others demand more computational resources, a factor to be considered especially in real-time applications. To summarize, the combination of individual model outcomes with ensemble method results, alongside the feature importance plots, equips readers with a comprehensive understanding of the results. It provides clarity on both the performance of each model and the influence of each feature within those models and their ensemble counterparts.

4. Discussion

Our findings indicate that ensemble models, particularly those utilizing the Borda count method, significantly enhance predictive accuracy for MetS. This suggests that combining multiple ML models can better capture the complex nature of MetS. Future research should explore the integration of additional variables and larger datasets to further validate these results.

Various studies have shown that HbA1c, WBC and UA are successful predictors of MetS [32–37]. In fact, there is an established causal relationship between the biochemical pathways indicated by these parameters and MetS. Glycated hemoglobin (HbA1c) is considered a reliable biomarker of long-term glucose maintenance and has been proposed

as a potential diagnostic criterium for MetS [38]. HbA1c is produced by the non-enzymatic reaction between sugars, mainly glucose, and hemoglobin. In case of glucose intolerance, as in MetS or diabetes mellitus, the level of HbA1c is correlated to the blood glucose level and the duration of the glucosemia [39]; therefore, it is a very useful biomarker for the diagnosis and follow-up of diabetes mellitus.

Chronic, low-grade inflammation has been shown to be a central underlying mechanism in the pathophysiology of MetS [40]. The exact relationship between elevated UA (hyperuricemia) and MetS has not yet been defined [41]. However, UA, which is the end product of purine metabolism, is implicated in inflammation and several mechanisms have been outlined, such as the activation of the inflammasome, the production of free radicals [42], and cytokines [43]. On the other hand, WBC is an objective parameter of systemic inflammation [34] and the positive association between WBC and MetS has been often underlined by several studies [33,35,44,45]. Consequently, it is not surprising that these three parameters, the biochemical background of which is so tightly intertwined in the pathophysiology if MetS, emerge as satisfactory, alternative predictors of MetS in our study.

In conclusion, the ensemble methods in particular demonstrate impressive performance despite a significantly reduced feature set. The three chosen features—HbA1C, WBC, and UA—emerge as critical predictors of metabolic conditions, with their importance magnified against the backdrop of more comprehensive models. Notably, while models like CatBoost and Random Forest, known for their reliance on a diverse feature set, show high accuracy and F1 scores, they are outperformed by simpler algorithms such as Quadratic Discriminant Analysis, Naive Bayes, and Linear Discriminant Analysis in the ensemble context. This shift underlines the importance of feature selection in both understanding metabolic states and in the strategic choice of algorithms for predictive accuracy.

A compelling insight from the heatmap analysis, both pre- and post-ensemble method application, is the notable change in model rankings. Models based on linear analysis gain prominence, overshadowing traditionally dominant models like CatBoost and Random Forest. This shift highlights the significant impact of feature reduction on model efficacy. Furthermore, certain anomalies, especially in the KNN algorithm, suggest the potential for overfitting or challenges associated with a limited feature set, emphasizing the need for rigorous model validation for broader applicability.

In contrast, the performance metrics of models using the full feature set offer a benchmark for comparison. These metrics reveal varied performance across models, with the CatBoost Classifier excelling in class differentiation due to its high AUC value. Conversely, models with lower Recall scores, like the Ridge Classifier and Naive Bayes, indicate challenges in accurately identifying true positives. The T-Sec metric underscores the importance of balancing predictive accuracy with computational efficiency, especially in real-time diagnostic applications.

The ensemble methods in our study exemplify the power of combining predictions from various machine learning algorithms to create a model that often surpasses the accuracy of individual components. These methods not only enhanced performance but also emphasized the effectiveness of a smaller feature set. By concentrating on just 3 critical features out of the initial 24, the ensemble approach achieved remarkable results, underscoring its ability to extract valuable insights from minimal data.

These performance measures highlight the ensemble's ability to harness the strengths of individual models while mitigating their weaknesses. The Random Forest model, for example, typically benefits from a diverse feature set but achieved notable accuracy and F1 scores even with the reduced feature set. This finding illustrates the ensemble's capability to enhance both feature selection and model performance. Moreover, the ensemble method offers a holistic view of feature relevance, providing a consensus on the most crucial variables for predicting metabolic states. This collective intelligence is invaluable in real-world applications, where understanding the interplay of various factors is crucial.

5. Conclusions

In conclusion, our study highlights the superior performance of the CatBoost Classifier in predicting MetS, as evidenced by its high AUC score. The effectiveness of ensemble models, especially with feature reduction to HbA1C, WBC, and UA, underscores the importance of strategic feature selection in improving diagnostic accuracy.

The varied performances across models like the Random Forest and Ridge Classifier underline the importance of matching model selection with specific project objectives, such as precision or recall. Further emphasizing the efficacy of strategic feature selection, our exploration of ensemble methods demonstrates remarkable predictive power by focusing on just three critical features—HbA1C, WBC, and UA. This not only showcases the potential of feature reduction but also accentuates the importance of each feature in MetS diagnosis. The study also brings to light the crucial balance between model performance and computational efficiency, an important consideration for real-time applications. Altogether, the integration of individual and ensemble model outcomes, coupled with feature importance analysis, provides a holistic understanding of machine learning's applicability in MetS prediction, contributing significantly to the advancement of non-invasive diagnostic tools and opening new avenues for future research in optimizing machine learning models for healthcare applications.

References

1. NCDs. Main NCDs. Available online: http://www.emro.who.int/noncommunicable-diseases/diseases/diseases.html (accessed on 19 May 2024).
2. Wang, Y.; Wang, J. Modelling and Prediction of Global Non-Communicable Diseases. *BMC Public Health* **2020**, *20*, 822. [CrossRef] [PubMed]
3. Saklayen, M.G. The Global Epidemic of the Metabolic Syndrome. *Curr. Hypertens. Rep.* **2018**, *20*, 12. [CrossRef] [PubMed]
4. Madadizadeh, F.; Bahrampour, A.; Mousavi, S.M.; Montazeri, M. Using Advanced Statistical Models to Predict the Non-Communicable Diseases. *Iran. J. Public Health* **2015**, *44*, 1714–1715. [PubMed]
5. Fahed, G.; Aoun, L.; Bou Zerdan, M.; Allam, S.; Bou Zerdan, M.; Bouferraa, Y.; Assi, H.I. Metabolic Syndrome: Updates on Pathophysiology and Management in 2021. *Int. J. Mol. Sci.* **2022**, *23*, 786. [CrossRef] [PubMed]
6. Mili, N.; Paschou, S.A.; Goulis, D.G.; Dimopoulos, M.-A.; Lambrinoudaki, I.; Psaltopoulou, T. Obesity, Metabolic Syndrome, and Cancer: Pathophysiological and Therapeutic Associations. *Endocrine* **2021**, *74*, 478–497. [CrossRef] [PubMed]
7. Lin, L.; Tan, W.; Pan, X.; Tian, E.; Wu, Z.; Yang, J. Metabolic Syndrome-Related Kidney Injury: A Review and Update. *Front. Endocrinol.* **2022**, *13*, 904001. [CrossRef]
8. Li, J.; Zhang, Y.; Lu, T.; Liang, R.; Wu, Z.; Liu, M.; Qin, L.; Chen, H.; Yan, X.; Deng, S.; et al. Identification of Diagnostic Genes for Both Alzheimer's Disease and Metabolic Syndrome by the Machine Learning Algorithm. *Front. Immunol.* **2022**, *13*, 1037318. [CrossRef] [PubMed]
9. Ali, A.; Ali, A.; Ahmad, W.; Ahmad, N.; Khan, S.; Nuruddin, S.M.; Husain, I. Deciphering the Role of WNT Signaling in Metabolic Syndrome-Linked Alzheimer's Disease. *Mol. Neurobiol.* **2020**, *57*, 302–314. [CrossRef]
10. Więckowska-Gacek, A.; Mietelska-Porowska, A.; Wydrych, M.; Wojda, U. Western Diet as a Trigger of Alzheimer's Disease: From Metabolic Syndrome and Systemic Inflammation to Neuroinflammation and Neurodegeneration. *Ageing Res. Rev.* **2021**, *70*, 101397. [CrossRef]

11. He, Y.; Lu, Y.; Zhu, Q.; Wang, Y.; Lindheim, S.R.; Qi, J.; Li, X.; Ding, Y.; Shi, Y.; Wei, D.; et al. Influence of Metabolic Syndrome on Female Fertility and in Vitro Fertilization Outcomes in PCOS Women. *Am. J. Obs. Gynecol.* **2019**, *221*, 138.e1–138.e12. [CrossRef]

12. Goulis, D.G.; Tarlatzis, B.C. Metabolic Syndrome and Reproduction: I. Testicular Function. *Gynecol. Endocrinol.* **2008**, *24*, 33–39. [CrossRef] [PubMed]

13. Fekete, M.; Szollosi, G.; Tarantini, S.; Lehoczki, A.; Nemeth, A.N.; Bodola, C.; Varga, L.; Varga, J.T. Metabolic Syndrome in Patients with COPD: Causes and Pathophysiological Consequences. *Physiol. Int.* **2022**, *109*, 90–105. [CrossRef] [PubMed]

14. Clini, E.; Crisafulli, E.; Radaeli, A.; Malerba, M. COPD and the Metabolic Syndrome: An Intriguing Association. *Intern. Emerg. Med.* **2013**, *8*, 283–289. [CrossRef] [PubMed]

15. Medina, G.; Vera-Lastra, O.; Peralta-Amaro, A.L.; Jiménez-Arellano, M.P.; Saavedra, M.A.; Cruz-Domínguez, M.P.; Jara, L.J. Metabolic Syndrome, Autoimmunity and Rheumatic Diseases. *Pharmacol. Res.* **2018**, *133*, 277–288. [CrossRef] [PubMed]

16. Wang, Y.; Huang, Z.; Xiao, Y.; Wan, W.; Yang, X. The Shared Biomarkers and Pathways of Systemic Lupus Erythematosus and Metabolic Syndrome Analyzed by Bioinformatics Combining Machine Learning Algorithm and Single-Cell Sequencing Analysis. *Front. Immunol.* **2022**, *13*, 1015882. [CrossRef]

17. Ünlü, B.; Türsen, Ü. Autoimmune Skin Diseases and the Metabolic Syndrome. *Clin. Dermatol.* **2018**, *36*, 67–71. [CrossRef]

18. Lima-Fontes, M.; Barata, P.; Falcão, M.; Carneiro, Â. Ocular Findings in Metabolic Syndrome: A Review. *Porto Biomed. J.* **2020**, *5*, e104. [CrossRef] [PubMed]

19. Roddy, G.W. Metabolic Syndrome and the Aging Retina. *Curr. Opin. Ophthalmol.* **2021**, *32*, 280–287. [CrossRef] [PubMed]

20. Wang, M.; Zhang, Y.H.; Yan, F.H. Research progress in the association of periodontitis and metabolic syndrome. *Zhonghua Kou Qiang Yi Xue Za Zhi* **2021**, *56*, 1138–1143. [CrossRef]

21. Kim, O.S.; Shin, M.H.; Kweon, S.S.; Lee, Y.H.; Kim, O.J.; Kim, Y.J.; Chung, H.J. The Severity of Periodontitis and Metabolic Syndrome in Korean Population: The Dong-Gu Study. *J. Periodontal Res.* **2018**, *53*, 362–368. [CrossRef]

22. Lu, Y.; Egedeuzu, C.S.; Taylor, P.G.; Wong, L.S. Development of Improved Spectrophotometric Assays for Biocatalytic Silyl Ether Hydrolysis. *Biomolecules* **2024**, *14*, 492. [CrossRef] [PubMed]

23. Park, J.-E.; Mun, S.; Lee, S. Metabolic Syndrome Prediction Models Using Machine Learning and Sasang Constitution Type. *Evid.-Based Complement. Altern. Med.* **2021**, *2021*, 8315047. [CrossRef] [PubMed]

24. Datta, S.; Schraplau, A.; Freitas Da Cruz, H.; Philipp Sachs, J.; Mayer, F.; Bottinger, E. A Machine Learning Approach for Non-Invasive Diagnosis of Metabolic Syndrome. In Proceedings of the 2019 IEEE 19th International Conference on Bioinformatics and Bioengineering (BIBE), Athens, Greece, 28–30 October 2019; IEEE: Piscataway, NJ, USA, 2019; pp. 933–940.

25. Karimi-Alavijeh, F.; Jalili, S.; Sadeghi, M. Predicting Metabolic Syndrome Using Decision Tree and Support Vector Machine Methods. *ARYA Atheroscler.* **2016**, *12*, 146–152. [PubMed]

26. Behadada, O.; Abi-Ayad, M.; Kontonatsios, G.; Trovati, M. Automatic Diagnosis Metabolic Syndrome via a *k*-Nearest Neighbour Classifier. In *Green, Pervasive, and Cloud Computing*; Lecture Notes in Computer Science; Au, M.H.A., Castiglione, A., Choo, K.-K.R., Palmieri, F., Li, K.-C., Eds.; Springer International Publishing: Cham, Switzerland, 2017; Volume 10232, pp. 627–637. ISBN 978-3-319-57185-0.

27. Choe, E.K.; Rhee, H.; Lee, S.; Shin, E.; Oh, S.-W.; Lee, J.-E.; Choi, S.H. Metabolic Syndrome Prediction Using Machine Learning Models with Genetic and Clinical Information from a Nonobese Healthy Population. *Genom. Inf.* **2018**, *16*, e31. [CrossRef] [PubMed]

28. Pawade, D.; Bakhai, D.; Admane, T.; Arya, R.; Salunke, Y.; Pawade, Y. Evaluating the Performance of Different Machine Learning Models for Metabolic Syndrome Prediction. *Procedia Comput. Sci.* **2024**, *235*, 2932–2941. [CrossRef]

29. Shin, H.; Shim, S.; Oh, S. Machine Learning-Based Predictive Model for Prevention of Metabolic Syndrome. *PLoS ONE* **2023**, *18*, e0286635. [CrossRef] [PubMed]

30. Paplomatas, P.; Krokidis, M.G.; Vlamos, P.; Vrahatis, A.G. An Ensemble Feature Selection Approach for Analysis and Modeling of Transcriptome Data in Alzheimer's Disease. *Appl. Sci.* **2023**, *13*, 2353. [CrossRef]

31. Rafieian, B.; Hermosilla, P.; Vázquez, P.-P. Improving Dimensionality Reduction Projections for Data Visualization. *Appl. Sci.* **2023**, *13*, 9967. [CrossRef]

32. Tao, X.; Jiang, M.; Liu, Y.; Hu, Q.; Zhu, B.; Hu, J.; Guo, W.; Wu, X.; Xiong, Y.; Shi, X.; et al. Predicting Three-Month Fasting Blood Glucose and Glycated Hemoglobin Changes in Patients with Type 2 Diabetes Mellitus Based on Multiple Machine Learning Algorithms. *Sci. Rep.* **2023**, *13*, 16437. [CrossRef]

33. Yang, H.; Yu, B.; OUYang, P.; Li, X.; Lai, X.; Zhang, G.; Zhang, H. Machine Learning-Aided Risk Prediction for Metabolic Syndrome Based on 3 Years Study. *Sci. Rep.* **2022**, *12*, 2248. [CrossRef]

34. Hedayati, M.-T.; Montazeri, M.; Rashidi, N.; Yousefi-Abdolmaleki, E.; Shafiee, M.-A.; Maleki, A.; Farmani, M.; Montazeri, M. White Blood Cell Count and Clustered Components of Metabolic Syndrome: A Study in Western Iran. *Casp. J. Intern. Med.* **2021**, *12*, 59–64. [CrossRef]

35. Raya-Cano, E.; Vaquero-Abellán, M.; Molina-Luque, R.; Molina-Recio, G.; Guzmán-García, J.M.; Jiménez-Mérida, R.; Romero-Saldaña, M. Association between Metabolic Syndrome and Leukocytes: Systematic Review and Meta-Analysis. *J. Clin. Med.* **2023**, *12*, 7044. [CrossRef] [PubMed]

36. Sampa, M.B.; Hossain, M.N.; Hoque, M.R.; Islam, R.; Yokota, F.; Nishikitani, M.; Ahmed, A. Blood Uric Acid Prediction With Machine Learning: Model Development and Performance Comparison. *JMIR Med. Inf.* **2020**, *8*, e18331. [CrossRef] [PubMed]

37. Trigka, M.; Dritsas, E. Predicting the Occurrence of Metabolic Syndrome Using Machine Learning Models. *Computation* **2023**, *11*, 170. [CrossRef]
38. Hung, C.-C.; Zhen, Y.-Y.; Niu, S.-W.; Lin, K.-D.; Lin, H.Y.-H.; Lee, J.-J.; Chang, J.-M.; Kuo, I.-C. Predictive Value of HbA1c and Metabolic Syndrome for Renal Outcome in Non-Diabetic CKD Stage 1–4 Patients. *Biomedicines* **2022**, *10*, 1858. [CrossRef] [PubMed]
39. Eyth, E.; Naik, R. Hemoglobin A1C. In *StatPearls*; StatPearls Publishing: Treasure Island, FL, USA, 2024.
40. Raya-Cano, E.; Vaquero-Abellán, M.; Molina-Luque, R.; De Pedro-Jiménez, D.; Molina-Recio, G.; Romero-Saldaña, M. Association between Metabolic Syndrome and Uric Acid: A Systematic Review and Meta-Analysis. *Sci. Rep.* **2022**, *12*, 18412. [CrossRef] [PubMed]
41. Lin, C.-R.; Tsai, P.-A.; Wang, C.; Chen, J.-Y. The Association between Uric Acid and Metabolic Syndrome in a Middle-Aged and Elderly Taiwanese Population: A Community-Based Cross-Sectional Study. *Healthcare* **2024**, *12*, 113. [CrossRef] [PubMed]
42. Kushiyama, A.; Nakatsu, Y.; Matsunaga, Y.; Yamamotoya, T.; Mori, K.; Ueda, K.; Inoue, Y.; Sakoda, H.; Fujishiro, M.; Ono, H.; et al. Role of Uric Acid Metabolism-Related Inflammation in the Pathogenesis of Metabolic Syndrome Components Such as Atherosclerosis and Nonalcoholic Steatohepatitis. *Mediat. Inflamm.* **2016**, *2016*, 8603164. [CrossRef] [PubMed]
43. Kimura, Y.; Yanagida, T.; Onda, A.; Tsukui, D.; Hosoyamada, M.; Kono, H. Soluble Uric Acid Promotes Atherosclerosis via AMPK (AMP-Activated Protein Kinase)-Mediated Inflammation. *Arterioscler. Thromb. Vasc. Biol.* **2020**, *40*, 570–582. [CrossRef]
44. Ren, Z.; Luo, S.; Liu, L. The Positive Association between White Blood Cell Count and Metabolic Syndrome Is Independent of Insulin Resistance among a Chinese Population: A Cross-Sectional Study. *Front. Immunol.* **2023**, *14*, 1104180. [CrossRef]
45. Odagiri, K.; Uehara, A.; Mizuta, I.; Yamamoto, M.; Kurata, C. Longitudinal Study on White Blood Cell Count and the Incidence of Metabolic Syndrome. *Intern. Med.* **2011**, *50*, 2491–2498. [CrossRef] [PubMed]

Review

A State-of-the-Art Review in Big Data Management Engineering: Real-Life Case Studies, Challenges, and Future Research Directions

Leonidas Theodorakopoulos [1,*], **Alexandra Theodoropoulou** [1] and **Yannis Stamatiou** [2]

[1] Department of Management Science and Technology, University of Patras, 26334 Patras, Greece; theodoropouloua@upatras.gr

[2] Department of Business Administration, University of Patras, 26504 Patras, Greece; stamatiu@upatras.gr

* Correspondence: theodleo@upatras.gr

Abstract: The explosion of data volume in the digital age has completely changed the corporate and industrial environments. In-depth analysis of large datasets to support strategic decision-making and innovation is the main focus of this paper's exploration of big data management engineering. A thorough examination of the basic elements and approaches necessary for efficient big data use—data collecting, storage, processing, analysis, and visualization—is given in this paper. With real-life case studies from several sectors to complement our exploration of cutting-edge methods in big data management, we present useful applications and results. This document lists the difficulties in handling big data, such as guaranteeing scalability, governance, and data quality. It also describes possible future study paths to deal with these issues and promote ongoing creativity. The results stress the need to combine cutting-edge technology with industry standards to improve decision-making based on data. Through an analysis of approaches such as machine learning, real-time data processing, and predictive analytics, this paper offers insightful information to companies hoping to use big data as a strategic advantage. Lastly, this paper presents real-life use cases in different sectors and discusses future trends such as the utilization of big data by emerging technologies.

Keywords: big data analytics; big data tools; decision-making; data lifecycle management; predictive analytics

1. Introduction

In today's fast-paced digital world, the explosion of data has completely reshaped the business and industrial landscapes. Organizations are now surrounded by data from numerous sources, including traditional systems, social media, and IoT devices. This influx of data offers a huge opportunity to gain valuable insights for strategic decisions and innovation, but it also brings the significant challenge of managing, processing, and analyzing vast and varied datasets effectively [1].

At the core of handling this data flood is big data information engineering—a discipline that merges art and science to unlock data's transformative power. It is the foundation on which data-driven companies build their strategies, helping them extract actionable insights, optimize operations, and stay competitive [2]. However, managing large-scale data involves complexities like scalability, data variety, and real-time processing, requiring advanced methods and technologies [3].

This paper explores big data information engineering in detail, highlighting its importance in our data-centric world. We provide a thorough analysis of its key components and principles, offering organizations a guide to using big data effectively for innovation and strategic goals. From data collection to storage, processing, analysis, and visualization, every aspect is crucial in revealing the value hidden in large datasets.

By examining the methodologies, tools, and best practices of big data information engineering, we aim to give organizations the knowledge they need to navigate today's complex data environment. Using real-world examples, case studies, and strategic insights, we seek to equip decision-makers, data practitioners, and industry stakeholders with the skills to leverage big data as a strategic asset. Embracing these principles will not only help organizations survive but also thrive in an era defined by data-driven innovation and disruption.

In this paper, as outlined in Table 1, we review and present the state-of-the-art papers in the field of big data management, describing their scope. Additionally, after discussing each work, we emphasize the scope of our research, consolidating all essential up-to-date knowledge about big data management.

Table 1. Summary of papers on big data management.

Reference	Survey	Scope
[4]	TinyML algorithms for big data management in large-scale IoT systems	Introduces a set of Tiny Machine Learning (TinyML) algorithms designed to improve big data management within large-scale IoT systems. These algorithms—TinyCleanEDF, EdgeClusterML, CompressEdgeML, CacheEdgeML, and TinyHybridSenseQ—address various aspects such as data processing, storage, and quality control using Edge AI capabilities.
[5]	Role of IoT technologies in big data management systems: A review and Smart Grid case study	Explores how IoT devices generate vast amounts of data and the subsequent challenges in processing, storing, and analyzing these data efficiently.
[6]	Efficient and secure medical big data management system using optimal map-reduce framework and deep learning	Focuses on managing and securing large-scale medical data using a combination of optimal map-reduce frameworks and deep learning techniques in a cloud environment. Proposes a system that includes patient authentication, big data management, secure data transfer, and big data classification, highlighting improvements in data processing efficiency, security, and classification accuracy.
[7]	Big data optimization and management in supply chain management: a systematic literature review	Aims to provide comprehensive insights into big data management and optimization technologies in SCM, highlighting current applications and identifying research gaps for future exploration.
[8]	Research on spatial big data management and high-performance computing based on information cloud platform	Explores the management of spatial big data and the implementation of high-performance computing (HPC) on an information cloud platform. Focuses on optimizing data storage, processing, and analysis to improve efficiency and performance in handling large-scale spatial datasets.
[9]	Integration of big data analytics and the cloud environment in harnessing valuable business insights	Explores the integration of big data analytics with cloud computing to generate valuable business insights. Discusses the selection of cloud service providers and tools, addressing challenges in data processing, storage, and security.
[10]	Research on the application of big data management in enterprise management decision-making	Explores how in-depth analysis and big data management can enhance decision-making ability and execution efficiency, promoting the realization of corporate strategic goals.
[11]	Big data management performance evaluation in Hadoop ecosystem	Examines various big data management tools within the Hadoop ecosystem, focusing on three levels including distributed file systems, NoSQL databases, and SQL-like components. Provides a comprehensive performance evaluation of typical technologies such as HDFS, HBase, MongoDB, and Hive, among others, comparing their features, advantages, and performance metrics.

Table 1. *Cont*.

Reference	Survey	Scope
Our work	A state-of-the-art review in big data information engineering: real-life case studies, challenges, and future research directions	Explores the complexities and opportunities in big data information engineering. Covers the full spectrum of big data management, including data collection, storage, processing, analysis, integration, and visualization. Emphasizes methodologies, technologies, and best practices essential for leveraging big data to drive strategic decision-making and innovation across various industries. Addresses challenges such as data quality, governance, scalability, and presents real-life case studies and future research directions.

The purpose of this work is to investigate, highlight, and contribute to the understanding and improvement of big data management engineering by presenting key factors and methodologies. This includes the following:

- Presenting an overview of state-of-the-art big data management through a comprehensive, specific, and up-to-date analysis of significant methodologies, tools, and best practices in the field.
- Analyzing real-life case studies and their implementations across various industries to showcase practical applications and outcomes, highlighting the successes and challenges encountered.
- Identifying and exploring unresolved issues and potential research directions in big data management, thereby creating a roadmap for future studies and innovations in academia and industry.
- Offering a thorough survey that aids readers in understanding the broader scope of big data management by summarizing knowledge from various sources, without the necessity to review all recent works individually.

Our paper also elaborates on the symbiotic relationship between big data and deep learning. We explore how big data technologies support the data lifecycle from collection to processing and analysis, which in turn facilitates the development and deployment of deep learning models. For instance, deep learning models for image recognition are trained on vast amounts of labeled images to achieve high accuracy [12]. Similarly, natural language processing models rely on extensive textual datasets to understand and generate human language [13].

The remainder of this article is organized as follows: Section 2 provides an overview of big data management engineering. Section 3 presents case studies, showcasing successful implementations of big data projects across different industries. Section 4 discusses challenges and future research directions. Finally, Section 5 concludes this article by summarizing key points and suggesting potential future directions. Figure 1 shows a general overview of a Big Data Management Framework.
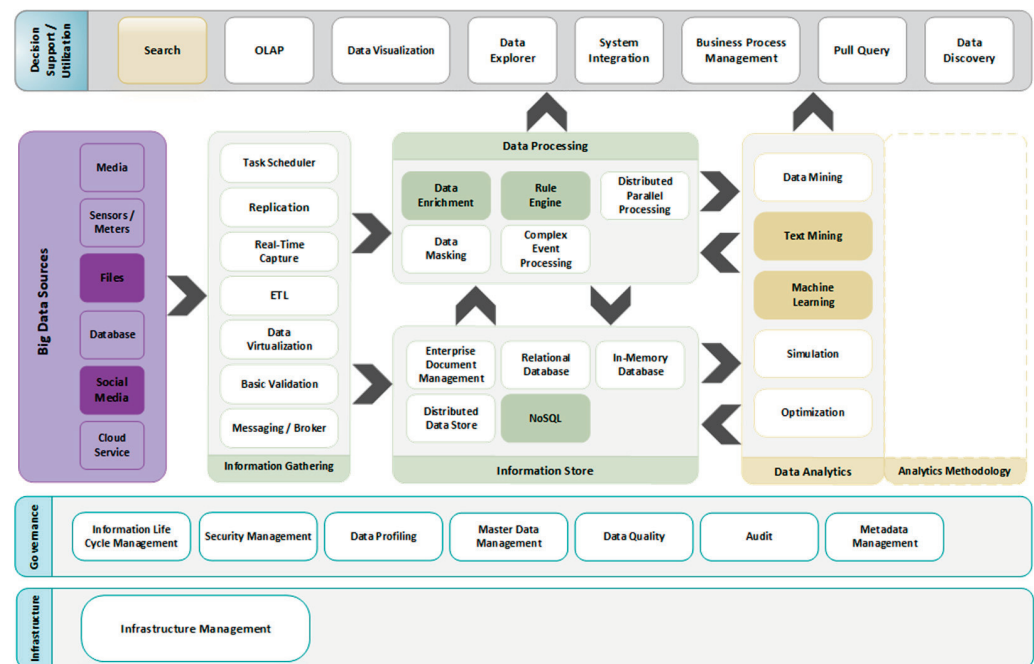
Figure 1. Big data management overview.

2. Overview of Big Data Management Engineering

In the current digital era, the term "big data" refers to datasets that are so large or complex that traditional data processing applications are inadequate. The characteristics of big data are commonly described by the "5Vs" framework, encompassing volume, velocity, variety, veracity, and value, which are described as follows:

(a) Volume: This refers to the vast amounts of data generated every second. Organizations collect data from various sources, including business transactions, social media, sensors, and more, leading to an explosion in data volume that requires scalable storage and processing solutions. For instance, social media platforms generate petabytes of data daily, which need to be managed efficiently.

(b) Velocity: This denotes the speed at which new data are generated and the pace at which they need to be processed. In the age of IoT and real-time analytics, the ability to process data streams rapidly and efficiently is crucial. Real-time data processing frameworks like Apache Kafka and Apache Flink are often employed to handle the high velocity of data inflow, enabling real-time decision-making.

(c) Variety: This aspect covers the different types of data, both structured (e.g., databases) and unstructured (e.g., text, images, videos), that organizations must manage and analyze. For example, healthcare data can range from patient records (structured) to medical imaging and doctors' notes (unstructured).

(d) Veracity: This refers to the trustworthiness and accuracy of the data. Data quality and reliability are critical for making informed decisions. Big data environments often deal with data from various sources, which may include noise, biases, and abnormalities. Techniques such as data cleansing and validation are essential to ensure high data veracity.

(e) Value: This represents the worth that can be extracted from data. Despite having large volumes of data, the real challenge lies in turning these data into actionable insights that can drive business decisions and innovation. Big data analytics, through methods like predictive analytics and machine learning, can unlock significant value by uncovering patterns, trends, and correlations that inform strategic decisions [14].

These five dimensions form the foundation of our exploration into big data management engineering. The core of handling this data flood is big data information engineering, a discipline that merges art and science to unlock data's transformative power. Our analysis is based on advanced methods and technologies necessary for managing large-scale data complexities such as scalability, data variety, and real-time processing.

2.1. Data Collection and Storage

At the start of any data project, the initial phase focuses on gathering data, serving as the crucial first step in information engineering. This stage involves collecting data from a variety of sources, including traditional databases and business systems as well as new technologies like sensors, IoT devices, social media platforms, and web scraping tools. By utilizing this array of sources, businesses can access a range of data types—structured, semi-structured, and unstructured—thereby enhancing their ability to analyze and derive valuable insights.

The methods employed for data collection are as diverse as the sources themselves, with organizations leveraging a combination of technologies and techniques tailored to their specific needs and objectives. For instance, sensors and IoT devices offer real-time data streams [4], providing instantaneous insights into operational metrics, environmental conditions, and consumer behaviors. Social media APIs enable the extraction of valuable sentiment analysis, demographic trends, and market sentiments, while web scraping tools empower organizations to gather data from the vast expanse of the internet, including news articles, forums, and product reviews.

After collecting data from various sources, the next crucial step is to store it efficiently for easier processing and analysis. In the realm of big data, where data volumes can reach petabytes and beyond, traditional storage options fall short of meeting scalability and performance needs. Therefore, companies opt for a variety of storage technologies and structures tailored to handle the specific demands of big data.

Among these technologies, distributed file systems such as the Hadoop Distributed File System (HDFS) emerge as a cornerstone, offering a scalable and fault-tolerant framework for storing vast datasets across clusters of commodity hardware. By distributing data across multiple nodes, HDFS not only ensures high availability and fault tolerance but also enables parallel processing, facilitating rapid data retrieval and analysis [15]. Furthermore, the emergence of NoSQL databases, including MongoDB, Cassandra, and HBase, provides organizations with flexible and schema-less alternatives to traditional relational databases, catering to the diverse data structures and access patterns prevalent in big data applications.

The rise of cloud computing has transformed data storage, complementing on-premises systems [9]. Cloud storage services like Amazon S3, Google Cloud Storage, and Microsoft Azure Blob Storage offer scalability, flexibility, and cost-effectiveness to businesses. They allow organizations to expand their storage capabilities easily as data needs fluctuate through a pay-as-you-go model [16]. Additionally, these cloud solutions come with managed services and data tools that streamline data management tasks, freeing up organizations to concentrate on innovation and extracting insights [8]. Figure 2 represents the architecture of cloud computing.

Data gathering and storage serve as the foundation for managing big data, paving the way for further steps such as processing, analyzing, and presenting information. Through the use of advanced technologies and structures, companies can not only receive and store large amounts of data but also establish a base for uncovering practical insights and guiding important decision-making in the age of big data.
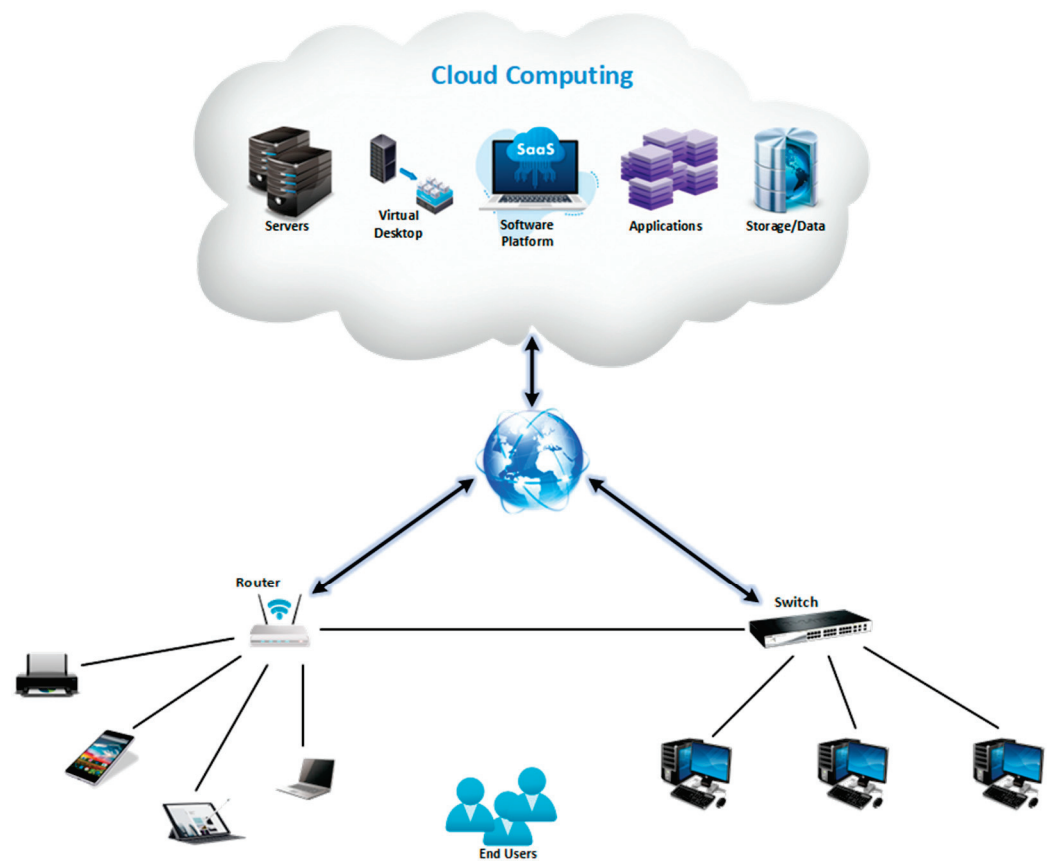
Figure 2. Cloud computing architecture.

2.2. Data Processing and Analysis

In the realm of big data information engineering, data processing stands as a cornerstone, representing the pivotal transition from raw data to valuable insights that drive informed decision-making and strategic initiatives [10]. This transformative process encompasses a spectrum of operations, including data cleansing, transformation, aggregation, and enrichment, aimed at harnessing the latent potential within vast datasets and converting it into actionable knowledge.

At the forefront of data processing technologies lies a suite of powerful frameworks and platforms tailored to meet the diverse needs of modern data-driven enterprises. Among these, Apache Hadoop emerges as a stalwart, offering a distributed processing framework that enables the parallel execution of data-intensive tasks across clusters of commodity hardware [11]. Through the MapReduce programming model, Hadoop facilitates the efficient processing of massive datasets by partitioning them into smaller, manageable chunks and distributing them across nodes for concurrent processing [5]. This enables organizations to tackle complex analytical tasks, such as batch processing and large-scale data transformations, with unparalleled scalability and fault tolerance. Figure 3 shows the main architecture of MapReduce.

Apache Spark complements Hadoop by offering a fast, in-memory processing engine that aims to overcome the constraints of conventional MapReduce methods. Utilizing resilient distributed datasets (RDDs) and a user-friendly API, Spark accelerates data processing tasks by storing interim results in memory, thereby reducing disk I/O demands and improving performance [17]. This feature makes Spark ideal for iterative algorithms, interactive queries, and live stream processing, enabling businesses to extract valuable insights from data quickly and efficiently. Figure 4 visualizes the architecture of Apache Spark.
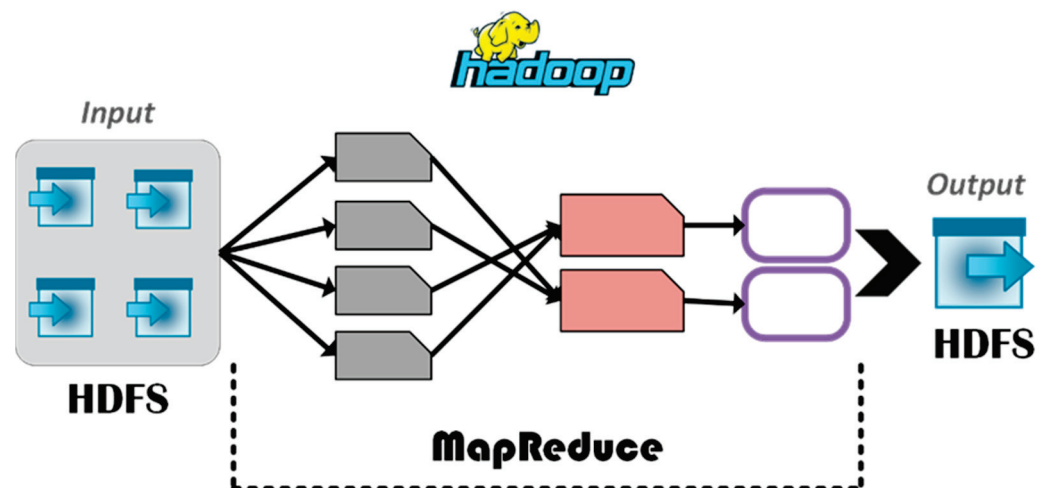
Figure 3. MapReduce architecture.
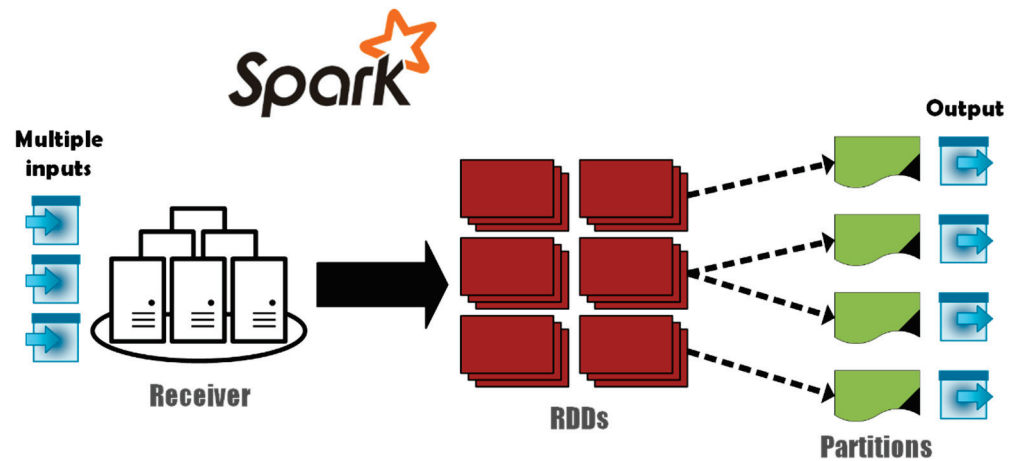
Figure 4. Apache Spark architecture.

Furthermore, Apache Flink emerges as a leader in the field of real-time stream processing. It provides low-latency and high-throughput capabilities for analyzing continuous data streams in a manner that is close to real-time [18]. Figure 5 shows the architecture of Apache Flink.
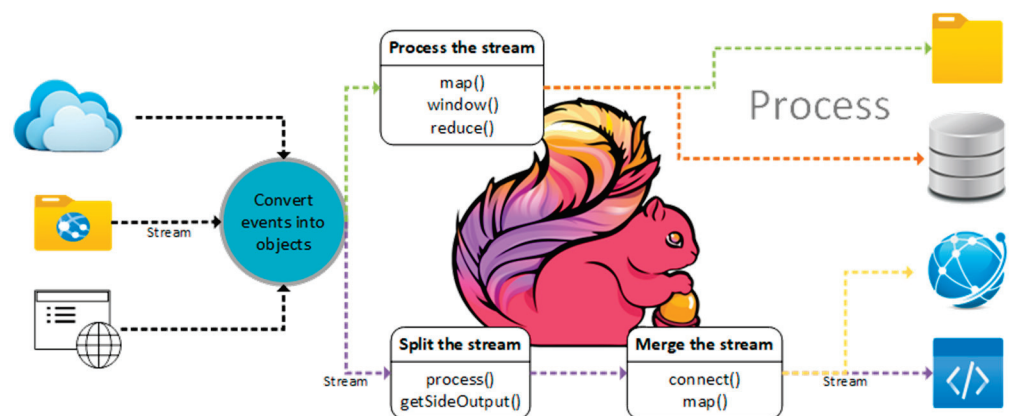
Figure 5. Apache Flink architecture.

Following the completion of the processing and transformation of the data, the next important step is to utilize rigorous analysis and exploration in order to extract the insights contained within the data. In this regard, a wide variety of approaches and procedures for data analysis come into play. These include more conventional statistical analyses and hypothesis testing, as well as more modern machine learning algorithms and data mining techniques [19]. For companies, statistical analysis acts as a basic pillar, allowing them to obtain descriptive and inferential insights from data. These insights might range from summary statistics and distributional studies to correlation and regression analyses. These techniques provide valuable insights into the underlying patterns, trends, and relationships within data, thereby informing strategic decision-making and guiding resource allocation.

Machine learning is becoming increasingly powerful in revealing insights and extracting useful information from data. By using techniques like classification, regression, clustering, and anomaly detection, businesses can discover patterns, predict upcoming trends, and streamline decision-making processes [20]. This gives them an advantage in fast-paced and unpredictable environments. Table 2 shows the most common Machine learning techniques.

Table 2. Machine learning techniques.

| Machine Learning Algorithm	Use Case and Description
Classification	Predicts the class or category of new observations based on training data. Commonly used for sentiment analysis, image recognition, and customer segmentation.
Regression	Models the relationship among variables to predict continuous outcomes. Used for sales forecasting, pricing optimization, and demand prediction.
Clustering	Identifies natural groupings within data, based on similarity. Helps in customer segmentation, anomaly detection, and pattern recognition in unlabeled datasets.
Anomaly Detection	Detects outliers or anomalies in data that deviate from the norm. Useful for fraud detection, network security monitoring, and predictive maintenance in manufacturing.

In addition, data mining techniques make it easier to find patterns and relationships within data that were not previously recognized. This allows for the discovery of significant insights that may have been masked by noise or complexity. Uncovering actionable insights, recognizing market trends, and optimizing business processes can all be accomplished by businesses through the utilization of exploratory data analysis, association rule mining, and clustering algorithms. This helps firms drive continuous improvement and innovation.

2.3. Data Integration and Visualization

The process of data integration acts as a key bridge in the complex terrain of big data information engineering. It connects different data sources and harmonizes heterogeneous datasets in order to produce a unified and coherent perspective of the information that lies under the surface. In its most fundamental form, data integration is the process of combining data from a variety of sources in a seamless manner [21]. This process encompasses organized, semi-structured, and unstructured forms, and it is designed to facilitate comprehensive analysis and decision-making.

Data integration involves a variety of tasks, starting with data cleansing, a process to fix errors, inconsistencies, and duplicates in the data. By using methods such as removing duplicates, identifying erroneous data points, and correcting mistakes, companies can ensure that the combined dataset is accurate, complete, and reliable, setting the stage for analysis and generating insights [22]. Also, data transformation is crucial in the data integration process as it helps unify data formats, structures, and meanings. This includes converting data from their original form into a standard representation to enable smooth compatibility across systems [23]. Through methods like standardization, summarization, and enrichment, companies can improve the usability and relevance of the combined dataset, leading to uncovering insights and promoting collaboration across different departments.

Furthermore, combining data structures into a single cohesive model through schema integration is crucial for organizations. This process involves aligning and connecting data elements, entities, and relationships from various sources to establish a shared semantic structure. It promotes analysis and decision-making regardless of the source or format of the data.

In tandem with the process of integrating data, data visualization is emerging as a strong tool that can translate complicated facts into insights that are easy to understand and can be put into action. These insights connect with stakeholders from all around the company. Organizations are able to condense complicated analytical results into visually captivating tales by utilizing charts, graphs, dashboards, and interactive visualizations. This enables stakeholders to understand essential insights at a glance and make choices with confidence that are informed by the information [24].

Data visualization plays a crucial role in communication, helping organizations present data analysis findings in a visually understandable way that transcends language barriers and specialized knowledge. By leveraging our ability to interpret visual information quickly, data visualization allows stakeholders to spot trends, detect patterns, and draw practical conclusions from data. This, in turn, aids decision-making and fosters a culture of data-driven decisions within the organization [25]. Additionally, data visualization promotes sharing insights and knowledge throughout the organization, enabling stakeholders to interact with data dynamically. With charts, dynamic dashboards, and self-service analytics tools, organizations empower stakeholders to explore data on their own terms, uncovering valuable insights that drive continuous growth and innovation.

It is important to note that data integration and visualization are two parts of big data information engineering that are interrelated. Data integration serves as the foundation for unified analysis, while data visualization helps to improve the dissemination of insights and provides support for decision-making capabilities. Big data may be utilized to their full potential by organizations through the combination of data integration and visualization [26]. This enables organizations to transform raw data into actionable insights that aid strategic decision-making, innovation, and growth.

2.4. Real-Time Data Processing

In today's fast-paced and interconnected digital world, quickly analyzing real-time data has become crucial for companies looking to stay ahead, react promptly to new trends, and seize fleeting opportunities. Real-time data processing marks a departure from traditional batch methods, allowing organizations to analyze and respond to data as they come in, leading to instant insights and actions based on the most up-to-date information. At the core of real-time data processing is the concept of data streams—limitless sequences of data that flow constantly from various sources such as sensors, IoT devices, social media platforms, and transactional systems [27]. These streams contain insights, passing trends, and important events that require immediate attention and action, underscoring the necessity of real-time processing for organizations navigating dynamic and rapidly changing landscapes. Figure 6 shows Real-time data processing.
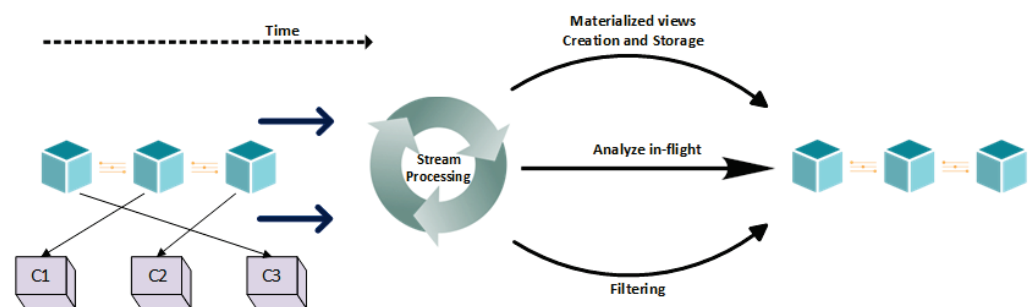
Figure 6. Real-time data processing.

Real-time data processing is built on a collection of cutting-edge technologies and frameworks that are designed to manage the speed, volume, and diversity of streaming data. This gives real-time data processing its basis. Among them, Apache Kafka stands out as a cornerstone because it provides a platform for distributed messaging that acts as the foundation for real-time data pipelines. Kafka makes it possible for businesses to ingest, process, and publish streams of data with low latency and high throughput [28]. This makes it possible for Kafka to provide seamless interaction with the downstream processing systems and analytics engines to be implemented. Figure 7 depicts the architecture of Apache Kafka.
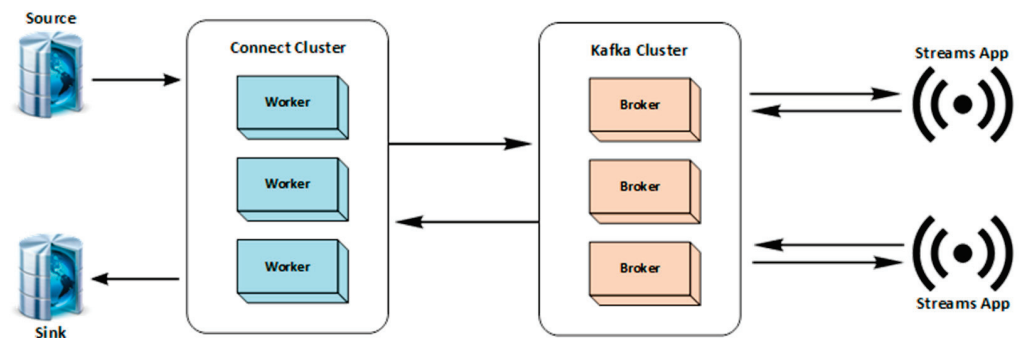
Figure 7. Apache Kafka architecture.

Kafka pairs well with Apache Storm, a framework designed for high-speed data stream processing. Storm allows organizations to analyze streaming data quickly and accurately by utilizing real-time processing and fault-tolerant mechanisms [29]. This capability helps in performing analytics, detecting anomalies, and recognizing patterns in real-time data, leading to timely decision-making and proactive actions. Figure 8 shows the architecture of Apache Storm.
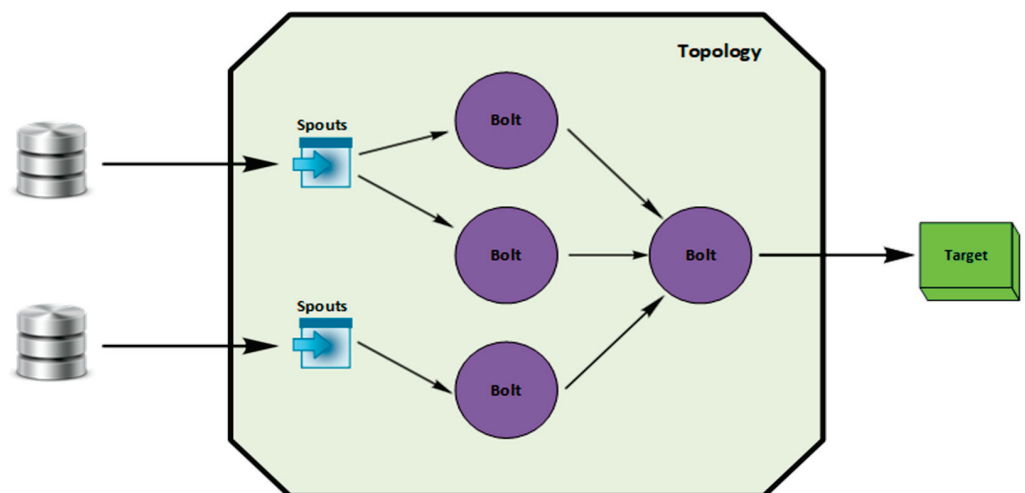
Figure 8. Apache Storm architecture.

In addition, Apache Flink has emerged as a leading contender in the field of real-time stream processing. It has low-latency and high-throughput capabilities, making it possible to analyze continuous data streams with a latency of less than one second. By utilizing a pipelined execution paradigm and stateful processing primitives, Flink gives businesses the ability to perform windowed aggregations, event-time processing, and complicated event processing on streaming data. This, in turn, enables organizations to obtain deeper insights and make decisions in real time. Figure 9 shows Real-time stream processing with Apache Flink.
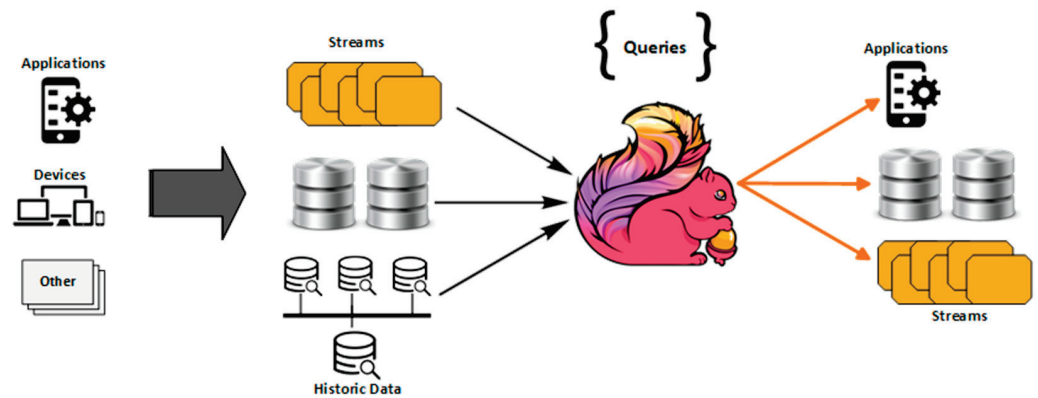
Figure 9. Real-time stream processing with Apache Flink.

In a wide variety of industries and use cases, real-time data processing is utilized in many applications that are both comprehensive and diverse. In the field of finance, real-time data processing offers opportunities for risk management, the identification of fraudulent activity, and algorithmic trading. These capabilities enable organizations to react rapidly to changes in the market and new hazards. In the retail industry, real-time processing makes it feasible to implement personalized marketing, inventory control, and dynamic pricing. This enables firms to give customers individualized experiences and swiftly capitalize on trends in customer behavior [30]. Real-time data processing is also utilized in the manufacturing, telecommunications, healthcare, and other industries. In these sectors, it assists businesses in enhancing their client experiences, streamlining operations, and fostering innovation via the utilization of data-driven decision-making. When businesses make use of the possibilities offered by real-time data processing in today's fast-paced and data-driven world, they have the opportunity to capture new opportunities, decrease risks, and gain an advantage over their competitors [31].

2.5. Data Quality and Preprocessing

In the field of data information engineering, data quality is crucial for ensuring the trustworthiness, accuracy, and relevance of analytical findings and decision-making processes. Data quality measures how well data align with their intended purpose, considering factors such as correctness, completeness, consistency, timeliness, and significance. In the realm of big data, characterized by extensive, diverse, and ever-changing datasets, maintaining high data quality is essential for extracting actionable insights and achieving strategic objectives [32].

One cannot stress enough how important data quality is to big data information engineering. The legitimacy and efficacy of data-driven projects can be undermined by incorrect findings, poorly considered actions, and lost opportunities brought about by poor data quality. Biased insights, faulty models, and less-than-ideal results can all originate from insufficient or inaccurate data. Furthermore, duplicate and inconsistent data might bring inefficiencies and mistakes into subsequent procedures, which would reduce operational effectiveness and impede creativity [33].

The term "data preprocessing" refers to the collection of many methodologies and approaches that are utilized by organizations in order to address the challenges that are posed by the level of data quality in big data environments. In the context of data, the term "preprocessing" refers to a collection of techniques that are intended to enhance the usefulness, quality, and relevance of raw data, laying the groundwork for meaningful analysis [34].

Data preprocessing involves a step known as data cleaning, where errors, inconsistencies, and anomalies in the dataset are identified and corrected. This process may include tasks such as eliminating duplicate entries, correcting typos, filling in missing information, and resolving discrepancies in data formats or measurements [35]. By ensuring data cleanliness, companies can reduce the chances of errors and biases in analysis outcomes, ultimately improving the reliability and credibility of the insights obtained from the data. Figure 10 depicts the Data cleansing process.
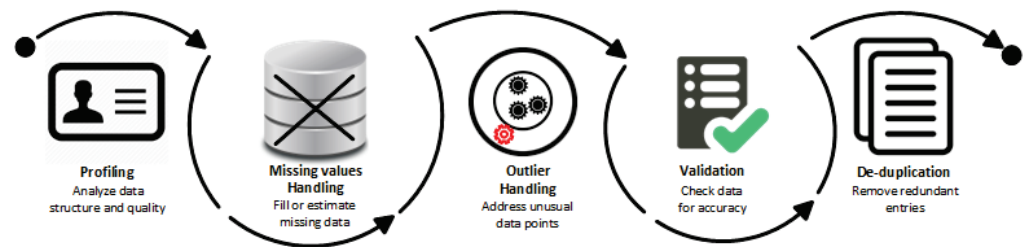
Figure 10. Data cleansing process.

An additional key component of data preparation is the process of normalizing data by converting it into a standard format or scale. This is performed in order to facilitate meaningful comparisons and analysis. A few examples of this include the normalization of categorical variables, the modification of skewed distributions in order to establish symmetry, and the scaling of numerical features to a common range. The capacity to assure consistency and comparability between different datasets and features is afforded to organizations that employ the process of normalizing their data representation. The process of identifying outliers, which involves locating and removing data points that significantly deviate from the expected or normal trend, may also be taken into consideration during the process of data preparation [36]. Outliers can be caused by a number of factors, including measurement noise, errors in data collection, or actual anomalies in the phenomenon that is being measured. Identifying and resolving outliers before they have a significant influence on analytical results and conclusions is one way for organizations to improve the accuracy and robustness of the insights that are generated from the data.

In addition, the methods of data quality assurance play a crucial part in assuring the correctness and dependability of analytical outputs in the field of big data information engineering. A wide variety of actions, including data profiling, validation, and monitoring, are included in these processes. The purpose of these activities is to evaluate and maintain the quality of the data during its entire lifespan. Through the implementation of stringent quality assurance methods, companies are able to discover and repair data quality concerns in a proactive manner, hence reducing the likelihood of mistakes and biases in the results of analytical processes.

2.6. Data Lifecycle Management

DLM stands for "data lifecycle management", which refers to the processes and procedures that are utilized in the management of data from the time they are created until they are finally discarded. The whole lifecycle of data is encompassed by it, beginning with the collection and storage of data and continuing through processing, analysis, and, finally, archiving or destruction. Effective data lifecycle management (DLM) ensures that data are maintained efficiently, safely, and in line with legal requirements throughout their entire duration [37]. This, in turn, maximizes the value of the data and minimizes the associated risks. Figure 11 shows the Data Lifecycle Management.
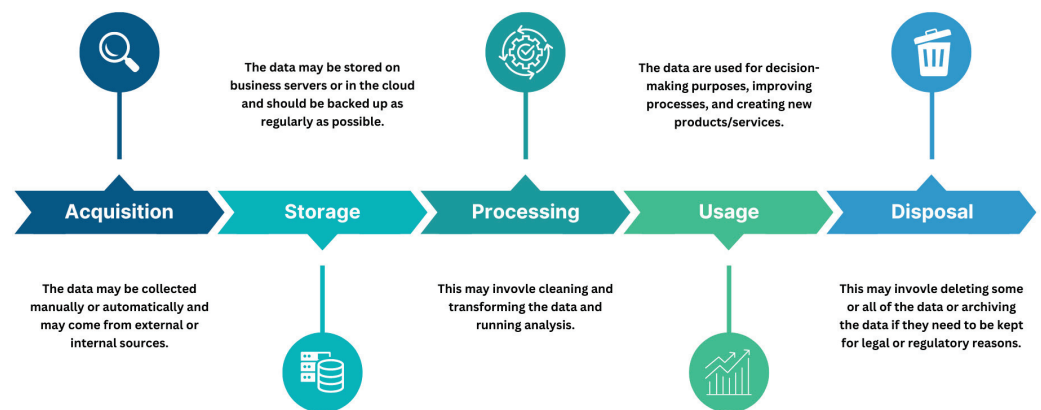
Figure 11. Data Lifecycle Management.

Stages of the Data Lifecycle

Acquisition: The data lifecycle kicks off with the acquisition stage, where data are gathered from a variety of sources such as internal systems, external databases, sensors, and IoT devices. This stage involves identifying data sources, deciding on data collection methods, and setting up protocols for data ingestion [38].

Storage: After data are collected, they move to storage. This could be in databases, data lakes, or cloud storage systems. Key decisions here include choosing data formats, structures, and access controls, along with planning for scalability, performance, and redundancy [39].

Processing: Once stored, data need to be processed to turn into useful information. This involves cleaning and enriching the data, aggregating various data points, and normalizing the datasets. This step can involve batch processing, real-time streaming analytics, or interactive querying to draw insights and add value [40].

Analysis: During the analysis stage, the processed data are scrutinized to identify patterns, trends, and correlations. This analysis can inform decision-making and drive business outcomes using statistical methods, machine learning, data mining, and visualization techniques [41].

Archiving: As data become older or less frequently accessed, they move into the archiving stage. Here, data are stored in long-term, cost-effective solutions. This stage involves setting retention policies, managing the data lifecycle, and ensuring that archived data remain intact and accessible for future reference or compliance purposes [42].

Managing data throughout their lifecycle is of the utmost importance for optimizing value and reducing risks associated with data assets. By adhering to best practices in data management and establishing strong data governance structures, companies can ensure compliance, efficiency, and reliability across the data lifecycle. This approach leads to better business outcomes and helps maintain a competitive advantage in today's data-focused environment.

3. Case Studies Showcasing Successful Implementations of Big Data Projects across Different Industries

3.1. Case Study: GE Healthcare—Predictive Maintenance for Medical Imaging

Challenge: The difficulties that GE Healthcare had with unplanned downtime and the price of maintenance for medical imaging equipment caused major interruptions to patient care and placed a financial burden on operating budgets. MRI (Magnetic Resonance Imaging) machines, CT (Computerized Tomography) scanners, and X-ray machines are examples of the types of medical imaging equipment that are essential assets in healthcare institutions. These instruments play an important part in the diagnostic processes and the treatment plans that are developed for patients. When it comes to providing timely and high-quality care to patients, the dependability and availability of these types of equipment are of the utmost importance.

Unexpected interruptions in the functioning of imaging devices can have severe repercussions. When these machines become unexpectedly unavailable, pre-scheduled patient appointments and procedures may face delays or cancellations, causing patient dissatisfaction, longer waiting periods, and potential negative effects on outcomes. In emergency situations requiring immediate trauma care or urgent diagnostic assessments, the inability to access imaging services promptly can jeopardize patient safety and quality of care.

Apart from the implications for patient care, unplanned downtimes also lead to operational expenses for healthcare providers. The costs associated with maintaining and repairing imaging equipment can be high, particularly when emergency repairs are needed outside of regular maintenance schedules. Additionally, downtime results in missed opportunities for revenue generation, as idle equipment cannot provide services during inactive periods. Prolonged downtimes can strain resources within healthcare facilities and diminish staff productivity, ultimately affecting operational efficiency and workflow management.

GE Healthcare and other manufacturers of medical equipment have begun looking into proactive maintenance programs that make use of the Internet of Things (IoT) and predictive analytics as a reaction to the problems that have been identified. Real-time monitoring of health metrics and equipment performance, which is made feasible by technology that enables predictive maintenance, helps medical professionals to anticipate potential issues before they develop into more significant failures. Through the analysis of data obtained from sensors that are included in imaging equipment, predictive maintenance algorithms are able to identify irregularities, identify new problems, and present alerts for early action intervention [43].

By adopting predictive maintenance solutions, GE Healthcare and healthcare facilities can shift from responding to equipment issues after they occur to anticipating and preventing them. Predictive maintenance helps reduce the chances of downtime by allowing for timely interventions, scheduling preventative maintenance based on equipment conditions and usage trends, and optimizing the management of spare parts inventory. This method not only enhances the reliability and availability of equipment but also cuts down on maintenance expenses and prolongs the lifespan of medical imaging resources.

The difficulties that GE Healthcare has had with unplanned downtime and maintenance expenses highlight the need to utilize new technologies like predictive analytics and the Internet of Things for the purpose of performing preventative equipment maintenance in healthcare organizations. It is possible for healthcare providers to improve the delivery of patient care, maximize operational efficiency, and reduce the financial risks associated with equipment downtime and maintenance charges by using techniques for predictive maintenance. When it comes to the management of medical imaging equipment, predictive maintenance is a game-changing technique that guarantees dependability, availability, and performance while also supporting the aim of providing timely and high-quality patient care.

Strategy: With the help of big data analytics, GE Healthcare put in place a revolutionary predictive maintenance system meant to prevent unexpected downtime for medical devices and actively manage equipment dependability. The goal of this project was to improve operational efficiency in hospital settings by using data integration and sophisticated analytics to anticipate equipment breakdowns before they happened.

The project involved integrating data from diverse sources critical for predictive maintenance, including real-time sensor data collected from medical devices, historical performance metrics, and maintenance logs. The medical dataset of patients contains hundreds of thousands or more data entries. The input dataset is initially preprocessed to improve data quality and reduce processing time [6]. By aggregating and analyzing these multidimensional data, GE Healthcare could gain comprehensive insights into equipment health, identify potential anomalies or patterns indicative of impending failures, and take proactive measures to prevent disruptions in service delivery.

Predictive maintenance at GE Healthcare was based mostly on sophisticated analytics methods, especially machine learning algorithms that could learn from past data to forecast future events with accuracy. These algorithms were trained on massive datasets including a variety of criteria like usage patterns, ambient conditions, sensor readings, and maintenance records. By real-time monitoring and analysis of various data streams, the predictive maintenance system might identify early warning indicators of equipment deterioration or failures, allowing for prompt intervention and preventative measures.

The initiative greatly benefitted from big data integration, as it provided a comprehensive view of equipment performance and health from various perspectives. By merging real-time sensor data with maintenance logs, GE Healthcare obtained a complete understanding of equipment performance and lifespan trends. This holistic perspective enabled decision-makers to focus on maintenance activities, allocate resources efficiently, and manage budgets more effectively using predictive analysis.

The introduction of predictive maintenance at GE Healthcare is a representative example of the revolutionary influence that big data analytics may have on the operations of healthcare facilities. Through the utilization of data-driven insights, healthcare providers are able to transition from reactive to proactive maintenance strategies, decrease the operational costs that are associated with unplanned downtime and emergency repairs, and ultimately improve the outcomes of patient care by ensuring the availability and dependability of essential medical equipment.

It is also important to note that this initiative highlights the larger ramifications that might result from the integration of advanced analytics and data into healthcare settings. Through the adoption of digital transformation and the utilization of big data, organizations such as GE Healthcare have the ability to foster innovation, maximize the utilization of resources, and open the door to healthcare delivery models that are more intelligent and efficient. The term "predictive maintenance" refers to an expenditure that is estimated in order to use data assets to produce insights, promote operational excellence, and eventually revolutionize the supply and administration of healthcare services.

Outcome: By proactively detecting maintenance requirements and scheduling interventions based on predictive insights, GE Healthcare was able to cut unexpected downtime by 20% and maintenance expenditures by 10%. This led to an increase in the dependability of the equipment, an improvement in the continuity of patient care, and an optimization of the allocation of resources [44]. Figure 12 shows GE healthcare's platform.
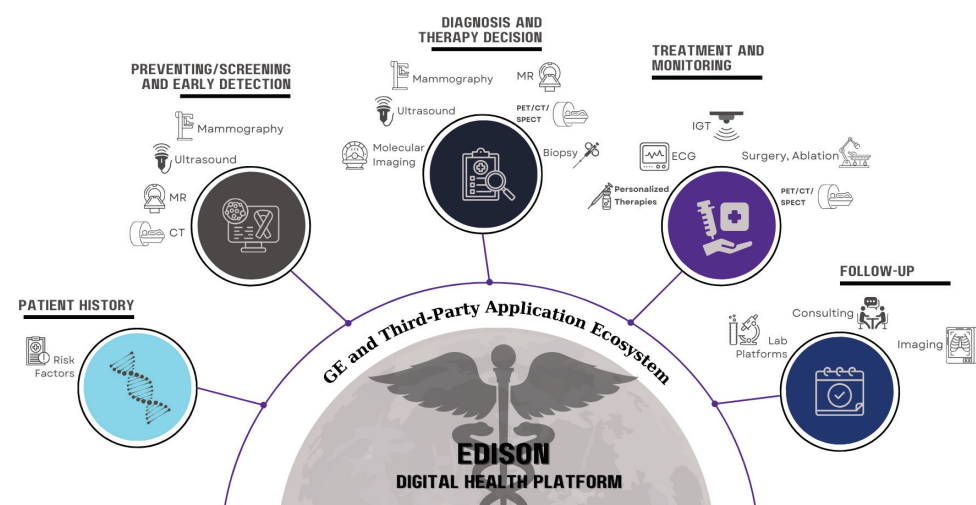

Figure 12. GE healthcare platform.

3.2. Case Study: Capital One—Personalized Customer Insights for Financial Services Industry

Challenge: The effort of Capital One to improve client engagement and retention through customized banking experiences is a strategic focus on using data-driven insights

and sophisticated analytics to provide customized services and solutions to each customer. Customer loyalty, contentment, and eventually keeping important clients are all greatly influenced by customer-centricity and individualized experiences in the cutthroat financial services industry of today.

In order to accomplish this goal, Capital One unquestionably initiated a comprehensive data-driven strategy, which included the use of transaction histories, demographic data, online activities, and behavioral patterns, amongst other sources of customer information. Through the use of big data analytics, machine learning, and artificial intelligence technologies, Capital One endeavored to obtain a comprehensive understanding of the specific requirements, financial behaviors, and preferences of each and every customer [45].

In this phase, Capital One would have started by combining and organizing various datasets to create a unified overview of each customer's information. This comprehensive data system likely included both structured and unstructured data sources, such as transaction records from banking activities, social media interactions, customer service logs, and external market data. By establishing a robust data management foundation, Capital One could access detailed, real-time insights about customers. By taking advantage of this wealth of information, Capital One could then use analytical methods to derive practical insights and identify tailored banking opportunities for individual customers. By utilizing machine learning algorithms, they could group customers based on their habits, forecast individual preferences, and anticipate future requirements. This would have enabled Capital One to offer targeted promotions, personalized product suggestions, and bespoke services that aligned with each customer's unique financial objectives and preferences.

The integration of customized banking services extended across various points of contact, including digital platforms (such as mobile apps and online banking sites), customer service interactions, and marketing messages. By tailoring engagements based on individual preferences and behaviors, Capital One aimed to provide smooth and captivating experiences that enhance customer satisfaction and foster lasting connections. Moreover, Capital One's approach to tailored banking services highlights a trend toward prioritizing customers in the financial sector. By using data-driven tactics and focusing on customer-centric strategies, companies like Capital One can stand out in a competitive market, cultivate customer loyalty, and ultimately achieve sustainable growth.

The initiative taken by Capital One to improve client engagement and retention through the provision of tailored banking experiences is a prime example of the revolutionary impact that data analytics and customer-centric initiatives provide in the financial services industry. Capital One's goal is to establish long-lasting connections with its customers, foster customer loyalty, and establish itself as a leader in the provision of innovative and personalized banking products. This will be accomplished by utilizing data-driven insights to comprehend, anticipate, and meet the requirements of individuals.

Strategy: Capital One's implementation of a data analysis system reflects a strategic effort to use data-driven insights effectively to improve customer interactions and provide personalized services in the financial sector. By utilizing data analytics, Capital One aimed to study extensive customer transaction records, spending habits, and engagements across different platforms to gain valuable insights and offer customized solutions to individual clients. The project encompassed various aspects of data analysis and artificial intelligence, starting with data consolidation. Capital One merged diverse datasets from multiple sources, such as transaction logs, client profiles, demographic details, online engagements, and external market statistics. By centralizing this information into a single platform, Capital One established a holistic understanding of each customer's financial activities, preferences, and requirements.

During the course of the project, the process of feature engineering was extremely important. This involved the identification of pertinent features and characteristics from the integrated dataset by data scientists and analysts in order to construct predictive models. For the purpose of capturing relevant patterns and insights, features such as transaction frequency, expenditure categories, geographic location, and customer segmentation were

developed. This procedure included the transformation of data, the normalization of data, and the enrichment of data in order to prepare the dataset for the construction of machine learning models.

One of the most important aspects of Capital One's analytics platform was the creation of machine learning models, which made it possible to provide tailored product suggestions and targeted marketing offers. For the purpose of analyzing client behavior and preferences, data scientists utilized sophisticated algorithms such as collaborative filtering, clustering, and recommendation engines. The purpose of these models is to find chances for cross-selling or upselling related financial products and services by predicting future purchase patterns and learning from previous data.

For Capital One, the utilization of this big data analytics platform makes it feasible for the company to provide individualized customer experiences on a large scale. Through the utilization of machine learning-driven insights, Capital One has the ability to personalize marketing materials, special offers, and product ideas in accordance with the distinguishing traits and behaviors of each individual customer. This tailored method increases relevance, improves consumer participation, and ultimately encourages customer loyalty and happiness from the perspective of the customer.

Capital One's dedication to utilizing data analytics highlights a strong focus on innovation and customer satisfaction within the financial industry. By adopting data-driven technologies and analytical tools, companies like Capital One can discover avenues for expansion, differentiate themselves in the market, and foster stronger connections with customers by understanding and meeting their evolving financial needs. The implementation of a data analytics system by Capital One serves as a prime example of how data-driven approaches can revolutionize personalized customer interactions and improve business outcomes. Through the application of analytics and machine learning methods, Capital One demonstrates how businesses can leverage data to offer enhanced services, boost customer engagement, and gain a competitive edge in today's fast-paced and data-centric environment.

Outcome: Capital One was able to achieve a 15% boost in customer satisfaction and a 20% improvement in the efficacy of cross-selling by utilizing big data analytics [46]. A better level of consumer involvement, enhanced loyalty, and improved business performance were all outcomes that resulted from the individualized insights. Figure 13 shows the Capital One's big data analytics platform.
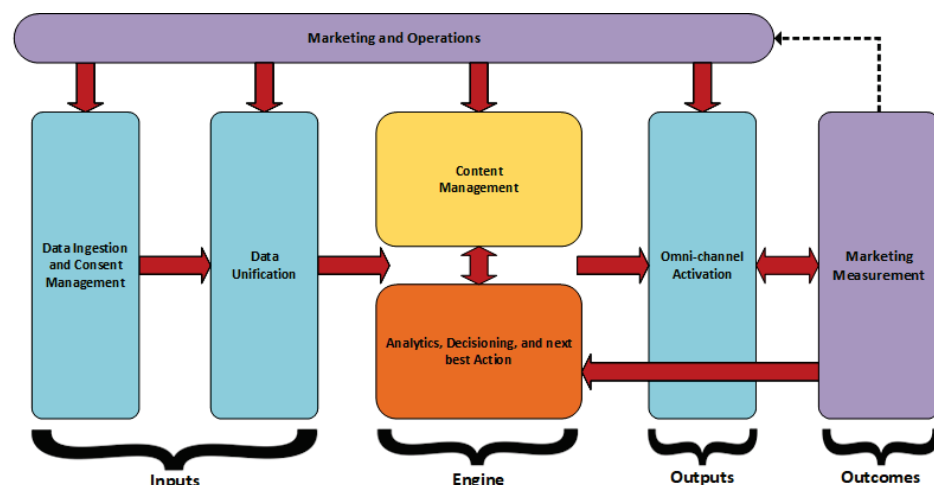

Figure 13. Capital One's big data analytics platform.

3.3. Case Study: Walmart—Supply Chain Optimization with Real-Time Analytics

Challenge: Walmart's initiative to improve inventory management, prevent stockouts, and streamline their supply chain demonstrates their commitment to leveraging data-

driven insights and advanced technology to meet the evolving needs of customers in a fast-paced retail environment. As one of the largest retailers globally, Walmart faces numerous challenges in managing inventory, ensuring an efficient supply chain, and maintaining customer satisfaction. By implementing innovative solutions based on data analysis and technology, Walmart aimed to boost operational efficiency, enhance product availability, and provide top-notch customer service.

Walmart most likely utilized a mix of big data analytics, machine learning, and Internet of Things (IoT) technology in order to accomplish these goals. This would have allowed the company to obtain real-time visibility into inventory levels, demand trends, and supply chain dynamics. Creating a complete and accurate view of inventory across the retail network would have been the goal of the project, which would have entailed the integration of data from a variety of sources, such as point-of-sale (POS) systems, inventory databases, vendor systems, and external market data.

Walmart relies on demand forecasting as a key component of its inventory management strategy. By analyzing sales data, seasonal patterns, customer preferences, and external factors such as weather and promotions, Walmart can predict future demand more accurately. Leveraging forecasting models powered by machine learning algorithms allows Walmart to anticipate customer needs, adjust inventory levels accordingly, and prevent stock shortages while enhancing inventory turnover efficiency. One other aspect Walmart is interested in is optimizing its supply chain. The company utilizes logistics and routing algorithms to streamline transportation routes, reduce delivery times, and lower operational expenses. Through real-time tracking of inventory and shipments using IoT devices, Walmart can closely monitor inventory movements, identify supply chain bottlenecks promptly, and proactively resolve any disruptions in the supply chain flow.

In addition, it is quite probable that Walmart makes use of data analytics in order to successfully execute dynamic pricing strategies and promotional campaigns that are based on demand patterns and the price of competitors. Walmart is able to alter its pricing and promotional plans in order to optimize income, boost sales, and improve customer happiness by conducting real-time analysis of customer behavior and the dynamics of the market. Walmart's dedication to simplifying supply chain processes also includes environmental programs like waste reduction and resource efficiency enhancement. Aligning with Walmart's larger sustainability objectives, data analytics are essential in maximizing inventory levels to decrease food waste and prevent overstocking.

Walmart's efforts to optimize inventory management, reduce stockouts, and streamline supply chain operations exemplify the transformative impact of data analytics and technology in the retail industry. By leveraging data-driven insights to make informed decisions, Walmart can enhance operational efficiency, improve product availability, and deliver exceptional customer experiences. This customer-centric approach underscores Walmart's commitment to innovation and continuous improvement in meeting the diverse and dynamic demands of modern retail consumers.

<u>**Strategy**</u>: The adoption of a real-time big data analytics platform by Walmart, with the goal of optimizing inventory management and demand forecasting, exemplifies the retailer's dedication to utilizing data-driven insights in order to improve both operational efficiency and consumer pleasure. Walmart's goal was to obtain real-time visibility into sales patterns, market dynamics, and supply chain performance by utilizing advanced analytics techniques and combining data from a wide variety of internal and external sources. This allows Walmart to make proactive choices and manage inventory levels.

The project involved combining data from various sources, such as internal sales figures, inventory records, weather trends, supplier performance metrics, and market data. Walmart standardized these diverse datasets into a single analytics platform to create a comprehensive data environment for thoroughly analyzing inventory management and supply chain operations. A significant aspect of Walmart's efforts focused on demand forecasting using analytics. By examining sales data, seasonal patterns, promotions, and external factors like weather conditions, Walmart developed advanced predictive models

to predict future demand accurately. These models helped Walmart anticipate changes in customer demand, optimize inventory levels effectively, and reduce the risk of shortages or excess inventory.

Walmart also quite likely utilized real-time data analytics in order to monitor and respond to crises involving customers and the market promptly. Walmart can adjust its inventory levels, enhance its product variety, and fine-tune its pricing tactics in order to better satisfy the preferences of its customers and optimize its profitability. This is accomplished by continuously monitoring sales patterns and supply chain performance indicators in real time.

The implementation of a real-time big data analytics platform also facilitated improved collaboration with suppliers and partners. Walmart can share actionable insights and performance metrics with suppliers, enabling collaborative demand planning and inventory management. This collaborative approach enhanced supply chain visibility, reduced lead times, and strengthened relationships with key stakeholders across the supply chain ecosystem [7]. Walmart's use of sophisticated analytics for inventory management also mirrors a larger retail sector movement toward operational excellence and data-driven decision-making. Big data analytics may be used by Walmart to improve inventory management procedures, cut operating expenses, and eventually provide better customer experiences by guaranteeing product availability and prompt order fulfillment.

Walmart's use of a real-time big data analytics platform for the purpose of inventory management and demand forecasting exemplifies the revolutionary nature of data analytics in terms of its ability to enhance the operational efficiency and competitive advantage of commercial retail businesses. Through the utilization of data-driven insights to optimize inventory levels and supply chain procedures, Walmart has the potential to enhance the satisfaction of its customers, boost its profitability, and position itself as a pioneer in the field of data-derived retail innovation. Walmart is demonstrating its commitment to using technology and analytics in order to meet the ever-evolving expectations of modern customers and to give exceptional value across all of its retail operations through this endeavor.

Outcome: Through the utilization of real-time analytics, Walmart was able to achieve a decrease of 10% in the number of out-of-stock situations and an improvement of 15% in the turnover of inventory. As a consequence of the supply chain being streamlined, operational efficiency was increased, carrying costs were decreased, and customer satisfaction was increased [47]. Figure 14 shows Walmart's online marketing platform architecture.
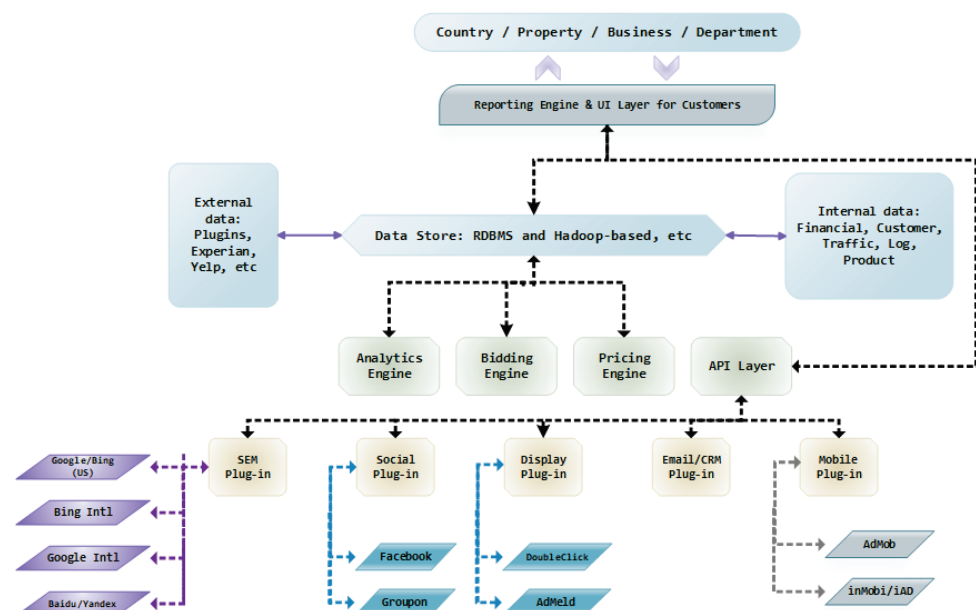

Figure 14. Walmart's online marketing platform architecture.

3.4. Tesla—Quality Control and Production Optimization in the Automotive Sector

Challenge: Tesla's goal of improving product quality, minimizing flaws, and streamlining production methods demonstrates an emphasis on utilizing data analysis, automation, and continuous enhancement techniques to meet the growing market demand for electric vehicles (EVs) while upholding high standards of excellence and efficiency. As a pioneer in the automotive sector, Tesla encounters distinct challenges related to expanding production capacity, ensuring reliability, and providing top-tier products that align with customer preferences.

Tesla most likely used a multidimensional strategy that incorporated data-driven insights and sophisticated technologies across the whole product lifecycle, beginning with the design and manufacturing stages and continuing through quality assurance and customer delivery. This was performed so that Tesla could fulfill these aims. The purpose of this effort was to optimize processes, discover problems at an early stage in the production cycle, and drive initiatives for continuous improvement by utilizing real-time data analytics, machine learning, and automation.

Tesla's strategy focuses on using data to ensure quality control and detect defects. Tesla relies on data analysis and machine learning to examine sensor data, production records, and quality measures in real time. By monitoring key performance indicators (KPIs) and identifying deviations from the norm, Tesla can proactively detect and address potential issues or irregularities during production, reducing rework and enhancing overall product quality. In addition, Tesla likely utilizes predictive maintenance techniques to optimize equipment performance and minimize downtime at their manufacturing plants. Using sensors and predictive analytics, Tesla can monitor the condition of their production machinery, forecast maintenance requirements, and plan maintenance tasks in advance to prevent unexpected interruptions in operations, thereby maintaining peak production efficiency.

Tesla's dedication to ongoing development also encompasses automation and process efficiency. Using data analytics, Tesla can find possibilities to streamline production processes as well as bottlenecks and inefficiencies. Tesla can scale production volumes, lower cycle times, and improve operational efficiency by putting automation technologies, robots, and AI-driven solutions into place to satisfy the expanding market demand for EVs without sacrificing quality or safety.

Tesla's approach to improving product quality and optimizing production processes exemplifies the transformative impact of data analytics and technology in the automotive industry. By leveraging data-driven insights to drive operational excellence and innovation, Tesla can deliver high-quality electric vehicles that exceed customer expectations, differentiate itself in a competitive market landscape, and drive sustainable growth. The emphasis Tesla places on improving product quality, lowering defects, and automating and data analytics manufacturing processes emphasizes how crucial it is to use cutting-edge technology to promote ongoing development and operational effectiveness in the automotive sector. Tesla is positioned to address the changing needs of customers for high-performance, environmentally friendly electric cars while preserving its reputation for quality and innovation in the automotive industry by using the potential of data-driven insights and technology-driven innovation.

Strategy: Tesla's use of data analysis and machine learning in manufacturing is a key strategy to improve efficiency, reduce defects, and enhance production quality. By utilizing real-time data analytics and proactive maintenance techniques, Tesla aims to streamline manufacturing processes, boost product quality, and meet the rising demand for vehicles while upholding high standards of performance and reliability.

Tesla's project involved integrating data from various sources in its production lines, such as sensor readings, production logs, quality control metrics, and equipment performance data. By consolidating and aligning these datasets within a single analytics platform, Tesla established a comprehensive data environment that enabled continuous monitoring and analysis of manufacturing operations in real time. A crucial aspect of Tesla's efforts was utilizing machine learning algorithms to examine manufacturing data and identify the

root causes of defects. Through the use of analytical methods, Tesla could detect patterns, anomalies, and deviations from expected performance metrics. Historical data were used to train machine learning models to anticipate defects, fine-tune process parameters, and suggest corrective measures to prevent quality issues and reduce production interruptions.

In addition, Tesla has incorporated predictive maintenance techniques to enhance the performance of its equipment and reduce downtime at its manufacturing plants. By using sensors and predictive analysis, Tesla can monitor the status and condition of production machinery in real time. Maintenance algorithms analyze data from equipment sensors to identify early signs of wear and predict potential malfunctions. This approach allows for the scheduling of maintenance tasks to avoid unexpected downtime and ensure efficient production operations.

The integration of data analysis and artificial intelligence into Tesla's manufacturing processes underscores the importance of data-driven decision-making and the adoption of technological advancements in the automotive sector. By utilizing real-time data analysis, Tesla can continuously refine production methods, enhance product quality, and achieve operational excellence to meet the rapidly changing demands of the electric vehicle market.

Tesla's deployment of big data analytics and machine learning for manufacturing optimization exemplifies the transformative impact of data-driven technologies on driving efficiency, quality, and innovation within automotive manufacturing. By leveraging advanced analytics and predictive maintenance strategies, Tesla is able to maintain a competitive edge, deliver high-quality electric vehicles, and uphold its commitment to sustainability and innovation in the automotive sector. This initiative demonstrates Tesla's strategic vision and commitment to leveraging technology to redefine manufacturing practices and deliver superior products to customers worldwide.

Outcome: By leveraging big data for quality control and process optimization, Tesla achieved a 20% reduction in manufacturing defects and a 30% improvement in production efficiency. The data-driven insights enabled Tesla to deliver high-quality vehicles at scale and maintain a competitive edge in the automotive market [48]. Figure 15 shows the Predictive maintenance process in the automotive sector.
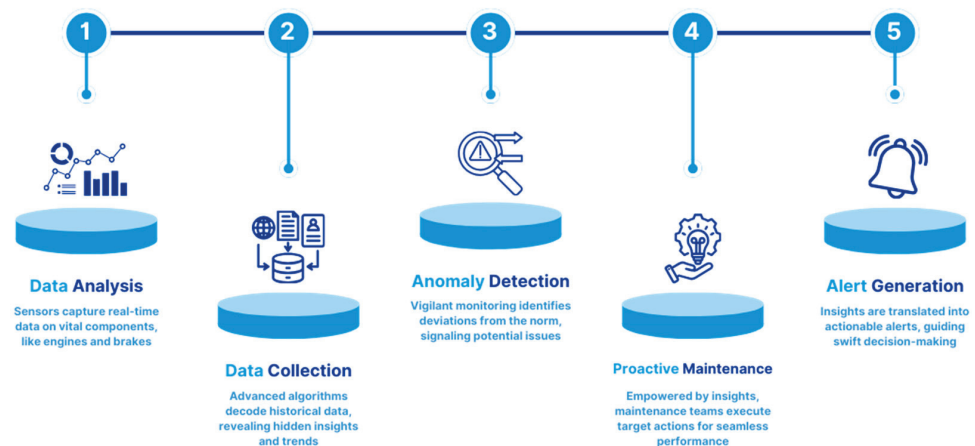
Figure 15. Predictive maintenance process in the automotive sector.

4. Discussion

4.1. Challenges and Future Research Directions

4.1.1. Edge Computing

In the realm of data processing and analytics, edge computing is a revolutionary trend that shifts the focus away from centralized cloud servers and toward distributed computing resources. These resources include Internet of Things devices, sensors, and edge servers, all of which are located closer to the source of the data [49]. This paradigm shift is being driven by the demand to minimize latency, reduce bandwidth usage, and reduce dependency on traditional cloud infrastructure. This is especially true in circumstances when real-time

responsiveness and low-latency applications are absolutely necessary. By utilizing their proximity to data sources, businesses are able to process and analyze massive volumes of data that are generated by Internet of Things devices and sensors that are located at the network edge. This is made possible by edge computing [50].

Edge computing advances real-time analytics and decentralized decision-making by allowing data processing to occur closer to the source. This enables data analysis and decision-making without the need to transmit large amounts of data to centralized data centers. It is particularly useful in applications requiring immediate responses based on real-time data, such as autonomous vehicles, industrial automation, and remote healthcare monitoring. Additionally, edge computing enhances context-aware applications by utilizing local data and environmental signals to provide personalized and adaptive user experiences [51].

Edge computing provides increased data privacy and security, which is another key breakthrough given by this technology. When enterprises handle sensitive data locally at the edge, they are able to reduce the exposure of data during transmission and storage, hence minimizing the risk of data breaches and unauthorized access. Edge computing makes it possible to secure sensitive information while still adhering to data protection requirements by enabling approaches such as data encryption, access control, and privacy-preserving methods. In addition, edge computing has the potential to improve resilience against cyber attacks by lowering the attack surface and making it possible for distributed edge systems to respond quickly to incidents [52].

Despite the fact that it has a number of benefits, edge computing also has a number of obstacles that need to be solved in order to achieve widespread acceptance and scalability. When dealing with dispersed edge settings, which are characterized by different and heterogeneous devices with varying capabilities and connections, one of the challenges that must be overcome is guaranteed dependability and consistency. It is of the utmost importance to effectively manage and orchestrate edge resources in order to guarantee consistent performance and dependability throughout a distributed infrastructure. Furthermore, in order to address security problems that are associated with the transmission and storage of data at the edge, it is necessary to implement effective encryption, authentication, and security protocols in order to safeguard the integrity and confidentiality of data in settings that are dynamic at the edge [53]. Table 3 shows the key aspects of edge computing, including trends, advancements, and challenges.

Table 3. Key aspects of edge computing, including trends, advancements, and challenges.

Aspect	Description
Trend: Edge Computing	Edge computing is an emerging paradigm shifting data processing and analytics closer to data sources (IoT devices, sensors, edge servers) rather than relying solely on centralized cloud servers. This reduces latency, bandwidth usage, and dependency on cloud infrastructure.
Advancements	- Enables real-time analytics and decentralized decision-making. - Supports context-aware applications. - Enhances data privacy and security by processing data at the network edge.
Challenges	- Ensuring reliability and consistency in distributed edge environments. - Managing heterogeneous edge devices and resources efficiently. - Addressing security concerns related to data transmission and storage at the edge.

4.1.2. Federated Learning

Federated learning is a new approach in machine learning that enables decentralized model training across various devices or edge nodes. This eliminates the need to collect sensitive data into centralized repositories, which is a common practice in traditional machine learning platforms [54]. Each participating device or node trains a local machine learning model using its own data in this manner. Only model changes (such as gradients) are exchanged with a central server or coordinator. This strategy is referred to as the "local machine learning algorithm". The decentralized training paradigm enables companies to

make use of dispersed data sources for the purpose of model training, while also limiting privacy problems that are connected with the centralized aggregation of user data [55].

Federated learning has made significant strides in privacy-focused machine learning. By training models directly on devices and keeping data local, this approach minimizes the risk of sensitive data exposure to central servers. This not only addresses privacy concerns but also ensures compliance with data protection laws. It allows organizations to utilize datasets spread across various devices or locations without compromising individual user privacy, making it ideal for sectors like healthcare, finance, and IoT [56]. Furthermore, federated learning enables the creation of personalized AI models tailored to specific users or devices. By training models on local data, personalized recommendations, predictions, and adjustments can be made based on user preferences and behaviors. This functionality enhances user interaction and experience while upholding data privacy and security standards.

While federated learning offers numerous benefits, it also presents several challenges that must be addressed to ensure smooth implementation and scalability. One major challenge is the communication among devices during model training and aggregation, especially in situations with limited bandwidth or unreliable network connections. Another key hurdle is maintaining model convergence and consistency across devices with varying computational capabilities and data distributions [57].

To tackle these issues, techniques such as adaptive learning rates, ensuring differential privacy, and employing secure aggregation methods are used to facilitate robust model training in federated learning setups [58]. Additionally, addressing concerns related to data distribution and bias among data sources is crucial for the success of federated learning. It is essential to have representative training data from all participating devices to create accurate and unbiased AI models. Strategies such as data sampling, augmentation, and model averaging play a significant role in managing discrepancies in data distribution and enhancing overall model performance within federated learning environments [59]. Table 4 shows the key aspects of federated learning, including trends, advancements, and challenges.

Table 4. Key aspects of federated learning, including trends, advancements, and challenges.

Aspect	Description
Trend: Federated Learning	Federated learning is a decentralized machine learning approach where multiple devices or edge nodes collaboratively train a shared model, without centrally aggregating data. Each device trains its local model using local data and only model updates are shared with a central server.
Advancements	- Enables privacy-preserving machine learning by keeping data local. - Supports personalized AI models while respecting data privacy regulations.
Challenges	- Dealing with communication overhead among devices. - Ensuring model convergence and consistency across heterogeneous devices. - Addressing issues related to data distribution and bias.

4.1.3. Explainable AI (XAI)

Explainable artificial intelligence, often known as XAI, is a prominent movement in the field of artificial intelligence. Its primary objective is to improve the interpretability and transparency of machine learning models. XAI approaches are designed to give explanations that are both obvious and intelligible for the judgments and predictions that are produced by artificial intelligence systems. This will ultimately improve the trustworthiness, accountability, and acceptance of AI technology across a variety of areas. The rising demand to simplify complicated machine learning algorithms and provide people with the ability to grasp and confirm the logic behind judgments powered by artificial intelligence is the driving force behind this development [60].

One of the main developments made possible by XAI approaches is the creation of methodologies for local interpretability, model-agnostic explanations, and feature significance analysis. The analysis of feature significance helps determine which input characteristics or variables have the biggest impact on model predictions, thus illuminating the fundamental principles behind AI judgments. Model behavior may be understood by users without a particular understanding of the internal architecture of a machine learning model thanks to model-agnostic explanations, which concentrate on methods applicable to any machine learning model. Local interpretability techniques give end users clearer and more understandable explanations at the level of individual forecasts, hence improving AI judgments [61].

Explainable AI (XAI) plays a crucial role in various fields, such as ensuring regulatory compliance, assessing risks, and enhancing collaboration between humans and AI. In heavily regulated industries like finance and healthcare, XAI techniques allow auditors and regulators to verify model decisions and ensure they meet legal requirements [62]. Additionally, XAI aids in risk assessment by providing insights into the factors influencing model predictions, helping organizations identify biases or errors in AI systems. Furthermore, explainable AI promotes collaboration between humans and AI technologies by empowering users to trust and engage with AI systems effectively [63].

Despite significant progress, XAI still faces hurdles that must be overcome to unlock its potential and scalability fully. One key challenge involves balancing model complexity and interpretability. For instance, more intricate models like deep learning algorithms might prioritize performance over transparency.

Deep learning, a subset of machine learning, involves neural networks with many layers (deep networks) that excel in analyzing large datasets. The success of deep learning algorithms is highly dependent on the availability of big data, as these models require substantial amounts of data for training in order to achieve high accuracy and performance. Big data provides the diverse and extensive datasets needed to train deep learning models effectively [64].

Furthermore, big data analytics tools help preprocess and manage the data required for deep learning, ensuring that the data fed into the models are clean, consistent, and relevant. This preprocessing includes tasks such as data normalization, augmentation, and transformation, which are critical for enhancing the performance of deep learning models [65].

Ongoing research focuses on developing XAI methods that can elucidate the decisions made by these complex algorithms. Moreover, it is important to ensure that the explanations provided by XAI techniques are not only meaningful and understandable but also actionable for end users. This is vital for building trust and acceptance of AI-powered solutions [66]. Table 5 shows the key aspects of Explainable AI (XAI), including trends, advancements, and challenges.

Table 5. Key aspects of Explainable AI (XAI), including trends, advancements, and challenges.

Aspect	Description
Trend: Explainable AI	Explainable AI focuses on developing machine learning models that provide transparent explanations for their decisions and predictions. XAI techniques aim to enhance the interpretability, trustworthiness, and accountability of AI systems.
Advancements	- Feature-importance analysis. - Model-agnostic explanations. - Local interpretability methods. - Supports regulatory compliance, risk assessment, and human–AI collaboration.
Challenges	- Balancing model complexity with interpretability. - Developing scalable XAI techniques for deep learning models. - Ensuring explanations are meaningful and actionable for end users.

4.1.4. Large Models in Big Data

Large models, such as ChatGPT and Sora, have fundamentally transformed the landscape of big data processing and analysis. These advanced neural networks leverage vast datasets to learn and generate valuable insights, making them indispensable tools in various applications. For instance, ChatGPT has found extensive use in natural language processing tasks, including text generation, translation, and summarization [67]. Similarly, Sora excels in analyzing and extracting patterns from massive datasets, making it highly effective for large-scale data tasks [68].

The deployment of these models has demonstrated significant benefits. One of the primary advantages is their ability to process and analyze unstructured data, such as text and images, which constitutes a considerable portion of big data. This capability enhances the comprehensiveness of data analysis, enabling the extraction of more complex insights. Furthermore, these models support improved decision-making through advanced predictive analytics and pattern recognition, which can identify trends and forecast outcomes with high accuracy. Additionally, the automation of complex tasks, such as customer service, content creation, and data extraction, leads to increased operational efficiency, allowing organizations to focus on more strategic activities [69].

Despite the considerable benefits, integrating large models into big data applications does not come by without issues that need to be addressed. One of the most significant obstacles is the requirement for substantial computational resources. Training and deploying large models demand immense computational power and memory, often leading to high costs that can be prohibitive for many organizations. Scalability also poses a considerable challenge. As datasets continue to grow, maintaining the performance of these models without degradation becomes increasingly difficult. Furthermore, ensuring data privacy and security is paramount, especially with stringent regulations such as the General Data Protection Regulation (GDPR). Protecting sensitive data during the training and inference processes is of great importance if we are to prevent breaches and unauthorized access [70].

The integration of large models with existing big data frameworks and infrastructures [71] is another complex challenge. This process often requires significant modifications to current systems, which can be resource-intensive and time-consuming. Additionally, the interpretability of these models remains a pressing issue. Understanding the decision-making process of large models is crucial for building trust and ensuring ethical use, yet it remains a challenging task because of the inherent complexity of these models [72].

To address these challenges and enhance the effectiveness of large models in big data applications, several future research directions are proposed. One key area is an improvement in model efficiency [73]. Developing more efficient algorithms and hardware can significantly reduce the computational and energy costs associated with training large models. Another vital area is the creation of scalable architectures. These architectures need to handle increasing data volumes seamlessly while maintaining performance, ensuring that the models can grow alongside the datasets they are designed to analyze.

Advanced privacy techniques, such as federated learning and differential privacy, are essential for protecting sensitive data while leveraging the power of large models [74]. These techniques allow models to learn from data without the need to centralize them, thereby enhancing privacy and security. Furthermore, hybrid models that combine the strengths of large models with traditional big data processing frameworks can offer a balanced approach, leveraging the best of both worlds.

Lastly, improving model interpretability is also an important research direction. Developing methods to make the inner workings of large models more transparent and understandable will enhance trust and usability, facilitating their broader adoption in the business and the academic world [75]. By focusing on these areas, future advancements can ensure that large models continue to play a pivotal role in extracting value from big data while effectively addressing the associated challenges.

4.2. Challenges and Potential Solutions in Big Data Management

When it comes to contemporary data management and analytics, one of the most critical issues is the management of data sources that are becoming increasingly complicated and diverse. As businesses amass varied datasets from a variety of sources, such as structured and unstructured data, Internet of Things devices, social media platforms, and enterprise systems, they are confronted with issues relating to the integration of data, quality assurance, governance, and scalability [76].

One of the biggest obstacles is data integration, which calls for the harmonization and consolidation of many datasets from many sources to produce a single perspective for analysis. Problems with interoperability, data silos, and inconsistencies arise from the complexity of the integration process brought on by the range of data formats, schemas, and storage systems. As data sources and quantities increase, conventional integration techniques become insufficient, and scalable and adaptable solutions to manage various data kinds and formats are needed [14]. Making sure data are consistent and of high quality from several sources is another problem. The reliability and efficacy of data-driven analytics and decision-making can be negatively impacted by data quality problems like missing values, duplication, and errors. Organizations that want to guarantee correct and trustworthy insights from heterogeneous datasets must put in place strong data quality assurance procedures, such as data cleansing, standardization, and validation, as data complexity grows [77].

Data governance also presents issues when it comes to managing data sources that are both complex and varied. In heterogeneous settings with distant data sources, the process of establishing and implementing policies for data governance, metadata management, and access restrictions becomes increasingly complicated. An additional degree of complexity is added to data governance processes by the necessity of ensuring compliance with legal requirements, privacy rules, and data security standards [78].

The capacity to scale is a significant obstacle to overcome when working with big amounts of complicated data originating from a variety of sources [79]. There is a possibility that traditional data management systems will have difficulty meeting the scalability requirements of big data analytics, real-time processing, and distributed computing. For the purpose of accommodating the increasing volume, velocity, and diversity of data sources, it is vital to use scalable architectures, cloud-based solutions, and distributed processing frameworks [80].

To address these challenges, organizations can leverage several potential solutions including the following:

Advanced Data Integration Tools: Utilizing up-to-date data integration tools and platforms is crucial for companies handling a mix of data sources and intricate data setups. These tools are specifically designed to tackle the complexities of merging datasets that come in different formats, have diverse schemas, and are stored in various systems. A notable feature of data integration tools is their support for schema-on-read, which offers flexibility in interpreting and processing data. Unlike schema-on-write methods that require predetermined schemas before storing data, schema-on-read allows for dynamic interpretation of data during query execution, accommodating a wide range of evolving data structures.

Data virtualization is yet another essential element that contemporary data integration systems make available to their users. Through the use of data virtualization, it is possible to have access to data from a variety of sources in real time without having to physically move or duplicate the data. Through the utilization of this strategy, companies are able to generate a unified, virtual picture of data that encompasses numerous systems, applications, and databases, hence allowing the smooth access and integration of data. Through the reduction in data movement latency and storage costs, data virtualization enables agile data provisioning and speeds up the creation of applications that are driven by data.

Moreover, contemporary data integration solutions often include features for data federation, which facilitate the coordination of data from various sources and environments.

Data federation enables organizations to gather and analyze data in real time from diverse systems such as local databases, cloud services, IoT devices, and external data repositories. This functionality is crucial for establishing a cohesive data infrastructure and supporting complex analytical scenarios that require information from multiple origins. In addition to streamlining data integration processes, modern tools support data manipulation and coordination, empowering organizations to adapt swiftly to evolving business needs and data requests. Real-time data processing capabilities also bolster streaming analytics, event-triggered architectures, and dynamic data workflows—enabling organizations to derive insights and make informed decisions almost instantly.

Companies can solve the obstacles that are encountered in heterogeneous data sources by utilizing current data integration tools and platforms that enable schema-on-read, data virtualization, and data federation. This allows enterprises to gain better agility, flexibility, and efficiency in data management and analytics. Unlocking the full potential of their unique data assets for business innovation and competitive advantage is made possible by these technologies, which enable businesses to adapt to changing data landscapes, embrace decision-making that is driven by data, and embrace data-driven decision-making.

Data Quality Management Practices: It has become imperative for organizations to prioritize data quality management practices to maintain the accuracy, reliability, and consistency of their data assets. Data quality management involves processes and methods aimed at evaluating and enhancing data quality throughout the data lifecycle. One important aspect is data profiling, which entails analyzing datasets to understand their structure, content, and quality attributes. Effective data governance plays a critical role in ensuring compliance with regulations, bolstering data security and integrity, building trust in data-driven decisions, and promoting organizational responsibility and transparency. Organizations must invest in data governance practices to optimize the value of their data assets while minimizing risks related to data misuse, security breaches, and regulatory non-compliance.

Scalable Infrastructure and Technologies: Organizations addressing the difficulties of effectively managing large-scale data processing and analytics must implement scalable infrastructure solutions. Often, the volume, velocity, and variety of data produced from many sources are too much for traditional on-premises infrastructure to handle. Big data processing frameworks like Hadoop and Spark, as well as cloud computing and distributed databases, provide the resources and flexibility needed to efficiently handle and analyze enormous amounts of information.

Providing on-demand access to computer resources, storage, and services over the internet, cloud computing is a game-changing technology that has the potential to revolutionize several industries. Amazon Web Services (AWS), Microsoft Azure, and Google Cloud Platform are examples of cloud platforms that provide scalable infrastructure components. These components include compute instances, storage solutions, and data analytics capabilities. By utilizing cloud computing, organizations are able to expand their resources dynamically in response to the needs of their workload. This allows for more cost-effective data processing and analytics rather than being constrained by the restrictions of on-premises technology.

Distributed databases utilize a multitude of nodes or servers for storage and processing in order to manage massive amounts of data. As data volumes increase, distributed database systems such as Apache Cassandra, MongoDB, and Amazon DynamoDB enable organizations to scale horizontally by adding nodes to the database cluster. By virtue of their fault tolerance, high availability, and efficient data retrieval capabilities, distributed databases are ideally adapted for scalable data storage and management.

Processing large amounts of data is made easier with tools like Apache Hadoop and Apache Spark. These platforms use distributed computing to analyze datasets by running tasks simultaneously across clusters of standard hardware. This approach allows for the execution of data operations, machine learning algorithms, and real-time analytics. By

utilizing distributed computing, companies can speed up data processing and manage various workloads effectively.

Organizations may enhance resource usage and facilitate scalability by utilizing serverless architectures and containerization, in addition to cloud computing and distributed databases. Serverless computing systems, such as AWS Lambda and Azure Functions, allow enterprises to execute code without the need to allocate or oversee servers. These platforms automatically adjust their capacity to match workload requirements. Containerization technologies like Docker and Kubernetes offer lightweight and portable environments for delivering and managing applications. They enable the effective allocation of resources and scalability across dispersed infrastructure.

Large-scale data processing and analytics encounter scalability issues that enterprises can address by implementing scalable infrastructure solutions like cloud computing, distributed databases, big data processing frameworks, serverless architectures, and containerization. These technologies let businesses support flexible, economic data-driven projects, optimize resource use, and expand resources dynamically. Putting money into scalable infrastructure sets the stage for using data as a strategic asset and promoting innovation in the data-heavy corporate environment of today.

5. Conclusions

The field of data information engineering is a diverse and evolving area that addresses the complexities and opportunities of handling, processing, and analyzing large volumes of data. It encompasses methods, technologies, and strategies designed to manage the challenges of today's data environments. By applying the elements and concepts discussed in this document, companies can effectively utilize big data to achieve significant business results, stay competitive in the market, and foster innovation across various sectors.

Data collection and storage that is both effective and efficient is one of the fundamental foundations that support big data information engineering. Distributed file systems, such as the Hadoop Distributed File System (HDFS), NoSQL databases, such as MongoDB and Cassandra, and scalable cloud storage solutions, such as Amazon S3 and Google Cloud Storage, are examples of the sophisticated technologies that are utilized by organizations. Organizations are able to ingest, store, and manage vast amounts of structured and unstructured data from a variety of sources, such as sensors, Internet of Things devices, social media platforms, and corporate applications, with the assistance of these technologies.

Data processing and analysis are essential components of big data information engineering. Apache Hadoop, Apache Spark, and Apache Flink represent essential technologies for managing extensive data processing activities, including batch processing, real-time streaming analytics, and intricate data transformations. Machine learning algorithms, statistical analysis, and data mining techniques are utilized to extract important insights, detect trends, and generate educated predictions from large datasets. This enables enterprises to obtain actionable knowledge from their data assets.

In data information engineering, an important aspect is the integration and management of data. Companies aim to unify datasets from various sources to create a cohesive view of their data. This process includes cleaning data, transforming it, and integrating schemas to ensure data accuracy and consistency. Effective governance structures are established to uphold data policies, adhere to regulations, and safeguard data security and privacy throughout the data lifecycle.

It is also important to note that big data information engineering places an emphasis on the significance of data visualization and interpretation. In order to convey complicated data insights in a manner that is visually intelligible, data visualization techniques like charts, graphs, and dashboards are utilized. This helps to facilitate effective decision-making and the sharing of insights among stakeholders. Additionally, approaches such as explainable artificial intelligence (XAI) are utilized in order to improve the interpretability and transparency of machine learning models. This makes it possible for stakeholders to comprehend the reasoning behind decisions that are driven by AI.

As the volume and complexity of data continue to grow exponentially, the role of big data information engineering becomes increasingly important in enabling data-driven decision-making and insights-driven strategies. Organizations that invest in robust big data practices and technologies are better positioned to leverage their data assets for strategic decision-making, innovation, and sustainable competitive advantage in today's data-centric business environment. The evolution of big data information engineering will continue to shape the future of industries, empowering organizations to unlock new opportunities and navigate the complexities of the digital era.

References

1. Aljumah, A.I.; Nuseir, M.T.; Alam, M.M. Organizational performance and capabilities to analyze big data: Do the ambidexterity and business value of big data analytics matter? *Bus. Process Manag. J.* **2021**, *27*, 1088–1107.
2. Wang, Y.; Kung, L.; Byrd, T.A. Big data analytics: Understanding its capabilities and potential benefits for healthcare organizations. *Technol. Forecast. Soc. Chang.* **2018**, *126*, 3–13. [CrossRef]
3. Günther, W.A.; Mehrizi, M.H.R.; Huysman, M.; Feldberg, F. Debating big data: A literature review on realizing value from big data. *J. Strateg. Inf. Syst.* **2017**, *26*, 191–209.
4. Karras, A.; Giannaros, A.; Karras, C.; Theodorakopoulos, L.; Mammassis, C.S.; Krimpas, G.A.; Sioutas, S. TinyML Algorithms for Big Data Management in Large-Scale IoT Systems. *Future Internet* **2024**, *16*, 42. [CrossRef]
5. Al-Ali, A.R.; Gupta, R.; Zualkernan, I.; Das, S.K. Role of IoT technologies in big data management systems: A review and Smart Grid case study. *Pervasive Mob. Comput.* **2024**, *100*, 101905.
6. Rajeshkumar, K.; Dhanasekaran, S.; Vasudevan, V. Efficient and secure medical big data management system using optimal map-reduce framework and deep learning. *Multimed. Tools Appl.* **2023**, *83*, 47111–47138. [CrossRef]
7. Alsolbi, I.; Shavaki, F.H.; Agarwal, R.; Bharathy, G.K.; Prakash, S.; Prasad, M. Big data optimisation and management in supply chain management: A systematic literature review. *Artif. Intell. Rev.* **2023**, *56* (Suppl. S1), 253–284. [CrossRef]
8. He, Z. Research on Spatial Big Data Management and High Performance Computing Based on Information Cloud Platform. In Proceedings of the 2021 5th Annual International Conference on Data Science and Business Analytics (ICDSBA), Changsha, China, 24–26 September 2021; IEEE: Piscataway, NJ, USA, 2021; pp. 23–28.
9. Rana, M.E. Integration of big data analytics and the cloud environment in harnessing valuable business insights. In Proceedings of the 2021 International Conference on Data Analytics for Business and Industry (ICDABI), Virtual, 25–26 October 2021; IEEE: Piscataway, NJ, USA, 2021; pp. 149–156.
10. Zhuo, Z.; Zhang, S. Research on the Application of Big Data Management in Enterprise Management Decision-making and Execution Literature Review. In Proceedings of the 2019 11th International Conference on Machine Learning and Computing, New York, NY, USA, 22–24 February 2019; pp. 268–273.
11. Liu, Q.; Fu, Y.; Ni, G.; Mei, J. Big Data Management Performance Evaluation in Hadoop Ecosystem. In Proceedings of the 2017 3rd International Conference on Big Data Computing and Communications (BIGCOM), Chengdu, China, 10–11 August 2017; IEEE: Piscataway, NJ, USA, 2017; pp. 413–421.
12. Shafiq, M.; Gu, Z. Deep residual learning for image recognition: A survey. *Appl. Sci.* **2022**, *12*, 8972. [CrossRef]
13. Dogra, V.; Verma, S.; Kavita Chatterjee, P.; Shafi, J.; Choi, J.; Ijaz, M.F. A Complete Process of Text Classification System Using State-of-the-Art NLP Models. *Comput. Intell. Neurosci.* **2022**, *2022*, 1883698.
14. Bagga, S.; Sharma, A. Big data and its challenges: A review. In Proceedings of the 2018 4th International Conference on Computing Sciences (ICCS), Jalandhar, India, 30 August 2018; IEEE: Piscataway, NJ, USA, 2018; pp. 183–187.
15. Elkawkagy, M.; Elbeh, H. High performance hadoop distributed file system. *Int. J. Networked Distrib. Comput.* **2020**, *8*, 119–123. [CrossRef]
16. Yang, P.; Xiong, N.; Ren, J. Data security and privacy protection for cloud storage: A survey. *IEEE Access* **2020**, *8*, 131723–131740.
17. Tekdogan, T.; Cakmak, A. Benchmarking apache spark and hadoop mapreduce on big data classification. In Proceedings of the 2021 5th International Conference on Cloud and Big Data Computing, Liverpool, UK, 13–15 August 2021; pp. 15–20.

18. Deepthi, B.G.; Rani, K.S.; Krishna, P.V.; Saritha, V. An efficient architecture for processing real-time traffic data streams using apache flink. *Multimed. Tools Appl.* **2024**, *83*, 37369–37385. [CrossRef]

19. Dogan, A.; Birant, D. Machine learning and data mining in manufacturing. *Expert Syst. Appl.* **2021**, *166*, 114060. [CrossRef]

20. Jayatilake SM DA, C.; Ganegoda, G.U. Involvement of machine learning tools in healthcare decision making. *J. Healthc. Eng.* **2021**, *2021*, 6679512. [CrossRef]

21. Yousif, O.S.; Zakaria, R.B.; Aminudin, E.; Yahya, K.; Sam, A.R.M.; Singaram, L.; Munikanan, V.; Yahya, M.A.; Wahi, N.; Shamsuddin, S.M. Review of big data integration in construction industry digitalization. *Front. Built Environ.* **2021**, *7*, 770496. [CrossRef]

22. Cho, D.; Lee, M.; Shin, J. Development of cost and schedule data integration algorithm based on big data technology. *Appl. Sci.* **2020**, *10*, 8917. [CrossRef]

23. Lutfi, A.; Alsyouf, A.; Almaiah, M.A.; Alrawad, M.; Abdo, A.A.K.; Al-Khasawneh, A.L.; Ibrahim, N.; Saad, M. Factors influencing the adoption of big data analytics in the digital transformation era: Case study of Jordanian SMEs. *Sustainability* **2022**, *14*, 1802. [CrossRef]

24. Qin, X.; Luo, Y.; Tang, N.; Li, G. Making data visualization more efficient and effective: A survey. *VLDB J.* **2020**, *29*, 93–117. [CrossRef]

25. Dimara, E.; Zhang, H.; Tory, M.; Franconeri, S. The unmet data visualization needs of decision makers within organizations. *IEEE Trans. Vis. Comput. Graph.* **2021**, *28*, 4101–4112. [CrossRef]

26. Naqvi, R.; Soomro, T.R.; Alzoubi, H.M.; Ghazal, T.M.; Alshurideh, M.T. The nexus between big data and decision-making: A study of big data techniques and technologies. In Proceedings of the International Conference on Artificial Intelligence and Computer Vision, Settat, Morocco, 29 May 2021; Springer International Publishing: Cham, Switzerland, 2021; pp. 838–853.

27. Mehmood, E.; Anees, T. Challenges and solutions for processing real-time big data stream: A systematic literature review. *IEEE Access* **2020**, *8*, 119123–119143. [CrossRef]

28. Peddireddy, K. Streamlining Enterprise Data Processing, Reporting and Realtime Alerting using Apache Kafka. In Proceedings of the 2023 11th International Symposium on Digital Forensics and Security (ISDFS), Chattanooga, TN, USA, 11–12 May 2023; IEEE: Piscataway, NJ, USA, 2023; pp. 1–4.

29. Vyas, S.; Tyagi, R.K.; Jain, C.; Sahu, S. Literature review: A comparative study of real time streaming technologies and apache kafka. In Proceedings of the 2021 Fourth International Conference on Computational Intelligence and Communication Technologies (CCICT), Sonepat, India, 3 July 2021; IEEE: Piscataway, NJ, USA, 2021; pp. 146–153.

30. Leow, K.R.; Leow, M.C.; Ong, L.Y. A New Big Data Processing Framework for the Online Roadshow. *Big Data Cogn. Comput.* **2023**, *7*, 123. [CrossRef]

31. Ochuba, N.A.; Amoo, O.O.; Okafor, E.S.; Akinrinola, O.; Usman, F.O. Strategies for leveraging big data and analytics for business development: A comprehensive review across sectors. *Comput. Sci. IT Res. J.* **2024**, *5*, 562–575. [CrossRef]

32. Elouataoui, W.; Alaoui, I.E.; Gahi, Y. Data quality in the era of big data: A global review. *Big Data Intell. Smart Appl.* **2022**, *994*, 1–25.

33. Taleb, I.; Serhani, M.A.; Bouhaddioui, C.; Dssouli, R. Big data quality framework: A holistic approach to continuous quality management. *J. Big Data* **2021**, *8*, 76. [CrossRef]

34. Mishra, P.; Biancolillo, A.; Roger, J.M.; Marini, F.; Rutledge, D.N. New data preprocessing trends based on ensemble of multiple preprocessing techniques. *TrAC Trends Anal. Chem.* **2020**, *132*, 116045. [CrossRef]

35. Kotiyal, B.; Pathak, H. Big Data Preprocessing Phase in Engendering Quality Data. In *Machine Learning, Advances in Computing, Renewable Energy and Communication: Proceedings of MARC 2020*; Springer: Singapore, 2021; pp. 65–74.

36. Prakash, A.; Navya, N.; Natarajan, J. Big Data Preprocessing for Modern World: Opportunities and Challenges. In *International Conference on Intelligent Data Communication Technologies and Internet of Things (ICICI) 2018*; Hemanth, J., Fernando, X., Lafata, P., Baig, Z., Eds.; ICICI 2018. Lecture Notes on Data Engineering and Communications Technologies; Springer: Cham, Switzerland, 2019; Volume 26.

37. Liu, X.L.; Wang, W.M.; Guo, H.; Barenji, A.V.; Li, Z.; Huang, G.Q. Industrial blockchain based framework for product lifecycle management in industry 4.0. *Robot. Comput. -Integr. Manuf.* **2020**, *63*, 101897. [CrossRef]

38. Munawar, H.S.; Qayyum, S.; Ullah, F.; Sepasgozar, S. Big data and its applications in smart real estate and the disaster management life cycle: A systematic analysis. *Big Data Cogn. Comput.* **2020**, *4*, 4. [CrossRef]

39. Lim, K.Y.H.; Zheng, P.; Chen, C.H. A state-of-the-art survey of Digital Twin: Techniques, engineering product lifecycle management and business innovation perspectives. *J. Intell. Manuf.* **2020**, *31*, 1313–1337. [CrossRef]

40. Stark, J. Product lifecycle management (PLM). In *Product Lifecycle Management (Volume 1) 21st Century Paradigm for Product Realisation*; Springer International Publishing: Cham, Switzerland, 2022; pp. 1–32.

41. Wang, J.; Xu, C.; Zhang, J.; Zhong, R. Big data analytics for intelligent manufacturing systems: A review. *J. Manuf. Syst.* **2022**, *62*, 738–752. [CrossRef]

42. Sabireen, H.; Kirthica, S.; Sridhar, R. Secure data archiving using enhanced data retention policies. In Proceedings of the Data Science Analytics and Applications: First International Conference, DaSAA 2017, Chennai, India, 4–6 January 2017; Revised Selected Papers 1; Springer: Singapore, 2018; pp. 139–152.

43. Çınar, Z.M.; Abdussalam Nuhu, A.; Zeeshan, Q.; Korhan, O.; Asmael, M.; Safaei, B. Machine learning in predictive maintenance towards sustainable smart manufacturing in industry 4.0. *Sustainability* **2020**, *12*, 8211. [CrossRef]

44. Meinert, E.; Milne-Ives, M.; Surodina, S.; Lam, C. Agile requirements engineering and software planning for a digital health platform to engage the effects of isolation caused by social distancing: Case study. *JMIR Public Health Surveill.* **2020**, *6*, e19297. [CrossRef]

45. Cook, E.; Merrick, J.R. Technology Implementation at Capital One. *INFORMS J. Appl. Anal.* **2023**, *53*, 178–191. [CrossRef]

46. Naseema, N.; Akhtar, S.; Al Hinai, A.A. Disrupting Financial Services: A Case Study on Capital One's Fintech Odyssey. In *Harnessing Blockchain-Digital Twin Fusion for Sustainable Investments*; IGI Global: Hershey, PA, USA, 2024; pp. 363–383.

47. Neebe, K. Sustainability at Walmart: Success over the long haul. *J. Appl. Corp. Financ.* **2020**, *32*, 64–71. [CrossRef]

48. Hamdan, A.; Ibekwe, K.I.; Ilojianya, V.I.; Sonko, S.; Etukudoh, E.A. AI in renewable energy: A review of predictive maintenance and energy optimization. *Int. J. Sci. Res. Arch.* **2024**, *11*, 718–729. [CrossRef]

49. Cao, K.; Liu, Y.; Meng, G.; Sun, Q. An overview on edge computing research. *IEEE Access* **2020**, *8*, 85714–85728. [CrossRef]

50. Khan, W.Z.; Ahmed, E.; Hakak, S.; Yaqoob, I.; Ahmed, A. Edge computing: A survey. *Future Gener. Comput. Syst.* **2019**, *97*, 219–235. [CrossRef]

51. Breitbach, M.; Schäfer, D.; Edinger, J.; Becker, C. Context-aware data and task placement in edge computing environments. In Proceedings of the 2019 IEEE International Conference on Pervasive Computing and Communications (PerCom), Kyoto, Japan, 11–15 March 2019; IEEE: Piscataway, NJ, USA, 2019; pp. 1–10.

52. Alwakeel, A.M. An overview of fog computing and edge computing security and privacy issues. *Sensors* **2021**, *21*, 8226. [CrossRef] [PubMed]

53. Shahzadi, S.; Iqbal, M.; Dagiuklas, T.; Qayyum, Z.U. Multi-access edge computing: Open issues, challenges and future perspectives. *J. Cloud Comput.* **2017**, *6*, 30. [CrossRef]

54. Zhang, C.; Xie, Y.; Bai, H.; Yu, B.; Li, W.; Gao, Y. A survey on federated learning. *Knowl.-Based Syst.* **2021**, *216*, 106775. [CrossRef]

55. Nilsson, A.; Smith, S.; Ulm, G.; Gustavsson, E.; Jirstrand, M. A performance evaluation of federated learning algorithms. In Proceedings of the Second Workshop on Distributed Infrastructures for Deep Learning, Rennes, France, 10–11 December 2018; pp. 1–8.

56. Chronis, C.; Varlamis, I.; Himeur, Y.; Sayed, A.N.; Al-Hasan, T.M.; Nhlabatsi, A.; Bensaali, F.; Dimitrakopoulos, G. A survey on the use of Federated Learning in Privacy-Preserving Recommender Systems. *IEEE Open J. Comput. Soc.* **2024**, *5*, 227–247. [CrossRef]

57. Kairouz, P.; McMahan, H.B.; Avent, B.; Bellet, A.; Bennis, M.; Bhagoji, A.N.; Bonawitz, K.; Charles, Z.; Cormode, G.; Cummings, R.; et al. Advances and open problems in federated learning. *Found. Trends® Mach. Learn.* **2021**, *14*, 1–210. [CrossRef]

58. Xu, C.; Liu, S.; Yang, Z.; Huang, Y.; Wong, K.K. Learning rate optimization for federated learning exploiting over-the-air computation. *IEEE J. Sel. Areas Commun.* **2021**, *39*, 3742–3756. [CrossRef]

59. Li, Q.; Wen, Z.; Wu, Z.; Hu, S.; Wang, N.; Li, Y.; Liu, X.; He, B. A survey on federated learning systems: Vision, hype and reality for data privacy and protection. *IEEE Trans. Knowl. Data Eng.* **2021**, *35*, 3347–3366. [CrossRef]

60. Angelov, P.P.; Soares, E.A.; Jiang, R.; Arnold, N.I.; Atkinson, P.M. Explainable artificial intelligence: An analytical review. *Wiley Interdiscip. Rev. Data Min. Knowl. Discov.* **2021**, *11*, e1424. [CrossRef]

61. Došilović, F.K.; Brčić, M.; Hlupić, N. Explainable artificial intelligence: A survey. In Proceedings of the 2018 41st International Convention on Information and Communication Technology, Electronics and Microelectronics (MIPRO), Opatija, Croatia, 21–25 May 2018; IEEE: Piscataway, NJ, USA, 2018; pp. 210–215.

62. Ahmed, I.; Jeon, G.; Piccialli, F. From artificial intelligence to explainable artificial intelligence in industry 4.0: A survey on what, how, and where. *IEEE Trans. Ind. Inform.* **2022**, *18*, 5031–5042. [CrossRef]

63. Arrieta, A.B.; Díaz-Rodríguez, N.; Del Ser, J.; Bennetot, A.; Tabik, S.; Barbado, A.; García, S.; Gil-López, S.; Molina, D.; Benjamins, R.; et al. Explainable Artificial Intelligence (XAI): Concepts, taxonomies, opportunities and challenges toward responsible AI. *Inf. Fusion* **2020**, *58*, 82–115. [CrossRef]

64. Zhang, Q.; Yang, L.T.; Chen, Z.; Li, P. A survey on deep learning for big data. *Inf. Fusion* **2018**, *42*, 146–157. [CrossRef]

65. Jan, B.; Farman, H.; Khan, M.; Imran, M.; Islam, I.U.; Ahmad, A.; Ali, S.; Jeon, G. Deep learning in big data analytics: A comparative study. *Comput. Electr. Eng.* **2019**, *75*, 275–287. [CrossRef]

66. Rawal, A.; McCoy, J.; Rawat, D.B.; Sadler, B.M.; Amant, R.S. Recent advances in trustworthy explainable artificial intelligence: Status, challenges, and perspectives. *IEEE Trans. Artif. Intell.* **2021**, *3*, 852–866. [CrossRef]

67. Alawida, M.; Mejri, S.; Mehmood, A.; Chikhaoui, B.; Isaac Abiodun, O. A comprehensive study of ChatGPT: Advancements, limitations, and ethical considerations in natural language processing and cybersecurity. *Information* **2023**, *14*, 462. [CrossRef]

68. Qin, R.; Wang, F.Y.; Zheng, X.; Ni, Q.; Li, J.; Xue, X.; Hu, B. Sora for computational social systems: From counterfactual experiments to artificiofactual experiments with parallel intelligence. *IEEE Trans. Comput. Soc. Syst.* **2024**, *11*, 1531–1550. [CrossRef]

69. Chang, Y.; Wang, X.; Wang, J.; Wu, Y.; Yang, L.; Zhu, K.; Chen, H.; Yi, X.; Wang, C.; Wang, Y.; et al. A survey on evaluation of large language models. *ACM Trans. Intell. Syst. Technol.* **2023**, *15*, 1–45. [CrossRef]

70. Raiaan, M.A.K.; Mukta, S.H.; Fatema, K.; Fahad, N.M.; Sakib, S.; Mim, M.M.J.; Ahmad, J.; Ali, M.E.; Azam, S. A review on large Language Models: Architectures, applications, taxonomies, open issues and challenges. *IEEE Access* **2024**, *12*, 26839–26874. [CrossRef]

71. Coussement, K.; Benoit, D.F. Interpretable data science for decision making. *Decis. Support Syst.* **2021**, *150*, 113664. [CrossRef]

72. Myers, D.; Mohawesh, R.; Chellaboina, V.I.; Sathvik, A.L.; Venkatesh, P.; Ho, Y.-H.; Henshaw, H.; Alhawawreh, M.; Berdik, D.; Jararweh, Y. Foundation and large language models: Fundamentals, challenges, opportunities, and social impacts. *Clust. Comput.* **2024**, *27*, 1–26. [CrossRef]

73. Chen, T.; Kornblith, S.; Swersky, K.; Norouzi, M.; Hinton, G.E. Big self-supervised models are strong semi-supervised learners. *Adv. Neural Inf. Process. Syst.* **2020**, *33*, 22243–22255.

74. Madan, S.; Bhardwaj, K.; Gupta, S. Critical Analysis of Big Data Privacy Preservation Techniques and Challenges. In *International Conference on Innovative Computing and Communications*; Khanna, A., Gupta, D., Bhattacharyya, S., Hassanien, A.E., Anand, S., Jaiswal, A., Eds.; Advances in Intelligent Systems and Computing; Springer: Singapore, 2022; Volume 1394.

75. Thunki, P.; Reddy SR, B.; Raparthi, M.; Maruthi, S.; Dodda, S.B.; Ravichandran, P. Explainable AI in Data Science-Enhancing Model Interpretability and Transparency. *Afr. J. Artif. Intell. Sustain. Dev.* **2021**, *1*, 1–8.

76. Hariri, R.H.; Fredericks, E.M.; Bowers, K.M. Uncertainty in big data analytics: Survey, opportunities, and challenges. *J. Big Data* **2019**, *6*, 44. [CrossRef]

77. Ridzuan, F.; Zainon, W.M.N.W. A Review on Data Quality Dimensions for Big Data. *Procedia Comput. Sci.* **2024**, *234*, 341–348.

78. Nair, S.R. A review on ethical concerns in big data management. *Int. J. Big Data Manag.* **2020**, *1*, 8–25. [CrossRef]

79. Gupta, D.; Rani, R. A study of big data evolution and research challenges. *J. Inf. Sci.* **2019**, *45*, 322–340. [CrossRef]

80. Karras, A.; Giannaros, A.; Theodorakopoulos, L.; Krimpas, G.A.; Kalogeratos, G.; Karras, C.; Sioutas, S. FLIBD: A Federated Learning-Based IoT Big Data Management Approach for Privacy-Preserving over Apache Spark with FATE. *Electronics* **2023**, *12*, 4633. [CrossRef]

An Investigation of Increased Power Transmission Capabilities of Elastic–Plastic-Designed Press–Fit Connections Using a Detachable Joining Device

Jan Falter *, Daniel Herburger, Hansgeorg Binz and Matthias Kreimeyer

Institute for Engineering Design and Industrial Design (IKTD), University of Stuttgart, Pfaffenwaldring 9, 70569 Stuttgart, Germany; hansgeorg.binz@iktd.uni-stuttgart.de (H.B.); matthias.kreimeyer@iktd.uni-stuttgart.de (M.K.)
* Correspondence: jan.falter@iktd.uni-stuttgart.de

Abstract: Drive systems are an important part of general mechanical engineering, automotive engineering, and various other fields, with shaft–hub connections being an important part of such systems. Decisive aspects in the development of such systems today are, for example, high transmittable forces and torques, low masses, and the cheapest possible production of components. A possibly threefold increase in the force and torque transmission capacity can be achieved by using press–fit connections with an elastic–plastic design as opposed to regular elastically designed alternatives. An elastic–plastic design of the press–fit connection is achieved by using a large interference. A large transition geometry on the shaft (which replaces the conventional chamfer) is required to join such an interference. The material and space requirements have a negative impact on lightweight applications and limited building spaces. Therefore, the objective of the research presented in this paper is to design and analyze a detachable joining device that substitutes this geometry. A simulation study was conducted to determine the geometry of the joining device that improves the stress state and consequently the force and torque transmission capacity of the connection. Moreover, the influence of manufacturing tolerances of the joining device and the shaft, corresponding risks, and measures to mitigate them are analyzed using finite element analysis. The results show that large transition radii, enabled by using a joining device, lead to a homogenous distribution of plastic strain and pressure in the press–fit connection, even for large interferences ξ and soft hub materials like wrought aluminum alloys. The influence of manufacturing tolerances on the stress state was quantified, leading to design guidelines that minimize the risk of, e.g., the front face collision of a shaft and hub, while maximizing the power transmission of the connection. The results show the capability of a detachable joining device to enable elastic–plastic press–fit connections and the corresponding threefold increase in the force and torque transmission capacity in lightweight applications, resulting from the substitution of the installation space consuming and mass increasing the transition geometry of the shaft.

Keywords: elastic–plastic design; finite element analysis; interference fit; joining device; power transmission; shaft–hub connection

1. Introduction

A primary objective in the development of drive systems is to increase the power density and to reduce the installation space and mass [1]. A crucial component to accomplish this goal is enhancing the force and torque transmission capacity of shaft–hub connections. A particularly important representative of these connections is the interference–fit connection, as it is characterized by its cost-effective production [1–4] and ability to transmit alternating forces and moments [5]. One effective way to increase the transmission capacity of interference–fit connections is to augment the diametral interference between the hub and shaft [3,6]. This is in engineering practice often restricted by the elastic limit of the used material, limiting the interference to approximately 1–2‰. However, a threefold increase in

the transmission capacity is achievable by allowing for the plastic deformation of the hub as part of an elastic–plastic design, using interferences up to 100‰ [7,8]. Due to the large interference, however, such press–fit connections cannot be joined using thermal expansion (shrink–fit connection), as this would require exceeding the annealing temperatures of the hub materials. It is therefore necessary to press the shaft into the bore of the hub (press–fit connection), e.g., by using a hydraulic press. This joining process is subject to extensive requirements due to its influence on the transmission capacity of the press–fit connection. Previous research [8] indicates that in order to achieve a stress state of the connection that allows for an increase in the transmission capacity, a specific transition radius between the shaft's cylindrical contact area and the end of the shaft is necessary.

This research article studies the potential of using a detachable joining device (JD) as a substitute for the shaft's transition radius to decrease weight, material consumption, and installation space while increasing the force and torque transmission capacity. Moreover, this research article examines the challenges of such a device related to manufacturing tolerances and corresponding corrective actions. Finite element simulations are used to find a suitable transition radius and to determine the influence of manufacturing tolerances on the pressure distribution and strains in the hub. Based upon this, a design recommendation for a joining device that is suitable for elastic–plastic-designed press–fit connections is presented.

1.1. Research Problem

Augmenting the diametral interference and therefore the transmission capacity of elastic–plastic-designed press–fit connections results in increasing the complexity of its prevailing triaxial stress condition [8]. Most importantly, the pressure between the shaft and hub, corresponding to the radial stress within the interface, becomes more inhomogeneous with rising diametral interferences. For larger interferences, an increasingly significant drop in the radial stress occurs within the interface in the region of the axial hub center, which is—according to [8]—related to increased local plastic strain. Consequently, this pressure reduction leads to a decreased transmission capacity of the press–fit connection. Moreover, the risk of failure due to fretting fatigue increases for connections with a locally decreased pressure that are subjected to dynamic torsional and bending moments. Increasing the transition radius leads to an increase in pressure within the axial hub center of elastic–plastic-designed press–fit connections. However, within prior research [7,8], it had to be considered that an augmented transition radius leads to an increase in mass and installation space for the shaft [8].

1.2. Research Objective

As described above, the elastic–plastic design requires a large transition radius to achieve a uniform pressure distribution without a strong decrease in the center of the hub. Only then will the average pressure in the interface between the shaft and hub be high, leading to an increased ability to transmit forces and torques. However, a large transition radius causes the shaft to grow in the axial direction and introduces undesired mass into the technical system.

Therefore, the main objective of this article is to apply the elastic–plastic design in such a way that high and uniform pressures are achieved between the hub and the shaft.

In addition, this article pursues the secondary objective of designing the geometry of the component required for the main objective to be as small and light as possible in order to meet the requirements of lightweight applications, which are becoming increasingly important.

By fulfilling these objectives, for the first time, a significantly increased force and torque transmission capacity, a small installation space, and a low mass of elastic–plastic-designed press–fit connections can be achieved simultaneously. The power density can thus be increased threefold [8], which opens up the use of press–fit connections in applications

that were previously restricted to more expensive and complex positive-fit shaft–hub connections.

1.3. Research Approach

To achieve the described objectives, it is proposed to use a detachable joining device, broadening the design flexibility substantially. With this, it will be possible to separate the necessary but disadvantageously large and heavy geometry of the transition radius from the press–fit connection. Finding the best possible geometry for the joining device, a first series of simulations is utilized to identify the relation between large transition radii and the homogeneity of the plastic strain distribution in the connection. For this simulation series, an initial examination of the aforementioned relation between the transition radius and the pressure distribution by Kröger et al. [7] is adopted and the examination space considerably increased. The obtained results serve as a quantified measure for the potential of large transition radii to increase the transmission capacity of press–fit connections and consequently the potential of the joining device as the enabler for their application (cf., Section 4.1). As a result, the most suitable transition radius will be found to meet the objective of a high and homogeneous pressure distribution, leading to an increased force and torque transmission capacity.

The potential of the detachable joining device to improve the stress state of the connection while decreasing the mass and installation space of the shaft relies on the feasibility of the transition of the hub from the joining device to the shaft. Consequently, a second series of simulations is used to investigate the influence of the junction geometry (shown in Figures 1 and 2) on the transmission capacity of the press–fit connection (cf., Section 4.2). Moreover, the effects of manufacturing tolerances in the junction region (cf., Figure 1) and resulting process risks are investigated (cf., Section 4.3). For this purpose, various achievable tolerance ranges are examined in finite element simulations. The objective of this set of iterative numerical investigations is to achieve the highest possible and most uniform pressure distribution in the interface between the shaft and hub.

The numerical simulations are built upon the investigations presented in [8]. The adopted experimentally validated elastic–plastic material model is described in Section 3.1. The definition of the finite element model used is given in Section 3.2. A validation of the numerical simulations of the joining process of the press–fit connections using the detachable joining device is given by experimental data in Section 4.4.

Subsequently, the results are discussed and a design recommendation for the joining device is derived and presented in Section 5. The research article is then closed by a general conclusion in Section 6.
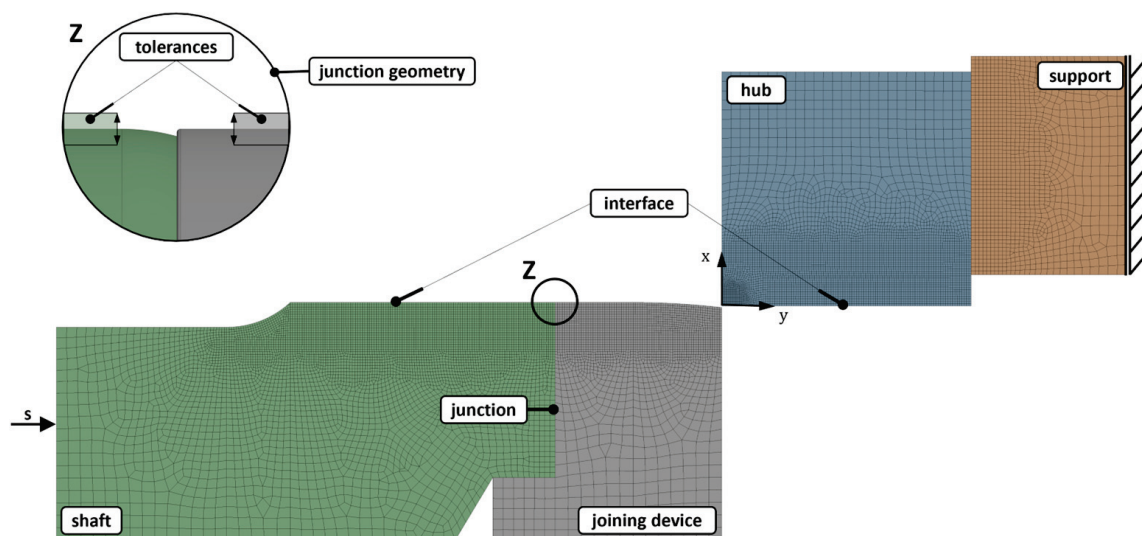

Figure 1. Geometry of the simulation model with detail Z (junction geometry).
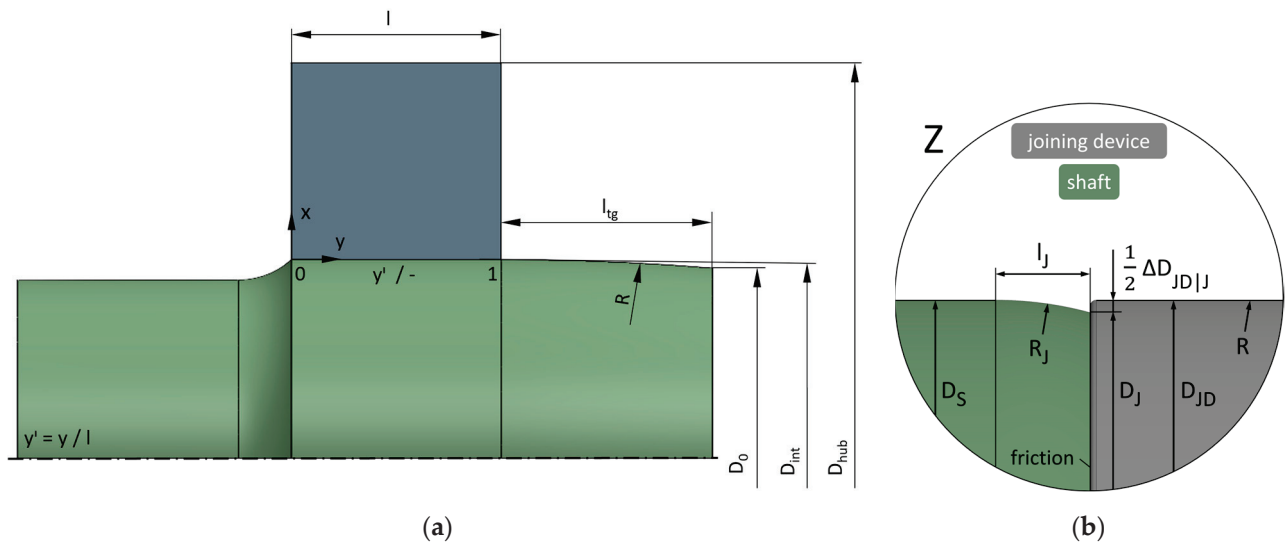
Figure 2. (**a**) Geometry of the simulation model for transition radius analysis and (**b**) geometry of the simulation model for junction geometry analysis.

2. Definitions and Fundamentals

2.1. Definition of the Press–Fit Geometry

To analyze the influence of the joining device on the stress state of the press–fit connection, a comparability of the results with previous research, such as [7–13], must be ensured. The investigations in all of these publications focus on connections with a diameter of the interface of $D_{int} = 30$ mm, a diameter ratio of the hub of $Q_{Hub} = 0.5$, and a length–diameter ratio of about $l/D_{int} \approx 0.5$. The diameter ratio Q_{Hub} (cf., Equation (1)) is of particular interest, as it is, together with the selected material and interference ξ (cf., Equation (2)), a primary influence on the stress state, the hardening behavior, and consequently the transmission capacity of the investigated connection. The geometric interference I_{geo} is given in millimeters. It is necessary to calculate the interference ξ according to Equation (2). All remaining parameters needed to solve Equations (1) and (2) are defined in Table 1 and Figure 2 [8]:

$$Q_{Hub} = \frac{D_{int}}{D_{Hub}} \tag{1}$$

$$\xi = \frac{I_{geo}}{D_{int}} \cdot 1000 \; [‰] \tag{2}$$

Table 1. Materials and geometry specification.

Material of the Shaft	Material of the Hub	Diameter Ratio of the Hub Q_{Hub}	Interference ξ Related to D_{int}	Diameter of the Interface D_{int}	Length-to-Diameter Ratio l/D_{int}
42CrMo4 +QT	EN AW-5083	0.5	10‰	30 mm	0.533

Therefore, the described geometry (cf., Figure 2a) was adopted, and the length–diameter ratio, in accordance with [8,9], was specified as $l/D_{int} = 0.533$. The material of the hub is aluminum wrought alloy EN AW-5083 (AlMg4.5Mn), and the material of the shaft is 42CrMo4 +QT, with a consistent interference of $\xi = 10‰$ applied throughout the analyses (cf., Table 1).

2.1.1. Geometry for Transition Radius Analyses

The geometry used to analyze the influence of the transition radius R on the stress state of the press–fit connection does not account for the junction geometry between the shaft and the joining device, since it is used specifically to evaluate the potential of large radii R. The length l_{tg} of the transition geometry is determined by the transition radius R used. The radius R ensures that the shaft becomes tapered towards its end face, resulting in a difference between the diameter of the shaft at its end face D_0 and the inner diameter of the hub D_{int} of 200 μm to account for tolerances and misalignments in the process (cf., Figure 2). The results are presented in Section 4.1. In the subsequent investigations, the modified transition radius R is applied to the joining device instead of to the shaft.

2.1.2. Geometry for Junction Geometry Analyses

As mentioned in Section 1, a second set of simulations is used to determine the influence of the junction between the shaft and the joining device on the stress state of the press–fit connection. Therefore, the junction geometry needs to be modeled explicitly. Hence, a radius R_J is applied to the shaft that accounts for misalignments and manufacturing tolerances of the shaft and the joining device to eliminate the risk of a front face collision between the shaft and the hub during the joining process. The interface between the shaft and the joining device is modelled using frictional contact (cf., Figure 2). The results of these investigations are presented in Sections 4.2 and 4.3.

3. Materials and Methods

3.1. Characterization of the Material Model

For the numerical investigations, the material properties of all materials used are required in order to be able to reliably calculate stress on the cylindrical press–fit connection. In accordance with Section 2.1 (cf., Table 1), tensile tests with precision strain measurements were carried out for the wrought aluminum alloy EN AW-5083 and the quenched and tempered steel 42CrMo4 +QT. The tensile specimens were taken from the same batch of material that was used for the experiments in Section 4.4. Table 2 shows the material properties which were ascertained with the experimental tensile tests.

Table 2. Material properties experimentally ascertained by uniaxial tensile tests.

Material	Young's Modulus E	Yield Strength $R_{p0.2}$	Tensile Strength R_m	Ultimate Strain A
42CrMo4 +QT	210 GPa	809 MPa	1081 MPa	14%
EN AW-5083	72 GPa	181 MPa	354 MPa	26%

In contrast to the elastic–ideal plastic design, the elastic–plastic design of cylindrical press–fit connections requires precise knowledge of the hardening behavior of the materials used. To describe the strain hardening behavior of the press–fit connection accurately, a non-linear material model is used. The model is based on the method of Li et al. [14], which allows for the combination of two parameterized Ramberg–Osgood [15] curves with a smooth transition [14,15]. This method was first adopted for press–fit connections by Kröger et al. [7,8] to account, with two different curves, for the varying hardening behavior occurring with increasing strain. Therefore, the Ramberg–Osgood model is extended by an index i (cf., Equation (3)) to approximate the region of low plastic strain with a curve corresponding to $i = 1$ and the region of large plastic strain with a curve corresponding to $i = 2$, respectively [8,14].

$$\varepsilon_{pl,i} = \left(\frac{\sigma_t}{K_i}\right)^{\frac{1}{m_i}} \text{ with : } i = 1,2 \mid \sigma_t : \text{ true stress} \mid K_i, m_i : \text{ model parameter} \quad (3)$$

According to Li et al. [14], the plastic strain ε_{pl} defined by the relationship between true plastic strain and true stress can be described as follows:

$$\varepsilon_{pl} = \frac{\varepsilon_{pl,2} \cdot e^{A \cdot \sigma_t + B} + \varepsilon_{pl,1}}{1 + e^{A \cdot \sigma_t + B}} \quad \text{with}: \ A, \ B: \ \text{model parameter} \tag{4}$$

Between the experimental stress–strain curve and the material, model deviations were occurring for larger strains, which could be eliminated with a modification of the model by the approach of Hertelé et al. [7,8,16]. An iteratively determined amount $\Delta\varepsilon$ is used to shift the Ramberg–Osgood curve for the range of larger plastic strains in order to increase the accuracy of the model by changing Equation (3) to the following:

$$\varepsilon_{pl,2} - \Delta\varepsilon = \left(\frac{\sigma_t}{K_2}\right)^{\frac{1}{m_2}} \quad \text{with}: \ \sigma_t: \ \text{true stress} \mid K_i, \ m_i: \ \text{model parameter} \tag{5}$$

The high accuracy of the non-linear material model was validated using uniaxial tensile tests with precision strain measurements (cf., Figure 3) [7,8].
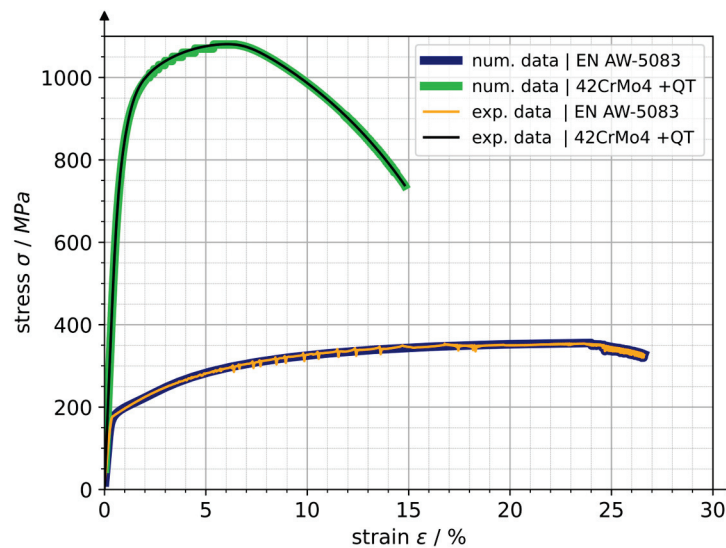

Figure 3. Validation of the material model (num. data) with experimental data (exp. data) based on [7,8].

The materials which were used for the shafts and hubs investigated in this research are from the same production lot as used in [7,8] to ensure comparability with these results. To rely on the numerical results of the finite element analysis, not only the material model but also the simulation model itself needs to be validated. An experimental procedure, described in Section 3.3, was used for this purpose [8].

3.2. Definition of the Finite Element Model Used for the Numerical Simulations

Finite element simulations are used to identify a suitable value for the transition radius *R* by analyzing the stresses and strains that occur and to ascertain the significance of the tolerances in the junction area between the shaft and the joining device. No further mathematical equations are required for this procedure, as the pressure distribution is approximated to the theoretical ideal (horizontal) distribution of the plane stress condition, according to [17]. Thus, no numerical optimization algorithms are needed. Due to the iterative approach, specific values for transition radii *R* and tolerances can be given as design recommendations, which are also useful for engineers in small- and medium-sized enterprises, where the financial and technical resources for complex numerical and mathematical optimizations are often limited.

The investigations described below were carried out using finite element analyses with ANSYS Workbench 2023 R1. Since the geometry investigated is axisymmetric, a 2D half model was used to simulate the joining process. Due to the significant deformations that the hub is subjected to as a result of the elastic–plastic design, the consideration of non-linearities and large deformations are activated in the software. The sample geometry—consisting of a shaft, a joining device, and a hub—is completed by a support for the hub, which is used to absorb the joining forces (cf., Figure 1). The support is rigidly fixed on its rear surface, whereas the contacts between the individual components are subjected to friction. The coefficient of friction in the contact area between the hub and the shaft, respectively, with the joining device, was set to $\mu = 0.08$, based on empirical values from [7]. The remaining contacts were set to a coefficient of friction of $\mu = 0.1$—in accordance with [17]. As a contact algorithm, the augmented Lagrange method was chosen, which proved to be suitable here, in conformity with [7]. The contact penetration tolerance was set to a maximum of 1 μm, as excessive penetration could change the interference ξ and thus the occurring stresses. Finally, the finite element model was meshed, whereby the element size was determined by means of a convergence study (cf., Figure 4).
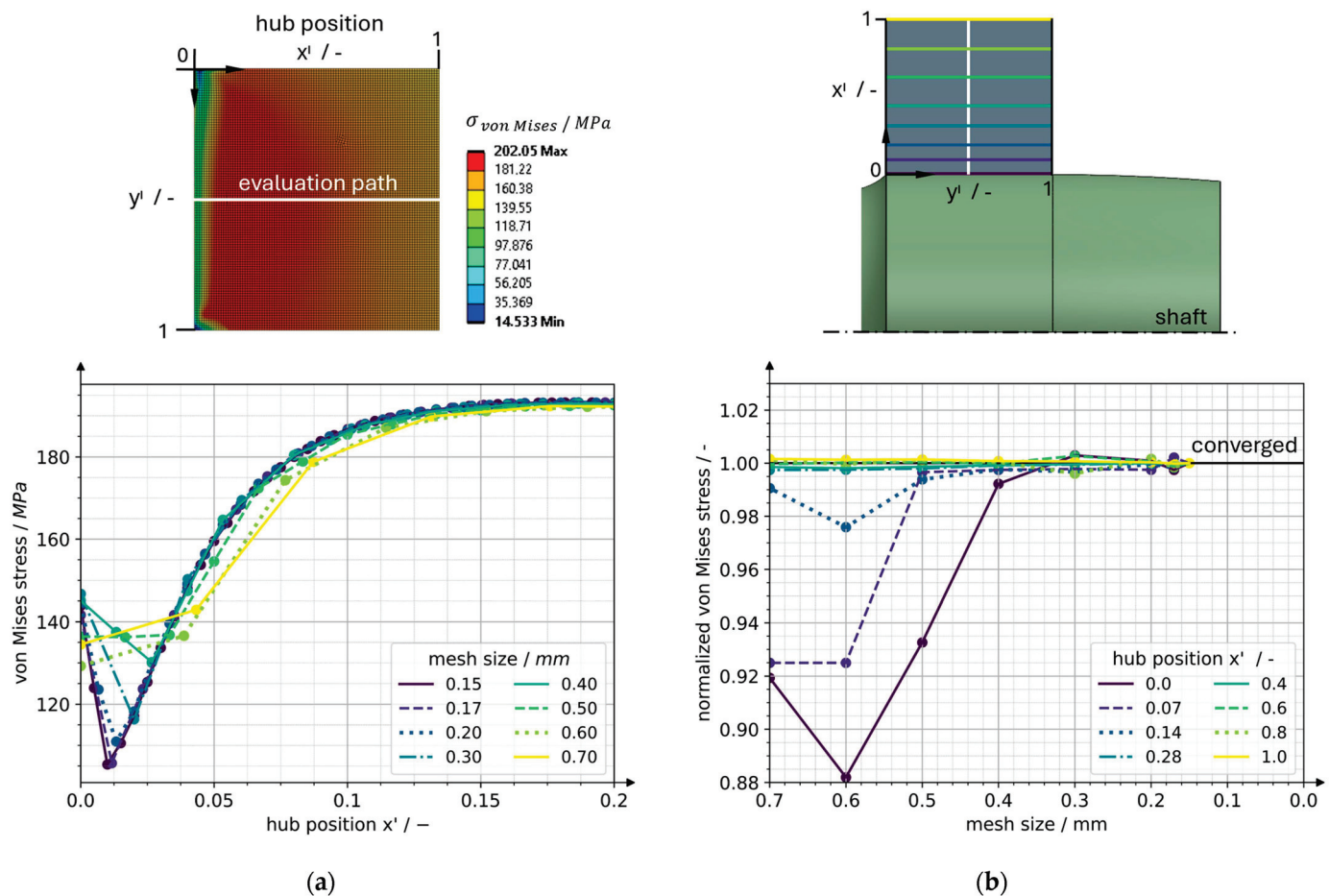

Figure 4. Mesh-convergence study to determine the mesh size. (**a**) von Mises stress for different mesh sizes along the evaluation path. (**b**) Convergence behavior depending on the mesh size at different positions in the hub.

The convergence study demonstrates that in the outer area of the hub, where the stresses are lower, the calculation already converges with element sizes of 0.7 mm (cf., Figure 4). In contrast, significantly smaller elements are required in areas close to the contact between the shaft and hub (cf., Figure 4) to achieve convergence. In the radial direction x', the hub was divided into two areas with different mesh sizes based on the convergence study in Figure 4. The area x' ≤ 0.267 was meshed with an element size of

0.15 mm. In the area closer to the outside of the hub ($0.267 < x' \leq 1.0$), the element size was set to 0.7 mm. The calculation results were visualized either in ANSYS Workbench (graphical illustrations) or using Python on the basis of the exported raw data (diagrams).

3.3. Experimental Procedure for the Validation of the Simulation Model

The experimental validation of the simulation model was performed in accordance with previous research [7,8,18,19]. The method utilizes the proportionality between the geometric changes of the hub related to deformation and the pressure within the interface *p*. For this, the approach is comparing numerically and experimentally determined deformations of the hub. With an experimental procedure containing measuring the components before and after joining, the change in diameter of the hub can be calculated and compared to the numerically determined data. Due to the proportionality between the deformation of the hub and the pressure within the interface *p* as described above, the simulation results can be validated by experimentally determining the hub deformation on a coordinate measuring machine. Unfortunately, there is currently no method for measuring the pressure directly in the contact surface. With the experimental procedure shown in Figure 5, the simulation model that was used in Section 4 of this research article was validated [8].
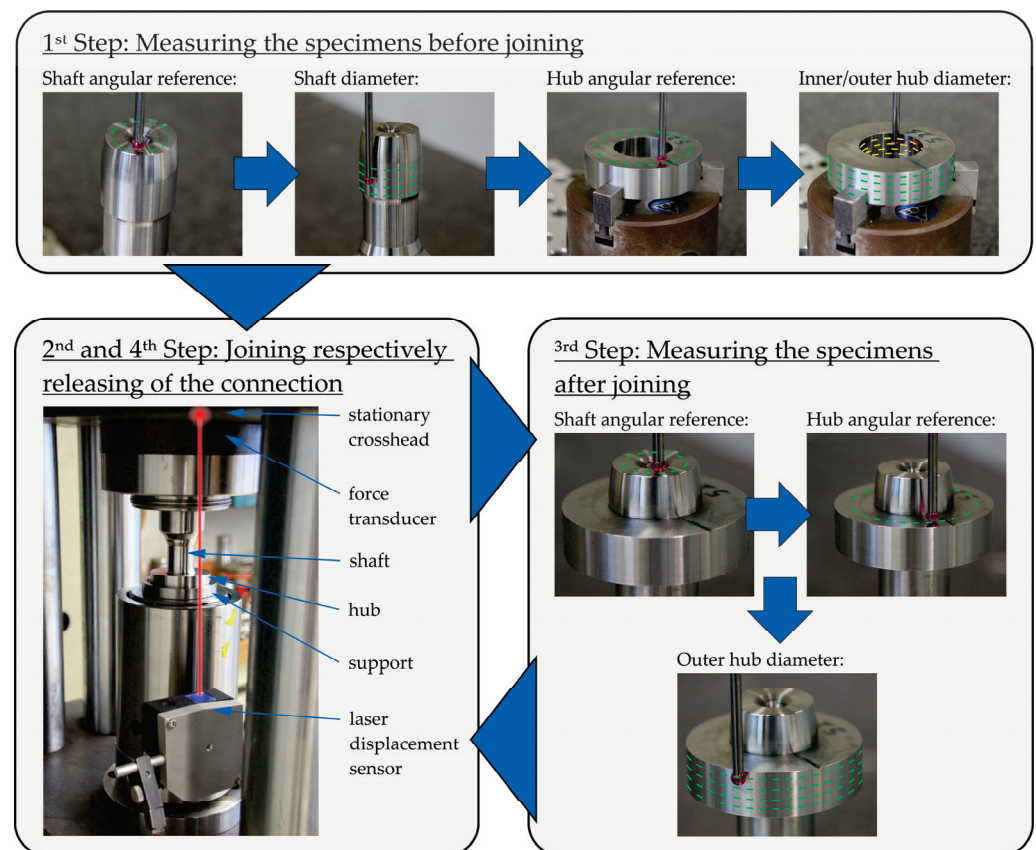
Figure 5. Experimental procedure validating the numerical results according to [8].

4. Results

4.1. Analysis of the Effect of Large Transition Radii R on the Stress State of the Press–Fit Connection

The numerical simulation of the joining process, as described in Section 2.1.1, shows that augmenting the transition radius *R* (cf., Figure 2) increases the average pressure between shaft and hub by reducing the pressure loss in the axial center region of the hub (cf., Figure 6). Moreover, pressure maxima are reduced, leading to increased fatigue strength. This is particularly beneficial for press–fit connections that are subject to bending moments that introduce further radial stresses, eventually approaching a stress state critical

to failure. Both the increase in average pressure and the reduction in pressure peaks correlate with the homogenized plastic strain distribution along the connection length that is achieved through larger transition radii *R*. For small radii *R*, this distribution is characterized by a localized peak at the inner edge of the hub ($y' = 0$) and by an increase in strain at the center of the hub ($y' = 0.5$) as depicted by the green semi-parabolic area (cf., Figure 6). The latter phenomenon is caused by joining forces, which similarly increase when the center part of the hub crosses the transition radius *R*.
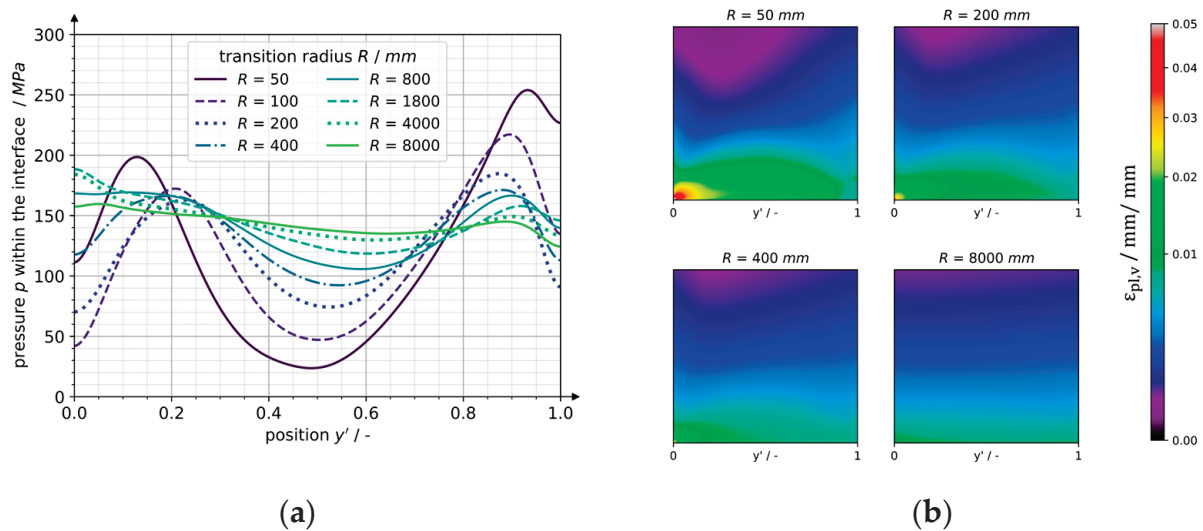

(**a**)

(**b**)

Figure 6. (**a**) Pressure distribution and (**b**) equivalent strain distribution in the hub. Both have a variation of the transition radii *R* for interference of $\xi = 10‰$, shaft made from 42CrMo4 +QT, and a hub made from EN AW-5083.

The stress state of the hub resulting in the joining process is dependent on the geometry of the press–fit connection (D_{int}, Q_{Hub}, *l*, and *R*) and on the interference ξ in particular. The quantitative evaluation of the aforementioned joining process shows that a transition radius of *R* = 8000 mm achieves an almost constant pressure (cf., Figure 6) as well as a homogenized plastic strain distribution. This value presents a limit to the significant improvement of the stress state of the press–fit connection, after which further increasing of the transition radius *R* is, in particular with respect to the anticipated manufacturing tolerances and lubrication challenges, not beneficial. From a pressure distribution for the interference of $\xi = 10‰$, it can be determined that a radius variation in the lower range *R* < 500 mm has a significant impact, corresponding to a reduction in pressure losses in the center of the hub of 58% for a radius increase from *R* = 50 mm to *R* = 400 mm. Increasing the radius *R* further leads to additional contributions to the homogeneity of the pressure *p* and plastic strain distribution, reaching a maximum reduction in pressure loss of 92% and a 22% increase in mean pressure in the connection for a transition radius of *R* = 8000 mm compared to the reference geometry with *R* = 50 mm.

4.2. Analysis of the Junction Geometry on Its Influence on the Stress State of the Press–Fit Connection

Resulting from the concept of a detachable joining device, the hub must overcome the junction between the joining device and shaft (cf., Figures 1 and 2). It must be considered that manufacturing tolerances do not allow for a sharp-edged junction as ideally assumed in Section 4.1. Due to inevitable manufacturing deviations, it is essential to apply a junction geometry that mitigates diametral differences and certain tolerances between the joining device and the shaft. Thus, a junction radius R_J on the shaft is introduced, which leads to a junction diameter D_J that is smaller than the diameter of the joining device D_{JD}, creating a difference between the diameters $\Delta D_{JD|J}$ (cf., Figure 2). This diametral difference $\Delta D_{JD|J}$

prevents the critical case of frontal contact between the shaft and the hub by allowing for manufacturing tolerances and misalignments proportional to its size.

To determine the influence of this radius R_J on the stress state of the press–fit connection, a simulation series is performed in which the junction radius R_J is systematically varied. Considering that a large radius R_J would diminish the advantages of a joining device in terms of its purpose to reduce the overall size of the shaft–hub connection, the unused length l_J of the shaft resulting from the radius R_J is restricted to a maximum of 1.5 mm. This is even less then the length of the transition geometry of a common press–fit connection, according to the design guideline of the German standard DIN 7190-1 [17].

The analysis shows that increasing the diametral difference $\Delta D_{JD|J}$, while leading to an improved assembling process safety, simultaneously decreases the transmission capacity by reducing the pressure p in the connection, establishing a corresponding trade-off (cf. Figure 7). However, the use of a joining device with a junction geometry with $\Delta D_{JD|J} = 200$ μm that allows for significant manufacturing tolerances and misalignments without an impairment of the joining process still achieves 90% of the average pressure that was obtained for a transition radius of $R = 8000$ mm in Section 4.1 while decreasing the unused length of the shaft from $l_{tg} = 63$ mm to $l_{tg} = l_J = 1.5$ mm by 98%. The analysis of the sensitivity of the pressure distribution to the size of the diametral difference $\Delta D_{JD|J}$ for a press–fit connection with an interference of $\xi = 10‰$ shows that decreasing $\Delta D_{JD|J}$ from 200 μm to 50 μm would allow for an increase in pressure of 6%.

Based on the analysis of the influence of large transition radii R and of the junction geometry on the stress state of the press–fit connection, the potential of the joining device in lightweight applications can be evaluated. The achieved reduction in pressure loss, the increase in average pressure, and therefore the increased transmission capacity are functions of the transition radius R employed (cf., Section 5). This transition radius in the current elastic–plastic design of press–fit connections without a joining device leads to a large non-usable shaft length l_J (cf., Section 5) that increases the mass and the size of the drive system substantially. The detachable joining device enables the implementation of large transition radii R, while maintaining a small non-usable shaft length of $l_J = 1.5$ mm on the shaft itself with only a small reduction in the force and torque transmission capacity compared to the idealized geometry shown in Section 4.1. The joining device therefore has the potential to significantly decrease the mass and installation space, yielding a substantial benefit in force and torque transmission as well as in lightweight applications (cf., Figure 8; cf., Table 3). With the presented joining device, the shaft geometry (a) can be used, which leads to a reduction in mass and length of 70% or 95% (compared to the shaft geometry (b), respectively, (c), as shown in Figure 8 and Table 3).

Table 3. Length and mass of different transition geometries and corresponding reductions achieved by using a joining device.

|	Shaft Geometry	Length of the Radius Geometry	Mass of the Radius Geometry
(a)	using a joining device to achieve an improved pressure distribution with $R = 8000$ mm and $\Delta D_{JD|J} = 200$ μm (cf., Figure 7a)	$l_1 = 1.5$ mm	8.3 g
(b)	used to achieve the reference pressure distribution with $R = 50$ mm (cf., Figure 7a)	$l_2 = 5.0$ mm	27.4 g
(c)	necessary to achieve the same pressure distribution as shaft geometry (a) without using a joining device	$l_3 = 28$ mm	153.8 g
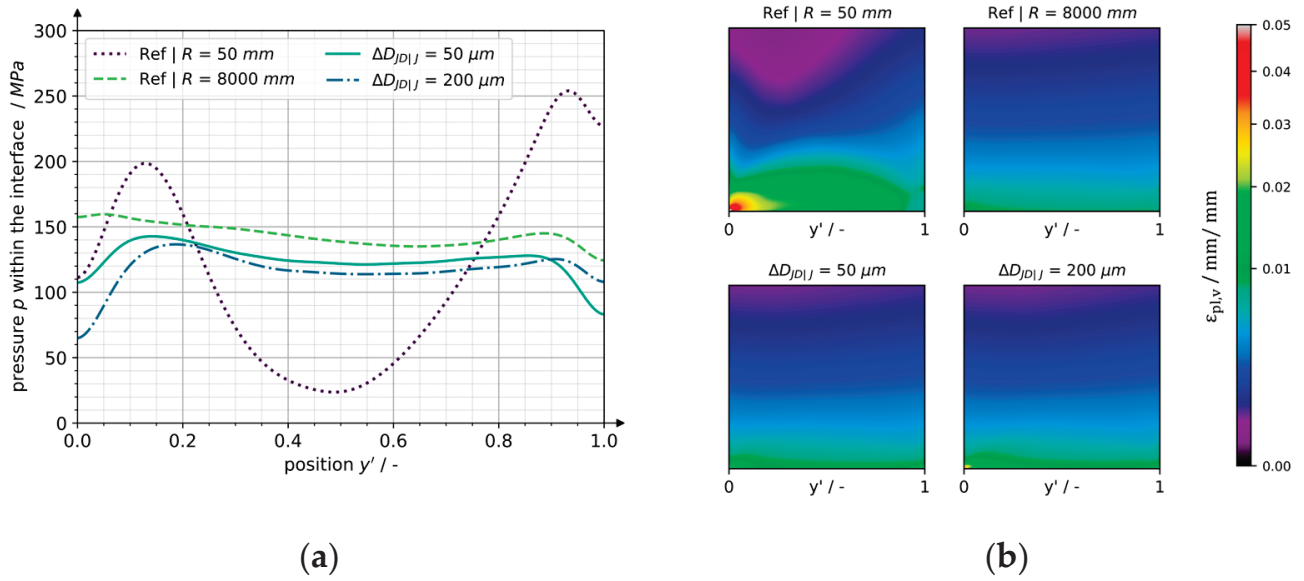
Figure 7. (**a**) Pressure distribution and (**b**) equivalent strain distribution in the hub. Both with a variation in the junction geometry for interference of $\xi = 10\,‰$, a shaft made from 42CrMo4 +QT, and a hub made from EN AW-5083.
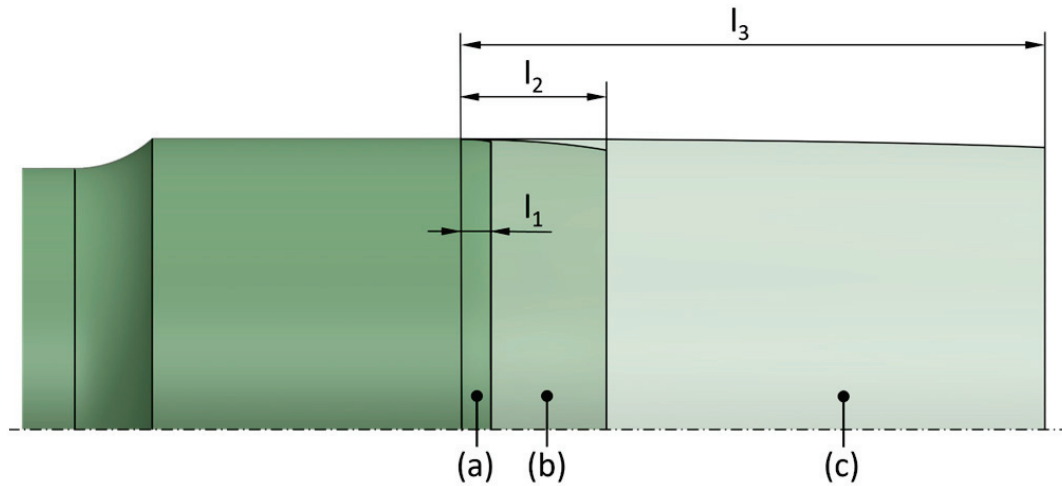

Figure 8. Shaft geometry: (**a**) small transition radius when using a joining device, (**b**) reference geometry with a transition radius of $R = 50$ mm (not to scale), and (**c**) large transition radius to achieve the same result as (**a**) without a joining device.

4.3. Analysis of Manufacturing Tolerances on Their Influence on the Stress State of the Press–Fit Connection

The proposed junction geometry ensures a secure joining process by accommodating anticipated manufacturing tolerances. However, the diameters of the shaft D_S and the joining device D_{JD} are still affected by tolerances, meaning that two further cases can arise in contrast to the assumption $D_S = D_{JD}$ made in Section 4.2. The following analysis targets the diametral difference between the joining device and the shaft $\Delta D_{JD|S}$, considering the two cases that either the diameter of the shaft D_S is larger than the diameter of the joining device D_{JD} (cf., Section 4.3.1 and Figure 9) or vice versa (cf., Section 4.3.2 and Figure 10). The results should assess the impact of these tolerances on the transmission capacity of the press–fit connection and the extent to which the potential of the joining device is diminished as a result.

4.3.1. Case of a Larger Shaft Diameter D$_S$

Joining a press–fit connection using a joining device with a diameter D_{JD} that is smaller than the diameter of the shaft D_S leads to partly opposing phenomena depending on the size of the diametral difference $\Delta D_{JD|S}$. Up to a certain limit (here, $\Delta D_{JD|S}$ = 40 µm), an increasing diameter of the shaft D_S caused by manufacturing tolerances induces additional interference ξ that increases the transmission capacity by slightly raising the pressure near to the axial center ($y' \approx 0.35$) of the shaft–hub connection. Once the difference between the joining device and shaft diameter $\Delta D_{JD|S}$ becomes too large (here, $\Delta D_{JD|S}$ = 80 µm), the prevailing phenomenon is a pressure loss that occurs at $0.2 \leq y' \leq 0.7$ (cf., Figure 9), which is caused by the increasing joining force required to overcome the additional interference ξ at the small radius of the joining geometry R_J (cf., Figure 2), similar to the more severe pressure loss caused by a small transition radius R that is described in Sections 1 and 4.1. Numerical investigations show that the latter phenomenon becomes predominant as soon as the tolerance exceeds $\Delta D_{JD|S}$ = 40 µm with stress extrema and local plastic deformations significantly increasing after surpassing this threshold. Basically, since the diameter of the shaft is larger than that of the joining device, high plastic deformations occur in the area of the inner hub edge when it comes in contact with the shaft radius R_J during the joining process. These plastic deformations did not occur for the reference geometry (cf., Section 4.2), since the diameters of the shaft and the joining device are the same and therefore no additional interference ξ has to be overcome at the small radius R_J of the shaft.
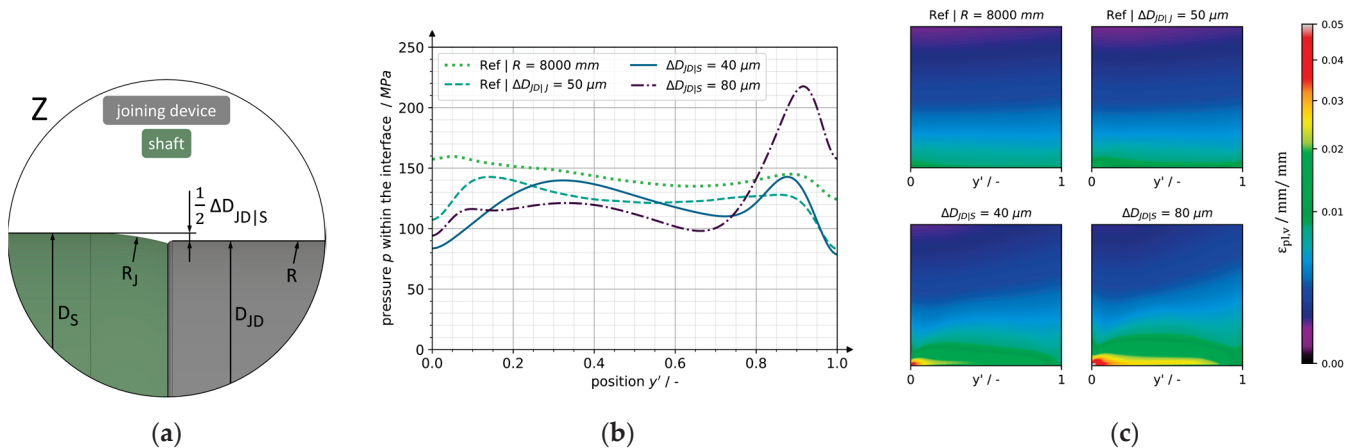

Figure 9. (**a**) Simulation geometry for varying tolerances between the shaft (larger) and joining device, (**b**) pressure distribution, and (**c**) equivalent plastic strain in the hub. For both, (**b**,**c**), tolerance between the shaft (larger) and joining device is varied for an interference of ξ = 10‰, the shaft is made from 42CrMo4 +QT, and the hub is made from EN AW-5083.

4.3.2. Case of a Larger Joining Device Diameter D$_{JD}$

A numerical analysis of manufacturing tolerances that lead to a diameter of the shaft D_S that is smaller than the diameter of the joining device D_{JD} (cf., Figure 10) shows that this case decreases the transmission capacity of the press–fit connection significantly. This is caused by the plastic deformation occurring at the inner diameter of the hub due to the large interference ξ that restricts the elastic recovery of the hub to a smaller diameter. The analysis shows that the pressure p decreases proportionately to the tolerance $\Delta D_{JD|S}$, with a pressure loss of approximately Δp = 12.5 MPa for each $\Delta D_{JD|S}$ = 10 µm increase in tolerance (cf., Figure 10).

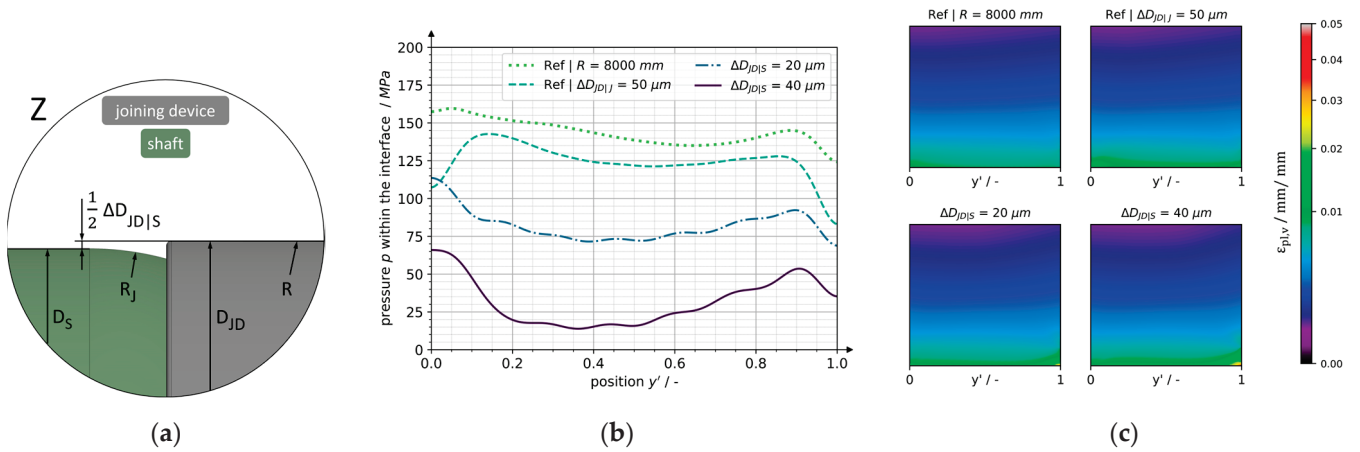**Figure 10.** (**a**) Simulation geometry for varying tolerances between the shaft (smaller) and joining device, (**b**) pressure distribution, and (**c**) equivalent plastic strain in the hub. For both, (**b**,**c**), tolerance between the shaft (smaller) and joining device is varied for an interference of $\xi = 10‰$, the shaft is made from 42CrMo4 +QT, and the hub is made from EN AW-5083.

The localized plastic deformations occur not as previously observed at the front edge of the hub but rather at the rear edge, as the load-bearing area gradually focuses on the rear part of the hub when crossing the junction geometry (cf., Figure 10). Concluding from this analysis, the upper deviation limit of the diameter of the joining device should not exceed the lower deviation limit of the shaft diameter.

4.4. Experimental Validation

To validate the numerical results, the geometry of the shaft and the associated joining device were designed based on the findings from Section 4.1 to Section 4.3. The transition radius of the joining device was selected as $R = 4000$ mm (Section 4.1), the diameter difference as $\Delta D_{JD|J} = 200$ µm, and the diameter difference as $\Delta D_{JD|S} = 20$ µm (Section 4.3). The specimens were then manufactured in the institute's workshop from the materials intended for this purpose (cf., Figure 11), considering the other geometry parameters (cf., Table 1). The joining device is centered in the shaft by a short pin to ensure radial alignment. Due to a suitable tolerance (Ø8 H7/g6), this pin ensures that, for the coaxiality of both the shaft and joining device, no collision can occur between their end faces, thus guaranteeing a reliable joining process.

Figure 11. (**a**) Specimens before joining and (**b**) press–fit connection after the joining process.

The procedure presented in Section 3.3 for validating the numerical calculation results, which is based on a comparison of the hub expansion, was carried out with the defined geometry. The joining experiment was carried out on a hydraulic press, which can achieve a maximum joining force of 250 kN. This ensures the required force avoids stick slip, which is recommended according to [17].

The axial force during the experiment was recorded using a force transducer. A laser sensor was used to record the joining distance of the press–fit connection, which corresponds to the change in the distance measured between the laser sensor and the stationary crosshead of the hydraulic press (cf., Figure 5). The accuracy of the measurement is 2000 data points within one second. Figure 12 shows the force during joining. Due to the very large transition radius of $R = 4000$ mm of the joining device, the interference ξ is overcome across a long distance. This leads to low and very evenly increasing joining forces (cf., $s < 32$ mm in Figure 12), which is also beneficial for the stress distribution in the hub and leads to a uniform pressure in the interface of the connection (cf., Figure 6 and [8]). Starting from $s > 32$ mm, the hub is forced onto the cylindrical shaft, whereby only a slight interference ξ at the radius R_J has to be overcome. However, this happens along a significantly shorter axial distance of $l_J = 1.5$ mm, causing the gradient of the force curve in Figure 12 to increase. After the joining process, the joining device can be removed manually from the shaft and reused for the next press–fit connection (cf., Figure 11). For mass production, the joining device can be finished with a DLC coating (diamond-like carbon), for example, to increase the durability of the device.
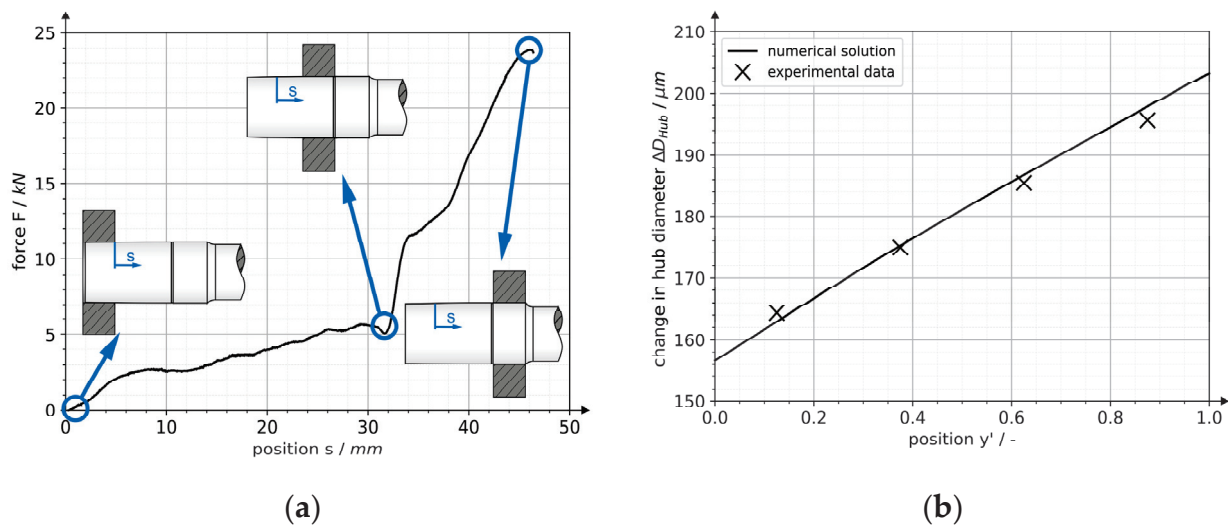

(**a**)

(**b**)

Figure 12. (**a**) Force during joining the press–fit connection using a joining device and (**b**) changes in hub diameter used for validation purposes.

The validation of the numerical results is completed by comparing the change in hub diameter between the experiment and the simulation. For this purpose, the specimens were measured on a coordinate measuring machine before and after the joining process, as described in Section 3.3. This first enabled a simulation of the joining process with the actual dimensions of the specimen and second, the determination of the hub expansion in the experiment. The latter was compared with the numerically calculated hub expansion in Figure 12. This clearly shows that the absolute values of the simulation and experiment deviate from each other by less than 3 µm (less than 2%). The numerically determined results from Section 4 can therefore be considered valid.

5. Discussion

5.1. Discussion and Design Recommendation

Consolidating the outcomes from Section 4 provides a foundation of information on which a design recommendation can be formulated. Section 4.1 demonstrates the

potential of large transition radii *R* for homogenizing the pressure distribution and therefore increasing the transmission capacity of press–fit connections. Sections 4.2 and 4.3 analyze the influence of the detachable joining device that enables this transition geometry for practical applications.

The results obtained in Section 4.1 suggest that increasing the transition radius *R* of the shaft from the reference radius from *R* = 50 mm to *R* = 8000 mm reduces the pressure loss that occurs for large interferences ζ in the center of the hub by 90% (cf., Figure 6). Assuming a difference between the diameter of the shaft at the connection to the hub D_0 and the inner diameter of the hub D_{int} of 200 μm to account for tolerances and misalignments in the process, this results in a non-usable shaft length of the transition geometry of $l_{tg} \approx 63$ mm (cf., Figure 2). This is not achievable in most applications due to restrictions on the mass and installation space.

The numerical analysis of the detachable joining device used to substitute this transition geometry (cf., Section 4.2) shows that despite the required junction geometry (cf., Figure 1), an average pressure of 90% of the pressure distribution, which was achieved for the transition geometry without a junction and with a radius of *R* = 8000 mm (cf., Section 4.1), can be realized (cf., Figure 13). Moreover, 78% of the pressure loss in the hub center seen for the reference radius of *R* = 50 mm can be recovered. Using this joining device therefore leads to a significant increased transmission capacity with a shaft radius R_J with an axial length l_J limited to 1.5 mm (cf., Figure 7), which is 92% less than the non-usable length l_{tg} (cf., Figure 2) necessary to achieve the same result without a joining device (cf., Figure 13).
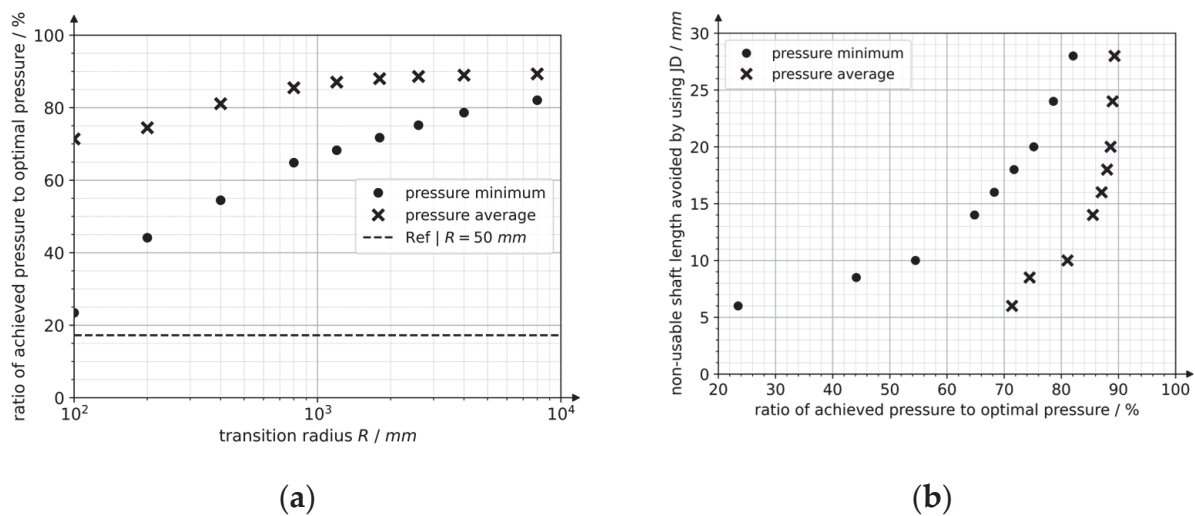

(a)   **(b)**

Figure 13. (**a**) Achieved pressure ratio for varying transition radii *R* and (**b**) non-usable shaft length avoided by using a joining device and the achieved pressure ratios.

Furthermore, the results of Section 4.2 present a relation between the pressure distribution and the diametral difference $\Delta D_{JD|J}$ (cf., Figure 7) that defines the maximal tolerances of the parts that can be accommodated and is therefore a measure for process safety. Increasing this diametral difference from $\Delta D_{JD|J}$ = 50 μm, which was used to achieve the aforementioned 78% pressure loss reduction, to $\Delta D_{JD|J}$ = 200 μm, which allows for significant manufacturing tolerances, only results in a 7% pressure decrease. This demonstrates the sensitivity of the pressure distribution and therefore the transmission capacity of the press–fit connection to the junction geometry needed to accommodate manufacturing tolerances. However, it does not present information on the influences of tolerances themselves that are analyzed in Section 4.3.

Focusing on the diametral difference between the joining device and the shaft $\Delta D_{JD|S}$, this tolerance leads to two different cases where either the diameter of the shaft D_S is larger than the diameter of the joining device D_{JD} or vice versa. The results show that

the upper deviation limit of the shaft diameter should not exceed the lower deviation limit of the joining device diameter by more than 40 μm (cf., Section 4.3.1) to prevent pressure maxima that can be critical in cyclic loading conditions for connections that are subject to bending stresses, especially for materials with limited ductility. Furthermore, the upper deviation limit of the joining device should never exceed the diameter resulting from the lower deviation limit of the shaft. Such tolerances show a rapid reduction in the transmission capacity, corresponding to a 10% pressure drop in the center of the hub per 10 μm tolerance, causing the diameter of the joining device to exceed the diameter of the shaft (cf., Section 4.3.2). Consolidating these findings into a recommendation for allowable manufacturing tolerances results in the tolerance field presented in Figure 14. Considering other geometries and materials, a general application of this recommendation has been identified. With these findings, the tolerance recommendation is 1.33‰ of D_{int}.
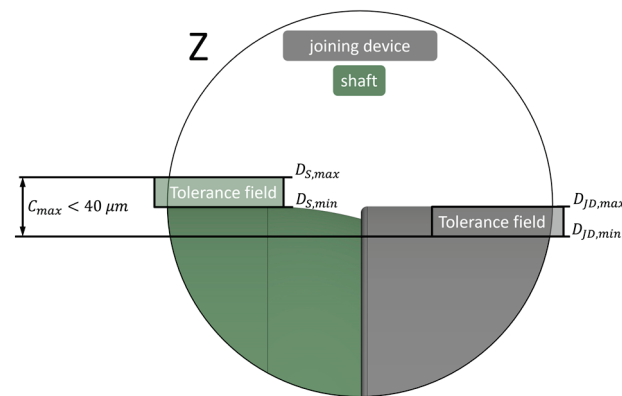

Figure 14. Proposed tolerances of junction geometry to maximize transmission capacity.

5.2. Summary of Key Findings

The key findings obtained from the presented research results are summarized in Table 4.

Table 4. Key findings obtained from discussed research results.

	Finding	Details and Recommendations	Section
(1)	Large transition radii R for increased transmission capacity	The pressure reduction Δp occurring for the elastic–plastic press–fit connection in the axial hub center can be reduced by 85% for a transition radius of R = 4000 mm and up to 90% for R = 8000 mm compared to the reference radius of R = 50 mm.	Section 4.1
(2)	Detachable joining device as enabler for large transition radii R in practical applications	The axial length of large transition radii R described in row (1) prevents their use in most applications, if these are conventionally provided as part of the shaft. Using a detachable joining device enables the use of such large transition radii R to obtain up to 90% of the pressure achieved in row (1) with a 95% reduction in the non-usable shaft length.	Sections 4.2 and 5.1
(3)	Design recommendation for reduced susceptibility to manufacturing tolerances	Identified tolerance fields for an improved transmission capacity (cf., Figure 14): • The upper deviation limit of the shaft should not exceed the lower deviation limit of the joining device by more than 40 μm. • The upper deviation limit of the joining device should never exceed the lower deviation limit of the shaft.	Sections 4.3 and 5.1

6. Conclusions

The results of this research article suggest the capability of a detachable joining device to enable the threefold increase in transmission capacity achieved by employing elastic–plastic instead of elastic press–fit connections. Large transition radii of the shaft that are necessary to join these connections often prevent this shaft–hub connection from being used in practical applications because of limitations in the mass and installation space. Substituting this transition geometry with a detachable joining device results in a significant reduction in the mass and installation space of the connection.

This article presents design recommendations on joining devices for elastic–plastic press–fit connections. For the first time, the possibility of separating the transition radius, which is generally necessary for press–fit connections to overcome geometric interferences, from the shaft by means of a detachable joining device is investigated. This results in the following advantages:

(1) The axial length of the transition radius and thus its size are no longer restricted by the installation-space limits of the assembly.
(2) The mass of the press–fit connection will not be affected by the size of the transition radius.

Using experimentally validated finite element simulations, this research article presents, in detail, the impact of large transition radii and manufacturing tolerances of a detachable joining device on stresses, strains, and force and torque transmissions in a press–fit connection. Finally, generalized design recommendations are given for the user, which can also be applied to other geometries and materials. The novel recommendations are as follows:

(1) A transition radius of at least 4000 mm should be selected for a high mean value of the pressure between the shaft and hub, as well as a uniform distribution of the pressure and the plastic strains.
(2) The upper limit of the joining device's tolerance field should never exceed the lower limit of the shaft's tolerance field.
(3) The upper limit of the shaft's tolerance field should not exceed the lower limit of the joining device's tolerance field by more than 1.33‰ of the diameter of the contact interface.

Therefore, the results significantly contribute to extending the application of elastic–plastic-designed press–fit connections. As a result, the performance of technical systems can be increased and the use of resources in production and operations can be reduced, thus achieving an important impact on resource protection.

References

1. Dausch, V.; Kröger, J.; Kreimeyer, M. An AI-Based Approach to Optimize Stress in Shrink Fits. *Proc. Des. Soc.* **2022**, *2*, 1549–1558. [CrossRef]
2. Gamer, U. The Rotating Elastic-Plastic Shrink Fit with Hardening. *Acta Mech.* **1986**, *61*, 15–27. [CrossRef]
3. Gamer, U. The Shrink Fit with Elastic-Plastic Hub Exhibiting Constant Yield Stress Followed by Hardening. *Int. J. Solids Struct.* **1987**, *23*, 1219–1224. [CrossRef]
4. Kittsteiner, J.; Ehrlenspiel, K. *Kostenanalyse von Welle-Nabe-Verbindungen in Zahnradgetrieben—Abschlussbericht zum FVA-Forschungsvorhaben Nr. 134, Heft 293*; Forschungsvereinigung Antriebstechnik e.V.: Frankfurt, Germany, 1989.
5. Kollmann, F.G. *Welle-Nabe-Verbindungen—Gestaltung, Auslegung, Auswahl*; Springer: Berlin/Heidelberg, Germany, 1984. [CrossRef]
6. Baldanzini, N. A General Formulation for Designing Interference-Fit Joints with Elastic-Plastic Components. *J. Mech. Des.* **2004**, *126*, 737–743. [CrossRef]
7. Kröger, J.; Binz, H. *Untersuchungen zu Auslegungsgrenzen und Steigerung der Maximalen Übermaße bei Zylindrischen Pressverbindungen—Abschlussbericht zum FVA-Forschungsvorhaben Nr. 810 I, Heft 1399*; Forschungsvereinigung Antriebstechnik e.V.: Frankfurt, Germany, 2020.
8. Falter, J.; Binz, H.; Kreimeyer, M. Investigations on design limits and improved material utilization of press-fit connections using elastic-plastic design. *Appl. Eng. Sci.* **2023**, *13*, 1–14. [CrossRef]
9. Önöz, I.E. *Die Auslegung Elastisch-Plastisch Beanspruchter Querpressverbände Unter Berücksichtigung der Werkstoffverfestigung*; VDI-Verlag: Düsseldorf, Germany, 1983.
10. Glöggler, C. Untersuchungen an Spannungshomogenisierten und Zylindrischen Pressverbindungen unter Torsionsbelastung. Dissertation, Universität Stuttgart, Stuttgart, Germany, 2003.
11. Blacha, M. Grundlagen zur Berechnung und Gestaltung von Querpressverbänden mit Naben aus Monolithischer Keramik. Dissertation, Universität Stuttgart, Stuttgart, Germany, 2009.
12. Heydt, J.F. Untersuchungen zum Dynamischen Verhalten von Topologisch Optimierten Pressverbänden bei Umlaufbiegung. Dissertation, Universität Stuttgart, Stuttgart, Germany, 2012.
13. Lohrengel, A.; Schäfer, G.; Mänz, T. *Untersuchung von Pressverbindungen mit geründelter Welle—Abschlussbericht zum FVA-Forschungsvorhaben Nr. 658 I, Heft 1247*; Forschungsvereinigung Antriebstechnik e.V.: Frankfurt, Germany, 2017.
14. Li, T.; Zheng, J.; Chen, Z. Description of full-range strain hardening behavior of steels. *SpringerPlus Eng.* **2016**, *5*, 1316. [CrossRef]
15. Ramberg, W.; Osgood, W.R. *Description of Stress-Strain-Curves by Three Parameters*; NACA Technical Note No. 902; National Advisory Committee for Aeronautics (NACA): Washington, DC, USA, 1943.
16. Hertelé, S.; De Waele, W.; Denys, R. A generic stress-strain model for metallic materials with two-stage strain hardening behavior. *Int. J. Non-Linear Mech.* **2011**, *46*, 519–531. [CrossRef]
17. *DIN 7190-1:2017-02*; Interference Fits—Part 1: Calculation and Design Rules for Cylindrical Self-Locking Pressfits. Beuth: Berlin, Germany, 2017.
18. Ulrich, D.; Binz, H. Einfluss von Schmierstoffen aus der Massivumformtechnik auf die Reibdauerbeanspruchung mikroschlupfanfälliger Welle-Nabe-Verbindungen—Numerische und experimentelle Untersuchungen anhand zylindrischer Querpressverbände mit beschichteten Wellen unter wechselnder Torsionslast. In Proceedings of the VDI-Fachtagung Welle-Nabe-Verbindungen Gestaltung—Fertigung—Anwendungen, Stuttgart, Germany, 28 November 2016. [CrossRef]
19. Kröger, J.; Binz, H.; Wagner, M. Spannungsoptimierung von Pressverbindungen mit additiv gefertigten Naben—Numerische und experimentelle Untersuchungen. In Proceedings of the VDI-Fachtagung Welle-Nabe-Verbindungen Dimensionierung—Fertigung—Anwendung, Stuttgart, Germany, 26–27 November 2018. [CrossRef]

Assessing the Suitability of Automation Using the Methods–Time–Measurement Basic System

Malte Jakschik [1,*], Felix Endemann [1], Patrick Adler [1], Lennart Lamers [2] and Bernd Kuhlenkötter [1]

[1] Chair of Production Systems, Ruhr-University Bochum, Industriestraße 38c, 44894 Bochum, Germany
[2] Production Automation, RIF Institute for Research and Transfer e. V., Joseph-von-Fraunhofer-Straße 20, 44227 Dortmund, Germany
* Correspondence: jakschik@lps.ruhr-uni-bochum.de; Tel.: +49-234-32-24611

Abstract: Due to its high complexity and the varied assembly processes, hybrid assembly systems characterized by human–robot collaboration (HRC) are meaningful. Suitable use cases must be identified efficiently to ensure cost-effectiveness and successful deployment in the respective assembly systems. This paper presents a method for evaluating the potential of HRC to derive automation suitability based on existing or to-be-collected time data. This should enable a quick and favorable statement to be made about processes, for efficient application in potential analyses. The method is based on the Methods–Time–Measurement Basic System (MTM-1) procedure, widely used in the industry. This ensures good adaptability in an industrial context. It extends existing models and examines how much assembly activities and processes can be optimized by efficiently allocating between humans and robots. In the process model, the assembly processes are subdivided and analyzed with the help of the specified MTM motion time system. The suitability of the individual activities and sub-processes for automation are evaluated based on criteria derived from existing methods. Two four-field matrices were used to interpret and classify the analysis results. The process is assessed using an example product from electrolyzer production, which is currently mainly assembled by hand. To achieve high statement reliability, further work is required to classify the results comprehensively.

Keywords: process automation; MTM-1; degree of automation suitability; human–robot collaboration; HRC

1. Introduction

Identifying automation potential can help standardize production processes, ensure quality, and reduce dependence on skilled workers. In the context of electrolyzer assembly, there are currently many manual activities. Added to this is the increasing shortage of skilled workers and the conflict of interest in filling monotonous, repetitive tasks with qualified personnel [1]. For a competitive assembly of such systems in Germany as an industrial location, there is a need for optimization in the development, manufacturing, and assembly processes [2].

One of the most established methods for time optimization in the production environment is the Methods–Time–Measurement (MTM). It can be used to determine and analyze times of the current actual situation and to determine planned times for optimized processes or a changed working method [3].

In addition to time optimization, increasing automation in the production process to raise efficiency is possible. Using the previously determined time data for an automation suitability test creates further synergies in the engineering process. Currently, there is a high degree of automation in manufacturing, whereas humans mostly perform the assembly processes. The high percentage of human activities during product manufacture makes up to 20% of the overall costs. The efficiency of planning and performing such processes must increase to reduce it [4].

Due to the high variability and complexity of the products, automating the entire assembly process is very demanding. An industrial robot as a production system is highly flexible for automation. Still, it cannot yet keep up with human dexterity in many applications, even depending on the tool used. Hybrid production could be one of the viable solutions in which robots and humans cooperate or work together in the same workspace [5]. Assessment of automation suitability is currently reserved for automation engineers or system integrators, which is time-consuming and costly. As described above, the use of MTM time data analysis is widespread, making it desirable to derive automation suitability based on these data.

1.1. Structure of the Article

Motivated by the abovementioned situation, this paper presents a procedure model for identifying HRC potential based on MTM-1. This allows the data previously collected for time optimization to be further used for automation suitability. For this purpose, a classification of existing methods and work in the state of the art (Section 2) is first given before Section 3 describes the developed method in detail. The process is then evaluated using an example product (Section 4) before the results are summarized in Section 5. Finally, an outlook and potential for further work are given in Section 6.

1.2. Requirements for the Procedure Model

Based on the challenges described above, requirements can be derived for developing the method and can be divided into three categories: (1) model structure, (2) method, and (3) results.

- To develop the model and enable a systematic approach for transparent results, an iterative and step-by-step approach and a description of the current situation should be provided. (1)
- Furthermore, due to the complexity of the assembly processes described above, the model should focus on the HRC and the assembly processes, considering the performance capabilities of humans and robots. (1)
- The method must include the possibility of a knockout (K.O.) criterion for HRC so that the evaluation can be terminated directly to prevent unnecessary planning processes. (2)
- Time measurement, more specifically the use of MTM, is necessary to ensure industry adaptability due to the method's high prevalence. (2)
- In addition, the method's evaluation criteria must be transparent regarding the suitability of the automation or the HRC for good reproducibility. (3)
- Finally, the results should be transparent and comparable next to economic efficiency. (3)

2. State of the Art

As described above, MTM is one of the most established methods for time optimization. Redundant movements can be eliminated by using MTM-1, workflows can be adapted, and ergonomic conditions can be optimized. The method focuses on optimizing the design of the work system from the outset. Waste is to be identified and avoided across the entire value chain with the help of method planning in line with the lean philosophy. While the lean concept focuses on the internal value stream, the global value flow, and the efficient design of value chains for industrial goods, MTM concentrates primarily on optimizing workstations [6].

The description, structuring, planning, and analysis of workflows are based on process modules defined in terms of topic and time, summarized on the MTM data cards. The values taken from the data card are all given in the time unit "Time Measurement Unit" (TMU); 1 TMU corresponds to 0.036 s, 1 h to 100,000 TMUs. The starting point is based on the MTM-1 basic system, which enables the modeling of the manual workflow by required basic movements. These movements are reaching (R), grasping (G), moving (M), positioning (P), releasing (RL), disengaging (D), applying pressure (AP), turning (T), body,

leg, and foot movements, and eye functions. Depending on defined parameters, standard times are assigned to each basic movement [3].

Several methods exist in the literature and industry to identify the potential for optimized assembly. Design for Assembly (DFA) in general and Design for Automatic Assembly (DFAA) are topics that have been extensively studied, and four methods have become established in the industry. The methods of *Boothroyd and Dewhurst* (*B&D*), *Lucas*, *Hitachi* (*AEM*), and the *modified Westinghouse* method are the most used. DFA or DFAA deals with how a product must be optimally designed for a well-automatable process. For that, the methods define various evaluation criteria to evaluate the suitability of automation. In specific further developments, the methods and the requirements described therein are combined in different constellations to consider better suitability of the method in connection with the product under consideration [7–13].

In addition, multiple methods for evaluating or introducing HRC have been identified in the literature. The following presents both model variants and shows the suitability of each approach.

2.1. Evaluation Methods with the Scope of an Assembly-Friendly Product Design

As described above, four established methods in the industry evaluate the product design in the context of the suitability for assembly. The overarching aim of the *B&D* method is to reduce costs by saving time during the handling and assembly processes. This is achieved by reducing the number of components within the assemblies [14,15].

The *Lucas* method is subdivided into three separate analyses and is based on a relative scoring system. In contrast to the *B&D* method, the functional analysis is used for early design analysis. Not all design questions must be fully answered at the time of application. The components are categorized into two groups: essential and non-essential components. Non-essential components should be eliminated to reduce the number of components to a minimum [16].

The *Westinghouse* method calculates product complexity using the assembly time, a complexity factor, the assembly time value, and the part efficiency. As in the previous methods, the complexity is determined using predefined influencing factors, resulting in the assembly time value. For the assembly time, the processes are classified as reaching, gripping, and bringing, and the process itself and the assembly time are calculated [17]. The *modified Westinghouse* method simplifies and differs from the superordinate method in creating the joining sequence diagram and eliminating non-essential components [9,13].

These methods are designed to identify weak points in the product design. However, this approach focuses on the assembly processes to identify tasks for humans and functions with a high automation potential. The *Hitachi-AEM* is categorized as an evaluation method for the assembly process [9,13,18]. According to the Hitachi AEM, two key figures are determined and evaluated to assess the product design. On the one hand, the complexity of the handling and assembly processes is determined using the evaluation factor *E.* On the other hand, the cost evaluation factor *K* is used to determine the savings potential through the optimized product design. As with the methods described above, predefined operations are used to classify and evaluate upcoming processes to estimate the handling and assembly effort. In contrast to the *B&D* and *Lucas* methods, the *Hitachi AEM* does not differentiate between a manual and an automated assembly because of the strong correlation between an assembly-friendly product design and the resulting simplified assembly [13]. With that in mind and the presented approach of an optimal distribution of the assembly task, this method is unsuitable for that procedure model.

The *MTM ASSOCIATION e.V*. has developed a method (*ProKon*) to minimize the costs during product development. It evaluates the assembly effort and focuses on low-cost solutions through targeted modification of parameters that the designs can influence. The procedure is divided into seven steps. The first step is remarkably similar to the methods described above, whereby various evaluation criteria such as weight, material, geometry, or specific handling conditions are analyzed. This is followed by the determination of

the assembly processes. In step three, the assembly position of the individual parts is determined on the assumption that the parts to be assembled are not in an optimum state of order. After that, in step four, the individual parts and higher-level assemblies are then evaluated by an evaluation matrix. This matrix differs from the card in that it analyzes the time estimation of the assembly process. Steps 5 to 7 deal with optimizing the product design, which is outside this approach's scope and is therefore not considered in more detail [3].

Since *ProKon* focuses on an assembly-friendly product design and process and does not distinguish between an automated or manual assembly task, this method does not fit this approach as well as the methods before.

2.2. Evaluation Methods with the Scope of Human–Robot Collaboration

Bauer et al. present a procedure model based on a cost-effective identification of practical HRC applications developed by the Fraunhofer Institute for Industrial Engineering (IAO). The model is divided into three steps and focuses on avoiding large volumes of data. Despite its simple structure and application, individual company goals are considered. In the first stage, assembly system data are analyzed for the three fundamental areas of classic system planning data: the problem situation, the degree of preparation of material provision, and potentials. The second stage is planning data at the workstation level, and potentials are considered. Finally, the last step is evaluating the process and product level. Subsequently, the assembly processes with the most significant automation potential can be selected, and HRC solutions can be implemented based on the preselection and evaluations [19].

Weber and Schüth developed a model for introducing HRC. It is structured on a step-by-step basis and is intended to enable companies to prioritize the factors to be checked successively. The focus shifts from the process to the product to the resource regarding HRC suitability. The first three steps consider component orientation, gripping properties, temperature, or flexural rigidity. In addition, the method evaluates the workstation and training needs. It concludes with an assessment of economic efficiency [20].

The model approach developed by *Petzold* et al. is divided into five steps. It defines six requirements for analyzing the potential for the use of HRC: specific focus on industrial assembly activities, method-supported analysis and evaluation, strong process orientation, consideration of quality, evaluation of economic efficiency, and consideration of ergonomics. The authors use MTM in their model approach for the assessment of economic efficiency but not for the identification of potential processes to be automated. To evaluate the use of HRC, both the assembly processes and the product design and geometry are considered [21].

The SafeMate method was developed to quickly and intuitively identify and assess the potential for using HRC. The research project of the Institute of Assembly Technology and the Institute of Production Systems and Logistics at the University of Hanover is intended to serve as a guideline for safe and accepted HRC implementations in companies. The SafeMate method consists of two successive stages. In the first stage, the added value of the HRC application is assessed, while the second stage evaluates the technical implementation [22].

The KoMPI Quick Check was also developed as part of a research project and focused on creating a new method for the integrated planning and realization of collaborative workstations for variable production scenarios. It is used to assess and identify HRC potential. This method, divided into three levels, uses a point system based on process criteria for evaluation. A good knowledge of the evaluated work system is a prerequisite. No other special prior knowledge is required [22,23].

Linsinger et al. present a method that identifies the suitability of HRC potentials in five steps. Step 1 begins with an overall analysis of the assembly system and is supplemented by a detailed examination in step 2. Here, the individual stations are analyzed using cycle time analysis and a checklist to assess their technical suitability. This depends on various factors, such as the dimensions and geometric characteristics of the product or the supplied

assembly part. The assembly station with the highest HRC potential is then analyzed in step 3. This analysis focuses on determining the division of labor between robots and humans. It uses the checklist described above and the MTM-1 for this purpose. Steps 4 and 5 deal with the application scenarios' design and implementation planning [24].

Teiwes et al. present a method to identify the HRC potential in automotive assembly lines based on the MTM Universal Analysis System (UAS). The authors describe their approach in three steps. Step 1 evaluates the automation potential for each movement within the assembly. For this purpose, each module of the MTM UAS is assigned a degree of automation potential based on the description of each module. The value determined from this is multiplied by the frequency of the activity in step 2. The final step summarizes the values to obtain an overview of the assembly line [25].

2.3. Classification of Described Literature

The literature will be categorized based on the state of the art presented and the previously derived requirements. This results in the following analysis shown in Scheme 1. Overall, no model in the literature meets all the requirements for this approach. Although the model structure and result categories fulfill the requirements placed on the model in various constellations, deviations from the requirements can be identified in the fulfillment of category 2. In particular, the combination of MTM time data analysis and the consideration of a K.O. criterion cannot be found in existing approaches.

			DFA					HRC						
						Authors / Models								
			Boothroyd & Dewhurst (1987)	Lucas (1989)	Hitachi AEM (1990)	Modified Westinghouse Method (1989)	ProKon	Bauer et al. (2018)	Weber und Schüth (2020)	Petzold et al. (2021)	SafeMate Hees et al. (2019)	KoMPI-Quick-Check Erner et al. (2019)	Linsinger et al. (2018)	Teiwes et al. (2016)
Categories		Requirements	1	2	3	4	5	6	7	8	9	11	10	11
1	A1	Step-by-step procedure	••	••	••	••	••	••	••	••	••	••	••	••
	A2	Iterative procedure	••	••	••	••	••	o	o	••	o	o	o	o
	A3	Presentation of the current status	•	•	•	•	••	••	••	••	••	••	••	••
	A4	Focus on HRC	o	o	o	o	o	••	••	••	••	••	••	••
	A5	Focus on assembly processes	•	•	••	••	••	••	•	••	••	••	••	••
	A6	Consideration of the strengths and weaknesses of human and robots	•	•	•	•	o	••	•	••	•	•	••	o
2	A7	Knockout Criterion for HRC	o	o	o	o	o	o	o	o	o	••	o	o
	A8	Time data determination	••	o	o	••	••	•	o	••	•	•	••	••
	A9	Usage of MTM-1	o	o	o	o	••	o	o	••	•	o	••	••
	A10	Transparent evaluation criteria	••	••	••	••	••	••	•	••	•	••	•	••
3	A11	Clarity and comparability of the results	••	••	••	••	••	••	•	•	•	••	••	••
	A12	Evaluation of the economic efficiency	••	o	o	•	•	••	••	••	••	o	••	•

Legend:

o → not fulfilled
• → partially fulfilled
•• → fulfilled

▮ → model structure
▮ → methodology
▮ → results

Scheme 1. Analysis of relevant valuation models in DFA and HRC [3,9,14,16,18–25].

With that in mind, the comprehensive development of a procedure model that fulfills all requirements is described below. Individual aspects and methods from the previous analysis are incorporated into the process model as steps are developed in-house. A detailed explanation of all aspects of the process model ensures a comparatively simple and transparent application. However, prior knowledge of performing an MTM-1 analysis is required.

3. Modelling of MTM-1 on HRC

The developed procedure model, derived from the state of the art described above, provides the potential of HRC based on MTM-1 and is divided into eight steps (Figure 1).
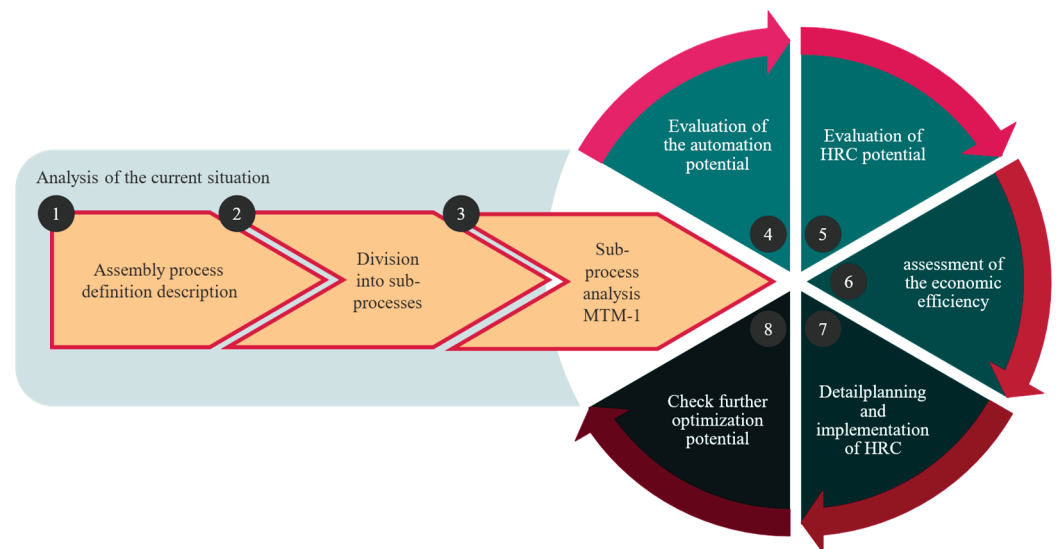
Figure 1. Structure of the presented model approach MTM-1-HRC.

The evaluation starts with analyzing the actual state (steps 1–3). Here, the assembly processes are defined, and the system is described in detail. The processes are then structured into sub-processes (SPs) before they are analyzed using MTM-1, which already corresponds to the current state of the art in using predefined motion time systems by many industrial users. For this reason, steps 1–3 can also be skipped for existing MTM-1 analyses, and existing data can be used. In step 4, the evaluation model MTM-1 is expanded to include an evaluation system determining the automation potential. The HRC potential is evaluated in step 5 before an economic efficiency assessment is performed (step 6). After a successful profitability check, the seventh phase involves detailed planning and HRC implementation. Finally, step 8 checks the assembly process for further optimization potential. For this purpose, processes with high time requirements and low suitability for automation are considered. Additional optimizations can consist of adjustments to the provision of parts and tools or pick-up options, path changes, or joining aids. After the completion of phase 8, an iteration occurs, starting with phase 4. It should be noted here that in the case of extensive process optimizations from the previous iteration, a new analysis of the process using MTM-1 can also be helpful. This results from adjustments to the workstation and new divisions of the processes, resulting in a different process and new MTM codes. In this case, the iteration starts in phase 2 or 3.

3.1. Analysis of the Actual State

The assembly processes are described in a process profile based on the MTM analysis [3]. The overall work task, including a brief process description, is recorded, and the workstation is defined. The structure of the workstation, as well as size and distance information, are particularly relevant. This step also includes a detailed explanation of the process or assembly result (output). Furthermore, all individual parts, machines, tools, and any means to facilitate the assembly process (input) are recorded. For complex assembly processes, the second phase divides the main overall work task into several individual SPs. Each SP fulfills a task within the overall process.

A coding technique is developed for uniform identification of the SPs, which is based on the 12-digit code of the MTM system but has been shortened and simplified. As this code is only used for error-free identification and is similar in principle to the existing code of the MTM system, the functionality of the code is not explained further here. After that, the SPs are analyzed by the MTM-1. The MTM-1 basic system is used, as it serves as a basis for other MTM systems and enables a high resolution or detailed activity descriptions using the numerous basic movement modules. For that approach, its formula has been extended by the column of the suitability of automation (Scheme 2).

					MTM-1 HRC Analysis			
No.	Description (L)	N x F (L)	MTM-1 Code (L)	TMU	Degree of automation	MTM-1 Code (R)	N x F (R)	Description (R)
				0	0			
				0	0			
					0			
				0	0			
			0	Gesamt 0	0		0	

DAS x (N x F):	0
Overall N x F:	0
Prelimainary average/ degree of automation:	0.00
Variance:	0.00
Standard deviation:	0.00
K.O. citeration evaluation factor:	1
Complexity factor:	0
Final average/degree of automation:	**0.00**

Scheme 2. Excerpt from the MTM-1-HRC Excel template based on the MTM analysis [3].

The individual time requirements are calculated based on the MTM-1 code, which describes the process step using the granular movement modules described. Double-handed tasks and similar restrictions for parallelization are also considered automatically. Behind this code, time requirements are stored so that at the end of the MTM analysis, the results show processes with a high optimization potential. Aspects such as long distances, many tasks with a high time requirement, or feeding of parts with an unknown orientation are made visible for short-term optimizations.

3.2. Evaluation of the Automation Potential

To evaluate the automation potential, the MTM-1 formula is extended by the column for the degree of automation suitability (DAS). It is important to note that this approach evaluates the potential of complete automation (step 5), a coexistence, or a synchronized assembly process regarding the requirements of HRC (step 6). The potential of the latter two will be described in the next section. Automation suitability is evaluated using a Likert scale with a point scale from zero to three, where high suitability is indicated by a three. In this approach, in addition to the time requirements, the automation capability ratings of the individual granular motion modules were also derived from the MTM-1 code. For this reason, the criteria used to assess the suitability for automation are also heavily dependent on the descriptions of the MTM basic movements, as found in the data cards [3].

If individual tasks are rated zero in terms of DAS, the entire SP is classified as non-automatable and is to be regarded as the required K.O. criterion. The same applies if at least three activities are assessed with one point. To evaluate the individual tasks regarding suitability for automation, evaluation criteria are defined that consider, among other things, the strengths and weaknesses of a robot as well as economic aspects. The approaches described in Section 2 have different combinations of evaluation criteria for automation suitability. Still, they all have in common that they are based on the four established methods. Due to the link with the MTM-1 code, the evaluation criteria are not to be understood as rigid but based on the cases depicted in the MTM-1 method. Nevertheless, the requirements described by the MTM cases can also be assigned to the methods mentioned, as you can see in Scheme 3. The established methods focus on the product design and its assembly; in addition, this approach rates the assignment of tasks between humans and robots so that the criterion of accuracy was added.

Categories	Evaluation criteria	Boothroyd & Dewhurst (1987)	Lucas (1989)	Hitachi AEM (1990)	Modified Westinghouse Method (1989)	ProKon
	o → not considered **● → partially considered** **●● → considered**					
		1	**2**	**3**	**4**	**5**
EC1	Range of movements	o	o	o	●●	o
EC2	Accessibility	●	●●	o	o	●●
EC3	Gripping operations	●	o	●	●	o
EC4	Weight	o	●	o	o	●●
EC5	Orientation	o	●●	o	●	o
EC6	Handling	●	●●	●	●●	o
EC7	Symmetrical joints	●	●●	●	o	●
EC8	Tolernace	o	o	o	o	●
EC9	Accuracy	o	o	o	o	o

Scheme 3. Assignment of selected evaluation criteria [3,9,14,16,18].

Movements over a more than 60 cm distance reduce the DAS by one. Longer distances are associated with increased effort or require a large, more cost-intensive robot replacement. How objects are approached and the different gripping movements are further criteria summarized under EC2.

Industrial robots can easily approach and pick up a single, easy-to-grasp object that is always in the same place (DAS = 3). Both grasping grips, touch grips, and transfer grips are possible. If the location of these objects changes, for example, when removing them from a pallet, additional programming must be carried out for precise positioning. Alternatively, coarse object recognition can be implemented, e.g., using a camera or sensors on the gripper. The evaluation factor is, therefore, reduced by one. For tiny (smaller than 3×3 mm^2) or fragile objects, increased financial expenditure must be expected for special grippers, sensors, and precise calibration. Gripping operations are like the need to reposition an object and are assessed under EC5.

The maximum load-bearing capacity of such robotic systems is a limiting factor in evaluating HRC suitability. Handling weights over 10 kg is regarded as an aggravating factor and leads to a reduction in the DAS by one. Moreover, handling, in general, is an essential factor in the suitability of automation. For example, parts that are difficult to grip, flexible, or oily make special programming necessary or may require gripper or robot adaptation. Difficult access to a part to be separated or a joining location diminishes the automation capability. In addition, the maximum travel speed of the robot can be negatively affected. For example, when joining or separating, this is considered by subtracting one point from the suitability for automation.

Depending on the fit class, symmetrical joints pose no difficulties for automation (DAS = 3). Semi-symmetry allows several joining positions, and the robot can only make minor alignment corrections. Thus, no points are deducted for this symmetry case. In the case of non-symmetry, on the other hand, some significant alignment corrections and a fixed joining position require increased effort on the part of the robot. Therefore, a maximum of two points are awarded for this characteristic.

With a loose fit class, there are no restrictions on automation suitability. Tight fits and joining tolerances can only be achieved with time-consuming calibration, hence minus one. Cases with fixed fit classes and, therefore, optionally low joining tolerances or high force requirements, are generally regarded as K.O. criteria and given zero points. Similarly, insertion and the associated application of pressure for fits are assessed. The need for a highly accurate process also impacts the DAS and is assessed under the last criterion of accuracy.

All other MTM-1 process modules whose actions can be carried out by a robot without complications or additional effort, e.g., simple gripping movements, releasing objects, light pressure, etc., receive three points and are rated with the highest suitability for automation.

To obtain an overall DAS, the column of suitability is multiplied by the corresponding values from the column of the "number and frequency (N × F)". The sum of all values and the subsequent division of it by the total number is used to calculate the provisional average and, thus, the provisional DAS. A high average indicates a high potential for automation, while a low value implies the exact opposite. Furthermore, the standard deviation is determined considering the respective variance. This serves to verify and refine the assessment, to identify potential "outliers", and to assess the suitability of HRC subsequently. Figure 2 uses a four-field matrix to illustrate the potential result areas and provides instructions for the next steps.
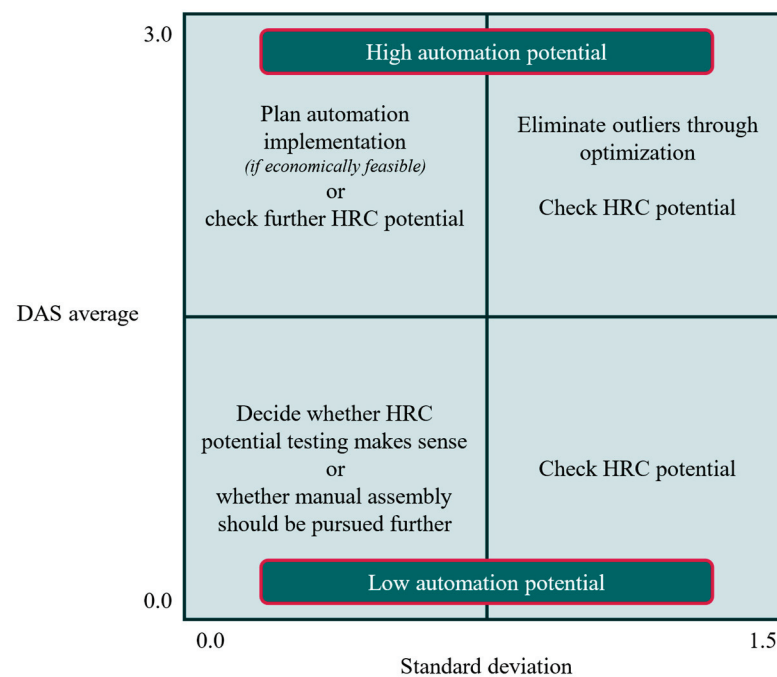
Figure 2. Four-field matrix to classify the potential of automation.

The SP under consideration should be in the second quadrant for suitable automation suitability. SPs in the first quadrant are outliers and should first be attempted to be minimized. The two lower quadrants indicate a low DAS, whereby the HRC potential should be investigated further in all cases.

3.3. Evaluation of the Human–Robot Collaboration Potential

In step 5, the HRC potential and allocation of labor is determined. The test is carried out in two stages:

1. Allocating the activities of the SP to humans and robots and subsequent testing of the changed DAS.
2. Testing of possible simultaneous execution of the activities.

Considering the strengths and weaknesses of humans and robots, the tasks of an SP are divided between these two actors. Activities with a low DAS are assigned to a human, and those with a high DAS are assigned to a robot. The human activities are entered on the left, and robot activities are on the right. For all activities classified as "manual", the automation suitability factor is deleted from the MTM-1 analysis. The updated final automation suitability level is then compared with the original value determined from the previous phase. If there is no significant improvement or a substantial imbalance in the allocation of tasks between humans and robots (greater than 75:25), the allocation is discarded. If there is a significant improvement in the value (average greater than two points) and no such imbalance in the allocation, there is a high HRC suitability.

Based on the previous interpretation of the results, the HRC potential is also depicted in a four-field matrix (Figure 3).
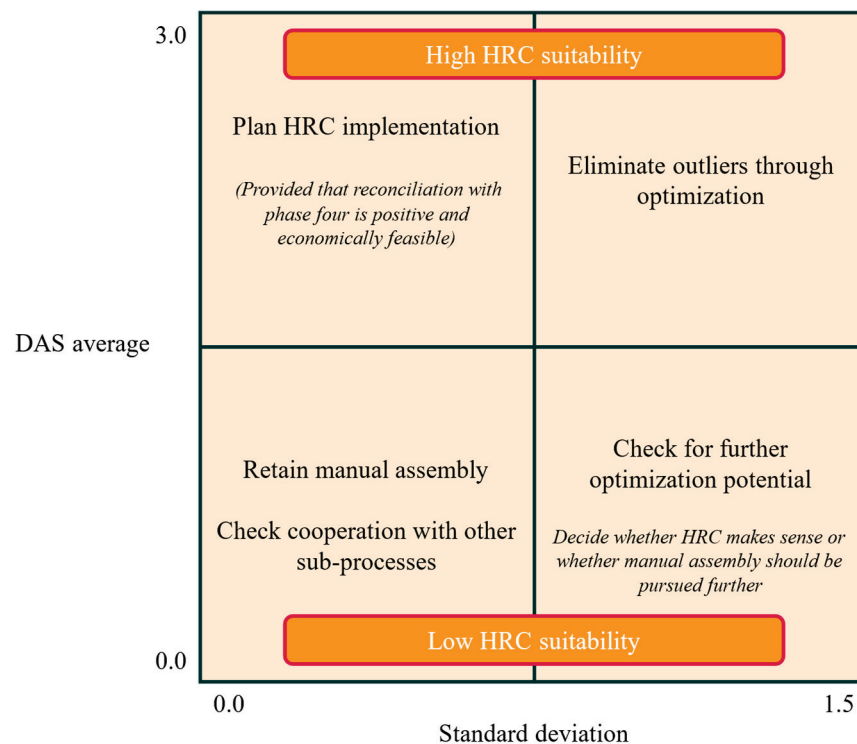
Figure 3. Four-field matrix to classify the HRC potential.

Depending on the characteristics of the final average or the DAS and their standard deviation, a result classification is made possible, and instructions for further procedures are derived.

3.4. Assessment of Economic Efficiency, Detailed Planning, and Optimization Potential

When applying the procedure model described here or from previous MTM 1 analysis, the respective times for the described SPs are available, based on which an economic application can be examined. For this purpose, the investment costs are compared with the expected productivity effects and time savings. Here, the total MTM times of the MTM-1 analyses are used as a basis, and the original actual times (before HRC) are compared with the planned times (after/with HRC). A subsequent amortization calculation provides information as to the duration from which the investment is worthwhile and helps with the risk assessment.

Phase 7 of the process model includes detailed planning and subsequent HRC implementation; the qualified HRC potentials are implemented for the respective assembly process, and the introduction, including all measures, is planned. The employees are informed about the planned steps and, if necessary, involved in developing the workstation

design. In addition, training on safety and the essential functions of the robots must be carried out. Depending on the type and scope of the HRC implementation, additional needs-specific qualifications may also be relevant.

Due to the high variability in assembly, further or new optimization potentials are examined after detailed planning and implementation. This focuses on activities in the respective analyses with high time requirement values or low suitability for automation. It is checked whether an improvement in the time requirement and the suitability for automation can be achieved through change measures. These can consist of further adjustments to the provision of parts and tools or pick-up options, path changes, or joining aids. In addition, scenarios with new cross-process automation solutions, e.g., acquiring additional machines, are considered in this phase. A redesign of the workstation is also possible. The process model is iterated to qualify further HRC potential. This begins with phase 4.

4. Evaluation Using the Industrial Example of Water Electrolysis

The evaluation focuses on selecting and qualifying HRC potential in an assembly process. A brief comparison of the time requirement values (before and after) is carried out based on phase 6. The subsequent realization or detailed planning and implementation (phase 7) is not dealt with further and would have to be investigated in the industrial context in additional work. Testing and optimization (phase 8), which involves the presentation of improvements as part of a cross-SP assembly, is not focused on here for the same reasons. The procedure for an MTM-1 analysis is not explained in detail. Therefore, the evaluation focuses on the first five phases of the developed process model.

In the context of electrolyzer production, instrument panels are required to control the process and ensure the quality of the processed media. Four different media are essential for the operation of electrolyzer systems, each requiring a different structure and composition of the panel. Figure 4a shows a customized nitrogen instrument panel, which is needed for purging the tubes for maintenance or emergencies. In addition, instrument panels differ in structure even with the same media, depending on the system size and customer. In summary, this product has a complex and very flexible product structure and is currently assembled by hand, as described in the beginning. Therefore, the product and the associated assembly processes are ideally suited as validation objects. Due to the frequency of the process, the focus of the evaluation is on the screwing of the tube elements.

The process is divided into five SPs, and the predicted time requirement is built by the sum of all time requirements (Figure 4b). Processes with high time requirements are time-consuming, cost-consuming, and need to be optimized. As there are already automation solutions for shortening pipes, the process with the second highest time requirement is considered, which is the screwing process. In addition to a tube, a double-ferrule fitting is required for a tight tube connection in the hydrogen context. Both must be taken from a stock and then joined together. The tube must be inserted into the fitting, and the nut must be tightened to assemble. The geometry of the screw connection component is like a standard hexagon nut. A tight connection is created when the nut is firsthand-tightened and then tightened by single $\frac{1}{4}$ turns, according to the quasi-industrial standard of Swagelok. The nut must be marked after hand-tightening for a subsequent visual check of the single $\frac{1}{4}$ turns. All in all, the process can be described by 32 basic movements and requires approx. 12 s in the MTM-1 prediction. In the following, the composition of the DAS for the ten superordinate classifications of basic movements for that SP 4 is shown in Table 1. The validation of the DAS is based on the assessment of the defined criteria, which are linked to the MTM-1 code. For example, the "reaching" process of category B is described as "Reaching out to a stand-alone counterpart that is located in a place that changes from work cycle to work cycle" [3] (p. 411), from which the evaluation criteria EC2, EC4, EC6, and EC9 can be derived. By adding the movement length to the MTM-1 code, the evaluation criterion EC1 can also be evaluated. The following basic movements can be interpreted similarly. As shown, the average of all fulfilled criteria has been calculated and rounded

down to reflect the worst possible case. This ensures that the most transparent processes for automation suitability are identified first.
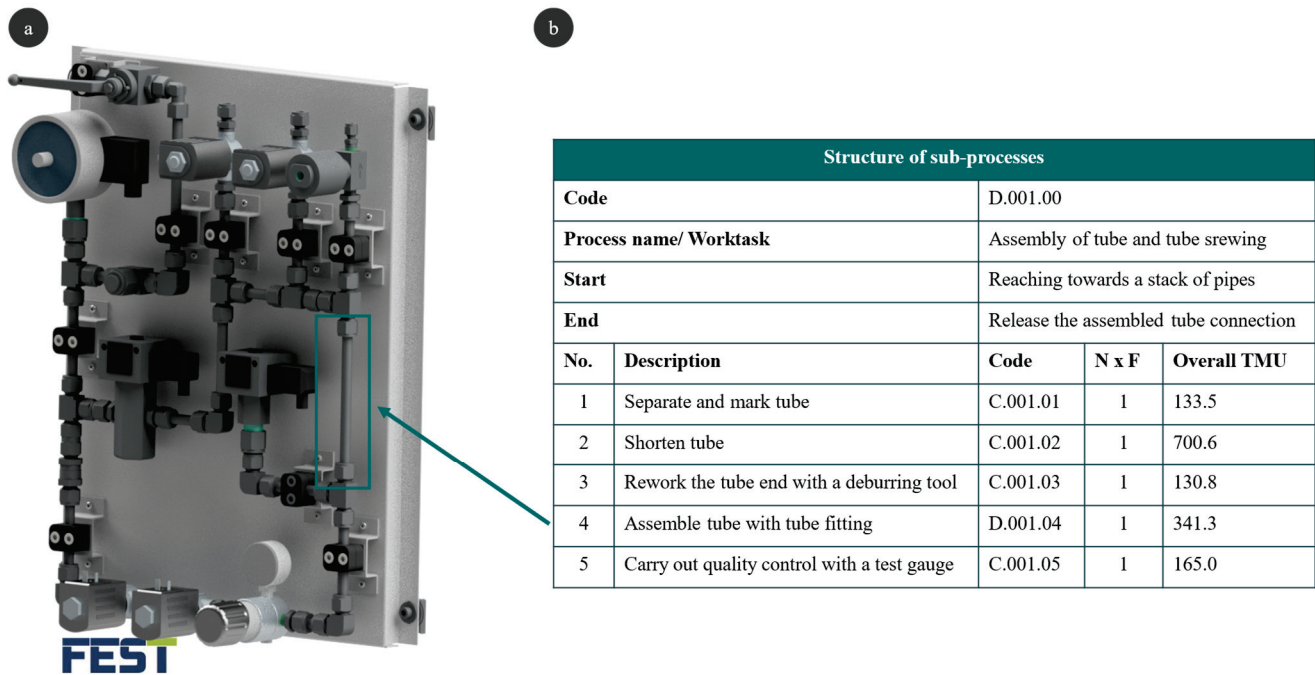

Structure of sub-processes				
Code	D.001.00			
Process name/ Worktask	Assembly of tube and tube srewing			
Start	Reaching towards a stack of pipes			
End	Release the assembled tube connection			
No.	**Description**	**Code**	**N x F**	**Overall TMU**
1	Separate and mark tube	C.001.01	1	133.5
2	Shorten tube	C.001.02	1	700.6
3	Rework the tube end with a deburring tool	C.001.03	1	130.8
4	Assemble tube with tube fitting	D.001.04	1	341.3
5	Carry out quality control with a test gauge	C.001.05	1	165.0

Figure 4. Nitrogen instrument panel (**a**) and associated process profile (**b**).

Table 1. Composition of the DAS (Extract) for the SP 4 under consideration.

	DAS	Average	EC1	EC2	EC3	EC4	EC5	EC6	EC7	EC8	EC9
R-B < 60 cm	2	2.33	3	2	\	3	1	3	\	\	2
G	3	3	\	3	3	\	\	3	\	\	\
M-C < 60 cm	3	3	3	\	\	3	\	3	\	3	3
M-B > 60 cm	2	2.80	2	\	\	3	\	3	\	3	3
R-A < 60 cm	3	3	3	3	\	3	3	3	\	\	3
P2SE	2	2.60	\	\	3	\	\	3	3	2	2
RL1	3	3	\	\	\	\	\	3	\	\	3
M-B < 60 cm	3	3	3	\	\	3	\	3	\	3	3
P1SSE	3	3	\	\	3	\	\	3	3	3	3
APA	3	3	\	\	\	\	\	3	\	\	3

As described above, the potential of the automation for the different SP is visualized in a four-field matrix (Figure 5a). The first four SPs exhibit a high potential for automation, whereas the SP 5 (quality testing) is categorized as "not automatable" based on the K.O. criterion. The lower suitability for automation in SP 4 compared to the first three SPs is mainly due to the high number of different activities and the associated high complexity factor. Points are also deducted for the vice clamping activities and two joining processes. Nevertheless, with a final average of 1.86 and a standard deviation of 0.31, SP 4 has a high automation potential.
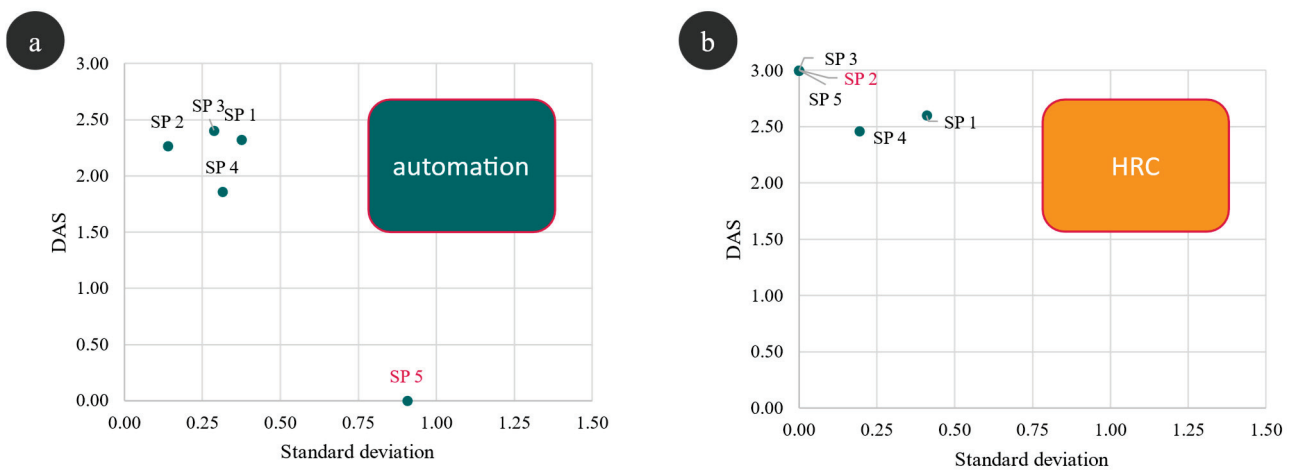
Figure 5. Potential of automation (**a**) and HRC (**b**) based on a four-field matrix.

Compared to the results from stage 4, the cooperative and collaborative HRC potential assessments show an improvement in the degree of automation suitability for all SPs (Figure 5b). Furthermore, allocating tasks between humans and robots eliminates the K.O. criterion for SP 5. All SPs have a high HRC potential. SP 4 has a complexity factor of 0.5 despite the division of activities and still loses one point in the analysis when moving to the tube fittings. Nevertheless, there is an improvement to an automation suitability factor of 2.46 and a standard deviation of 0.19. SP 4 has a high HRC potential. Table 2 shows the total time required for the process model's individual analyses of phases 3, 4, and 5, as well as the DAS for all SPs in the context of full automation and HRC. The reduction in the time requirements of the MTM-1 column and the Automation column results solely from the optimizations about picking up and storing items at the assembly station based on the MTM-1 analysis (phase 3) for a time improvement. The time required for the process modules for a fully automated solution is assessed as being equivalent to the time needed for manual activities. In SP 4, a reduction in time requirements of just under 9% can be achieved, corresponding to a time saving of approx. 1.1 s.

Table 2. Comparison of time requirements from the different phases.

	Structure of Sub-Processes					
No.	**MTM-1 TMU**	**Automation TMU**	**Automation DAS**	**HRC TMU**	**HRC DAS**	**Total Time Saving**
1	133.5	117.0	2.82	91.5	2.60	42.0
2	700.6	697.3	2.76	691.7	3.00	8.9
3	130.8	127.5	2.90	127.5	3.00	3.3
4	341.3	336.7	2.86	309.9	2.96	31.4
5	165.0	164.8	2.31	164.8	3.00	0.2
Sum	1471.2	1446.3	-	1385.4	-	85.8

The considered assembly process of screwing together tube elements and all the SPs involved is highly suitable for HRC. However, the high values of the DAS are also due to the allocation of tasks, as the robot only has to work on suitable tasks here. Therefore, the average rating is also significantly better. The preferred form of interaction varies, as the evaluations of the different phases show. While SP 1 and SP 5 benefit from cooperative or collaborative collaboration, coexistence or synchronization should be selected for SP 2. SP 3 and SP 4 are suitable for all forms of HRC.

5. Conclusions of the Procedure Model MTM-1-HRC

The procedure model developed makes it possible to describe complex assembly processes and divide them into SPs. It is based on the basic MTM-1 modular process system, which is already used in many industries and companies of all sizes. The MTM-1 analysis is used to determine actual times and provides initial approaches for optimizations in assembly. In the subsequent MTM-1-HRC cycle, the SPs can be checked for suitability for automation and HRC. The different forms of HRC are considered in the various phases. The high level of detail of the model makes it possible to determine the respective suitability of the various activities based on the defined evaluation criteria and to identify individual problems or knock-out criteria directly. Criteria from established DFA methods are used and linked using the process description of the individual MTM-1 modules. In addition, the interpretation matrices support the classification of the analysis results and the evaluation of automation and HRC potentials. They provide information for further action. In a final investigation of further optimization potential, new and cross-process measures can be identified, and thus, approaches for new iterations of the process model can be derived. The developed process model can be seen as further developing existing models and fulfilling all requirements.

6. Outlook and Further Work

However, the model presented also has some potential for further development, which must be mentioned and addressed in subsequent work. To evaluate the time savings, the approach developed is based on the exact time requirements for both actors, humans and robots. However, humans are significantly faster than robots for various tasks, particularly in assembly. This results in a certain lack of precision in evaluating economic efficiency by comparing the time requirements. Furthermore, there is no linking of pre- and post-movements. This would be useful for an accurate assessment of the economic viability of implementing such automation solutions. In addition, the use of various tools such as screwdrivers or wrenches for the assembly process would become much more important. At this stage, the method presented evaluates the suitability of the individual components regarding automation. In the future, a holistic evaluation of the SP would be possible. One possible solution could be the rule base for multi-hand movements. As described above, MTM-1 considers the time estimation of human multi-hand movements. HRC could be considered as a further specification of this movement and could, therefore, be used to derive new rules and, thus, times. This connection must be investigated further.

It should also be noted that, although established criteria were used to assess the suitability of automation, the grading of the assessment is based on several assumptions that need to be further investigated and adjusted afterward with the help of a panel of experts. No distinction is made between autonomous industrial robots and collaborative robots, nor is there consideration of the respective size. Hence, the validity of the assumptions is questionable depending on the context of the application. Adjustments, e.g., to the robot accuracy, the movement radii, or the weight handling, would lead to changed evaluation criteria and thus differing degrees of automation suitability. For that, a more dynamic system for the evaluation criteria must be researched and implemented in the future. Moreover, comprehensive knowledge of the processes is required to apply this method. Therefore, the application area of this method lies in detailed engineering or the downstream optimization of existing production systems. However, basic engineering significantly impacts costs, so adapting this method for early use would make sense.

Author Contributions: Conceptualization, M.J., F.E. and P.A.; Methodology, M.J., F.E., P.A., L.L. and B.K.; Writing—original draft, M.J.; Writing—review & editing, P.A., L.L. and B.K.; Visualization, M.J. and F.E.; Supervision, B.K. All authors have read and agreed to the published version of the manuscript.

Data Availability Statement: The data presented in this study are available on request from the corresponding author. The data are not publicly available.

Conflicts of Interest: The authors declare no conflict of interest.

References

1. Smolinka, T.; Wiebe, N.; Sterchele, P.; Palzer, A.; Lehner, F.; Jansen, M.; Kiemel, S.; Miehe, R.; Wahren, S.; Zimmermann, F. *Studie IndWEDe: Industrialisierung der Wasser Elektrolyse in Deutschland: Chancen und Herausforderungen für Nachhaltigen Wasserstoff für Verkehr, Strom und Wärme*; NOW GmbH: Berlin, Germany, 2018.
2. Hebling, C.; Ragwitz, M.; Fleiter, T.; Groos, U.; Härle, D.; Held, A.; Jahn, M.; Müller, N.; Pfeifer, T.; Plötz, P.; et al. *Eine Wasserstoff-Roadmap für Deutschland*; Fraunhofer-Institut für System- und Innovationsforschung ISI, Karlsruhe Fraunhofer-Institut für Solare Energiesysteme ISE: Freiburg, Germany, 2019.
3. Bokranz, R.; Landau, K. *Handbuch Industrial Engineering: Produktivitätsmanagement mit MTM*, 2nd ed.; Schäffer-Poeschel: Stuttgart, Germany, 2012.
4. Neb, A.; Göke, J. Generation of assembly restrictions and evaluation of assembly criteria from 3D assembly models by collision analysis. *Procedia CIRP* **2021**, *97*, 33–38. [CrossRef]
5. Linsinger, M.; Stecken, J.; Kutschinski, J.; Kuhlenkötter, B. Orts- und aufgabenflexibler Einsatz von Leichtbaurobotern in der Montage. *Wt Werkstattstech. Online* **2019**, *109*, 94–99. [CrossRef]
6. Becker, T. *Prozesse in Produktion und Supply Chain Optimieren*, 2nd ed.; Springer: Berlin/Heidelberg, Germany, 2008.
7. Alfadhlani; Samadhi, T.; Ma'ruf, A.; Toha, I. A Framework for the Development of Automatic DFA Method to Minimize the Number of Components and Assembly Reorientations. *IOP Conf. Ser. Mater. Sci. Eng.* **2018**, *319*, 12083. [CrossRef]
8. Eskilander, S. *Design for Automatic Assembly: A Method for Product Design: DFA2. Dissertation*; Kungliga Tekniska Högskolan: Stockholm, Sweden, 2001.
9. Ezpeleta, I.; Justel, D.; Bereau, U.; Zubelzu, J. DFA-SPDP, a new DFA method to improve the assembly during all the product development phases. *Procedia CIRP* **2019**, *84*, 673–679. [CrossRef]
10. Formentini, G.; Rodríguez, N.; Favi, C. Design for manufacturing and assembly methods in the product development process of mechanical products: A systematic literature review. *Int. J. Adv. Manuf. Technol.* **2022**, *120*, 4307–4334. [CrossRef]
11. Madappilly, P.; Mork, O. Review and modification of DFA2 methodology to support design for automatic assembly (DFAA) in the maritime industry. *Procedia CIRP* **2021**, *100*, 744–749. [CrossRef]
12. Shetty, D.; Ali, A. A new design tool for DFA/DFD based on rating factors. *Assem. Autom.* **2015**, *35*, 348–357. [CrossRef]
13. Trommnau, J. Methodik zur Bewertung und Optimierung der Automatisierungseignung des Zusammenbaus von Bauteilkombinationen mit Forminstabilen Einzelteilen. 2022. Available online: https://elib.uni-stuttgart.de/bitstream/11682/12555/3/2022 TrommnauJerome.pdf (accessed on 14 May 2024).
14. Boothroyd, G. Design for assembly—The key to design for manufacture. *Int. J. Adv. Manuf. Technol.* **1987**, *2*, 3–11. [CrossRef]
15. Boothroyd, G.; Dewhurst, P.; Knight, W.A. (Eds.) *Product Design for Manufacture and Assembly*; Dekker: New York, NY, USA, 2002.
16. Miles, B.L. Design for Assembly—A Key Element within Design for Manufacture. Proceedings of the Institution of Mechanical Engineers. *Part D J. Automob. Eng.* **1989**, *203*, 29–38. [CrossRef]
17. Sturges, R.H. A quantification of manual dexterity: The design for an assembly calculator. *Robot. Comput.-Integr. Manuf.* **1989**, *6*, 237–252. [CrossRef]
18. Desai, A.; Mital, A. Facilitating design for assembly through the adoption of a comprehensive design methodology. *Int. J. Ind. Eng. Theory Appl. Pract.* **2010**. [CrossRef]
19. Bauer, W.; Rally, P.; Scholtz, O. Schnelle Ermittlung sinnvoller MRK-Anwendungen. *Z. Für Wirtsch. Fabr.* **2018**, *113*, 554–559. [CrossRef]
20. Weber, M.-A.; Schüth, N.J. Integration der Mensch-Roboter-Kollaboration unter Beachtung technischer und personeller Rahmenbedingungen. In *Frühjahrskongress*; Gesellschaft für Arbeitswissenschaft (GfA): Dortmund/Berlin, Germany, 2020; Available online: https://www.arbeitswissenschaft.net/fileadmin/Downloads/Angebote_und_Produkte/Publikationen/GfA_2020_B-13-5_Weber_Schueth.pdf (accessed on 14 May 2024).
21. Petzoldt, C.; Keiser, D.; Siesenis, H.; Beinke, T.; Freitag, M. Ermittlung und Bewertung von Einsatzpotenzialen der Mensch-Roboter-Kollaboration. *Z. Für Wirtsch. Fabr.* **2021**, *116*, 8–15. [CrossRef]
22. Hees, F.; Müller-Abdelrazeq, S.L.; Langer, T.; Voss, M.; Schmitt, R.; Hüttemann, G. (Eds.) *Projektatlas Kompetenz Montage: Kollaborativ und wandlungsfähig*; RWTH Aachen University Lehrstuhl für Informationsmanagement im Maschinenbau: Aachen, Germany, 2019.
23. Ermer, A.-K.; Seckelmann, T.; Barthelmey, A.; Lemmerz, K.; Glogowski, P.; Kuhlenkötter, B.; Deuse, J. A Quick-Check to Evaluate Assembly Systems' HRI Potential. In *Tagungsband des 4. Kongresses Montage Handhabung Industrieroboter*; Schüppstuhl, T., Tracht, K., Roßmann, J., Eds.; Springer: Berlin/Heidelberg, Germany, 2019; pp. 128–137.

24. Linsinger, M.; Sudhoff, M.; Lemmerz, K.; Glogowski, P.; Kuhlenkötter, B. Task-based Potential Analysis for Human-Robot Collaboration within Assembly Systems. In *Tagungsband des 3. Kongresses Montage Handhabung Industrieroboter*; Schüppstuhl, T., Tracht, K., Franke, J., Eds.; Springer: Berlin/Heidelberg, Germany, 2018; pp. 1–12.
25. Teiwes, J.; Banziger, T.; Kunz, A.; Wegener, K. Identifying the Potential of Human-Robot Collaboration in Automotive Assembly Lines using a Standardised Work Description. In Proceedings of the 2016 22nd International Conference on Automation and Computing (ICAC), Colchester, UK, 7–8 September 2016; IEEE: New York, NY, USA, 2016; pp. 78–83.

Article

Effects of Initial Small-Scale Material Nonlinearity on the Pre-Yield and Pre-Buckling Response of an Externally Pressurized Ring

Reaz A. Chaudhuri [1,*,†] **and Deokjoo Kim** [2,‡]

1   Department of Materials Science & Engineering, University of Utah, Salt Lake City, UT 84112, USA
2   Department of Mechanical Engineering, University of Utah, Salt Lake City, UT 84112, USA
*   Correspondence: r.chaudhuri@utah.edu
†   Retired Faculty, Tel.: +1-(801)-550-0661; reaz.chaudhuri@gmail.com.
‡   Current address: TAEJIN Technology, Seoul 06126, Republic of Korea.

Abstract: The effects of initial small-scale material nonlinearity on the pre-yield and pre-buckling response of externally pressurized metallic (plane strain) perfect rings (very long cylindrical shells) is investigated. The cylindrically curved 16-node element, based on an assumed quadratic displacement field (in surface-parallel coordinates) and the assumption of linear distribution of displacements through thickness (LDT), is employed to obtain the discretized system equations. The effect of initial small-scale material nonlinearity (assumed hypo-elastic) on the deformation and stress in the pre-yield and pre-buckling regime of a very long relatively thin metallic cylindrical shell (plane strain ring) is numerically investigated. These numerical results demonstrate that the enhanced responses for metallic rings due to initial small-scale nonlinearity are significant enough to not miss attentions from designers and operators of submersibles alike.

Keywords: compression failure; pre-buckling; buckling; pre-yield stress; yield; material nonlinearity; stainless steel

1. Introduction

The present study is primarily motivated by the recent compression failure of the Titan submersible in the North Atlantic at about 12,500 ft. depth [1]. The findings are consistent with what had long-earlier been observed both analytically/computationally as well as experimentally by the first author and his co-authors; see the brief literature review below [2–6].

Observations made from the fractured portion and detailed theoretical analysis indicate that the failure may have initiated at a stress concentration site such as initial fiber waviness or misalignment, shown, e.g., in Figure 3 of Chaudhuri [7], and associated resin-rich areas. Finally, Chaudhuri and Garala [8] published a successful analytical/experimental effort at improving the compressive strength/toughness of the CFRP material by using a then-unavailable hybrid carbon/glass commingling concept.

Some of the uncertainties in the failure of thick CFRP cylindrical shells under compressive loading relate to very fundamental questions pertaining to (i) linkage between macro-structural instability, such as buckling/post-buckling failure of a structural component, e.g., a ring or cylindrical shell at the geometric scale of at least several centimeters and larger [9–21], and micro-structural instability, such as kink band type failure at the fiber-matrix level (at the geometric scale of about 10 μm) investigated by Chaudhuri [7,19–23], Chaudhuri and Garala [8], Chaudhuri et al. [24], Moran and Shih [25] and Gutkin et al. [26] among others.

Buckling and post-buckling responses of arch/ring/cylindrical shell/panel type structures have been extensively studied in the literature [27–45]. It may be remarked here

that since the elastic post-buckling of a ring involves deformation hardening type non-linearity [16,31,32,35,46], there is no final loss of stability in the post-buckling stage. This is in sharp contrast to the deformation softening type nonlinearity caused by, e.g., the thickness effect, [11–15], the presence of distributed fiber misalignments (in fiber reinforced composites) [16,47], and hypo-elastic or inelastic material properties [17,46,47], in addition to the thickness effect [18–21]. An arch (an open ring with pinned or fixed ends) is, it may be pointed out in this context, probably the simplest special case which exhibits such behaviors as nonlinear load-deflection path, bifurcation and snapping (and combinations thereof) of a general shell, depending on the range of its specific elasto-geometric parameter, defined in terms of its (modified) slenderness ratio [30,38]. Furthermore, as has been pointed out earlier by Chaudhuri et al. [40], the hydrostatic buckling pressure of a complete ring can be obtained as a special case of a hinged uniformly compressed arch with a central angle π.

One major necessary-cum-looked-forward-to item to designers and operators alike is the heretofore unaddressed analysis on the sensitivity of compressive responses of very long cylindrical shells (plane strain rings) to initial small-scale material nonlinearity, which is the primary objective of the present investigation. Applications include but are not limited to submersibles as well as buried and submerged pipelines, and can be of varying thicknesses. The fact that many a metallic material/alloy, such as aluminum, molybdenum, cast iron, stainless steel (304 and 316) among others, is characterized by initial small-scale nonlinearity in the absence of a well-defined yield point, is well-known in the literature. The initial small-scale nonlinearity of longitudinal Young's modulus of a unidirectional composite under global or macroscopic compression, but local or micro-/nano-scale shear, caused by crystallite disorientations, as detected by the Raman and X-ray measurements, inside a carbon fiber [48] is still unavailable in the literature. An approximate derivation of this is currently underway (and will be reported at a future date).

In what follows, a materials-only [49] nonlinear three-dimensional cylindrical shell finite element analysis is presented in order to obtain the discretized system of equations. A cylindrically curved 16-node isoparametric element is employed, which is based on an assumed quadratic displacement field (in surface-parallel coordinates) and the assumption of linear distribution of displacements through thickness (LDT) [42,50]. The effect of initial small-scale material nonlinearity (assumed hypo-elastic) on the pre-buckling as well as the pre-yield response of a metallic (plane strain) ring is thoroughly investigated. Results relating to the extension to the same effect on the deformation and through-thickness stress distribution in the pre-buckling regime of a long asymmetric cross-ply cylindrical shell (plane strain ring) are deferred to a future date. Finally, physically meaningful conclusions are drawn from these numerical results.

2. Three-Dimensional Kinematic Relations for a Shell

Referring to Figure 1 and invoking the theory of parallel surfaces, the coefficients of the first fundamental differential quadratic form of a surface inside a cylindrical shell can be written in terms of their bottom surface (inside wall) counterparts as follows [45,50–53]:

$$g_x(z) = 1; \ g_\theta(z) = \bar{g}_\theta(1 + \frac{z}{R_i}); \ g_z(z) = 1. \tag{1}$$

As has been explained earlier by Chaudhuri and Kim [19], the inner surface of the cylindrical shell/ring is, from the book-keeping point of view, considered more convenient to serve as the reference surface, since the state of stresses and deformation are primarily three-dimensional in nature. This is in contrast to what is commonly adopted by the classical lamination theory (CLT) or first-order shear deformation theory (FSDT), wherein transverse inextensibility is assumed. The components of the engineering strain in terms of the physical components of the displacement vector at an arbitrary point inside the shell are obtained as follows [50–54]:

$$\varepsilon_x(x, \theta, z) = \frac{\partial u}{\partial x}, \tag{2a}$$

$$\varepsilon_\theta(x,\theta,z) = \frac{1}{g_\theta}\left(\frac{\partial v}{\partial \theta} + w\right),$$ (2b)

$$\varepsilon_{x\theta}(x,\theta,z) = \frac{\partial v}{\partial x} + \frac{1}{g_\theta}\frac{\partial u}{\partial \theta},$$ (2c)

$$\varepsilon_z(x,\theta,z) = \frac{\partial w}{\partial z},$$ (2d)

$$\varepsilon_{xz}(x,\theta,z) = \frac{\partial w}{\partial x} + \frac{\partial u}{\partial z},$$ (2e)

$$\varepsilon_{yz}(x,\theta,z) = \frac{1}{g_\theta}\left(\frac{\partial w}{\partial \theta} - v\right) + \frac{\partial v}{\partial z}.$$ (2f)
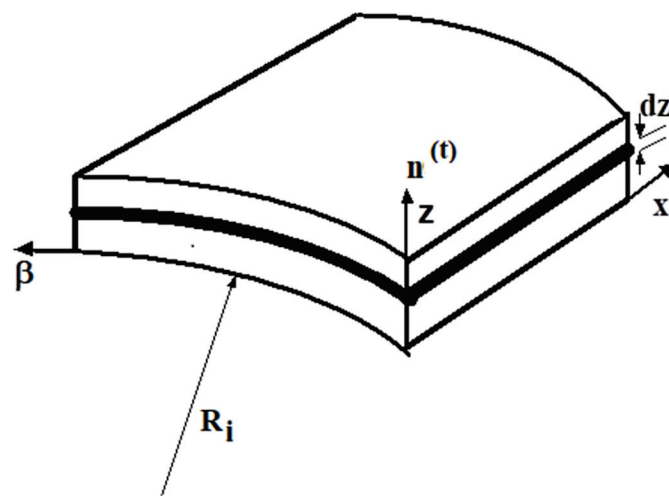
Figure 1. An infinitesimal element cylindrical shell.

3. Equations of Motion and the Method of Virtual Work

The second Piola-Kirchhoff stress tensor is conjugate to the Green-Lagrange strain tensor in that their properties are also invariant under rigid body motions. When the equilibrium of the body at time $t + \Delta t$ is first expressed using the principle of virtual displacements with tensor notation, the total Lagrangian formulation requires that

$$\int_V {}^{t+\Delta t}S_{ij}\delta^{t+\Delta t}\bar{\varepsilon}_{ij}dV = {}^{t+\Delta t}R,$$ (3)

where the ${}^{t+\Delta t}S_{ij}$ and ${}^{t+\Delta t}\bar{\varepsilon}_{ij}$ are the Cartesian components of the second Piola-Kirchhoff stress tensor and the total Green-Lagrange strain tensor defined at time $t + \Delta t$, respectively, referred to the initial configurations, while ${}^{t+\Delta t}R$ represents the external virtual work. Furthermore,

$$^{t+\Delta t}S_{ij} = {}^{t}S_{ij} + S_{ij},$$ (4)

and

$$^{t+\Delta t}\bar{\varepsilon}_{ij} = {}^{t}\bar{\varepsilon}_{ij} + \bar{e}_{ij},$$ (5)

where ${}^{t}S_{ij}$ and S_{ij} represent components of the second Piola-Kirchhoff stress tensor defined at time t, and the incremental components of the same during the subsequent time step Δt, respectively, both referred to the initial configuration. The quantities $\bar{e}_{ij}$ in Equation (5) denote the linear incremental strain. The incremental constitutive relation, which relates

the components of incremental stress and incremental strain both referred to the initial configuration, is given by

$$S_{ij} = C_{ijrs} \, \bar{e}_{rs}, \tag{6}$$

in which C_{ijrs} is the incremental elastic stiffness (material property) tensor, referred to the initial configuration and represented as [Q] in matrix notation (see Section 4 and also refer to Figure 2 below). Substituting Equations (4)–(6) into the left hand side of the Equation (3) finally yields the equations needed for the finite element formulation. The details are available in Chaudhuri and Kim [11,12].

Because the variation in the strain components is equivalent to the virtual strains, the right hand side of Equation (3) is the virtual work done when the body is subjected to a virtual displacement at time $t + \Delta t$. The corresponding virtual work is given by

$$^{t+\Delta t}R \quad \int_{^{t+\Delta t}S} {}^{t+\Delta t}f_{\,j}^{\,s} \, \delta_0 u_j^s \, {}^{t+\Delta t}ds, \tag{7a}$$

where $^{t+\Delta t}f_{\,j}^{\,s}$ is the surface force vector applied on the surface, S, at time $t + \Delta t$, and δu_j^s is the jth component of the incremental virtual displacement vector evaluated on the loaded surface. When the hydrostatic pressure is applied, the loading path is always deformation-dependent, and the load vector should be evaluated at the current configuration. The external virtual work can, however, be approximated to a sufficient accuracy using the intensity of loading corresponding to time $t + \Delta t$, integrated over the surface area, $^{t+\Delta t}s \, ^{(i-1)}$ calculated at the $(i-1)$th iteration as follows:

$$^{t+\Delta t}R = \int_{^{t+\Delta t}S \, ^{(i-1)}} {}^{t+\Delta t}f_{\,j}^{\,s} \, \delta_0 u_j^s \, {}^{t+\Delta t}ds. \tag{7b}$$

4. Constitutive Relations for an Orthotropic Lamina

Taking into account nonlinear elastic (hypo-elastic) behavior (as opposed to plasticity) and neglecting the thermal and hygrothermal effects, the incremental strain vs. incremental stress relation of an isotropic material in terms of the principal material directions (x, θ, z) is given as follows [11,12,18,19]:

$$[\Sigma] = \begin{bmatrix} 1/{}^tE & -v/{}^tE & -v/{}^tE & 0 & 0 & 0 \\ -v/{}^tE & 1/{}^tE & -v/{}^tE & 0 & 0 & 0 \\ -v/{}^tE & -v/{}^tE & 1/{}^tE & 0 & 0 & 0 \\ 0 & 0 & 0 & 2(1+v)/{}^tE & 0 & 0 \\ 0 & 0 & 0 & 0 & 2(1+v)/{}^tE & 0 \\ 0 & 0 & 0 & 0 & 0 & 2(1+v)/{}^tE \end{bmatrix}. \tag{8}$$

In the above equation, the compliance matrix components, Σ_{ij}, $i, j = 1, \ldots, 6$, can be approximated analytically by the method of Ramberg and Osgood [55], who have suggested that rising stress-strain curves with a smooth knee be represented by the relation [18].

$$\frac{1}{{}^tE} = \frac{1}{E}\left[1 + \frac{3}{7}\left(\frac{{}^tS}{S_R}\right)^{n-1}\right], \tag{9}$$

where ^tE and $^tS = \sigma$ denote Young's modulus and normal stress component at time t, respectively, of the material. Details of nomenclature and property definitions of this nonlinear (hypo-elastic) material are shown in Figure 2.
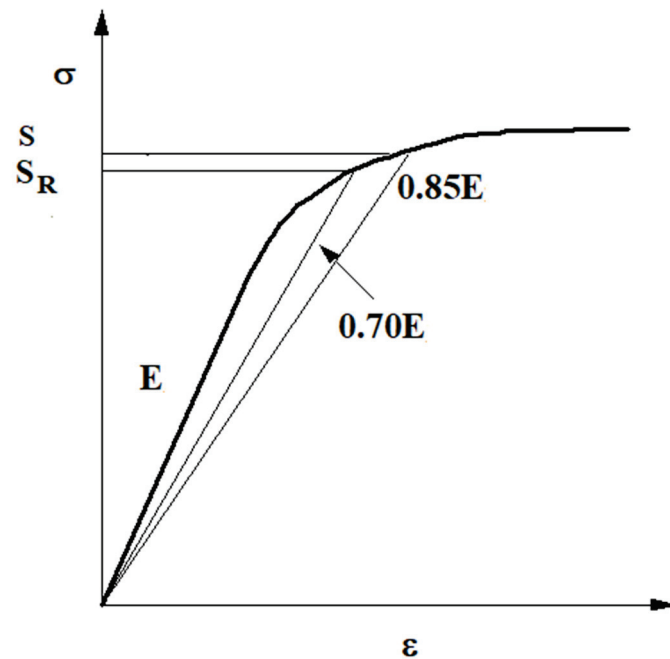
Figure 2. Definition of parameters in Ramberg-Osgood representation of stress-strain curves [18,19].

The reference "yield" stress $\sigma_Y = S_R$ is defined as the normal stress at which $E_s = (\Sigma_s)^{-1} = 0.7E$, where E_s is the secant modulus. The exponent, n, known as the hardening parameter, is found from the expression for the secant modulus thus defined:

$$\frac{E}{E_s} = 1 + \frac{3}{7} \left(\frac{{}_0^t S}{S_R} \right)^{n-1}, \tag{10a}$$

with

$$S_R = mE. \tag{10b}$$

Evaluation of Equation (10a) at $E_s = 0.85E$ gives

$$n = \frac{\log_{10}(0.441)}{\log_{10}(S/S_R)} + 1, \tag{11}$$

where S is the stress at $E_s = 0.85E$. It may be noted that the linear elastic and the perfectly elastic-plastic (no unloading) cases can be obtained by substituting $S = \infty$ and $n = \infty$, respectively, into Equation (9). The incremental stress vs. incremental strain relation can be obtained by inversion of Equation (8) as follows:

$$[Q] = [\Sigma]^{-1}. \tag{12}$$

5. Isoparametric Finite Element Discretization

In this section, a materially-nonlinear-only displacement-based three-dimensional finite element formulation is presented. An alternative approach to the formulation of thick (laminated) shell nonlinear finite element has recently been developed by Chaudhuri [10]. The Rayleigh–Ritz finite element method (local shape function), which is useful for modeling structures with somewhat less complex geometrical shapes, such as beams, rings and arches [30], has recently been extended to nonlinear analysis of symmetrically laminated shallow circular arches by Kim and Chaudhuri [38]. A then-unavailable nonlinear resonance (eigenvalue) based semi-analytical approach was introduced by Chaudhuri [39] and Chaudhuri et al. [40,41] for computation of the elastic mode 2 collapse pressure of a moderately-thick to thin isotropic and cross-ply harmonically imperfect rings, which

is the harmonically imperfect ring counterpart to the Euler type buckling pressure of a hydrostatically pressurized thin perfect ring [27].

The basic steps in the derivation of isoparametric finite element equations are to select the interpolation functions of the displacements and the element coordinates. Because the new element coordinates are obtained by adding the element displacements to the original coordinates in the incremental analysis, the same interpolations can be employed for the displacements and coordinates. In the present study, 16-node quadrilateral elements (Figure 3) are employed because of their computational efficiency, as compared to their lower-order linear counterparts, which are too stiff to model the shear deformation. The details are available in Chaudhuri and Kim [11], and are, therefore, omitted here in the interest of brevity of presentation.
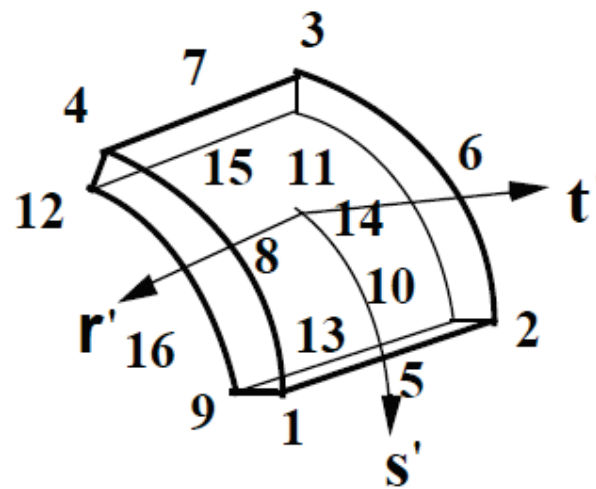
Figure 3. A 16-node curvilinear side surface-parallel quadratic isoparametric cylindrical shell element [11,18,19,34].

On computing the left and right sides of Equations (3) and (7) as sums of integrals over the volume and areas of all finite elements, followed by equating them, and incorporating the boundary conditions, the principle of virtual displacement, in conjunction with the materially-nonlinear-only formulation, is invoked to obtain the incremental equations of motion as follows [11,16,43]:

$$[\mathbf{K_L}]\{\mathbf{V}\} = \{\mathbf{f_L}\} - \{\mathbf{f_N}\}, \tag{13}$$

where

$$[\mathbf{K_L}] = \sum_{m=1}^{N} \int_{S^{(m)}} \int_0^h \left([\mathbf{B}_{LL}] \,[\mathrm{T}_{BT}] \,[\Phi]\right)^T [Q] \,[\mathbf{B}_{LL}] \,[\mathrm{T}_{BT}] \,[\Phi] \, R_i dz dS, \tag{14}$$

$$[\mathbf{f_L}] = \sum_{m=1}^{N} \int_{S^{(m)}} \left([\mathbf{B}_{LL}][\mathrm{T}_{BT}]\,[\Phi]\right)^T \begin{Bmatrix} n^{(t)} \\ 0 \end{Bmatrix} p_r \,(R_i + h) dS, \tag{15a}$$

$$[\mathbf{f_N}] = \sum_{m=1}^{N_L} \int_{S^{(m)}} \int_0^h \left([\mathbf{B}_{LL}] \,[\mathrm{T}_{BT}]\,[\Phi]\right)^T [^t\overline{S}] \, R_i dz dS, \tag{15b}$$

in which the matrices, $[\mathbf{B}_{LL}]$, $[\mathrm{T}_{BT}]$ and $[\Phi]$ are defined in Equations, (A1), (A2) and (A3), respectively, in Appendix A, while $[Q]$ is defined in Equation (12) above, and $\{\mathbf{V}\}$ is given as follows:

$$\{\mathbf{V}\}^T = \{U_{b1}, \dots, U_{b8}, \, V_{b1}, \dots, V_{b8}, \, W_{b1}, \dots, W_{b8}, \, U_{t1}, \dots, U_{t8}, \, V_{t1}, \dots, V_{t8}, \, W_{t1}, \dots, W_{t8}\}, \tag{16}$$

Because the nodal point forces at time $t + \Delta t$ depend nonlinearly on the nodal point displacements, it is necessary to iterate for obtaining a reasonably accurate solution of Equation (13). The most frequently used iteration scheme for solutions of nonlinear finite element equations is the Newton-Raphson iteration, because reformations and triangularizations of stiffness matrices at selective load and iteration steps are more computationally efficient without a significant loss of accuracy. In the Newton-Raphson method, only the stress force vector (i.e., the right hand side of Equation (13)) is modified without changing the stiffness matrix, after each iteration within a certain load step. The details of the algorithm employed for solving Equation (13) are available in Section 5 of Chaudhuri and Kim [12], and Appendix-C of Kim and Chaudhuri [14], and will not be repeated here in the interest of brevity of presentation.

In actual computer programming, the active columns and the addresses of the diagonal elements of the total stiffness matrix are stored effectively in an one-dimensional array, and an effective subroutine COLSOL (active column solver) is used to finally obtain the incremental displacement for the unbalanced force, $^{t+\Delta t}\Delta R^{(i-1)} = {}^{t+\Delta t}\{f_L\} - {}^{t+\Delta t}\{f_N\}^{(i-1)}$ in the $(i-1)$th iteration. The iteration is continued until the out-of-balance load vector and the displacement increments are sufficiently small, i.e., the iteration scheme is terminated at the current load step and moves to the next load step, when the force convergence criterion,

$$\frac{\left\| {}^{t+\Delta t}\{\mathbf{f_L}\} - {}^{t+\Delta t}\{\mathbf{f_N}\}^{(i)} \right\|}{\left\| {}^{t+\Delta t}\{\mathbf{f_L}\} - {}^{t}\{\mathbf{f_L}\} \right\|} < \varepsilon_f, \tag{17a}$$

with $\| \cdot \|$ denoting the Euclidean norm of the column vector, and the energy convergence criterion,

$$\frac{\{\mathbf{_0V}\}^{(i)T}\left({}^{t+\Delta t}\{\mathbf{f_L}\} - {}^{t+\Delta t}\{\mathbf{f_N}\}^{(i-1)}\right)}{\{\mathbf{_0V}\}^{(1)T}\left({}^{t+\Delta t}\{\mathbf{f_L}\} - {}^{t}\{\mathbf{f_L}\}\right)} < \varepsilon_e, \tag{17b}$$

are simultaneously satisfied. Here $\varepsilon_f, \varepsilon_e = 5 \times 10^{-3}$ represent the preset force and energy tolerances. In the nonlinear regime, which starts right at the start in the present initial small-scale material nonlinearity scenario, the Newton-Raphson method with a relatively smaller magnitude of the load increment would require, as expected, similarly smaller number of iterations, and vice versa. Otherwise, it may introduce serious errors and, indeed, diverge from the exact solution. Solution of the resulting nonlinear equations by the Newton-Raphson (with Aitken acceleration) has earlier been verified by the BFGS (Broyden Fletcher Goldfarb Shanno) iterative scheme, thus validating computational accuracy of both the schemes [44,45]. Furthermore, the importance of selection of proper step size of the loading in the nonlinear range is amply demonstrated by Chaudhuri and Abu-Arja [56]. One improperly chosen large step size in the middle of this process can induce an artificially created chaotic situation, even if the previous and subsequent load step sizes are properly selected.

Bathe and Cimento [57] have provided general guidelines for the number of iterations needed to achieve convergence within the prescribed tolerance in the context of Aitken acceleration, while cautioning about the empirical nature of the topic of rate of convergence. Rapid convergence rate is defined as one, when convergence with prescribed tolerance (such as what is described above) is achieved for a given load step within 4 iterations or less. The physical situation reflected by the relatively steeply rising stress-strain plot and/or pressure-deflection curves, presented in Section 6 below, that arises from the initial small-scale nonlinearity and that does not deviate too far from linear elastic equilibrium path fits this description. When a similar convergence with prescribed tolerance is achieved within 4 to 12 iterations, it is classified as the moderately fast convergence. This physico-computational scenario arises when the computed equilibrium path passes through the knee region with rapidly decreasing stiffness, as depicted in, e.g., Figure 4 of Kim and Chaudhuri [35], Figure 7 of Hsia and Chaudhuri [42], Figure 5 of Kim and Chaudhuri [43], Figure 8 of Chaudhuri and Hsia [45], Figure 6 of Kim and Chaudhuri [13], Figures 8 and 11 of Chaudhuri and Kim [11],

Figure 11 of Chaudhuri and Kim [12], Figure 6 of Chaudhuri [16], Figure 11 of Kim and Chaudhuri [14], Figure 7 of Chaudhuri and Kim [17], Figures 8, 9 and 11 of Chaudhuri and Kim [18], Figures 8–11 of Chaudhuri and Kim [19], Figures 4 and 5 of Chaudhuri [15], Figure 8 of Chaudhuri [20], Figure 5 of Chaudhuri [21], and Figure 3 of Chaudhuri [46]. Finally, when a similar convergence with prescribed tolerance takes more than 12 iterations, it is classified as slow. This is exemplified by the physico-computational scenario that entails almost flat or flattening region close to the limit point on the computed equilibrium path with approaching zero-stiffness or nearly so signaling the onset of localization, as displayed in Figure 6 of Kim and Chaudhuri [13], Figures 8 and 11 of Chaudhuri and Kim [11], Figure 11 of Chaudhuri and Kim [12], Figure 6 of Chaudhuri [16], Figure 11 of Kim and Chaudhuri [14], Figure 7 of Chaudhuri and Kim [17], Figures 8, 9 and 11 of Chaudhuri and Kim [18], Figures 8–11 of Chaudhuri and Kim [19], Figures 4 and 5 of Chaudhuri [15], Figure 8 of Chaudhuri [20], and Figure 5 of Chaudhuri [21].

The procedure for computation of the hydrostatic buckling pressure of a ring is outlined by Kim and Chaudhuri [34].

The finite element model of a quarter of the plane strain (perfect) ring along with the prescribed boundary conditions is presented in Figure 4. Double-symmetry conditions permit every model under consideration to be limited to only a quarter of the ring such that the corresponding surface-parallel displacements vanish along the center lines and the buckled shapes are assumed to be symmetric. Because the loading and geometric symmetries are assumed, boundary conditions on the surfaces in Figure 4 can be prescribed as follows [35]:

(a) Geometric Symmetry:

$$\text{On the surfaces ABFE and CDHG}: \ v(x,0,z) = 0 \ \text{and} \ v(x,\pi/2,z) = 0, \tag{18}$$

$$\text{On the surface EHGF}: \ u(x,\theta,z) = 0; \tag{19}$$

(b) Loading Symmetry:

$$\text{Traction force on the surface BCGF}: \ f_i^S = p(x,\theta,R_i + h)n_i^{(t)}. \tag{20}$$
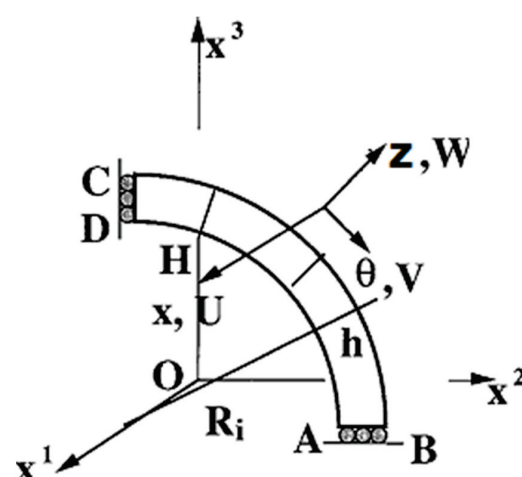
Boundary AB: w = 0;

Boundary AB & CD: V = 0;

Surface ABCD: $\sigma_x = 0$.

Figure 4. Finite element model of a perfect ring [35].

The plane strain condition in the three-dimensional model is obtained by applying the displacement constraints as shown below:

$$u_j^{(i)} = 0, \ i = b, t, \ j = 1, \ldots, 16 \tag{21a}$$

$$v_1^{(i)} = v_2^{(i)} = v_5^{(i)}, v_9^{(i)} = v_{10}^{(i)} = v_{13}^{(i)}, v_{11}^{(i)} = v_{12}^{(i)} = v_{15}^{(i)}, v_6^{(i)} = v_8^{(i)}, v_{14}^{(i)} = v_{16}^{(i)}, \tag{21b}$$

$$w_1^{(i)} = w_2^{(i)} = w_5^{(i)}, w_9^{(i)} = w_{10}^{(i)} = w_{13}^{(i)}, w_3^{(i)} = w_4^{(i)} = w_7^{(i)}, w_{11}^{(i)} = w_{12}^{(i)} = w_{15}^{(i)}, w_6^{(i)} = w_8^{(i)}, w_{14}^{(i)} = w_{16}^{(i)}, \ i = b, t \tag{21c}$$

where the superscript, *i*, denotes element number.

6. Results and Discussion

Hsia and Chaudhuri [42] have established the accuracy as well as relatively rapid convergence characteristics of the present 16 node isoparametric element, employed for fully nonlinear analysis of perfect shallow homogeneous isotropic cylindrical panels. Kim and Chaudhuri [14] have shown the convergence of the critical buckling pressure, computed by the finite element analysis, of a perfect thin finite cylindrical shell; see their Table 1. They also have compared thus-converged buckling pressure, $p_{cr,FE}$, with its classical counterpart, $p_{cr,Donell}$, obtained using the Donnell shell theory [58]. The 4.5% (approximately) higher magnitude of the "converged" finite element buckling pressure (in comparison to its classical Donnell theory counterpart) is attributable to the simplified nature of the Donnell shell theory in which certain curvature effect is neglected, in a manner similar to the von Karman type nonlinearity. Chaudhuri and Hsia [44] have shown, in their Figure 2, a comparison of results, computed using their serendipity-type cubic (24-node) and the present quadratic (16-node) quadrilateral shell elements, of a homogeneous isotropic shallow thin panel. Kim and Chaudhuri [35] and Hsia and Chaudhuri [42] have examined the accuracy of the von Karman type nonlinearity on the computed response of a moderately thick isotropic ring and a thin-shallow clamped cylindrical panel, respectively.

Example 1. Pre-Buckling and Pre-Yield Response of Relatively Thin Perfect Isotropic Rings with Small-Scale Material Nonlinearity Subjected to External Pressures

Pre-buckling and pre-yield response of a relatively thin ($R_i/h = 25.64$) perfect isotropic stainless steel 316 ring with small-scale material nonlinearity, subjected to external pressure, is numerically investigated. The inner radius, R_i, and thickness, h, of the ring under investigation are 10.16 cm (4 in.) and 3.9624 mm (0.156 in.), respectively. The initial elastic properties are given as follows: *E* = 206.85 GPa (30 Msi) and ν = 0.3.

The yield stress is 206.843 MPa (30 ksi). A typical stress–strain curve for stainless steel with definitions of key material parameters is depicted in Figure 1 of Arrayago et al. [59]. The initial (pre-yield/pre-buckling) portion of the stress-strain plot for stainless steel 316, showing small scale material nonlinearity is displayed in Figure 5.

Before presenting numerical results for relatively thin isotropic perfect rings with initial small-scale material nonlinearity, those pertaining to thin and moderately thick linear elastic perfect rings are reproduced first and compared with their classical counterparts [27,28], $p_{cr,classical}$, under two different loading conditions (see Table 1 of Chaudhuri [39]). As has been discussed above in Section 4, double-symmetry conditions permit the model under consideration to be limited to only a quarter of the geometry such that the corresponding surface-parallel displacements vanish along the centerlines and the buckled shapes are assumed to be symmetric. The ring geometry is described in detail in Figure 2 of Kim and Chaudhuri [47].

A convergence check of the present analysis is available in Table 1 of Kim and Chaudhuri [47], which shows that the displacement and buckling pressure of the perfect ring converge reasonably fast with the 10 × 1 mesh, used in conjunction with the reduced integration scheme to prevent shear locking [35,47]. The present computed values for hydrostatic buckling pressure are somewhat higher than their classical counterparts,

$p_{cr,classical}$ = E/[4(h/R)^3], because of the effects of the transverse shear/normal (primarily shear) deformation and circumferential compressibility, which have softening effects, being not accounted for in the classical buckling analysis. The exact buckling pressure and displacement are, however, obtained for the constant directional pressure as shown in Table 1 of Kim and Chaudhuri [47], which are higher than the computed hydrostatic buckling pressure because of the membrane action.
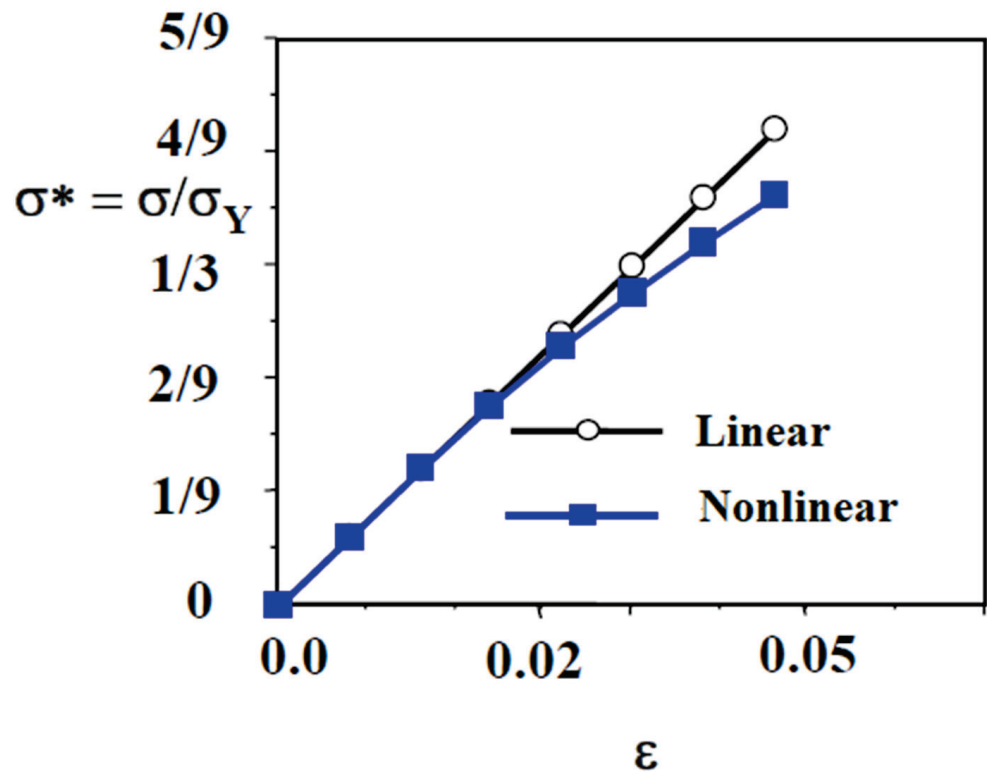

Figure 5. Initial pre-yield stress–strain curve for stainless steel 316 with initial small-scale nonlinearity.

Table 2 of Chaudhuri [39] has presented comparison of the buckling pressure, p_{cr}, computed by using the present FEA (see also Ref. [34]) with its nonlinear resonance counterpart, for the afore-mentioned two loading conditions. The relative difference, defined as, $\left| \frac{Present\ FEA - Nonlin\ Resonance}{Present\ FEA} \right|$ 100%, for the hydrostatic pressure and radial pressure loading cases are 1.006% and 1.215%, respectively, which testifies to the accuracy of both sets of results. The slight difference is possibly due to the assumption of transverse inextensibility in the nonlinear resonance analysis [39], while the present FEA permits transverse normal deformation. $p_{cr,classical}$ = 2.895 MPa (419.849262 psi).

Figure 6 presents the comparison for plots, depicting the normalized pressure, $p^* = p/p_{cr,classical}$ vs. normalized deflection, w* = w/h, of the crown of the relatively thin (R_i/h = 25.64) perfect quarter-ring (see point D, Figure 4), for linear elastic and initial small-scale nonlinear material properties. This plot shows that the pressure-deflection curve for the perfect ring with initial small-scale material nonlinearity deviates from the corresponding linear elastic response by as much as 15% (approx.) as the buckling pressure is approached (88% of $p_{cr,classical}$).
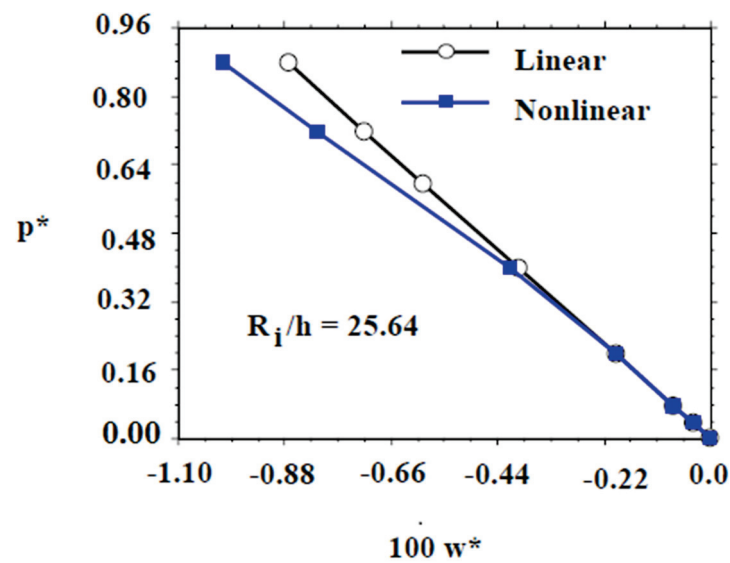
Figure 6. Normalized hydrostatic pressure vs. normalized deflection curve for a perfect relatively thin ($R_i/h = 25.64$) stainless steel 316 ring.

Figures 7 and 8 exhibit similar comparisons for plots, depicting the normalized pressure, $p^* = p/p_{cr,classical}$ vs. normalized radial or transverse (ε_r) and hoop or circumferential (ε_θ) strains, respectively, of the crown of the relatively thin ($R_i/h = 25.64$) perfect quarterring (see point D, Figure 4), for linear elastic and initial small-scale nonlinear material properties. These plots similarly show that the pressure-strain curves for the perfect ring with initial small-scale material nonlinearity deviate from their linear elastic response counterparts by as much as 16.67% and 13.64%, respectively, as the buckling pressure is approached (88% of $p_{cr,classical}$). As expected, the transverse normal strain values are about two orders of magnitude smaller than their circumferential strain counterparts, because of the relative thinness of the ring. It is interesting to observe the trends of the two deviations exhibiting opposite directions. The reason is the Poisson effect. However, the radial strains are so small, that this effect does not have any practical impact.
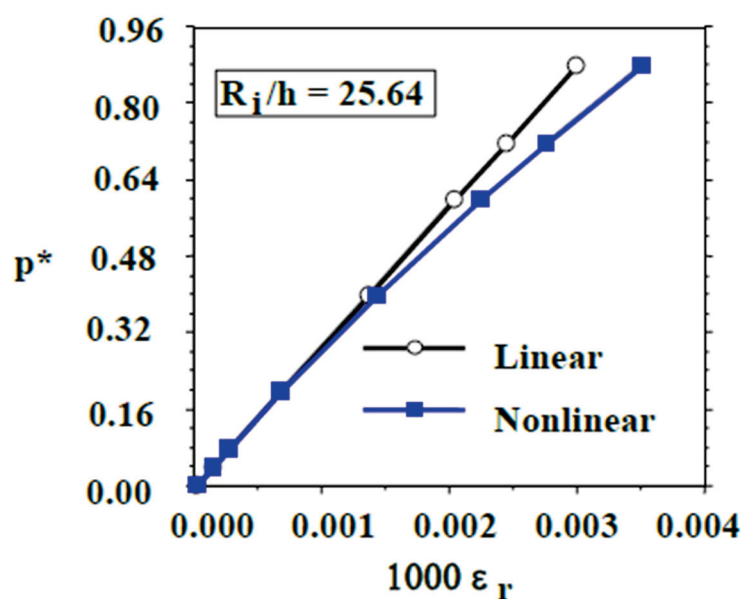
Figure 7. Normalized hydrostatic pressure vs. transverse normal strain curve for a perfect relatively thin ($R_i/h = 25.64$) stainless steel 316 ring.
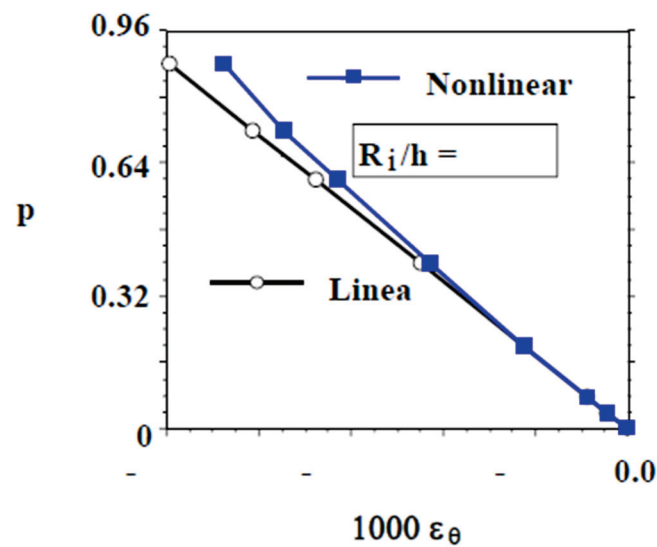
Figure 8. Normalized hydrostatic pressure vs. circumferential strain curve for a perfect relatively thin ($R_i/h = 25.64$) stainless steel 316 ring.

Plots, depicting the normalized pressure, $p^* = p/p_{cr,classical}$ vs. normalized circumferential or hoop ($\sigma_\theta* = \sigma_\theta/\sigma_Y$) stress, of the crown of the relatively thin ($R_i/h = 25.64$) perfect quarter-ring, for linear elastic and initial small-scale nonlinear material properties, are displayed in Figure 9. Again, the pressure vs. hoop stress curve for the perfect ring with initial small-scale material nonlinearity deviates from its linear elastic response counterpart by as much as 10.89% (approx.) as the buckling pressure is approached (88% of $p_{cr,classical}$). These enhanced responses due to initial small-scale nonlinearity are significant enough to not miss attentions from designers and operators of submersibles alike.
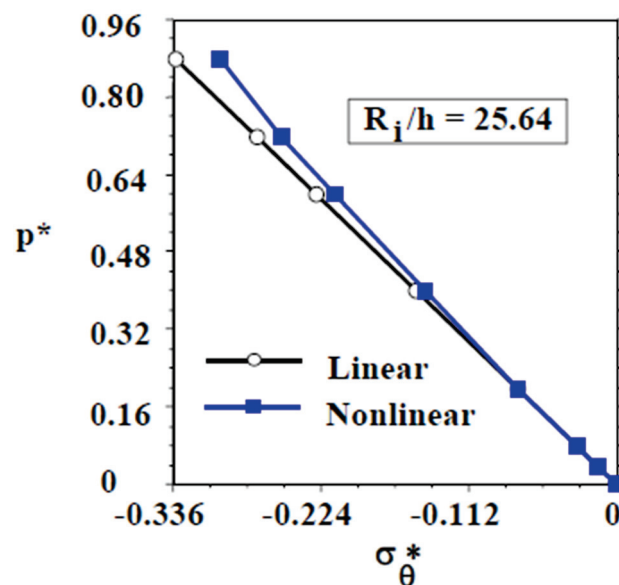
Figure 9. Normalized hydrostatic pressure vs. circumferential stress curve for a perfect relatively thin ($R_i/h = 25.64$) stainless steel 316 ring.

7. Summary and Conclusions

The effects of initial small-scale material nonlinearity on the pre-yield and pre-buckling response of externally pressurized metallic (plane strain) perfect rings (very long cylindrical shells) is investigated. The cylindrically curved 16-node isoparametric element, based on an assumed quadratic displacement field (in surface-parallel coordinates) and the assumption

of linear distribution of displacements through thickness (LDT), is utilized to obtain the discretized system of equations. The effect of initial small-scale material nonlinearity (assumed hypo-elastic) on the deformation and stress field in the pre-yield stress and pre-buckling regime of a perfect relatively thin (R_i/h = 25.64) metallic very long cylindrical shell (plane strain ring) is numerically investigated, with the objective of understanding its early-stage compressive behavior. What follows is a list of useful and physically meaningful conclusions drawn from the numerical results:

(i) Initial small-scale material nonlinearity has a pronounced effect on the pre-yield stress and pre buckling compressive response a perfect metallic relatively thin (R_i/h = 25.64) very long cylindrical shell (plane strain ring) under investigation.

(ii) Numerical results suggest that the pressure-deflection curve for a perfect relatively thin (R_i/h = 25.64) stainless steel 316 ring with initial small-scale material nonlinearity deviates from the corresponding linear elastic response by as much as 15% (approx.) as the buckling pressure is approached (88% of $p_{cr,classical}$).

(iii) The pressure vs. transverse and circumferential strain curves for the perfect relatively thin (R_i/h = 25.64) stainless steel 316 ring with initial small-scale material nonlinearity deviate from their linear elastic response counterparts by as much as 16.67% and 13.64%, respectively, as the buckling pressure is approached (88% of $p_{cr,classical}$).

(iv) The transverse normal strain values are about two orders of magnitude smaller than their circumferential strain counterparts, because of the relative thinness of the ring.

(v) The pressure vs. hoop stress curve for the perfect relatively thin (R_i/h = 25.64) stainless steel 316 ring with initial small-scale material nonlinearity deviates from its linear elastic response counterpart by as much as 10.89% (approx.) as the buckling pressure is approached (88% of $p_{cr,classical}$).

(vi) These enhanced responses for metallic rings due to initial small-scale nonlinearity are significant enough to not miss attentions from designers and operators of submersibles alike.

Nomenclature

$[\mathbf{B}_{LL}]$	Linear differential operator matrix relating the linear incremental strain components to incremental displacement components
b, t	Subscript or superscript indicating the bottom and the top surface, respectively
C_{ijrs}	Incremental elastic stiffness (material property) tensor
$^{t+\Delta t}_{d}S$	Differential loading surface area evaluated at the first iteration of each load step when hydrostatic pressure is applied
dV	Infinitesimal control volume
$\bar{e}_{ij}$	Linear incremental component of the 6×1 strain vector
$\{f_L\}$	Applied load vector
$^{t+\Delta t}\{f_L\}$	Applied load vector at the time $t + \Delta t$

$\{f_N\}$	Nonlinear internal force vector
$^{t+\Delta t}\{f_N\}^{(i)}$	Nonlinear internal force vector at the *i*th iteration of the time step between *t* and *t* + Δ*t*
$g_j(z)$	Coefficient of the first fundamental differential quadratic form of a parallel surface in the *j*th direction, *j* = 1 (*x*), 2 (*θ*), 3 (*z*)
$\bar{g}_\theta$	Coefficient of the first fundamental differential quadratic form of the bottom surface in the θ direction
h	Thickness of the shell/ring
$[K_L]$	Linear global stiffness matrix
m, n	Ratio of reference yield stress to the corresponding modulus, and strain hardening parameter, respectively, in the Ramberg-Osgood representation
N	Total number of elements
$\mathbf{n}^{(t)}$	Unit normal vector for the top surface with respect to the fixed coordinate system
p_r, p	Applied general and uniform, respectively, hydrostatic pressure
p_{cr}	Classical buckling pressure of a long cylindrical shell (plane strain ring)
$[Q]$, Q_{ij}	Incremental elastic stiffness (material property) matrix, and its components, respectively
R_i	Inner radius of a long perfect cylindrical shell (plane strain ring)
$^{t+\Delta t}R$	External virtual work done on a body
r	Radial coordinate of a point in an undeformed perfect ring
$^{t+\Delta t}S$	Loading surface area evaluated at the first iteration of each load step when hydrostatic pressure is applied
S_{ij}	Incremental stress component
$^{t+\Delta t}S_{ij}$	Second Piola-Kirchhoff stress tensor at time *t* + Δ*t*
$^{t}\hat{S}_{ij}$	9 × 9 stress matrix evaluated at time *t*
$^{t}\bar{S}_{ij}$	6 × 1 stress vector evaluated at time *t*
t	Time as an index
U_{bj}, V_{bj}, W_{bj}	Incremental nodal displacement components at the *j*th node on the bottom surface in x_1 (or *x*), x_2 (or *θ*), and *z* directions, respectively
U_{tj}, V_{tj}, W_{tj}	Incremental nodal displacement components at the *j*th node on the top surface in x_1 (or *x*), x_2 (or *θ*), and *z* directions, respectively
x, θ, z	Coordinates of a point
$^{t+\Delta t}\bar{\varepsilon}_{ij}$	Total Green-Lagrangian strain tensor evaluated at time *t* + Δ*t*
ε_f, f, ε_e	Force and energy convergence criteria, respectively
$[\Phi]$	Quadratic global interpolation function matrix
$\psi_j(r', s')$	Quadratic element interpolation function in terms of r' and s'

Appendix A. Definition of Certain Matrix Operators

The matrix $[\mathbf{B}_{LL}]$ referred to in Equations (14) and (15a,b) is given by [18,19,43]

$$[\mathbf{B}_{LL}] = \begin{bmatrix} \frac{\partial}{\partial x} & 0 & 0 \\ 0 & \frac{1}{g_\theta}\frac{\partial}{\partial \theta} & \frac{1}{g_\theta} \\ 0 & 0 & \frac{\partial}{\partial z} \\ 0 & \frac{\partial}{\partial z} - \frac{1}{g_\theta} & \frac{1}{g_\theta}\frac{\partial}{\partial \theta} \\ \frac{\partial}{\partial z} & 0 & \frac{\partial}{\partial x} \\ \frac{1}{g_\theta}\frac{\partial}{\partial \theta} & \frac{\partial}{\partial x} & 0 \end{bmatrix}, \tag{A1}$$

The layer-wise linear distribution of displacement matrix, $[T_{BT}]$, referred to in Equations (14) and (15a,b), can be written as follows:

$$[T_{BT}(z)] = \begin{bmatrix} 1 - \frac{z}{h} & & & \frac{z}{h} & & \\ & 1 - \frac{z}{h} & & & \frac{z}{h} & \\ & & 1 - \frac{z}{h} & & & \frac{z}{h} \end{bmatrix}, \tag{A2}$$

The quadratic global interpolation function matrix, $[\Phi]$, referred to in Equations (14) and (15a,b), is given by [18,19,34,43]

$$[\Phi(r',s')] = \begin{bmatrix} \{\psi\} & \{0\} & \{0\} & \{0\} & \{0\} & \{0\} \\ \{0\} & \{\psi\} & \{0\} & \{0\} & \{0\} & \{0\} \\ \{0\} & \{0\} & \{\psi\} & \{0\} & \{0\} & \{0\} \\ \{0\} & \{0\} & \{0\} & \{\psi\} & \{0\} & \{0\} \\ \{0\} & \{0\} & \{0\} & \{0\} & \{\psi\} & \{0\} \\ \{0\} & \{0\} & \{0\} & \{0\} & \{0\} & \{\psi\} \end{bmatrix}, \tag{A3}$$

wherein

$$\{\psi\} = \{\psi_1\ \psi_2\ \psi_3\ \psi_4\ \psi_5\ \psi_6\ \psi_7\ \psi_8\}, \tag{A4}$$

and $\{0\}$ is 1×8 null matrix. $\psi_j(r',s')$, $j = 1, \ldots, 8$, are the shape functions as used for displacements and coordinates. Finally, stress vector, $\left\{{}^t\overline{S}_{ij}\right\}$, referred to in Equation (15b), is given as follows:

$$\left\{{}^t\overline{S}_{ij}\right\}^T = \left\{{}^tS_{11}\ {}^tS_{22}\ {}^tS_{33}\ {}^tS_{23}\ {}^tS_{13}\ {}^tS_{12}\right\}. \tag{A5}$$

References

1. Casey, S. The Abyss: The Titan Submersible Disaster Was Years in the Making, New Details Reveal. Vanit, 17 August 2023. Available online: https://www.vanityfair.com/news/2023/08/titan-submersible-implosion-warnings (accessed on 29 January 2024).
2. Couch, W.P.; Ward, G.D.; Blumenberg, W.F. *Investigation of Filament-Reinforced Plastic Deep Submergence Pressure Hulls July 1966 to March 1969*; Department of the Navy, Naval Ship Research & Development Center: Washington, DC, USA, 1969.
3. Garala, H.J. *Structural Evaluation of 8-Inch Diameter Graphite-Epoxy Composite Cylinders Subjected to External Hydrostatic Compressive Loading*; DTRC Report 89/016; David Taylor Research Center: Bethesda, MD, USA, 1989.
4. Garala, H.J.; Chaudhuri, R.A. Structural evaluation of advanced composite thick-section cylinders under bi-axial compressive loading. In *Mechanics of Thick Composites*; Rajapakse, Y., Ed.; ASME AMD: New York, NY, USA, 1993; Volume 162, pp. 227–236.
5. Hahn, H.T.; Sohi, M.M. Buckling of a fiber bundle embedded in epoxy. *Compos. Sci. Technol.* **1986**, *27*, 25–41. [CrossRef]
6. Abdallah, M.G.; Gascoigne, H.E.; Cairnes, D.S.; Patton, K.B. Measurement of deformation in thick composite rings subjected to external pressure. In Proceedings of the SEM's Spring Conference on Experimental Mechanics and Manufacturer's Exhibit, Albuquerque, NM, USA, 4–6 June 1990.
7. Chaudhuri, R.A. Prediction of the compressive strength of thick-section advanced composite laminates. *J. Compos. Mater.* **1991**, *25*, 1244–1276. [CrossRef]
8. Chaudhuri, R.A.; Garala, H.J. Analytical/experimental evaluation of hybrid commingled carbon/glass/epoxy thick-section composites under compression. *J. Compos. Mater.* **1995**, *29*, 1695–1718. [CrossRef]
9. Hunt, G.W.; Lucena Neto, E. Localized buckling in long axially-loaded cylindrical shells. *J. Mech. Phys. Solids* **1991**, *39*, 881–894. [CrossRef]
10. Chaudhuri, R.A. A nonlinear zigzag theory for finite element analysis of highly shear-deformable laminated anisotropic shells. *Compos. Struct.* **2008**, *85*, 350–359. [CrossRef]
11. Chaudhuri, R.A.; Kim, D. On propagation of shear crippling (kinkband) instability in a long imperfect laminated composite cylindrical shell under external pressure. *Int. J. Solids Struct.* **1997**, *34*, 3455–3486. [CrossRef]
12. Chaudhuri, R.A.; Kim, D. Localization and shear-crippling (kinkband) instability in a thick imperfect laminated composite ring under hydrostatic pressure. *Int. J. Solids Struct.* **2003**, *40*, 7063–7092. [CrossRef]
13. Kim, D.; Chaudhuri, R.A. Effect of lamination sequence on the localization and shear crippling instability in thick imperfect cross-ply rings under external pressure. *Compos. Struct.* **2007**, *80*, 504–513. [CrossRef]
14. Kim, D.; Chaudhuri, R.A. Influence of localized imperfection on the instability of isotropic/cross-ply cylindrical shells/rings under external pressure. *Compos. Struct.* **2005**, *67*, 57–70. [CrossRef]
15. Chaudhuri, R.A. Effects of thickness and fibre misalignment on compression fracture in cross-ply (very) long cylindrical shells under external pressure. *Proc. R. Soc. A Lond.* **2015**, *471*, 20150147. [CrossRef]
16. Chaudhuri, R.A. Effects of fiber misalignment and transverse shear modulus on localization and shear crippling instability in thick imperfect cross-ply rings under external pressure. *Compos. Struct.* **2008**, *82*, 587–599. [CrossRef]
17. Chaudhuri, R.A.; Kim, D. Influence of localized imperfection and surface-parallel shear modulus nonlinearity on the instability of a thin cross-ply cylindrical shell under external pressure. *Compos. Struct.* **2008**, *82*, 235–244. [CrossRef]
18. Chaudhuri, R.A.; Kim, D. Sensitivity of the post-localization response of a thick cross-ply imperfect ring to transverse Young's modulus nonlinearity. *Compos. Struct.* **2008**, *84*, 44–55. [CrossRef]
19. Chaudhuri, R.A.; Kim, D. Effects of thickness and transverse shear modulus nonlinearity on the post-"yield" and post-localization response of an externally pressurized imperfect cross-ply ring. *Compos. Struct.* **2009**, *88*, 83–96. [CrossRef]

20. Chaudhuri, R.A. Stress intensity factor and energy release rate of externally pressurized thick cross-ply (very) long cylindrical shells with low-hardening transverse shear modulus nonlinearity. *Eng. Fract. Mech.* **2016**, *151*, 138–160. [CrossRef]

21. Chaudhuri, R.A. Localization, delocalization and compression fracture in externally pressurized thick cross-ply (very) long cylindrical shells with material non-linearity: A multi-scale and multi-physics analysis. *Int. J. Non-Linear Mech.* **2016**, *84*, 68–81. [CrossRef]

22. Chaudhuri, R.A. Comparison of stress singularities of kinked carbon and glass fibres weakening compressed unidirectional composites: A three-dimensional trimaterial junction stress singularity analysis. *Philos. Mag.* **2014**, *94L*, 625–667. [CrossRef]

23. Chaudhuri, R.A. A micro-kink theory for determination of shear modulus of a unidirectional composite lamina. *Compos. Struct.* **2010**, *92*, 395–400. [CrossRef]

24. Chaudhuri, R.A.; Xie, M.S.; Garala, H.J. Stress singularity due to kink band weakening a unidirectional composite under compression. *J. Compos. Mater.* **1996**, *30*, 672–691. [CrossRef]

25. Moran, P.M.; Shih, C.F. Kink band propagation and broadening in ductile matrix fiber composites, experiments and analysis. *Int. J. Solids Struct.* **1998**, *35*, 1709–1722. [CrossRef]

26. Gutkin, R.; Pinho, S.T.; Robinson, P.; Curtis, P.T. On the transition from shear-driven fibre compressive failure to fibre kinking in notched CFRP laminates under longitudinal compression. *Compos. Sci. Tech.* **2010**, *70*, 1223–1231. [CrossRef]

27. Timoshenko, S.P.; Gere, J.M. *Theory of Elastic Stability*, 2nd ed.; McGraw-Hill: New York, NY, USA, 1961.

28. Simitses, G.J. Buckling and post-buckling of imperfect cylindrical shells: A review. *Appl. Mech. Rev.* **1986**, *39*, 1517–1524. [CrossRef]

29. Jones, R.M.; Morgan, H.S. Buckling and vibration of cross-ply laminated circular cylindrical shells. *AIAA J.* **1975**, *13*, 664–671. [CrossRef]

30. Bradford, M.A.; Uy, B.; Pi, Y.L. In-plane elastic stability of arches under a central load. *ASCE J. Eng. Mech.* **2002**, *128*, 710–719. [CrossRef]

31. Fu, L.; Waas, A.M. Initial postbuckling behavior of thick rings under uniform external hydrostatic pressure. *ASME J. Appl. Mech.* **1995**, *62*, 338–345. [CrossRef]

32. Wu, B.; Yu, Y.; Li, Z. Analytical approximations to large post-buckling deformation of elastic rings under uniform hydrostatic pressure. *Int. J. Mech. Sci.* **2007**, *49*, 661–668. [CrossRef]

33. Djondjorov, P.A.; Vassilev, V.M.; Mladenov, I.M. Analytic description and explicit parametrization of the equilibrium shapes of elastic rings and tubes under uniform hydrostatic pressure. *Int. J. Mech. Sci.* **2011**, *53*, 355–364. [CrossRef]

34. Kim, D.; Chaudhuri, R.A. Effect of thickness on buckling of perfect cross-ply rings under external pressure. *Compos. Struct.* **2007**, *81*, 525–532. [CrossRef]

35. Kim, D.; Chaudhuri, R.A. Postbuckling of moderately thick imperfect rings under external pressure. *ASCE J. Eng. Mech.* **2006**, *132*, 1273–1276. [CrossRef]

36. Kerdegarbakhsh, M.; Kiani, Y.; Esfahani, S.E.; Eslami, M.R. Postbuckling of FGM rings. *Int. J. Solids Struct.* **2014**, *85*, 187–195. [CrossRef]

37. Asemi, K.; Kiani, Y. Postbuckling up to collapse of polar orthotropic linearly elastic rings subjected to external pressure. *Int. J. Struct. Stab. Dyn.* **2016**, *16*, 1450091. [CrossRef]

38. Kim, D.; Chaudhuri, R.A. Postbuckling behavior of symmetrically laminated thin shallow circular arches. *Compos. Struct.* **2009**, *87*, 101–108. [CrossRef]

39. Chaudhuri, R.A. A nonlinear resonance (eigenvalue) approach for computation of elastic collapse pressures of harmonically imperfect relatively thin rings. *Thin-Walled Struct.* **2018**, *127*, 344–353. [CrossRef]

40. Chaudhuri, R.A.; Kim, D.; Pavliga, J.R. A nonlinear resonance (eigenvalue) approach for computing elastic collapse pressure of a moderately thick cross-ply imperfect ring. *Compos. Struct.* **2008**, *82*, 117–126. [CrossRef]

41. Chaudhuri, R.A.; Kim, D.; Pavliga, J.R. Effects of thickness and modal imperfection amplitude on elastic collapse pressure of a cross-ply imperfect ring. *Compos. Struct.* **2008**, *86*, 370–384. [CrossRef]

42. Hsia, R.L.; Chaudhuri, R.A. Geometrically nonlinear analysis of cylindrical shells using surface-parallel quadratic elements. *Comput. Struct.* **1996**, *61*, 1143–1154. [CrossRef]

43. Kim, D.; Chaudhuri, R.A. Full and von Karman geometrically nonlinear analyses of laminated cylindrical panels. *AIAA J.* **1995**, *33*, 2173–2181. [CrossRef]

44. Chaudhuri, R.A.; Hsia, R.L. Effect of thickness on large-deflection behavior of shells. *AIAA J.* **1999**, *37*, 403–405. [CrossRef]

45. Chaudhuri, R.A.; Hsia, R.L. Effect of thickness on the large elastic deformation behavior of laminated shells. *Compos. Struct.* **1999**, *44*, 117–128. [CrossRef]

46. Chaudhuri, R.A. Localization, delocalization, and compression fracture in moderately thick transversely isotropic bilinear rings under external pressure. *ASME J. Eng. Mater. Technol.* **2006**, *128*, 603–610. [CrossRef]

47. Kim, D.; Chaudhuri, R.A. Localized buckling of a bilinear elastic ring under external pressure. *ASCE J. Eng. Mech.* **2005**, *131*, 221–224. [CrossRef]

48. Chaudhuri, S.N.; Chaudhuri, R.A.; Benner, R.E.; Penugonda, M. Raman spectroscopy for characterization of interfacial debonds between carbon fibers and polymer matrices. *Compos. Struct.* **2006**, *76*, 375–387. [CrossRef]

49. Bathe, K.J. *Finite Element Procedures in Engineering Analysis*; Prentice-Hall: Englewood Cliffs, NJ, USA, 1982.

50. Chaudhuri, R.A. A degenerate triangular shell element with constant cross-sectional warping. *Comput. Struct.* **1988**, *28*, 315–325. [CrossRef]

51. Seide, P.; Chaudhuri, R.A. Triangular finite element for analysis of thick laminated shells. *Int. J. Numer. Methods Eng.* **1987**, *24*, 1563–1579. [CrossRef]

52. Chaudhuri, R.A. A new three-dimensional shell theory in general (non-lines-of-curvature) coordinates for analysis of curved panels weakened by through/part-through holes. *Compos. Struct.* **2009**, *89*, 321–332. [CrossRef]

53. Chaudhuri, R.A.; Seide, P. An approximate method for prediction of transverse shear stresses in a laminated shell. *Int. J. Solids Struct.* **1987**, *23*, 1145–1161. [CrossRef]

54. Chaudhuri, R.A. On the prediction of interlaminar shear stresses in a thick laminated general shell. *Int. J. Solids Struct.* **1990**, *26*, 499–510. [CrossRef]

55. Ramberg, W.; Osgood, W.R. *Description of Stress Strain Curves by Three Parameters*; NACA-TN 902; National Advisory Committee for Aeronautics: Washington, DC, USA, 1934.

56. Chaudhuri, R.A.; Abu-Arja, K.R. Plastic deformation of a boron/aluminum tube under multi-axial loadings. *Comput. Struct.* **1986**, *24*, 915–921. [CrossRef]

57. Bathe, K.J.; Cimento, A.P. Some practical procedures for the solution of nonlinear finite element equations. *J. Comput. Meth. Appl. Mech. Eng.* **1980**, *22*, 59–85. [CrossRef]

58. Amazigo, J.C.; Frazer, W.B. Buckling under external pressure of cylindrical shells with dimple shaped initial imperfections. *Int. J. Solids Struct.* **1971**, *7*, 883–900. [CrossRef]

59. Arrayago, I.; Real, E.; Gardner, L. Description of stress–strain curves for stainless steel alloys. *Mater. Design* **2015**, *87*, 540–552. [CrossRef]

Current Status, Sizing Methodologies, Optimization Techniques, and Energy Management and Control Strategies for Co-Located Utility-Scale Wind–Solar-Based Hybrid Power Plants: A Review

Shree O. Bade *, Ajan Meenakshisundaram and Olusegun S. Tomomewo *

College of Engineering & Mines, Energy and Petroleum Department, University of North Dakota, Grand Forks, ND 58202, USA

* Correspondence: shree.bade@und.edu (S.O.B.); olusegun.tomomewo@und.edu (O.S.T.)

Abstract: The integration of renewable energy sources, such as wind and solar, into co-located hybrid power plants (HPPs) has gained significant attention as an innovative solution to address the intermittency and variability inherent in renewable systems among plant developers because of advancements in technology, economies of scale, and government policies. However, it is essential to examine different challenges and aspects during the development of a major work on large-scale hybrid plants. This includes the need for optimization, sizing, energy management, and a control strategy. Hence, this research offers a thorough examination of the present state of co-located utility-scale wind–solar-based HPPs, with a specific emphasis on the problems related to their sizing, optimization, and energy management and control strategies. The authors developed a review approach that includes compiling a database of articles, formulating inclusion and exclusion criteria, and conducting comprehensive analyses. This review highlights the limited number of peer-reviewed studies on utility-scale HPPs, indicating the need for further research, particularly in comparative studies. The integration of machine learning, artificial intelligence, and advanced optimization algorithms for real-time decision-making is highlighted as a potential avenue for addressing complex energy management challenges. The insights provided in this manuscript will be valuable for researchers aiming to further explore HPPs, contributing to the development of a cleaner, economically viable, efficient, and reliable power system.

Keywords: control strategies; energy management strategies; hybrid power plant; optimal sizing; optimization; utility-s

1. Introduction

The importance of sustainable energy sources in mitigating global greenhouse gas emissions and ensuring a reliable energy supply is underscored by both the Paris Agreement and the United Nations Sustainable Development Goals [1]. Adopting new, clean, and renewable energy sources (RESs) helps decarbonize the transportation and power generation industries. Research and development, economies of scale, and government policies have driven recent improvements in wind and solar energy technology. As a result, wind and solar are becoming more cost-competitive with conventional fossil fuels [2,3], and traditional power plants are gradually decommissioning [4].

There is limited market penetration for wind and solar energy, resulting in a lesser need for dispatchable renewable energy plants. As renewable energy usage increases, these facilities will play a crucial role in providing grid services, ensuring a consistent electricity supply [3], and addressing any issues arising from unknown resources, grid problems, or unusual situations [5]. Unpredictable weather patterns and geographical location-dependent availability limit the effectiveness of renewable energy, severely impacting the

reliability and stability of their power supply and necessitating the use of complementary sources like batteries.

Several studies have looked into ways to deal with the problem that wind and solar resources change over time. These have included storing and limiting resources [6–8] to make them more useful, combining hybrid resources like hydropower [9], bioenergy [10], hydrogen/fuel cells [11], and the possibility of wind and solar resources working together [2,12–14]. Previous studies [13,15–18] have highlighted that researchers mainly studied wind and solar hybrid systems for off-grid environments, focusing on small-scale generation units to reduce reliance on fossil fuel generators and fulfill specific energy needs. Therefore, this study refers to HPPs (>1 MW) as co-located utility-scale wind farms and solar farms with or without battery storage connected at the point of common connection (PCC). Several key factors drive the main motivations behind HPPs compared with standalone renewable power plants or standalone energy storage [2,7,12,14]. Wind and solar power combine to counteract each energy source's intermittent power output, ensuring stable, continuous power output. Wind turbines generate power on windy days with limited sunlight, while solar panels produce electricity on cloudy or low-wind days, ensuring a stable electricity supply. The negative correlation between wind and solar resources helps provide more consistent power for hybrid plants [2]. In markets with no direct correlation between wind and solar resources, HPPs can benefit from power dispatching. If electricity market prices show a negative correlation with wind power, HPPs can capitalize on their solar resources to generate revenue during high market prices [2]. They promote energy independence by reducing reliance on centralized power plants and distant energy sources, ensuring a reliable and stable electricity supply. Therefore, HPPs that consist of wind, solar, and energy storage have been active in research.

Manufacturers and project developers are currently developing HPPs to ensure their economic viability in markets with a high demand for predictable and manageable energy supply to maintain grid reliability and dispatchability [13]. However, the installation costs remain high. On top of this, combining these technologies intensifies the complexity, requiring additional models specific to each discipline, understanding power generation sources, and accommodating supplementary design variables [2]. Therefore, efficient sizing and optimization methodologies, as well as energy management and control strategies, are essential to exploring the optimal configuration of parameters such as system cost, reliability, and the size of photovoltaic systems, batteries, and wind turbines.

Researchers have documented numerous methodologies in the literature related to sizing [3,19–22], optimization [23,24], and various tools [2,25–27] that consider economic and reliability factors. The economic assessment of renewable energy entails an analysis of total expenses, cost of energy (COE), annualized system cost (ASC), levelized cost of energy (LCOE), and life cycle cost (LCC) [21,22,28]. It takes into account initial investment, operational and maintenance costs, as well as replacement expenses. The assessment of reliability involves examining the disparity between the supply of renewable energy and the corresponding demand, employing several metrics such as loss of load probability (LLP), loss of power supply probability (LSSP), renewable fraction (RF), energy unmet, and renewable energy factor (REF).

Constraints related to minimizing grid-injected power, decreasing fluctuation rates, and improving the utilization factor guide system size optimization. These considerations, along with the main objective of minimizing costs, collectively shape the optimization process [29]. Achieving the best possible design of an HPP requires careful consideration of technical, economic, reliability, environmental, and social factors to ensure the best possible design feasibility. The Appendix A (Table A1) provides a detailed description of these factors.

Recent research has shown a preference for hybrid methodologies over traditional methods, as well as an increase in modern algorithmic techniques [30], relying on individual artificial intelligence (AI) algorithms and hybrid methods, which are gaining prominence compared with traditional methods because of their capabilities in resolving intricate

optimization challenges. These techniques primarily consider multi-objective functions, mainly cost and LPSP [31,32], with other criteria like COE, LPSP, REF, etc., as constraints [33]. Iterative, graphical, probabilistic, and analytical techniques, including algorithms like the genetic algorithm (GA) and particle swarm optimization (PSO) [23,24], achieved the objectives. Commercially available software tools, such as HOMER, aid in sizing and optimizing standalone solar photovoltaic and wind-based systems, identifying optimal energy system sizes, and conducting sensitivity analyses to explore varying input variables or uncertainties. Energy management [11,34,35] and control strategies [3,13,34,36–42] drive the effective functioning of HPPs, enhance system performance, and meet energy demands. Various methods, such as centralized, distributed, and hybrid, control hybrid renewable power systems. Most energy management methods focus on power requirements and economic, technical, and techno-economic-oriented strategies [42,43], making it critical to establish a well-defined and suitable management approach. Figure 1 illustrates the overall scope of this study. Appendix A (Table A2) summarizes the essential findings from the review studies.
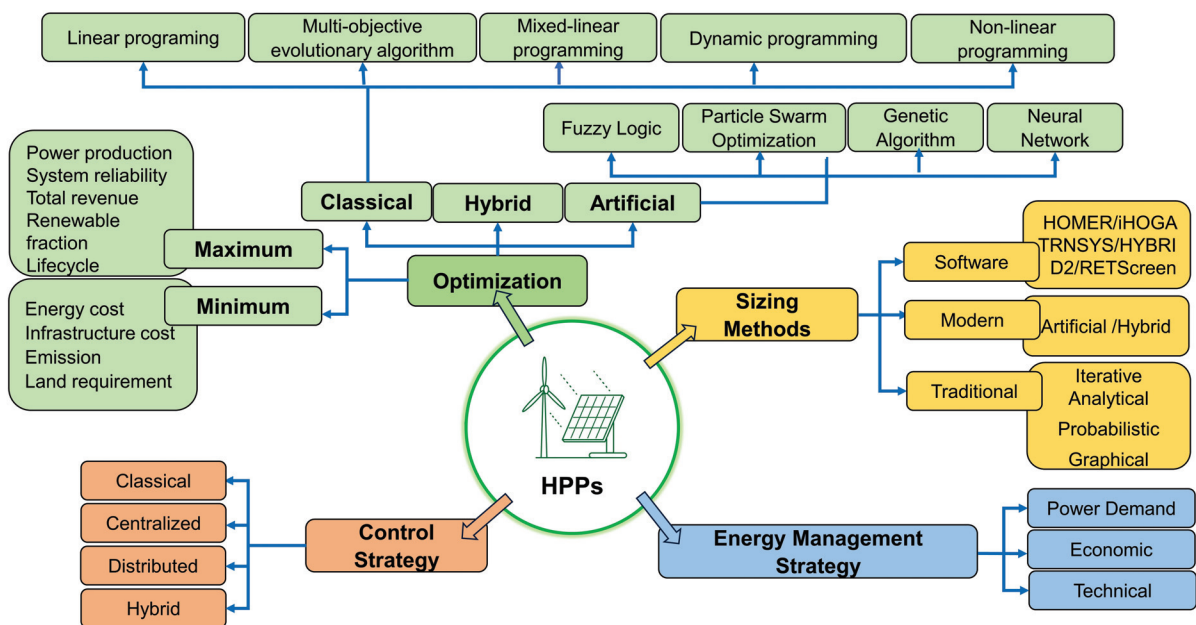
Figure 1. Graphical representation of the scope of this study.

Contribution of this Review Paper

The absence of a universally agreed-upon definition for HPPs presents a challenge in exploring this emerging field. This discrepancy could lead to misleading conclusions, given the limited literature on co-located utility-scale HPPs. Despite the potential benefits of HPPs, particularly in co-locating wind and solar farms, their long-term economic viability remains uncertain. However, the studies conducted thus far have not placed significant attention on the exploration of optimization, size, and energy management, specifically within the context of utility-scale operations. This study aims to fill this research gap by examining various energy management and control tactics, optimization techniques, and sizing methodologies employed by the research community over the past decade using wind and solar energy. Researchers use an interdisciplinary approach to bridge the knowledge gap and enhance the efficiency of utility-scale HPPs in the renewable energy sector. This study also serves as a valuable resource for developers and researchers engaged in HPPs, providing them with the means to evaluate decision-making tools, energy management, and control strategies to optimize the financial performance of these projects. This assessment considers various factors, including local resources, land availability, costs, and market prices. Recent developments in HPPs are comprehensively analyzed in this article, offering readers a convenient source of information categorized according

to their specific interests. Additionally, this study aims to enhance knowledge and foster discussions among policymakers, academics, and industry professionals.

This study includes sections that cover a review approach, exploration of various available topologies in the scientific literature, the global status of HPPs, optimization techniques, sizing methodologies, energy management systems and control strategies, discussions, challenges, and future aspects of HPPs, and conclusions.

2. Review Approach

The evaluation of the existing literature on the sizing, optimization, energy management, and control strategies of utility-scale HPPs involved the following procedure: The first stage involved gathering a wide range of scholarly articles from several databases and online platforms, such as Science Direct, Google Scholar, IEEE Xplore, and Web of Science. Since utility-scale HPPs are in their early stages, there is limited research, which mainly comprises wind and solar. By extrapolating key findings and methodologies from HRES studies, the authors intend to shed light on the potential applicability and viability of these insights within the context of HPPs. The data collection process involved a four-step approach, as shown in Figure 2. Initially, a Boolean search was conducted, utilizing the following combination of keywords: ("large-scale hybrid power plant" OR "hybrid renewable energy system") AND ("optimization software tools" OR ("optimal sizing" OR sizing")) OR ("energy management" AND "control strategies"). The focus was limited to the database's topic section, encompassing article titles, abstracts, and keywords, as well as all possible combinations thereof. All articles chosen exclusively covered hybrid systems that incorporated both wind and PV elements.
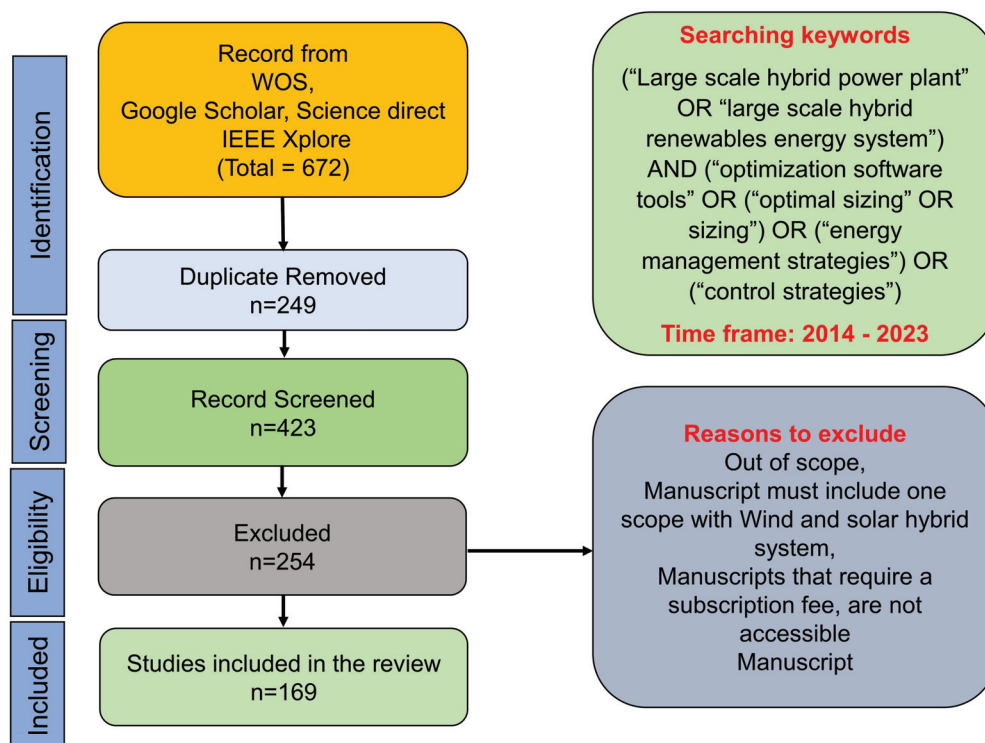
Figure 2. PRISMA model for the literature selection.

Subsequently, the acquired research papers underwent a screening process adhering to predetermined criteria for inclusion and exclusion. Inclusion criteria encompassed studies focused on co-located wind and solar plants coupled with or without energy storage. This hybrid must include either optimization techniques, sizing methodologies, energy management systems, or control strategies. Exclusion criteria pertained to studies out of scope, centered on single-source renewable energy systems, and those that did not employ

optimization techniques or energy management systems and control strategies. This study also excluded the hybrid system used for residential applications, papers that required a paid subscription, and papers not published in the English language. The results from the chosen studies were then put together to give a full picture of the latest progress in system optimization, EMS, and control strategies for HPPs that store energy.

Utility-scale HPPs are in the early stages of implementation compared with the hybrid renewable energy system (HRES); therefore, the authors mainly focused on a decade-long timeframe, i.e., 2014–2023. Initially, the search yielded 672 articles from the IEEE Xplore, Google Scholar, Science Direct, and Web of Science (WoS) databases, as illustrated in Figure 2. Endnote software version 20 was used to merge the results and eliminate duplicates. The abstract and conclusion sections of the remaining articles were scrutinized to ascertain the relevance to the objectives of this review study. This narrowed down the number of articles to 171. To summarize, each collected article was meticulously studied to acquire a comprehensive grasp of the research findings.

3. Topologies and Configuration

The basic components of the reviewed HPPs mainly comprise wind farms, solar farms, and battery storage. Several studies have analyzed the arrangement of co-located wind–solar hybrid power facilities. Petersen et al. [36] described two different configurations for co-located wind solar-based HPPs, in which wind is the main energy source. These configurations provide choices for either grid connection or off-grid operation. Additionally, Vivas illustrated different topologies based on grid connection and integration techniques [11]. The deployment of HPPs as standalone or grid-connected operations depends on the application's requirements and available funds. Standalone HPP systems continue to meet load demands while operating independently from the grid. However, because of resource constraints and excess energy waste, this strategy poses performance and reliability issues [11]. Technically and economically, it works best when connecting to the grid is either too expensive or unfeasible.

On the other hand, a grid-connected system allows for bidirectional power flow by integrating an HPP with the main electrical grid. When the production of renewable energy is inadequate, this feature enables the system to take power from the grid and return excess energy when the need for renewable energy is greater [11,44]. Solar and wind power plants can be set up in three different ways, as explained in [7,11,45,46], including the following: an AC-coupled topology (Figure 3), a DC-coupled topology (Figure 4), or a hybrid DC/AC-coupled topology (Figure 5). Several studies have noted the AC-coupled system as the most common form of hybrid power plants [3,8,37–39]. Table 1 compares the advantages and disadvantages of each method with the coupling topology.
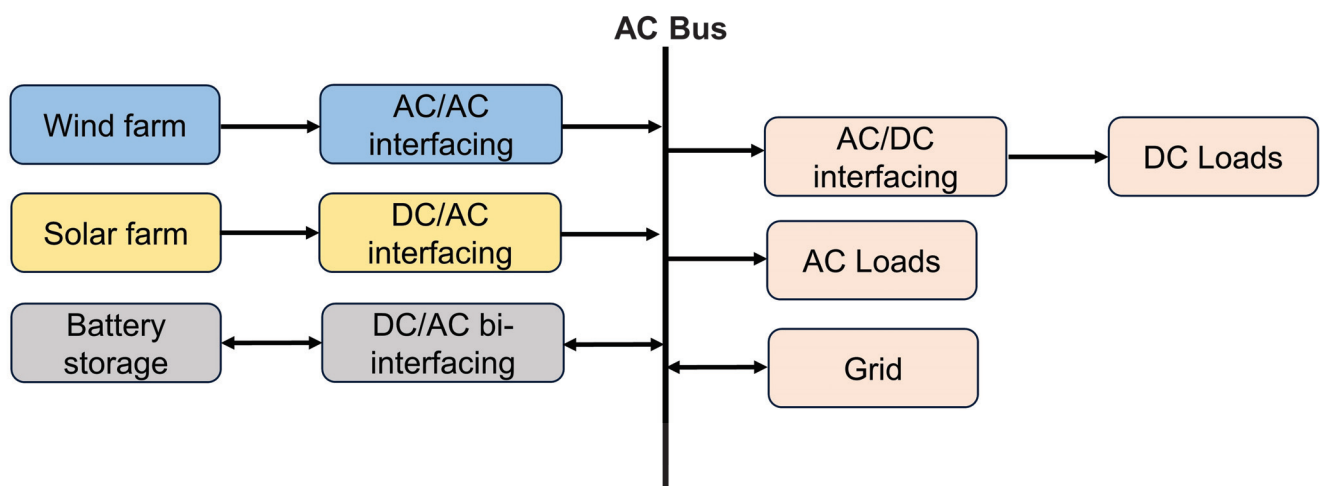
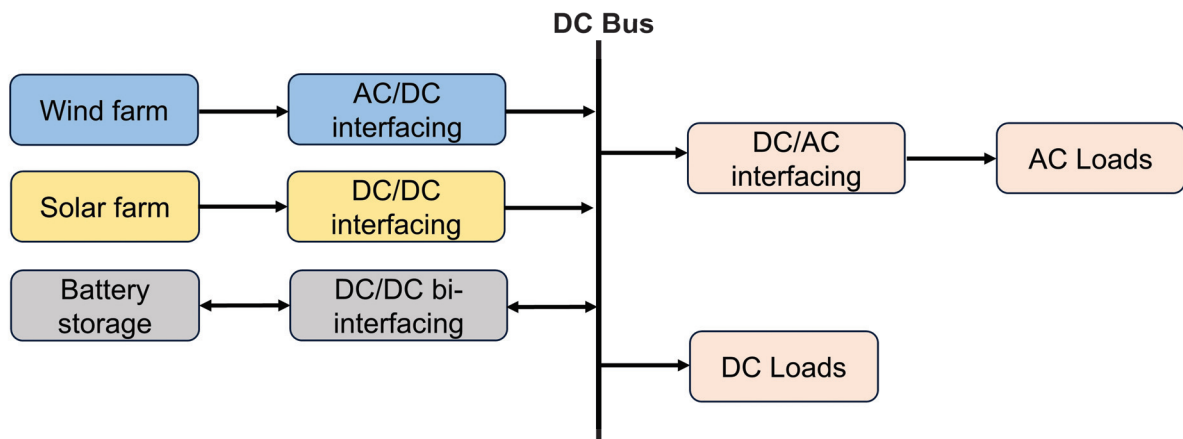**Figure 3.** Grid-connected AC-coupled configuration.

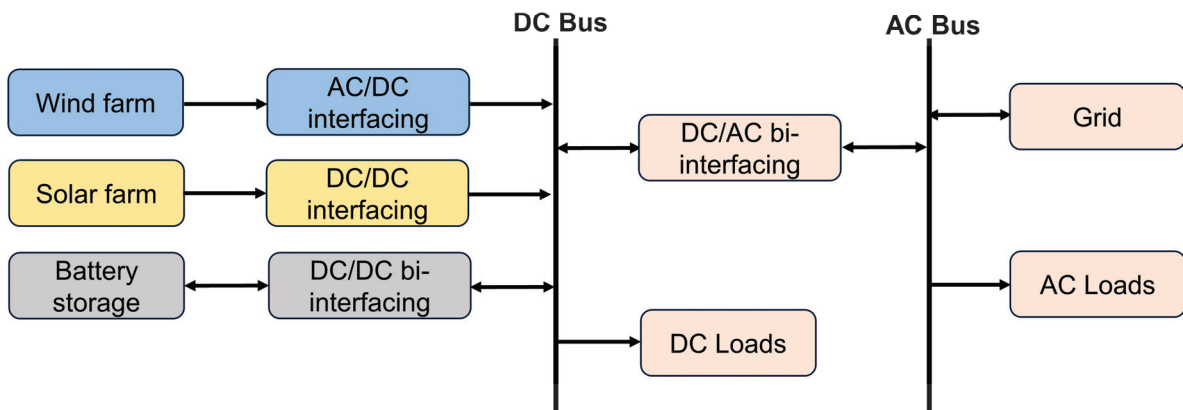**Figure 4.** Grid-connected DC-coupled configuration.

Figure 5. Hybrid configuration.

Table 1. A comparison of coupling topologies with advantages and disadvantages [7,17,46].

Configuration	Advantage	Disadvantage	Application
DC-coupled	• Synchronization not needed. • Fewer components used.	• Requires a large number of conversion components. • If converter is out of order, the whole supply is disturbed.	• Low voltage. • DC microgrid. • Long-distance transmission.
AC-coupled	• Standard interface and modular structure. • Protection system is easier. • Ready to grid connection.	• Potential risks to system stability and integrity due to the need for power quality correction elements. • Synchronization required. • Not suitable for long transmission.	• Medium- and high-production applications. • AC microgrid.
Hybrid	• Flexible system compared with AC and DC. • High efficiency.	• Controlling and managing energy is complex.	• Domestic and industrial applications.

In the AC-coupled topology, all HPP resources are interconnected to a common AC bus using dedicated power electronics interfacing [7,11,17]. The wind farm is connected to the AC bus, but the solar farm utilizes a system inverter (DC-AC) to convert the DC output into AC. Using a bidirectional DC-AC converter, the Battery Energy Storage System (BESS) is linked to the AC bus, guaranteeing a consistent supply–demand balance at its

pre-established capacity. An AC/DC rectifier can power DC loads. In the AC-coupled architecture, the only bidirectional energy transfer takes place between the grid and the AC bus [36]. In certain cases, if the hybrid installation is located close to a grid source, the inverter may provide an on-grid or off-grid option that permits grid connection. When the BESS is completely charged, excess electricity generation may be sent to the grid. Alternatively, the inverter connects to the grid to maintain energy balance at times when daily output from renewable energy sources is small and BESS discharge is fully used.

In the DC-coupled topology, all energy sources are linked to a shared DC bus via power electronics interfacing, offering cost savings in capital expenditure [11,36]. DC loads receive direct power from the DC bus, while AC loads require a DC/AC inverter for operation. In this setup, wind and solar farms generate variable electric energy, while the electronic interface helps regulate electric energy to meet system demands. The bidirectional DC-DC converter connects BESS to the DC bus, ensuring a consistent supply–demand balance at its designated capacity.

In the DC/AC-coupled topology, a combination of DC and AC-coupled features is utilized. The solar farm is connected through a DC-DC converter, while the wind farm is linked to the DC bus through a rectifier and DC/DC converter. A bidirectional DC/AC inverter facilitates energy conversion between the DC and AC buses. The AC bus can power multiple AC loads and connect to the grid when available. The hybrid configuration offers higher efficiency and lower system cost for domestic and industrial applications [7,11,17], but managing energy can be challenging as a result of accommodating AC and DC loads/grid.

4. Global Status of HPPs

Hybrid plants are becoming more and more popular because of advancements in battery technology, variable renewable energy, and cost reduction. For many years, different hybrid configurations and the integration of multiple energy sources have been an essential part of the energy landscape. Most of the current emphasis has been on connecting solar plants with batteries. The wind-based hybrid power plant (HPP) has acquired significant traction lately [12,13,47]. An updated list of co-located HPPs that are now operating and planned throughout the world—particularly those that are using solar and wind energy—is provided in this section. Plants with a capacity of one megawatt or more are the main emphasis; smaller projects are becoming more common but are not included in this data synthesis. In 2017, WindEurope [12] shared a database on co-located power plants integrating wind and storage technologies. To further promote awareness and knowledge about HPPs, WindEurope expanded this database to include HPPs that combined both wind and solar technologies, with or without storage components, as shown in Figure 6.

There are presently only a small number of operating or in-development HPPs based on solar and wind energy in the world, and these projects' business cases are still in the planning or assessment phases. Utility-scale HPPs have attracted interest throughout the last five years, especially in the USA and Europe [12,13,47]. HPPs aim to maximize energy production, improve grid stability, and ensure a steady supply of electricity by using wind, solar sources, and energy storage. This section highlights these fundamental features, which are explained briefly in the following paragraphs. Table 2 summarizes some of the innovative initiatives undertaken by HPP developers.

Vattenfall has developed a commercial PV–wind hybrid project in Cynog Park, U.K., to evaluate the feasibility of combining solar and wind technologies. In 2016, the project underwent upgrades to incorporate a 4.95 MWp solar PV farm and a 3.6 MVA onshore wind farm, showcasing the advantages of integrating a battery storage system to optimize energy production. Manufacturers emphasize the need for regular curtailment simulations to manage output and ensure efficient energy utilization, such as every 10 or 15 min, according to WindEurope [12] and Klonari [47].

Haringvliet, a Dutch project integrating wind (21 MW), solar (41 MW), and battery power capacity (12 MW), aims to stay competitive and generate revenue by participating in the wholesale electricity market and Guarantees of Origin. The plant provides frequency

containment reserves and time-shifting services, ensuring its sustainability and competitiveness [12,47]. The Kennedy Energy Park in northwest Queensland, Australia, is a 60.2 MW hybrid renewable energy facility that combines 19.3 MW solar PV, 43.2 MW wind, and 4 MWh lithium-ion energy capacity to meet local energy demand without excessive storage capacity [12,48].
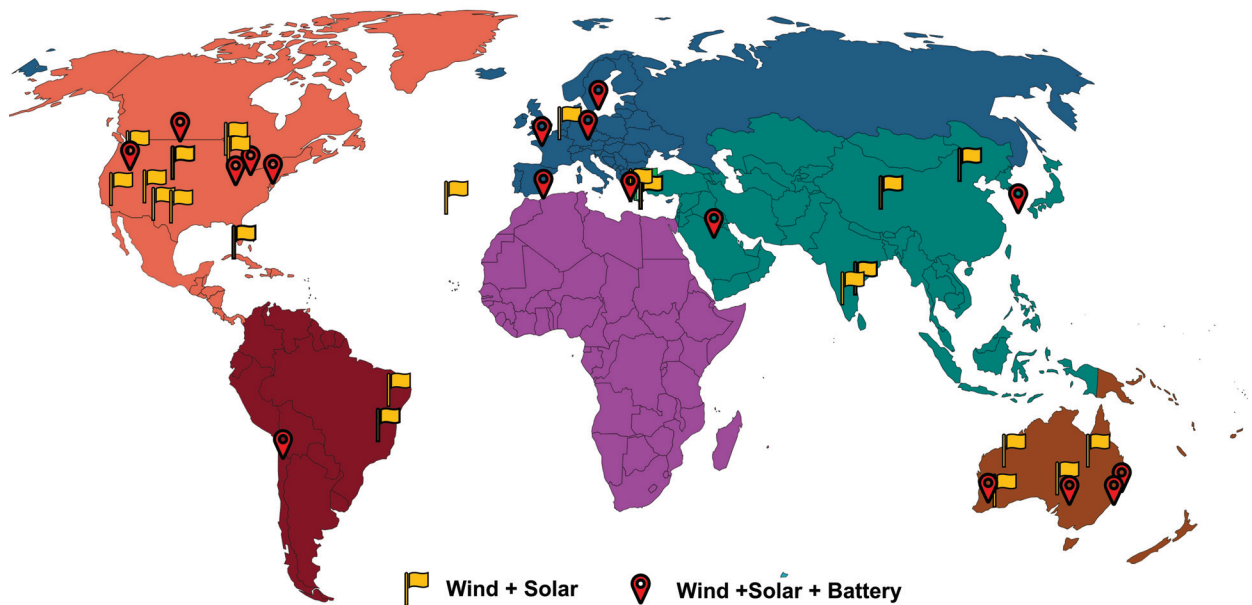

Figure 6. Wind–solar hybrid power plants (adopted and in addition to WindEurope).

The Minnesota Community Site in the USA is the first U.S. wind and solar HPP, combining wind (5 MW) and solar (0.5 MW) to generate electricity for a local municipality, but ensuring grid connection compliance remains a significant challenge [12,47]. The Kavithal Solar Wind Project in Raichur, India, combines a 50 MW wind farm with a 28.8 MW solar PV site to create a hybrid system to address grid-integration challenges with fluctuating renewable energy output and benefits from shared transmission infrastructure and operations, leading to cost reductions [49].

Siemens Gamesa in La Muela, Spain, developed a PV–wind hybrid initiative, combining an 850 kW wind turbine, a 245 kW PV module, 222 kW diesel generators, and a 429 kW battery power capacity system to provide dependable green power to remote areas without access to the main electricity grid and minimize diesel consumption [50]. The Ollague Microgrid in Chile uses wind (0.3 MW), PV (0.205 MW), lithium-ion battery power capacity (0.3 MW), and a diesel generator to provide a continuous 24-h energy supply. Storing the grid's surplus energy in the BESS for nighttime use in an off-grid village results in significant energy and cost savings compared with relying solely on a diesel generator [47].

The Tilos hybrid plant in Greece is the first energy-self-sufficient island, consisting of wind (0.8 MW), PV (0.16 MW), and storage power capacity (0.8 MW) systems [12]. It will meet 70% of the island's energy needs, reducing costs and enhancing stability. Excess energy will charge electric vehicles for local transportation [51]. Wheatridge Renewable Energy Facilities in the USA are the first utility-scale HPP plant in North America, featuring a 300 MW wind farm, 50 MW solar facility, and 30 MW storage power capacity system aiming to reduce greenhouse gas emissions by at least 80% by 2030 [52].

The Grand Ridge Project in Illinois, USA, combines 210 MW of wind, 20 MW of solar, and 36 MW of battery storage power, offering advantages like shorter development timelines, reduced construction costs, enhanced energy supply stability, and optimized infrastructure productivity [53]. Graciosa, Portugal, uses a hybrid plant that combines wind (4.5 MW), PV (1 MW), storage power capacity (6 MW), and a diesel generator to meet 70% of the island's power needs, with diesel generators serving as backup plants.

Table 2. HPP projects operating, under development, or approved.

Project	Location	Wind (MW)	Solar (MW)	Storage (MW/MWh)	Main Function	Status	Reference
Wind + Solar Project							
Cynog park	U.K.	3.6	5		Maximizing grid utilization	Operating (2016)	[47]
Minnesota Community Site	U.S.	5	0.5		Local municipality, but ensuring grid connection compliance	Operating (2018)	[12]
Kavithal Solar Wind Project	India	50	28.8		Enhanced and flatter power output, shared transmission infrastructure	Operating (2018)	[49]
Louzes	Greece	24	1			Operating (2012)	[12]
Wind + Solar + Battery							
Haringvliet	Netherlands	21	41	12	Frequency containment reserve services and time-shifting services	Operating (2020)	[12,47]
Kennedy Energy Park	Australia	43.2	15	2/4 *	Meet local energy demand without excessive storage capacity	Operating (2017)	[12,47]
La Plana	Spain	0.85	0.245	0.4/0.5 *	Support remote areas without access to the gird and minimize diesel consumption	Operating (2017)	[50]
Tilos Hybrid Plant	Greece	0.8	0.16	0.8	Power demand and enhanced stability	Operating (2018)	[51]
Wheattridge Renewable Energy	USA	300	50	30	Contribution to GHG reduction	Operating (2020)	[52]
Graciosa	Portugal	4.5	1	6	Meet power demand	Operating (2020)	
Grand Ridge	USA	210	20	36	Enhanced energy supply stability	Operating (2020)	[53]
Upcoming, under development, and approved [12]							
Kendinin	Australia	120	50	N/A	Enhanced and flatter power output	Under feasibility study	
Clarke Creek	Australia	800	N/A	N/A	Enhanced and flatter power output	Under feasibility study	
Andra Pradesh hybrid project	India	16	25	10	Enhanced and flatter power output	Contracted	
Tender Project	India	N/A	N/A	N/A	Enhanced and flatter power output	Approved	[12]
Three Gorges, Inner Mongolia	China	2.7 GW	300	880	Enhanced and flatter power output	Under construction	
Northwest Ohio	USA	105	3.5	1	Enhanced and flatter power output	Under development	
Megisti hybrid project	Greece	1	0.85	1.44	Weak power grid	Under licensing	
Angios Elestratios Green Island	Greece	1	0.101	0.72	Weak power grid	Under development	
Endesa	Portugal	264	365	168	Enhanced and flatter power output	Under Planning	

* Battery storage energy capacity.

5. Optimization Techniques

Optimization in energy systems aims to achieve optimal outcomes within specific conditions and constraints, considering stakeholders' needs. Optimization entails optimizing resource utilization, including energy sources, sizing, financial means, control, and energy management, while adhering to grid requirements and constraints. Selecting multiple parameters to maximize or minimize can achieve optimization (as depicted in Figure 7). Common optimization approaches include classical methods, artificial methods, and hybrid methods (as depicted in Figure 8), which are used in various applications [11,20,34,42,43,54,55]. The main objectives of optimizations could be to optimize existing infrastructure by combining multiple energy sources in a single power plant, reduce redundant infrastructure, maximize land use efficiency, achieve higher profitability, and minimize energy loss [12,13].
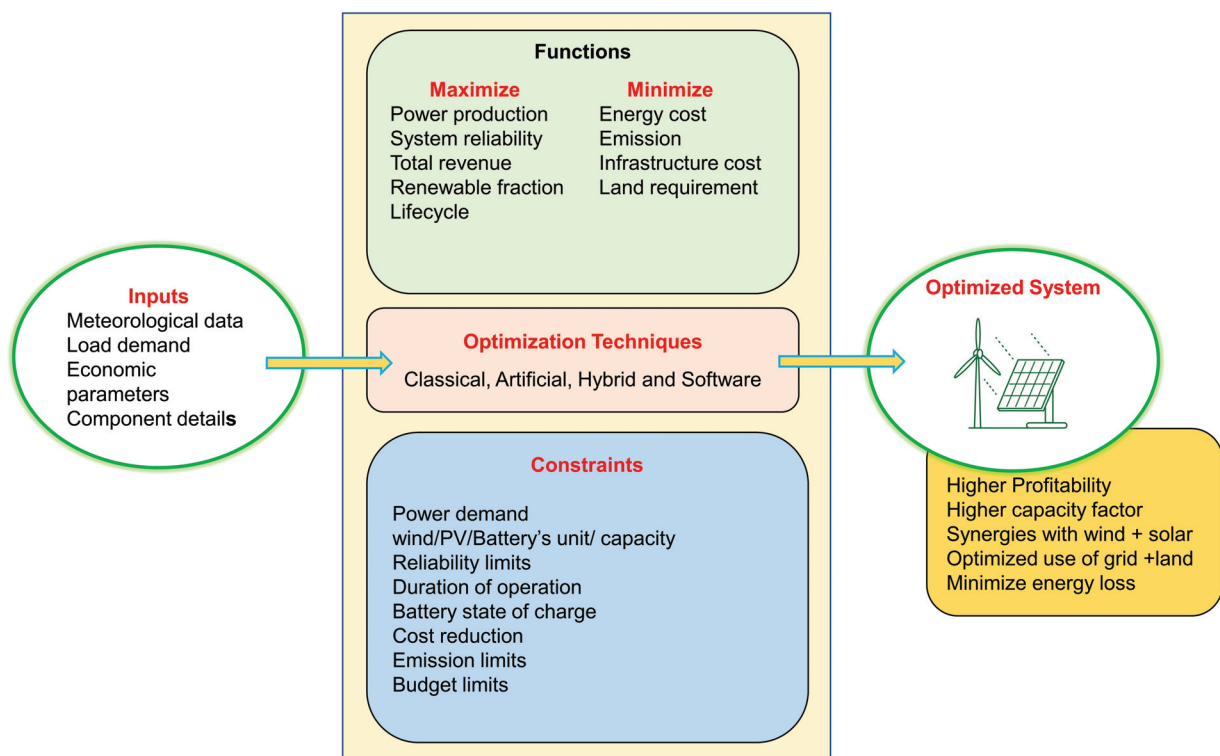
Figure 7. Optimization procedures for HPPs.

Classical optimization methods use mathematical formulations to determine globally optimal solutions in a deterministic fashion, but they face challenges when dealing with complex variables. Classical approaches, such as iterative, analytical, graphical, and probabilistic analyses, use differential calculus to compute energy models. Methods are limited by objective functions that lack continuity or differentiability. Examples of iterative techniques include the linear programming model (LPM) [25], multi-choice goal programming [56], multi-objective evolutionary algorithms (MOEAs) [57], mixed-integer linear programming (MILP) [58–60], and nonlinear programming (NLP) [61]. These techniques aim to achieve outcomes like null energy deficits, minimized system costs, and consistent power supply. The optimal arrangement for a hybrid system varies depending on factors such as location and demand patterns. However, because of their limited optimization capacity, these methods are limited in use among researchers. Probabilistic approaches provide statistical explanations for variable designs, whereas deterministic approaches view load demand and resources as predictable quantities with known time-series variation. Graphical construction procedures are created when optimization functions and outlines are drawn in the same graph, focusing on the implementation region.
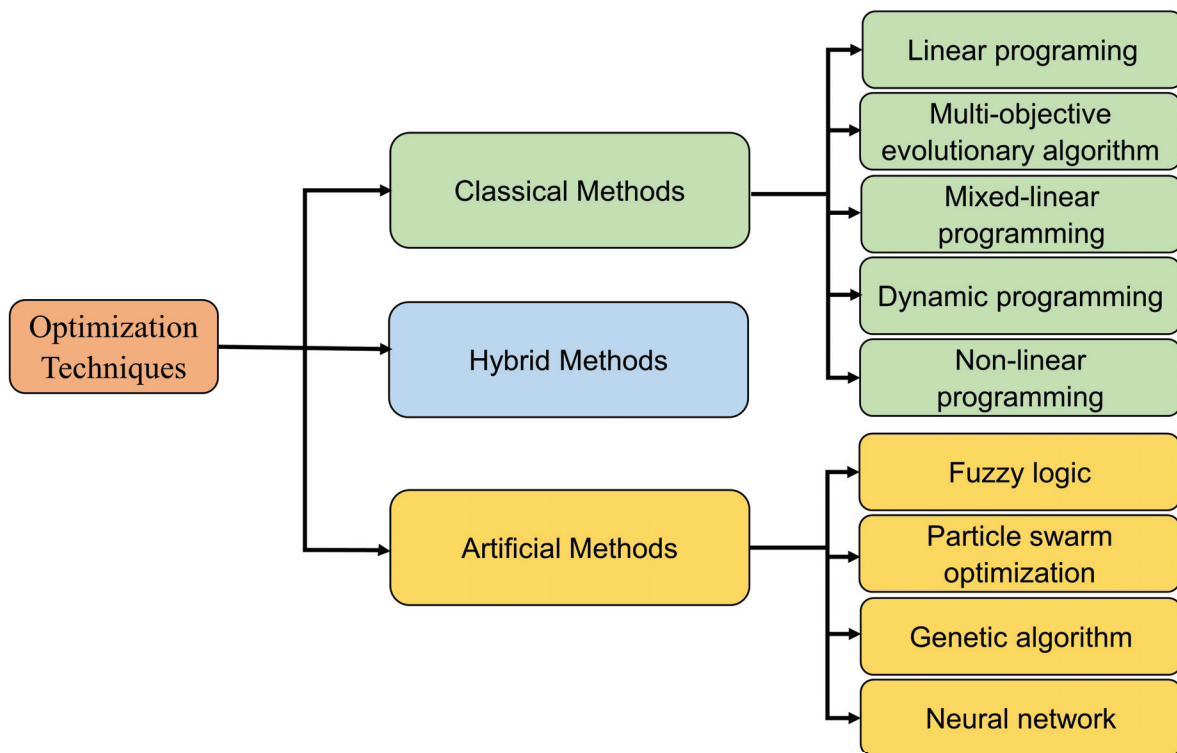
Figure 8. Optimization techniques for HPPs.

In the literature [11,34,42,43,55], many artificial techniques, including GA, PSO, the harmony search algorithm (HSA), simulated annealing (SA), the ant colony algorithm (ACA), the bacterial foraging algorithm (BFO), the artificial bee colony algorithm (ABC), and cuckoo search (CS), have been reported for sizing renewable sources. These algorithms are capable of addressing the non-linear characteristics of renewable energy system components or the intermittent behavior of solar and wind energy sources. These algorithms have shown reduced computation times, improved accuracy, and superior convergence rates compared with conventional methods. However, the focus in this section is directed solely towards the methods that have been commonly and recently employed by researchers.

In hybrid renewable energy systems, evolutionary heuristic search methods use GA to optimize dimensions. Researchers have successfully used it in several different areas, such as planning day-ahead schedules for hybrid plants [62], optimizing the design and layout of hybrid wind–solar-storage plants [21], and balancing life cycle cost, system embodied energy, and the chance of losing power supply in PV–wind–battery hybrid systems [63]. However, the success of these approaches depends on steady wind speeds and consistent voltage output from PV cells, which can be challenging in real renewable energy setups. PSO is an optimization search algorithm that minimizes LCOE while maintaining a suitable production range. It has been used for many things, like lowering the cost of energy storage [64] in HPPs, lowering the cost of energy (COE) [65], LPSP, total annual cost (TAC), and emissions [66], solving multi-objective optimization problems, making sure the system works reliably, and lowering the total cost, unmet load, and fuel emissions [67].

Artificial neural networks (ANNs) are dynamic adaptive computing systems that can process information in parallel. Enhancing HPP performance has resulted in improved efficiency, reliability, and cost-effectiveness [68]. These methods enable better resource allocation, load management, and overall system operation. They also improve energy capture, reduce energy waste, and optimize power generation. Neural network optimization also shows promise in predictive maintenance, preventing costly breakdowns and downtime. Faria et al. [69] and Singh and Lather [70] introduced ANNs as a power management approach for hybrid PV–energy storage systems, analyzing the State of Charge

(SOC) of individual ESSs. Mohandes et al. [71] used neural networks to predict hourly energy distribution for renewable energy sources and battery storage systems. However, this approach did not consider the gradual deterioration of energy storage systems, which can significantly impact an HPP's operational performance.

Fuzzy logic control (FLC) is a method that is easier to understand and less affected by changes in parameters compared with ANNs. It operates based on rules [11] defined by membership functions. Athari and Ardehali [72] used FLC to analyze the impact of changing electricity prices on energy storage performance in a grid-connected HRES. The shuffled frog leap algorithm was used to fine-tune membership functions, aiming to minimize operational expenses and improve the performance of HRES energy storage components. Fuzzy logic has been used to manage energy flux in hybrid systems with solar, wind, and battery components, demonstrating successful control of energy flux [73]. Yahyaoui and De La Peña [74] used fuzzy logic to enhance energy management systems for wind, solar, battery, and diesel generator systems. Ammari et al. [34] identified various fuzzy logic algorithms, such as the adaptive neuro-fuzzy inference system (ANFIS), the fuzzy analytic hierarchy process (FAHP), ANP, fuzzy clustering, the genetic algorithm, fuzzy particle swarm optimization, fuzzy honeybee optimization, and quantum-behaved particle swarm optimization.

Hybrid methods are techniques that combine multiple algorithms to address the limitations of a single algorithm. This flexibility allows soft computing approaches to manage complex optimization problems more effectively, leading to more accurate results [42]. Tito et al. [75] optimized a hybrid PV, WT, and battery system using GA and an exhaustive search. Singh et al. [76] used enhanced differential evolution and PSO to determine the best sizes for each component of their sizing model. Hybridization can take various forms; a few examples include Monte Carlo simulation with multi-energy balance and financial equations [77] or the fusion of GA and PSO (GAPSO) [32]. Alshammari and Asumadu [78] used Harmony Search, Jaya, and particle swarm optimization to find the best configuration for an HRES comprising wind, photovoltaic, biomass, and battery technologies. The primary goal was to meet customers' electricity needs in a cost-effective and reliable manner while ensuring efficiency.

Furthermore, many approaches to optimizing hybrid renewable resources focus on cost reduction, including LPSP constraints to lower system expenses. Other constraints include minimizing grid-injected power, decreasing fluctuation rates, and enhancing the utilization factor. These considerations drive the optimization process, with cost reduction as the single objective [29,79]. In contrast to single-objective and multi-criteria decision-making techniques, multi-objective optimization methods offer a range of optimal solutions. Modern techniques using AI algorithms and hybrid methods are gaining popularity over traditional methods for resolving complex optimization challenges. These techniques consider multi-objective functions, primarily cost and LPSP, with constraints like COE, LPSP, and REF [31–33].

Summary and Evaluation

HPPs are complex because of uncertainties and limitations, leading to the adoption of soft computing methods with meta-heuristic algorithms. These techniques, which come in single-objective optimization (SOO) and multi-objective optimization (MOO), offer increased adaptability and accuracy. However, their complexity is a common drawback. Traditional methods are highly effective but have limitations due to parameters. Contemporary optimization approaches require robust hardware performance because of their intricate procedures and codebase. Their strengths include efficiency, rapidity, and accuracy. Combining conventional and modern optimization techniques creates an approach with remarkable speed and resilience, requiring sophisticated design and code creation. Table 3 and the Appendix A (Tables A3 and A4) outline the advantages and disadvantages of each method and summarize the study of single and multiple objective functions.

Table 3. Advantages and disadvantages of optimization methods adapted from [25,43,54].

Techniques	Advantage	Disadvantage
Classical	• Efficient multi-objective solutions that are valuable for investment decision-making. • Quicker processing time.	• Limitations in optimizing space, and exhibit linear relationships with the variables. • Require a mix of discrete and continuous probability.
Artificial	• Offer more efficiency. • More accurate. • Fast convergence.	• Complex solving process. • Require more memory space.
Hybrid	• High convergence. • Offer time efficiency. • Robustness. • Quick convergence.	• Design complexity. • Code generation challenges.

6. Sizing Methodologies

In HPPs, determining the appropriate wind farm, solar farm, and battery storage energy capacity is crucial for establishing the system's capacity. Incorrect sizing can lead to undersized or oversized systems. Designing HPPs considers factors like cost reduction, reliability enhancement, and emissions reduction [28]. Accurately assessing real loads as well as wind and solar metrological data is critical, as climatic conditions affect energy availability at specific locations [54]. Researchers often rely on average data from hours [75,80] or months [17] to analyze system performance. Figure 9 shows how size optimization methodologies fall into classical, modern, and software-based approaches. Traditional methods use iterative, numerical, analytical, probabilistic, and graphical methods based on differential calculus, simplifying the process of identifying optimal continuous and differentiated solutions, while modern techniques use artificial and hybrid methods [43,46,54]. Commercially available software tools, such as HOMER, aid in sizing and optimizing standalone solar photovoltaic and wind-based systems, identifying optimal energy system sizes, and conducting sensitivity analyses to explore varying input variables or uncertainties.
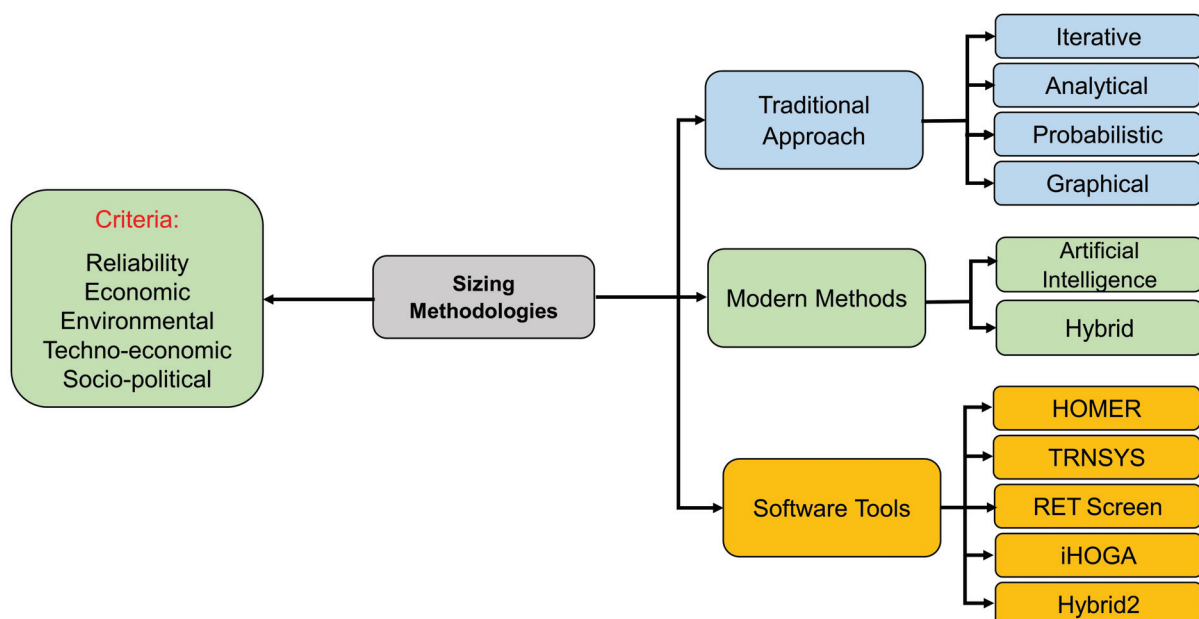
Figure 9. Sizing methodologies.

6.1. Sizing HPPs Using the Classical Approach

Several studies [33,54,81] explored various approaches for sizing solar and wind-based hybrid systems. A classical approach includes probabilistic, graphical, analytical, numerical, and iterative methods. However, only widely used approaches are considered in this study. Iterative methodologies are used to evaluate performance in HPPs using a recursive process. The framework uses the LPSP model for power reliability and integrates LCOE and net present value (NPV) models to account for system costs. Identifying the optimal system configuration is based on achieving the lowest LCOE/NPV, leading to cost reduction through linear parameter adjustments or linear programming methods. Akram et al. [80] presented two iterative search algorithms for optimal sizing components in a grid-connected microgrid configuration for maximum reliability and minimum cost.

The probabilistic approach is a method for determining system size, but its results may not be suitable for identifying the optimal solution. Li et al. [82] proposed a new probabilistic method for optimizing an off-grid hybrid energy system, estimating power distribution probability in the South China Sea region. Lian et al. [83] highlighted the use of probabilistic methodologies for assessing reliability simultaneously. Analytical methods describe HPPs using computational models that determine the size of the hybrid system based on feasibility [84]. The approach is faster than the Monte Carlo simulation and requires less time. This approach views the hybrid system as a numerical model and defines its size as a function of viability [15]. Karve et al. [85] used mathematical methods and improved particle swarm optimization (IPSO) to find the best size for a hybrid PV–wind–battery system that could work on its own. They performed the study to lower the system's annual costs.

6.2. Modern Methods

Modern methods utilize artificial intelligence and hybrid methodologies, enhancing their adaptability and ability to handle complex optimization challenges with more accurate results [43,55]. The design of renewable HPPs is complex because of uncertainties, technical considerations, and site limitations. Conventional methods are inadequate, leading to a shift towards soft computing techniques, often relying on meta-heuristic algorithms [42,43,55]. Contemporary techniques incorporate both single and hybrid algorithms to address a wider range of challenges, enabling more efficient and refined optimization outcomes [42]. Numerous techniques have been documented in the literature [11,28,34,42,46,54,55], including GA, PSO, HSA, SA, ACA, BFO, ABC, and CS. These algorithms can address the non-linear characteristics of renewable energy system components or the intermittent behavior of solar and wind energy sources. Kiehbadroudinezhad et al. [86] used a division algorithm and an enhanced genetic algorithm to model, design, and optimize wind, PV, and battery hybrid systems for water desalination. Muthukumar and Balamurugan [87] used a bee algorithm and neural architecture to optimize wind and solar hybrid systems, as well as test various solar irradiance and wind velocities. Roy et al. [64] used PSO in HPPs to reduce energy storage costs by utilizing multiple energy storage systems.

Hybrid techniques combine different methods to achieve optimal design outcomes. Riaz et al. [88] presented a hybrid of PSO with grey wolf optimization (GWO) used for optimal power flow. Ghorbani et al. [32] used the fusion of GA and PSO (GAPSO). Zhang et al. [89] developed a hybrid approach that combined the Harmony Search Optimization (HSO) method with the simulated annealing (SA) technique, enhancing chaotic search and demonstrating better results for optimizing HRES sizing than either method individually. Abdelshafy et al. [90] used a PSO-GWO approach to find the best HRES design. The method converges optimally faster and better.

6.3. Sizing HPPs Using Software Tools

Software tools efficiently and cost-effectively design, analyze, optimize, and assess HPPs. These tools are designed to operate under optimal conditions for investment and power reliability [17,34,35,43,83,91]. The National Renewable Energy Laboratory (NREL)

developed HOMER to evaluate energy based on resource costs and availability. Several studies [92–96] have used HOMER software (Homer Pro) to determine the most cost-effective configuration for hybrid systems, with some finding a combination of solar panels and wind turbines as the optimal approach. Other software tools used for sizing include IHOGA, HYBRIDS2, TRNSYS, and RETScreen.

The Renewable Energy Research Laboratory (RERL) at the University of Massachusetts developed Hybrid2 software (version 1.3), a computer model for analyzing hybrid power systems that include electrical loads, wind turbines, photovoltaic installations, diesel generators, battery storage units, and power conversion devices [34]. The Electric Engineering Department at the University of Zaragoza developed HOGA as a hybrid system optimization tool, while HYBRIDS is a Microsoft Excel spreadsheet-based application used for renewable energy assessments [97].

For simulation purposes, TRNSYS software (version 18) from the University of Wisconsin allows programmers to define time steps ranging from 0.01 s to 1 h. TYRSYN optimizes generation system combinations and sizes energy storage capacity to achieve the LCOE across renewable energy fractions [98]. RETScreen evaluates the technical and financial viability of renewable energy, energy efficiency, and cogeneration projects.

Table 4 displays a comparison of various tools, revealing their respective qualities and limitations [25,26,34,43,99]. Table 5 provides a comprehensive overview of various size methodologies, including the system components and objective functions.

Table 4. Summary of the input and output for sizing optimization software tools.

Software	Input	Output	Limitations	Availability
HOMER	• Load demand. • System control. • Resource input. • Component details. • Emission data. • Constraints. • Capital and maintenance cost.	• Sizing optimization. • Techno-economic analysis. • Environmental analysis. • Risk assessment and sensitivity analysis. • Analytical probability.	• Use first order linear equations. • Time series data cannot be used. • Needs more information to get started.	Free access www.homerenergy.com (accessed on 15 Decmeber 2023)
HYBRID2	• Load demand. • Resource input. • Component details. • Financial data.	• Sizing optimization. • Percentage of GHG emissions. • Techno-economic analysis.	• Simulations take a long time. • Only one configuration can be simulated at a time.	Free access https://www.umass.edu/ windenergy/research/topics/ tools/software/hybrid2 (accessed on 7 Februaryr2024)
HYBRIDS	• Component details.	• Cost of energy. • Percentage emission of GHGs.		-
IHOGA	• Resource input. • Constraints. • Economic data. • Component details. • Emission data.	• Cost of energy. • Multi-objective optimization. • Life cycle emission. • Sizing optimization. • Analytical probability.	• Only one configuration can be simulated at a time. • Lacks sensitivity analysis and probability analysis.	The EDU version is free, while the PRO version is priced www.ihoga.unizar.es/en/ (accessed on 7 February 2024)
RETScreen	• Resource input. • Load data. • Project database. • Product database.	• Costs. • Techno-economic analysis. • Emission reduction. • Sensitivity and risk analysis. • Analytical probability.	• Input data are reduced. • Time series data cannot be used.	Free access www.retscreen.net (accessed on 22 Decmeber 2023)
TRNSYS	• Resource input. • Inbuilt model/	• Dynamic simulation behavior. • Technical evaluation. • Thermal behavior.	• No option for optimization.	Priced www.trnsys.com (accessed on 20 Decmeber 2023)

Table 5. Summary of various studies conducted on HPPs/HRES using sizing software tools.

Software	Energy Resources				Objective of the Study	Reference
	Wind	**Solar**	**Battery**	**Other**		
HOMER	✓	✓	✓		Cost-effective configuration of HRES	Muller et al. [92]
	✓	✓		FC	Evaluate technical and financial performance	Al-Badi et al. [100]
	✓	✓	✓		Sizing design of HRES	Hoarca et al. [101]
HYBRID2	✓	✓	✓		Sizing method of standalone RES based on techno-economic analysis and object-oriented programming	Belmili et al. [102]
IHOGA	✓	✓			Optimal sizing of RES	Fadaeenejad et al. [103]
	✓	✓	✓		Sizing design of HRES	Hoarca et al. [101]
HOMER PRO	✓	✓			Minimize LCOE, life cycle cost	Ranaboldo et al. [104]
HOMER	✓	✓	✓		Energy production, net present cost, and levelized cost of electricity	Baker [105]
HOMER	✓	✓	✓	Hydrogen	Total net present cost	Babatunde et al. [106]
RETScreen	✓	✓	✓	Biomass	Feasibility study based on economics and the environment	Hossen and Shezan [107]
TRNSYS	✓	✓			Optimal sizing of wind–PV-based hybrid system	Anoune et al. [17]
	✓	✓	✓		Energy performance of the system	Mazzeo et al. [108]

Summary and Evaluation

The speed and ease of use of traditional methods for scaling hybrid systems may be overcome by using artificial intelligence techniques. AI techniques leverage multi-objective functions to tackle complex challenges. Iterative approaches, which use recursive processes, can mitigate the constraint but may overlook critical parameters. Artificial intelligence offers versatility and favorable outcomes for complex tasks, but the complexity of the codes in the algorithms poses challenges. Table 6 presents a comparison of various sizing methods used in hybrid systems.

Table 6. Comparison of various studies on sizing methods/tools.

Techniques/Tools	Advantage	Disadvantage	Reference
Iterative	• User-friendly and capable of early-stage threat detection. • Easy to code. • Use of linear variable parameters or linear programming techniques is highly efficient in achieving cost minimization.	• Suboptimal solutions result from linear adjustments in decision variables, not optimizing factors like PV module slope angle and wind turbine installation height, which have a more significant effect on cost.	Chauhan and Saini [109]
Probabilistic	• The system is stochastic and can randomly identify the optimal solution based on the provided data. • Simple sizing methods do not require time-series data.	• Optimization considers limited performance parameters, potentially not suitable for identifying optimal solutions. • Less efficient in representing the dynamic nature of performance changes within a hybrid system.	Ganguly et al. [84]; Lian et al. [83]
Analytical	• Size determination is simpler and requires less computational resources than Monte Carlo simulation.	• System design becomes less flexible as performance is evaluated using computational models. • Model is unable to predict the coefficient of the mathematical equation related to position.	Lian et al. [83]
Graphical	• The most straightforward method for depicting complex problems or situations involving numerous mathematical equations.	• The method is limited to handling problems with multiple dimensions because of scale and graphical interpretation complexities, making its reliability uncertain. It faces difficulties in graphing non-linear, exponential, logarithmic, and trigonometric expressions and is impractical when combined with other approaches.	Rathore and Patidar [110]
LP	• The model exhibits a linear relationship among variables, is renowned for its favorable convergence, and is less stringent.	• The system may become stuck in a local search, reducing accuracy and confidence over time, and not considering variable evolution and changes.	Saiprasad et al. [111]

Table 6. *Cont.*

Techniques/Tools	Advantage	Disadvantage	Reference
GA	• GAs are powerful tools that can manage multiple parameters, including integers, discrete values, and non-differential attributes, simultaneously. Their parallelism allows for simultaneous evaluation of multiple strategies, enhancing the likelihood of achieving optimal solutions. GA has proven superior in cost and environmental analysis compared with HOMER Pro software and SA.	• GAs are time-consuming but less computationally intensive than the analytical method, as they are specifically designed for local searches.	Iweh et al. [35]; Riaz et al. [88]
PSO	• Proficient in executing parallel computations, achieving rapid convergence, efficiently finding the optimal global solution, and effectively resolving complex problems.	• The system exhibits poor local search performance when dealing with complex problems with numerous dimensions, with a notable tendency towards premature convergence.	Dubey et al. [112]; Gad et al. [113]; Wang et al. [114]; Gupta and Srivastava [115]
ACO	• The algorithm quickly identifies optimal solutions through feedback mechanisms, demonstrates parallelism, is adaptable, and can be combined with another algorithm for a potent, reliable approach. It achieves the global minimum with fewer iterations compared with particle swarm optimization.	• Insufficient parameter selection can lead to stagnation, premature convergence, and inability to reach optimal solutions, especially when addressing discrete problems, with potential challenges in continuous problems.	Gupta and Srivastava [115]
CS	• The algorithm, which incorporates Levi's flight trait, enhances its performance by enabling convergence towards global optimal solutions, boasts robust random searching paths and optimization capabilities, and is highly prone to hybridization with other algorithms.	• Incorrect initial parameters can lead to a local search trap and slow convergence rate.	Shen et al. [116]
SA	• The process of achieving optimal outcomes is methodical and predictable, with programming being straightforward, resilient, and flexible, enabling smooth transitions between local and global search modes.	• The system exhibits limited efficiency and prolonged computational durations.	Iweh et al. [35]

Table 6. *Cont.*

Techniques/Tools	Advantage	Disadvantage	Reference
HS	• The method requires fewer adjustable control parameters, no initial decision variable configuration, and operates without requiring derivative information.	• Exhibits gradual and premature convergence, with limited ability to constrain and adjust search ranges.	Dubey et al. [112]
GWO	• Fewer parameters. • Easy to implement.	• The algorithm's precision and accuracy have been reduced because of a slow convergence pace during later iterations, resulting in a lack of local search presence.	Wang et al. [114]
HOMER	• An expedient approach to obtaining a desired solution for a singular objective.	• The linear equation model's initial attributes are undefined, and it assumes a fixed state throughout the investigation. It does not allow users to choose suitable equipment, does not consider future developments, and is constrained by input parameters. It does not support control strategies like iHOGA and is overshadowed by nature-inspired algorithms. A well-informed criterion is needed for a satisfactory solution in the optimization process.	Saiprasad et al. [111]; Kavadias et al. [117]
iHOGA	• Ability to directly implement a control strategy during the sizing of HRES.	• The focus is on achieving individual objectives and addressing non-linear problem scenarios.	Saiprasad et al. [111]
RETScreen	• Drastically lowers the expenses linked to the identification and evaluation of potential energy projects in comparison with Homer Pro.	• The task involves manually compiling data into a workbook or Excel sheet.	Ramli et al. [118]

7. Control and Energy Management Strategies

HPPs, which combine wind and solar power, face challenges such as power quality, voltage fluctuations, network stability, frequency disparities, and efficient dispatch. To ensure system reliability, effective power management, and optimal performance, an effective control system and an energy management strategy (EMS) are crucial. The approach can regulate power allocation from generators, stabilize voltage and frequency, optimize resource utilization, minimize operational costs, and prolong the system's lifespan.

7.1. Control Strategies

The literature [3,7,8,36–40] presents a variety of control systems for wind turbines, with few studies focusing on the combination of HPPs with batteries. The typical composition of HPP controllers includes a plant model and an embedded dispatch function. The plant model includes power-generating units (PGUs) that contribute to power production at the PCC. The controller is programmed with predefined reference values and can be adjusted to parameters like curtailment set-points, grid limitations, or frequency variations [3,38,39]. The dispatch function optimizes power utilization from different PGUs by processing the output. Few have adopted a supervisory hierarchical control framework with multiple levels dedicated to specific objectives, such as active power management [39], frequency regulation, reactive power and voltage control [38,39], and maximizing revenue [119]. This structure aims to optimize power management, maintain frequency stability, and regulate voltage levels effectively. Petersen et al. [7] developed and verified a reduced-order performance model for wind turbines, photovoltaic parks, and BESS, testing it in two scenarios. For controller design, comprehensive resource simulations are essential.

HPPs can be controlled using various methods, such as centralized, distributed, and hybrid [11,34,35], as shown in Figure 10, and proportional-integral control [8,39]. Moreover, another study by Olatomiwa et al. [120] classifies control strategies into classical and intelligent control. Traditional approaches include ANNs, FLC, multi-objective PSO, and adaptive neuro-fuzzy inference systems. These strategies can enhance the cost-effectiveness of the system and ensure seamless energy flow.
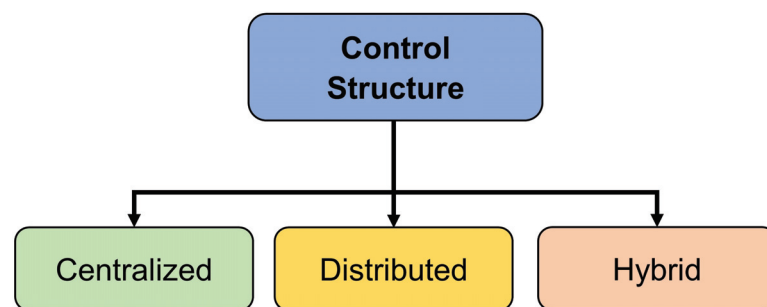
Figure 10. HPP control strategies.

Intelligent control algorithms drive the centralized approach for conventional energy coordination control [80]. The STATCOM (Static Synchronous Compensator) system is critical to efficiently managing power in multisource energy systems because it regulates reactive power [80]. However, as wind farms, photovoltaic arrays, and composite energy storage systems become more prevalent, the limitations of this centralized approach pose challenges for large-scale integrated power-generation systems.

To overcome these drawbacks, the multi-agent system has emerged as a viable alternative, offering intelligent and adaptable responses to varying working conditions and demands [121]. Wu and Hua [121] created a multi-agent-based energy coordination control system (MA-ECCS) to make large-scale wind–photovoltaic energy storage power-generation units more stable, efficient, and good at making decisions. It enables non-fixed client–server cooperation among agents by using a negotiation model inspired by the contract net protocol.

The flow chart algorithm [8,39], linear programming [122], model predictive control [123], the Pareto algorithm [124], and the adaptive neuro-fuzzy inference system [125] are some of the control algorithms that are used. However, these algorithms require precise models of the entire system, as well as accurate demand and weather resource data. Hybrid systems often use distributed or hybrid control strategies for efficiency, system failure minimization, and incorporating multiple control methods. Agrawal et al. [126] developed a two-tier optimization approach to improve the operational efficiency of HRESs, while Hashemi and Zarif [127] introduced a two-phase method to manage reactive power in power systems. Shibl et al. [128] introduced a dual-phase energy dispatch management framework for HPPs, integrating machine learning techniques.

Summary and Evaluation

Control methods in practical applications are chosen based on system complexity, optimization, robustness, communication capabilities, and potential failure consequences. Real-world systems employ various strategies to balance efficiency, adaptability, and reliability, ensuring a harmonious equilibrium. Hybrid systems widely use distributed or hybrid control methods because they effectively decentralize control, reduce system failures, and integrate multiple control strategies, although the interconnection and processing codes are complex. Table 7 provides a comprehensive overview of the various control categories, outlining their advantages and disadvantages.

Table 7. A comparison of various control methods [28,34,35,43].

Control Method	Advantage	Disadvantage
Centralized	• Efficient optimization and coordination. • Easier implementation and management for simpler systems. • Maintaining the lowest possible energy costs.	• Single point of failure. • Scalability issues in complex systems. • Lack of robustness in the face of controller malfunctions.
Distributed	• Scalability for complex systems. • Adaptability to environmental changes. • Robustness against failures.	• Necessitate more intricate communication and synchronization mechanisms. • Most solutions are not optimal. • Coordinating decisions among distributed agents can be challenging.
Hybrid	• Combines the advantages of centralized and distributed approaches. • Customized control strategies for various system components. • Local controllers are seldom utilized.	• Management of both central and local decision-making processes is complex. • Present potential integration challenges.

7.2. Energy Management Strategies

Effective energy management of HPPs aims to achieve optimal efficiency and reliability while minimizing costs, ensuring a continuous energy supply throughout the year [11]. This can lead to benefits such as extended component lifespan, reduced economic parameters, and enhanced overall system performance [15]. Energy management methods include rule-based, optimization-based, reinforcement-based, and learning-based methods [35,42,129]. This review provides an overview of different EMSs studied in the literature [11,34,35,42]. Figure 11 illustrates the major management strategies.

The power-oriented strategy aims to meet energy demand by controlling the power balance and battery state of charge, which define the operational limits of major energy storage systems [11,34,42]. This strategy is simple and controlled through algorithms in flowchart diagrams, guided by flowchart diagrams. Similarly, the technical objective-oriented strategy aims to optimize the technical parameters of a hybrid system to meet load demand [130,131], prolong equipment lifespan [132], enhance system performance, ensure stability [133], extend storage component lifespan [134], and optimize generator

parameters. This involves using various algorithms like predictive control [135], PSO [136], real-time optimization [137], neural network techniques [138], and software tools like HOMER [137]. Implementing these strategies requires design constraints, power storage system state management, and consideration of degradation parameters. Depending on the optimization objectives, these strategies offer medium complexity and promising system performance and lifespan outcomes. Brka et al. [139] employ a flowchart algorithm, while Cano et al. [140] use model predictive control and fuzzy logic. A strategy's effectiveness is dependent on precise forecasting and reliable system models for accurate operations, which affect the system's performance.
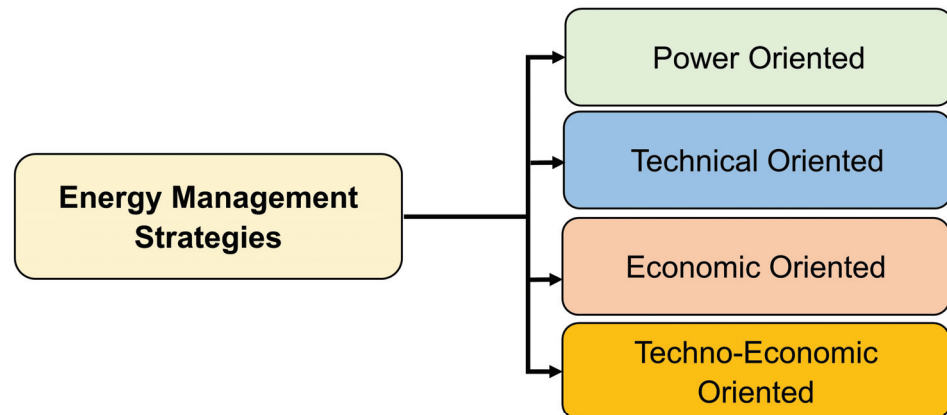
Figure 11. Energy management strategies.

An economic-oriented strategy involves assessing energy demand and minimizing system expenses. Research in this area uses various algorithms, including genetic algorithms, differential evolution algorithms, model predictive control, mixed-integer linear programming, fuzzy logic, and commercial software like HOMER. A dual-tier energy management system for microgrids was developed using a hierarchical dispatch framework, focusing on reducing operational expenses and mitigating forecast inaccuracies, as outlined in Ju et al. [141]. However, the model does not account for stochastic variations in renewable energy output.

Finally, a techno-economic objective-oriented approach improves system performance by balancing supply and demand, taking into account technical and economic factors to extend equipment lifespan and reduce maintenance costs [11,43]. It offers an ideal solution compared with conventional generation alternatives. Existing approaches involve solving nonlinear optimization problems by incorporating costs and equipment depreciation into a multi-objective function. Various techniques ensure a harmonious power distribution for optimal system functioning by determining the power output from each component. The solution to extreme energy shortages depends on the system's configuration. Hamdi et al. [142] implemented an ANN and MATLAB program to examine LCOE, zero power loss supply probability, and curtail energy for a wind- and solar-based hybrid system.

Summary and Evaluation

EMS is essential for managing power movement across various components. Utilizing strategies such as rule-based, optimization-based, learning-based, and reinforcement learning (RL) enhances the efficiency of hybrid energy systems. Rule-based strategies commonly handle practical scenarios, while optimization-based approaches address complex optimization issues using algorithms. Machine learning techniques train controllers in RL-based energy management, enabling decisions based on system status and objectives. This approach minimizes maintenance costs and prolongs the lifespan of equipment. However, complex optimization algorithms may increase the complexity of the system in real-world scenarios. Table 8 provides a comprehensive examination of the optimization objectives, design constraints, and control algorithms associated with energy management strategies.

Table 8. Management methods and their characteristics [11,34,43].

Management Strategy	Design Constraint	Control Algorithm	Advantages	Disadvantages
Power requirements	• Power balance. • Battery state of charge.	• Flow chart algorithm. • SOC based on the algorithm. • Supervisory centralized control algorithm. • Distributed control algorithm. • Artificial intelligence method. • Linear programming. • Predictive control.	• Simplicity in design and control.	• Lifetime not optimized. • O and M not optimized. • Performance not optimized.
Technical-oriented	• Power balance. • Battery state of charge. • Battery degradation.	• Flow chart algorithm. • SOC based on the algorithm. • Supervisory centralized control power algorithm. • Battery short time.	• Increase performance. • Improve lifetime. • Less complex.	• Operation and maintenance cost are not optimized.
Economic-oriented	• Power balance. • Battery state of charge. • Cost function.	• Cost minimize algorithm. • Power reference and priority algorithm.	• Optimal system response. • Minimize system cost.	• Complex algorithm. • Increases operation and maintenance costs. • Not optimized for lifetime.
Techno-economic-oriented	• Power balance, • Battery state of charge. • Cost function. • Battery degradation.	• Optimization algorithm is used to determine the power reference of a multi-objective function.	• High performance.	• Complex algorithm. • Increases operation and maintenance costs.

8. Discussion

The lack of a universally accepted definition of HPPs poses a challenge to exploring this emerging field. This disparity can lead to misguided conclusions, as there is limited literature on co-located utility-scale HPPs. HPPs offer potential advantages, especially from co-locating wind and photovoltaic facilities. However, their long-term economic viability is uncertain because of a lack of standardized definitions and existing park instances. Previous research has improved the understanding of hybrid systems on a small scale, but there is a noticeable lack of comprehensive review articles on energy management and control strategies and optimization methodologies for HPPs at the utility scale. This study aims to address this gap by extrapolating key findings and methodologies from HRES studies. The Discussion Section is categorized by the topics explored in this manuscript, considering its structure and issues.

Topologies: Regarding the topologies and configurations of HPPs, there exists limited research into the consequences of varying topologies on the outcomes of dimensioning. Each topology, including AC-coupled, DC-coupled, and hybrid, has unique converters and equipment, potentially affecting the system's technological and economic efficiency. As a result, it is imperative to undertake a comprehensive comparative assessment of distinct HPP topologies.

Optimization: The primary goal of employing optimization techniques in HPP is to achieve superior overall performance while also meeting grid requirements and constraints. Optimization studies primarily focus on three methodologies including classical, artificial, and hybrid approaches. Classical methods are quick and efficient but limited in optimization space. Artificial methods are efficient, precise, and fast, but they require complex processing procedures. Research has shifted towards hybrid algorithms for multi-objective optimization, with HOMER software becoming popular for its robustness and cost-effectiveness. Artificial intelligence-based optimization models have shown superiority over conventional methods because of their adaptability, enabling solutions for both single and multi-objective design problems, but they face usability challenges and involve complex implementation processes. Hybrid methods combine the strengths of conventional and advanced optimization techniques to improve efficiency and reduce processing time. However, the design and code delivery add to the complexity and the need for a specific code. Based on the literature reviewed, most of the research is carried out using SOO, while there has been an increase in the use of hybrid algorithm techniques to solve MOO problems in the last five years, as shown in Figure 12.
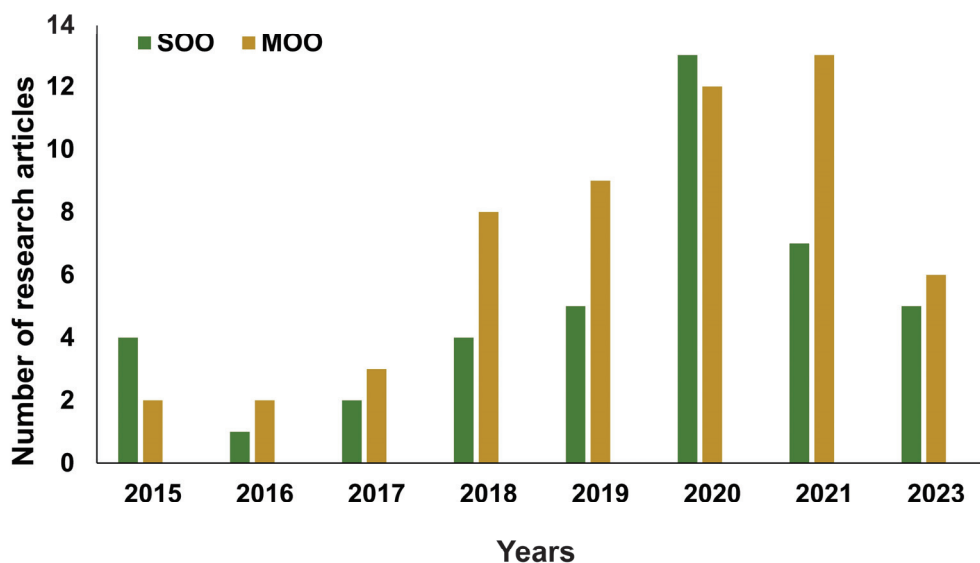
Figure 12. The use of SOO vs. MOO in the reviewed research articles.

Sizing: The optimization of sizing and proportions for solar–wind hybrid system components is crucial for cost reduction and operational satisfaction. However, as system complexity increases because of uncertainties such as output fluctuations, load variation, and constraints, a single algorithm may not be effective. A novel approach that combines the strengths of multiple methods holds promise for optimized sizing with increased precision and reduced computational time, addressing complex system dynamics challenges. Future optimization of HPP sizes involves considering not only minimizing annual and fuel costs but also enhancing reliability through factors like the human development index and job market, as well as bolstering sustainability and resilience. Exploring sizing methodologies that incorporate operational safety, sustainability, and resilience indicators could help address these challenges. Figures 13 and 14 show the sizing methodologies and evaluation criteria used in the literature. The occurrence frequency of meta-heuristic algorithms and software tools is the highest.
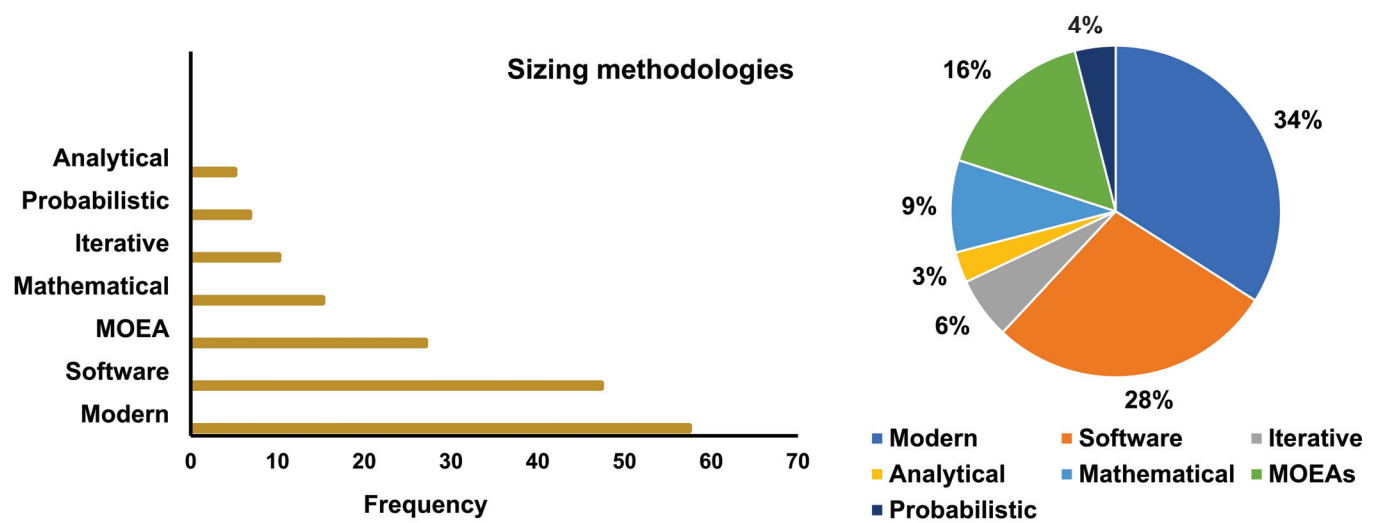
Figure 13. Summary of sizing methodologies used in the literature.
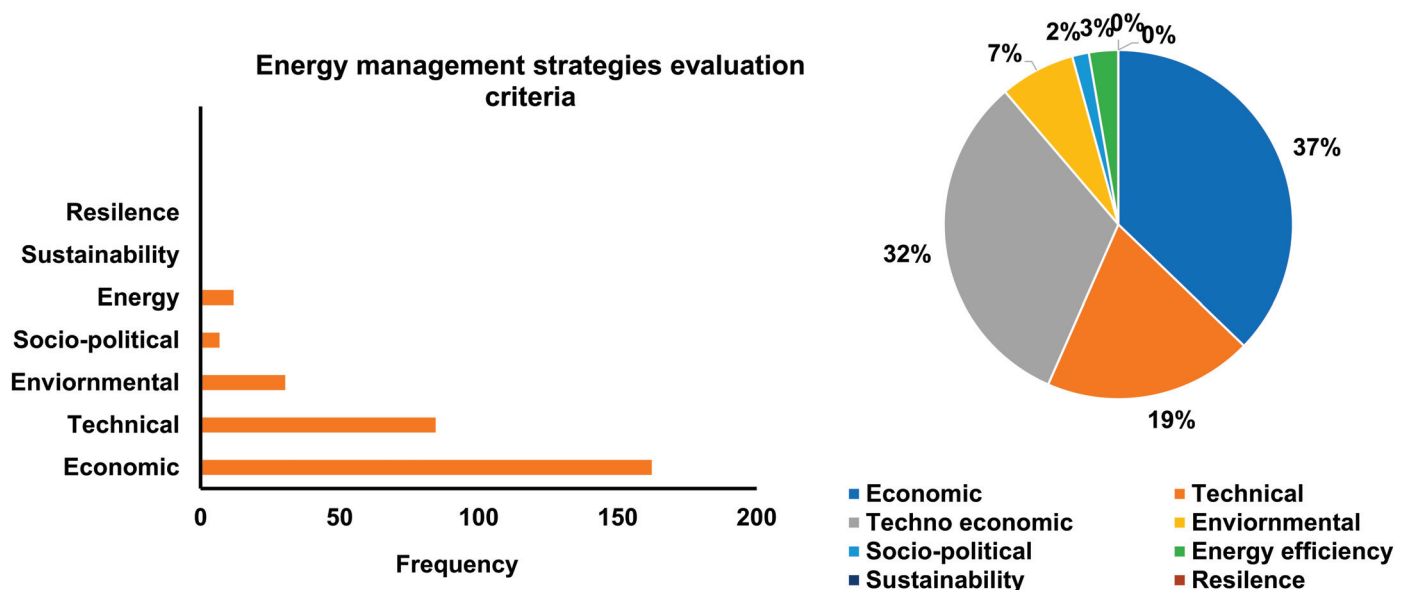
Figure 14. Summary of optimization evaluation criteria used in the literature.

Control and Energy Management Strategies

Control strategies for HPPs employ various control strategies, including centralized, distributed, and hybrid. Distributed and hybrid control methods are effective in managing generators autonomously, reducing system failure risk, extending system lifespan, and enabling advanced control techniques. However, the most challenging aspect lies in the complexity of interconnections or programming logic processing within the system. Energy management strategies are designed to optimize energy flow and determine operational equipment and power levels. The complexity of a strategy depends on optimization goals, system topology, and configuration. This study reveals that researchers favor rule-based energy management strategies over complex optimization techniques because of their ease of application and quick calculations. Economic considerations are a key factor in sizing optimization models for HPPs. Simplistic strategies focus on demand fulfillment but lack optimization parameters considering operating costs and equipment degradation. Technical strategies aim to amplify the system response and minimize equipment wear, while economic strategies aim to minimize cost functions by establishing priority and reference power levels for system elements. However, these strategies require intricate optimization algorithms, introducing an extra layer of complexity. Despite this complexity, these strategies yield optimal solutions for energy storage systems, aiding in the design of effective energy control systems to enhance overall system performance. In general, the developed sizing optimization model is used to assess the HPP characteristics that characterize a feasible project from the beginning. However, more sophisticated strategies must be developed to take into consideration several variables, including battery deterioration, the choice of turbine technology, uncertainties, diverse market engagement, and more. The research community should focus on refining artificial intelligence techniques and strategically integrating them to address various objective functions. As autonomous microgrid systems grow, robust communication and real-time energy management strategies are crucial. Table 9 summarizes control algorithms, optimization objectives, limitations, and descriptions of EMS from the recent literature.

Table 9. Summary of the control algorithms, optimization goals, constraints, and EMS descriptions obtained from the recent literature.

Management Strategies	Control Algorithm/Approach	Energy System	Design Constraints	Objectives	Reference
Power requirement	Flowchart	Wind/solar/FC	Power balance, SOC, H$_2$ stock	Ensure demand sizing	Cozzolino et al. [143]
	Flowchart	Wind/solar/H$_2$	Power balance, SOC, H$_2$ stock	Ensure demand	Zhang et al. [144]
	Flowchart	Wind/solar/battery	Power balance, SOC	Ensure demand	Bade et al. [40]
Technical	ANN	Wind/solar/battery	Power balance, SOC, battery degradation	Redue LPSP, ensure demand	Q. Li et al. [145]
	Flowchart	Wind/solar/battery	Power balance, SOC	Ensure demand, quality of service	Long et al. [39]
	PMC/multi-objective approach	Wind/solar/battery/FC	Power balance, SOC, battery degradation, H$_2$	Increase reliability, ensure demand	Eriksson and Gray [135]
	PSO Recurrent neural network Flowchart	Wind/solar/battery/FC	Power balance, SOC, battery degradation, H$_2$	Reduce LPSP, ensure demand	Yan et al. [137]
	Multi-stage machine learning	Wind/solar/battery/FC	Power balance, SOC, battery degradation, H$_2$	Ensure demand, reliability	Shibl et al. [128]
Economical	Linear programing and simulation	Wind/solar/battery	Power demand, SOC, cost	Reduce system cost	Nogueira et al. [146]
	MLIP	Wind/solar	Power demand, SOC, cost	Reduce total operating cost	Lamedica et al. [147]
	FL	Wind/solar/battery/FC	Power demand, SOC, cost, H$_2$	Ensure demand	Rouholamini and Mohammadian [148]
	Flowchart, supervisory hierarchical control system	Wind/solar/battery/auxiliary	Power demand, SOC, cost	Ensure demand, increase revenue	Long et al. [39]
Techno-economic	FL	Wind/solar	Power balance, cost	Increase reliability and reduced loss	García-Triviño et al. [149]
	PSO	Wind/solar/battery/FC	Power demand, SOC, cost, H$_2$, battery and electrolyzer degradation	Ensure demand, minimize operating and maintenance cost, increase reliability and performance	Valverde et al. [150]
	Lyapunov technique, simultaneous perturbation stochastic approximation	Wind/solar/battery	Power demand, SOC, cost, battery degradation	Increase reliability and performance	Ciupageanu et al. [151]
	GA	Wind/solar/battery/thermal load	Cost	Cost reduction and sustainability	Das et al. [152]
	ANN, MATLAB	Wind/solar/battery/electrolyzer/FC/	LCOE	Reduce LCOE, reduce power curtail	Hamdi et al. [142]
	HOMER	Wind/solar/battery/electrolyzer/FC/thermal load	Power demand, SOC, cost, battery/FC/electrolyzer degradation,	Ensure demand, cost of energy	Priyanka et al. [153]
	Improve search space reduction	Wind/solar/battery	power demand, SOC, cost	Ensure demand, reduce levelized cost of energy	Nirbheram et al. [154]

9. Research Opportunities

Research gaps in hybrid power plants (HPPs) have been discovered, emphasizing the need for more study to solve operational issues related to solar intermittency and wind output curtailment. Because of the lack of long-term performance data from such systems, research papers that use modeling tools for system design and optimization of hybrid systems incorporating solar photovoltaic and wind turbine technologies frequently have limitations because they are not always compared to real-world results.

HPP systems work in a complex way, with several controllers and control loops that are connected via connections. Communication breakdowns may have a significant effect on how well HPPs operate as a whole. The control architecture, goals, and topology of the HPP determine how data are exchanged and communicated. Grid compliance and auxiliary services need appropriate data exchange and communication frameworks, as well as time resolution, management of communication failures, and determination of variables transferred.

Moreover, with differing control techniques and flexibility in manipulating various variables, the integration of controllers from multiple suppliers increases complexity. As such, it is essential to examine these problems while designing the control architecture and fine-tuning control settings.

Artificial intelligence (AI) has proven useful in several renewable energy-related fields. Advanced dynamic modeling and the identification of various causes of uncertainty may be accomplished via the application of AI and machine learning techniques. Notably, AI-driven model-free methods for HPPs have not yet been investigated in the field of regulating unknown parameters. The incorporation of such methodologies may affect HPPs' control structure, hence augmenting its dependability and resilience to uncertainties.

10. Future Trends

Anticipated advancements, government incentives, and policies in solar and wind technologies are expected to decrease costs for renewable energy sources, contrasting with the annual increase in expenses for traditional energy resources. As a result, this combination of energy sources will become more cost-effective in the future, and the positive environmental impacts are likely to promote its adoption.

Additionally, the integration of artificial intelligence into energy management is expected to enhance the hybrid system's performance in the near term. This involves optimizing resource allocation based on demand and predicting renewable resource availability, which can significantly cut down operational expenses. The future optimization of HPP sizes involves considering not only minimizing annual and fuel costs but also maximizing the profit and utilization of the infrastructure and environmental aspects like the human development index and job market, as well as bolstering sustainability and resilience. This requires implementing sophisticated control methods through a distributed and hybrid controller, which holds the potential to enhance the efficiency of modular HPPs. Lastly, applying modern control techniques to monitor the operation of these modular HPPs further optimizes the utilization of renewable resources and enhances energy management.

11. Conclusions

This paper reviewed and analyzed the available research articles on sizing, optimization, energy management, and control strategies to develop co-located wind- and solar-based HPPs. This review shows that the number of published papers on HPPs has increased because of growing interest from both the industry and the scientific community in recent times. There are a large number of review articles related to the scope of this paper; however, only a few of them have considered utility-scale wind- and solar-based HPPs without explicitly covering them. Therefore, a comprehensive comparative assessment is needed. This paper reviewed various approaches used by academics to optimize these systems, whether grid-tied or not. Meta-heuristic algorithms are the most popular methods for sizing wind–solar hybrid systems. No single approach has outperformed across all problem

types. Using a hybrid approach that combines two or more meta-heuristic optimization techniques helped find the global best system configurations and made risk assessments more thorough by taking into account more factors. HOMER stands out as the most widely used software tool because of its comprehensive incorporation of renewable energy systems. It facilitates optimization and sensitivity analyses, streamlining the evaluation process for a multitude of potential system configurations. In terms of control and energy management strategies, hybrid centralized and distributed control strategies appear to be effective for efficient operation, meeting demand, and improving performance. Centralized control optimizes local groups, while distributed control ensures global coordination among groups, minimizes system failure risks, and enables the integration of multiple control methods within a single system. The findings suggest the need for further advancements in algorithms and multi-objective strategies for widespread use in distributed energy applications. Comparative studies are also needed to draw general conclusions about co-locating wind and PV farms. Future research should address larger-scale challenges, complex objective spaces, and inherent uncertainty, as well as incorporate a diverse range of methods to develop robust hybrid algorithms.

Abbreviations

HPP	hybrid power plant
RES	renewable energy sources
MW	mega watt
PCC	point of common connection
COE	cost of energy
ASC	annualized system cost
LCOE	levelized cost of energy
LCC	life cycle cost
LLP	loss of load probability
LPSP	loss of power supply probability
RF	renewable fraction
REF	renewable energy factor
AI	artificial intelligence
GA	genetic algorithm
PSO	particle swarm optimization
HOMER	hybrid optimization of multiple energy resources
EMSs	energy management strategies
PV	photovoltaic
WT	wind turbine
HRES	hybrid renewable energy system
WoS	Web of Science
AC	alternate current
DC	direct current
LPM	linear programming model

MOEA	multi-objective evolutionary algorithms
MILP	multi-integer linear programming
NLP	non-linear programming
HSA	harmony search algorithm
SA	simulated annealing
ACA	ant colony algorithm
BFO	bacterial foraging algorithm
ABC	artificial bee colony algorithm
CS	cuckoo search
ANN	artificial neural network
SOC	state of charge
FLC	fuzzy logic control
FL	fuzzy logic
ANFIS	adaptive neuro-fuzzy inference system
FAHP	fuzzy analytic hierarchy process
GAPSO	generic algorithm particle swarm optimization
SOO	single-objective optimization
MOO	multi-objective optimization
NPV	net present value
IPSO	improved particle swarm optimization
GWO	grey wolf optimization
NREL	National Renewable Energy Laboratory
HOGA	hybrid optimization of generic algorithm
TRNSYS	transient system simulation software
RETSCreen	renewable-energy and energy-efficiency technology screening software
FC	fuel cell
PGUs	power generating units
STATCOM	static synchronous compensator
MPC	model predictive control
TLBO	teaching learning-based optimization
EDE	enhanced differential evolution
SSA	slap swarm algorithm
FPA	flower pollination algorithm
GSA	gravitation search algorithm
CSA	crow search algorithm

Appendix A

See Tables A1–A4.

Table A1. Economic, reliability, social, energy efficiencies, and environmental indices, and their main formulas (adapted from: [129]).

Assessment	Preferred Indicators	Functions
Technical indicator	LPSP	$LPSP = \dfrac{\sum_{t=1}^{T} \lvert P_{load}(t) - P_{supply}(t) \rvert}{\sum_{t=1}^{T} P_{load}(t)}$
Economic indicator	NPC	$NPC = C_{ini} + \sum_{n=1}^{N_s} \left(\dfrac{C_{annual}}{(1+r)^n} + \dfrac{C_{replace}}{(1+r)^{N_R}} + \dfrac{C_{salvage}}{(1+r)^{N_s}} \right)$
	ACS	$ACS = C_{ini} + C_{replace} \, x \, \dfrac{r(1+r)^{N_s}}{(1+r)^{N_s}-1} + C_{annual}$
	LCOE	$LCOE = \dfrac{C_{ini} + \sum_{m=1}^{N_s} \left(\frac{C_{annual}}{(1+r)^n} + \frac{C_{replace}}{(1+r)^{N_R}} + \frac{C_{salvage}}{(1+r)^{N_s}} \right)}{\sum_{m=1}^{N_s} \frac{E_{first}(1-d)^n}{(1+r)^n}}$
Social political indicator	HDI	$HDI = 0.0978 \; x \; ln\left(\sum_{t=1}^{8760} E_{load}(t) \right) - 0.0319$
	JC	$JC = \sum_{m=1}^{M} jC_m \cdot C_{renew \cdot m}$
Energy Efficiency indicator	ECR	$ECR = \dfrac{\sum_{t=1}^{T} \lvert P_{renew}(t) - P_{load}(t) \rvert}{\sum_{t=1}^{T} P_{renew}(t)}$
Environmental indicator	E_{carbon}	$E_{carbon} = \sum_{t=1}^{T} \sum_{n=1}^{N} \theta_n \cdot P_{fossil}(t)$
	LCCF	$LCCF = E_{carbon} + \sum_{n=1}^{N} \delta_n \cdot C_{fossil \cdot n} + \sum_{m=1}^{M} \delta_m \cdot C_{renew \cdot m}$
	LEOE	$LEOE = \dfrac{E_{carbon} + \sum_{n=1}^{N} \delta_n \cdot C_{fossil \cdot n} + \sum_{m=1}^{M} \delta_m \cdot C_{renew \cdot m}}{\sum_{m=1}^{N_s} E_{first}(1-d)^n}$

HDI = human development index. JC = job creation. $P_{load}(t)$ = load demand at time t. $P_{supply}(t)$ = power supply of HPP at time t. T = simulation period. C_{ini} = initial investment cost. C_{annual} = operation and maintenance cost. $C_{replace}$ = replacement cost. $C_{salvage}$ = salvage value at the end of lifetime. N_R = year of component replacement. N_s = design lifetime. r = discount rate. E_{first} = first-year energy production. d = degradation rate. $E_{load}(t)$ = load demand at time t. jc_n = job creation factor of renewable installed capacity. jc_n = job creation coefficient of electricity generated by fossil-based technologies. $C_{fossil \cdot n}$ = rated capacity of the n-th fossil-based technology. $C_{renew \cdot m}$ = rated capacity of the m-th renewable energy technology. $P_{renew}(t)$ = renewable energy generation at time t. $P_{load}(t)$ = load demand at time t. E_{carbon} = direct carbon emissions produced by non-renewable energy technologies. θ_n = direct carbon emission coefficient of fossil-based technologies per kilowatt-hour. $P_{fossil \cdot n}(t)$ = power output of the n-th fossil-based technology at time t. δ_m and δ_n = indirect carbon emission coefficients of renewable and fossil-based technologies per kilowatt-hour. $C_{fossil \cdot n}$ = rated capacity of the n-th fossil-based technology. $C_{renew \cdot m}$ = rated capacity of the m-th renewable energy technology.

Table A2. Highlights of review studies on sizing and optimization and energy management strategies of renewable energy-based hybrid systems from 2014 to 2023.

Reference/Year of Study	System Studied	Topic Covered	Highlights
Chauhan and Saini [109]	HRES	• Reviewed various configurations (AC/DC) and energy storage technology options for system control and management. • Mathematical models for wind, micro-hydro, solar, and biomass gasifier energy systems. • Sizing techniques including AI, multi-objective design, iterative approaches, analytical methods, probabilistic approaches, and graphical construction methods. • Software tools including HOMER, HOGA, RETScreen, HYBRIDS, and TRNSYS for assessing and analyzing hybrid energy systems.	• DC-AC-coupled is efficient and the least-cost scheme. • A combination of centralized and distributed control approaches is acknowledged as optimal to ensure strong control in IRES without single point failure issues.
Siddaiah and Saini [25]	HRES	• Review on planning, configurations, and modeling and optimization techniques of hybrid renewable energy systems for off-grid applications. • Mathematical model for cost minimization. • Optimization models including classic, artificial intelligence, and hybrid. • Sizing methodologies including classical techniques, artificial intelligence, and hybrid techniques.	• Reliability-centric models improve system performance and reduce uncertainty in renewable energy resources.
Al-falahi et al. [55]	HRES	• Various combinations of wind/solar. • Sizing techniques including single algorithms and hybrid algorithms. • Software tools including HOMER and iHOGA.	• AI algorithms are increasingly popular for solving complex optimization challenges, while hybrid algorithms are increasingly preferred because of their favorable results in recent times.
Khan et al. [28]	Solar photovoltaic and wind hybrid energy systems	• Economic feasibility, sizing strategies, and future prospects. • Optimization techniques including graphical construction, iterative methodologies, direct programming, multi objectives optimization function, and probabilistic. • New approach including GA, PSO, SA, ACA, and ABC.	• Artificial intelligence and hybrid algorithms performed better than traditional approach. However, the hybridization of more than two algorithms is recommended for better performance.
Anoune et al. [17]	PV–wind based HRES	• Various configurations of hybrid renewable energy systems. • Hybrid systems' performance metrics including reliability and system cost. • Sizing methods including AI, GA, PSO, SA, CS, MOO, HSA, iterative, probabilistic, and analytical. • Software tools including HOMER, HYBRID2, HOGA, HYBRIDS, TRNSYS, etc.	• The literature shows hybrid renewable energy systems lack cost competitiveness compared with conventional fossil fuel-based power systems. • Methods of optimization, such as those centered around artificial intelligence algorithms and heuristic techniques, are more favorably received compared with conventional approaches. Among these, HOMER stands out as the predominantly utilized tool.

Table A2. *Cont.*

Reference/Year of Study	System Studied	Topic Covered	Highlights
Lian et al. [83]	HRES	• Various configurations of hybrid renewable energy systems. • Sizing methodologies including analytical, probabilistic, iterative, numerical, graphic construction, GA, PSO, SA, ACO, ABC, CS, and hybrid methods. • Software tools including HOMER, iHOGA, HYBRIDS, and HYBRID2.	• Hybrid optimization techniques are recommended because of their adaptability and optimization capabilities, enabling a comprehensive exploration of the subject.
Lindberg et al. [13]	Wind–solar battery HPP	• Co-located wind and solar park modeling methodologies. • Physical design, control strategies, market participation, and quantification of possible synergies.	• Energy management systems require intelligence and dispatch models to optimize resource utilization and maximize resource utilization.
Ammari et al. [34]	HRES	• Reviewed sizing, optimization, and control and energy management. • Sizing methods including traditional and software, optimization techniques including classical, artificial, and hybrid methods. • Control methods including centralized, distributed, and hybrid control. • Energy management objectives including technical, economic, and techno-economic.	• Highlighted that the use machine learning, commercial software, and neural networks is a good option for hybrid systems. • Hybrid renewable energy systems utilize fuzzy logic, particle swarm optimization, neural networks, and commercial software like HOMER for overseeing components.
Emad et al. [91]	Wind–solar battery	• Reviewed mathematical formulations for wind, solar and energy storage • Economic aspects including NPC, LCC, TAC, and COE TLBO. • Sizing approaches including classical techniques, meta-heuristic techniques, and hybrid techniques. • Software tools including HOMER.	• Meta-heuristic optimization methods offer higher precision and reduced computational time compared with conventional techniques.
Thirunavukkarasu et al. [81]	HRES	• Reviewed various optimization techniques. • Optimization techniques including classical, artificial, hybrid, and software tools. • Types of optimization problems included constraints, variables, problem structure, nature of equations, permissible value of the design variables, separability of the function, and the number of objective functions.	• Hybrid optimization algorithms provide a faster, more reliable, and efficient method for problem-solving.
Iweh et al. [35]	HRES	• Reviewed hybrid system performance indicators. • Optimization methods including classical, meta-heuristic, and software. • Software tools including HOMER, iHOGA, RETScreen, TRNSYS, HYCROGEM, HYBRIDS, and INSEL.	• AI-based hybrid methodologies offer superior system optimization effectiveness.

Table A3. Summary of various studies on optimization methods for a single objective.

Optimization Method	System Configurations	Optimization Function	Constraints	Reference
GA FL	Wind/PV/battery	Minimize total cost	Power balance State of charge	Adbelhak et al. [155]
ACA, Integer LPM	Wind/PV	Minimize total cost	Number of PV panels, wind turbines, and batteries	Fetanat et al. [156]
PSO SA	Wind/PV/battery	Minimize total present cost	Number of hybrid components, energy not supplied, battery SOC	Ahmadi et al. [157]
CS	Wind/PV/battery	Minimize total cost	Seasonal variation in the load	Sanajaoba and Fernandez, [158]
SA, CS, Improved HS	PV–wind–reverse osmosis–battery	Minimize total LCC	Surface area of PV arrays, wind turbine blades, quantity of batteries, LPSP, and SOC	Peng et al. [159]
TLBO, EDE, and SSA	Wind–PV	Minimize TAC, reliability	Number of hybrid system components, LPSP, DOD	Khan et al. [20]
Jaya, TLBO	Wind/PV/battery	Minimize TAC	Number of hybrid system components, LPSP, SOC	Khan et al. [160]
AC, firefly algorithm, PSO, GA	Wind/PV/battery	NPC	Number of hybrid system components, SOC	Javed et al. [161]
Crow and PSO	Wind/PV/battery	Minimize COE	Distribution of power supply and demand planning	Guneser et al. [162]
GWO Sine cosine Algorithm	Wind/PV/H$_2$	Minimize LCC	Number of hybrid system components	Jahannoosh et al. [163]

Table A4. Summary of various studies on optimization methods for multiple objective functions.

Optimization Method	System Configurations	Optimization Function	Constraints	Reference
FPA SA	Wind/PV/battery	Minimize LPSP Maximize cumulative saving	PV panel tilt angle, number of PVs, wind turbines, and batteries	Tahani et al. [164]
PSO GA	Wind/PV/battery	Minimize LPSP Minimize LCC Minimize fluctuation rate Minimize loss of energy probability	Numbers of PVs, wind turbines, and batteries	Ma et al. [165]
PSO Nelder Mead Algorithm	PV/wind/fuel cell	Minimize power loss	Power balance, bus voltage	Senthil et al. [166]
PSO GSA	PV/wind	Minimize total energy loss Maximize voltage profit	Power flow m bus voltage, load constraints, PV/wind capacity	Radosavljevic et al. [167]
Biogeography-based optimization, PSO	Wind/PV/battery	Minimize cost Minimize system index reliability	Power balance between supply and demand	Abuelrub et al. [168]
CSA, PSO	Wind/PV/battery	Minimize cost Minimize loss Minimize voltage profile	Number of hybrid system components, size of batteries, network bus voltage constraint, allowable current constraint, peak capacity of each renewable DG constraint, and power balance constraint	Aliabadi et al. [169]

References

1. United Nation [UN]. *Adoption of the Paris Agreement 2015*; United Nation: New York, NY, USA, 2015.
2. Dykes, K.; King, J.; DiOrio, N.; King, R.; Gevorgian, V.; Corbus, D.; Blair, N.; Anderson, K.; Stark, G.; Turchi, C.; et al. Opportunities for Research and Development of Hybrid Power Plants. National Renewable Energy Laboratory 2020; NREL/TP-5000-75026. Available online: https://www.nrel.gov/docs/fy20osti/75026.pdf (accessed on 7 April 2023).
3. Das, K.; Hansen, A.D.; Vangari, D.H.; Koivisto, M.J.; Sørensen, P.E.; Altin, M. Enhanced Features of Wind-based Hybrid Power Plants. In Proceedings of the 4th International Hybrid Power Systems Workshop 2019, Crete, Greece, 22–23 May 2019.
4. Kryonidis, G.C.; Kontis, E.O.; Papadopoulos, T.A.; Pippi, K.D.; Nousdilis, A.I.; Barzegkar-Ntovom, G.A.; Boubaris, A.; Papanikolaou, N. Ancillary services in active distribution networks: A review of technological trends from operational and online analysis perspective. *Renew. Sustain. Energy Rev.* **2021**, *147*, 111198. [CrossRef]
5. Mar, A.; Pereira, P.; Martins, J. A survey on power grid faults and their origins: A contribution to improving power grid resilience. *Energies* **2019**, *12*, 4667. [CrossRef]
6. Buonomano, A.; Calise, F.; D'Accadia, M.D.; Vicidomini, M. A hybrid renewable system based on wind and solar energy coupled with an electrical storage: Dynamic simulation and economic assessment. *Energy* **2018**, *155*, 174–189. [CrossRef]
7. Petersen, L.; Iov, F.; Tarnowski, G.C.; Gevorgian, V.; Koralewicz, P.; Stroe, D. Validating Performance Models for Hybrid Power Plant Control Assessment. *Energies* **2019**, *12*, 4330. [CrossRef]
8. Bade, S.O.; Meenakshisundaram, A.; Omojiba, T.; Tomomewo, O. Battery Uses for Regulating Active Power in Utility-scale Wind-based Hybrid Power Plant. *Am. J. Energy Res.* **2023**, *11*, 82–92. [CrossRef]
9. François, B.; Hingray, B.; Raynaud, D. Increasing climate-related-energy penetration by integrating run-of-the river hydropower to wind/solar mix. *Renew. Energy* **2016**, *87*, 686–696. [CrossRef]
10. Guangqian, D.; Bekhrad, K.; Azarikhah, P. A hybrid algorithm-based optimization on modeling of grid-independent biodiesel-based hybrid solar/wind systems. *Renew. Energy* **2018**, *122*, 551–560. [CrossRef]
11. Vivas, F.; De Las Heras, A.; Segura, F.; Andújar, J.M. A review of energy management strategies for renewable hybrid energy systems with hydrogen backup. *Renew. Sustain. Energy Rev.* **2018**, *82*, 126–155. [CrossRef]
12. Wind Europe. Renewable Hybrid Power Plants-Exploring the Benefits and Market Opportunities. 2019. Available online: https://windeurope.org/wp-content/uploads/files/policy/position-papers/WindEurope-renewable-hybrid-power-plants-dasbenefits-and-market-opportunities.pdf (accessed on 7 April 2023).
13. Lindberg, O.; Arnqvist, J.; Munkhammar, J.; Lingfors, D. Review on power-production modeling of hybrid wind and PV power parks. *J. Renew. Sustain. Energy* **2021**, *13*, 042702. [CrossRef]
14. Lawan, S.M.; Abidin, W.A.W.Z. A review of hybrid renewable energy systems based on wind and solar Energy: Modeling, design and Optimization. In *Wind Solar Hybrid Renewable Energy System*; IntechOpen: London, UK, 2020. [CrossRef]
15. Mahesh, A.; Sandhu, K.S. Hybrid wind/photovoltaic energy system developments: Critical review and findings. *Renew. Sustain. Energy Rev.* **2015**, *52*, 1135–1147. [CrossRef]
16. Khare, V.; Nema, S.; Baredar, P. Solar–wind hybrid renewable energy system: A review. *Renew. Sustain. Energy Rev.* **2016**, *58*, 23–33. [CrossRef]
17. Anoune, K.; Bouya, M.; Astito, A.; Abdellah, A.B. Sizing methods and optimization techniques for PV-wind based hybrid renewable energy system: A review. *Renew. Sustain. Energy Rev.* **2018**, *93*, 652–673. [CrossRef]
18. Jurasz, J.; Canales, F.A.; Kies, A.; Ma, T.; Beluco, A. A review on the complementarity of renewable energy sources: Concept, metrics, application and future research directions. *Sol. Energy* **2020**, *195*, 703–724. [CrossRef]
19. Ding, Z.; Hou, H.; Yu, G.; Hu, E.; Duan, L.; Zhao, J. Performance analysis of a wind-solar hybrid power generation system. *Energy Convers. Manag.* **2019**, *181*, 223–234. [CrossRef]
20. Khan, A.; Alghamdi, T.A.; Khan, Z.A.; Fatima, A.; Abid, S.; Khalid, A.; Javaid, N. Enhanced evolutionary sizing algorithms for optimal sizing of a Stand-Alone PV-WT-Battery hybrid system. *Appl. Sci.* **2019**, *9*, 5197. [CrossRef]
21. Stanley, A.P.J.; King, J. Optimizing the physical design and layout of a resilient wind, solar, and storage hybrid power plant. *Appl. Energy* **2022**, *317*, 119139. [CrossRef]
22. González-Ramírez, J.M.; Arcos-Vargas, Á.; Hernández, F.N. Optimal sizing of hybrid wind-photovoltaic plants: A factorial analysis. *Sustain. Energy Technol. Assess.* **2023**, *57*, 103155. [CrossRef]
23. Hu, W.; Zhang, H.; Dong, Y.; Wang, Y.; Dong, L.; Xiao, M. Short-term optimal operation of hydro-wind-solar hybrid system with improved generative adversarial networks. *Appl. Energy* **2019**, *250*, 389–403. [CrossRef]
24. Ishraque, M.F.; Shezan, S.A.; Ali, M.; Rashid, M.M. Optimization of load dispatch strategies for an islanded microgrid connected with renewable energy sources. *Appl. Energy* **2021**, *292*, 116879. [CrossRef]
25. Siddaiah, R.; Saini, R. A review on planning, configurations, modeling and optimization techniques of hybrid renewable energy systems for off grid applications. *Renew. Sustain. Energy Rev.* **2016**, *58*, 376–396. [CrossRef]
26. Ma, W.; Xue, X.; Liu, G. Techno-economic evaluation for hybrid renewable energy system: Application and merits. *Energy* **2018**, *159*, 385–409. [CrossRef]
27. Tripp, C.; Guittet, D.; King, J.; Barker, A. A simplified, efficient approach to hybrid wind and solar plant site optimization. *Wind Energ. Sci.* **2022**, *7*, 697–713. [CrossRef]
28. Khan, F.A.; Pal, N.; Saeed, S.H. Review of solar photovoltaic and wind hybrid energy systems for sizing strategies optimization techniques and cost analysis methodologies. *Renew. Sustain. Energy Rev.* **2018**, *92*, 937–947. [CrossRef]

29. Mahesh, A.; Sandhu, K.S. A genetic algorithm based improved optimal sizing strategy for solar-wind-battery hybrid system using energy filter algorithm. *Front. Energy* **2020**, *14*, 139–151. [CrossRef]

30. Ghofrani, M.; Hosseini, N.N. Optimizing hybrid renewable energy systems: A review. *Sustain. Energy-Technol. Issues Appl. Case Stud.* **2016**, *8*, 161–176.

31. Belouda, M.; Hajjaji, M.A.; Sliti, H.; Mami, A. Bi-objective optimization of a standalone hybrid PV–Wind–battery system generation in a remote area in Tunisia. *Sustain. Energy Grids Netw.* **2018**, *16*, 315–326. [CrossRef]

32. Ghorbani, N.; Kasaeian, A.; Toopshekan, A.; Bahrami, L.; Maghami, A. Optimizing a hybrid wind-PV-battery system using GA-PSO and MOPSO for reducing cost and increasing reliability. *Energy* **2018**, *154*, 581–591. [CrossRef]

33. Barakat, S.; Ibrahim, H.; Elbaset, A.A. Multi-objective optimization of grid-connected PV-wind hybrid system considering reliability, cost, and environmental aspects. *Sustain. Cities Soc.* **2020**, *60*, 102178. [CrossRef]

34. Ammari, C.; Belatrache, D.; Touhami, B.; Makhloufi, S. Sizing, optimization, control and energy management of hybrid renewable energy system—A review. *Energy Built Environ.* **2022**, *3*, 399–411. [CrossRef]

35. Iweh, C.D.; Clarence, S.G.; Roger, A.H. The optimization of hybrid renewables for rural electrification: Techniques and the design problem. *Int. J. Eng. Trends Technol.* **2022**, *70*, 222–239. [CrossRef]

36. Petersen, L.; Hesselbak, B.; Martinez, A.; Borsotti-Andruszkiewicz, R.M.; Tarnowski, G.C.; Steggel, N.; Osmond, D. Vestas power plant solutions integrating wind, solar PV and energy storage. In Proceedings of the 3rd International Hybrid Power Systems Workshop, Tenerife, Spain, 8–9 May 2018.

37. Raducu, A.; Styliaras, N.; Funkqvist, J.; Ionita, C. Design and implementation of a hybrid power plant controller. In Proceedings of the 3rd International Hybrid Power Systems Workshop, Tenerife, Spain, 8–9 May 2018.

38. Pombo, D.V.; Iov, F.; Stroe, D. A Novel Control Architecture for Hybrid Power Plants to Provide Coordinated Frequency Reserves. *Energies* **2019**, *12*, 919. [CrossRef]

39. Long, Q.; Das, K.; Sørensen, P.E. Hierarchical Control Architecture of Co-located Hybrid Power Plants. *IEEE TechRxiv* **2021**, *143*, 108407. [CrossRef]

40. Bade, S.O.; Tomomewo, O.; Meenakshisundaram, A. Utility-Scale Wind-Based Hybrid Power Plants and Control Strategy. *Sustain. Energy* **2023**, *11*, 12–20. [CrossRef]

41. Nallolla, C.A.; Vijayapriya, P.; Dhanamjayulu, C.; Padmanaban, S. Multi-Objective Optimization Algorithms for a hybrid AC/DC microgrid using RES: A Comprehensive review. *Electronics* **2023**, *12*, 1062. [CrossRef]

42. Modu, B.; Abdullah, P.; Bukar, A.L.; Hamza, M.F. A systematic review of hybrid renewable energy systems with hydrogen storage: Sizing, optimization, and energy management strategy. *Int. J. Hydrogen Energy* **2023**, *48*, 38354–38373. [CrossRef]

43. Khan, A.A.; Minai, A.F.; Pachauri, R.K.; Malik, H. Optimal Sizing, control, and Management Strategies for Hybrid Renewable Energy Systems: A Comprehensive Review. *Energies* **2022**, *15*, 6249. [CrossRef]

44. Rullo, P.; Costa-Castelló, R.; Roda, V.; Feroldi, D. Energy Management strategy for a bioethanol isolated hybrid system: Simulations and experiments. *Energies* **2018**, *11*, 1362. [CrossRef]

45. Silva, A.R.; Estanqueiro, A. From Wind to Hybrid: A contribution to the optimal design of Utility-Scale Hybrid Power Plants. *Energies* **2022**, *15*, 2560. [CrossRef]

46. Upadhyay, S.; Sharma, M. A review on configurations, control and sizing methodologies of hybrid energy systems. *Renew. Sustain. Energy Rev.* **2014**, *38*, 47–63. [CrossRef]

47. Klonari, V.; Fraile, D.; Rossi, R.; Schmela, M. Exploring the Viability of HybridWind-Solar Power Plants. 2019. Available online: https://hybridpowersystems.org/crete2019/wp-content/uploads/sites/13/2020/03/3A_1_HYB19_063_paper_Klonari_Vasiliki.pdf (accessed on 29 July 2023).

48. Australian Renewable Energy Agency [ARENA]. Knowledge Sharing (Finclose Report). 2018. Available online: https://arena.gov.au/assets/2017/02/Kennedy-Park-FinClose-Report-Windlab.pdf (accessed on 30 July 2023).

49. India Energy Storage Alliance. Hero Launches India's First Solar-Wind Hybrid Project, n.d. Available online: https://indiaesa.info/buzz/news/industry-news/1192-hero-launches-india-s-first-solar-wind-hybrid-project (accessed on 29 July 2023).

50. Energymatters. Gamesa Commissions Hybrid System's Battery Storage 2016. Available online: https://www.energymatters.com.au/renewable-news/gamesa-offgrid-battery-em5744/ (accessed on 30 July 2023).

51. Kokkinidis, T. Tilos, Greece's First Energy-Self-Sufficient Island. Greekreporter 2022. Available online: https://greekreporter.com/2022/01/21/tilos-greece-first-energy-self-sufficient-island/ (accessed on 30 July 2023).

52. Gearino, D. A Clean Energy Trifecta: Wind, Solar and Storage in the Same Project. Inside Climate News 2022. Available online: https://insideclimatenews.org/news/06102022/a-clean-energy-trifecta-wind-solar-and-storage-in-the-same-project/ (accessed on 30 July 2023).

53. Invenergy. Grand Ridge Energy Center-Case Study Invenergy n.d. Available online: https://invenergy.com/projects/case-studies/blt0d2f2a9438d0674c (accessed on 30 July 2023).

54. Eriksson, E.; Gray, E.M. Optimization and integration of hybrid renewable energy hydrogen fuel cell energy systems—A critical review. *Appl. Energy* **2017**, *202*, 348–364. [CrossRef]

55. Al-Falahi, M.D.; Jayasinghe, S.G.; Enshaei, H. A review on recent size optimization methodologies for standalone solar and wind hybrid renewable energy system. *Energy Convers. Manag.* **2017**, *143*, 252–274. [CrossRef]

56. Chang, C. Multi-choice goal programming model for the optimal location of renewable energy facilities. *Renew. Sustain. Energy Rev.* **2015**, *41*, 379–389. [CrossRef]

57. Wang, R.; Li, G.; Ming, M.; Wu, G.; Wang, L. An efficient multi-objective model and algorithm for sizing a stand-alone hybrid renewable energy system. *Energy* **2017**, *141*, 2288–2299. [CrossRef]

58. Khan, A.; Naeem, M.; Iqbal, M.; Qaisar, S.; Anpalagan, A. A compendium of optimization objectives, constraints, tools and algorithms for energy management in microgrids. *Renew. Sustain. Energy Rev.* **2016**, *58*, 1664–1683. [CrossRef]

59. Moretti, L.; Astolfi, M.; Vergara, C.; Macchi, E.; Pérez-Arriaga, J.I.; Manzolini, G. A design and dispatch optimization algorithm based on mixed integer linear programming for rural electrification. *Appl. Energy* **2019**, *233–234*, 1104–1121. [CrossRef]

60. Wu, N.; Wang, H. Deep learning adaptive dynamic programming for real time energy management and control strategy of micro-grid. *J. Clean. Prod.* **2018**, *204*, 1169–1177. [CrossRef]

61. Das, B.; Kumar, A. A NLP approach to optimally size an energy storage system for proper utilization of renewable energy sources. *Procedia Comput. Sci.* **2018**, *125*, 483–491. [CrossRef]

62. Reddy, S.S.; Momoh, J.A. Realistic and transparent optimum scheduling strategy for hybrid power system. *IEEE Trans. Smart Grid* **2015**, *6*, 3114–3125. [CrossRef]

63. Abbes, D.; Martinez, A.; Champenois, G. Life cycle cost, embodied energy and loss of power supply probability for the optimal design of hybrid power systems. *Math. Comput. Simul.* **2014**, *98*, 46–62. [CrossRef]

64. Roy, P.; He, J.; Liao, Y. Cost minimization of Battery-Supercapacitor hybrid energy storage for hourly dispatching Wind-Solar hybrid power system. *IEEE Access* **2020**, *8*, 210099–210115. [CrossRef]

65. Sawle, Y.; Gupta, S.; Bohre, A.K. Techno-economic scrutiny of HRES through GA and PSO technique. *Int. J. Renew. Energy Technol.* **2018**, *9*, 84. [CrossRef]

66. Muleta, N.; Badar, A.Q.H. Designing of an optimal standalone hybrid renewable energy micro-grid model through different algorithms. *J. Eng. Res.* **2023**, *11*, 100011. [CrossRef]

67. Sharafi, M.; ElMekkawy, T.Y. Multi-objective optimal design of hybrid renewable energy systems using PSO-simulation based approach. *Renew. Energy* **2014**, *68*, 67–79. [CrossRef]

68. Sutikno, T.; Arsadiando, W.; Wangsupphaphol, A.; Yudhana, A.; Facta, M. A review of recent advances on hybrid energy storage system for solar photovoltaics power generation. *IEEE Access* **2022**, *10*, 42346–42364. [CrossRef]

69. Faria, J.; Pombo, J.; Calado, M.; Mariano, S. Power Management Control Strategy Based on Artificial Neural Networks for Standalone PV Applications with a Hybrid Energy Storage System. *Energies* **2019**, *12*, 902. [CrossRef]

70. Singh, P.; Lather, J.S. Dynamic power management and control for low voltage DC microgrid with hybrid energy storage system using hybrid bat search algorithm and artificial neural network. *J. Energy Storage* **2020**, *32*, 101974. [CrossRef]

71. Mohandes, B.; Wahbah, M.; Moursi, M.S.E.; El-Fouly, T.H.M. Renewable energy Management System: Optimum design and hourly dispatch. *IEEE Trans. Sustain. Energy* **2021**, *12*, 1615–1628. [CrossRef]

72. Athari, M.H.; Ardehali, M. Operational performance of energy storage as function of electricity prices for on-grid hybrid renewable energy system by optimized fuzzy logic controller. *Renew. Energy* **2016**, *85*, 890–902. [CrossRef]

73. Derrouazin, A.; Aillerie, M.; Mekkakia-Maaza, N.; Charles, J. Multi input-output fuzzy logic smart controller for a residential hybrid solar-wind-storage energy system. *Energy Convers. Manag.* **2017**, *148*, 238–250. [CrossRef]

74. Yahyaoui, I.; De La Peña, N.V. Energy management strategy for an autonomous hybrid power plant destined to supply controllable loads. *Sensors* **2022**, *22*, 357. [CrossRef] [PubMed]

75. Tito, S.R.; Lie, T.T.; Anderson, T. Optimal sizing of a wind-photovoltaic-battery hybrid renewable energy system considering socio-demographic factors. *Sol. Energy* **2016**, *136*, 525–532. [CrossRef]

76. Singh, P.; Pandit, M.; Srivastava, L. Multi-objective optimal sizing of hybrid micro-grid system using an integrated intelligent technique. *Energy* **2023**, *269*, 126756. [CrossRef]

77. Gu, Y.; Zhang, X.; Han, M.; Chen, X.; Yuan, Y. Techno-economic analysis of a solar photovoltaic/thermal (PV/T) concentrator for building application in Sweden using Monte Carlo method. *Energy Convers. Manag.* **2018**, *165*, 8–24. [CrossRef]

78. Alshammari, N.; Asumadu, J. Optimum unit sizing of hybrid renewable energy system utilizing harmony search, Jaya and particle swarm optimization algorithms. *Sustain. Cities Soc.* **2020**, *60*, 102255. [CrossRef]

79. Akram, U.; Khalid, M.; Shafiq, S. Optimal sizing of a wind/solar/battery hybrid grid-connected microgrid system. *Iet Renew. Power Gener.* **2017**, *12*, 72–80. [CrossRef]

80. Kong, L.; Cai, G.; Xue, S.; Li, S. Modeling and coordinated control strategy of large-scale Grid-Connected Wind/Photovoltaic/Energy Storage hybrid energy conversion system. *Math. Probl. Eng.* **2015**, *2015*, 682321. [CrossRef]

81. Thirunavukkarasu, M.; Sawle, Y.; Lala, H. A comprehensive review on optimization of hybrid renewable energy systems using various optimization techniques. *Renew. Sustain. Energy Rev.* **2023**, *176*, 113192. [CrossRef]

82. Li, W.; Jikang, L.; Hu, Z.; Li, S.; Chan, P.W. A novel probabilistic approach to optimize Stand-Alone Hybrid Wind-Photovoltaic renewable energy system. *Energies* **2020**, *13*, 4945. [CrossRef]

83. Lian, J.; Zhang, Y.; Ma, C.; Yang, Y.; Chaima, E. A Review on Recent Sizing Methodologies of Hybrid Renewable Energy Systems. *Energy Convers. Manag.* **2019**, *199*, 112027. [CrossRef]

84. Ganguly, P.; Kalam, A.; Zayegh, A. Solar–wind hybrid renewable energy system: Current status of research on configurations, control, and sizing methodologies. In *Hybrid-Renewable Energy Systems in Microgrids*; Elsevier: Amsterdam, The Netherlands, 2018; pp. 219–248. [CrossRef]

85. Karve, G.M.; Kurundkar, K.; Vaidya, G.A. Implementation of Analytical Method and Improved Particle Swarm Optimization Method for Optimal Sizing of a Standalone PV/Wind and Battery Energy Storage Hybrid System. In Proceedings of the 2019 IEEE 5th International Conference for Convergence in Technology, Bombay, India, 29–31 March 2019. [CrossRef]

86. Kiehbadroudinezhad, M.; Rajabipour, A.; Cada, M.; Khanali, M. Modeling, Design, and Optimization of a Cost-Effective and Reliable Hybrid Renewable Energy System Integrated with Desalination Using the Division Algorithm. *Int. J. Energy Res.* **2021**, *45*, 429–452. [CrossRef]

87. Muthukumar, R.; Balamurugan, P. A Novel Power Optimized Hybrid Renewable Energy System Using Neural Computing and bee Algorithm. *Automatika* **2019**, *60*, 332–339. [CrossRef]

88. Riaz, M.; Ahmad, S.; Hussain, I.; Naeem, M.; Mihet-Popa, L. Probabilistic Optimization Techniques in Smart Power System. *Energies* **2022**, *15*, 825. [CrossRef]

89. Zhang, W.; Maleki, A.; Rosen, M.A.; Liu, J. Sizing a stand-alone solar-wind-hydrogen energy system using weather forecasting and a hybrid search optimization algorithm. *Energy Convers. Manag.* **2019**, *180*, 609–621. [CrossRef]

90. Abdelshafy, A.M.; Hassan, H.; Jurasz, J. Optimal design of a grid-connected desalination plant powered by renewable energy resources using a hybrid PSO–GWO approach. *Energy Convers. Manag.* **2018**, *173*, 331–347. [CrossRef]

91. Emad, D.; El-Hameed, M.A.; Yousef, M.T.; El-Fergany, A.A. Computational methods for optimal planning of hybrid renewable microgrids: A comprehensive review and challenges. *Arch. Comput. Methods Eng* **2020**, *27*, 1297–1319. [CrossRef]

92. Müller, D.; Selvanathan, S.P.; Cuce, E.; Sudhakar, K. Hybrid solar, wind, and energy storage system for a sustainable campus: A simulation study. *Sci. Technol. Energy Transit.* **2023**, *78*, 13. [CrossRef]

93. Ur Rehman, S.; Rehman, S.; Qazi, M.U.; Shoaib, M.; Lashin, A. Feasibility Study of Hybrid Energy System for off-Grid Rural Electrification in Southern Pakistan. *Energy Explor. Exploit.* **2016**, *34*, 468–482. [CrossRef]

94. Das, B.; Hassan, R.; Tushar, M.S.H.K.; Zaman, F.; Hasan, M.; Das, P. Techno-economic and environmental assessment of a hybrid renewable energy system using multi-objective genetic algorithm: A case study for remote Island in Bangladesh. *Energy Convers. Manag.* **2021**, *230*, 113823. [CrossRef]

95. Elkadeem Younes, A.; Sharshir, S.W.; Campana, P.E.; Wang, S. Sustainable siting and design optimization of hybrid renewable energy system: A geospatial multi-criteria analysis. *Appl. Energy* **2021**, *295*, 117071. [CrossRef]

96. Sambhi, S.; Sharma, H.; Bhadoria, V.S.; Kumar, P.; Chaurasia, R.; Fotis, G.; Vita, V. Technical and Economic analysis of Solar PV/Diesel Generator Smart Hybrid Power Plant using different battery Storage Technologies for SRM IST, Delhi-NCR Campus. *Sustainability* **2023**, *15*, 3666. [CrossRef]

97. Sinha, S.; Chandel, S. Review of software tools for hybrid renewable energy systems. *Renew. Sustain. Energy Rev.* **2014**, *32*, 192–205. [CrossRef]

98. Brumana, G.; Franchini, G.; Ghirardi, E.; Perdichizzi, A.G. Techno-economic optimization of hybrid power generation systems: A renewables community case study. *Energy* **2022**, *246*, 123427. [CrossRef]

99. Tawfik, T.; Badr, M.A.; EYEl-Kady; Abdellatif, O.E. Optimization and energy management of hybrid standalone energy system: A case study. *Renew. Energy Focus* **2018**, *25*, 48–56. [CrossRef]

100. Al-Badi, A.; Wahaibi, A.A.; Ahshan, R.; Malik, A. Techno-Economic feasibility of a Solar-Wind-Fuel cell energy system in Duqm, Oman. *Energies* **2022**, *15*, 5379. [CrossRef]

101. Hoarca, I.C.; Bizon, N.; Sorlei, I.S.; Thounthong, P. Sizing design for a hybrid renewable power system using HOMER and iHOGA simulators. *Energies* **2023**, *16*, 1926. [CrossRef]

102. Belmili, H.; Haddadi, M.; Bacha, S.; Almi, M.; Bendib, B. Sizing stand-alone photovoltaic–wind hybrid system: Techno-economic analysis and optimization. *Renew. Sustain. Energy Rev.* **2014**, *30*, 821–832. [CrossRef]

103. Fadaeenejad, M.; Radzi, M.A.M.; AbKadir, M.Z.A.; Hizam, H. Assessment of hybrid renewable power sources for rural electrification in Malaysia. *Renew. Sustain. Energy Rev.* **2014**, *30*, 299–305. [CrossRef]

104. Ranaboldo, M.; Domenech, B.; Reyes, G.A.; Ferrer-Martí, L.; Moreno, R.P.; García-Villoria, A. Off-grid Community Electrification Projects Based on Wind and Solar Energies: A Case Study in Nicaragua. *Sol. Energy* **2015**, *117*, 268–281. [CrossRef]

105. Baker, D.K. Sizing of Photovoltaic-Wind-Battery Hybrid System for a Mediterranean Island Community Based on Estimated and Measured Meteorological Data. *J. Sol. Energy Eng.* **2018**, *140*, 011006. [CrossRef]

106. Babatunde, O.M.; Munda, J.L.; Hamam, Y. Hybridized off-grid fuel cell/wind/solar PV /battery for energy generation in a small household: A multi-criteria perspective. *Int. J. Hydrogen Energy* **2022**, *47*, 6437–6452. [CrossRef]

107. Hossen, D.; Shezan, S.A. Optimization and Assessment of a Hybrid Solar-Wind-Biomass Renewable Energy System for Kiribati Island. *Int. J. Eng. Trends Technol.* **2019**, *9*, 58–64. [CrossRef]

108. Mazzeo, D.; Baglivo, C.; Matera, N.; De Luca, P.; Congedo, P.M.; Oliveti, G. Energy and economic dataset of the worldwide optimal photovoltaic-wind hybrid renewable energy systems. *Data Brief* **2020**, *33*, 106476. [CrossRef]

109. Chauhan, A.; Saini, R. A review on Integrated Renewable Energy System based power generation for stand-alone applications: Configurations, storage options, sizing methodologies and control. *Renew. Sustain. Energy Rev.* **2014**, *38*, 99–120. [CrossRef]

110. Rathore, A.; Patidar, N.P. Reliability assessment using probabilistic modelling of pumped storage hydro plant with PV-Wind based standalone microgrid. *Int. J. Electr. Power Energy Syst.* **2019**, *106*, 17–32. [CrossRef]

111. Saiprasad, N.; Kalam, A.; Zayegh, A. Comparative Study of Optimization of HRES Using HOMER and iHOGA Software. *J. Sci. Ind. Res.* **2018**, *77*, 677–683.

112. Dubey, M.; Kumar, V.; Kaur, M.; Dao, T.P. A Systematic Review on Harmony Search Algorithm: Theory, Literature, and Applications. *Math. Probl. Eng.* **2021**, *2021*, 5594267. [CrossRef]

113. Gad, A.G. Particle Swarm Optimization Algorithm and Its Applications: A Systematic Review. *Arch. Comput. Methods Eng.* **2022**, *29*, 2531–2561. [CrossRef]

114. Wang, Y.; Wang, T.; Dong, S.; Yao, C. An Improved Grey-Wolf Optimization Algorithm Based on Circle Map. *J. Physics Conf. Ser.* **2020**, *1682*, 012020. [CrossRef]

115. Gupta, A.; Srivastava, S. Comparative Analysis of Ant Colony and Particle Swarm Optimization Algorithms for Distance Optimization. *Procedia Comput. Sci.* **2020**, *173*, 245–253. [CrossRef]

116. Shen, D.; Ming, W.; Ren, X.; Xie, Z.; Zhang, Y.; Liu, X. A Cuckoo Search Algorithm Using Improved Beta Distributing and its Application in the Process of edm. *Crystals* **2021**, *11*, 916. [CrossRef]

117. Kavadias, K.A.; Triantafyllou, P. Hybrid Renewable Energy Systems' Optimisation. *A Review and Extended Comparison of the Most-Used Software Tools. Energies* **2021**, *14*, 8268. [CrossRef]

118. Ramli, M.S.; Wahid, S.S.A.; Hassan, K.K. A comparison of renewable energy technologies using two simulation softwares: HOMER and RETScreen. *AIP Conf. Proc.* **2017**, *1875*, 030013. [CrossRef]

119. Long, Q.; Zhu, R.; Das, K.; Sørensen, P.E. Interfacing energy management with supervisory control for hybrid power plants. In Proceedings of the 20th International Workshop on Large-Scale Integration of Wind Power into Power Systems as well as on Transmission Networks for Offshore Wind Power Plants (WIW 2021), Hybrid Conference, Berlin, Germany, 29–30 September 2021. [CrossRef]

120. Olatomiwa, L.; Mekhilef, S.; Ismail, M.I.; Moghavvemi, M. Energy management strategies in hybrid renewable energy systems: A review. *Renew. Sustain. Energy Rev.* **2016**, *62*, 821–835. [CrossRef]

121. Wu, K.; Hua, Z. A multi-agent-based energy-coordination control system for grid-connected large-scale wind–photovoltaic energy storage power-generation units. *Sol. Energy* **2014**, *107*, 245–259. [CrossRef]

122. Karami, N.; Moubayed, N.; Outbib, R. Energy management for a PEMFC–PV hybrid system. *Energy Convers. Manag.* **2014**, *82*, 154–168. [CrossRef]

123. Torreglosa, J.P.; García, P.L.; Fernández, L.M.S.; Jurado, F. Energy dispatching based on predictive controller of an off-grid wind turbine/photovoltaic/hydrogen/battery hybrid system. *Renew. Energy* **2015**, *74*, 326–336. [CrossRef]

124. Behzadi, M.S.; Niasati, M. Comparative performance analysis of a hybrid PV/FC/battery stand-alone system using different power management strategies and sizing approaches. *Int. J. Hydrogen Energy* **2015**, *40*, 538–548. [CrossRef]

125. García, P.L.; Garcia, C.A.; Fernández, L.M.S.; Llorens, F.; Jurado, F. ANFIS-Based control of a Grid-Connected hybrid system integrating renewable energies, hydrogen and batteries. *IEEE Trans. Ind. Inform.* **2014**, *10*, 1107–1117. [CrossRef]

126. Agrawal, D.; Sharma, R.; Ramteke, M.; Kodamana, H. Hierarchical two-tier optimization framework for the optimal operation of a network of hybrid renewable energy systems. *Chem. Eng. Res. Des.* **2021**, *175*, 37–50. [CrossRef]

127. Hashemi, M.; Zarif, M.H. A novel two-stage distributed structure for reactive power control. *Eng. Sci. Technol. Int. J.* **2020**, *23*, 168–188. [CrossRef]

128. Shibl, M.; Ismail, L.; Massoud, A.M. An Intelligent Two-Stage energy dispatch Management System for hybrid power plants: Impact of machine learning deployment. *IEEE Access* **2023**, *11*, 13091–13102. [CrossRef]

129. He, Y.; Guo, S.; Dong, P.; Zhang, Y.; Huang, J.; Zhou, J. A state-of-the-art review and bibliometric analysis on the sizing optimization of off-grid hybrid renewable energy systems. *Renew. Sustain. Energy Rev.* **2023**, *183*, 113476. [CrossRef]

130. Zhu, J.; Yuan, Y.; Wang, W. Multi-stage active management of renewable-rich power distribution network to promote the renewable energy consumption and mitigate the system uncertainty. *Int. J. Electr. Power Energy Syst.* **2019**, *111*, 436–446. [CrossRef]

131. Forough, A.B.; Roshandel, R. Lifetime optimization framework for a hybrid renewable energy system based on receding horizon optimization. *Energy* **2018**, *150*, 617–630. [CrossRef]

132. Bonkile, M.P.; Ramadesigan, V. Power management control strategy using physics-based battery models in standalone PV-battery hybrid systems. *J. Energy Storage* **2019**, *23*, 258–268. [CrossRef]

133. Kosmadakis, I.; Elmasides, C. Towards performance enhancement of hybrid power supply systems based on renewable energy sources. *Energy Procedia* **2019**, *157*, 977–991. [CrossRef]

134. Rullo, P.; Braccia, L.; Luppi, P.; Zumoffen, D.; Feroldi, D. Integration of sizing and energy management based on economic predictive control for standalone hybrid renewable energy systems. *Renew. Energy* **2019**, *140*, 436–451. [CrossRef]

135. Eriksson, E.; Gray, E.M. Optimization of renewable hybrid energy systems—A multi-objective approach. *Renew. Energy* **2019**, *133*, 971–999. [CrossRef]

136. Yan, J.; Menghwar, M.; Asghar, E.; Panjwani, M.K.; Liu, Y. Real-time energy management for a smart-community microgrid with battery swapping and renewables. *Appl. Energy* **2019**, *238*, 180–194. [CrossRef]

137. Vaccari, M.; Mancuso, G.; Riccardi, J.; Cantù, M.; Pannocchia, G. A Sequential Linear Programming algorithm for economic optimization of Hybrid Renewable Energy Systems. *J. Process Control* **2019**, *74*, 189–201. [CrossRef]

138. Padrón, I.; Avila, D.; Marichal, G.; Rodríguez, J.Á.S. Assessment of Hybrid Renewable Energy Systems to supplied energy to Autonomous Desalination Systems in two islands of the Canary Archipelago. *Renew. Sustain. Energy Rev.* **2019**, *101*, 221–230. [CrossRef]

139. Brka, A.; Kothapalli, G.; Al-Abdeli, Y.M. Predictive power management strategies for stand-alone hydrogen systems: Lab-scale validation. *Int. J. Hydrogen Energy* **2015**, *40*, 9907–9916. [CrossRef]

140. Cano, M.H.; Kelouwani, S.; Agbossou, K.; Dubé, Y. Power management system for off-grid hydrogen production based on uncertainty. *Int. J. Hydrogen Energy* **2015**, *40*, 7260–7272. [CrossRef]

141. Ju, C.; Wang, P.; Goel, L.; Xu, Y. A Two-Layer energy management system for microgrids with hybrid energy storage considering degradation costs. *IEEE Trans. Smart Grid* **2018**, *9*, 6047–6057. [CrossRef]

142. Hamdi, M.; Salmawy, H.A.E.; Ragab, R. Optimum configuration of a dispatchable hybrid renewable energy plant using artificial neural networks: Case study of Ras Ghareb, Egypt. *AIMS Energy* **2023**, *11*, 171–196. [CrossRef]

143. Cozzolino, R.; Triboli, L.; Bella, G. Power management of a hybrid renewable system for artificial islands: A case study. *Energy* **2016**, *106*, 774–789. [CrossRef]

144. Zhang, W.; Maleki, A.; Nazari, M.A. Optimal operation of a hydrogen station using multi-source renewable energy (solar/wind) by a new approach. *J. Energy Storage* **2022**, *53*, 104983. [CrossRef]

145. Li, Q.; Loy-Benitez, J.; Nam, K.; Hwangbo, S.; Rashidi, J.; Yoo, C. Sustainable and reliable design of reverse osmosis desalination with hybrid renewable energy systems through supply chain forecasting using recurrent neural networks. *Energy* **2019**, *178*, 277–292. [CrossRef]

146. Nogueira, C.E.C.; Vidotto, M.L.; Niedzialkoski, R.K.; De Souza, S.N.M.; Chaves, L.I.; Edwiges, T.; Santos, D.B.D.; Werncke, I. Sizing and simulation of a photovoltaic-wind energy system using batteries, applied for a small rural property located in the south of Brazil. *Renew. Sustain. Energy Rev.* **2014**, *29*, 151–157. [CrossRef]

147. Lamedica, R.; Santini, E.; Ruvio, A.; Palagi, L.; Rossetta, I. A MILP methodology to optimize sizing of PV-Wind renewable energy systems. *Energy* **2018**, *165*, 385–398. [CrossRef]

148. Rouholamini, M.; Mohammadian, M. Heuristic-based power management of a grid-connected hybrid energy system combined with hydrogen storage. *Renew. Energy* **2016**, *96*, 354–365. [CrossRef]

149. García-Triviño, P.; Fernández-Ramírez, L.M.; Mena, A.J.G.; Llorens-Iborra, F.; García-Vázquez, C.A.; Jurado, F. Optimized operation combining costs, efficiency and lifetime of a hybrid renewable energy system with energy storage by battery and hydrogen in grid-connected applications. *Int. J. Hydrogen Energy* **2016**, *41*, 23132–23144. [CrossRef]

150. Valverde, L.; Lucena, F.J.P.; Guerra, J.; Rosa, F. Definition, analysis and experimental investigation of operation modes in hydrogen-renewable-based power plants incorporating hybrid energy storage. *Energy Convers. Manag.* **2016**, *113*, 290–311. [CrossRef]

151. Ciupageanu, D.; Barelli, L.; Lazaroiu, G. Real-time stochastic power management strategies in hybrid renewable energy systems: A review of key applications and perspectives. *Electr. Power Syst. Res.* **2020**, *187*, 106497. [CrossRef]

152. Das, B.; Tushar, M.S.H.K.; Hassan, R. Techno-economic optimisation of stand-alone hybrid renewable energy systems for concurrently meeting electric and heating demand. *Sustain. Cities Soc.* **2021**, *68*, 102763. [CrossRef]

153. Priyanka, T.J.; Atre, S.; Billal, M.M.; Arani, M. Techno-economic analysis of a renewable-based hybrid energy system for utility and transportation facilities in a remote community of Northern Alberta. *Clean. Energy Syst.* **2023**, *6*, 100073. [CrossRef]

154. Nirbheram, J.S.; Mahesh, A.; Bhimaraju, A. Techno-economic analysis of grid-connected hybrid renewable energy system adapting hybrid demand response program and novel energy management strategy. *Renew. Energy* **2023**, *212*, 1–16. [CrossRef]

155. Abdelhak, B.J.; Essounbouli, N.; Hamzaoui, A.; Hnaien, F.; Yalaoui, F. Optimum sizing of hybrid PV/wind/battery using Fuzzy-Adaptive Genetic Algorithm in real and average battery service life. In Proceedings of the 2014 International Symposium on Power Electronics, Electrical Drives, Automation and Motion, Ischia, Italy, 18–20 June 2014. [CrossRef]

156. Fetanat, A.; Khorasaninejad, E. Size optimization for hybrid photovoltaic-wind energy system using ant colony optimization for continuous domains-based integer programming. *Appl. Soft. Comput.* **2015**, *31*, 196–209. [CrossRef]

157. Ahmadi, S.; Abdi, S. Application of the hybrid big bang-big crunch algorithm for optimal sizing of a stand-alone hybrid pv/wind/battery system. *Sol. Energy* **2016**, *134*, 366–374. [CrossRef]

158. Sanajaoba, S.; Fernandez, E. Maiden application of Cuckoo Search algorithm for optimal sizing of a remote hybrid renewable energy System. *Renew. Energy* **2016**, *96*, 1–10. [CrossRef]

159. Peng, W.; Maleki, A.; Rosen, M.A.; Azarikhah, P. Optimization of a hybrid system for solar-wind-based water desalination by reverse osmosis comparison of approaches. *Desalination* **2018**, *442*, 16–31. [CrossRef]

160. Khan, A.; Javaid, N. Jaya learning-based optimization for optimal sizing of stand-alone photovoltaic, wind turbine, and battery systems. *Engineering* **2020**, *6*, 812–826. [CrossRef]

161. Javed, M.; Jurasz, J.; Ahmed, S.; Mikulik, J. Performance comparison of heuristic algorithms for optimization of hybrid off-grid renewable energy systems. *Energy* **2020**, *210*, 118599. [CrossRef]

162. Guneser, M.T.; Elbaz, A.; Seker, C. Hybrid optimization methods application on sizing and solving the economic dispatch problems of hybrid renewable power systems. In *Applications of Nature-Inspired Computing in Renewable Energy Systems*; IGI Global: Hershey, PA, USA, 2022; pp. 136–165.

163. Jahannoosh, M.; Nowdeh, S.A.; Naderipour, A.; Kamyab, H.; Faraji Davoudkhani, I.; Jaromír Klemeš, J. New hybrid meta-heuristic algorithm for reliable and cost-effective designing of photovoltaic/wind/fuel cell energy system considering load interruption probability. *J. Clean. Prod.* **2021**, *278*, 123406. [CrossRef]

164. Tahani, M.; Babayan, N.; Pouyaei, A. Optimization of pv/wind/battery stand-alone system, using hybrid fpa/sa algorithm and cfd simulation, case study: Tehran. *Energy Convers Manag.* **2015**, *106*, 644–659. [CrossRef]

165. Ma, G.; Guchao, X.; Chen, Y.; Rong, J. Multi-objective optimal configuration method for a standalone wind-solar-battery hybrid power system. *IET Renew Power Gener* **2016**, *11*, 194–202. [CrossRef]
166. Senthil, K.J.; Charles, R.S.; Srinivasan, D.; Venkatesh, P. Hybrid renewable energy-based distribution system for seasonal load variations. *Int. J. Energy Res.* **2018**, *42*, 1066–1087. [CrossRef]
167. Radosavljević, J.; Arsić, N.; Milovanović, M.; Ktena, A. Optimal placement and sizing of renewable distributed generation using hybrid metaheuristic algorithm. *J. Mod. Power Syst. Clean Energy* **2020**, *8*, 499–510. [CrossRef]
168. Aliabadi, M.J.; Radmehr, M. Optimization of hybrid renewable energy system in radial distribution networks considering uncertainty using meta-heuristic crow search algorithm. *Appl. Soft. Comput.* **2021**, *107*, 107384. [CrossRef]
169. Abuelrub, A.; Khamees, M.; Ababneh, J.; Al-Masri, H. Hybrid energy system design using greedy particle swarm and biogeography-based optimisation. *IET Renew. Power Gener.* **2020**, *14*, 1657–1667. [CrossRef]

Numerical Analysis of Bearing Capacity in Deep Excavation Support Structures: A Comparative Study of Nailing Systems and Helical Anchors

Seyyed Alireza Taghavi [1,2], Farhad Mahmoudi Jalali [3], Reza Moezzi [4], Reza Yeganeh Khaksar [1,*], Stanisław Wacławek [5], Mohammad Gheibi [5] and Andres Annuk [4,*]

[1] Department of Civil Engineering, Sadjad University of Technology, Mashhad 9188148848, Iran; seyed@tultech.eu
[2] Association of Talent under Liberty in Technology (TULTECH), 10615 Tallinn, Estonia
[3] Department of Civil Engineering, Faculty of Engineering, Islamic Azad University, Tabriz Branch 5157944533, Iran; farhadmahmoudijalali@gmail.com
[4] Institute of Forestry and Engineering, Estonian University of Life Science, Kreutzwaldi 56/1, 51014 Tartu, Estonia; reza.moezzi@emu.ee
[5] Institute for Nanomaterials, Advanced Technologies and Innovation, Technical University of Liberec, Studentská 1402/2, 461 17 Liberec, Czech Republic; stanislaw.waclawek@tul.cz (S.W.); mohammad.gheibi@tul.cz (M.G.)
* Correspondence: rezayeganeh@sadjad.ac.ir (R.Y.K.); andres.annuk@emu.ee (A.A.)

Abstract: The increasing demand for deep excavations in construction projects emphasizes the necessity of robust support structures to ensure safety and stability. Support structures are critical in stabilizing excavation pits, with a primary focus on enhancing their bearing capacity. This paper employs finite element modeling techniques to conduct a numerical analysis of nails and helical anchors' bearing capacity. To reinforce the stability of pit walls, selecting an appropriate method for guard structure construction is imperative. The chosen method should efficiently redistribute forces induced by soil mass weight, displacements, and potential loads in the pit vicinity to the ground. Various techniques, including trusses, piles, cross-bracing systems, nailing, and anchorage systems, are utilized for this purpose. The study evaluates numerical models for two guard structure configurations: nailing systems and helical anchorage. It examines the impact of parameters such as displacement, helical helix count, helix diameter variations, and the integration of nailing systems with helices. Comparative analyses are conducted, including displacement comparisons between different nailing systems and helical anchor systems, along with laboratory-sampled data. The research yields significant insights, with a notable finding highlighting the superior performance of helical bracings compared to nailing systems. The conclusions drawn from this study provide specific outcomes that contribute valuable knowledge to the field of deep excavation support structures, guiding future design and implementation practices.

Keywords: geotechnical simulation; Abaqus software; helical anchors; soil stability; nailing analysis; soil displacement assessment

1. Introduction

With the growth of population and urbanization, the optimal use of land has become a crucial issue. The construction of residential, administrative, and commercial complexes in urban areas, especially in large cities, highlights the importance of detailed field and geotechnical studies to ensure the proper design and stability of the guard structures [1]. The stability of excavations and the bearing capacity of foundations are critical factors [2–4], and the method of pit excavation and stabilization of open pits are key considerations for successful construction projects [5].

Excavations at great depths require careful consideration of effective land use, time constraints, and the stability of pit walls, which some experimental studies have conducted recently [6,7]. In order to minimize the disturbance to the surrounding area and prevent potential collapse, guard structures are implemented before foundation construction to increase the strength of the excavated walls. Various methods can be used for restraining and building a guard structure, but nailing or anchoring is one of the most effective and commonly used methods [8,9]. With the unpredictable behavior of soil and the presence of adjacent buildings and facilities, it is necessary to take action to ensure the stability of the excavation site and protect against potential risks [10].

Soil nail walls are constructed by erecting a front face support and inserting closely spaced steel bars or sections in the existing ground to provide passive reinforcement. Various parameters are influential on the stability of the nailed wall, such as nail spacing, whose effect on the global stability of soil-nailed walls has been well studied [11]. Anchoring, on the other hand, is a more complex and specialized method of providing stability to structures. Anchors come in a variety of types, including helical anchors, driven piles, and drilled shafts, and are designed to provide support in a variety of soil and geologic conditions. Anchors are commonly used in foundation work, including building foundations, retaining walls, and bridges, where they are used to transfer the load of the structure to the ground [12]. The problems of designing a well and implementing guard structures in the field of civil engineering vary widely, and therefore there is a need to review and study geotechnical data, available materials, implementation methods, financial costs, and project construction time. To select the stabilization system of the pit walls using guard structures, factors such as excavation depth, soil type, existing overhead, boundary conditions, materials, and equipment are influential. The following are a few current, pertinent studies: In a superdeep excavation in Beijing, Wang et al. [13] studied the stress and deformation properties of a composite soil-nailed wall and an anchored soldier pile wall combined retaining system. Their study shed light on the variables influencing the performance of the retaining structure and emphasized the need to limit lateral displacement during excavation. Similar to this, during the construction of a deep foundation pit, Sun et al. [14] examined the behavior of a three-pile and two-anchor rod support system in an anhydrous sand pebble strata. Their investigation clarified the axial force distribution along anchor rods and the passive force-bearing property of soil-nailed walls, which advances our knowledge of the behavior of support systems in a range of scenarios. Mun et al. [15] employed a hybrid soldier pile, tieback, and soil-nailed shoring wall to reduce shoring wall displacement in crowded metropolitan locations. Their results illustrated the usefulness of using thorough numerical simulations in shoring system design by proving how well this hybrid technique reduced wall displacement below allowable bounds. In order to enlarge a hillside roadway, Zhou et al. [16] devised a laterally cantilevered space frame system that uses ground tieback anchors as essential structural elements. They successfully redistributed surcharge loadings on slopes, which provided advantages over traditional approaches in terms of lower construction costs and environmental impact. Additionally, in soft soil places close to the sea, Junding Liu et al. [17] looked into the deformation management of deep foundation pit excavation. Using both numerical modeling and long-term in situ monitoring, their study examined the deformation characteristics of a geometrically difficult deep foundation hole project in Taizhou. Future projects with comparable conditions might refer to the study's insightful findings on the deformation features of deep foundation pit excavation in soft soil areas.

A prestressed anchor holding system with a bearing structure under the anchor head was presented by Jia et al. [18] as an alternative to rigid retaining techniques in deep foundation pits. Their study proved how well the technology controlled deformation and reduced environmental impact, providing useful solutions for excavation operations in metropolitan areas. Furthermore, in large-scale deep foundation pit situations, Liu et al. [19] examined the "corner effect" in the optimum design of soil-nailed wall-retaining pile-anchor cable supporting systems. Their work underlined the need to take lateral forces

into account in support structure design by proposing an optimization technique to lower construction costs while meeting safety criteria. A case study of a deep excavation next to a residential structure in Tehran using high-pressure grouted soil nails and anchors for lateral support was given by Mirlatifi [20]. His research validated the efficacy of the chosen design techniques by demonstrating the relationship between numerical forecasts and observed displacements and reinforcing pressures. In order to conduct a deep foundation excavation in a second-tier inland city, Chen et al. [21] examined several retaining system designs, highlighting the significance of striking a balance between structural capabilities and cost-effectiveness. Their results highlighted the advantages of hybrid methods in lowering displacements and improving safety during excavation, such as soil-nailed walls in conjunction with pile anchors. Nisha et al. [22] examined the difficulties in urban design and construction while presenting a case study of deep excavation for an office building in Bengaluru. Their research made clear how crucial numerical modeling is to the efficient design of shoring systems and the prompt implementation of corrective actions to reduce the risk to nearby structures. In their investigation of several stabilizing techniques for deep excavation pit walls in Ardabil, Zolfegharifar et al. [23] emphasized the need to establish a stable and safe environment prior to excavation. In order to evaluate the stability of excavation walls, their study used finite element and limit equilibrium analysis, which gave important insights into geological and geotechnical issues. In addition to the above studies, Table 1 also summarizes an approach-based literature review that aims to explore the current state of research on the topic of the bearing capacity of nails and helical anchors in order to provide a more comprehensive overview of the existing literature and identify gaps in the research that need to be addressed.

Table 1. The literature review of the bearing capacity of nails and helical anchors.

Method	Approach	Reference
Numerical analysis	The paper presents the design process for the micropiles, including the determination of the load capacity and the spacing and depth of the micropiles.	[24]
Laboratory tests	The authors conducted a series of laboratory tests to investigate the effects of various factors, such as pile diameter, helix spacing, and soil density, on the bearing capacity of helical piles.	[25]
Laboratory tests	The paper gives details about the testing program and the results of the tests, which showed that the CPT or CPTu methods can be used to accurately predict the bearing capacity of helical piles.	[26]
Finite element analysis	The authors used finite element analysis to study how a retaining wall with helical anchors behaved when the anchors were set up in different ways.	[27]
Numerical modelling	The paper presents a case study on the performance of a helical soil-nailed wall used to support a bridge abutment.	[9]
Finite element analysis	The study showed that the pull-out capacity of the helical multiple anchors increased with an increase in the number of helixes and the embedment depth of the anchors.	[28]
Finite element analysis	This study investigates the ideal ratio of S/Dh, which represents the spacing between helical plates and the diameter of the helical plate, for multiple helical piles.	[29]

Table 1 shows that most of the previous studies that looked at the effect of different factors on the bearing capacity of nails and helical anchors used numerical and finite element modeling. As mentioned in Table 1, several researchers have pointed out the effects of spacing between helical plates on bearing capacity, but extensive and practical research has not been conducted in this case.

This novel study examines the comparison of the final bearing capacity of nails and helical anchors in a very detailed and rigorous way to address a gap in the field. We aim to use Abaqus v. 6.12 [30] software to examine an excavated model with helical anchors to calculate their maximum capacity when expanded in the specified soil. A method for accurately assessing soil behavior is simulation, which provides insightful information for

improving and stabilizing soil [31–35]. At first, numerical modeling is used to verify the validity of the topic discussed in the selected basic article, and then by making changes in the implementation of helical anchors, such as changing the diameter of helixes, combining simple anchors with helixes, increasing the number of helixes, and a gradual increase in the load, the change in the head of the wall reaches the allowed value of the regulation. In this research, an attempt has been made to discuss and investigate the impact of excavation behaviors and the values obtained from the displacement and deformation of the pit wall, which are modeled by the various implementations of helical and simple anchors in Abaqus.

2. Material and Methods

2.1. Model Planning

Before carrying out any excavation operation, geotechnical studies and research should be conducted to determine the soil type of the site. In this research, the existing dug wells, water aqueducts from the past to the present, and underground facilities should also be examined. The underground water level is another issue that should be paid special attention to. If there is a heavy load, especially dynamic and seismic loads such as pools around the drilling site, the necessary measures must be included in the process requirements to reduce these loads.

One of the most significant, and perhaps one of the most crucial, influencing factors in geotechnical studies is the soil behavior model. The results and analysis design may be significantly impacted by the selection of appropriate soil behavior models. In the research that has been conducted, an effort has been made to look into the behavior of the drilling process and the values of displacements and deformations of the pit wall. These values are first verified by numerical modeling with a laboratory model, and then the drilled model with a nailing system and helical bracing system is analyzed using the Abaqus software. The models created by the software are introduced in Table 2. Figure 1 shows the descriptive diagram parameters used in Table 2.

Table 2. Specifications of models introduced in Abaqus software.

Model Number	Helix Diameter (mm)	Type of Bracing System	The Number of Helixes
1	-	Nailing	-
2	15	Helical anchor	3
3	15	Helical anchor	4
4	40	Helical anchor	3
5	40	Helical anchor	4
6	45	A combination of helixes and nailing	3
7	45	Helical anchor	3
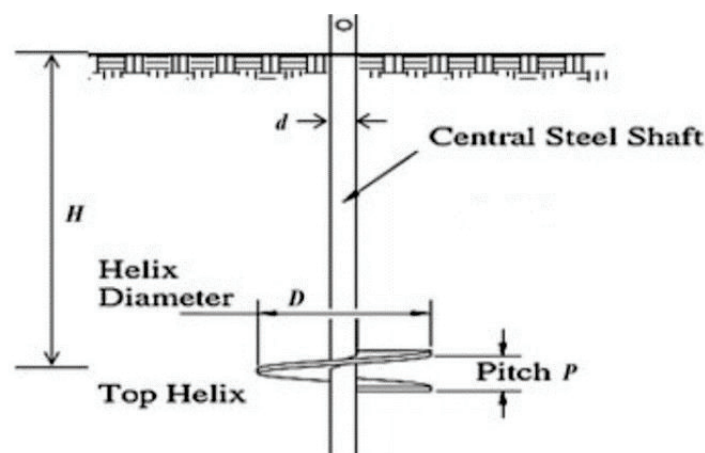
Figure 1. Details of helical anchor.

In contrast to other models, model 7 gradually applies a load to the model until the top of the wall changes to the permitted value of the regulation. This results in a different amount of load on the soil than other models.

2.2. Material Specifications

It should be noted that the main scales are not always practical and applicable due to constraints, which will be discussed further. Two Helical anchor and nailing systems are taken into consideration in this modeling and analysis under entirely identical conditions. In the Abaqus modeling, the excavation wall height is 80 cm, whereas in the actual excavation operation, the walls are 8 m high. After the excavation operation is complete, a top wall made of mesh network and shotcrete concrete is used in the two implementation methods of nailing and helical anchor systems. These walls typically range in thickness from 5 to 10 cm in reality, though this can vary depending on the soil type and other project-specific factors. A 5 cm thick concrete wall has been selected for the design and modeling of the final procedure. Materials that can provide the compressive and tensile strengths of shotcrete concrete as well as the tensile strength of the mesh network used in the excavated wall should be used for the design of the wall. In order to provide this feature, polymer derivatives were used. A compressed Teflon sheet that is fireproof (PTF) and has a compressive strength and high hardness of approximately 1 GPa is used in the numerical modeling.

Based on calculations in Appendix A, it was determined that a 5 cm concrete wall in the real model is equivalent to a Teflon wall with a thickness of 1.5 cm in the software model for designing the wall thickness in numerical modeling with a laboratory scale of 1:10. Steel plates of a certain weight were used for loading in both models. In terms of soil moisture percentage, it was determined that the value during the experiments was equal to 10%. In modeling, the soil density was also set to 70% based on the characteristics of the soil, which will be covered in more detail. And in the designs, the heel of the wall was taken into account as the heel of the stuck wall. In the real model, holes with a diameter of 10 to 25 cm are used for the drilling design of the nailing system. For this model, holes with a 10 cm diameter served as the basis, and they were scaled down to a 1 cm diameter in a 1:10 ratio. The used strands' diameter can range from 15 to 40 mm, and they can be made of a variety of materials and alloys. The strands used in the software modeling had a 15 mm diameter, which was converted to 1.5 mm by applying the modeling scale. In the real model, the nails are spaced apart by 150 to 300 cm and 100 to 250 cm, respectively. For the purposes of this simulation, the horizontal and vertical distances between the holes were set, as depicted in Figure 2a.
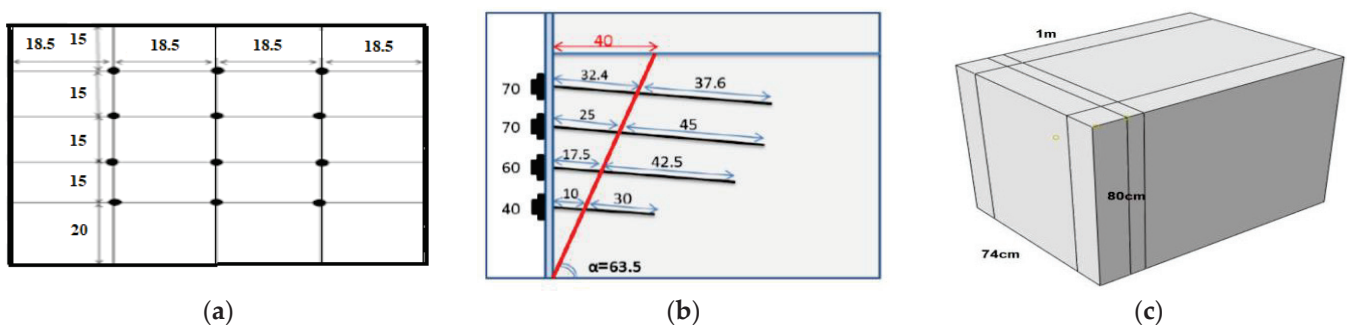
Figure 2. General configuration in this study. (**a**) The distance between the holes; (**b**) simulated model geometry; (**c**) soil geometry in modelling.

We determined the nail length based on the required carrying capacity and the technical characteristics of the soil. Most of these designs shared similar implementation strategies and guiding principles. The regulations for the size and length of the bars in Figure 2b suggested the following models. Figure 2c also displays the spatial shape of the simulation element.

The diameter of the helix can range from 15 to 45 cm in accordance with American regulations and taking into account the circumstances and characteristics of the soil. So, using a scale of 1:10, 4.5 cm plates were used in this simulation.

The use of square and solid rods would improve the tensile performance of bracings, but since these materials were not available for this modeling, solid circular rods were chosen instead. Typically, square and curved sections of rods with diameters ranging from 1.5 to 4 cm are used. Iron wire with a 1.5 mm diameter was used in this simulation, scale-adjusted. Additionally, it is advised that the distance between two helical anchors be 2.5 to 3.5 times the diameter of helixes in relation to each other in order to comply with the current regulations regarding the distance of the helixes from one another. As a result, in the simulation, the ratio of the distance between the helix was taken to be roughly three times the helix's diameter in length.

The helical bracing, the soil, and the guard structure make up the model's three main components. In the experiment, three different types of helixes with lengths of 40, 60, and 70 cm were used. The rows were positioned in the soil at an angle of 10 degrees, with the bottom row being 40 cm long, the second row being 60 cm long, and the top two rows being 70 cm long. The soil in this model had the following measurements: $100 \times 80 \times 74$ cm. Its geometry is shown in Figure 2c, and Table 3 lists the material properties of the soil.

Table 3. Soil characteristics.

Stickiness	Internal Friction Angle (Degrees)	Dry Density (kg/m^3)	Minimum Dry Density (kg/m^3)	Maximum Dry Density (kg/m^3)	Sand
0.05	37	1546.03	1392	1644	Chiruk WT60 (Regional)

The main rod's diameter was 1.5 mm, its plates' diameter was 4.5 cm, and their thickness is 1.5 mm. Three times the plates' diameter, or 13.5 cm, separates them from one another. It has three dimensions, each 40, 60, and 70 cm in length. In Figure 3, all three models are displayed.
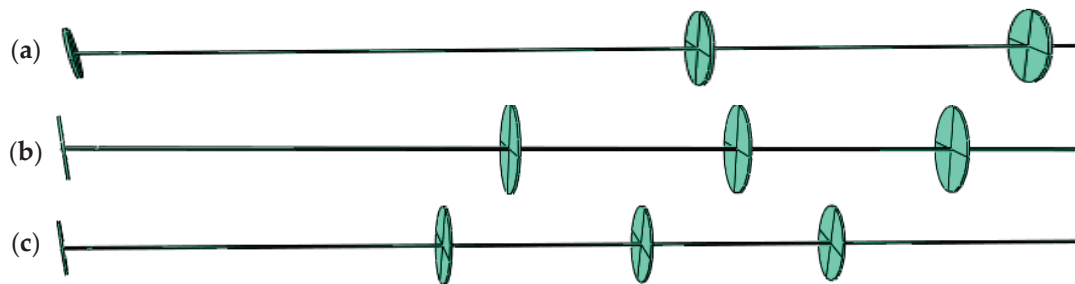
Figure 3. (**a**) Helical anchor with dimensions of 40 cm; (**b**) helical anchor with dimensions of 60 cm; (**c**) helical anchor with dimensions of 70 cm.

2.3. Loading, Boundary Conditions, and Meshing

As can be seen, the horizontal distance between the helixes is 18.5 cm, and the vertical distance between them is 15 cm. The assembly model for this layout in Abaqus software is also presented in Figure 4a.

Given that the soil is modeled as a solid, Figure 4b should be followed when placing the helical bracings in the ground and arming them. The next step is to ascertain the friction coefficient and contact properties on all surfaces after all helical bracings have been defined. Typically, 0.3 is thought to be the approximate value of the coefficient of friction between soil and other components. By choosing the General Contact type after calculating the friction coefficient, it is possible that the software will take into account contact wherever

it exists in the models. The model's loading and boundary conditions are established in this section. The lower portion of the soil is completely bound, as shown in Figure 4c, in accordance with the type of model.
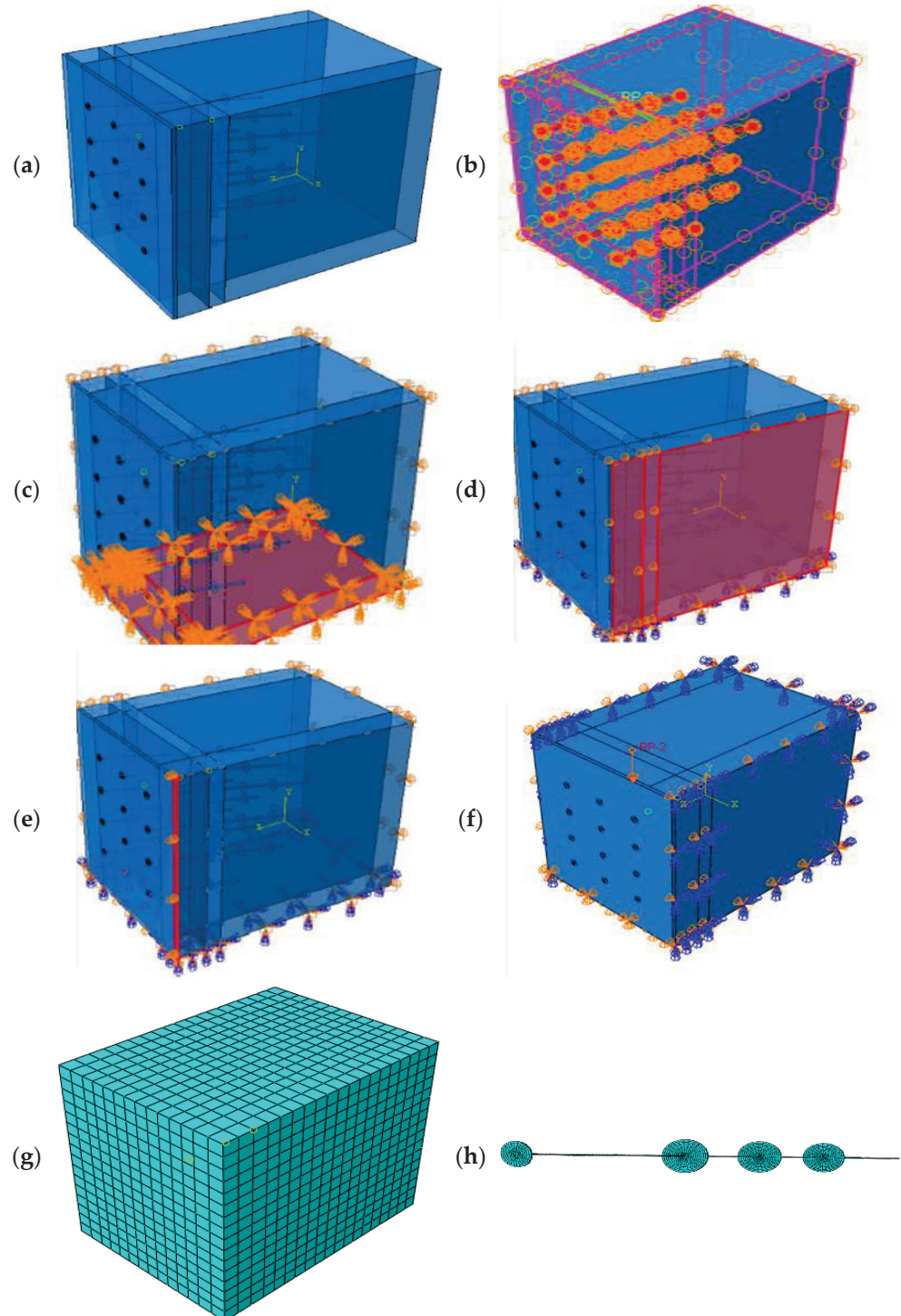
Figure 4. (**a**) Assembly model with helical anchor; (**b**) defining the model for burying the anchor in the soil; (**c**) complete binding of the lower part of the soil; (**d**) binding of the right wall in the structure; (**e**) binding the guard wall; (**f**) applying load on the upper part of the soil; (**g**) soil model meshing; (**h**) helical anchor meshing.

The upper surface of the soil is the only surface that is bounded and Figure 4d depicts one of these walls. The upper and lower sides of the guard wall are tied vertically; the

other degrees of freedom are left free. Figure 4e represents how one of the surfaces has been bound. The final step involves applying the incoming load, whose maximum weight is 288 kg, to the soil as a point load at the location depicted in Figure 4f. The model's meshing section is then shown. Figure 4g displays the mesh model for the soil, which has a granularity of 0.01 m (10 mm). Figure 4h shows the meshing model of one of the helical anchors, which was produced using 0.0079 m as the mesh size. Finally, the meshing of the guard wall is appropriately considered.

3. Numerical Model

Validation of the Base Numerical Model

In this section, the results of the numerical model for verification are compared with the results of the base physical model.

The calibration test specifications depicted in Figure 5b encompass a thorough experimental setup designed to refine the model's accuracy. It is imperative to note that the dataset employed for this calibration is sourced from an authentic project carried out in Mashhad City, Iran. Notably, the calibration process uniquely incorporates a specific segment of the project data within the ambit of the current research undertaking.

During the experimental phase, a scaling factor of 1:10 is applied, aligning the scale of the experiment with that of the simulation for accurate comparison. As delineated in Figure 5b, the experimental setup adopts a backfill approach, distinct from real-world activities where soil immersion via screwing is commonplace. Consequently, the phenomenon of soil loosening, inherent to screwing methods, is absent in the laboratory analysis and results. Consequently, in the simulation procedure, the effect of soil loosening is omitted, mirroring the conditions of the experimental setup. This meticulous alignment ensures that the simulation faithfully reflects the experimental conditions, enhancing the reliability and applicability of the model's outcomes.

The comparison of the change in horizontal locations obtained by the numerical model and the physical model based on Figure 5a shows that the displacement along the wall in the two models has a slight difference, which indicates the acceptable performance of the numerical model (Table 4). Comparing the change in horizontal locations obtained by numerical models and physical models is a crucial aspect of validating numerical simulations in various fields, including engineering and fluid dynamics. It helps assess the accuracy and reliability of numerical models in representing real-world phenomena. Our findings are distinct because, in some cases, earlier studies have not been able to compare the horizontal displacement along the wall from both numerical and physical results. For example, the study by Misir discusses the numerical model calibration of U-shaped multi-leaf stone masonry wall specimens tested under ambient vibrations. While the exact details of the results are not provided In the search results, It can be Inferred that the comparison of numerical and physical models was conducted to assess the performance of the numerical model in predicting horizontal displacements along the wall [36]. Another study by J García-Alba evaluates numerical models' performance in describing flows of positively buoyant jets. While it does not directly mention the comparison of horizontal displacements, it indicates the use of numerical models to simulate physical phenomena [37]. In a study by MA Bouarroudj, the differences between numerical and experimental results in single-strut models are discussed. This could potentially include the comparison of horizontal displacements, although specific details are not provided [38].

Table 4. Comparison of displacement of two models (physical and numerical).

Difference Percentage of Experimental and Numerical Model	Difference between Experimental and Numerical Model (cm)	Displacement Rate in the Numerical Model (cm)	Displacement Rate in the Physical Model (cm)
2%	0.1	4.7	4.8
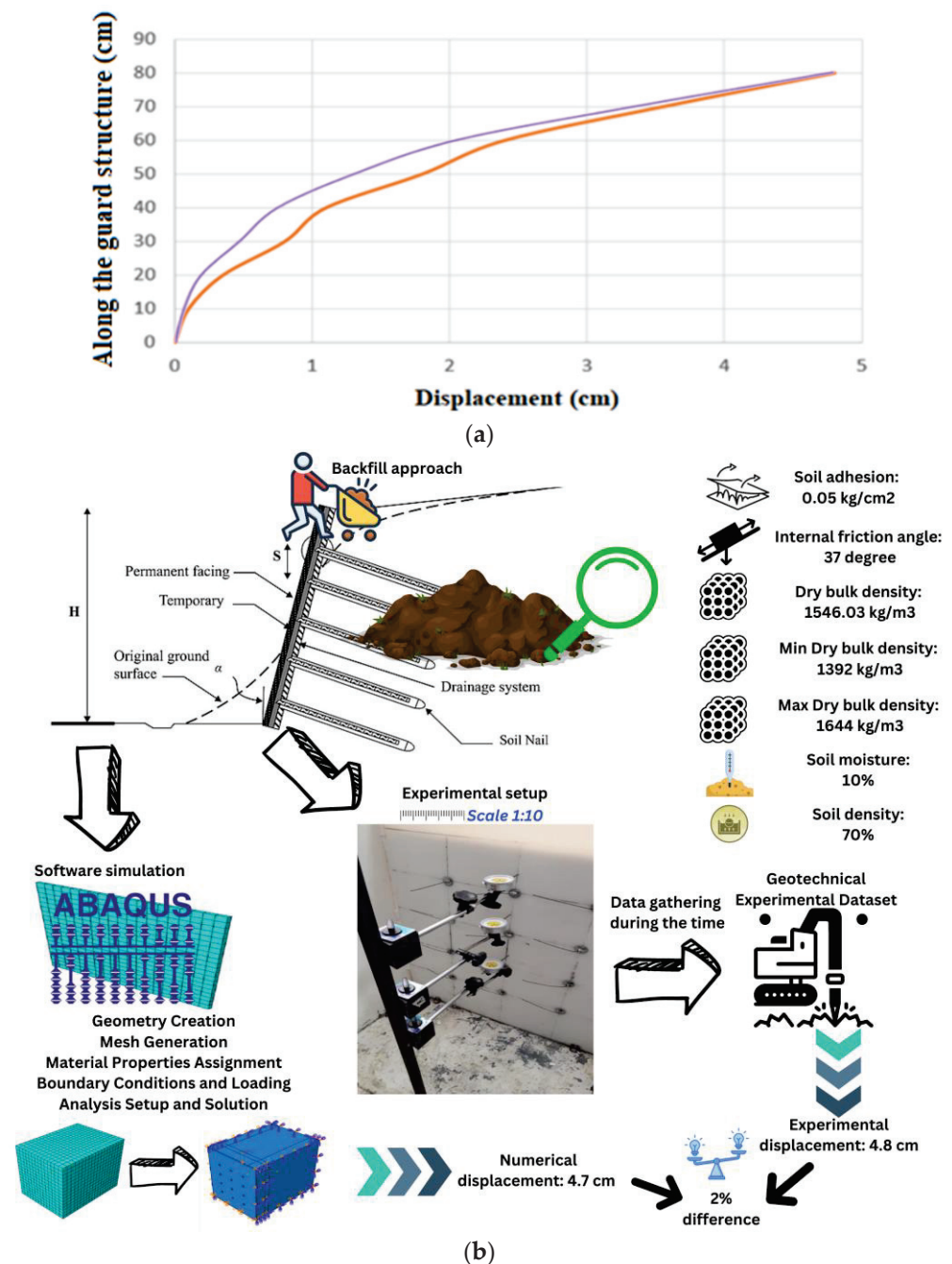
Figure 5. The descriptions of (**a**) displacement along the wall from the Abaqus model in orange; displacement along the wall from the base in the physical model in purple; and (**b**) experimental setup specifications.

4. Results and Discussion

In this section of the research, the results extracted from the modelling are presented. In the modelling performed by the Abaqus software, the changes and displacement of the pit wall are studied during the use of nailing and helical bracing. The helical model is divided into six different models, including changes in the number of helixes, the diameter of the helixes, and the gradual addition of load until reaching the permitted position change of the regulation. In this research, two basic models, including nailing and helical bracing, are used to stabilize the pit wall.

The results are analyzed in seven models; the main characteristics of each model are described below:

1. Nailing with a diameter of 45 mm and 3 helixes;
2. Helical anchor with a diameter of 15 mm and 3 helixes;
3. Helical anchor with a diameter of 15 mm and 4 helixes;
4. Helical anchor with a diameter of 40 mm and 3 helixes;
5. Helical anchor with a diameter of 40 mm and 4 helixes;
6. The combination of helical and nailing with a diameter of 45 mm and 3 helixes with an arrangement of one in between;
7. Helical bracing as a gradual increase in load permitted by the regulations with a diameter of 45 mm and 3 helixes.

Each model is modelled while taking into account the parameters, and the results are then saved in an Excel file. As a result, at the conclusion of the work, the effects of the change in the shape of the pit wall, capacity, and incoming energy have been compared.

4.1. Type of Bracing

To study the impact of different bracing systems on embankment stability, models 1 (nailing system), 7 (bracing helical anchor system), and 6 (combined nailing and helical bracing system) are being compared in Figure 6.
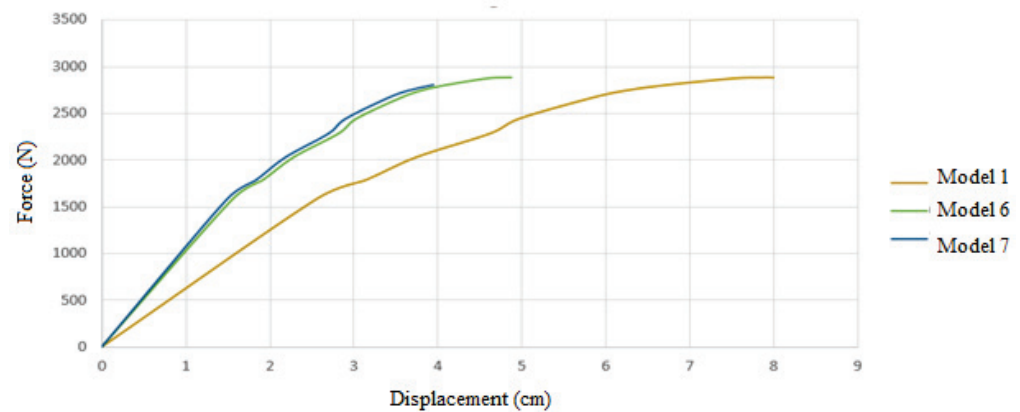
Figure 6. Comparison of three models based on bearing force.

In Figure 6, the displacement of the applied force for each of the models can be seen until the end of the analysis.

With a digging height of 80 cm and a horizontal displacement of the wall equal to 0.002 times that height, the allowable displacement is determined to be 0.16 cm. In order to establish the bearing capacity of the models according to the permissible displacement authorized by laws, it is essential to identify the force value that causes this displacement in the models, as seen in Figure 7.
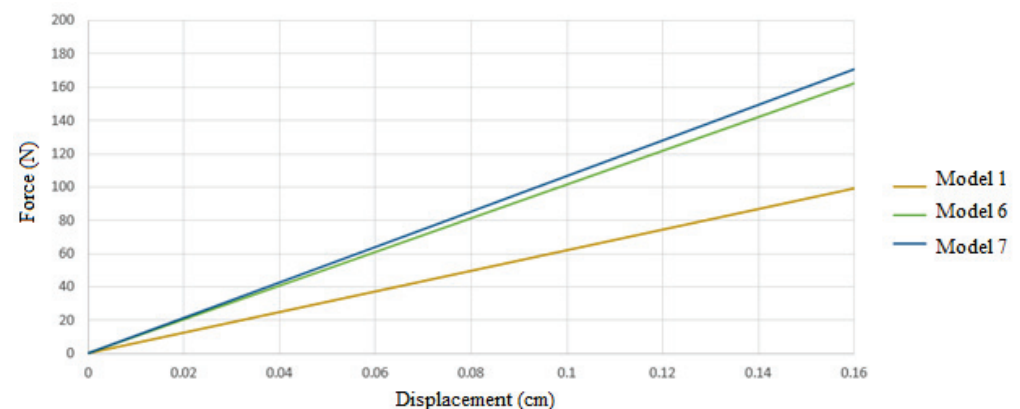
Figure 7. Comparison of the model's displacement depending on the standard's allowable limit.

Figure 8 displays the wall displacement for each model. Model number 7 (3 to 35 mm helixes) experiences the least amount of wall displacement.
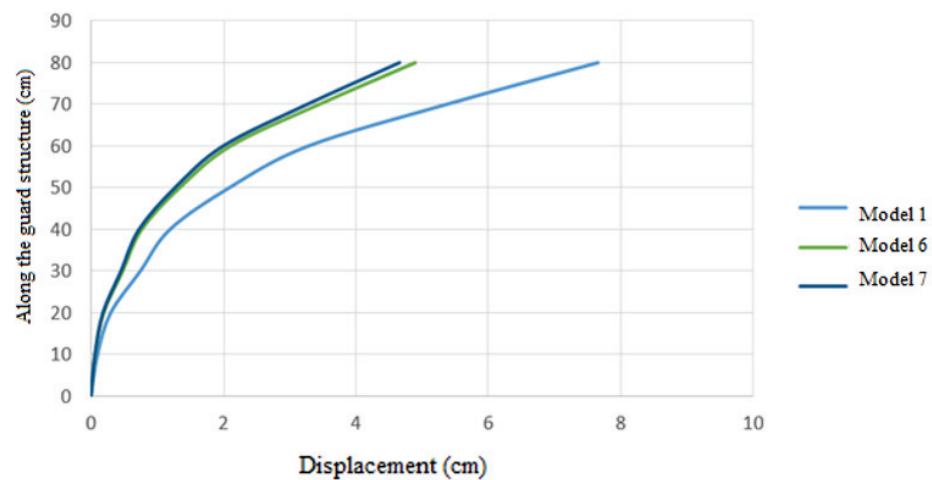
Figure 8. Comparing displacement along the guard structure.

Figure 9 displays the energy input for each model taken from the software, indicating that model number one necessitates the most energy input.
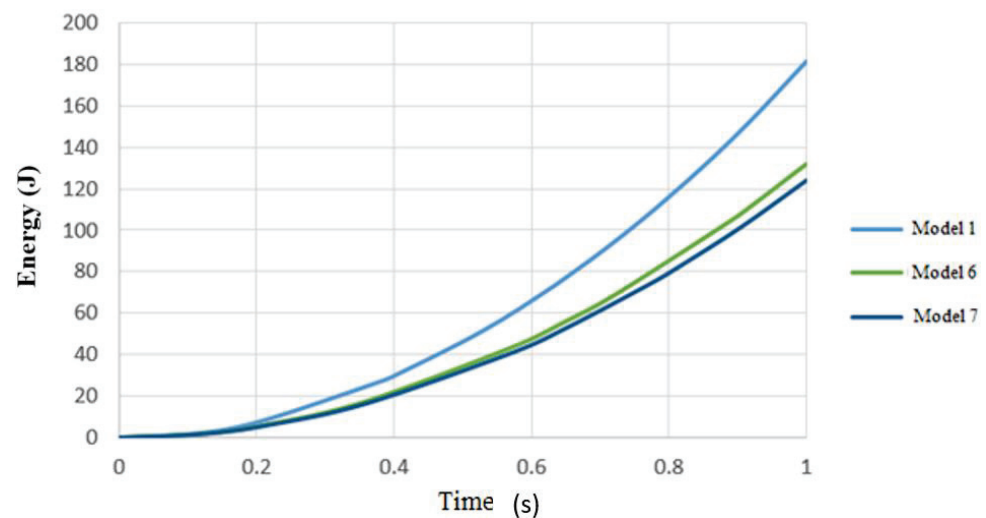
Figure 9. Comparing the energy input required by various models.

Table 5 displays the maximum energy input, displacements, and bearing capacity for each model. The final conclusion will be drawn based on these statistics.

Table 5. Results obtained from the analysis of models.

The Maximum Energy Input to the Model (J)	Maximum Displacement of the Model (cm)	The Capacity of the Model Is Based on the Amount of Displacement Allowed by the Regulations (N)	Model Number
181	7.66	100	1
132	4.88	162	6
124	4.66	170	7

4.2. The Diameter of the Helixes

In order to check the effect of the diameter of the helix used in the helical bracing system, model number 2, which has a diameter of 15 mm, and model number 4, which has

a diameter of 40 mm, and model number 7, which has a diameter of 45 mm, were compared with each other.

In Figure 10, the displacement of the applied force for each of the models can be seen until the end of the analysis.
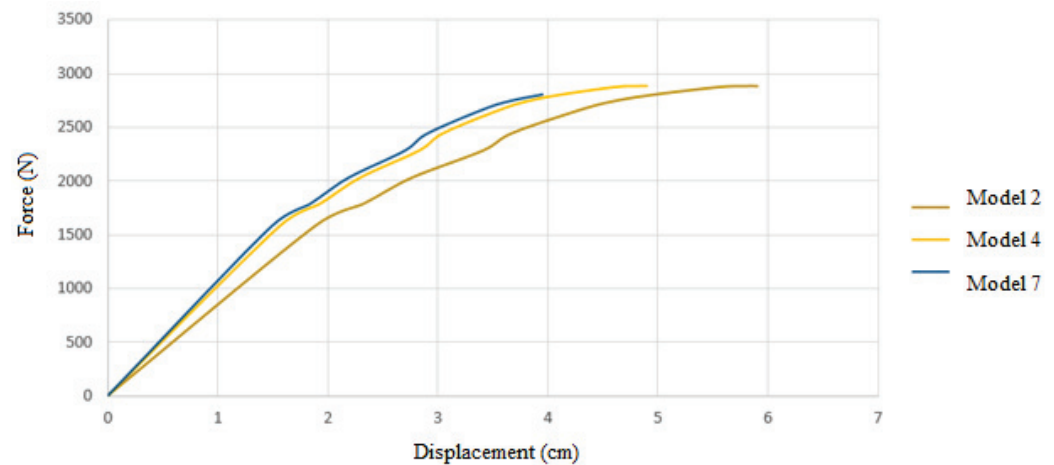
Figure 10. Comparison of three models based on bearing force.

Considering that the amount of horizontal displacement of the wall is equal to 0.002 of the digging height and that the digging height is 80 cm, the allowed displacement is calculated as 0.16 cm. Therefore, by obtaining the amount of force that causes this displacement in the models according to Figure 11, it is possible to calculate the bearing capacity of the models based on the permissible displacement of the regulations.
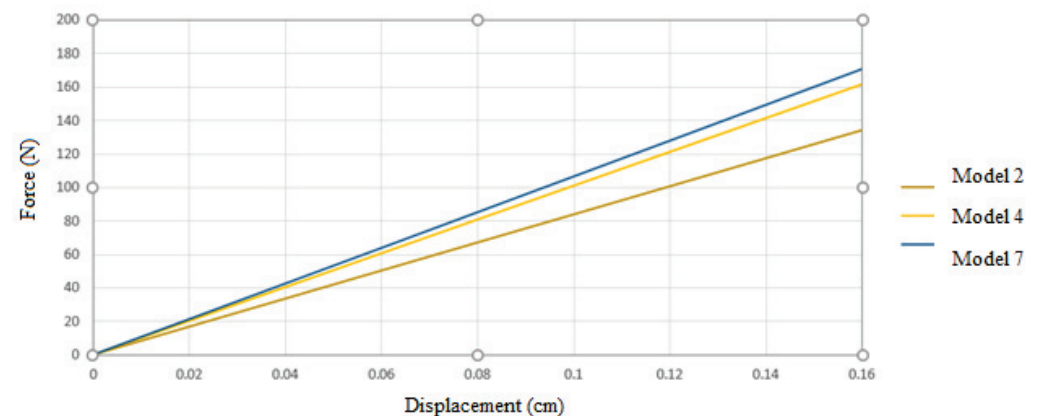
Figure 11. Comparison of the model's displacement depending on the standard's allowable limit.

In Figure 12, the displacement along the wall is shown for each of the models; according to the diagram, the lowest amount of wall displacement occurred in model number 7 (3 to 45 mm helixes).

In Figure 13, the energy input to each of the models extracted from the software can be seen.

Table 6 provides data on the maximum energy input, displacements, and bearing capacity of each model, which will be used to draw the ultimate conclusion in the summary.
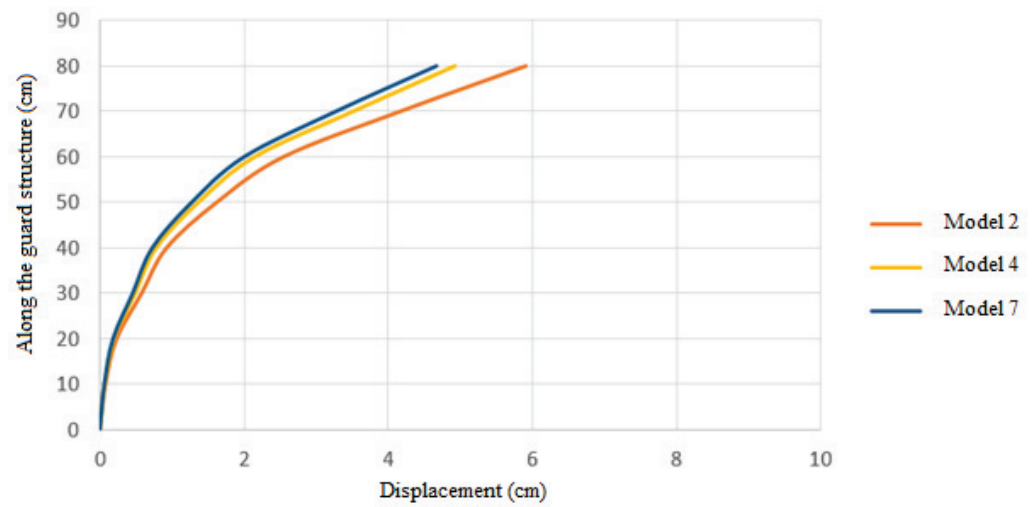
Figure 12. Comparing displacement along the guard structure.
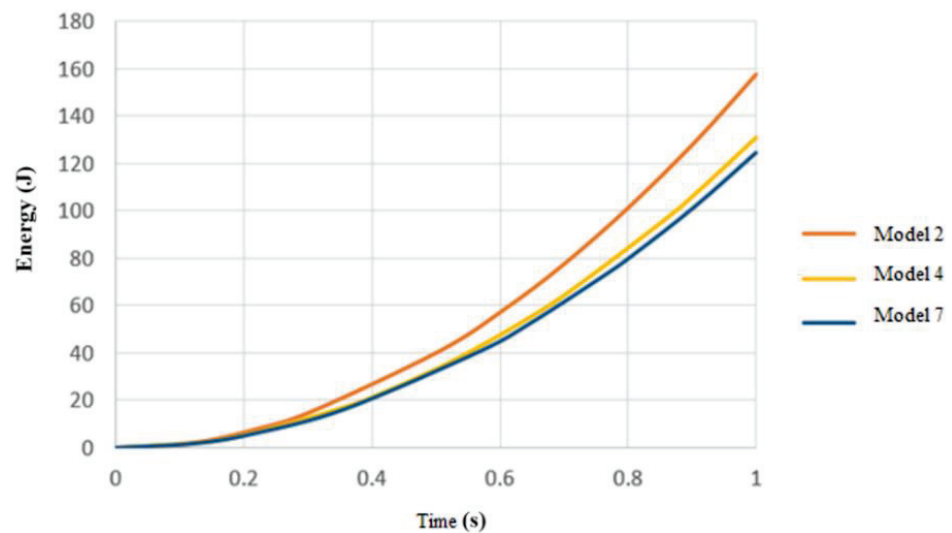
Figure 13. Comparing the energy input required by various models.

Table 6. Results obtained from the analysis of models.

The Maximum Energy Input to the Model (J)	Maximum Displacement of the Model (cm)	The Capacity of the Model Is Based on the Displacement Allowed by the Regulations (N)	Model Number
158	5.9	130	2
131	4.9	164	4
124	4.66	170	7

4.3. The Number of Helixes

In order to check the effect of the number of helix plates used in the helical bracing system, considering the constant consideration of the plate diameter, once for the plate diameter of 15 mm, model number 2, which has 3 helix plates, and model number 3, which has 4 helix plates, are compared with each other. Again, for the 40 mm plate diameter, model No. 4, which has 3 helixes, and model No. 5, which has 4 helixes, are compared.

4.3.1. Helixes with Diameter of 15 mm

For the case with helixes of 15 mm diameter, the results are as below.

In Figure 14, the displacement of the applied force for each of the models can be seen until the end of the analysis.
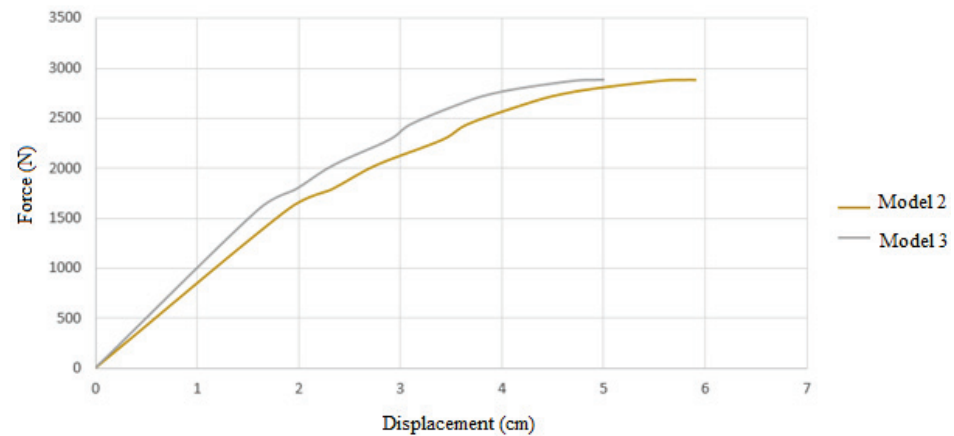
Figure 14. Comparison of two models based on bearing force.

Considering that the amount of horizontal displacement of the wall is equal to 0.002 of the digging height and that the digging height is 80 cm, the allowed displacement is calculated as 0.16 cm, according to Figure 15. Therefore, by obtaining the amount of force that causes this displacement in the models, it is possible to calculate the bearing capacity of the models based on the permissible displacement of the regulations.
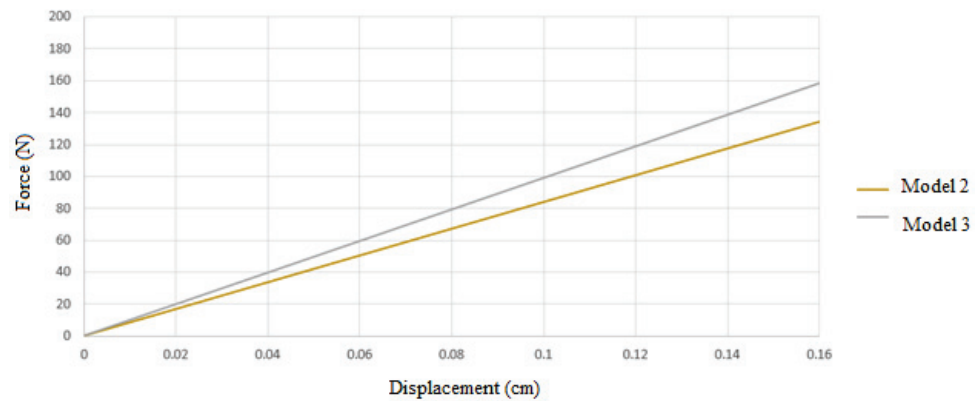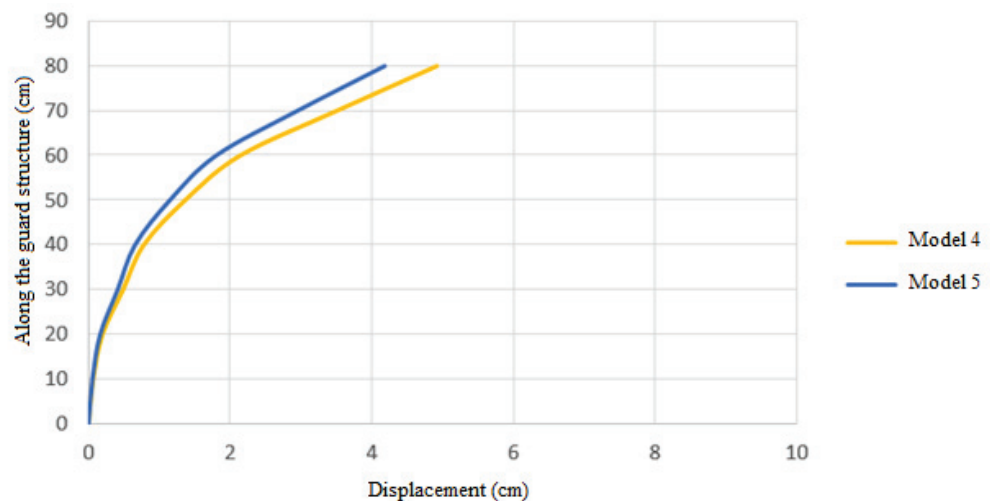

Figure 15. Comparison of the model's displacement depending on the standard's allowable limit.

In Figure 16, the displacement along the wall is shown for each of the models. According to the diagram, the lowest amount of wall displacement occurred in model number 3 (4 to 15 mm helixes).
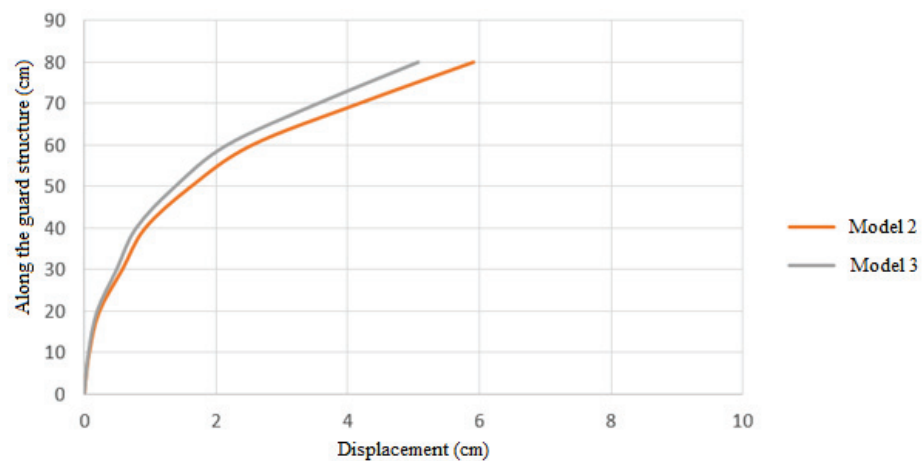
Figure 16. Comparing displacement along the guard structure.

In Figure 17, the amount of energy input to each of the models extracted from the software can be seen.
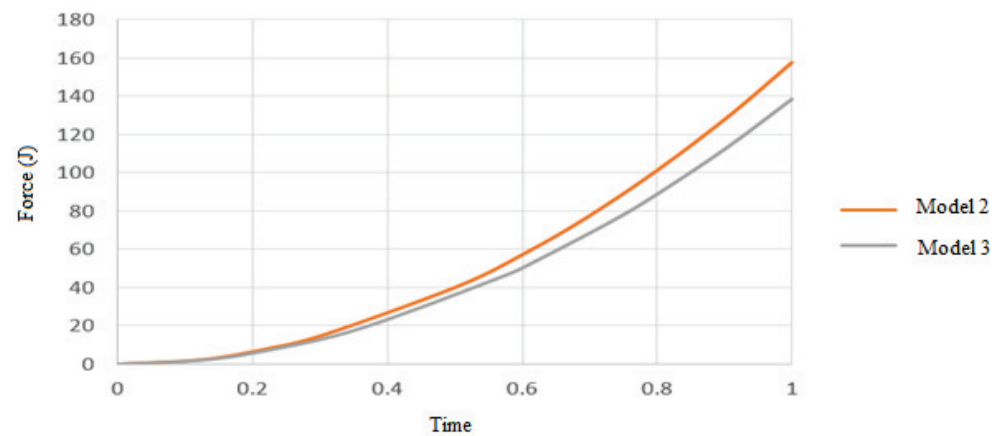
Figure 17. Comparing the energy input required by various models.

In Table 7, the maximum amount of energy entered into the structure, the displacements, and the bearing capacity of each model are presented, and in the summary of the results, the ultimate conclusion will be derived from these data.

Table 7. The results obtained from the analysis of the models.

The Maximum Energy Input to the Model (J)	Maximum Displacement of the Model (cm)	The Capacity of the Model Is Based on the Displacement Allowed by the Regulations (N)	Model Number
158	5.9	130	2
138	5	159	3

4.3.2. Helixes with a Diameter of 40 mm

In Figure 18, the displacement of the applied force for each of the models can be seen until the end of the analysis.
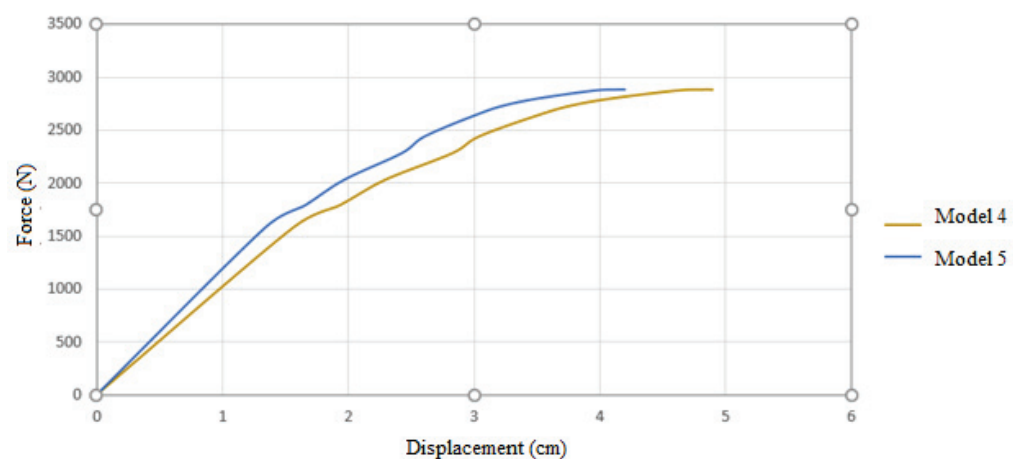
Figure 18. Comparison of two models based on bearing force.

The permitted displacement is computed as 0.16 cm, taking into account that the wall's horizontal displacement is equal to 0.002 of the digging height and that the digging height is 80 cm (according to Figure 19). Therefore, based on the permitted displacement of the regulations, it is possible to compute the bearing capacity of the models by obtaining the amount of force that generates this displacement in the models.
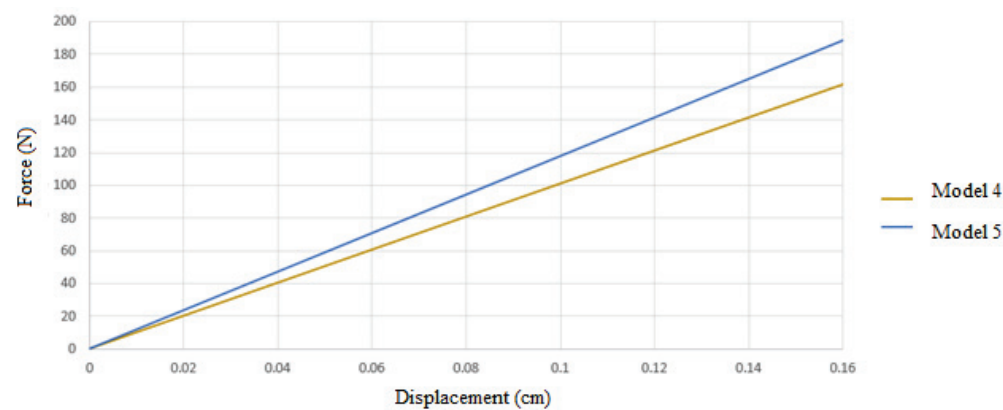
Figure 19. Comparison of the model's displacement depending on the standard's allowable limit.

In Figure 20, the displacement along the wall is shown for each of the models. According to the diagram, the lowest amount of wall displacement occurred in model number 5 (4 to 40 mm helixes).

Figure 20. Comparing displacement along the guard structure.

In Figure 21, the amount of energy input to each of the models extracted from the software can be seen.
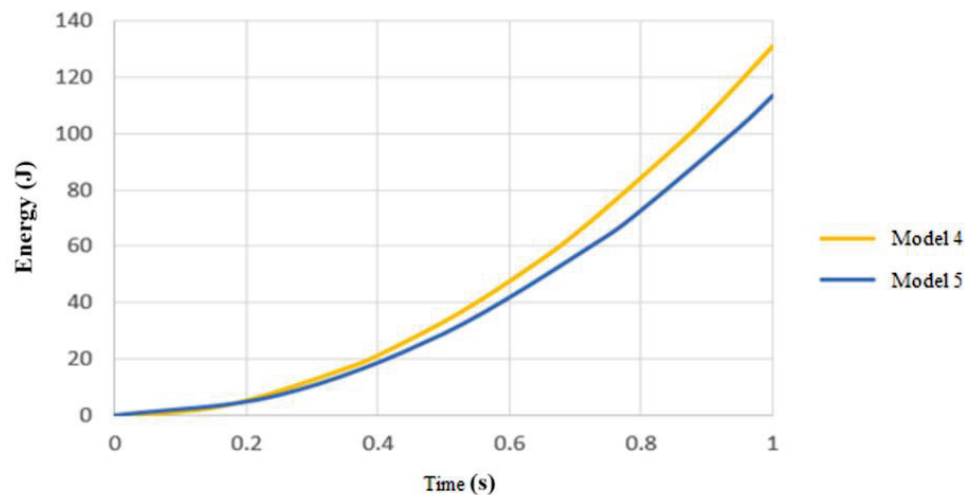
Figure 21. Comparing the energy input required by various models.

The maximum energy entered into the structure, the displacements, and the load capacity of each model are listed in Table 8, and the conclusions that follow will be based on these data and the findings summary.

Table 8. The results obtained from the analysis of the models.

The Maximum Energy Input to the Model (J)	Maximum Displacement of the Model (cm)	The Capacity of the Model Is Based on the Displacement Allowed by the Regulations (N)	Model Number
131	4.9	164	4
113	4.2	190	5

The existing model has been carried out in order to obtain a numerical analysis of the bearing capacity of helical and nailing through finite element modeling. In this way, the conclusion of the research is of great importance because it can be a foundation for solving the problems or improving the current situation and pave the way to a more optimized solution. Based on the available results, we can observe the effect of parameters such as the type of bracing system, the diameter, and the number of helixes. Based on this, in order to check the type of bracing system, models 1, 6, and 7 were used, and for the helical anchor system, compared to the nailing system, the bearing capacity, wall displacement, and energy input to the structure increased by 41%, 39%, and 31%, respectively.

For the helical and nailing combined restraining and bracing system, compared to the nailing system, the amount of capacity, wall displacement, and energy input to the structure increased by 38%, 36%, and 17%, respectively. Now, according to the comparisons made regarding the type of bracing system, the bracing helical anchor system performed better than other systems and improved the performance and capacity of the model.

In order to check the diameter of the helixes, model numbers 2, 4, and 7 were used, and according to the comparisons made, the helical anchor with a plate diameter of 45 mm performed better than other systems and improved the performance and capacity of the model. By changing the diameter of the plate from 40 to 45 mm, the capacity of the structure increased by 3.5%, and also, by changing the diameter from 15 to 45 mm, the bearing capacity of the structure increased by 23%.

The effect of the number of helixes on the structural responses was investigated in two cases; the first case was for a helical anchor with a helix diameter of 15 mm and 3 and 4 helixes. And the second model was the helical anchor with a helix diameter of 40 mm and 3 and 4 helixes. In both cases, increasing the number of helixes improved the performance and capacity of the model. In the first case, the increase in the bearing capacity was 18%, and in the second case, it was 13%.

The study's results reveal the performance and effectiveness of two distinct deep excavation support systems: the nailing system and the helical anchor system. The behavioral variations across these systems offer vital insights into their structural features and operational mechanisms. The nailing system's brittle and fragile behavior, along with its rapid upward deformations as it reaches the breaking point, emphasize the significance of comprehending the impact of injected concrete on its load-bearing capability. This trend indicates that the effectiveness of the nailing method could be affected by factors like the quality of concrete injection and soil adhesion. In contrast, the helical anchor system operates more softly, displaying steady upward deformations until breaking. The flexibility of steel helixes in the helical anchor system contributes to its overall performance against overhead loads, making it a promising option for deep excavation support. The comparative analysis reveals that the helical anchor system, particularly configurations with multiple helixes of larger diameters, outperforms the nailing system in terms of displacement and energy input. This underscores the importance of considering the design parameters and configurations when selecting the most suitable support system for a given excavation project.

5. Conclusions

- The analysis results indicate distinct behavioral differences between the nailing system and the helical anchor system.
- The nailing system exhibits brittle, fragile behavior with rapid upward deformations upon reaching the breaking threshold, likely attributed to the contribution of injected concrete to its bearing capacity.
- In contrast, the helical anchor system operates more softly, showing steady upward deformations until breaking, with steel helixes contributing to its flexibility and overall performance against overhead loads.
- Based on the available results, the capacity of load-bearing, displacement, and energy input in the bracing system with four plates of 40 mm compared to the nailing system changed, with a 47% increase, 45% decrease, and 37% decrease, respectively. These values indicate the highest level of performance of the bracing systems compared to the nailing system.
- The capacity of the construction is increased by 3.5 percent by increasing the diameter of the plate from 40 to 45 mm. Additionally, the structure's capacity increases by 23% when the diameter is changed from 15 to 45 mm.
- Based on the conducted investigations, the best-performing bracing system configurations are ranked as follows:
  1. Anchor with 4 helixes of 40 mm diameter.
  2. Anchor with 3 helixes of 45 mm diameter.
  3. Combined mode of helical anchor and nailing.
  4. Anchor with 3 helixes of 40 mm diameter.
  5. Anchor with 4 helixes of 15 mm diameter.
  6. Anchor with 3 helixes of 15 mm diameter.
- The conclusions drawn from this research suggest several areas for further investigation, including consideration of soil saturation, comparison of outcomes using another software such as Analysis System (ANSYS), and variations in soil properties.

Appendix A

$$E_p = 1 \, \text{GPa}; E_c = 25 \, \text{GPa}$$

$$N = \frac{1}{10} \rightarrow I = \left[\frac{1}{10^4}\right] \rightarrow 10^4 = \frac{E_c \frac{b \, h^3}{12}}{E_p \frac{b \, h^3}{12}} \rightarrow \frac{b = 740 * h = 5}{b = 74 * h = ?}$$

$$h^3 = \frac{25 \times 10 \times 5^3}{10^3} = 3.15 \rightarrow h = 1.46 \cong 1.5 \, \text{cm}$$

References

1. Satyanaga, A.; Aventian, G.D.; Makenova, Y.; Zhakiyeva, A.; Kamaliyeva, Z.; Moon, S.-W.; Kim, J. Building Information Modelling for Application in Geotechnical Engineering. *Infrastructures* **2023**, *8*, 103. [CrossRef]
2. Chaabani, W.; Remadna, M.S.; Abu-Farsakh, M. Numerical Modeling of the Ultimate Bearing Capacity of Strip Footings on Reinforced Sand Layer Overlying Clay with Voids. *Infrastructures* **2023**, *8*, 3. [CrossRef]
3. Gokceoglu, C.; Aygar, E.B.; Nefeslioglu, H.A.; Karahan, S.; Gullu, S. A Geotechnical Perspective on a Complex Geological Environment in a High-Speed Railway Tunnel Excavation (A Case Study from Türkiye). *Infrastructures* **2022**, *7*, 155. [CrossRef]
4. Islam, M.N. Small Scale Experiments to Assess the Bearing Capacity of Footings on the Sloped Surface. *Eng* **2020**, *1*, 240–248. [CrossRef]
5. De Bruyn, I.; Prado, D.; Mylvaganam, J.; Walker, D. Geotechnical Considerations for the Stability of Open Pit Excavations at Mine Closure, Some Scenarios. In Proceedings of the 13th International Conference on Mine Closure, Perth, Australia, 3–5 September 2019; pp. 235–248. [CrossRef]
6. Tian, Y.; Motalleb Qaytmas, A.; Lu, D.; Du, X. Stress Path of the Surrounding Soil during Tunnel Excavation: An Experimental Study. *Transp. Geotech.* **2023**, *38*, 100917. [CrossRef]
7. Zhao, Y.; Chen, X.; Hu, B.; Huang, L.; Li, W.; Fan, J. Evolution of Tunnel Uplift and Deformation Induced by an Upper and Collinear Excavation: A Case Study from Shenzhen Metro. *Transp. Geotech.* **2023**, *39*, 100953. [CrossRef]
8. Cheng, S.-H.; Chen, S.-S.; Yang, K.-H. Self-Inspection System for Ground Anchors Monitoring on Long-Term Load Change. *Transp. Geotech.* **2022**, *36*, 100825. [CrossRef]
9. Yadegari, S.; Yazdandoust, M.; Momeniyan, M. Performance of Helical Soil-Nailed Walls under Bridge Abutment. *Transp. Geotech.* **2023**, *38*, 100788. [CrossRef]
10. Koerner, R.M. In-Situ Stabilization of Soil Slopes Using Nailed or Anchored Geosynthetics. *Int. J. Geosynth. Ground Eng.* **2015**, *1*, 2. [CrossRef]
11. Villalobos, S.A.; Villalobos, F.A. Effect of Nail Spacing on the Global Stability of Soil Nailed Walls Using Limit Equilibrium and Finite Element Methods. *Transp. Geotech.* **2021**, *26*, 100454. [CrossRef]
12. Juran, I.; Elias, V. Ground Anchors and Soil Nails in Retaining Structures. In *Foundation Engineering Handbook*; Fang, H.-Y., Ed.; Springer: Boston, MA, USA, 1991; pp. 868–905, ISBN 9781461367529.
13. Wang, S.; Li, Q.; Dong, J.; Wang, J.; Wang, M. Comparative Investigation on Deformation Monitoring and Numerical Simulation of the Deepest Excavation in Beijing. *Bull. Eng. Geol. Environ.* **2021**, *80*, 1233–1247. [CrossRef]
14. Sun, Y.; Li, Z. Analysis of Deep Foundation Pit Pile-Anchor Supporting System Based on FLAC3D. *Geofluids* **2022**, *2022*, 1699292. [CrossRef]
15. Mun, B.; Oh, J. Hybrid Soil Nail, Tieback, and Soldier Pile Wall—Case History and Numerical Simulation. *Int. J. Geotech. Eng.* **2017**, *11*, 1–9. [CrossRef]
16. Zhou, Z.; Li, F.; Qujue, A. Laterally Cantilevered Space Frame for the Roadway Widening in Steep-Sloped Mountainous Areas. *Struct. Eng. Int.* **2008**, *18*, 254–258. [CrossRef]
17. Liu, J.; Ye, J.; Shen, X.; Yu, J.; Wu, T.; Yuan, J.; Ye, Q.; Wang, S.; He, H. In-Situ Monitoring and Numerical Analysis of Deformation in Deep Foundation Pit Support: A Case Study in Taizhou. *Appl. Sci.* **2023**, *13*, 6288. [CrossRef]
18. Jia, J.; Gao, R.; Tu, B.; Zhou, C. Application of Flexible Retaining with Prestressed Anchor to Reduce the Effect That Excavations Have on Urban Environment. *Ekoloji Derg.* **2018**, *2018*, 1833–1840.
19. Liu, L.; Wu, R.; Congress, S.S.C.; Du, Q.; Cai, G.; Li, Z. Design Optimization of the Soil Nail Wall-Retaining Pile-Anchor Cable Supporting System in a Large-Scale Deep Foundation Pit. *Acta Geotech.* **2021**, *16*, 2251–2274. [CrossRef]
20. Mirlatifi, S. Performance Evaluation of a 21m Deep Excavation Stabilised by Combined Soil Nails and Anchors—A Case Study. *Aust. Geomech. J.* **2013**, *48*, 203–209.
21. Chen, A.; Wang, Q.; Chen, Z.; Chen, J.; Chen, Z.; Yang, J. Investigating Pile Anchor Support System for Deep Foundation Pit in a Congested Area of Changchun. *Bull. Eng. Geol. Environ.* **2021**, *80*, 1125–1136. [CrossRef]
22. Nisha, J.J.; Muttharam, M.; Vinoth, M.; Prasad, C.R.E. Design, Construction and Uncertainties of a Deep Excavation Adjacent to the High-Rise Building. *Indian Geotech. J.* **2019**, *49*, 580–594. [CrossRef]
23. Zolfegharifar, S.Y.; Kuchesfahani, A. Geotechnical study and analysis of the stability of pit walls. *Fen Bilim. Derg. (CFD)* **2015**, *36*, 1285–1297.
24. Babu, G.L.S.; Murthy, B.S.; Murthy, D.S.N.; Nataraj, M.S. Bearing Capacity Improvement Using Micropiles: A Case Study. In Proceedings of the GeoSupport 2004; American Society of Civil Engineers: Orlando, FL, USA, 2004; pp. 692–699.
25. Abd El-Rahim, H.H.A.; Taha, Y.K.; Mohamed, W.E.D.E.S. The compression and uplift bearing capacities of helical piles in cohesionless soil. *JES J. Eng. Sci.* **2013**, *41*, 2055–2064. [CrossRef]
26. Fateh, A.M.A.; Eslami, A.; Fahimifar, A. Direct CPT and CPTu Methods for Determining Bearing Capacity of Helical Piles. *Mar. Georesour. Geotechnol.* **2017**, *35*, 193–207. [CrossRef]
27. Mahmoudi-Mehrizi, M.-E.; Ghanbari, A.; Sabermahani, M. The Study of Configuration Effect of Helical Anchor Group on Retaining Wall Displacement. *Geomech. Geoengin.* **2022**, *17*, 598–612. [CrossRef]
28. Abdoli, M.; Mehrnahad, H.; Hazeghian, M. Numerical Study of Pullout Capacity of Helical Multiple Anchors for Supporting Excavations. *Road* **2023**, *31*, 279–290.

29. Vijayakumar, S.; Muttharam, M. Numerical Study on Uplift Capacity of Helical Pile Embedded in Homogeneous and Layered Soil. In *Proceedings of the Soil Dynamics, Earthquake and Computational Geotechnical Engineering*; Muthukkumaran, K., Ayothiraman, R., Kolathayar, S., Eds.; Springer Nature: Singapore, 2023; pp. 97–108.
30. *ABAQUS, Analysis User's Manual*; Version 6.12; Dassault Systemes Simulia, Inc.: Johnston, RI, USA, 2012.
31. Bozkurt, S.; Abed, A.; Karstunen, M. Finite Element Analysis for a Deep Excavation in Soft Clay Supported by Lime-Cement Columns. *Comput. Geotech.* **2023**, *162*, 105687. [CrossRef]
32. Giner, E.; Sukumar, N.; Tarancón, J.E.; Fuenmayor, F.J. An Abaqus Implementation of the Extended Finite Element Method. *Eng. Fract. Mech.* **2009**, *76*, 347–368. [CrossRef]
33. Siemens, G.A.; Bathurst, R.J.; Miyata, Y. Numerical Simulation and Parametric Analysis of Multi-Anchor Walls Using the Finite Element Method. *Transp. Geotech.* **2018**, *15*, 57–69. [CrossRef]
34. Zhuang, Y.; Wang, K. Finite Element Analysis on the Dynamic Behavior of Soil Arching Effect in Piled Embankment. *Transp. Geotech.* **2018**, *14*, 8–21. [CrossRef]
35. Al Hasani, S.; Nasrellah , H.A.; Abdulraeg, A.A. Numerical Study of Reinforced Concrete Beam by Using ABAQUS Software. *Int. J. Innov. Technol. Interdiscip. Sci.* **2021**, *4*, 733–741 . [CrossRef]
36. Misir, I.S.; Yucel, G. Numerical Model Calibration and a Parametric Study Based on the Out-Of-Plane Drift Capacity of Stone Masonry Walls. *Buildings* **2023**, *13*, 437. [CrossRef]
37. García-Alba, J.; Bárcena, J.F.; García, A. Zonation of Positively Buoyant Jets Interacting with the Water-Free Surface Quantified by Physical and Numerical Modelling. *Water* **2020**, *12*, 1324. [CrossRef]
38. Bouarroudj, M.A.; Boudaoud, Z. Numerical Investigation of Predicting the In-Plane Behavior of Infilled Frame with Single Diagonal Strut Models. *Struct. Eng. Mech.* **2022**, *81*, 131–146. [CrossRef]

Investigating Collaborative Robotic Assembly: A Case Study of the FANUC CRX-10 iA/L in Industrial Automation at i-Labs

Albin Bajrami *, Daniele Costa, Matteo Claudio Palpacelli and Federico Emiliani

Department of Industrial Engineering and Mathematical Sciences, Marche Polytechnic University,
60121 Ancona, Italy; d.costa@univpm.it (D.C.); m.palpacelli@univpm.it (M.C.P.); f.emiliani@pm.univpm.it (F.E.)
* Correspondence: a.bajrami@pm.univpm.it

Abstract: This study examines the practicality and limitations of using a FANUC CRX-10 iA/l collaborative robot to assemble a product component, highlighting the trade-offs between increased robotization and reduced manual intervention. Through a detailed case study in the i-Labs laboratory, critical factors affecting precision assembly such as station layout, tooling design and robot programming are discussed. The findings highlight the benefits of robots for nonstop operation, freeing up human operators for higher value tasks despite longer cycle times. In addition, the paper advocates further research into reliable gripping of small components, a current challenge for robotics. The work contributes to open science by sharing partial results and methods that could inform future problem solving in robotic assembly.

Keywords: robotic; assembly; FANUC; industrial collaborative robot; 3D printing; industrial automation; case study; i-Labs research; rapid prototyping

1. Introduction

The contemporary industry is experiencing an acceleration in changes to productive paradigms, with an increasingly pressing demand for flexibility and product customization. To meet these needs, it is essential to have a flexible production system. Jain et al. [1] point out that there is no unique definition of a flexible production system; specifically, they distinguish between an adaptive approach, reactive to circumstances, and a proactive approach, planned in advance. Regardless of these categories, it is clear that the adaptability of a production system is crucial, especially for small and medium enterprises (SMEs). This has generated the need for more flexible production systems and complex products with a high degree of variation. Gustavsson et al. [2] add that it is often necessary to choose in advance between productivity and flexibility during the system's design, offering methodologies for this definition.

Automation has played a key role in this evolution. As Jovane [3] indicates, flexible production systems have made mass customization possible. However, traditional manufacturing solutions might not be sufficient to meet the new requirements, requiring a greater emphasis on flexibility and reconfigurability as suggested by Urbani [4]. In this context, the industry must not only adapt to changes but also anticipate them, integrating systems that are both efficient and capable of evolving in line with market trends.

Subsequently, as highlighted by Mourtzis [5], the evolution of production systems, driven by changing customer needs and technological advancements, has led to a shift from functional paradigms to customer-oriented ones (User-Centered Design, UCD). In [6], Chammas et al. explore the fundamental concepts of UCD, emphasizing the growing importance of project management through a proper balance of budget, time, and quality, necessary for more personalized production. The use of cobots (collaborative robots) in industry can benefit this triad of elements (quality, time, and budget).

Collaborative robots, or cobots, are emerging as crucial enablers in this context, not only aiding in reducing physical strain on workers but also in optimizing process efficiency through their high reconfigurability and the establishment of optimized work trajectories [7].

As emphasized by Fager et al. in [8], in the case of object sorting in a picking system, cobots can reduce costs and improve performance (time and budget) when there is significant sorting work to be done. El Makrini et al. in [9] demonstrate how the integration of cobots and humans in car assembly leads to improvements in process quality, combining human dexterity and problem-solving with the precision and strength of cobots. Another study in this direction was conducted by Safeea et al. in [10], where it is stated that a cobot can act as a 'third assistant hand' that lifts and holds parts while humans perform assembly tasks. In this way, the use of cobots can improve working conditions and productivity, and reduce safety risks.

While several studies highlight the advantages of adopting robots (both collaborative and industrial) in production processes compared to fully manual solutions, a detailed comparison of the benefits of integrating collaborative robots versus industrial robots still seems to be lacking. An article attempting to assess which solution is better between collaborative and industrial robots is that of Barravecchia et al. [11]. This study presents a methodology for evaluating the optimal layout, especially for customized production, in the use of collaborative robots in assembly. In Barravecchia's proposed model, costs related to learning and assembly time are also included. The learning process is faster in collaborative solutions than in the industrial one. The study shows that the cobot solution is ideal in situations of low production volumes, as they can reduce the frequency of defects and do not require reallocating or laying off workers. In the study by Heredia et al. [12], a comparison is made between industrial robots (IR) and collaborative ones (cobots), focusing on the energy consumption behavior of electronic components (EC) and shows that while industrial robots consume more energy, more of it is used to handle loads, in contrast to cobots which consume a large proportion of energy to power electronic components, although in absolute terms, cobots generally consume less. This observation might point out a potential downside in integrating cobots in industrial environments. Cobots allocate a significant part of their energy to powering EC (Electronic Components), unlike industrial robots, which predominantly use energy for direct task execution, like handling heavy loads. For example, a cobot might use a considerable amount of its energy just to keep its sensors and control systems running, even when not actively manipulating objects.

Comparing industrial robots with collaborative ones in terms of production flexibility, the collaborative solution brings numerous benefits over industrial robots. Collaborative robotics significantly enhances the flexibility of production as shown by several studies. In the literature review by Keshvarparast et al. [13], the authors report that in the designing phase of cobots, flexibility is considered a key feature as is the importance attached to safety. They define two types of flexibility: "Flexible cobots" (how quickly the robot can be reprogrammed) and "Flexible Collaboration" (how many tasks a robot can perform in a given time). Furthermore, there are several works that speak about the importance of cobots for flexible manufacturing, for instance, Giberti et al. in [14] define flexibility as the system's ability to quickly reconfigure itself to adapt to a new product within the same product family. The authors propose an approach to simplify the programming of collaborative robots, called Interactive Refinement Programming (IRP). This approach is based on primitives and general skills developed by expert engineers, which can then be connected in a tree structure to generate a specific task.

Lee et al. in [15] highlight that, for more high production flexibility, it is necessary to have a close collaboration between humans and robots. The authors propose a production structure specifically designed for this collaboration, demonstrating its feasibility. This is particularly important in the context of the Fourth Industrial Revolution, where customer demands are diverse and rapidly changing as also evidenced by the work of Sherwani et al. [16]. Strassmair et al. [17] further emphasize the importance of worker acceptance, which can be facilitated by granting more flexibility and considering spatial

constraints in the collaboration. These findings collectively underscore the role of collaborative robotics in enhancing production flexibility. Furthermore, Othman et al. [18] highlight that Human–Robot Collaboration (HRC) has become a prominent feature of smart manufacturing environments and conduct a systematic review about new technologies that can help in the HRC system, like AI, collaborative robots, Augmented Reality, and Digital Twin, providing insights on how this topic should be addressed. A similar work is performed by Michalos et al. [19], where the authors aim to present the existing approaches to the implementation of human collaborative applications and highlight the trends towards achieving seamless integration and robots as coworkers in the factories of the future.

In the context of flexible manufacturing, robotic assembly stands out as a key solution in many contemporary industrial applications, evident in the diverse range of products on the market. The integration of advanced technologies such as collaborative robotics and 3D printing is becoming increasingly significant. Rapid prototyping, particularly bolstered by low-cost 3D printing, represents a pivotal development in this landscape. Rapid prototyping (RP) is a technology for fabricating physical objects directly from CAD parts using additive layer manufacturing techniques, eliminating the need for extensive manufacturing process planning, tooling, or fixtures [20]. Three-dimensional printing, or additive manufacturing, plays a vital role in this industrial transformation, thanks to its capability to create objects layer by layer from CAD models. This technology is increasingly utilized in various sectors, including healthcare, automotive, and aerospace. It enables mass customization and the use of diverse materials, marking a significant step towards manufacturing agility [21]. The synergy between cobots and 3D printing is crucial in enhancing the efficiency and adaptability of manufacturing processes. It facilitates a quicker turnaround from design to final product and enables greater customization in response to market demands. Notable examples of rapid prototyping include the work of Geonea et al. [22], who develop a new exoskeleton robotic system for locomotor assistance, utilizing a novel structural solution and virtual prototyping. This is followed by dynamic simulations and stress analysis. Ciceri et al. [23] analyze building designs using a genetic algorithm with parameters such as shadow length, transportation, and outdoor area. Khalid et al. [24] review developments in additive manufacturing of cellulose nanocrystals (CNCs), highlighting their applications across fields like tissue engineering, robotics, and wearable electronics. These are just a few examples from the extensive literature on rapid prototyping, indicating its widespread impact and application.

The principle underlying this article is that of open science, with a commitment to sharing detailed insights related to a specific industrial application. Our aim is to contribute to the broader dissemination of knowledge by presenting methods, solutions, and critical observations gleaned from our research. To this end, we detail a comprehensive case study conducted at the i-Labs Industry Laboratory in Jesi, Italy. This study centers on a robotic assembly operation and rapid prototyping [25], offering a practical demonstration of these advanced technologies in an industrial setting and exploration of their operational the impacts on the manufacturing process. Through this approach, we aspire to provide valuable information that can be leveraged by other practitioners and researchers in the field. Furthermore, this article follows the same philosophy as the one proposed in [26], where it not only provides practical results but also defines a procedure for solving problems.

The structure of the paper is outlined as follows: Section 2 delves deeper into the topic of robotic assembly, highlighting its importance and relevance in the current industrial landscape. This section sets the context for the subsequent discussions and underscores the significance of robotic automation in manufacturing. Section 3 explains the specific task that the study aims to accomplish, providing insights into how the task is traditionally performed manually. Section 4 details the tools and methods utilized in this project. It encompasses a comprehensive exposition of the technologies, strategies, and programming techniques employed. Section 5 presents the results of the study. This section is dedicated to discussing the findings, observations, and data analysis, providing a critical evaluation of the project outcomes. Finally, Section 6 offers the conclusions of the paper. It synthesizes

the key takeaways, assesses the impact of the study, and discusses the broader implications of the findings within the field of robotic assembly. This section also contemplates future directions and potential areas for further research.

2. Robotic Assembly Task

The field of robotic assembly has long been a critical area of research and development. Initially explored in the early 1980s [27], it continues to be a pivotal topic in modern industries, with applications ranging from precision operations [28] to complex tasks like in-space assembly [29]. The inherent complexity of robotic assembly as outlined by Sanderson et al. in 1983 [30] lies in the need for precise positioning, handling complex geometries, and managing physical interactions. Within this complexity, an essential element is the development of methods for instructing robots to perform task independently, an area explored by Eicker in 1989 [31]. These advancements in robotic assembly are crucial for improving adaptability, reliability, and performance across various industries.

The literature is fit with works that address the multifaceted challenges of robotic assembly. For instance, Popa et al. [32] tackle the issue through a multilayer approach, dividing the workspace into mesoscale and microscale operations. Part of the robotic system is developed for coarse operations like positioning, while manipulation tasks are executed at the microscale using grippers and fixtures.

Similarly, Chen et al. [33] focus on high-precision assembly in semi-structured environments, such as inserting a piston into the hole of a valve body. To do this, they utilize a vision system to identify the position and orientation of parts, coupled with a force/torque control algorithm for tight-tolerance assembly.

Saric et al. [34] propose a method to estimate and correct part positioning uncertainties in assembly tasks, using contact trajectory data collected during active part interaction. This approach effectively addresses uncertainties through sensing.

Lastly, Peña-Cabrera et al. [35] discuss the challenge of threaded fastening operations in small batch production industries, which demand flexibility due to varied product types. They introduce and test a novel identification algorithm in a semi-structured environment.

Through these diverse approaches, the literature demonstrates the ongoing evolution and problem-solving in robotic assembly, highlighting the field's dynamic nature and its critical role in modern manufacturing.

3. The Task to Be Accomplished

The assembly of the subcomponent, which is the focus of this study and depicted in Figure 1, was initially performed manually by an operators. Although the operations were straightforward for the human operator, they consisted of repetitive tasks that lacked perceived added value for the end user, yet were essential for the completion of the product.

The sequence of operation that should be performed to assemble the product is as follows:

- Pick and place the *Cap*.
- Pick and place the *Magazine*.
- Pick and place the *Cone* (the cone is a reusable tool for inserting the ring into the housing. The principle of the cone could be seen in reference [36], shown in Figure 2).
- Pick and place the *Ring*.
- Insert the *Ring* into its seat.
- Remove the *Cone* from the piece and reposition it in its base.

The cone, a reusable tool depicted in Figure 2, is instrumental in the component to be assembled process of the system shown in Figure 1. It is used to guide the insertion of the ring into its housing, a method well established and commonly employed as referenced in [36]. The cone is designed to facilitate the elastic deformation of the ring as it is pressed towards the wider part of the cone, which is its base. This process causes the ring to expand and conform to the dimensions of its housing. Upon insertion, the ring attempts to return to its original size, thereby securing the CAP to the MAG through a clamping action. The

subsequent step of palletizing the assembled product, although integral to the process, is not within the purview of this paper's discussion.
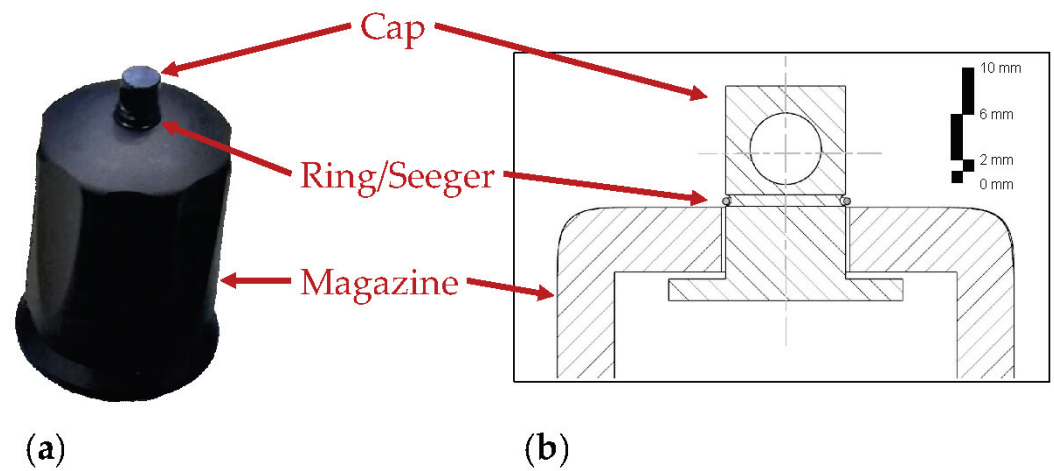

Figure 1. The sub-component subject of the assembly study. On the left (**a**), a real image of the component is shown; on the right (**b**), a simplified cross-section is presented to demonstrate the assembly of the sub-components.
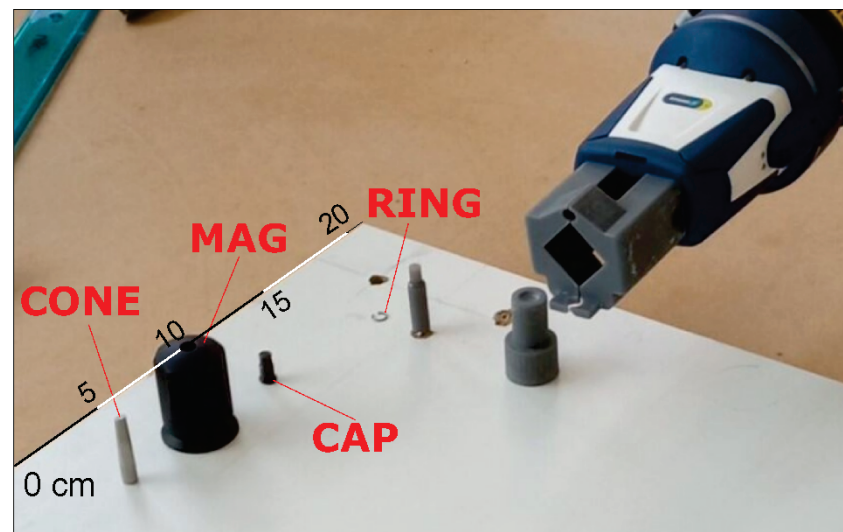

Figure 2. Set-up of the assembly system used for this operation. At the bottom left, you can see the cone used for the assembly of the part. The graduated scale in black and white is to be considered for a better understanding of the distances involved.

The list of operations we provided outlines the essential steps required for the assembly process. However, it does not dictate the actual sequence that must be followed. Figure 3 illustrates a potential assembly process solution, where operations can be parallelized rather than being sequential, enabling simultaneous task execution. This is achievable using dual anthropomorphic arms like YUMI [37]. The solution adopted with YUMI, although not elaborated upon here because it was explored in a separate research project, essentially revolves around the use of the robot's double anthropomorphic arms to parallelize certain steps, shown in the UML (Unified Modeling Language) diagram (Figure 3).

The assembly steps performed in this research begin with "Pick CAP", grasping a cap, and is succeeded by "Place CAP", for positioning. This pattern continues with other components like "Pick MAG" and "Place MAG", leading up to the picking and placing of a "CONE" and a "RING". The "Push RING" operation secures the ring within its seat. Post assembly, the "CONE" is detached ("Remove CONE") and is reverted to the starting point ("Home CONE"). The concluding stages involve lifting the assembled component

("Pick Assembled Component") and its palletization ("Palletize"), marking the process completion. A summary of the main steps performed is illustrated in Figure 4.
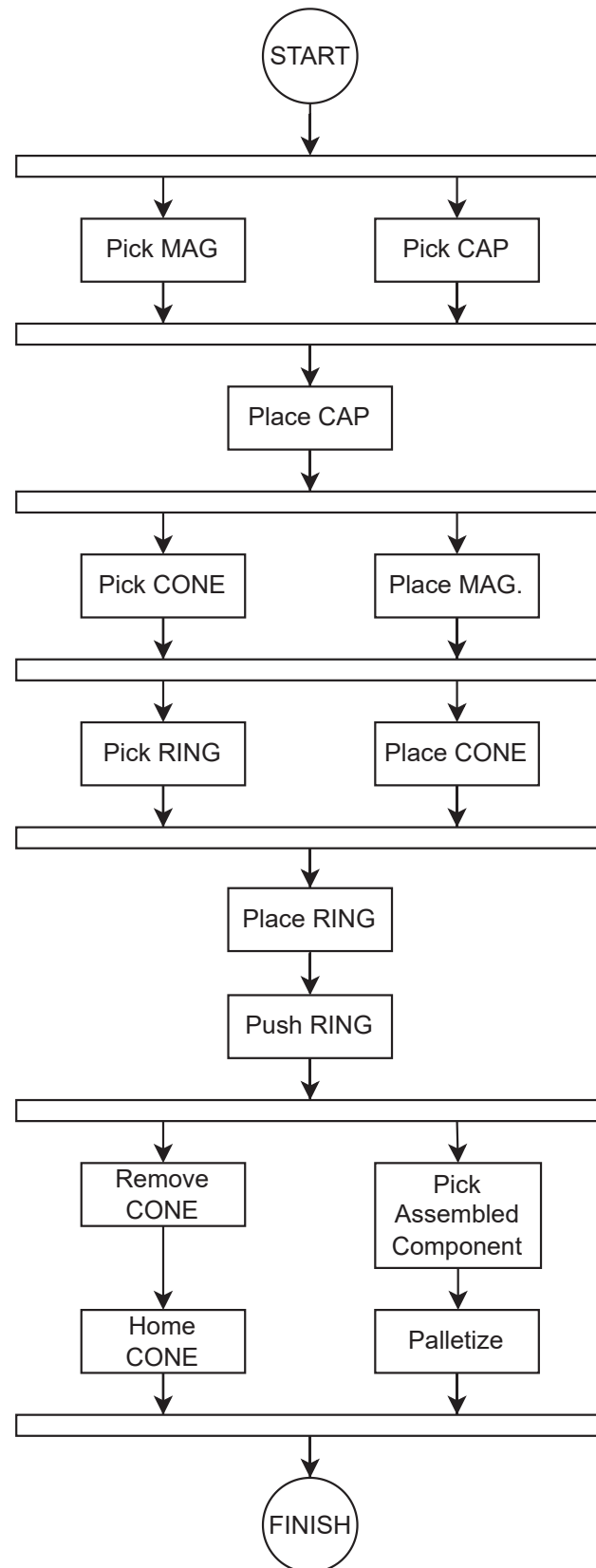
Figure 3. The UML diagram visually represents the parallelized step-by-step automated assembly process, from component selection to final assembly completion.
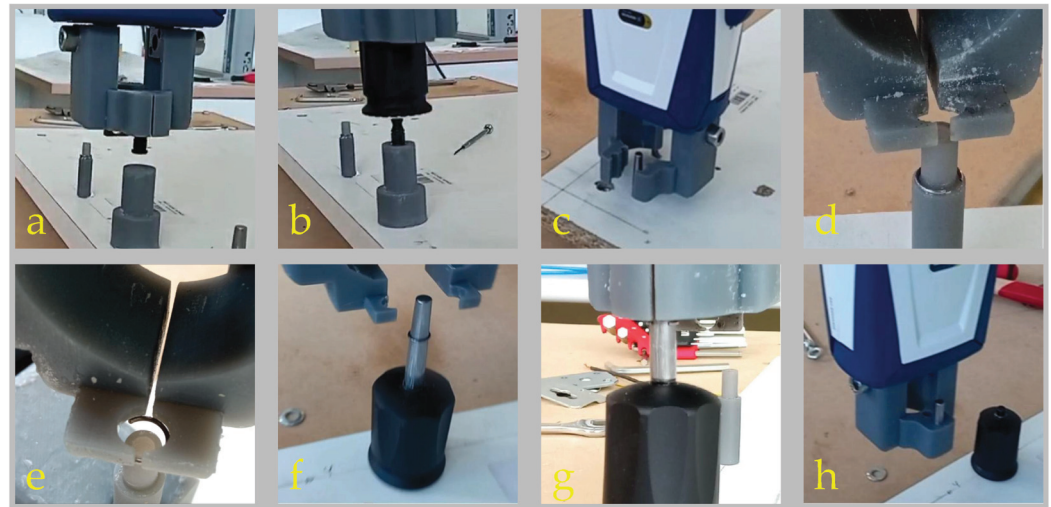
Figure 4. Automated assembly sequence: (**a**) positioning of the CAP, (**b**) positioning of the MAG, (**c**) gripping of the guiding cone (CONE) by the robot, (**d**) detail of the approach position for gripping the RING, (**e**) close-up view of the RING correctly gripped by the robot, (**f**) positioning stage of the RING in preparation for insertion, (**g**) insertion of the ring into its housing assisted by the CONE, and (**h**) removal of the CONE after assembly, signaling the preparation of the component for subsequent palletization.

4. Tools and Methods

The project primarily utilizes the FANUC CRX 10iA/L robot [38] and the Formlabs 3 SLA 3D printer [39]. The Formlabs 3, employing laser technology for resin curing, ensures high precision and detail, though it comes with limitations such as slower print speeds and additional post-processing. Complementing these tools, the SCHUNK Co-act EGP-C gripper [40] is optimized for collaborative operations, enhancing safety and versatility in handling diverse tasks. Further, Siemens NX [41] is used for creating CAD models, which are subsequently exported in STL format for the Formlabs printer through the proprietary software PreForm [42], showcasing Siemens NX's extensive capabilities in computer-aided design and manufacturing.

This integration of advanced technologies illustrates the project's alignment with Industry 4.0's emphasis on flexible automation and customized production.

The process followed a trial-and-error approach, testing various CAD solutions and setups. Results from these attempts were shared online, adhering to open science principles. However, certain proprietary data, like the final product version, remain exclusive to the company.

The procedure followed to obtain the company's compliance with the order is as follows:

- Understanding customer requirements.
- Determining what tasks can be executed solely by the robot and which need automation.
- Identifying various tasks and figuring out their execution.
- Testing and evaluating functionality.
- Using the results to make modifications, greatly aided by 3D printing.
- Repeating this process until a satisfactory solution is achieved.

This sequence of steps led to two distinct outcomes: a corporate solution and a research-focused one. The solution detailed in this research diverges from the one implemented by the company. It is important to note that the company did not fund this specific project. What has been undertaken is the extraction of an innovative resolution from the corporate solution, aiming to explore new methodologies in the application of cobots.

Figure 2 showcases the setup used to test the assembly operation described in this paper. The setup is straightforward and allows for the required evaluation to be conducted

effectively. The components (MAG, CAP, RING, and CONE) are arranged in a line to the left, although their positioning is not mandatory for the operation's success. Additionally, in the same figure, the RING holder and the assembly support near the gripper are depicted. The entire assembly process is carried out directly on this support. In the git repository of the project, there is a video that shows the complete procedure to assembly the component [43].

In this project, the programming of the robot was carried out using Fanuc's TP (Teach Pendant) language as requested by the company. The TP language is known for its relative simplicity, which facilitated the programming process. Specifically, it allowed for precise fine-tuning, a critical feature for this project. This meant that we could approximate the robot's positioning and orientation and then make exact adjustments as needed, enhancing the accuracy and effectiveness of the robot's operations in the assembly process. This capability proved essential in achieving the desired precision in the assembly tasks.

5. Results

The key findings in this paper are categorized into two main areas: practical industry applications and conceptual research insights. For the industrial application, significant outcomes include the comprehensive operational cycle time of the setup and the development of CAD models, specifically detailing the final dimensions of the robotic fingers. These results offer valuable insights for both industrial implementation and academic study. The upcoming sections will focus on conceptual results, aimed more at research-oriented discussions and generalizations, furthering the theoretical understanding in this field.

5.1. Design of the Fingers

The design of the fingers in this project is tailored to perform multiple tasks within a single setup. This section will showcase the various functionalities of these fingers, aiming to share problem-solving methodologies that could be useful for addressing new challenges, applying the principle of problem abstraction.

Figure 5 presents two global views of the fingers designed for this project. Developed using Siemens NX, the designs were exported in STL format for printing with the Formlabs 3 SLA printer. The fingers were printed using gray resin, and their specifications can be found in [44].

Figure 5. The left view is a top–down perspective highlighting the central decagonal (10-sided) hole for gripping the MAG. Moving to the right, there is a hole for the CAP and a conical hole for gripping the CONE.

Description of the Functional Parts of the Fingers

The fingers of the gripping mechanism are multi-purpose. There are several parts specifically designed to perform specific tasks. In the remainder of this section, the individual parts will be explained. Table 1 gives a summary description of the parts that make up the fingers and their functionality.

Table 1. Summary description of the functional parts of the robot fingers.

Component	Shape and Function	Special Features
MAG Grip	Irregular cylindrical, decagonal shape	Adaptable to various positions
CAP Grip	Cylindrical with linear geometry	Ensures secure and universal grip
CONE Grip	Negative form, narrow at base	Prevents CONE from being pushed out
RING Grip	Triangular and elliptical internal space	Selects and grips small rings (Ø 9 mm, thickness 0.7 mm)

Note: The RING Grip is critical due to the small size of the rings it needs to handle.

MAG Grip: The MAG has an irregular cylindrical shape. The adoption of a decagonal shape for the grip interface has shown practical effectiveness, as its geometry increases the contact points. This design advantage was observed through empirical testing, where the decagonal grip consistently accommodated various placements of the MAG, resulting in stable and secure handling without the need for precise positioning. *CAP Grip*: The CAP grip utilizes a similar principle to the MAG grip. With the cylindrical shape of CAP, a linear geometry aids in ensuring a more secure and universal grip. Figure 5 illustrates the concept behind this choice for both MAG and the CAP. *CONE Grip*: The CONE grip is designed for interference with a negative form fit. To ensure a firm grip on the CONE and prevent it from being pushed outward, the negative form is designed narrower at the base and wider towards the top. Forces at play tend to push the CONE upwards, which is then blocked by form interference. This part of the fingers also serves to push the ring into its final seat. Being narrower at the base ensures that the ring does not get trapped inside the CONE. *RING Grip*: This component is the most critical because of the small size of the ring it has to take (outer diameter of 9 mm and thickness of about 0.7 mm), which makes it difficult to grip. To better understand how this part of the fingers must work, the procedure by which the rings are gripped is explained: the rings are inserted into a special holder, lined up one above the other. The gripper is brought into position and then closed with the component shown in the Figure 6. The lower triangular geometry selects only one ring, and the inner space of the housing allows only one ring to enter. Furthermore, the internal space is elliptical, not circular, to accommodate the ring and allow for slight deformation. The ring is then transported and inserted into the upper part of the CONE already positioned over the previously assembled component. The ring is released and, with the seat of the CONE, is pushed into its final position.
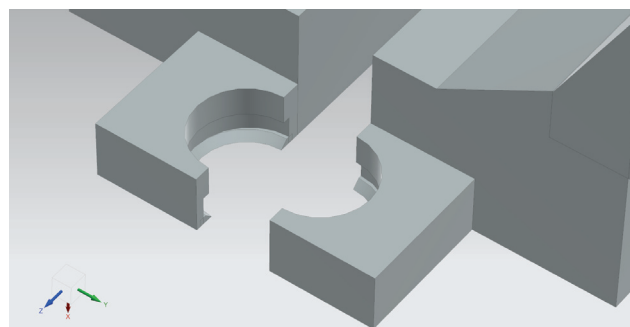
Figure 6. The image illustrates in isometric view the particular RING (Figure 5) of the pliers' fingers. Its particular geometry makes it possible to take a single ring with an external diameter of 9 mm and a thickness of 0.7 from a pile of rings arranged one above the other.

Normally, the pushing force does not require more than 3 kg, but the presence of various frictions can increase the necessary force to unacceptable levels. Additionally, during this phase, the CONE and the gripper must be vertically aligned, as misalignments can lead to a force development that could exceed the robot's 10 kg payload or even break the gripper. This could be avoided by a force control, here not developed.

5.2. Cycle Time

The manual assembly process, normally taking about 15 s, contrasts sharply with the robotic operation's 50 s cycle time, which is longer due to the serialized nature of the tasks. However, the robotic solution offers significant advantages, such as enabling continuous assembly outside of regular working hours or with fewer staff. This allows operators to focus on more critical and value-adding tasks within the product development process.

6. Conclusions

In conclusion, this study underscores that, while the task could technically be executed entirely by a collaborative robot, it is not recommended due to the complexity of tasks such as gripping and inserting small-sized rings. The sensitivity and malleability of human hands facilitate a simpler grip, which is challenging to replicate with current robotic technology. This limitation has spurred the idea for further research aimed at reliable ring gripping.

The key conclusions of the study are as follows:

- Shifting from manual to robotic assembly in this application is feasible but not advisable. It is important to consider redesigning products with robotic assembly in mind, incorporating specific design features to simplify robot training and facilitate easier assembly by robots.
- Slower operational speeds are crucial for maintaining precision in assembly tasks, particularly due to vibrations caused by motors in various configurations.
- The use of wait commands is essential to minimize vibrations and enhance the repeatability of the cycle.
- The introduction of vibrations during assembly, especially for handling rings, is suggested as a method to reduce interference and improve operational efficiency.

All results obtained in this study are freely available online in the project's GitHub repository [43]. The outputs of this research have also been instrumental in better understanding the potential challenges in executing certain robotic assembly operations. This has allowed us to provide solutions that can be utilized by other companies or researchers, while also highlighting the weaknesses of this process. The aim is to use these findings to enhance the flexible framework proposed in [45], thereby improving its efficacy and applicability.

References

1. Jain, A.; Jain, P.; Chan, F.T.; Singh, S. A review on manufacturing flexibility. *Int. J. Prod. Res.* **2013**, *51*, 5946–5970. [CrossRef]
2. Gustavsson, S.O. Flexibility and productivity in complex production processes. *Int. J. Prod. Res.* **1984**, *22*, 801–808. [CrossRef]
3. Jovane, F.; Koren, Y.; Boër, C. Present and Future of Flexible Automation: Towards New Paradigms. *CIRP Ann.* **2003**, *52*, 543–560. [CrossRef]
4. Urbani, A.; Molinari-Tosatti, L.; Pierpaoli, F. New frontiers for manufacturing in mass customization. In Proceedings of the 5th Biannual World Automation Congress, WAC-02, Orlando, FL, USA, 9–13 June 2002. [CrossRef]
5. Mourtzis, D.; Doukas, M. The Evolution of Manufacturing Systems: From Craftsmanship to the Era of Customisation. In *Advances in Logistics, Operations, and Management Science*; IGI Global: Hershey, PA, USA, 2014; pp. 1–29. [CrossRef]

6. Chammas, A.; Quaresma, M.; Mont'Alvão, C. A Closer Look on the User Centred Design. *Procedia Manuf.* **2015**, *3*, 5397–5404. [CrossRef]
7. Bragança, S.; Costa, E.; Castellucci, I.; Arezes, P.M. A Brief Overview of the Use of Collaborative Robots in Industry 4.0: Human Role and Safety. In *Occupational and Environmental Safety and Health*; Springer International Publishing: Cham, Switzerland, 2019; pp. 641–650. [CrossRef]
8. Fager, P.; Sgarbossa, F.; Calzavara, M. Cost modelling of onboard cobot-supported item sorting in a picking system. *Int. J. Prod. Res.* **2020**, *59*, 3269–3284. [CrossRef]
9. El Makrini, I.; Elprama, S.A.; Van den Bergh, J.; Vanderborght, B.; Knevels, A.J.; Jewell, C.I.; Stals, F.; De Coppel, G.; Ravyse, I.; Potargent, J.; et al. Working with Walt: How a Cobot Was Developed and Inserted on an Auto Assembly Line. *IEEE Robot. Autom. Mag.* **2018**, *25*, 51–58. [CrossRef]
10. Safeea, M.; Neto, P.; Béarée, R. The Third Hand, Cobots Assisted Precise Assembly. In *Lecture Notes in Computer Science*; Springer International Publishing: Cham, Switzerland, 2019; pp. 454–457. [CrossRef]
11. Barravecchia, F.; Mastrogiacomo, L.; Franceschini, F. A general cost model to assess the implementation of collaborative robots in assembly processes. *Int. J. Adv. Manuf. Technol.* **2023**, *125*, 5247–5266. [CrossRef]
12. Heredia, J.; Schlette, C.; Kjærgaard, M.B. Breaking Down the Energy Consumption of Industrial and Collaborative Robots: A Comparative Study. In Proceedings of the 2023 IEEE 28th International Conference on Emerging Technologies and Factory Automation (ETFA), Sinaia, Romania, 12–15 September 2023. [CrossRef]
13. Keshvarparast, A.; Battini, D.; Battaia, O.; Pirayesh, A. Collaborative robots in manufacturing and assembly systems: Literature review and future research agenda. *J. Intell. Manuf.* **2023**. [CrossRef]
14. Giberti, H.; Abbattista, T.; Carnevale, M.; Giagu, L.; Cristini, F. A Methodology for Flexible Implementation of Collaborative Robots in Smart Manufacturing Systems. *Robotics* **2022**, *11*, 9. [CrossRef]
15. Lee, E.; Barthelmey, A.; Reckelkamm, T.; Kang, H.; Son, J. A Study on Human-Robot Collaboration based Hybrid Assembly System for Flexible Manufacturing. In Proceedings of the IECON 2019—45th Annual Conference of the IEEE Industrial Electronics Society, Lisbon, Portugal, 14–17 October 2019. [CrossRef]
16. Sherwani, F.; Asad, M.M.; Ibrahim, B. Collaborative Robots and Industrial Revolution 4.0 (IR 4.0). In Proceedings of the 2020 International Conference on Emerging Trends in Smart Technologies (ICETST), Karachi, Pakistan, 26–27 March 2020. [CrossRef]
17. Strassmair, C.; Taylor, N. Human Robot Collaboration in Production Environments. In Proceedings of the 23rd IEEE International Symposium on Robot and Human Interactive Communication 2014: Towards a Framework for Joint Action Workshop, IEEE RO-MAN 2014, Edinburgh, UK, 25–29 August 2014.
18. Othman, U.; Yang, E. Human–Robot Collaborations in Smart Manufacturing Environments: Review and Outlook. *Sensors* **2023**, *23*, 5663. [CrossRef]
19. Michalos, G.; Karagiannis, P.; Dimitropoulos, N.; Andronas, D.; Makris, S. Human Robot Collaboration in Industrial Environments. In *Intelligent Systems, Control and Automation: Science and Engineering*; Springer International Publishing: Cham, Switzerland, 2021; pp. 17–39. [CrossRef]
20. Chang, K.H. Rapid Prototyping. In *e-Design*; Elsevier: Amsterdam, The Netherlands, 2015; pp. 743–786. [CrossRef]
21. Shahrubudin, N.; Lee, T.; Ramlan, R. An Overview on 3D Printing Technology: Technological, Materials, and Applications. *Procedia Manuf.* **2019**, *35*, 1286–1296. [CrossRef]
22. Geonea, I.; Copilusi, C.; Dumitru, S.; Margine, A.; Rosca, A.; Tarnita, D. A New Exoskeleton Prototype for Lower Limb Rehabilitation. *Machines* **2023**, *11*, 1000. [CrossRef]
23. Ciceri, M.; Gauterio, M.; Scaccabarozzi, S.; Paz, J.; Garcia-Carmona, R.; Aruanno, B.; Covarrubias, M. Rapid Prototyping in Engineering Education: Developing a Hand Exoskeleton for Personalized Rehabilitation. *Comput. Aided Des. Appl.* **2023**, *21*, 474–486. [CrossRef]
24. Khalid, M.Y.; Arif, Z.U.; Noroozi, R.; Hossain, M.; Ramakrishna, S.; Umer, R. 3D/4D printing of cellulose nanocrystals-based biomaterials: Additives for sustainable applications. *Int. J. Biol. Macromol.* **2023**, *251*, 126287. [CrossRef] [PubMed]
25. Bajrami, A.; Palpacelli, M.C. From Traditional Automation to Collaborative Robotics in Fine Robotic Assembly: A Case Study at i-Labs. In Proceedings of the 2023 I-RIM Conference, Rome, Italy, 23–25 May 2023.
26. Bajrami, A.; Palpacelli, M.C. A Proposal for a Simplified Systematic Procedure for the Selection of Electric Motors for Land Vehicles with an Emphasis on Fuel Economy. *Machines* **2023**, *11*, 420. [CrossRef]
27. Fox, B.; Kempf, K. Opportunistic scheduling for robotic assembly. In Proceedings of the 1985 IEEE International Conference on Robotics and Automation, St. Louis, MO, USA, 25–28 March 1985; Volume 2, pp. 880–889. [CrossRef]
28. Cho, H.S.; Warnecke, H.J.; Gweon, D.G. Robotic assembly: A synthesizing overview. *Robotica* **1987**, *5*, 153–165. [CrossRef]
29. Roa Garzón, M.A.; Nottensteiner, K.; Wedler, A.; Grunwald, G. Robotic Technologies for In-Space Assembly Operations. In Proceedings of the 14th Symposium on Advanced Space Technologies in Robotics and Automation (ASTRA), Leiden, The Netherlands, 20–22 June 2017.
30. Sanderson, A.; Perry, G. Sensor-based robotic assembly systems: Research and applications in electronic manufacturing. *Proc. IEEE* **1983**, *71*, 856–871. [CrossRef]
31. Eicker, P.; Strip, D. Current research in robotics and automation-automated planning and programming for robotic batch mechanical assembly. *Computer* **1989**, *22*, 53–54. [CrossRef]
32. Popa, D.O.; Stephanou, H.E. Micro and Mesoscale Robotic Assembly. *J. Manuf. Process.* **2004**, *6*, 52–71. [CrossRef]

33. Chen, H.; Zhang, G.; Zhang, H.; Fuhlbrigge, T.A. Integrated robotic system for high precision assembly in a semi-structured environment. *Assem. Autom.* **2007**, *27*, 247–252. [CrossRef]
34. Sarić, A.; Xiao, J.; Shi, J. Reducing uncertainty in robotic surface assembly tasks based on contact information. In Proceedings of the 2014 IEEE International Workshop on Advanced Robotics and its Social Impacts, Evanston, IL, USA, 11–13 September 2014; pp. 94–100. [CrossRef]
35. Peña-Cabrera, M.; Lopez-Juarez, I.; Rios-Cabrera, R.; Corona-Castuera, J. Machine vision approach for robotic assembly. *Assem. Autom.* **2005**, *25*, 204–216. [CrossRef]
36. BM MECCANICA—Assembly Line Solution—Coni per Guarnizione di Diverse Misure. Available online: https://www.bmmeccanica.com/prodotti/coni-per-guarnizioni-o-ring-di-diverse-misure/ (accessed on 18 January 2024).
37. Dual-Arm YuMi Collaborative Robot—ABB Group. Available online: https://new.abb.com/products/robotics/robots/collaborative-robots/yumi/dual-arm (accessed on 18 January 2024).
38. FANUC. CRX-10iA/L. 2024. Available online: https://www.fanuc.eu/it/it/robot/robot-filter-page/robot-collaborativi/crx-10ial (accessed on 19 January 2024).
39. Formlabs. Form 3. 2024. Available online: https://formlabs.com/it/3d-printers/form-3/ (accessed on 19 January 2024).
40. SCHUNK. Co-act EGP-C Collaborating Gripper for Small Components. Available online: https://schunk.com/gb/en/gripping-systems/parallel-gripper/co-act-egp-c/c/pgr_3995 (accessed on 19 January 2024).
41. NX Software Including CAD and CAM—Siemens Software. Available online: https://plm.sw.siemens.com/en-US/nx/ (accessed on 19 January 2024).
42. Formlabs. Software PreForm. Available online: https://formlabs.com/it/software/ (accessed on 19 January 2024).
43. AlbinEV. Miscellaneous Projects. 2024. Available online: https://github.com/AlbinEV/miscellaneous_projects/tree/main/Progetto_1 (accessed on 19 January 2024).
44. Formlabs. Grey Resin—Formlabs. Available online: https://formlabs.com/it/negozio/materials/grey-resin/ (accessed on 19 January 2024).
45. Bajrami, A.; Palpacelli, M.C. A Flexible Framework for Robotic Post-Processing of 3D Printed Components. In Proceedings of the Volume 7: 19th IEEE/ASME International Conference on Mechatronic and Embedded Systems and Applications (MESA). American Society of Mechanical Engineers, IDETC-CIE2023, Boston, MA USA, 20–23 August 2023. [CrossRef]

Process Mining Organization (PMO) Based on Machine Learning Decision Making for Prevention of Chronic Diseases

Angelo Rosa [1,2,*,†] **and Alessandro Massaro** [1,2,3,†]

1. Department of Management, Finance and Technology, LUM, Libera Università Mediterranea "Giuseppe Degennaro", S.S. 100-Km.18, Parco il Baricentro, 70010 Bari, Italy; massaro@lum.it
2. Department of Engeneering, LUM, Libera Università Mediterranea "Giuseppe Degennaro", S.S. 100-Km.18, Parco il Baricentro, 70010 Bari, Italy
3. LUM Enterprise S.r.l., S.S. 100-Km.18, Parco il Baricentro, 70010 Bari, Italy
* Correspondence: rosa@lum.it
† These authors contributed equally to this work.

Abstract: This paper discusses a methodology to improve the prevention processes of chronic diseases such as diabetes and strokes. The research motivation is to find a new methodological approach to design advanced Diagnostic and Therapeutic Care Pathways (PDTAs) based on the prediction of chronic disease using telemedicine technologies and machine learning (ML) data processing techniques. The aim is to decrease health risk and avoid hospitalizations through prevention. The proposed method defines a Process Mining Organization (PMO) model, managing risks using a PDTA structured to prevent chronic risk. Specifically, the data analysis is focused on stroke risk. First, we applied and compared the Random Forest (RF) and Gradient Boosted Trees (GBT) supervised algorithms to predict stroke risk, and then, the Fuzzy c-Means unsupervised algorithm to cluster information on the predicted results. The application of the proposed approach is able to increase the efficiency of healthcare human resources and drastically decrease care costs.

Keywords: prevention of chronic disease; process mining; Process Mining Organization (PMO); machine learning; decision making; telemedicine

1. Introduction

Process mining (PM) is an important approach suitable for designing processes based on machine learning (ML) decision-making engines. PM has been applied to improve industrial processes [1,2] and subsequently to design healthcare processes [3,4] regarding the cost optimization of healthcare services [5], telemedicine [6], and patient fall risk management [7]. The application of PM is important for the design of organizational models based on workflows integrating ML algorithms and supporting decisions about human resource (HR) allocation or engagement [6]. The ML-HR decision-making engine upgrades the PM model to a Process Mining Organization (PMO) model. A method suitable for representing and sketching processes is the Business Process Modeling and Notation (BPMN) approach [8]. BPMN is an international standard [9,10], providing graphical elements to map processes. The BPMN is useful to design healthcare processes such as Diagnostic and Therapeutic Care Pathways (PDTAs). An example of a PDTA mapped by BPMN is illustrated in Figure 1, representing the 'AS IS' care path of diabetics [11]. As observed in Figure 1, the Italian diabetic PDTA is exhaustive for the chronic pathology, but no details are provided for primary prevention highlighted by the green box (prevention task). The goal of the proposed paper is therefore precisely the optimization of the prevention task using telemedicine and ML facilities. Specifically, we have proposed a basic organizational model and technological facilities that can be used to implement a prevention PDTA with the goal of eliminating the risk of chronic degeneration, and, consequently, avoiding the

execution of the whole PDTA process of chronic care, which requires high resource costs. Figure 2 presents the sketch of a diagram summarizing the goal of the paper.
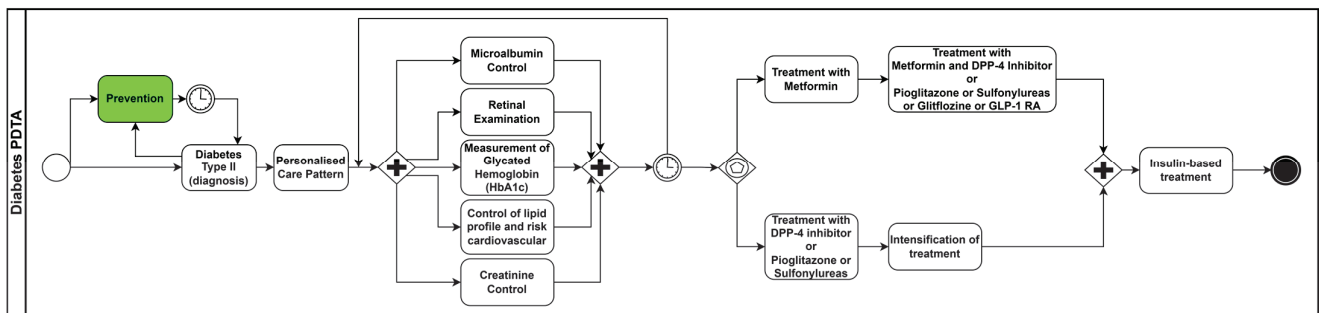

Figure 1. 'AS IS' PDTA process of type 2 diabetes (translation of the procedure indicated in [11]). The green box highlights the prevention task goal of the proposed work. No stroke PDTA is available in Italy.
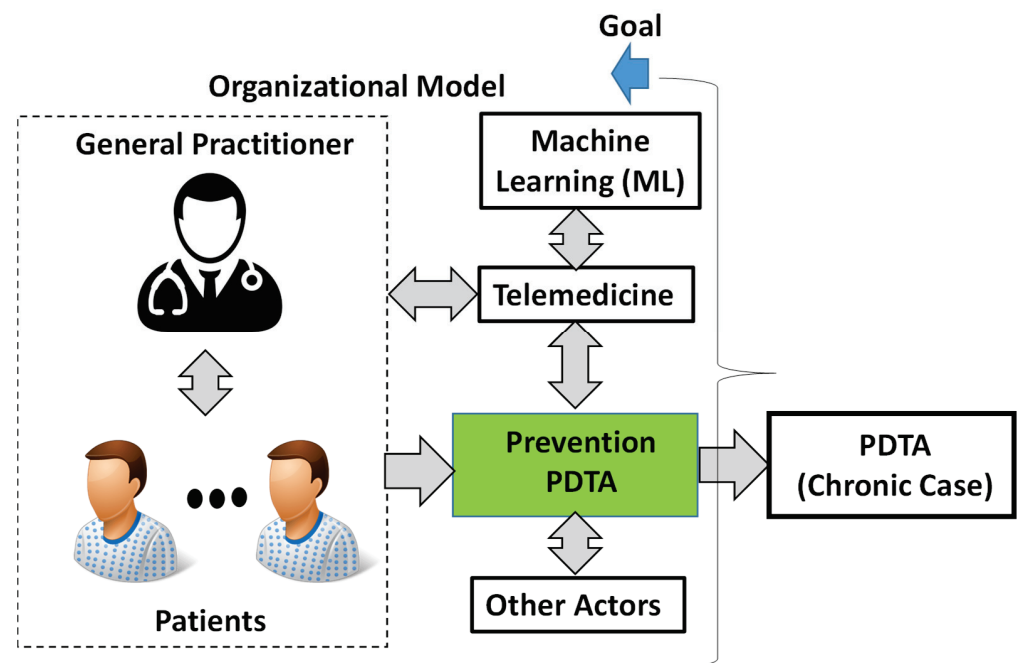

Figure 2. Basic organizational model and technological facilities for implementing a prevention PDTA with the goal of avoiding chronic risk.

In Italy, high care costs are estimated for chronic diabetic patients; by analyzing the socio-economic impact of diabetes, it is noted that in only the Italian Puglia region, approximately 5% of the adult population aged 18–69 years is affected by diabetes [12]; furthermore, the average annual cost per diabetic patient is EUR 2792 [13], and for the Puglia region alone, there are an estimated 232,000 diabetic people (Source: Istat 2020), corresponding to a total annual cost for the region of EUR 647,744,000. Concerning the stroke cost, in Italy, there are 100 thousand new cases a year, corresponding to an estimated cost of EUR 16 billion for the whole National Healthcare Service (source: 'Sanità 24', 2018). These initial analyses highlight the importance of finding a solution capable of reducing, from a predictive perspective, the onset of chronic diseases in various possible forms.

The prevention of diabetes could also have implications in the prediction of the risk of stroke. In particular, cases of hypoglycemia or hyperglycemia represent stroke risks [14,15]. Other elements concerning risks which are correlated with strokes are hypertension [16] and heart disease [17]. These risk elements are analyzed in the paper.

Regarding prevention, telemedicine could improve healthcare organization by optimizing care processes [6]. For this reason, the goal of the proposed work is to design a prevention process matching diabetes and stroke risks by highlighting ML data processing aspects in decision-making procedures and in organizational aspects.

The purpose of the study is to provide ML tools and process mapping methods to actuate the new PDTA to prevent chronic diseases. The PDTA prevention process is modeled in this paper through BPMN, thus suggesting an innovative workflow to follow the patient monitoring care patterns through telemedicine tools. Furthermore, telemedicine provides digital data useful for executing the preventive decision-making procedures.

The paper is structured as follows:

- In Section 2, we provide information about the materials and methods, discussing the analyzed dataset and the ML data processing workflow.
- In Section 3, we propose a PDTA BPMN workflow management prevention process and care service organization, including telemedicine monitoring tools to decrease the risks of diabetes and stroke.
- In Section 3, we apply supervised and unsupervised ML algorithms, improving the initial decision making about possible risks and focusing the data analysis on stroke risk.
- In Section 4 and in the appendices, we provide information about organizational aspects supported by telemedicine facilities and improved by other possible healthcare actors.
- In Section 4 and in the appendices, we also discuss advantages, disadvantages, limitations, and perspectives of the proposed approaches and technologies.

2. Materials and Methods

In this section, we discuss the ML tools and the dataset processed by the ML algorithms.

2.1. Dataset Testing Machine Learning Algorithms to Predict Stroke Risk

The open dataset [18] is used for the testing of the ML algorithms, focusing attention on stroke prediction. The dataset is available in the *Kaggle* dataset repository [18] as a .csv file containing 5110 observations with the following 12 attributes:

- *id*: unique identifier of the patient;
- *gender*: 'Male' or 'Female';
- *age*: age of the patient;
- *hypertension*: 0 for patients without hypertension, 1 for patients with hypertension;
- *heart_disease*: 0 for patients without any heart diseases, 1 for patients affected by heart disease;
- *ever_married*: 'No' (never married) or 'Yes' (married);
- *work_type*: 'children' (not a worker), 'Govt_jov' (public worker), 'Never_worked' (unemployed), 'Private' (worker of a private company), or 'Self-employed' (professionals or managers);
- *Residence_type*: 'Rural' or 'Urban';
- *avg_glucose_level*: average glucose level measured in blood;
- *bmi:* body mass index;
- *smoking_status:* 'formerly smoked' (smoker in the past), 'never smoked' (not a smoker), 'smokes' (smoker), or 'Unknown' (no information is available);
- *stroke:* 1 if the patient had a stroke, or 0 if not.

In Figure 3, a screenshot is shown of the dataset imported in the local repository (local memory) of the personal computer (11th Gen Intel(R) Core(TM) i5-1135G7, 2.42 GHz) used for the data processing. The figure shows all the attributes listed above as digital records locally imported.

Row ID	S gender	D age	I hypertension	I heart_disease	S ever_married	S work_type	S Residence_type	D avg_glucose_level	D bmi	S smoking_status	S stroke
Row90	Female	79	0	1	Yes	Private	Urban	226.98	29.8	never smoked	1
Row91	Male	81	0	0	Yes	Private	Urban	72.81	26.3	never smoked	1
Row92	Female	57	0	0	No	Self-employed	Urban	68.02	37.5	never smoked	1
Row93	Female	80	1	0	Yes	Self-employed	Urban	68.56	26.2	Unknown	1
Row94	Male	45	0	0	Yes	Private	Rural	64.14	29.4	never smoked	1
Row95	Female	78	0	0	Yes	Private	Rural	235.63	32.3	never smoked	1
Row96	Female	70	0	0	Yes	Self-employed	Rural	76.34	24.4	formerly smoked	1
Row97	Male	58	0	1	Yes	Private	Rural	240.59	31.4	smokes	1
Row98	Male	57	1	0	Yes	Govt_job	Urban	78.92	27.7	formerly smoked	1
Row99	Female	69	0	0	Yes	Govt_job	Urban	82.81	28	never smoked	1
Row100	Male	64	0	1	Yes	Govt_job	Urban	74.1	28.8	Unknown	1
Row101	Female	77	0	0	Yes	Govt_job	Rural	190.32	31.4	never smoked	1
Row102	Female	74	0	0	Yes	Private	Rural	231.61	34.6	formerly smoked	1
Row103	Female	81	0	1	Yes	Self-employed	Rural	78.7	19.4	Unknown	1
Row104	Female	57	0	0	Yes	Govt_job	Urban	110.52	28.5	Unknown	1

Figure 3. Dataset extraction (data imported in the local repository), indicating the attributes to be processed by the ML algorithms.

2.2. Machine Learning Algorithms

The ML data processing model is structured in the following three data processing steps:

(1) *Stage I*: data pre-processing, preparing the input dataset;
(2) *Stage II:* supervised ML algorithm data processing, predicting stroke risks;
(3) *Stage III:* unsupervised ML algorithm data processing, supporting data interpretation and clustering of the results.

Random Forest (RF) and Gradient Boosted Trees (GBT) are applied as ML supervised algorithms. The choice of these algorithms is due to their ability to efficiently process heterogeneous attributes [19–22], including numerical and categorical ones. Specifically, RF is an ensemble ML algorithm consisting of the use of a chosen number of decision trees by combining the outputs of the decision trees into a single result. RF has many further advantages, such as the ability to also process qualitative data, high performance with a good classification accuracy, good robustness regarding numerical entropy introduced by missing values or wrong information, and good ability to analyze complex attribute interdependencies.

On the other hand, the GBT algorithm adopts very shallow regression trees and a special form of boosting to build an ensemble of trees [23]. The used base learner for this ensemble method is a simple regression tree, as for the RF algorithm. For each iteration step, the parameters are adjusted to minimize the loss function, indicating the difference between the classified/predicted and actual values. The gradient represents the incremental parameter adjustment and the boost is the method to accelerate the improvement of the accuracy.

The supervised RF and GBT algorithms are applied in this work to classify the patients to be controlled. These patients are initially characterized with no stroke risk; some patients initially with no stroke risk are classified by the RF and GBT algorithms as patients with a possible stroke risk (patients to be monitored).

The output of the ML supervised algorithms is successively clustered to facilitate data reading and data interpretation by simultaneously analyzing more clustered attributes. The adopted ML unsupervised algorithm is the Fuzzy c-Means [24]; fuzzy clustering allows each data point to fit in different clusters, defining a degree of membership to each cluster.

The tool adopted for ML data processing is the Konstanz Information Miner (KNIME). KNIME is an open-source tool [25] providing a large set of ML algorithms. Its versatility is in the use of interconnected graphical block (or nodes) behaving as interfaces, allowing data processing parameters to be changed. All the blocks are linked to structure the workflow. In Figure 4, the KNIME workflow executed in this work is illustrated. The workflow is structured into the three stages:

- *Stage I:* Containing blocks suitable for data pre-processing operations, such as importing the .csv input dataset into the local repository environment ('CSV Reader'), attribute conversion ('String to Number'), attribute section filtering more significant

attributes ('Column Filter'), and data partition (partition by the 'Partitioning' block of the dataset into a training and a testing dataset).

- *Stage II:* Implementing blocks to execute the RF and GBT supervised algorithms, including learning models processing the training dataset ('Random Forest Learner' and 'Gradient Boosted Trees Learner'), prediction models processing the testing dataset ('Random Forest Predictor' and 'Gradient Boosted Trees Predictor'), visual representation of results ('Scatter Plot', 'Color Manager' and 'Statistic'), and algorithm performance score ('Scorer' and 'Numeric Scorer').
- *Stage III:* Implementing blocks to run the unsupervised Fuzzy c-Means algorithm ('Fuzzy c-Means') and visual representation blocks.
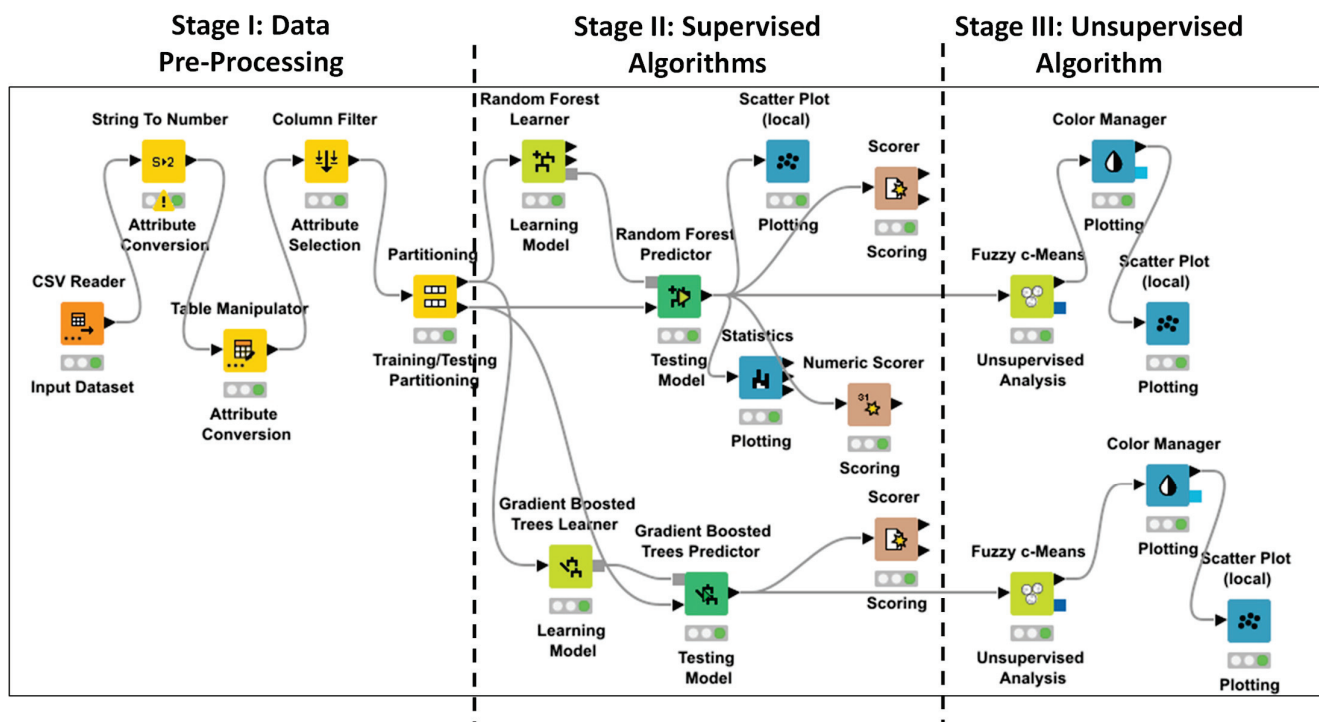
Figure 4. KNIME workflow implementing ML supervised and unsupervised algorithms, following from left to right the three stages of data processing (Stage I, Stage II, Stage III).

For both the FR and GBT algorithms, the original dataset is partitioned into training (2146 records containing stroke conditions important for training the ML models) and testing datasets (last 2964 records). The 'stroke' attribute (see Section 2.1) is chosen as a class to predict. The hyper parameters of the used GBT algorithm are as follows: limit the number of levels, indicating that the tree depth equals 4, learning rate equals 0, 1, and 100 is the number of models (number of decision trees to learn). Concerning RF, the used split criterion is the *Information Gain Ratio*, which is able to normalize the standard information gain by split entropy to overcome any unfair preference for nominal splits with many child nodes.

3. Results

The first result is obtained by discussing the ML application with medical staff (general practitioners and specialists validating the methodology) and by evaluating the feasibility of deploying a telemedicine platform by adopting certified medical kits (standard CE: 93/42/CEE, 2017/745/UE, class 2a) for diabetes and stroke prevention.

The BPMN workflow of Figure 5 is the result of the validated design, describing the platform monitoring patients during the prevention phase. The workflow examines the combined risk of patients to be affected by diabetes or to be injured by a stroke, thus defining a PDTA of prevention. The same workflow is also suitable for the prevention of

the hypertension risk by adopting specific sensors, mainly measuring heart disease. The diagram in Figure 5 is structured into three pools, indicating the processes of the three main actors involved in the system:

- patient to be monitored for diabetes risk (pool named 'Diabetes Prevention Process');
- patient to be monitored for stroke risk (pool named 'Stroke Prevention Process');
- general practitioner deciding the medical kit to assign and analyze data to decide on possible exams or drug assignments after the detection of digital alerting conditions (alerting thresholds overcoming critical values of physiological parameters, or alerting predicted results).

The model is designed by considering real-time monitoring of the patient's physiological parameters, and an automatic alerting condition enabling the decision of the general practitioner.
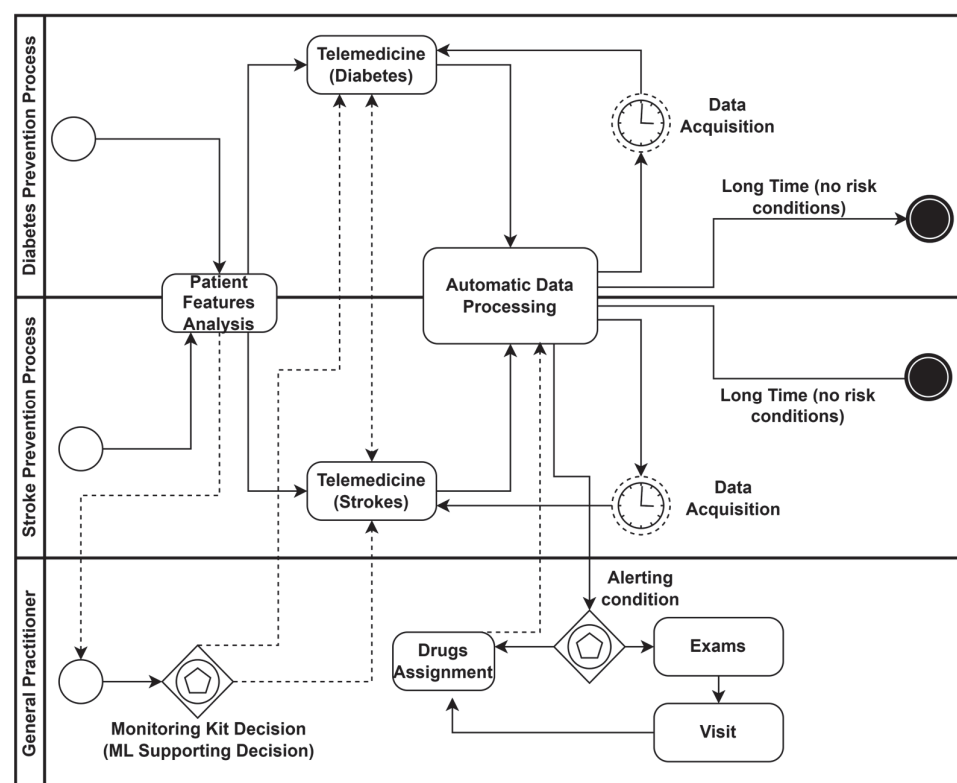
Figure 5. BPMN PDTA prevention process matching stroke and diabetes risk. The automatic data processing activates the general practitioner decision making.

Data Result Interpretation and Decision-Making Processs Preventing Stroke Risk

The dataset [18] is processed by the two algorithms RF and GBT. In Figure 6a,b, two screenshots are shown, indicating the stroke prediction of the same records by executing both the ML RF and GBT algorithms; the algorithms provide the same alerting condition with a weakly different confidence (0.7 in the case of RF and 0.776 for GBT). The algorithms provide similar prediction results and good performances (see performance parameters of Table 1). In Figure 7 can be seen the Receiver Operating Characteristic Curves (ROCs) of both the approaches, providing the values of the Area Under the ROC Curve (AUC) of Table 1, furthermore confirming the high algorithm performance. A further estimated performance index indicated in Table 1 is the F-measure (or F-score), measuring the predictive performance. The F-measure is typically adopted for statistical analysis of binary classification and information retrieval systems.

(a)

Row ID	S gender	D age	I hypertension	I heart_disease	S ever_married	S work_type	S Residence_type	D avg_glucose_level	D bmi	S smoking_sta...	S stroke	S Prediction (stroke)	D Prediction (stroke) (Confidence)
Row2542	Male	14	0	0	No	children	Urban	101.87	20.3	never smoked	0	0	1
Row2543	Female	13	0	0	No	children	Rural	77.55	21.3	Unknown	0	0	1
Row2544	Male	71	0	1	Yes	Private	Urban	215.72	39.2	smokes	0	1 → Alerting	0.7
Row2545	Female	66	0	0	Yes	Private	Rural	87.84	52.8	Unknown	0	0	0.88
Row2546	Male	32	0	0	No	Govt_job	Rural	91.93	30.2	never smoked	0	0	0.98

(b)

Row ID	S gender	D age	I hypertension	I heart_disease	S ever_married	S work_type	S Residence_type	D avg_glucose_level	D bmi	S smoking_status	S stroke	S Prediction (stroke)	D Prediction (stroke) (Confidence)
Row2542	Male	14	0	0	No	children	Urban	101.87	20.3	never smoked	0	0	0.995
Row2543	Female	13	0	0	No	children	Rural	77.55	21.3	Unknown	0	0	0.995
Row2544	Male	71	0	1	Yes	Private	Urban	215.72	39.2	smokes	0	1 → Alerting	0.776
Row2545	Female	66	0	0	Yes	Private	Rural	87.84	52.8	Unknown	0	0	0.958
Row2546	Male	32	0	0	No	Govt_job	Rural	91.93	30.2	never smoked	0	0	0.993

Figure 6. Prediction of the alerting case: (**a**) samples processed by RF algorithm; (**b**) same samples processed by GBT algorithm.

Table 1. Estimated accuracy, AUC, and F-measure of the adopted ML algorithms. All of the indexes confirm the good performance of the adopted RF and GBT algorithms.

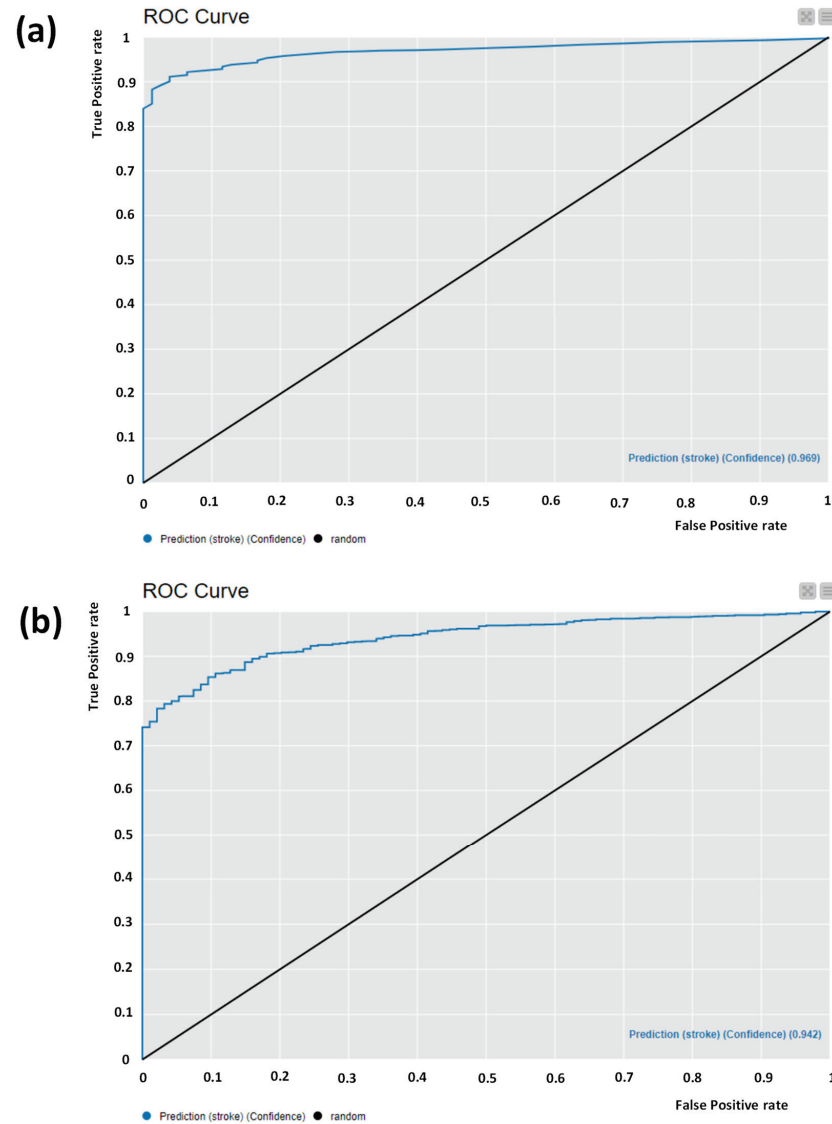| ML Algorithm	Accuracy	AUC	F-Measure
Random Forest (RF)	0.974	0.969	0.987
Gradient Boosted Trees (GBT)	0.968	0.942	0.984

Figure 7. (**a**) RF ROC curve. (**b**) GBT ROC curve (implementation of the KNIME 'ROC Curve' node).

We observe that the results to pay attention to are those where the risk of stroke is predicted even though there has not been an alert condition in the past. In order to group the results, the RF and GBT outputs are clustered by the Fuzzy c-Means algorithm, highlighting in red the predicted risk cases of stroke (the red color indicates the cluster of the predicted stroke risk). By considering three clusters, it is observed that the predicted stroke cases do not appertain to the first cluster characterized by patients having an age lower than 40 years old (this allows for excluding the preventive monitoring of these patients). In Figure 8, a comparison is presented of RF and GBT risk cases due to hyperglycemia and hypoglycemia status, by confirming the results expected in the literature [14,15]. The results of both algorithms present few differences.
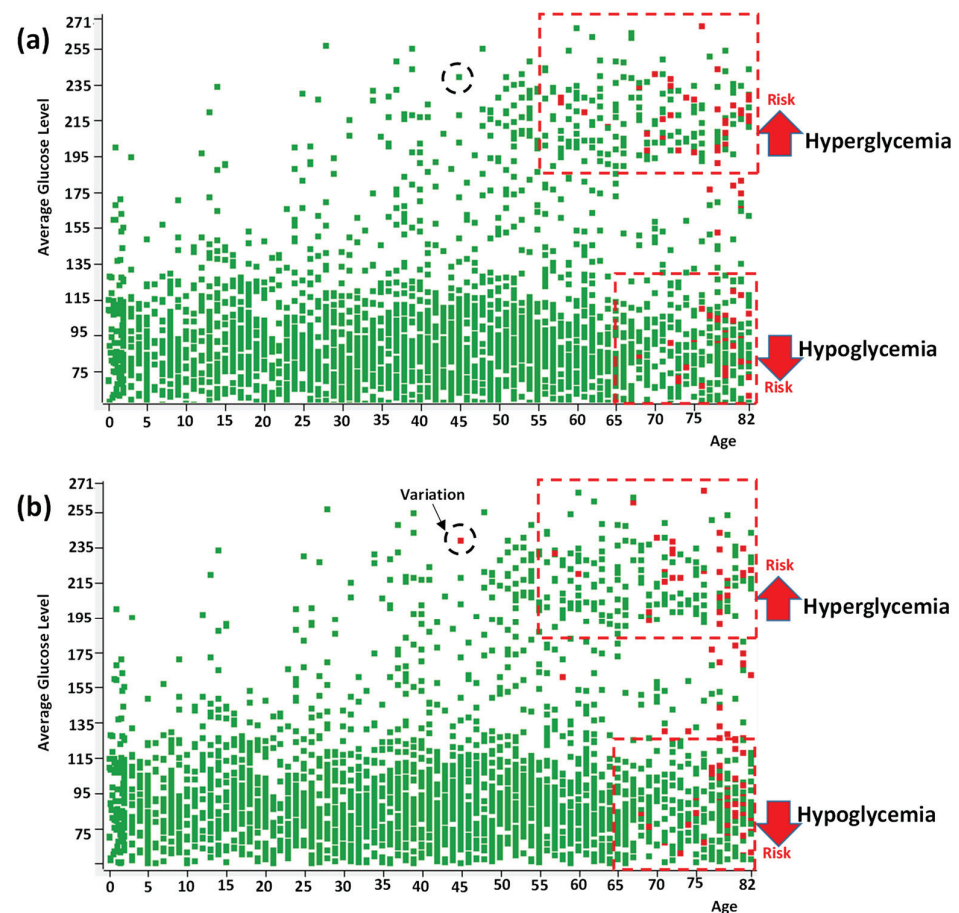
Figure 8. RF (**a**,**b**) GBT risk cases matching the variables of average glucose level and patient's age. An example of result variation is indicated by the black dashed circle.

In Figure 9a,b, the RF and the GBT stroke risks are shown, matching patient age and patient work type, respectively. Also, in this case, both algorithms provide similar results by highlighting that private companies employees or managers are characterized by a high stroke risk. This result enhances the impact of the work about the stroke risk and could enable the formulation of new welfare policies in private work environments; according to the results, possible interventions could be applied regarding the optimization of working conditions, improving the quality of life, and consequently decreasing the health risk.
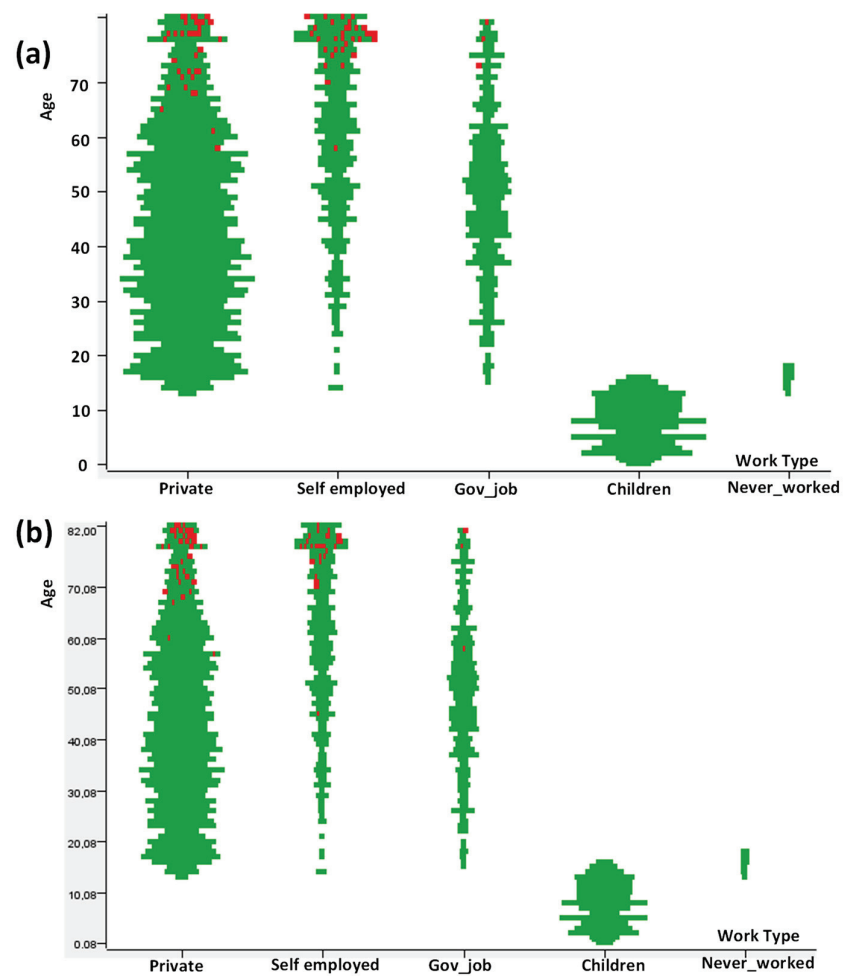
Figure 9. RF (**a**,**b**) GBT risk cases matching the variables of patient age and work type.

As expected in the literature, stroke risk happens when heart disease and hypertension cases are checked [16,17]. The results of Figures 10 and 11 confirm these scientific expectations.

Figure 10. RF stroke risk matching variables of patient age and past verified heart disease conditions.
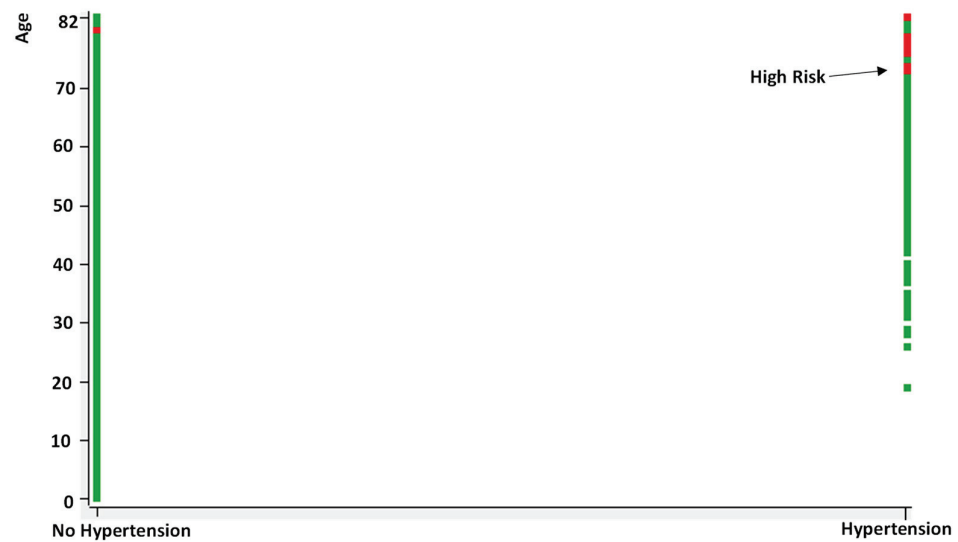
Figure 11. RF stroke risk matching variables of patient age and past verified hypertension conditions.

In addition, social conditions could also have an impact on the risk. Figure 12 demonstrates that no married patients are characterized by a possible stroke risk; this can be explained by the fact that that unmarried workers overwork themselves (work hard) and are therefore subject to a greater risk of stroke.
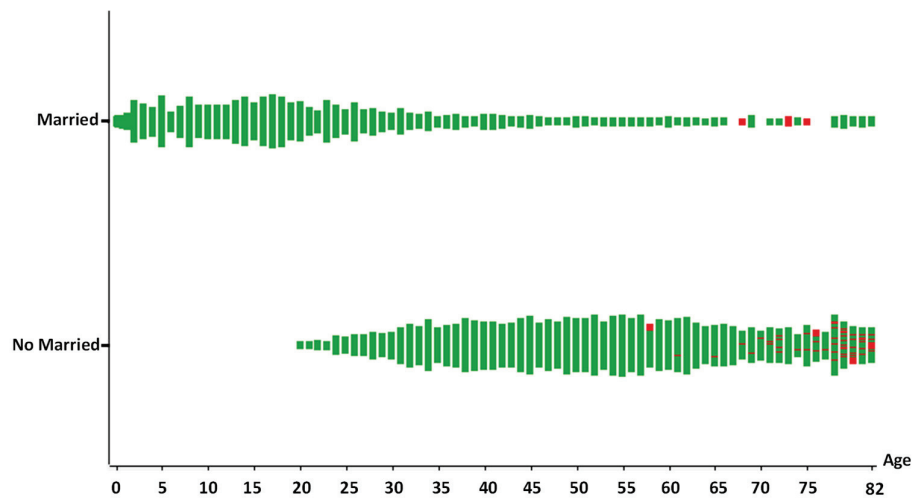
Figure 12. RF stroke risk, matching variables of marriage status and patient age.

4. Discussion: The Telemedicine Framework

The BPMN workflow of Figure 5 is a basic process involving only the patient and the general practitioner actors. More actors could be involved by further optimizing the whole prevention process. The ML results discussed in Section 3 are to be used for the decision of patients to enroll, for the assignment of the medical kit, and for the decisions of the general practitioner upon reading the alerting conditions (corresponding to the 'Exclusive Event-Based' symbols of Figure 5). For example, concerning the diabetes risk, an important parameter to predict with ML is glycemic values. In Table 2, a list of further actors is presented which could collaborate to prevent chronic cases or dangerous health status conditions. In Appendix A, we detail the whole ecosystem involving actors, companies, and research units, improving the telemedicine system and describing the interconnections (action fluxes) between the actions required to perform a preventive PDTA. The realization of a telemedicine platform suitable for chronic prevention requires investment in technology having a high Key Performance Indicator (KPI) of technology readiness (see Appendix B).

The technology readiness KPI indicates the company's capabilities in terms of technology development and organization management.

Table 2. Possible further actors for improving prevention actions and related organizational aspects.

Possible Further Actor to Involve in the Prevention Process	Role	New Organizational Aspects
Pharmacist	Support for patient enrollment in monitoring activities	Coordination with the general practitioner to select the patient to control (the monitoring kit is available in pharmacy)
Dietician	Especially for diabetic risk, a dietician could be important to prevent chronic risk (as for obesity cases [26])	Dietician is involved when it is difficult to control diet and a nutritional balance. Useful solutions for children could be enabled through mobile apps and gaming [27] (organizational aspects are addressed mainly on the management of the mobile app data)
Psychologist	If eating disorders are serious, the help of a psychologist may be required	The psychologist should collaborate with the dietician. The psychological care process should be synchronized with the prevention process, including dietician interactions
Cardiologist	Mainly for stroke cases, the reading of alerting conditions could require the intervention of a cardiologist to provide a second opinion	The prevention process should be synchronized with the cardiologist monitoring process
Private Nurse	Private nurses are required for non-self-sufficient patients	The general practitioner could be relieved of the workload through the work of the nurse
Educational Trainer	Educational trainers to facilitate technology transfer	Organizational aspects are mainly in the planning of the training courses about the use of digital technologies
Public Teachers (schools and universities)	Educational interventions about correct diet and lifestyles in schools and universities could have important effects on risk prevention	Organizational aspects are mainly in the planning of the training courses about lifestyles and nutrition
Politicians (welfare policies)	Important interventions in the social environment require political laws supporting a sustainable prevention platform	Politicians should have a list of available actors or health structures to hypothesize possible collaborative frameworks

The advantages of the use of a telemedicine platform can be estimated by KPIs. For example, in Table 3, we list and comment on some qualitative and quantitative KPIs associated with a telediabetology platform.

Table 3. Possible qualitative and quantitative KPI in telediabetology.

KPI	Description
Qualitative KPI	• Level of functioning of the new PDTA processes of diabetics with the use of the telediabetology platform; • Decrease in cases of hypo- and hyperglycemia (for monitored patients); • Amount of data recorded in the backend system (useful for georeferenced monitoring of diabetics); • Socio-economic impact deriving from the implemented system; • Level of satisfaction of actors (general practitioners, pharmacists, clinical staff, patients, etc.);
Quantitative KPI	• Number of enrolled patients; • Number of hospitalizations and percentage of incidence of monitored diabetic patients; • Number of comorbidities (percentage annual incidence of monitored patients); • Number of electronic health records connected to the project platform and used to predict chronicity; • Number of PDTA processes implemented with integration of the telediabetology facilities; • Risk stratification of hyper- and hypoglycemia; • Percentage reduction in episodes of hypo- and hyperglycemia classified as high risk; • Level of reliability of ML predictive and classification algorithms (evaluation of some parameters such as accuracy, recall, Mean Squared Error—MSE, Root Mean Squared Error—RMSE, ROC curve, etc.); • Scoring of TO BE process monitoring sheets; • Quality of Life (QoL) of monitored diabetic patients.

Table 4 indicates limitations and perspectives of telemedicine technology. The listed limits are common for all telemedicine platforms.

Table 4. Limitations and perspectives of telemedicine technologies.

Technological Limits	Technology Description	Technological Perspectives
Limited availability in the market of certified medical kits (standard CE: 93/42/CEE, 2017/745/UE, class 2a) for diabetes and stroke diagnoses	A certified medical kit groups different sensors in terms of function of the pathology to control. For example, the kit for diabetes includes the following certified devices: • glucometer; • profile analyzer lipid; • balance; • blood pressure meter; • glycated hemoglobin meter; • saliva tester for nutrigenic test. The kit for stroke monitoring includes the following certified sensors: • heart rate sensor; • inertial motion sensor; • pulse oximeter.	The certified devices will require a protocol validating the detected measurements (control room activity)
Digital solution integrated in PDTA	• The integration of digital solutions (electronic health records, sensor data, telemedicine platform databases, etc.) requires data flow integration into a digital PDTA; • the policies of privacy could block data integration in the backend system; • the Software Development Kit (SDK) [28] is necessary to integrate and manipulate data detected by medical sensors.	Future prevention PDTA could include ML decision-making engine and big data analytics tools [29]
Dataset availability	Supervised ML algorithms require a large amount of digital data and clean dataset to optimize the training model	Big data, data fusion techniques, and augmented data are to be considered to improve ML performance

In Appendix B, we discuss an example of the KPI technology readiness model structured by the Ishikawa diagram, typically adopted to model organizational aspects in healthcare [30,31] and production management processes [32]. For the stroke telemonitoring platform, different KPIs should be considered, including neurological assessment, nutritional assessment, hyperthermia management, lipid management [33], stroke education, and screening actions [34]. Another approach useful for mapping processes is the Unified Modeling Language (UML) [35,36], used in Appendix A, where we detail a complete framework of a telemedicine platform. In Appendix C, we list some PMO aspects associated with actors listed in Table 2, and possible advantages and disadvantages following the corrective actions.

The limitations about the adoption of the new PDTA based on ML data processing are mainly in the availability of enough clinical data to learn an ML model, and in the execution of new organizational models capable of ensuring the correct functioning of the PDTA. In this direction, future developments are in the design of new structured process workflows able to efficiently manage new human resources having new roles.

The results proposed in this paper regarding stroke analysis highlight that there are many aspects to consider for risk assessment decision processes in order to prevent dangerous cases. For example, the risk could be reduced over time, improving the social quality of life or optimizing the work conditions, as well as suggesting the inclusion of corrective actions or lifestyles, including the choice of a specific diet. The limitations mainly involve the deployment of an organizational model suitable for directing patients to the correct health path. The organizational model implies new human resources and a synergic

collaboration between them by executing efficient processes. The future direction of the research is to integrate as much as possible into the PDTA the automatisms of AI decision making and the synergies between all the actors that serve to implement risk prevention.

Other alternative ML algorithms adopted in the literature for stroke classification or prediction are Artificial Neural Networks (ANNs) and Support Vector Machine (SVM) [37–40]. In Table 5, we compare the performance of the ANN and SVM methods found in the literature with the FR and GBT algorithms applied in this work; the ANN and the SVM algorithms exhibit a performance lower or slightly lower than that of the FR and GBT algorithms.

Table 5. ML comparison of the accuracy and AUC parameters.

ML Algorithm	Accuracy	AUC
RF (this work)	0.974	0.969
GBT (this work)	0.968	0.942
ANN ([37])	0.91	0.90
ANN ([38])	0.97	0.6587
ANN ([39])	0.875	0.914
ANN ([40])	0.902	No data
SVM ([37])	0.84	0.93
SVM ([38])	0.90	0.5622

Future works will apply the experimentation of the proposed PDTA of Figure 5 and of the use of medical kits, which will be assigned to the hospitalization units characterized by many confirmed cases, as for the Italian district units represented in Figure 13 and Table 6 (Unit 1, Unit 6, and Unit 7).
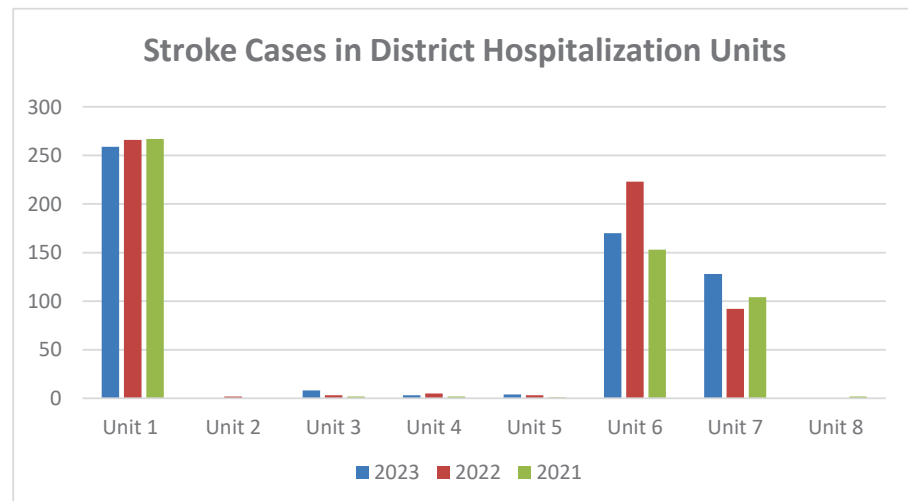
Figure 13. Confirmed stroke cases of different hospitalization units appertaining to a local healthcare district.

Table 6. Stroke cases of hospitalization units of a local regional healthcare district.

Hospitalization Unit	Year 2021	Year 2022	Year 2023
Unit 1	267	266	259
Unit 2	0	2	0
Unit 3	2	3	8
Unit 4	2	5	3
Unit 5	1	3	4
Unit 6	153	223	170
Unit 7	104	92	128
Unit 8	2	9	0

The proposed framework will be able to integrate decision-making procedures suggested by research topics, such as the use of efficient dietary components [41], sentiment analysis [42] matching with the psychological profile of the patient, the metabolism balancing approach [43], the improvement of psychological processes of consumer purchase decision making [44], and the detailed analyses of etiological aspects [45].

5. Conclusions

The proposed paper introduces a methodology to apply ML in order to improve a telemedicine prevention platform for diabetes and stroke, and discusses the related organizational models. Specifically, alerting conditions could be predicted by means of data processing of supervised and unsupervised algorithms to enable a preventive control process of patients, thus avoiding the risk of injuries or becoming chronic cases. The study is focused on the design of a prevention PDTA based on telemedicine platforms adopting a PMO approach. The ML algorithms are applied using an open dataset with the goal of explaining the data processing methodology and how it could interact with the decisions to be made. Important aspects about organization management and technology development are highlighted. The study has been developed within the framework of projects in collaboration with hospitals and companies working in telemedicine. The presented approach is suitable for the design of different prevention healthcare platforms for other chronic risks or comorbidities, allowing the processing of new digital data useful for medical and clinical advances. Furthermore, the discussed methodology allows the researchers to write telemedicine research projects based on ML data processing. The paper is mainly addressed to provide a new PMO methodology to consider PDTA based on prevention processes and optimized by telemedicine tools and ML. Actually, there is an active collaboration with local hospitalization units to collect data about stroke cases in order to define an operative plan financed by projects, including the software and hardware of telemedicine platforms. Today, few data related to the more significant aspects of the post-COVID 19 situation have been collected. Future works will process local clinical datasets to validate the proposed PDTA prevention process, which may be subject to possible further revisions.

Appendix A

A further graphical approach to designing telemedicine processes is based on the standard Unified Modelling Language (UML). In Figure A1, we illustrate the UML Use Case Diagram (UCD) involving different actors and related activities. The telemedicine ecosystem is composed of the following main actors:

- Patients;
- Specialists;
- General Practitioners;
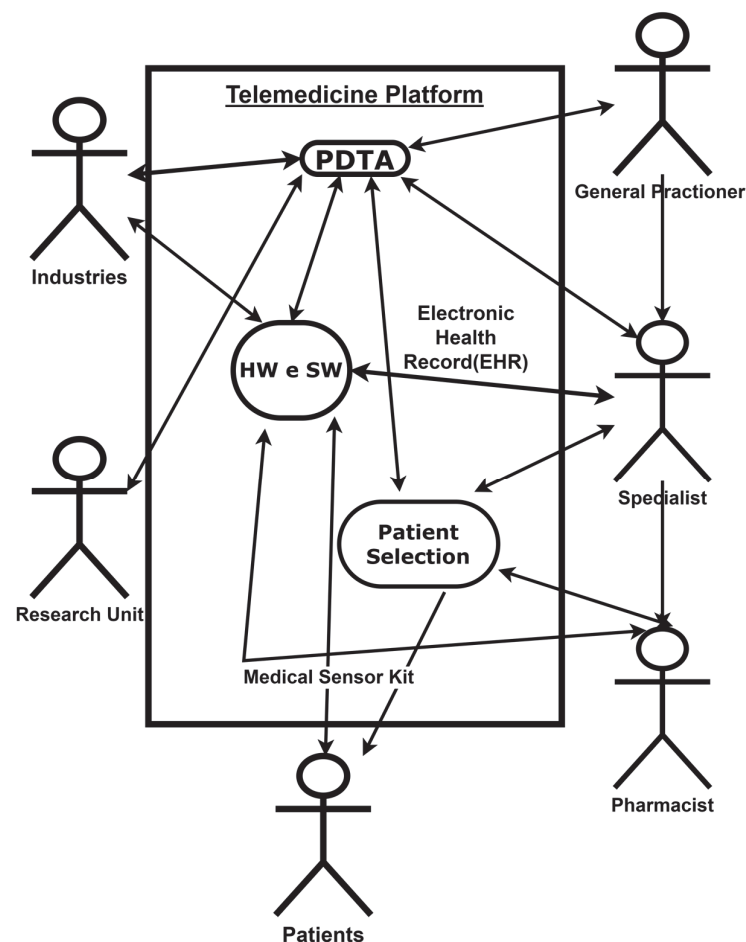- Industries developing telemedicine tools;
- Pharmacists;
- Research units.

Figure A1. UML UCD of a telemedicine ecosystem for the prevention of chronic disease.

Appendix B

The Ishikawa diagram turns out to be the most effective and efficient tool for problem solving. According to a study, 95% of problems in processes can be solved by using the Ishikawa "Quality Control" (QC) tool, exploring their validity in the healthcare sector.

The Ishikawa diagram of Figure A2 illustrates a methodology to formulate the KPI of technology readiness for a company oriented towards the development of telemedicine tools.

The diagram is structured into the following two main groups of variables:

- Upper part (variables of technological aspects): The orange color indicates the readiness aspects for the development of hardware, software, and the whole embedded telemedicine system.

- Lower part (variables correlated with management and organizational aspects): The green color represents the ability to manage the project developments, the suppliers, the licenses, and the patients.

The diagram of Figure A2 is representative of the hi-tech industrial and social ecosystem of the telemedicine platforms.
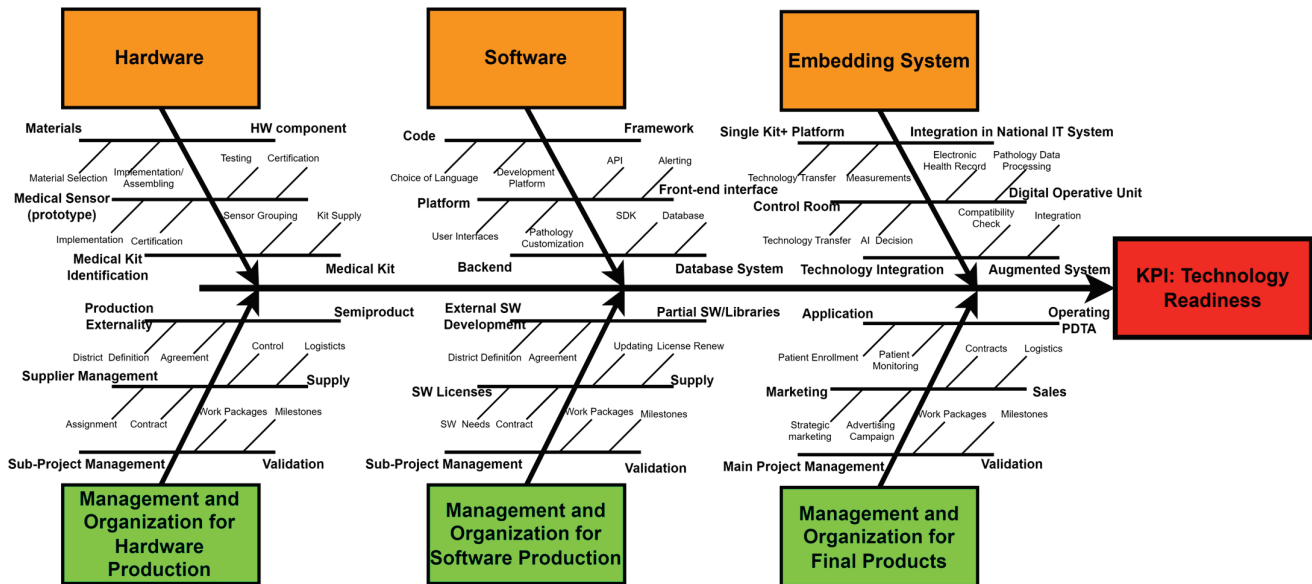

Figure A2. Ishikawa diagram defining the KPI of technology readiness (orange color: technological aspects; green color: organizational and management aspects).

Appendix C

In Table A1, we list some PMO aspects correlated to the management of the medical staff, including the management of the activities of actors listed in Table 2. The table enhances solutions of human resource (HR) interventions in telemedicine, improving the prevention process by specifying possible negative impacts and action guidelines.

Table A1. Framework and action guidelines to optimize the prevention process using a telemedicine platform.

HR Intervention Typology	Goal	Possible Correlated Negative Impact	Action Guidelines
Training of the health HR staff	Decrease in the health risk about chronic pathologies and of irreversible cases (mainly for stroke cases)	In cases of limited staff, the training could generate inefficiencies for PDTA processes, as for the process of Figure 1	Reskilling and upskilling of HR about new technologies enabling telemedicine
Further actor allocation and displacement	• Improvement of prevention processes allocating new actors; • HR allocation according to priorities (patients with high risk); • decrease in the visit delay due to the real-time monitoring of patients.	Imbalances of working times between traditional PDTA and new prevention processes	HR management synchronizing prevention processes and tracing patients which become chronic
HR recruitment	Recruitment of new medical staff skilled in telemedicine (biomedical engineers, specialists, etc.)	Increase in costs due to the engagement of new HR	Recruitment is executed according to the HR necessary to realize an operating prevention platform

Table A1. *Cont.*

HR Intervention Typology	Goal	Possible Correlated Negative Impact	Action Guidelines
Definition of new roles in prevention processes	Formulation of new protocols by designating new staff roles	Possible confusion in the initial organization and HR management due to the interventions of the new actors. This stage requires a patient enrollment phase which could take a long time	Formulation of the new procedures to be performed by the new actors (possibly using BPMN workflows)
HR for control room of telemedicine platforms	Designation of a part of the medical staff to control patients remotely at home (homecare assistance)	Convince patients to use wearable sensors	Guidelines about data privacy and information procedures of patients to be monitored by a telemedicine platform

In Table A2, we describe possible corrective actions to optimize a telemedicine framework by showing related advantages and disadvantages following the corrective actions.

Table A2. Main advantages and disadvantages of the PMO related to the telemedicine framework.

HR Corrective Action	Advantages	Disadvantages
Training on the use of medical kits	• Decrease in the chronic risk; • decrease in injuries (strokes and heart disease).	The training requires a specific plan: different training courses should cover all the HR skills. The training is also to apply for reskill and upskill operations about technology transfer in telemedicine (more complex planning)
Increase in the medical staff or HR allocation/displacement	• Formulation of new prevention care protocols to be integrated into more efficient PDTA; • creation of new operation units for prevention based on telemedicine platforms.	Increase in the HR management impact due to new organization, with a part of the staff operating in the prevention process and in the new integrated PDTA
Monitoring of the prevention risk (control room action)	The patient traceability allows for the estimation of the prevention efficacy	Possible confusions in the reconstruction of the care pattern of the monitored patients

References

1. Massaro, A. Advanced Control Systems in Industry 5.0 Enabling Process Mining. *Sensors* **2022**, *22*, 8677. [CrossRef] [PubMed]
2. Massaro, A. Process Mining in Production Management, Intelligent Control, and Advanced KPI for Dynamic Process Optimization: Industry 5.0 Production Processes. In *Advances in Systems Analysis, Software Engineering, and High Performance Computing*; IGI Global: Hershey, PA, USA, 2023; pp. 1–17.
3. Martin, N.; Wittig, N.; Munoz-Gama, J. Using Process Mining in Healthcare. In *Lecture Notes in Business Information Processing*; Springer International Publishing: Cham, Switzerland, 2022; pp. 416–444.
4. Munoz-Gama, J.; Martin, N.; Fernandez-Llatas, C.; Johnson, O.A.; Sepúlveda, M.; Helm, E.; Galvez-Yanjari, V.; Rojas, E.; Martinez-Millana, A.; Aloini, D.; et al. Process Mining for Healthcare: Characteristics and Challenges. *J. Biomed. Inform.* **2022**, *127*, 103994. [CrossRef] [PubMed]
5. Zerbino, P.; Stefanini, A.; Aloini, D. Process Science in Action: A Literature Review on Process Mining in Business Management. *Technol. Forecast. Soc. Chang.* **2021**, *172*, 121021. [CrossRef]
6. Rosa, A.; Massaro, A. Process Mining Organization (PMO) Modeling and Healthcare Processes. *Knowledge* **2023**, *3*, 662–678. [CrossRef]
7. Rosa, A.; Massaro, A.; McDermott, O. Process Mining Applied to Lean Management Model Improving Decision Making in Healthcare Organizations. In Proceedings of the 18th International Forum on Knowledge Asset Dynamics, Matera, Italy, 7–9 June 2023; pp. 222–231, ISBN 978-88-96687-16-1. Available online: https://aran.library.nuigalway.ie/handle/10379/17801 (accessed on 11 December 2023).
8. Pufahl, L.; Zerbato, F.; Weber, B.; Weber, I. BPMN in Healthcare: Challenges and Best Practices. *Inf. Syst.* **2022**, *107*, 102013. [CrossRef]

9. *ISO/IEC 19150:2013*; Information Technology—Object Management Group Business Process Model and Notation. ISO: London, UK, 2013. Available online: https://www.iso.org/standard/62652.html (accessed on 11 December 2023).
10. Object Management Group Business Process Model and Notation. Available online: https://www.bpmn.org/ (accessed on 11 December 2023).
11. PDTA Diabete. Available online: https://www.salute.gov.it/portale/lea/documenti/pdta/Risultati_2017_PDTA_Diabete.pdf (accessed on 11 December 2023).
12. Epicentro. I Dati PASSI sul Diabete. Available online: https://www.regione.puglia.it/web/ufficio-statistico/-/epicentro.-i-dati-passi-sul-diabete (accessed on 11 December 2023).
13. Il Costo della Malattia Diabetica. Available online: https://www.sanita24.ilsole24ore.com/art/focus-diabete/2018-06-27/il-costo-malattia-diabetica-105318.php?uuid=AE02hEDF (accessed on 11 December 2023).
14. Smith, L.; Chakraborty, D.; Bhattacharya, P.; Sarmah, D.; Koch, S.; Dave, K.R. Exposure to Hypoglycemia and Risk of Stroke. *Ann. N. Y. Acad. Sci.* **2018**, *1431*, 25–34. [CrossRef] [PubMed]
15. Jingqi Yan, Z.Z. Hyperglycemia as a Risk Factor of Ischemic Stroke. *J. Drug Metab. Toxicol.* **2013**, *4*, 4. [CrossRef]
16. Wajngarten, M.; Silva, G.S. Hypertension and Stroke: Update on Treatment. *Eur. Cardiol.* **2019**, *14*, 111–115. [CrossRef]
17. Tsao, C.W.; Aday, A.W.; Almarzooq, Z.I.; Alonso, A.; Beaton, A.Z.; Bittencourt, M.S.; Boehme, A.K.; Buxton, A.E.; Carson, A.P.; Commodore-Mensah, Y.; et al. Heart Disease and Stroke Statistics—2022 Update: A Report from the American Heart Association. *Circulation* **2022**, *145*, e153–e639. [CrossRef]
18. Stroke Prediction Dataset. Available online: https://www.kaggle.com/datasets/fedesoriano/stroke-prediction-dataset (accessed on 11 December 2023).
19. Fan, Z.; Yuan, C.; Xin, L.; Wang, X.; Jiang, J.; Wang, Q. HSRF: Community Detection Based on Heterogeneous Attributes and Semi-Supervised Random Forest. In Proceedings of the 2021 IEEE 24th International Conference on Computer Supported Cooperative Work in Design (CSCWD), Dalian, China, 5–7 May 2021; pp. 1141–1147. [CrossRef]
20. Yao, D.; Zhang, T.; Zhan, X.; Zhang, S.; Zhan, X.; Zhang, C. Geometric Complement Heterogeneous Information and Random Forest for Predicting lncRNA-Disease Associations. *Front. Genet.* **2022**, *13*, 995532. [CrossRef]
21. Luetto, S.; Garuti, F.; Sangineto, E.; Forni, L.; Cucchiara, R. One Transformer for All Time Series: Representing and Training with Time-Dependent Heterogeneous Tabular Data. 2023. Available online: https://www.arxiv-vanity.com/papers/2302.06375/ (accessed on 11 December 2023).
22. Khan, N.U.; Wan, W.; Riaz, R.; Jiang, S.; Wang, X. Prediction and Classification of User Activities Using Machine Learning Models from Location-Based Social Network Data. *Appl. Sci.* **2023**, *13*, 3517. [CrossRef]
23. Friedman, J.H. Greedy Function Approximation: A Gradient Boosting Machine. *Ann. Stat.* **2001**, *29*, 1189–1232. [CrossRef]
24. Hashemi, S.E.; Gholian-Jouybari, F.; Hajiaghaei-Keshteli, M. A Fuzzy C-Means Algorithm for Optimizing Data Clustering. *Expert Syst. Appl.* **2023**, *227*, 120377. [CrossRef]
25. KNIME. Available online: https://www.knime.com/ (accessed on 11 December 2023).
26. Siopis, G.; Colagiuri, S.; Allman-Farinelli, M. Effectiveness of Dietetic Intervention for People with Type 2 Diabetes: A Meta-Analysis. *Clin. Nutr.* **2021**, *40*, 3114–3122. [CrossRef] [PubMed]
27. Álvarez, R.; Torres, J.; Artola, G.; Epelde, G.; Arranz, S.; Marrugat, G. OBINTER: A Holistic Approach to Catalyse the Self-Management of Chronic Obesity. *Sensors* **2020**, *20*, 5060. [CrossRef] [PubMed]
28. Henriksen, A.; Haugen Mikalsen, M.; Woldaregay, A.Z.; Muzny, M.; Hartvigsen, G.; Hopstock, L.A.; Grimsgaard, S. Using Fitness Trackers and Smartwatches to Measure Physical Activity in Research: Analysis of Consumer Wrist-Worn Wearables. *J. Med. Internet Res.* **2018**, *20*, e110. [CrossRef] [PubMed]
29. Massaro, A.; Ricci, G.; Selicato, S.; Raminelli, S.; Galiano, A. Decisional Support System with Artificial Intelligence oriented on Health Prediction using a Wearable Device and Big Data. In Proceedings of the 2020 IEEE International Workshop on Metrology for Industry 4.0 & IoT, Roma, Italy, 3–5 June 2020; pp. 718–723. [CrossRef]
30. Chang, H. Evaluation Framework for Telemedicine Using the Logical Framework Approach and a Fishbone Diagram. *Healthc. Inform. Res.* **2015**, *21*, 230. [CrossRef] [PubMed]
31. McDermott, O.; Antony, J.; Sony, M.; Rosa, A.; Hickey, M.; Grant, T.A. A study on Ishikawa's original basic tools of quality control in healthcare. *TQM J.* **2023**, *35*, 1686–1705. [CrossRef]
32. Botezatu, C.; Condrea, I.; Oroian, B.; Hrițuc, A.; Ețcu, M.; Slătineanu, L. Use of the Ishikawa Diagram in the Investigation of Some Industrial Processes. *IOP Conf. Ser. Mater. Sci. Eng.* **2019**, *682*, 012012. [CrossRef]
33. Urimubenshi, G.; Langhorne, P.; Cadilhac, D.A.; Kagwiza, J.N.; Wu, O. Association between Patient Outcomes and Key Performance Indicators of Stroke Care Quality: A Systematic Review and Meta-Analysis. *Eur. Stroke J.* **2017**, *2*, 287–307. [CrossRef]
34. Mohammed, M.; Zainal, H.; Tangiisuran, B.; Harun, S.N.; Ghadzi, S.M.; Looi, I.; Sidek, N.N.; Yee, K.L.; Aziz, Z.A. Impact of Adherence to Key Performance Indicators on Mortality among Patients Managed for Ischemic Stroke. *Pharm. Pract.* **2020**, *18*, 1760. [CrossRef]
35. *ISO/IEC 19505-1/2:2012*; Information Technology—Object Management Group Unified Modeling Language (OMG UML). ISO: London, UK, 2012. Available online: https://www.iso.org/obp/ui/#iso:std:iso-iec:19505:-2:ed-1:v1:en (accessed on 31 December 2023).
36. Suriya, S.; Nivetha, S. Design of UML Diagrams for WEBMED—Healthcare Service System Services. *ICST Trans. e-Educ. e-Learn.* **2023**, *8*, e5. [CrossRef]

37. Sohn, J.; Jung, I.-Y.; Ku, Y.; Kim, Y. Machine-Learning-Based Rehabilitation Prognosis Prediction in Patients with Ischemic Stroke Using Brainstem Auditory Evoked Potential. *Diagnostics* **2021**, *11*, 673. [CrossRef] [PubMed]
38. Srinivasu, P.N.; Sirisha, U.; Sandeep, K.; Praveen, S.P.; Maguluri, L.P.; Bikku, T. An Interpretable Approach with Explainable AI for Heart Stroke Prediction. *Diagnostics* **2024**, *14*, 128. [CrossRef] [PubMed]
39. Iosa, M.; Paolucci, S.; Antonucci, G.; Ciancarelli, I.; Morone, G. Application of an Artificial Neural Network to Identify the Factors Influencing Neurorehabilitation Outcomes of Patients with Ischemic Stroke Treated with Thrombolysis. *Biomolecules* **2023**, *13*, 334. [CrossRef] [PubMed]
40. Usama, N.; Niazi, I.K.; Dremstrup, K.; Jochumsen, M. Detection of Error-Related Potentials in Stroke Patients from EEG Using an Artificial Neural Network. *Sensors* **2021**, *21*, 6274. [CrossRef] [PubMed]
41. Hill, C.R.; Shafaei, A.; Balmer, L.; Lewis, J.R.; Hodgson, J.M.; Millar, A.H.; Blekkenhorst, L.C. Sulfur Compounds: From Plants to Humans and Their Role in Chronic Disease Prevention. *Crit. Rev. Food Sci. Nutr.* **2023**, *63*, 8616–8638. [CrossRef] [PubMed]
42. Cai, Y.; Ke, W.; Cui, E.; Yu, F. A Deep Recommendation Model of Cross-Grained Sentiments of User Reviews and Ratings. *Inf. Process. Manag.* **2022**, *59*, 102842. [CrossRef]
43. He, W.-J.; Lv, C.-H.; Chen, Z.; Shi, M.; Zeng, C.-X.; Hou, D.-X.; Qin, S. The Regulatory Effect of Phytochemicals on Chronic Diseases by Targeting Nrf2-ARE Signaling Pathway. *Antioxidants* **2023**, *12*, 236. [CrossRef]
44. Zhu, P.; Miao, C.; Wang, Z.; Li, X. Informational Cascade, Regulatory Focus and Purchase Intention in Online Flash Shopping. *Electron. Commer. Res. Appl.* **2023**, *62*, 101343. [CrossRef]
45. Darnton-Hill, I.; Nishida, C.; James, W.P.T. A Life Course Approach to Diet, Nutrition and the Prevention of Chronic Diseases. *Public Health Nutr.* **2004**, *7*, 101–121. [CrossRef]

Optimum Path Planning Using Dragonfly-Fuzzy Hybrid Controller for Autonomous Vehicle

Brijesh Patel [1,2,*], Varsha Dubey [3], Snehlata Barde [3] and Nidhi Sharma [4]

[1] School of Engineering and Information Technology, MATS University, Raipur 492001, CG, India
[2] Department of Mechanical Engineering, National Taiwan University of Science and Technology, Taipei 106335, Taiwan
[3] School of Information Technology, MATS University, Raipur 492001, CG, India; sharmavarsha20@gmail.com (V.D.); v.snehabarde@gmail.com (S.B.)
[4] Department of Mathematics, Government Co.Ed. Polytechnic, Raipur 492001, CG, India; nsharma630@gmail.com
* Correspondence: aero.brijesh@gmail.com; Tel.: +91-9926119575

Abstract: Navigation poses a significant challenge for autonomous vehicles, prompting the exploration of various bio-inspired artificial intelligence techniques to address issues related to path generation, obstacle avoidance, and optimal path planning. Numerous studies have delved into bio-inspired approaches to navigate and overcome obstacles. In this paper, we introduce the dragonfly algorithm (DA), a novel bio-inspired meta-heuristic optimization technique to autonomously set goals, detect obstacles, and minimize human intervention. To enhance efficacy in unstructured environments, we propose and analyze the dragonfly–fuzzy hybrid algorithm, leveraging the strengths of both approaches. This hybrid controller amalgamates diverse features from different methods into a unified framework, offering a multifaceted solution. Through a comparative analysis of simulation and experimental results under varied environmental conditions, the hybrid dragonfly–fuzzy controller demonstrates superior performance in terms of time and path optimization compared to individual algorithms and traditional controllers. This research aims to contribute to the advancement of autonomous vehicle navigation through the innovative integration of bio-inspired meta-heuristic optimization techniques.

Keywords: autonomous vehicle; path planning; hybrid controller; dragonfly algorithm; fuzzy logic

1. Introduction

The rapid evolution of the logistics industry has spurred the demand for intelligent autonomous vehicles to enhance efficiency and streamline processes [1]. The substitution of human labor in labor-intensive, repetitive, and hazardous tasks with autonomous vehicles has garnered significant attention and proven vital for optimizing operational efficiency and resource utilization in modern factories and warehouses [2]. An autonomous vehicle is characterized as an intelligent entity capable of perceiving its surroundings, collecting and analyzing pertinent information from sensors, and determining its current position. Additionally, such a vehicle can generate a viable path from its initial location to the target destination by employing decision control mechanisms to navigate along a planned trajectory [3]. Path-planning methods play a pivotal role in realizing the intelligence of autonomous vehicles and entail the determination of an optimal path from the starting point to the destination in intricate spatial environments. This involves considering the initial and target positions provided during vehicle operation [4]. Path-planning problems are categorized into static and dynamic environments and address challenges related to both static and dynamic obstacle avoidance [5,6].

Path-planning algorithms play a prevalent role in both outdoor and indoor navigation scenarios. Various navigation and motion-planning techniques, including classical

approaches, heuristic methods, and bioinspired algorithms, have been employed in the realm of autonomous vehicle technologies, specifically within the context of pathfinding algorithms. Classical path-planning methods such as A*, RRT, and PRM, characterized as traditional approaches, have been extensively utilized and studied to address path-planning challenges across diverse domains. These methods have demonstrated their efficacy in discovering viable paths within known environments and established themselves as foundational elements in the field of path-planning research over an extended period. A* [7] is a popular heuristic search algorithm that guarantees an optimal path in a discretized state space, making it efficient for small and structured environments. RRT [8,9] (rapidly-exploring random trees) is a sampling-based algorithm that efficiently explores high-dimensional spaces and has shown promise in handling complex and dynamic environments. PRM (probabilistic roadmap) [10] is another sampling-based technique that constructs a roadmap of the configuration space and enables quick path-planning by connecting waypoints. Although traditional methods have their merits, bioinspired algorithms offer distinct advantages that make them superior for certain path-planning scenarios. Bioinspired algorithms, inspired by natural systems, emulate collective behaviors to solve optimization problems. These algorithms possess several strengths that set them apart from traditional methods: robustness in complex environments, a balance of exploration–exploitation, handling of dynamic environments, scalability, and flexibility in parameter tuning. In dynamic environments where obstacles or target locations change over time, bioinspired algorithms can dynamically adapt their search strategies, making them more suitable for real-time applications. Additionally, their stochastic nature enables a good balance between exploration and exploitation, which allows them to escape local optima and find better global solutions in uncertain environments.

Bio-inspired algorithms, or biologically inspired algorithms, constitute a specialized category of stochastic and metaheuristic search algorithms within the realm of computational sciences. Recognized for their effectiveness in addressing distributed and multimodal optimization problems [11], these algorithms employ robust search procedures that facilitate diversity maintenance, steering clear of local optimal convergence and increasing the likelihood of achieving globally optimal solutions [12,13]. The concern over the lack of control in exploration noises is inherent in bio-inspired methods, which prompts strategies to incorporate exploratory behavior through noise injection into the action space or agent parameters and fosters more reliable exploration and a wider range of behaviors. Bio-inspired algorithms, which foster agent interactions and leverage feedback mechanisms for cooperative dynamics, find applications in various scientific and engineering domains such as data mining and neural networks. Specifically applied to path optimization for autonomous vehicles, a range of swarm intelligence algorithms, including ant colony optimization (ACO) [14], particle swarm optimization (PSO) [15], the firefly algorithm (FA) [16], the fruit fly algorithm (FFA) [17], the bat algorithm [18], grey wolf optimization [19], and the grasshopper optimization algorithm (GOA) [20], contribute collectively to addressing diverse navigational challenges encountered by autonomous vehicles.

However, the existing path-planning algorithms have certain limitations, especially when dealing with multi-objective optimization and navigating in unstructured environments. In real-world scenarios, it is essential to consider multiple elements simultaneously, such as travel distance, collision safety, and path flexibility, rather than focusing on just one component. Hybrid approaches that combine bioinspired algorithms with heuristic techniques, such as A* [21] and fuzzy logic [22], have shown promise in improving the efficiency of autonomous vehicles. For instance, the A*–fuzzy hybrid approach optimizes the shortest path while avoiding obstacles [23], and quarter orbits particle swarm optimization (QOPSO) ensures an optimal path free of collisions [24]. However, these hybrid approaches still face challenges, such as high power consumption and unsmooth paths, when considered independently.

Fuzzy logic control and inferencing systems have been applied in various path-planning methods, as demonstrated in prior research [25]. This soft-computing approach

allows for the utilization of knowledge represented in linguistic rules [26], which enables the incorporation of expert human knowledge and experience, particularly in obstacle avoidance scenarios [27]. Fuzzy logic is well suited for handling imprecise variables and uncertainties, making it capable of addressing unknown conditions and dynamically reacting to changing environments [28]. As a result, it serves as an ideal tool to tackle obstacle avoidance problems effectively. The dragonfly algorithm (DA) [29] has been extended to and applied in various optimization tasks. A binary version of the algorithm (BDA) was proposed for solving the 0–1 knapsack problem [30] and showcased strong convergence and stability. In the context of feature selection, modified versions of BDA were introduced that incorporated penalty functions [31] and other methods to enhance performance. The integration of time-varying transfer functions into BDA demonstrated its effectiveness in feature selection tasks, outperforming other algorithms on benchmark datasets [32]. Additionally, DA has been utilized for swarm mobile robots with obstacle avoidance and showed efficiency in rescue scenarios [33]. Chaotic dragonfly algorithm (CDA) variations incorporated chaos to accelerate convergence in feature selection tasks [34], and the adaptive dragonfly [35] algorithm (ADF) was presented as a self-adaptive approach for multilevel segmentation by achieving superior solutions compared to standard DA and other optimization techniques. These diverse variants and applications highlight the versatility and performance of DA in solving different optimization challenges.

The task of autonomous vehicle path planning holds significant importance, as it aims to determine the optimal trajectory under diverse circumstances. This involves generating real-time high-quality paths while considering factors such as path quality, efficiency, and computational resource consumption. Ji et al. [36] introduced an innovative method employing a 3-D virtual dangerous potential field to navigate potential collisions, relying on complex calculations of collision-free trajectories. Simultaneously, obstacle avoidance, which is crucial for vehicle safety, requires careful consideration of dynamic and static obstacles, vehicle-maneuvering capabilities, comfort, and handling stability. To address conflicts arising from various objectives, inventive control structures such as Fernando et al.'s MIMO method for autonomous vehicle path tracking address network-induced delays and incorporate roll dynamics to enhance safety and passenger comfort [37]. Path-tracking control is essential for guiding actuators along the planned route by utilizing various algorithms such as PID-based, feedforward and feedback, model predictive control (MPC), robust control, and optimal preview methods for automated ground vehicles [38]. The interaction between path-tracking control and vehicle dynamics control presents a central challenge. Hu et al. [39] and Chen et al. [40] introduced output constraint controllers and simultaneous path-following and lateral stability control methods, respectively. However, there remains a need for real-time simulation evaluations and practical experimentation to validate the efficacy of these approaches.

To address the challenges and improve path-planning efficiency for autonomous vehicles operating in static and dynamic environments, this study introduces a novel strategy termed the dragonfly–fuzzy hybrid approach. This method harnesses the collective intelligence of the dragonfly algorithm and the adaptability of fuzzy logic to identify the most direct collision-free path. The proposed dragonfly–fuzzy algorithm provides an innovative solution that takes into account both obstacle avoidance and the optimization of path length. Through the integration of bioinspired, traditional, and hybrid techniques, our approach aims to deliver a path-planning solution that is both efficient and effective. Comparative analysis against standalone algorithms illustrates the superior performance of the dragonfly–fuzzy hybrid strategy in terms of optimizing path length and computational time. This research represents a promising advancement in autonomous vehicle path planning, particularly in unstructured environments, contributing to ongoing efforts to enhance navigation and motion planning in the field of autonomous vehicles.

2. Path-Planning Algorithms

The key issue with moving an autonomous vehicle from one position to another is identifying the best or close to the best desired path by avoiding obstacles in order to reach the target with desirable accuracy. Hence, the most crucial function of any navigational technique is safe path planning along with obstacle avoidance from the initial place to the target position. As a result, when working in a simple or complex environment, the proper selection of the navigational strategy is the most critical phase in the planning of an autonomous vehicle's course. This study used fuzzy logic and the dragonfly algorithm for path planning and autonomous mobile robot obstacle detection.

2.1. Dragonfly Algorithm

In 2015, Seyedali Mirjalili introduced the dragonfly algorithm [29] as a solution to address multi-objective optimization challenges. The inspiration for the dragonfly algorithm (DA) was drawn from swarming behaviors related to static and dynamic scenarios, mirroring the exploration and exploitation phases inherent in metaheuristic optimization. Static swarming behavior, referred to as hunting, involves a small group of dragonflies swiftly adjusting their movements in search of food. On the other hand, dynamic swarming, known as migratory swarming, involves a large group of dragonflies covering extensive distances for migration. These swarming behaviors, in line with Reynolds' concepts from 1987, encompass separation, alignment, cohesion, attraction to food, and distraction from opponents. The dragonfly algorithm is designed to emulate these social interactions, incorporating two primary optimization phases: exploration and exploitation. Various versions of the algorithm, such as the binary dragonfly algorithm (BDA), multi-objective dragonfly algorithm (MODA), and single-objective dragonfly algorithm (SODA), cater to dynamic navigation, food hunting, and engaging enemies in a compiled manner.

The fundamental principles governing the dragonfly algorithm encompass five core rules: separation, alignment, cohesion, attraction, and distraction. The population size, denoted as M, serves as an indicator of the total number of individual dragonflies. The position of the ith dragonfly is defined as

$$P_i = (p_i^1, p_i^d, \ldots p_i^M) \tag{1}$$

In the given context of $i = 1, 2, 3, \ldots \ldots M$, p_i^d denotes the ith dragonfly's position within the dth dimension of the search space, and M corresponds to the total number of search agents. The symbol P_n signifies the position of the current individual fly.

1. The dragonfly algorithm's segregation principle pertains to the internal avoidance of collisions with other individuals within the algorithm's proximity. This concept is expressed mathematically in Equation (2).

$$S_{(i,t)} = \sum_{j=1}^{M} P_{(i,t)} - P_{(j,t)} \tag{2}$$

where separation $S_{(i,t)}$ represents the separation vector for the ith individual at the tth iteration, and $P_{(i,t)}$ is the position of the current individual "i" at the tth iteration, whereas $P_{(j,t)}$ is the position of the neighboring individual "j" at the tth iteration.

2. The concept of alignment ($A_{(i,t)}$) in the given context signifies the synchronization of velocities among neighboring individuals within the same group. This mathematical representation is given in Equation (3).

$$A_{(i,t)} = \frac{\sum_{j=1}^{M} V_{(j,t)}}{M} \tag{3}$$

In this context, $A_{(i,t)}$ as the term "alignment motion" denotes the motion of the current individual "i" at the tth iteration. Similarly, $V_{(j,t)}$ is the velocity of the neighboring individual "j" at the tth iteration.

3. Cohesion $(C_{(i,t)})$ in this context signifies the inclination of individuals to move towards the center of the mass within their neighborhood. This tendency is expressed mathematically, as illustrated in Equation (4).

$$C_{(i,t)} = \frac{\sum_{j=1}^{M} P_{(j,t)}}{M} - P_{(i,t)} \qquad (4)$$

In this scenario, $C_{(i,t)}$ is the term "cohesion motion", referring to the movement of the present individual "*i*" during the *t*th iteration.

4. Attraction $(F_{(i,t)})$ in this context signifies the food source, which is mathematically represented in Equation (5).

$$F_{(i,t)} = P_{(fd,t)} - P_{(i,t)} \qquad (5)$$

In the above scenario, the term $P_{(fd,t)}$ represents the food source at the *t*th iteration and $F_{(i,t)}$ represents the food attraction motion of the current individual "*i*".

5. Distraction $(E_{(i,t)})$ represents the distraction from the enemy as shown in the Equation (6).

$$E_{(i,t)} = P_{(enemy,t)} + P_{(i,t)} \qquad (6)$$

In this context, $P_{(enemy,t)}$ represents the enemy position at *t*th iteration. The distraction of the enemy is represented by $E_{(i,t)}$ for the current individual "*i*" at the *t*th iteration.

Regarding the dragonfly's position, its entities share similarities with the step vector update characteristic observed in the particle swarm optimization method [41]. In this context, the step vector $(\Delta P_{(i,t)})$ and the position vector $(P_{(i,t)})$ assume crucial roles in adapting the dragonflies' positions within the exploration domain, effectively directing their movements. The step vector delineates the direction of the dragonflies' motion, whereas the position vector defines the specific locations of individual dragonflies in the exploration space. The computation of the step vector follows the subsequent formula.

$$\Delta P_{(i,t+1)} = s \times S_{(i,t)} + a \times A_{(i,t)} + c \times C_{(i,t)} + f \times F_{(i,t)} + e \times E_{(i,t)} + w \Delta P_{(i,t)} \qquad (7)$$

In this context, the symbol *s* represents the current step vectors denoting separation, *a* indicates alignment, *c* represents cohesion, *f* signifies the influence of the food source, and *e* represents a distraction. Additionally, *w* is the inertia weight. Initially, each operator is assigned initial weights through a random process, and subsequently, these weights are dynamically adjusted to facilitate the convergence of dragonflies towards an optimal solution. Following the computation of the step vector, the position vector can be determined using the following procedure.

$$P_{(i,t+1)} = P_{(i,t)} + \Delta P_{(i,t)} \qquad (8)$$

In the above equation, *t* represents the current iteration, the next position is represented by $P_{(i,t+1)}$, and $P_{(i,t)}$ represents the current position.

As the optimization process advances, the dragonfly's neighborhood radius undergoes expansion. When the dragonfly has at least one neighboring entity, the procedures involving $(\Delta P_{(i,t+1)})$ and $(P_{(i,t+1)})$ come into play to update its velocity and position. Nevertheless, in instances where the dragonfly algorithm encounters situations without any neighbors, it resorts to a random movement strategy. During such occurrences, the Levy flight technique is applied to adjust both the position and the velocity of the dragonflies. The incorporation of the Levy flight technique introduces heightened levels of randomness and chaotic behavior, thereby augmenting the algorithm's global search capabilities. In this particular circumstance, the position undergoes an update using Levy flight, as outlined in Equation (9).

$$P_{(i,t+1)} = P_{(i,t)} + \text{Levy}(d) \times P_{(i,t)} \qquad (9)$$

In the above context, the number of decision variables is represented by "*d*", whereas the Levy flight function is denoted by "Levy(*d*)."

The main objective of using the dragonfly algorithm (DA) is to navigate an autonomous vehicle in an unstructured environment consisting of different obstacles. This objective is transformed into a minimization problem with two functions. The first is to avoid obstacles, and the second is to find the shortest possible path. Figure 1 depicts the environment of the autonomous vehicle's target and goal positions.
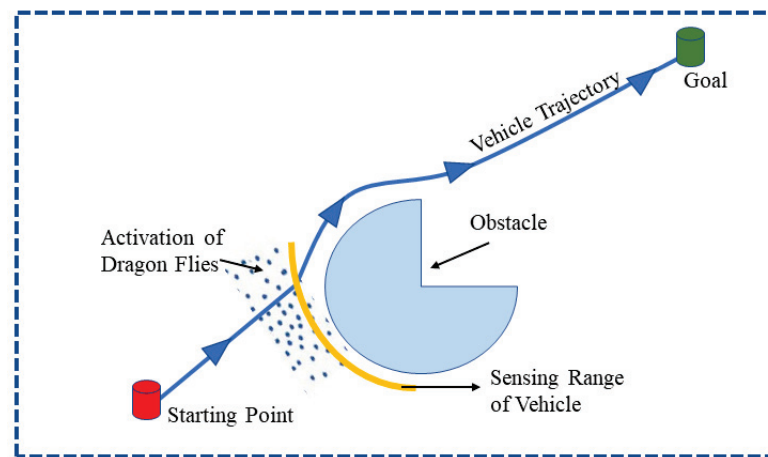
Figure 1. Autonomous vehicle positioning in the presence of an obstacle.

Figure 2 depicts the architecture of the proposed DA controller, and Algorithm 1 illustrates the pseudo-code for the DA to describe its execution.
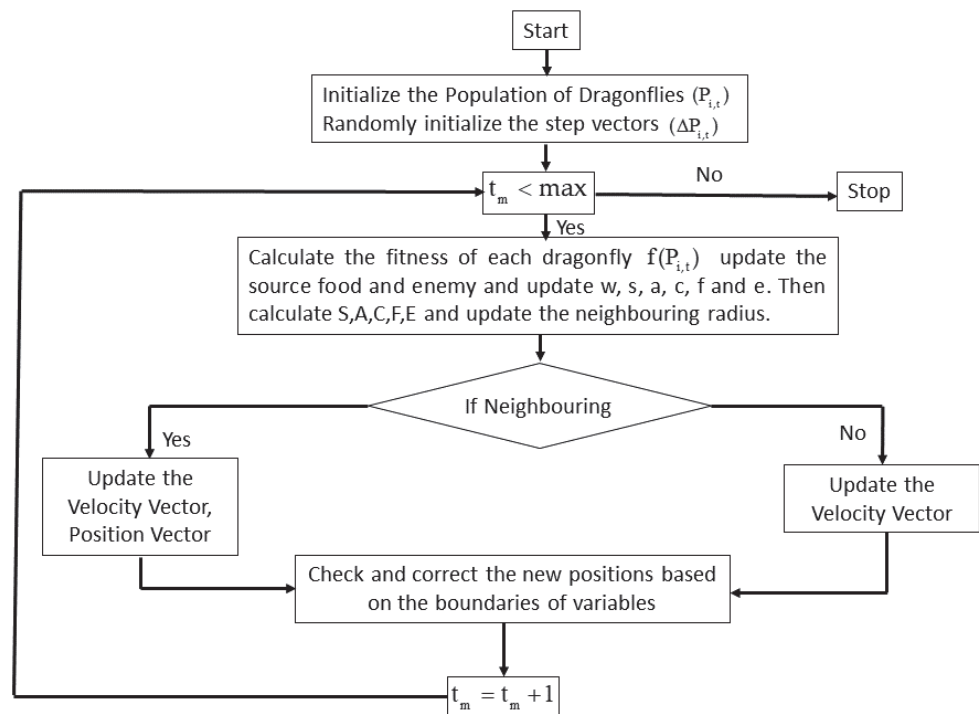
Figure 2. Dragonfly algorithm architecture.

The dragonfly algorithm is a metaheuristic approach that stands as an optimization technique inspired by the collective behavior of dragonflies. Its initiation involves the setup of a dragonfly population along with their corresponding step vectors. The algorithm iteratively computes the objective values of dragonflies while dynamically adjusting parameters

such as food source, enemy, separation, alignment, cohesion, attraction, and distraction. Adjustments to the neighborhood radius are applied, and if a dragonfly has at least one neighboring counterpart, updates are made to both the velocity vector and the position vector. To enhance adaptability, the algorithm integrates Levy flight for position adjustments and conducts boundary checks for corrections. Exhibiting efficiency and scalability, the dragonfly algorithm boasts a time complexity of O(N), where N denotes the number of iterations. The standard algorithm steps are outlined as follows.

Algorithm 1 Dragonfly Algorithm

```
# Dragonfly algorithm
# Complexity analysis: O(N), where N is the number of iterations
def dragonfly_algorithm():
    # Initialization
    population = initialize_population()
    step_vectors = initialize_step_vectors()
    # Iterative optimization loop
    while not end_condition_satisfied():
        # Objective value calculation
        calculate_objective_values(population)
        # Update food source and enemy
        update_food_source_and_enemy()
        # Update factors: separation, alignment, cohesion, food, and enemy
        update_factors()
        # Calculate and update vectors using equations
        calculate_and_update_vectors()
        # Update neighboring radius
        update_neighboring_radius()
        # Update position and velocity vectors based on neighbors
        for dragonfly in population:
            if dragonfly_has_neighboring_dragonflies(dragonfly):
                update_velocity_and_position(dragonfly):
            else:
                update_position_levy_flight(dragonfly)
            # Check and correct new positions based on variable boundaries
            check_and_correct_positions(dragonfly)
    # End of the algorithm
# Time complexity: O(N), where N is the number of iterations
```

2.2. Fuzzy Logic Concept

The inception of fuzzy logic methodologies was introduced by Lotfi Zadeh in 1965 [42]. This approach draws inspiration from human decision-making, encompassing nuanced responses beyond binary choices like yes or no. Fuzzy logic addresses multifaceted scenarios by employing if–else rules, which capture the essence of complex decision processes. It operates by processing imperfect and non-uniform data across various concerns. Unlike conventional linear logic, fuzzy logic adeptly handles intricate data challenges characterized by substantial uncertainty. The fundamental framework of fuzzy logic is depicted in Figure 3.

The fundamental elements of fuzzy logic encompass several crucial facets:

- Fuzzification: This involves employing membership functions to delineate input variables.
- Inference and aggregation: This factor determines the final output resulting from fuzzy rules, accomplished through a process of inference and aggregation.
- Defuzzification: The transformation of fuzzy-based output into a precise value is achieved through the process of defuzzification.
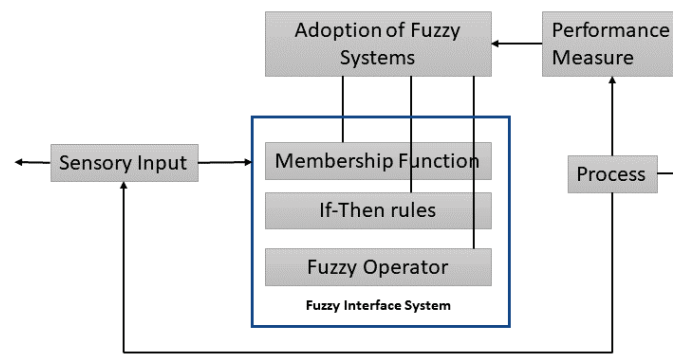
Figure 3. Schematic diagram of fuzzy logic.

The core principle of fuzzy inference revolves around elementary mapping strategies that use input data to produce output variables. Within fuzzy inference, the crucial utilization of if–then rules plays a central role and forms the basis for the decision-making process. Let the various objects denoted by "*x*" be represented by *X* and "*x*", forming a known pair for the fuzzy set "*A*".

$$A = \{(x, \mu_A(x) | x \in X\} \tag{10}$$

As depicted in Equation (10), the fuzzy membership function is defined by $\mu_A(x)$ for set *A*. The membership function $\mu_A(\cdot)$ maps *X* for membership space *M*, i.e., $\mu_A : X \to M$.

In the interval [0, 1] lies the membership values, which indicate the range of the membership function with a subset of non-negative real numbers. The fundamental problem in fuzzy logic is addressed through two types of functions, namely, trapezoidal and triangular. Equation (11) delineates the triangular membership function.

$$\text{Triangle}(x, p, q, r) = \begin{cases} 0, x < p \\ \frac{x-p}{q-p} & p \leq x \leq q \\ \frac{r-x}{r-q} & q \leq x \leq r \\ 0, r \leq X \end{cases} \tag{11}$$

By using the principle of maxima and minima above Equation (11) can be represented by Equation (12), respectively..

$$\text{Triangle}(x, p, q, r) = \max\left(\min\left\{\frac{x-p}{q-p}, \frac{r-x}{r-q}\right\}, 0\right) \tag{12}$$

Similarly, the given trapezoidal function can be explained by using the four parameters $\{p, q, r, s\}$, as represented Equation (13) below.

$$\text{Trapezoid}(x, p, q, r, s) = \begin{cases} 0, x < p \\ \frac{x-p}{q-p} & p \leq x \leq q \\ 1, q \leq x \leq r \\ \frac{s-x}{s-q} & r \leq x \leq s \\ 0, s \leq X \end{cases} \tag{13}$$

In the above equation, the value denoting x-coordinates is (p, q, r, s), which states that $p < q < r < s$. This is in the corners of the defuzzification–trapezoidal membership function.

Defuzzification is mathematically explained in the subsequent equation, which employs the center of sums. The center of sums is faster in comparison to other defuzzification techniques. It is given by the algebraic expression in Equation (14).

$$Z^* = \frac{\sum\limits_{i=1}^{n} \mu_i(z) \int (\bar{z}dz)}{\sum\limits_{i=1}^{n} \mu_i(z) \int (dz)} \tag{14}$$

where $\bar{z}$ is defined as the distance of the centroid of each relevant membership function, and i and μ_i reflect the area under the membership function.

3. Dragonfly–Fuzzy Hybrid Controller

The hybrid control system proposed in this study was designed by taking into account various parameters, including the distance between the vehicle and obstacles, the distance between the vehicle and the goal, and the relative distance between the vehicle and its motion. This controller effectively processes navigation parameters to determine the appropriate angle for autonomous vehicle movement. In the hybrid controller, the dragonfly algorithm (DA) controller takes precedence, receiving inputs such as front obstacle distance (FOD), left obstacle distance (LOD), and right obstacle distance (ROD) and producing the steep heading angle (SHA) as an output. The output of the DA controller and the current position of the vehicle (FOD, LOD, ROD) serve as inputs for the fuzzy logic controller. The overall architecture of the hybrid controller is illustrated in Figure 4.
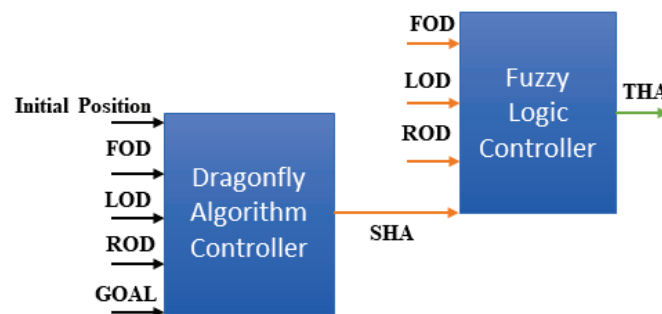
Figure 4. Dragonfly–fuzzy hybrid controller architecture.

In this study, the autonomous vehicle employs eight sensors distributed around its periphery to detect obstacles and determine the goal's position, enabling the calculation of key pointers such as front obstacle distance (FOD), left obstacle distance (LOD), and right obstacle distance (ROD). The hybrid controller integrates inputs from the DA controller and obstacle distances to generate the steep heading angle (SHA). The output from the DA controller is utilized to train the fuzzy logic controller, which, in turn, determines the total heading angle (THA), which is applicable to various environmental conditions.

The design incorporates an obstacle avoidance feature to prevent collisions with obstacles in the vehicle's environment. Emphasis is placed on positioning the food source in the global best position, ensuring it is kept as far away as possible from the nearest obstacle. This strategy aims to optimize the vehicle's trajectory and enhance obstacle avoidance capabilities. The Euclidean distance $(Dist)_{F-OB}$ between the global best position (food source) and the most immediate environmental obstacle is used to calculate the objective function, given by the Equation (15).

$$(Dist)_{F-OB} = \sqrt{(x_{OB} - x_{Fi})^2 + (y_{OB} - y_{Fi})^2} \tag{15}$$

where x_{Fi} and y_{Fi} are the best position, and x_{OB} and y_{OB} is the position of the closest obstacle. The Euclidean distance between the most relative obstacle and the vehicle is calculated using Equation (16).

$$(Dist)_{V-OB} = \sqrt{(x_{OB_n} - x_V)^2 + (y_{OB_n} - y_V)^2} \tag{16}$$

The best position for the dragonfly's food source should be as close to the goal as possible. The target-seeking objective function is defined as the Euclidean distance between the best position and the goal in the environment, given by Equation (17).

$$(Dist)_{F-G} = \sqrt{(x_G - x_{F_i})^2 + (y_G - y_{F_i})^2} \tag{17}$$

where x_G and y_G are the goal position, and $(Dist)_{F-G}$ is the minimum Euclidean distance from the vehicle to the position of the food source.

The equation defines the objective function of path optimization, which combines obstacle-seeking and target-seeking behavior.

$$\text{Objective Function}(f_1) = C_1 \frac{1}{\min_{OB_j} \in OB_d \|Dist_{F-OB_d}\|} + C_2 \|Dist_{F-G}\| \tag{18}$$

When the vehicle moves in an unstructured environment, it encounter different obstacles, known as $OB_d \in \{OB_1, OB_2, \ldots, OB_n\}$. In this objective function, it is clearly specified that when F_i comes closer to the goal, the $\|Dist_{F-G}\|$ value will decrease, and when F_i moves far away from the obstacles, the objective function value $\min_{OB_j} \in OB_d \|Dist_{F-OB_d}\|$ will be larger. The objective function incorporates parameters denoted as C_1 and C_2, which are recognized as fitting and controlling parameters, respectively, and it is evident that these parameters significantly impact the trajectory of the vehicle. When C_1 is excessively large, the robot tends to maintain a considerable distance from obstacles, whereas overly small values of C_1 may lead to collisions with objects in the surroundings. Similarly, a large value of C_2 inclines the robot towards a shorter and more optimal path to the target, whereas smaller values result in longer pathways. These control settings play a crucial role in expediting the convergence of the objective function and eliminating local minima. The determination of these control settings in this study involved a trial-and-error approach.

The dragonfly algorithm (DA) controller produces an output that serves as input for the fuzzy logic (FL) controller in the hybrid system. Following this, the FL controller refines the parameters from the DA controller, leading to the determination of the optimal values for the hybrid controller. Fuzzy logic, acknowledged for its universal approximation properties, demonstrates the ability to perform any nonlinear mapping between input sensor data and the central variable output. Linguistic expressions assigned to front obstacle distance (FOD), left obstacle distance (LOD), and right obstacle distance (ROD) encompass terms such as "too close", "very close", "close", "far", "very far", and "too far." Correspondingly, the heading angle utilizes linguistic terms such as "too wide", "moderately wide", "wide", "short", "moderately short", and "too short" as outputs. The membership functions employed for these linguistic terms are visually represented in Figure 5. Detailed illustrations of all fuzzy if–then rule mechanisms can be found in Tables 1 and 2.

Table 1. FL parameters for obstacles.

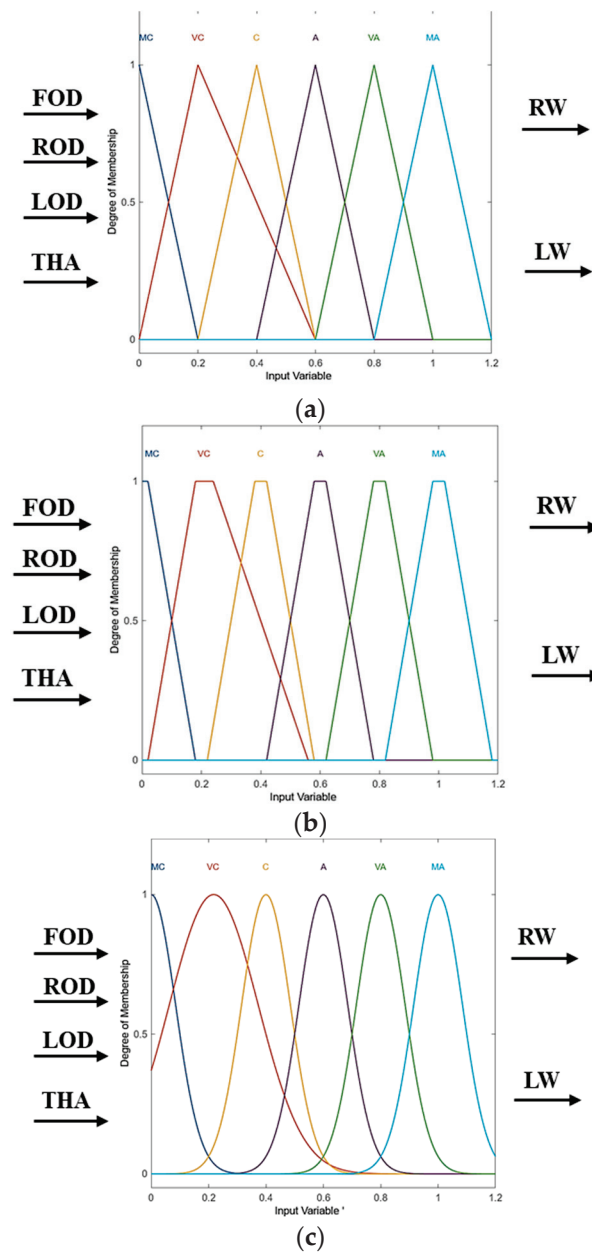| Linguistic Variable	Too Close (TC)	Very Close (VC)	Close (C)	Far (F)	Very Far (VF)	Too Far (TF)
LOD	0.0	0.2	0.4	0.6	0.8	1.0
ROD	0.2	0.4	0.6	0.8	1.0	1.2
FOD	0.4	0.6	0.8	1.0	1.2	0.0

(a)

(b)

(c)

Figure 5. Fuzzy logic membership functions: (**a**) triangular; (**b**) trapezoidal; (**c**) Gaussian.

Table 2. FL parameters for heading angle.

Linguistic Variable	Highly Negative (HN)	Negetive (N)	Zero (Z)	Positive (P)	Highly Postitive (HP)
	−180	−120	−10	10	60
Target heading angle (THA)	−120	−60	0.0	60	60
	−60	0	10	120	180

Selected fuzzy logic rules for robot navigation:

1. If the front obstacle distance (FOD) is negative (N), the left obstacle distance (LOD) is negative (N), and the right obstacle distance (ROD) is positive (F), then the heading angle (HA) is positive, the left velocity (LV) is slow, and the right velocity (RV) is fast.

2. If the FOD is medium (M), the LOD is negative (N), and the ROD is positive (F), then the HA is zero, the LV is medium, and the RV is medium.

3. If the FOD is positive (F), the LOD is negative (N), and the ROD is positive (F), then the HA is negative, the LV is fast, and the RV is slow.
4. If the FOD is negative (N), the LOD is medium (M), and the ROD is positive (F), then the HA is positive, the LV is slow, and the RV is fast.
5. If the FOD is medium (M), the LOD is medium (M), and the ROD is positive (F), then the HA is zero, the LV is medium, and the RV is medium.
6. If the FOD is positive (F), the LOD is medium (M), and the ROD is positive (F), then the HA is negative, the LV is fast, and the RV is slow.
7. If the FOD is negative (N), the LOD is negative (N), and the ROD is negative (N), then the HA is positive, the LV is slow, and the RV is fast.
8. If the FOD is medium (M), the LOD is negative (N), and the ROD is negative (N), then the HA is zero, the LV is medium, and the RV is medium.
9. If the FOD is positive (F), the LOD is negative (N), and the ROD is negative (N), then the HA is negative, the LV is Fast, and the RV is slow.
10. If the FOD is negative (N), the LOD is medium (M), and the ROD is negative (N), then the HA is positive, the LV is slow, and the RV is fast.

4. Experimental and Simulation Results

The presentation of both simulation and experimental outcomes is included herein to authenticate the suggested experimental controller. Utilizing the Fire Bird V robot in this trial, as depicted in Figure 6, enhanced the versatility of the experiment. The Fire Bird V is equipped with an ATMEGA2560 (AVR) microcontroller adaptor board, contributing to its adaptability.

Figure 6. Fire Bird V robot.

A simulation environment featuring obstacles was employed using the MATLAB R2021a simulation software to assess the efficiency of the suggested controller based on the dragonfly algorithm (DA). The evaluation focused on determining the optimality with respect to both the path length and the time needed for navigation. In order to identify the optimal parameters for the previously described objective function, systematic experiments were carried out involving the variation of multiple controlled parameters, as outlined in Table 3.

Table 3. Optimal tuning parameters for the DA-based controller.

Symbol	Description	Value
N	Dragonfly population size	30
T	Iteration count	350
s	Separation weight	0.1
a	Alignment weight	0.1
c	Cohesion weight	0.7
f	Food factor	1

Table 3. *Cont.*

Symbol	Description	Value
e	Enemy factor	1
w	Inertia weight	0.9–0.4
r_1, r_2	Random values	[0, 1]
C_1	Controlling parameter 1	1
C_2	Controlling parameter 2	1×10^{-6}

The computational time was analyzed across different population sizes for the dragonfly algorithm, providing insights into how the algorithm's performance scaled with the number of individuals in the population. Figure 7 illustrates that the computational time was particularly efficient with a population size of N = 30.
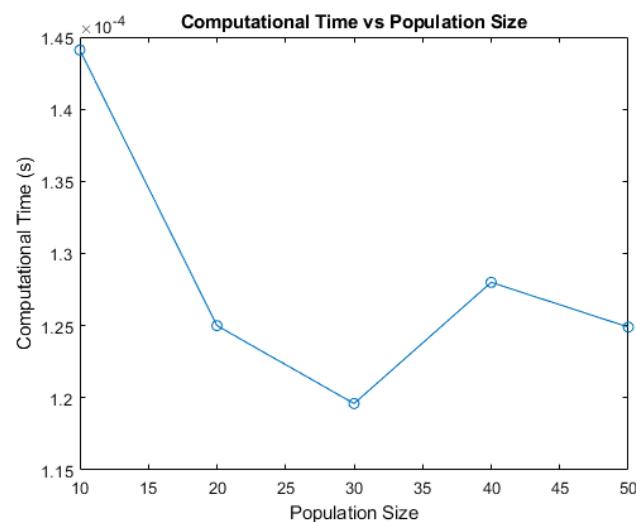
Figure 7. Population size analysis.

This study showcases the efficacy of our newly devised methodology under a range of environmental circumstances. We performed numerous experiments in settings characterized by static conditions and incorporated diverse obstacles. Utilizing the MATLAB R2021a software for simulation analysis provided us with the capability to tailor the environment by manipulating obstacle locations, robot placements, and objectives. In static scenarios, obstacles were stationary, which permitted modifications solely in the initial positions of the robot and the goal. Our software was configured to adapt to a varying number of robots and goals, thereby ensuring versatility in the experimental setups. The simulation results confirm that the three controllers (DA, FL, DA-FL) were used for navigation in the presence of obstacles represented by green blocks, and the outcome as a navigated path from a red circle representing the start position, while red square representing goal position are depicted in Figures 8–10. The path length and the time of the three controllers are shown in Table 4.

Table 4. Simulation path length and time of DA, FL, and DA–FL.

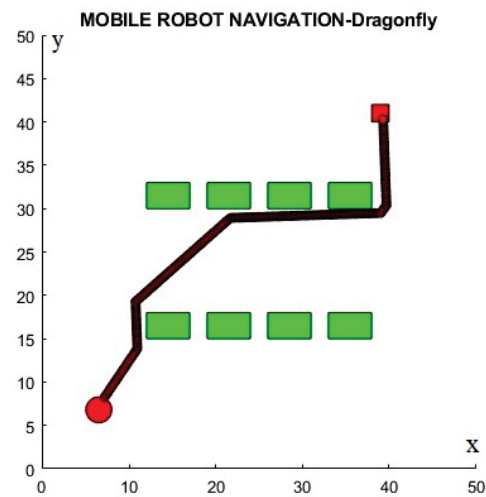| S. No.	Controller	Simulation Path Length (cm)	Simulation Path Time (seconds)
1	Dragonfly	120.4	11.8
2	Fuzzy logic	169.8	13.2
3	DA–FL hybrid	113.0	10.9

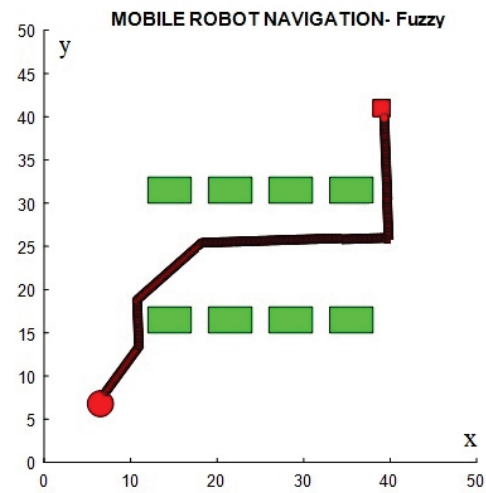**Figure 8.** Navigation using standalone DA.

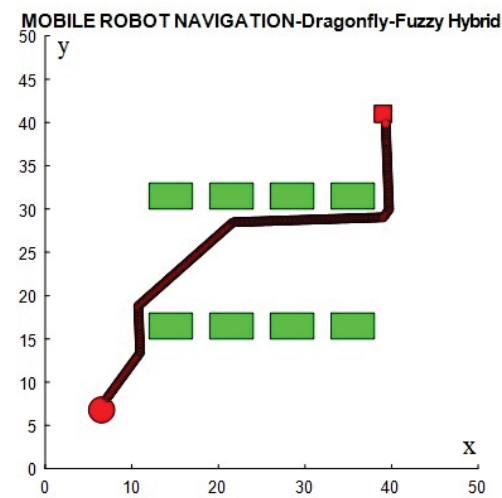**Figure 9.** Navigation using standalone FL.

Figure 10. Navigation using the DA–FL hybrid.

All three controllers (DA, FL, DA–FL) were experimentally run in a similar environment to validate the simulation results, as shown in Figure 11, where the movement is shown in four phases from 1–4 and the red dotted line is the path followed by the mobile

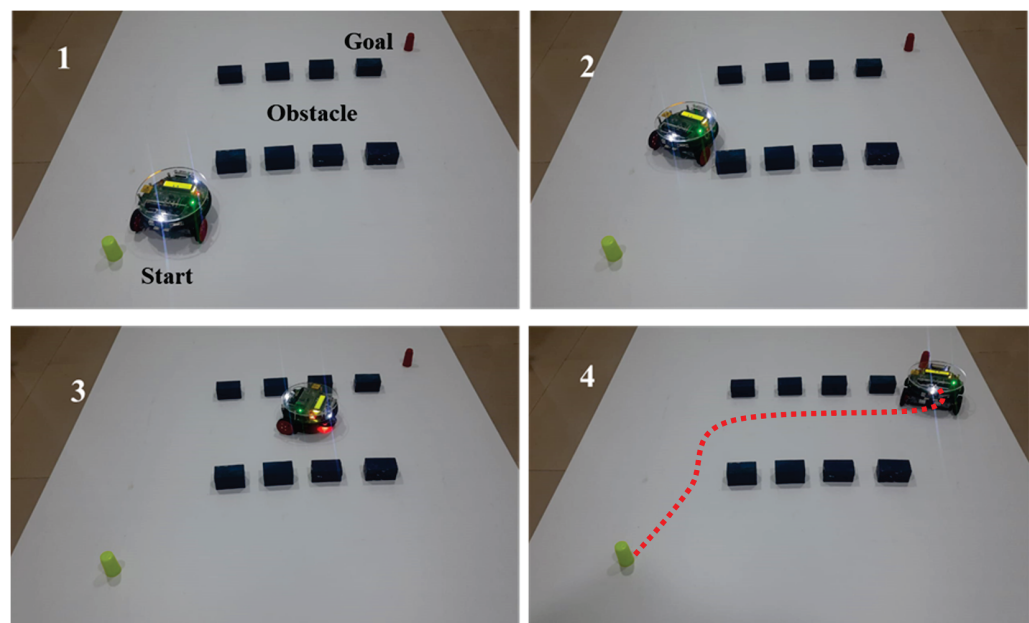robot. These experimental results are presented for the path length and navigation time, as shown in Table 5.

Figure 11. Experimental setup for mobile robot navigation of all controllers.

Table 5. Experimental path length and time of DA, FL, and DA–FL.

S. No.	Controller	Experimental Path Length (cm)	Experimental Path Time (seconds)
1	Dragonfly	126.22	12.6
2	Fuzzy logic	136.68	14
3	DA–FL hybrid	118.66	11.5

The proposed dragonfly–fuzzy hybrid controller was compared to existing standalone navigational controllers in the same environmental configuration configuration showcasing phase 4 (reached goal), as shown in Figure 12, to determine its success. Tables 6 and 7 compare the simulation and experimental results for all three controllers in terms of time and path length.
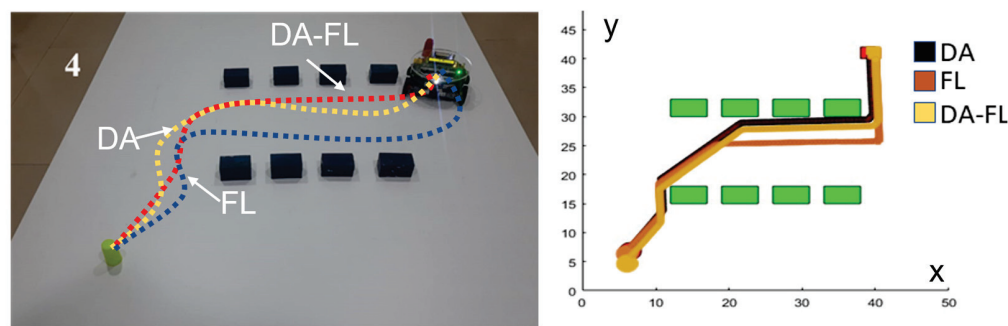
Figure 12. DA–FL hybrid controller versus another controller.

The performance evaluation of the proposed dragonfly–fuzzy controller was meticulously conducted through simulation analysis, enhancing the clarity and transparency in the comparison with two existing controllers under two distinct environmental setups. Figure 13a showcases Joshi and Zaveri's [43] neuro–fuzzy controller, whereas Figure 14a

depicts Patle et al.'s [44] firefly–fuzzy algorithm leveraged for mobile robot navigation in a simulated environment. Correspondingly, Figures 13b and 14b demonstrate that consistent environmental conditions were maintained and detail the number, dimensions, and positions of the obstacles, as well as the initial and final positions of the unmanned vehicle. These enhancements aim to provide comprehensive insight into the scenarios tested.

Table 6. Path length comparison of DA, FL, and DA–FL.

Controller	Experimental Path Length (cm)	Simulation Path Length (cm)	% Error
Dragonfly	126.3	120.4	4.58
Fuzzy logic	136.7	169.8	5.10
DA–FL hybrid	118.6	113.0	4.40

Table 7. Navigational time comparison of DA, FL, and DA–FL.

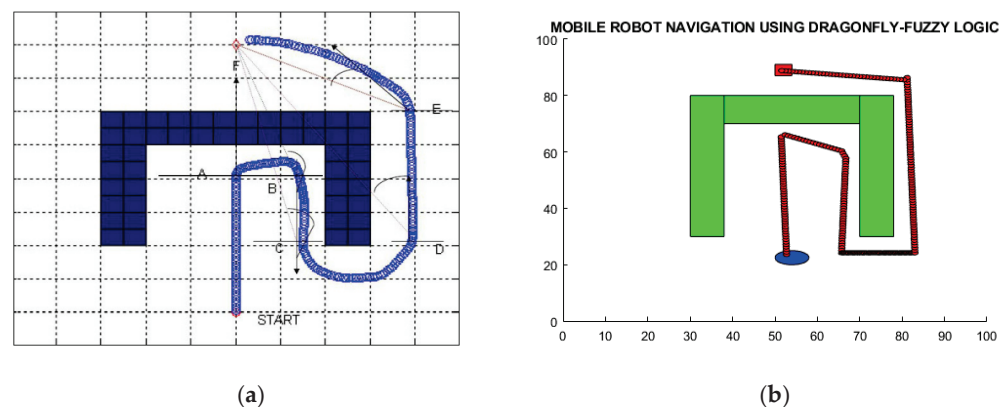| Controller	Experimental Path Time (s)	Simulation Path Time (s)	% Error
Dragonfly	12.6	11.8	5.80
Fuzzy logic	14	13.2	5.76
DA–FL hybrid	11.5	10.9	5.20

(**a**)　　　　　　　　　　　　　　　　(**b**)

Figure 13. Comparison of dragonfly–fuzzy algorithm with neuro–fuzzy algorithm: (**a**) neuro–fuzzy algorithm [43]; (**b**) dragonfly–fuzzy algorithm.
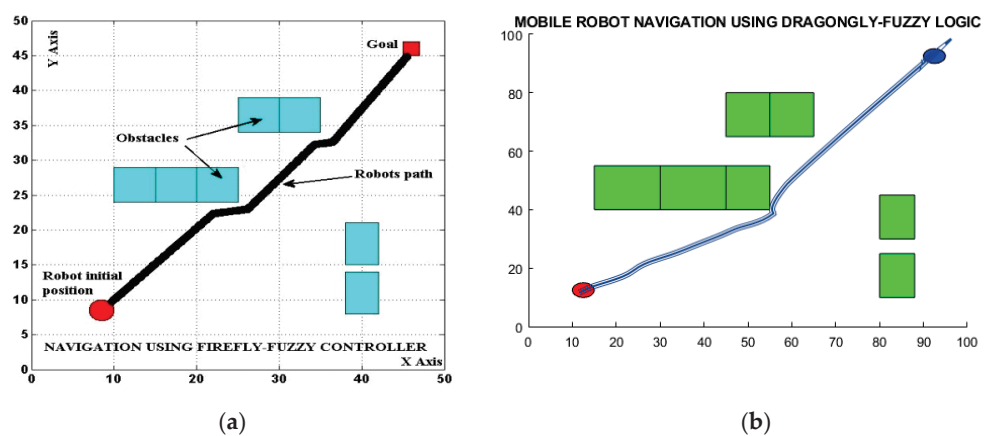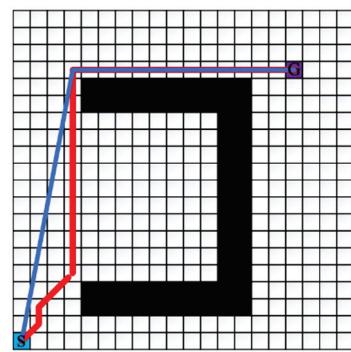

(**a**)　　　　　　　　　　　　　　　　(**b**)

Figure 14. Comparison of dragonfly–fuzzy algorithm with firefly–fuzzy algorithm: (**a**) firefly–fuzzy algorithm [44]; (**b**) dragonfly–fuzzy algorithm.

Upon comparing the performance, the dragonfly–fuzzy controller consistently outperformed both alternatives, achieving path savings of approximately 8.62% against the

neuro–fuzzy controller and of around 4.2% against the firefly–fuzzy controller, as detailed in Table 8. This underscores the dragonfly–fuzzy controller's superior path efficiency in simulated environments, ensuring optimized and effective navigation for unmanned vehicles. The results affirm its proficiency in discovering shorter and more efficient paths while adeptly avoiding unnecessary detours around obstacles. Notably, the controller's adaptive trajectory optimization for unmanned vehicles positions it as a promising and effective choice for path planning in mobile robot navigation scenarios. The provided systematic contrast analysis, incorporating environmental setups and detailed performance metrics, strengthens the validity and comprehensibility of the evaluation.

Table 8. Simulation results with other hybrid controllers.

Controller	Simulation Path Time (s)	Simulation Path Length (cm)	% Change Length with Dragonfly–Fuzzy	% Change Time with Dragonfly–Fuzzy
Dragonfly–fuzzy (Figure 13b)	20.8	143.0	----------	--------
Neurofuzzy logic (Figure 13a)	22.2	156.5	+8.62	+6.30
Dragonfly–fuzzy (Figure 14b)	15.3	113.05	----------	--------
Firefly–fuzzy (Figure 14a)	17.2	118.0	+4.2	+11.04
Dragonfly–fuzzy (Figure 15b)	16.3	126.0	----------	--------
A*–greedy (Figure 15a)	18.2	131.0	+3.9	+11.6
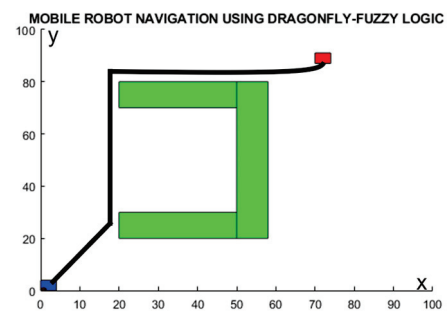
(**a**)   (**b**)

Figure 15. Comparison of A*–greedy algorithm with dragonfly–fuzzy algorithm: (**a**) A*–greedy algorithm [45]; (**b**) dragonfly–fuzzy algorithm.

In a comparative study conducted by Xiang et al. [45], the effectiveness of the dragonfly–fuzzy algorithm for mobile robot navigation was assessed against traditional A* and A*–greedy algorithms, as illustrated through the simulation depicted in Figure 15. The results of the comparison detailed in Table 8 reveal notable advantages of the dragonfly–fuzzy algorithm over the conventional A* algorithm. Specifically, it was observed that the dragonfly–fuzzy algorithm achieved a 3.6% reduction in path length compared to the traditional A* algorithm. Additionally, the computational time was significantly reduced, showcasing an 11% improvement. When compared to the A*–greedy algorithm, the

dragonfly–fuzzy algorithm demonstrated a similar path length with only minor variations, yet it exhibited significant savings in computational time. These findings underscore the efficiency and effectiveness of the dragonfly fuzzy algorithm in mobile robot navigation, making it a promising alternative for optimizing path planning and reducing computational overhead when compared to traditional A* and A*–greedy approaches.

5. Conclusions

Different standalone metaheuristic algorithms were investigated in this work to solve the navigational problem of an autonomous vehicle, and a new hybrid method was introduced. The proposed DA–FL controller was tested successfully against the standalone DA and FL controllers in a static obstacle environment. A set of experiments was performed to adjust the autonomous vehicle's parameters, which are directly connected to the smoothness of the generated path. The suggested technique allowed the autonomous vehicle to reach its destination while avoiding obstacles and following a significantly optimized path. Experimental and simulation findings demonstrate that the variation percentage was around 4% to 5% with the optimum path and time. When comparing the proposed hybrid controller and the standalone controller, it was found that the DA–FL hybrid controller took the shortest path and time. Also, the simulation was compared with other results by creating the same environment, and it was found that the dragonfly–fuzzy controller outperformed in terms of saving path length and time. In the future, the dragonfly–fuzzy controller can be implemented in a dynamic environment. It can be tested for navigation for underwater robots and aerial vehicles.

Author Contributions: Conceptualization and supervision, B.P. and S.B.; methodology and validation, B.P. and N.S.; software and investigation, V.D.; writing—original draft preparation, B.P. and V.D. All authors have read and agreed to the published version of the manuscript.

Institutional Review Board Statement: Not applicable.

Informed Consent Statement: Not applicable.

Data Availability Statement: The data presented in this study are available on request from the corresponding author. The data are not publicly available due to privacy.

Conflicts of Interest: The authors declare no conflicts of interest.

References

1. Oleari, F.; Magnani, M.; Ronzoni, D.; Sabattini, L. Industrial AGVs: Toward a pervasive diffusion in modern factory warehouses. In Proceedings of the 2014 IEEE 10th International Conference on Intelligent Computer Communication and Processing (ICCP), Cluj-Napoca, Romania, 4–6 September 2014; pp. 233–238.
2. Monios, J.; Bergqvist, R. Logistics and the networked society: A conceptual framework for smart network business models using electric autonomous vehicles (EAVs). *Technol. Forecast. Soc. Chang.* **2020**, *151*, 119824. [CrossRef]
3. Nakhaeinia, D.; Tang, S.H.; Noor, S.M.; Motlagh, O. A review of control architectures for autonomous navigation of mobile robots. *Int. J. Phys. Sci.* **2011**, *6*, 169–174.
4. Sudhakara, P.; Ganapathy, V.; Priyadharshini, B.; Sundaran, K. Obstacle avoidance and navigation planning of a wheeled mobile robot using amended artificial potential field method. *Procedia Comput. Sci.* **2018**, *133*, 998–1004. [CrossRef]
5. Yazici, A.; Kirlik, G.; Parlaktuna, O.; Sipahioglu, A. A dynamic path planning approach for multirobot sensor-based coverage considering energy constraints. *IEEE Trans. Cybern.* **2013**, *44*, 305–314. [CrossRef]
6. Patle, B.; Patel, B.; Jha, A. Rule-Based Fuzzy Decision Path Planning Approach for Mobile Robot. In Proceedings of the 2018 Fourth International Conference on Computing Communication Control and Automation (ICCUBEA), Pune, India, 16–18 August 2018; pp. 1–7.
7. Hart, P.E.; Nilsson, N.J.; Raphael, B. A formal basis for the heuristic determination of minimum cost paths. *IEEE Trans. Syst. Sci. Cybern.* **1968**, *4*, 100–107. [CrossRef]
8. Karaman, S.; Walter, M.R.; Perez, A.; Frazzoli, E.; Teller, S. Anytime motion planning using the RRT. In Proceedings of the 2011 IEEE International Conference on Robotics and Automation, Shanghai, China, 9–13 May 2011; pp. 1478–1483.

9. Hauer, F.; Tsiotras, P. Deformable Rapidly-Exploring Random Trees. In Proceedings of the Robotics: Science and Systems, Cambridge, MA, USA, 12–16 July 2017.

10. Kavraki, L.; Latombe, J. Probabilistic roadmaps for robot path planning. In *Pratical Motion Planning in Robotics: Current Aproaches and Future Challenges*; Wiley: Hoboken, NJ, USA, 1998; pp. 33–53.

11. Sun, Z.; Wu, J.; Yang, J.; Huang, Y.; Li, C.; Li, D. Path planning for GEO-UAV bistatic SAR using constrained adaptive multiobjective differential evolution. *IEEE Trans. Geosci. Remote Sens.* **2016**, *54*, 6444–6457. [CrossRef]

12. Dujari, R.; Patel, B.; Patle, B. Adaptive Mayfly Algorithm for UAV Path Planning and Obstacle Avoidance in Indoor Environment. In Proceedings of the 2023 International Conference on Network, Multimedia and Information Technology (NMITCON), Bengaluru, India, 1–2 September 2023; pp. 1–7.

13. Yi, X.; Zhu, A.; Yang, S. MPPTM: A Bio-Inspired Approach for Online Path Planning and High-Accuracy Tracking of UAVs. *Front. Neurorobot.* **2022**, *15*, 798428. [CrossRef] [PubMed]

14. Ganapathy, V.; Sudhakara, P.; Jie, T.J.; Parasuraman, S. Mobile robot navigation using amended ant colony optimization algorithm. *Indian J. Sci. Technol.* **2016**, *9*, 1–10. [CrossRef]

15. Xin, J.; Li, S.; Sheng, J.; Zhang, Y.; Cui, Y. Application of improved particle swarm optimization for navigation of unmanned surface vehicles. *Sensors* **2019**, *19*, 3096. [CrossRef] [PubMed]

16. Patel, B.; Patle, B. Analysis of firefly–fuzzy hybrid algorithm for navigation of quad-rotor unmanned aerial vehicle. *Inventions* **2020**, *5*, 48. [CrossRef]

17. Xing, B.; Gao, W.-J.; Xing, B.; Gao, W.-J. Fruit fly optimization algorithm. In *Innovative Computational Intelligence: A Rough Guide to 134 Clever Algorithms*; Springer: Cham, Switzerland, 2014; pp. 167–170.

18. Wang, G.-G.; Chu, H.E.; Mirjalili, S. Three-dimensional path planning for UCAV using an improved bat algorithm. *Aerosp. Sci. Technol.* **2016**, *49*, 231–238. [CrossRef]

19. Liu, J.; Wei, X.; Huang, H. An improved grey wolf optimization algorithm and its application in path planning. *IEEE Access* **2021**, *9*, 121944–121956. [CrossRef]

20. Meraihi, Y.; Gabis, A.B.; Mirjalili, S.; Ramdane-Cherif, A. Grasshopper optimization algorithm: Theory, variants, and applications. *IEEE Access* **2021**, *9*, 50001–50024. [CrossRef]

21. Guruji, A.K.; Agarwal, H.; Parsediya, D. Time-efficient A* algorithm for robot path planning. *Procedia Technol.* **2016**, *23*, 144–149. [CrossRef]

22. Antonelli, G.; Chiaverini, S.; Fusco, G. A fuzzy-logic-based approach for mobile robot path tracking. *IEEE Trans. Fuzzy Syst.* **2007**, *15*, 211–221. [CrossRef]

23. Dubey, V.; Barde, S.; Patel, B. Obstacle Finding and Path Planning of Unmanned Vehicle by Hybrid Techniques. In *Information Systems and Management Science, Proceedings of the 4th International Conference on Information Systems and Management Science (ISMS) 2021, Msida, Malta, 14–15 December 2021*; Springer: Cham, Switzerland, 2022; pp. 28–36.

24. Kanoon, Z.E.; Araji, A.; Abdullah, M.N. Enhancement of Cell Decomposition Path-Planning Algorithm for Autonomous Mobile Robot Based on an Intelligent Hybrid Optimization Method. *Int. J. Intell. Eng. Syst.* **2022**, *15*, 161–175.

25. Murofushi, T.; Sugeno, M. Fuzzy control of model car. *J. Robot. Soc. Jpn.* **1988**, *6*, 536–541. [CrossRef]

26. Langari, R. Past, present and future of fuzzy control: A case for application of fuzzy logic in hierarchical control. In Proceedings of the 18th International Conference of the North American Fuzzy Information Processing Society-NAFIPS (Cat. No. 99TH8397), New York, NY, USA, 10–12 June 1999; pp. 760–765.

27. Berisha, J.; Bajrami, X.; Shala, A.; Likaj, R. Application of Fuzzy Logic Controller for obstacle detection and avoidance on real autonomous mobile robot. In Proceedings of the 2016 5th Mediterranean Conference on Embedded Computing (MECO), Bar, Montenegro, 12–16 June 2016; pp. 200–205.

28. Fernando, T.; Gammulle, H.; Walgampaya, C. Fuzzy logic based mobile robot target tracking in dynamic hostile environment. In Proceedings of the 2015 IEEE International Conference on Computational Intelligence and Virtual Environments for Measurement Systems and Applications (CIVEMSA), Shenzhen, China, 12–14 June 2015; pp. 1–6.

29. Mirjalili, S. Dragonfly algorithm: A new meta-heuristic optimization technique for solving single-objective, discrete, and multi-objective problems. *Neural Comput. Appl.* **2016**, *27*, 1053–1073. [CrossRef]

30. Abdel-Basset, M.; Luo, Q.; Miao, F.; Zhou, Y. Solving 0–1 knapsack problems by binary dragonfly algorithm. In *Intelligent Computing Methodologies, Proceedings of the 13th International Conference, ICIC 2017, Liverpool, UK, 7–10 August 2017*; Proceedings, Part III 13; Springer: Cham, Switzerland, 2017; pp. 491–502.

31. Sawhney, R.; Jain, R. Modified binary dragonfly algorithm for feature selection in human papillomavirus-mediated disease treatment. In Proceedings of the 2018 International Conference on Communication, Computing and Internet of Things (IC3IoT), Chennai, India, 15–17 February 2018; pp. 91–95.

32. Mafarja, M.; Aljarah, I.; Heidari, A.A.; Faris, H.; Fournier-Viger, P.; Li, X.; Mirjalili, S. Binary dragonfly optimization for feature selection using time-varying transfer functions. *Knowl.-Based Syst.* **2018**, *161*, 185–204. [CrossRef]

33. Abuomar, L.; Al-Aubidy, K. Cooperative search and rescue with swarm of robots using binary dragonfly algoritlnn. In Proceedings of the 2018 15th International Multi-Conference on Systems, Signals & Devices (SSD), Yassmine Hammamet, Tunisia, 19–22 March 2018; pp. 653–659.

34. Sayed, G.I.; Tharwat, A.; Hassanien, A.E. Chaotic dragonfly algorithm: An improved metaheuristic algorithm for feature selection. *Appl. Intell.* **2019**, *49*, 188–205. [CrossRef]

35. Sambandam, R.K.; Jayaraman, S. Self-adaptive dragonfly based optimal thresholding for multilevel segmentation of digital images. *J. King Saud Univ.-Comput. Inf. Sci.* **2018**, *30*, 449–461. [CrossRef]
36. Ji, J.; Khajepour, A.; Melek, W.W.; Huang, Y. Path planning and tracking for vehicle collision avoidance based on model predictive control with multiconstraints. *IEEE Trans. Veh. Technol.* **2016**, *66*, 952–964. [CrossRef]
37. Viadero-Monasterio, F.; Nguyen, A.-T.; Lauber, J.; Boada, M.J.L.; Boada, B.L. Event-triggered robust path tracking control considering roll stability under network-induced delays for autonomous vehicles. *IEEE Trans. Intell. Transp. Syst.* **2023**. [CrossRef]
38. Xu, S.; Peng, H. Design, analysis, and experiments of preview path tracking control for autonomous vehicles. *IEEE Trans. Intell. Transp. Syst.* **2019**, *21*, 48–58. [CrossRef]
39. Hu, C.; Wang, R.; Yan, F.; Chen, N. Output constraint control on path following of four-wheel independently actuated autonomous ground vehicles. *IEEE Trans. Veh. Technol.* **2015**, *65*, 4033–4043. [CrossRef]
40. Chen, T.; Chen, L.; Xu, X.; Cai, Y.; Sun, X. Simultaneous path following and lateral stability control of 4WD-4WS autonomous electric vehicles with actuator saturation. *Adv. Eng. Softw.* **2019**, *128*, 46–54. [CrossRef]
41. Kennedy, J.; Eberhart, R. Particle swarm optimization. In Proceedings of the ICNN'95—International Conference on Neural Networks, Perth, WA, Australia, 27 November–1 December 1995; pp. 1942–1948.
42. Zadeh, L.A. Fuzzy sets. *Inf. Control* **1965**, *8*, 338–353. [CrossRef]
43. Joshi, M.M.; Zaveri, M.A. Reactive navigation of autonomous mobile robot using neuro-fuzzy system. *Int. J. Robot. Autom. (IJRA)* **2011**, *2*, 128.
44. Patle, B.; Patel, B.; Pandey, A.; Sahu, O.; Parhi, D. Analysis of Firefly-Fuzzy Hybrid Controller for Wheeled Mobile Robot. In Proceedings of the 2019 3rd International Conference on Computing and Communications Technologies (ICCCT), Chennai, India, 21–22 February 2019; pp. 187–194.
45. Xiang, D.; Lin, H.; Ouyang, J.; Huang, D. Combined improved A* and greedy algorithm for path planning of multi-objective mobile robot. *Sci. Rep.* **2022**, *12*, 13273. [CrossRef] [PubMed]